

DEVELOPMENT OF STRUCTURALLY AND ELECTRONICALLY VERSATILE AMINOPYRIDINE COBALT COMPLEXES FOR PHOTO-(ELECTRO)REDUCTION OF WATER AND KETONES

Arnau Call Quintana

Per citar o enllaçar aquest document:

Para citar o enlazar este documento:

Use this url to cite or link to this publication:

<http://hdl.handle.net/10803/674245>

ADVERTIMENT. L'accés als continguts d'aquesta tesi doctoral i la seva utilització ha de respectar els drets de la persona autora. Pot ser utilitzada per a consulta o estudi personal, així com en activitats o materials d'investigació i docència en els termes establerts a l'art. 32 del Text Refós de la Llei de Propietat Intel·lectual (RDL 1/1996). Per altres utilitzacions es requereix l'autorització prèvia i expressa de la persona autora. En qualsevol cas, en la utilització dels seus continguts caldrà indicar de forma clara el nom i cognoms de la persona autora i el títol de la tesi doctoral. No s'autoritza la seva reproducció o altres formes d'explotació efectuades amb finalitats de lucre ni la seva comunicació pública des d'un lloc aliè al servei TDX. Tampoc s'autoritza la presentació del seu contingut en una finestra o marc aliè a TDX (framing). Aquesta reserva de drets afecta tant als continguts de la tesi com als seus resums i índexs.

ADVERTENCIA. El acceso a los contenidos de esta tesis doctoral y su utilización debe respetar los derechos de la persona autora. Puede ser utilizada para consulta o estudio personal, así como en actividades o materiales de investigación y docencia en los términos establecidos en el art. 32 del Texto Refundido de la Ley de Propiedad Intelectual (RDL 1/1996). Para otros usos se requiere la autorización previa y expresa de la persona autora. En cualquier caso, en la utilización de sus contenidos se deberá indicar de forma clara el nombre y apellidos de la persona autora y el título de la tesis doctoral. No se autoriza su reproducción u otras formas de explotación efectuadas con fines lucrativos ni su comunicación pública desde un sitio ajeno al servicio TDR. Tampoco se autoriza la presentación de su contenido en una ventana o marco ajeno a TDR (framing). Esta reserva de derechos afecta tanto al contenido de la tesis como a sus resúmenes e índices.

WARNING. Access to the contents of this doctoral thesis and its use must respect the rights of the author. It can be used for reference or private study, as well as research and learning activities or materials in the terms established by the 32nd article of the Spanish Consolidated Copyright Act (RDL 1/1996). Express and previous authorization of the author is required for any other uses. In any case, when using its content, full name of the author and title of the thesis must be clearly indicated. Reproduction or other forms of for profit use or public communication from outside TDX service is not allowed. Presentation of its content in a window or frame external to TDX (framing) is not authorized either. These rights affect both the content of the thesis and its abstracts and indexes.



DOCTORAL THESIS

Development of Structurally and
Electronically Versatile Aminopyridine
Cobalt Complexes for Photo-
(Electro)reduction of Water and Ketones

Arnau Call Quintana

2016

Doctoral Programme in Experimental Sciences and Sustainability

Supervised by: Dr. Julio Lloret Fillol and Dr. Miquel Costas
Salgueiro

Tutor: Miquel Costas Salgueiro

Presented in partial fulfilment of the requirements for a doctoral
degree from University of Girona



Dr. Julio Lloret Fillol, of Institut Català d'Investigació Química and Dr. Miquel Costas Salgueiro, of Universitat de Girona,

WE DECLARE

That the thesis entitled “Development of Structurally and Electronically Versatile Aminopyridine Cobalt Complexes for Photo-(Electro)reduction of Water and Ketones”, presented by Arnau Call Quintana to obtain a doctoral degree, has been completed under our supervision and meets the requirements to opt for an International Doctorate

For all intents and purposes, we hereby sign this document.

Dr. Julio Lloret Fillol

Dr. Miquel Costas Salgueiro

Girona, November 11th, 2016

Dedicat a la meva família i amics

A la Marina

*Science, my lad, has been built upon
many errors; but they are errors which
it was good to fall into, for they led to the truth*

Jules Verne (1864)

*I am among those who think that science has great beauty. A scientist in his
laboratory is not only a technician: he is also a child placed before natural
phenomena which impress him like a fairy tale. We should not allow it to be
believed that all scientific progress can be reduced to mechanisms, machines,
gearings, even though such machinery has its own beauty*

Marie Curie (1933)

List of Publications

Photo and Electrocatalytic H₂ production by new first-row transition metal complexes based on an Aminopyridine Pentadentate Ligand. Call, A.; Codolà, Z.; Acuña-Parés, F.; Lloret-Fillol, J. *Chem. Eur. J.* **2014**, *20*, 6171.

Influence of the Electronic Effects on the H₂ Evolution Catalyzed by Cobalt Complexes Based on N-tetradentate Pytacn type ligands. Call, A.; Fernández, S.; Lloret-Fillol, J. *In preparation*

Improved Activity and Stability of a Cobalt Reduction Catalyst by Supramolecular Confinement in Streptavidin. Call, A.; Ghirlanda, G.; Lloret-Fillol, J. *In preparation*

Synthesis, Characterization and Reactivity of Cobalt Intermediates in Low-Oxidation State. Call, A.; Casadevall, C.; Martin, V.; Lloret-Fillol, J. *In preparation*

Cobalt Complexes Catalyzed Light-Driven Reduction of Ketones and Aldehydes Using Water and Et₃N as Source of Hydride. Call, A.; Acuña-Parés, F.; Lloret-Fillol, J. *Submitted*

Influence of the Electronic Effects in Cobalt Catalysts on Photocatalytic Ketone Reduction. Call, A.; Lloret-Fillol, J. *In preparation*

Mechanistic Studies on Photochemical Reduction of Ketones Catalyzed by Cobalt Complexes. Call, A.; Lloret-Fillol, J. *In preparation*

The candidate has also contributed in the following publication but it is not included in the thesis:

Catalizadores para la conversión de la energía solar en enlaces químicos. Casadevall, C.; Call, A.; Codolà, Z.; Acuña-Pares, F.; Lloret-Fillol, J. *An. Quím.* **2016**, *112*, 133.

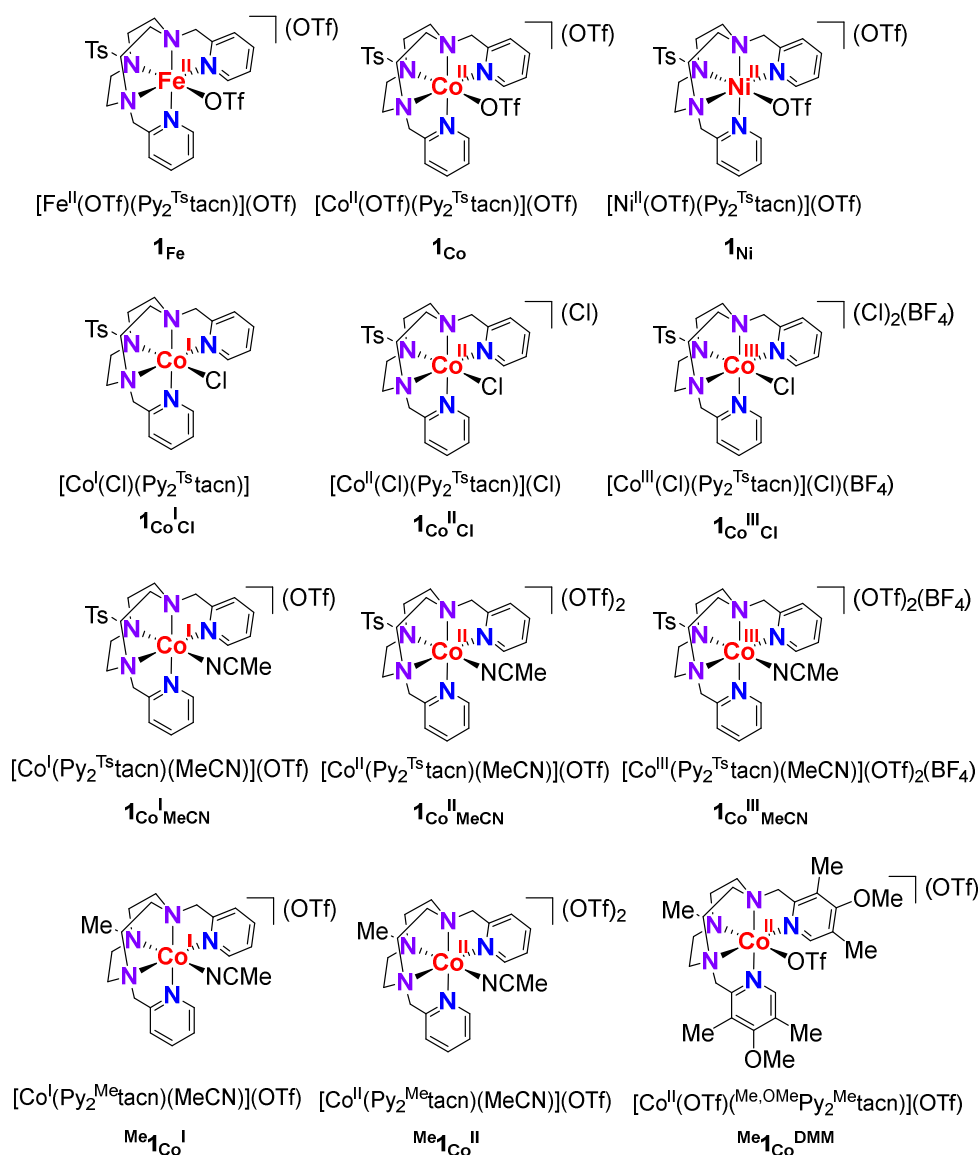
Glossary of Abbreviations

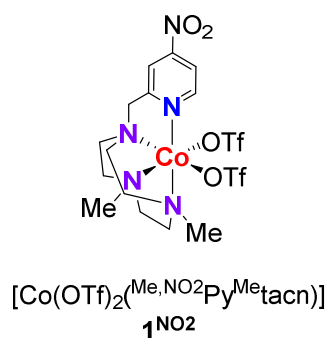
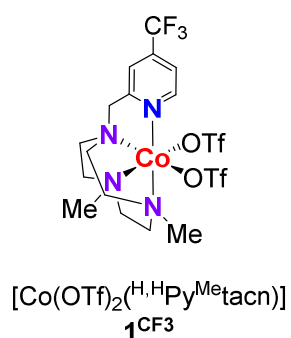
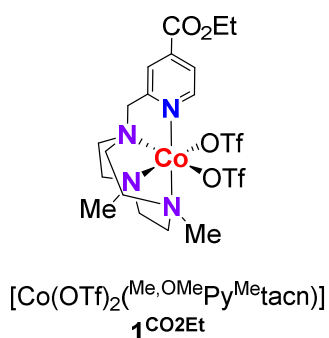
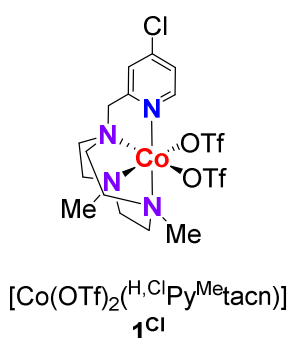
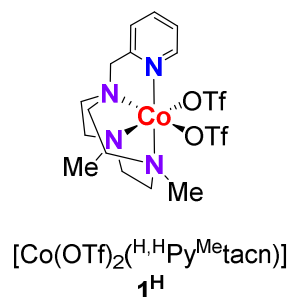
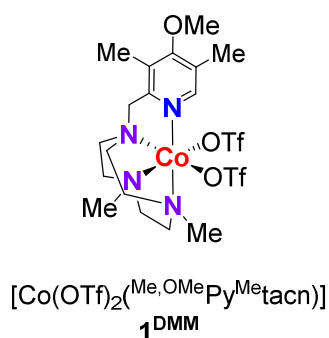
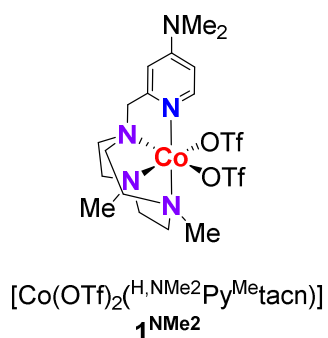
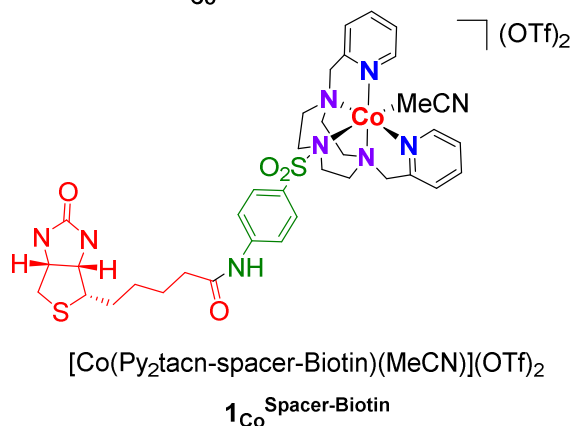
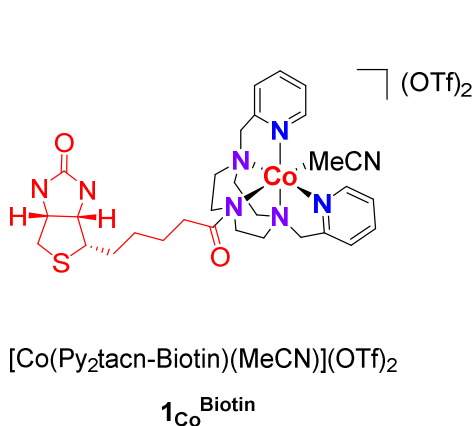
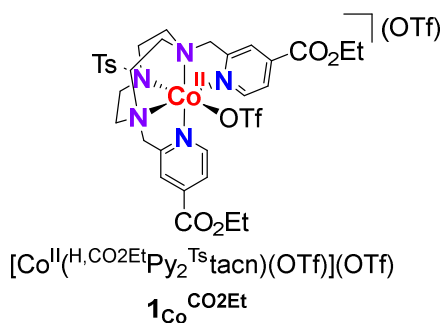
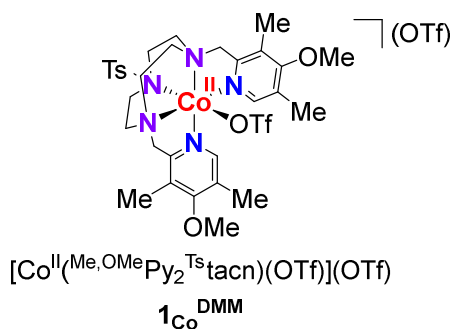
Å: Angstrom
AcOEt: Ethyl acetate
aq: Aqueous
cal: Caloria
cat: Catalyst
bpy: 2,2'-bipyridine
CD: Circular dichroism
Cp: Cyclopentadienyl
Cp*: Pentamethylcyclopentadienyl
CV: Cyclic voltammetry
δ: Chemical shift
DFT: Density functional theory
DLS: Dynamic Light Scattering
DMF: Dimethyl formamide
E_{1/2}: Thermodynamic potential
eq: Equivalent
EB: Erythrosin B photosensitizer
EPR: Electron paramagnetic resonance
ESI-MS: Electrospray Ionization Mass Spectroscopy
Et₂O: Diethylether
eV: Electronvolt
EXAFS: Extended X-Ray Adsorption Fine Structure
FT-IR: (Fourier Transform) Infrared spectroscopy
GC: Gas chromatography
K: Kelvin
Kcal: Kilocalorie
KIE: Kinetic isotope effect
HABA: 2-(4'-hydroxyazobenzene)benzoic acid
HAT: Hydrogen atom transfer
HM: Heterolytic mechanism
HR-ESI-MS: High-resolution electrospray ionization mass spectrometry
ICP: Inductively coupled plasma
J: Joule
Kg: Kilogram
KIE: Kinetic isotopic effect
KRA: Ketyl radical anion
KIE: Kinetic isotopic effect
L: Liter
LED: Light emitting diode
LLCT: Ligand-to-ligand charge transfer
L-XTA: Laser - X-ray Transient Absorption Spectroscopy
M: Molar

MeCN: Acetonitrile
MeOH: Methanol
MJ: Mega joules= 10^6 joules= 10^6 W/s
MLCT: Metal-to-ligand charge transfer
Mol: Mole
MS: Mass spectrometry
NMR: Nuclear Magnetic Resonance
NP: Nanoparticles
N4Py: *N,N'*-bis(2-pyridylmethyl)-*N*-(bis-2-pyridylmethyl)amine
NTA: Nanoparticle Tracking Analysis
 η : Overpotential
ORTEP: Oak Ridge Thermal Ellipsoid Plot Program
OTf: Trifluoromethanesulfonate anion
P: Pressure
PCET: Proton-coupled electron transfer
PDP: *N,N'*-bis(2-pyridylmethyl)2,2'-bypyrrolidine
Ph: Phenyl group
PPh₃: Triphenyl phosphine
ppm: Part per million
PSI: Photosystem I
PSII: Photosystem II
PS_{Cu}: [Cu(Bathocuproine)(Xantphos)]PF₆ photosensitizer
PS_{Ir}: [Ir^{III}(ppy)₂(bpy)]PF₆ photosensitizer
PS_{Ru}: [Ru(bpy)₃]²⁺ photosensitizer
ppy: 2-phenylpyridine
PS: Photosensitizer
Py: Pyridine
rds: Rate-determining step
RNILs: Redox non-innocent ligands
RT: Room temperature, 298 K
SA: Streptavidin
SET: Single electron transfer
SCE: Saturated Calomel Electrode
SDKIE: Secondary Deuterium Kinetic Isotopic Effect
tacn: 1,4,7-triazacycononane
Ts: Tosyl moiety
TCD: Thermal conductivity detector
TEMPO: 2,2,6,6-tetramethyl-1-piperidinyloxy free radical
TEOA: Triethanolamine
TFA: Trifluoroacetic acid
THF: Tetrahydrofuran
TOF: Turnover frequency (TON·h⁻¹)
TON: Turnover number, (number the molecules of H₂ produced)/(number of molecules of catalyst used)

TPA: Tris(2-pyridylmethyl)amine
 TS: Transition state
 UV/Vis: Ultraviolet-visible spectroscopy
 V: Volt
 VT-¹H-NMR: ¹H-NMR at varied temperatures
 WO: Water oxidation
 WR: Water reduction
 WS: Water splitting
 XANES: X-ray absorption near edge structure
 XAS: X-ray absorption spectroscopy

Structures and abbreviations of the catalysts employed in this thesis





List of Figures

CHAPTER I

- Figure I. 1.** Structure of the active centers of the dinuclear and mononuclear hydrogenases. . 11
- Figure I. 2.** Selected biomimetic iron complexes used in proton reduction. 12
- Figure I. 3.** Selected NiFe biomimetic systems 13
- Figure I. 4.** Evolution of H₂ oxidation and production catalysts containing amine pendant arms. 14
- Figure I. 5.** Left: Selected nickel thiolene complexes. Right: Proposed mechanism of hydrogen formation by thiolene complexes. 15
- Figure I. 6.** Selected Ni complexes for H₂ production containing nitrogen ligands. 16
- Figure I. 7.** Selected cobalt macrocyclic platforms for H₂ evolution. 18
- Figure I. 8.** Selected cobalt polypyridyl catalysts for H₂ evolution. 21
- Figure I. 9.** Selected cobalt catalysts based on aminopyridine ligands for H₂ evolution. 23
- Figure I. 10.** Structures of some selected cobalt dithiolene catalysts. 23
- Figure I. 11.** Homolytic and heterolytic mechanisms for H₂ evolution catalyzed by molecular cobalt complexes. The electrons can be provided by a photoredox catalyst or from an electrode. 24
- Figure I. 12.** Artificial hydrogenases based on diiron-complexes and a peptide chain. A) Synthetic α -helical peptide containing [Fe₂(CO)₆] developed by Ghirlanda and co-workers. B) Proposed mechanism for proton reduction catalyzed by H-apocyt c containing the iron carbonyl cluster. Reprinted with permission from ref 169 Copyright 2011 Royal Society of Chemistry. C) Scheme of the photocatalytic reduction reaction of protons by [FeFe][Ru]Pep-18 in aqueous media. Reprinted with permission from ref 171. Copyright 2012 Elsevier..... 27
- Figure I. 13.** The modified hydrogen evolving complex (μ -S)₂Fe₂(CO)₆ reacts with a cysteine residue located inside of the protein nitrobindin cavity. B) Structure of SwMb-cobaloxime computed at the QC-MM level. C) Photocatalytic H₂ production scheme in Ru-Fd-Co biohybrids with two possible pathways for electron transfer from PS to catalyst. Reprinted with permission from (A) ref 172, (B) ref 173 and (C) ref 179. Copyright 2014 American Chemical Society..... 28
- Figure I. 14.** Biocatalytic systems for H₂ evolution based on cobalt. A) Synthetic CoMyo system developed by Ghirlanda and co-workers. Reprinted with permission from ref 184. Copyright 2014 Royal Society of Chemistry. B) Structure of the synthetic CoMP11-Ac system. C) Biocatalytic system Ht-CoM61A developed by Bren and co-workers. Reprinted with permission from ref 187. Copyright 2016 American Chemical Society. 32
- Figure I. 15.** Photocatalytic reduction of water to hydrogen and alkenes catalyzed by B₁₂-TiO₂ hybrid system. 44

CHAPTER II

- Figure II. 1.** Promising first-row transition metal complexes based on penta and tetradentate aminopyridine ligands for catalytic proton reduction to H₂. 49
- Figure II. 2.** General selected cobalt biotinylated complexes for the construction of cobalt metalloenzymes. 50
- Figure II. 3.** Reduction of ketones using aminopyridine cobalt complexes. 51

CHAPTER III

- Figure III. 1.** $^1\text{H-NMR}$ (CD_3CN , 400 MHz, 300 K) spectrum of **1_{Fe}**, **1_{Co}** and **1_{Ni}**. 58
- Figure III.2.** ORTEP structures with ellipsoids set at the 50% probability level of **1_{Co}** (Left) and **1_{Ni}** (Right) from the X-ray diffraction analysis. Hydrogen atoms have been omitted for clarity. 59
- Figure III. 3.** UV/Vis absorption spectra of **1_{Fe}** (0.1 mM, Blue), **1_{Co}** (0.1 mM, red) and **1_{Ni}** (0.1 mM, green) in MeCN at 298 K. 60
- Figure III. 4.** Left: On-line time dependent traces of photochemical H_2 generated (TON) by **1_{Co}** (50 μM , red), **1_{Fe}** (50 μM , orange), **1_{Ni}** (50 μM , blue) and $[\text{Co}(\text{OTf})_2(\text{MeCN})_2]$ (50 μM , green) with **PS_{Ir}** (250 μM) in $\text{CH}_3\text{CN}:\text{H}_2\text{O}:\text{Et}_3\text{N}$ (3:7:0.2 mL) solvent mixture, irradiated at 447 nm, under N_2 . Right: On-line time dependent traces of photochemical H_2 generated (TON) by **1_{Co}** (50 μM) with **PS_{Ir}** (250 μM , blue), **PS_{Ru}** (250 μM , red) or **PS_{EB}** (250 μM , green) in $\text{CH}_3\text{CN}:\text{H}_2\text{O}:\text{Et}_3\text{N}$ (2:8:0.2 mL) solvent mixture, irradiated at 447 nm, under N_2 62
- Figure III.5.** Study of the effect of solvent mixture, $[\text{Et}_3\text{N}]$, $[\text{PS}_{\text{Ir}}]$ and $[\mathbf{1}_{\text{Co}}]$ in the photocatalytic H_2 formation by **1_{Co}**. Top left: effect of $\text{Et}_3\text{N}\%$ v/v in the solvent mixture, $\text{CH}_3\text{CN}/\text{H}_2\text{O}$ (2:8 mL), **1_{Co}** (50 μM) and **PS_{Ir}** (250 μM). Top right: effect of the $\text{CH}_3\text{CN}/\text{H}_2\text{O}$ solvent mixture (total volume 10 mL), Et_3N (0.2 mL), **1_{Co}** (50 μM), **PS_{Ir}** (250 μM). Bottom left: $\text{TON}_{\mathbf{1}_{\text{Co}}}$ and TON_{PS} as a function of $[\text{PS}_{\text{Ir}}]$ in $\text{CH}_3\text{CN}/\text{H}_2\text{O}/\text{Et}_3\text{N}$ (2:8:0.2 mL), **1_{Co}** (50 μM). Bottom right: $\text{TON}_{\mathbf{1}_{\text{Co}}}$ and TON_{PS} as a function of $[\mathbf{1}_{\text{Co}}]$, $\text{CH}_3\text{CN}/\text{H}_2\text{O}/\text{Et}_3\text{N}$ (2:8:0.2 mL), **PS_{Ir}** (100 μM). $\text{TON}_{\text{cat}}=n_{\text{H}_2}/n_{\text{cat}}$, $\text{TON}_{\text{PS}}=n_{\text{H}_2}/n_{\text{PSIr}}$ 63
- Figure III.6.** Plots of on-line pressure monitored versus time for reactions using $\text{CH}_3\text{CN}/\text{H}_2\text{O}/\text{Et}_3\text{N}$ (2:8:0.2) as solvent mixture under irradiation at $\lambda=447$ nm. Top: **PS_{Ir}** (100 μM) and $[\mathbf{1}_{\text{Co}}]$ from 5 μM to 100 μM . Inset: double-ln plot of initial H_2 evolution rates versus $[\mathbf{1}_{\text{Co}}]$. Bottom: **1_{Co}** (50 μM) and $[\text{PS}_{\text{Ir}}]$ from 25 μM to 125 μM . Inset: double-ln plot of initial H_2 evolution rates versus $[\text{PS}_{\text{Ir}}]$ 64
- Figure III. 7.** Photochemical H_2 production experiments after a 1st H_2 photogeneration run. 1st run (from $t=0$ to 2h, blue dark line) **1_{Co}** (50 μM) and **PS_{Ir}** (250 μM) in $\text{MeCN}:\text{H}_2\text{O}:\text{Et}_3\text{N}$ (3:7:0.2 mL). $t=2-5$ h, red line) H_2 produced after addition of an extra **1_{Co}** (50 μM) and **PS_{Ir}** (250 μM) at $t=2$ h. $t=2-5$ h, blue pale line). H_2 produced after addition of an extra **1_{Co}** (50 μM) and **PS_{Ir}** (250 μM) and Et_3N (0.2 mL) at $t=2$ h. 65
- Figure III. 8.** Photocatalytic H_2 production under inert conditions (blue curve) and in the presence of 21 % of O_2 . Reaction conditions: **1_{Co}** (50 μM) and **PS_{Ir}**, (250 μM) in $\text{MeCN}:\text{H}_2\text{O}:\text{Et}_3\text{N}$ (3:7:0.2 mL) solvent mixture irradiated at $\lambda=447$ nm. 66
- Figure III.9.** UV/Vis monitoring of **PS_{Ir}^{III}** (0.1 mM) reductive quenching with Et_3N (1000 eq.) to form **PS_{Ir}^{II}** at $\lambda=447$ nm, and subsequent addition of one equivalent of **1_{Fe}**, **1_{Co}** or **1_{Ni}** in anhydrous CH_3CN at -20°C , under N_2 atmosphere. 67
- Figure III.10.** Top: UV/Vis monitoring of the reductive quenching of **PS_{Ir}^{II}** species generated by irradiating at $\lambda=447$ nm, upon addition of one equivalent of **1_{Fe}**, **1_{Co}** and **1_{Ni}**. Conditions: $[\text{PS}_{\text{Ir}}]=0.1$ mM, $\text{Et}_3\text{N}=1000$ eq., reaction volume= 2 mL, $\text{CH}_3\text{CN}/\text{H}_2\text{O}$ (0.6:1.4) at 25°C . Bottom: Time-dependent photocatalytic H_2 evolution activities measured in the UV/Vis cell upon addition of one equivalent of **1_{Fe}** (green triangles), **1_{Co}** (red diamonds) and **1_{Ni}** (blue squares). Inset: Magnification in the case of **1_{Co}**. 68
- Figure III. 11.** Number of nanoparticles distribution after different irradiation times: before irradiation (black line), 5 min (drack-blue line), 30 min (light-blue line), 1 h (purple line), 2 h (red line) and 3 h (brown line). Conditions: Left) **1_{Co}** (50 μM), **PS_{Ir}** (200 μM), $\text{CH}_3\text{CN}:\text{H}_2\text{O}:\text{Et}_3\text{N}$ (5:5:0.2 mL) as solvent mixture irradiated at 447 nm. Right) **1_{Co}** (500 μM), **PS_{Ir}** (200 μM), $\text{CH}_3\text{CN}:\text{H}_2\text{O}:\text{Et}_3\text{N}$ (5:5:0.2 mL) as solvent mixture irradiated at 447 nm..... 69
- Figure III. 12.** Hg^0 poisoning experiments. Effect of the addition of Hg^0 to photochemical H_2 production carried out using **1_{Co}** (50 μM), **PS_{Ir}** (250 μM), Et_3N (2% v/v) and irradiated at 447 nm

in CH₃CN:H₂O (3:7 mL). *Left*) Reactions: without Hg⁰ (green dots), with the presence of 1000 eq. of Hg⁰ (Orange dots) and with the presence of 1.5 mL (15% of the total volume of the reaction) of Hg⁰ (blue dots) from the 5 min before irradiation. Bars represent the errors (usually below 10%) of reactions in triplicate. *Right*) Reactions: without Hg⁰ (blue dots) and with the addition of 0.5 mL Hg⁰ after t = 0.23 h and t = 0.37 h (red dots) from the beginning of irradiation..... 71

Figure III. 13. CVs of **1_{Fe}**, **1_{Co}** and **1_{Ni}**. Experimental conditions: Bu₄NPF₆ (0.1 M) as supporting electrolyte in acetonitrile, using a glassy carbon as working and SCE as reference electrodes. Scan rate of 100 mV·s⁻¹. 71

Figure III.14. Successive CVs of **1_{Fe}** (top), **1_{Co}** (middle) and **1_{Ni}** (bottom) (1 mM) in acetonitrile containing Bu₄NPF₆ (0.1 M) in the presence of TFA (0–60 mM). Scan rate=100 mV·s⁻¹, glassy carbon as working electrode. Insets: *i*_{cat}/*i*_p versus [TFA]..... 73

Figure III.15. *i*_{cat}/*i*_p ratio as a function of the [TFA] in a 1 mM concentration solution of **1_{Fe}**, **1_{Co}** or **1_{Ni}**. Scan rate=100 mV·s⁻¹. Glassy carbon working electrode and SCE as reference. *i*_{cat}/*i*_p values were measured at the M^{II/I} redox potential. 74

Figure III. 16. Cyclic voltammetry in acetonitrile using 0.1 M Bu₄NPF₆ as supporting electrolyte at scan rate of 100 mV/s using a glassy carbon working electrode: a) of **1_{Co}** (1 mM) and TFA (100 mM, red) and b) after CV after (a) without **1_{Co}** but under the same condition using the same glassy carbon working electrode without polishing. 74

Figure III. 17. Top: plots of *i*_{cat}/*i*_p versus [TFA] for a 1 mM solution of **1_{Co}** at different scan rates. Bottom: Plot of the *i*_{cat}/*i*_p slopes at different scan rates versus [TFA] as function of the v^{-1/2}.... 75

Figure III. 18. Successive cyclic voltammograms of **1_{Co}** (1 mM) in acetonitrile containing Bu₄NPF₆ (0.1 M) in the presence of acid: TFA (blue: 0 mM, red: 1 mM, green: 3 mM, purple: 10 mM, black: 20 mM, orange: 40 mM and grey: 60 mM), measured at different scan rates (50, 100, 200, 300, 400 and 500 mV/s). Glassy carbon electrode and SCE electrodes were used as working and reference electrodes, respectively..... 76

Figure III. 19. Successive CVs at increasing [**1_{Co}**]. Conditions: [TFA]=100 mM, Supporting electrolyte: Bu₄NPF₆ (0.1 M), scan rate=100 mV·s⁻¹, Glassy Carbon working electrode. Inset: Electrocatalytic current versus [**1_{Co}**] (0.1–0.8 mM) showing a first order kinetics. 77

Figure III. 20. Successive CVs of **1_{Co}** (1 mM) in water containing KNO₃ (0.1 M) and TFA acid: from bottom to top 0, 1, 3, 10, 20, 40, and 60 mM. Scan rate=100 mV·s⁻¹, glassy carbon as working electrode. 77

Figure III. 21. Determination of the overpotential in the case of **1_{Co}** using TFA..... 89

CHAPTER IV

Figure IV. 1. Selected cobalt complexes based containing different electronic substituents studied in catalytic hydrogen production. 95

Figure IV. 2. Paramagnetic ¹H-NMR spectrum of **1^H** complex in CD₃CN at 280 K. Peak width measured at half peak intensity (Δδ, in ppm): 242.9 (0.6), 201.9 (4.3), 141.1 (0.61), 111.7 (0.81), 91.9 (0.10), 83.93 (4.24), 65.55 (0.12), 28.91 (0.04). 99

Figure IV. 3. Linear plot of H_α chemical shift (T = 298 K) of the **1^R** complexes versus the Hammett σ parameter..... 100

Figure IV. 4. Paramagnetic ¹H-NMR spectra of **1^R** complexes in CD₃CN at 298 K..... 101

Figure IV. 5. ¹H-NMR spectra (500 MHz) of **1^H** in CD₃CN at different temperatures..... 102

Figure IV. 6. Representation of the chemical shift of aromatic protons of **1^R** complexes (in CD₃CN) in front of temperature in the ¹H-NMR spectrum in CD₃CN 103

Figure IV. 7. *Left*: Representation of the chemical shift of H_α signals in front of temperature in the ¹H-NMR spectrum of **1^R** complexes in CD₃CN..... 104

Figure IV. 8. Representation of the effective magnetic moment of 1^R complexes as a function of the temperature. μ_{eff} values were obtained in CD_3CN using the Evans' method	104
Figure IV. 9. Thermal ellipsoid plots of complex $[\text{Co}^{\text{H,NO}_2}\text{Py}^{\text{Me}_t}\text{tacn})(\text{MeCN})_2](\text{OTf})_2$ (50% probability) measured at 298 K. Hydrogen atoms have been omitted for clarity. The crystal data and the selected bond and angles are collected in the section IV.3.12.3.	105
Figure IV. 10. UV/Vis spectra of 100 mM solution of 1^{NMe_2} (green), 1^{DMM} (red), 1^{H} (orange), 1^{Cl} (blue), $1^{\text{CO}_2\text{Et}}$ (brown), 1^{CF_3} (purple) and 1^{NO_2} (black), in MeCN at 298 K.	106
Figure IV. 11. Thermal ellipsoid plots of $1^{\text{NO}_2}_{\text{OTf}}$, $1^{\text{CO}_2\text{Et}}_{\text{OTf}}$, $1^{\text{Cl}}_{\text{OTf}}$, $1^{\text{H}}_{\text{OTf}}$, $1^{\text{DMM}}_{\text{OTf}}$ (50% probability) and 1^{NMe_2} (30% probability). Solvent molecules and hydrogen atoms are omitted for clarity. Color code: cobalt (blue), nitrogen (light blue), oxygen (red), fluor (yellow), carbon (grey) and sulfur (orange).....	107
Figure IV. 12. <i>Left:</i> Electrochemical wave of 1^{NMe_2} (green), 1^{DMM} (red), 1^{H} (grey), 1^{Cl} (orange), $1^{\text{CO}_2\text{Et}}$ (blue) and 1^{CF_3} (black). <i>Right:</i> Redox potentials of $\text{Co}^{\text{II/I}}$ versus the Hammett constant ($\sigma_p + \sigma_m$) for the R substituents. Experimental conditions: 1^R (1 mM), Bu_4NPF_6 (100 mM) as supporting electrolyte in dry acetonitrile, using glassy carbon as working and SCE as reference electrodes. Scan rate: $100 \text{ mV}\cdot\text{s}^{-1}$. Potentials are quoted versus SCE.....	109
Figure IV. 13. Cyclic voltammograms of 1^R (1 mM) complexes measured in MeCN containing Bu_4NPF_6 (100 mM) as supporting electrolyte, using glassy carbon as working and SCE as reference electrodes. Scan rate: $100 \text{ mV}\cdot\text{s}^{-1}$. Potentials are quoted versus SCE.	110
Figure IV. 14. Photocatalytic hydrogen production in the presence (dashed line) and absence (solid line) of Hg^0 . Conditions: 1^{H} (50 μM), PS_{Ir} (250 μM) using $\text{CH}_3\text{CN}:\text{H}_2\text{O}:\text{Et}_3\text{N}$ (4:6:0.2 mL) as solvent and irradiated ($\lambda = 447 \text{ nm}$) at 25 $^\circ\text{C}$. The reaction using Hg^0 was performed using 1.5 mL of Hg^0 (15 % of the total volume of the reaction).....	112
Figure IV. 15. On-line H_2 evolved vs time for 1^R complexes (50 μM), PS_{Ir} (150 μM) in $\text{CH}_3\text{CN}:\text{H}_2\text{O}:\text{Et}_3\text{N}$ (4:6:0.2 mL) as solvent mixture and irradiated ($\lambda = 447 \text{ nm}$) at 25 $^\circ\text{C}$. $1^{\text{CO}_2\text{Et}}$ (blue), 1^{Cl} (orange), 1^{H} (grey), 1^{CF_3} (black), 1^{DMM} (red), 1^{NO_2} (green) and 1^{NMe_2} (purple). $\text{TON} = n(\text{H}_2)/n(1^R)$	113
Figure IV. 16. Top: Rate profiles in H_2 evolution for $1^{\text{CO}_2\text{Et}}$ (blue), 1^{Cl} (orange), 1^{H} (grey), 1^{CF_3} (black), 1^{DMM} (red), 1^{NO_2} (green) and 1^{NMe_2} (purple). Conditions: 1^R (50 μM), PS_{Ir} (150 μM) using $\text{CH}_3\text{CN}:\text{H}_2\text{O}:\text{Et}_3\text{N}$ (4:6:0.2 mL) as solvent and irradiated ($\lambda = 447 \text{ nm}$) at 25 $^\circ\text{C}$	114
Figure IV. 17. Hammett plot of the relative reaction rates versus the Hammett substituent value (σ). v : Initial reaction rate determined at 10% conversion.	115
Figure IV. 18. Hydrogen production (mL H_2) versus the concentration of $1^{\text{CO}_2\text{Et}}$. Conditions: $1^{\text{CO}_2\text{Et}}$ (0.25-100 μM), PS_{Ir} (150 μM) using $\text{CH}_3\text{CN}:\text{H}_2\text{O}:\text{Et}_3\text{N}$ (4:6:0.2 mL) as solvent and irradiated ($\lambda = 447 \text{ nm}$) at 25 $^\circ\text{C}$	116
Figure IV. 19. Study of the dependence of the cobalt concentration. <i>Top left:</i> On-line hydrogen evolution traces with different concentrations of $1^{\text{CO}_2\text{Et}}$ (0.25 – 100 μM). <i>Top right:</i> Initial reaction rates (TOF) vs $[1^{\text{CO}_2\text{Et}}]$. <i>Bottom left:</i> Rate profiles in H_2 evolution at different concentrations of $1^{\text{CO}_2\text{Et}}$: TOF_{max} (h^{-1}): 425 (100 μM), 780 (50 μM), 1420 (25 μM), 2965 (12.5 μM), 6720 (5 μM), 19075 (2.5 μM), 28610 (1 μM), 52485 (0.5 μM) and 52570 (0.25 μM). <i>Bottom left:</i> Double-ln plot of initial H_2 evolution rates vs $[\text{Co}]$. Conditions: $1^{\text{CO}_2\text{Et}}$ (0.25-100 μM), PS_{Ir} (150 μM) using $\text{CH}_3\text{CN}:\text{H}_2\text{O}:\text{Et}_3\text{N}$ (4:6:0.2 mL) as solvent and irradiated ($\lambda = 447 \text{ nm}$) at 25 $^\circ\text{C}$	117
Figure IV. 20. Top: UV/Vis monitoring at 527 nm associated with the formation of $\text{PS}_{\text{Ir}}^{\text{II}}$ species by irradiating at $\lambda = 447 \text{ nm}$, upon addition of 1^R complex (0.1 eq. vs. PS_{Ir}). Conditions: $[\text{PS}_{\text{Ir}}] = 0.25 \text{ mM}$, $[\text{Et}_3\text{N}] = 100 \text{ mM}$, $\text{CH}_3\text{CN}:\text{H}_2\text{O}$ (0.8:1.2 mL) at 25 $^\circ\text{C}$. Bottom: Time-dependent photocatalytic H_2 evolution. Inset: Magnification in the first seconds after the addition of 1^R	118

Figure IV. 21. UV/Vis monitoring at 527 nm of the self-decay of the photogenerated $\text{PS}_{\text{ir}}^{\text{II}}$ species by irradiating at $\lambda = 447$ nm. Conditions: $[\text{PS}_{\text{ir}}] = 0.1$ mM, $[\text{Et}_3\text{N}] = 100$ mM, $\text{CH}_3\text{CN}/\text{H}_2\text{O}$ (0.8:1.2 mL) at 25 °C.....	119
Figure IV. 22. Elementary steps where H/D selectivity can take place in the water reduction reaction and the equations to calculate the combined KIE^{Sel}	121
Figure IV. 23. <i>Left:</i> On-line hydrogen evolved versus time with $\mathbf{1}^{\text{CO}_2\text{Et}}$ (50 μM), PS_{ir} (150 μM) using $\text{CH}_3\text{CN}:\text{H}_2\text{O}:\text{Et}_3\text{N}$ (4:6:0.2 mL) (blue), $\text{CH}_3\text{CN}:\text{H}_2\text{O}:\text{D}_2\text{O}:\text{Et}_3\text{N}$ (4:3:3:0.2 mL) (green) or $\text{CH}_3\text{CN}:\text{D}_2\text{O}:\text{Et}_3\text{N}$ (4:6:0.2 mL) (red) as solvent mixture and irradiated ($\lambda = 447$ nm) at 25 °C. Activities using a) H_2O : 500 \pm 20 TON, initial rate = 760 \pm 10 h^{-1} , b) $\text{H}_2\text{O}/\text{D}_2\text{O}$ (1:1): 230 \pm 30 TON, initial rate = 740 \pm 20 h^{-1} and c) D_2O : 145 \pm 1 TON, initial rate = 670 \pm 20 h^{-1} . <i>Right:</i> Hydrogen evolved by $\mathbf{1}^{\text{CO}_2\text{Et}}$ (blue), $\mathbf{1}^{\text{H}}$ (green) and $\mathbf{1}^{\text{DMMM}}$ (red) using $\text{CH}_3\text{CN}:\text{H}_2\text{O}:\text{Et}_3\text{N}$ (4:6:0.2 mL) (solid traces) or $\text{CH}_3\text{CN}:\text{H}_2\text{O}:\text{D}_2\text{O}:\text{Et}_3\text{N}$ (4:3:3:0.2 mL) (dashed traces).	122
Figure IV. 24. On-line monitoring of the formation (Ion current) of H_2 (Solid trace), HD (dashed trace) and D_2 (dotted line) versus time using D_2O (99 % in deuterium). The current response was corrected relative to a previous calibration of HD and D_2 . Conditions: $\mathbf{1}^{\text{CO}_2\text{Et}}$ (50 μM), PS_{ir} (150 μM), $\text{MeCN}:\text{D}_2\text{O}$ (0.8:1.2 mL), Et_3N (40 μL), reaction volume = 2 mL, irradiated at $\lambda = 447$ nm, under N_2 atmosphere.....	123
Figure IV. 25. Top: On-line monitoring of the formation (Ion current) of H_2 (Solid trace), HD (dashed trace) and D_2 (dotted line) versus time in a mixture of $\text{H}_2\text{O}:\text{D}_2\text{O}$ (1:1). Bottom: Ratios of H_2/D_2 (dots), HD/D_2 (diamonds) and H_2/HD (squares) obtained from the ion current data. For the ratio determination, the ion current response was corrected relative to a previous calibration of HD and D_2 . Conditions: $\mathbf{1}^{\text{CO}_2\text{Et}}$ (50 μM), PS_{ir} (150 μM), $\text{MeCN}:\text{H}_2\text{O}:\text{D}_2\text{O}$ (0.8:0.6:0.6 mL), Et_3N (40 μL), reaction volume = 2 mL, irradiated at $\lambda = 447$ nm, under N_2 atmosphere.....	125
Figure IV. 26. Eyring plot with the catalyst $\mathbf{1}^{\text{CO}_2\text{Et}}$	126
Figure IV. 27. Top: On-line hydrogen evolved versus time with $\mathbf{1}^{\text{CO}_2\text{Et}}$ (35 μM), PS_{ir} (150 μM) using $\text{CH}_3\text{CN}:\text{H}_2\text{O}:\text{Et}_3\text{N}$ (4:6:0.2 mL) as solvent and irradiated ($\lambda = 447$ nm) at 25 °C, in the presence of different concentrations of O_2 . Bottom: Initial reaction rates for hydrogen evolution at different concentrations of O_2 in the headspace. Relative photocatalytic H_2 evolution activity compared to that under anaerobic conditions. TON: 512 \pm 20 (0 % O_2), 410 \pm 14 (0.5 % O_2), 340 \pm 20 (1 % O_2), 305 \pm 24 (2.5 % O_2), 200 \pm 14 (6.5 % O_2), 69 \pm 12 (12.5 % O_2), 4 \pm 2 (15 % O_2).....	127
Figure IV. 28. TON of electrons (mmol e^- / mmol Cat) consumed for the formation of H_2 (blue dots) and O_2 reduction (red dots) versus the initial amount of O_2 (mmol) in the headspace..	129
Figure IV. 29. <i>Left:</i> Thermal ellipsoid plots of Co^{III} ($\mathbf{1}^{\text{H}}$) with (50 % probability). Solvent molecules and hydrogen atoms are omitted for clarity. Color code: cobalt (blue), nitrogen (light blue) and carbon (grey). <i>Right:</i> Comparison between the experimental and theoretical Co-N distances.	130
Figure IV. 30. Spin density isosurfaces of the seven formal Co^{I} intermediates in the triplet spin state computed at the B3LYP/6-31+G* level of theory. The spin density in the positive sign is coloured in blue and the spin density in the negative one is coloured in green.	131
Figure IV. 31. Hammett plot of experimental (red) and theoretical (blue) A) $E(\text{Co}^{\text{III/I}})$ (V), B) $E(\text{Co}^{\text{III/II}})$ (V), C) Theoretical pK_a values and E) experimental $E(\text{Co}^{\text{III/II}})$ (V) and theoretical pK_a values and D) experimental $E(\text{Co}^{\text{III/II}})$ and $E(\text{Co}^{\text{II/I}})$ vs. theoretical pK_a values	133
Figure IV. 32. Top: Experimental E (V) ($\text{Co}^{\text{III/II}}$) and computed pK_a values vs. the Hammett constant. The dashed black trace corresponds to the cyclic voltammogram of the photosensitizer PS_{ir} ($E(\text{V}) \text{PS}_{\text{ir}}(\text{III/II}) = -1.38$ V vs. SCE). Bottom: Hammett plot of the relative reaction rates versus the Hammett substituent value (σ). v : Initial reaction rate determined at 10% conversion. The	

two main trends in reactivity are emphasized by green (redox dependent) and red (pK _a dependent).....	134
Figure IV. 33. Cyclic voltammograms of 1^R complexes (1 mM) showing the growth of a new electrocatalytic wave due to the addition of TFA (red: 0 mM, light blue: 1 mM, green: 3 mM, black: 10 mM). A) Half wave potential of the electrocatalytic wave. B) Onset potential of the electrocatalytic wave C) Standard potential in proton reduction using TFA. Conditions: 0.1 M Bu ₄ NPF ₆ (0.1 M) in MeCN, using a scan rate of 100 mV·s ⁻¹ . Glassy carbon electrode and SCE electrodes were used as working and reference electrodes, respectively.....	136
Figure IV. 34. Successive cyclic voltammograms of 1^R complexes (1 mM) in acetonitrile containing Bu ₄ NPF ₆ (0.1 M) in the presence of acid: TFA (red: 0 mM, light blue: 1 mM, green: 3 mM, black: 10 mM, purple: 20 mM, orange: 40 mM, grey: 60 mM, dark blue: 80 mM and yellow: 100 mM), measured at 100 mV·s ⁻¹ . Glassy carbon electrode and SCE electrodes were used as working and reference electrodes, respectively.....	137
Figure IV. 35. A) Proposed structure of the [FeFe] hydrogenase active site based on crystallographic data. ¹⁰ B) Possible pathway for hydrogen evolution involving PCET processes and protonated ligand.....	138
Figure IV. 36. Cyclic voltammograms of 1^H (1 mM) in acetonitrile containing Bu ₄ NPF ₆ (0.1 M) in the presence of different Et ₃ N TfOH concentrations (red: 0 mM, light blue: 1 mM, green: 3 mM, black: 10 mM, purple: 20 mM, orange: 40 mM and grey: 60 mM), measured at 100 mV·s ⁻¹ . Glassy carbon electrode and SCE electrodes were used as working and reference electrodes, respectively.	139
Figure IV. 37. Setup for UV/Vis measurement with on-line irradiation.	144
Figure IV. 38. Calibration of the response of H ₂ , DH and D ₂ in the on-line mass spectrometer apparatus.	145

CHAPTER V

Figure V. 1. ¹ H-NMR (CDCl ₃ , 500 MHz, 300 K) spectrum of Py₂tacn-Biotin	165
Figure V. 2. ¹ H- ¹ H COSY (CDCl ₃ , 500 MHz, 300 K) spectrum of Py₂tacn-Biotin	166
Figure V. 3. ¹³ C-NMR (CDCl ₃ , 126 MHz, 300 K) spectrum of Py₂tacn-Biotin	166
Figure V. 4. ¹ H- ¹³ C HSQC (CDCl ₃ , 126 MHz, 300 K) spectrum of Py₂tacn-Biotin	167
Figure V. 5. UV/Vis absorption decay of the HABA ⊂ SA complex upon the addition of different amounts of 1^{Biotin} (<i>left</i>) and 1^{Spacer-Biotin} (<i>right</i>). Conditions: 26 μM of SA in 20 mM phosphate, 150 mM NaCl, pH 7.5 and saturated with 500 μM HABA.	169
Figure V. 6. HABA displacement assay of streptavidin by 1^{Biotin} (Orange dots) and 1^{Spacer-Biotin} (Blue dots). Absorbance at 500 nm was monitored as a function of the biotinylated compound concentration. The titration with free D-Biotin has been included for comparative reasons. The dashed black trace is the theoretical fitted curve for the K _{exch} determination.....	170
Figure V. 7. Differences in affinity with streptavidin measured by HABA titration.....	171
Figure V. 8. Computed models of the cobalt catalyst (1^{Biotin} (A), 1^{Spacer-Biotin} (B)) inside streptavidin (transparent surface).	172
Figure V. 9. Left: CD spectra of SA (Black trace), 1^{Biotin} (red trace) and 1^{Spacer-Biotin} (green trace). Conditions: 5 μM protein, 100 mM Tris·HCl buffer, pH 7.5 at 20 °C. Right: UV/Vis spectra of 5 μM solution of SA (solid black trace), 1^{Biotin} (solid red trace) and 1^{Spacer-Biotin} (solid green trace) measured in 100 mM Tris·HCl buffer, pH 7.5 at 20 °C. The absorption of 1^{Biotin} (dashed blue trace) and 1^{Spacer-Biotin} (dashed grey trace) are included for comparative reasons.....	173
Figure V. 10. Positive MALDI-TOF spectra of SA (left) and 1^{Biotin} ⊂ SA (right). Spectra were obtained by mixing directly on the target 1 μL of the SA solution (from 20 μM stock solution) with 1 μL of the matrix (sinapinic acid, 5·10 ⁻² M in acetonitrile/H ₂ O, 4:1 v/v).	174

Figure V. 11. Single crystals obtained of $\mathbf{1}^{\text{Biotin}} \subset \text{SA}$ and $\mathbf{1}^{\text{Spacer-Biotin}} \subset \text{SA}$	175
Figure V. 12. Successive cyclic voltammograms of 1 mM cobalt catalysts $\mathbf{1}^{\text{Biotin}}$ (A) and $\mathbf{1}^{\text{Spacer-Biotin}}$ (B) in 100 mM citrate buffer, 100 mM NaCl, at pH in the 3.5 to 6.0 range. Scan rate of $100 \text{ mV}\cdot\text{s}^{-1}$ using a 0.28 cm^2 glassy carbon working electrode. Potentials are quoted versus SCE. C) Maximum peak intensity values versus the pH value in the case of $\mathbf{1}^{\text{Biotin}}$. D) Maximum peak intensity values versus the pH value in the case of $\mathbf{1}^{\text{Spacer-Biotin}}$	176
Figure V. 13. Successive CVs at increasing concentrations $\mathbf{1}^{\text{Biotin}}$ (left) and $\mathbf{1}^{\text{Spacer-Biotin}}$ (right). Conditions: 100 mM citrate buffer, 100 mM NaCl, at pH 3.5 using different catalyst concentrations: 0 mM (dashed grey) 0.5 mM (orange), 1 mM (blue), 1.5 mM (purple), 2 mM (red) and 2.5 mM (black). Scan rate of $100 \text{ mV}\cdot\text{s}^{-1}$ using a 0.28 cm^2 glassy carbon working electrode. Potentials are quoted versus SCE. <i>Inset</i> : Electrocatalytic current (i_c) versus [Catalyst] showing a first order kinetics.	177
Figure V. 14. Cyclic voltammograms in 100 mM citrate buffer, 100 mM NaCl, at different pH values in the absence (dashed grey trace), and presence of 1 mM catalyst $\mathbf{1}^{\text{Biotin}}$ (red trace) and $\mathbf{1}^{\text{Spacer-Biotin}}$ (blue trace). The black CV correspond to the electrocatalytic current obtained after rinsing the electrode after the measurement of the cobalt solution. Scan rate of $100 \text{ mV}\cdot\text{s}^{-1}$ using a 0.28 cm^2 glassy carbon working electrode. Potentials are quoted versus SCE.....	178
Figure V. 15. Left: Cyclic voltammogram of $\mathbf{1}^{\text{Biotin}} \subset \text{SA}$ adduct thin film on the surface (red trace) and in solution (black trace). The CV scan for bare electrode under the same conditions (dashed grey trace) and the CV of a thin film of SA alone (green trace) are included. Conditions: 100 mM citrate buffer, 100 mM NaCl, at pH 3.5. Scan rate of $100 \text{ mV}\cdot\text{s}^{-1}$ using a 0.28 cm^2 glassy carbon working electrode. Potentials are quoted vs SCE. Right: Plot of the peak potential (E_p) as a function of pH. The E_p value of $\mathbf{1}^{\text{Biotin}}$ at pH = 3.5 was removed from the plot E_p (V) vs. pH because it did not fit with the linear plot.....	179
Figure V. 16. Successive cyclic voltammograms of $\mathbf{1}^{\text{Biotin}} \subset \text{SA}$ (A) and $\mathbf{1}^{\text{Spacer-Biotin}} \subset \text{SA}$ (B) adducts thin film on the surface in 100 mM citrate buffer, 100 mM NaCl, at pH in the 3.5 to 6.0 range. Scan rate of $100 \text{ mV}\cdot\text{s}^{-1}$ using a 0.28 cm^2 glassy carbon working electrode. Potentials are quoted versus SCE. C) Maximum peak intensity values versus the pH value in the case of $\mathbf{1}^{\text{Biotin}} \subset \text{SA}$. D) Maximum peak intensity values versus the pH value in the case of $\mathbf{1}^{\text{Spacer-Biotin}} \subset \text{SA}$	180
Figure V. 17. Cyclic voltammograms of $\mathbf{1}^{\text{Biotin}} \subset \text{SA}$ (red trace) and $\mathbf{1}^{\text{Spacer-Biotin}} \subset \text{SA}$ (blue trace) adducts thin film on the surface in 100 mM citrate buffer, 100 mM NaCl, at pH in the 3.5 to 6.0 range. The CV scan for bare electrode under the same conditions (grey trace) and the CV obtained from a thin of SA alone (green trace) are included. Scan rate of $100 \text{ mV}\cdot\text{s}^{-1}$ using a 0.28 cm^2 glassy carbon working electrode. Potentials are quoted versus SCE.....	182
Figure V. 18. Cyclic voltammograms of left) $\mathbf{1}^{\text{Biotin}}$ (black trace) $\mathbf{1}^{\text{Biotin}} \subset \text{SA}$ (red trace) Right) $\mathbf{1}^{\text{Spacer-Biotin}}$ (black trace) $\mathbf{1}^{\text{Spacer-Biotin}} \subset \text{SA}$ (red trace). CVs measured in 100 mM citrate buffer, 100 mM NaCl, at pH 3.5. Scan rate of $100 \text{ mV}\cdot\text{s}^{-1}$ using a 0.28 cm^2 glassy carbon working electrode. Potentials are quoted versus SCE.....	183
Figure V. 19. Photoinduced hydrogen production with 5 μM catalyst, 250 μM PS_{Ir} , 0.4 M TEOA in 0.4 mL aqueous phosphate buffer containing 100 mM NaCl, measured at different pH values. Irradiation with $1100 \text{ W}\cdot\text{m}^{-2}$ of visible light ($\lambda > 400 \text{ nm}$). A) Time traces of hydrogen evolved using $\mathbf{1}^{\text{Spacer-Biotin}}$. B) Time traces of hydrogen evolved using $\mathbf{1}^{\text{Spacer-Biotin}} \subset \text{SA}$. C) Activities represented as TON at different pH values in the case of $\mathbf{1}^{\text{Spacer-Biotin}}$ (grey) and $\mathbf{1}^{\text{Spacer-Biotin}} \subset \text{SA}$ (black).The red trace represents the TON enhance factor ($\text{TON}_{\mathbf{1}^{\text{Spacer-Biotin}} \subset \text{SA}} / \text{TON}_{\mathbf{1}^{\text{Spacer-Biotin}}}$) at different pH values. D) Activities represented as initial TOF (h^{-1}) at different pH values in the case of $\mathbf{1}^{\text{Spacer-Biotin}}$ (grey) and $\mathbf{1}^{\text{Spacer-Biotin}} \subset \text{SA}$ (black).The red trace represents the enhance factor in TOF ($\text{TOF}_{\mathbf{1}^{\text{Spacer-Biotin}} \subset \text{SA}} / \text{TOF}_{\mathbf{1}^{\text{Spacer-Biotin}}}$) at different pH values.....	186

Figure V. 20. CD spectra of 1^{Spacer-Biotin} C SA at different percentages of MeCN in the solvent mixture. Conditions: 5 μ M protein, 100 mM Tris·HCl buffer, pH 7.5 at 20 °C. The CD signals were corrected according to the dilution of the addition.	187
Figure V. 21. Time-traces in H ₂ evolution catalyzed by 1^{Biotin} (empty red dots), 1^{Spacer-Biotin} (empty black dots), 1^{Biotin} C SA (full red dots) and 1^{Spacer-Biotin} C SA (full black dots). Conditions: 5 μ M catalyst, 250 μ M PS_{Cu} , 0.4 M Et ₃ N in 0.4 mL of MeCN:H ₂ O (4:6). Irradiation with 1100 W·m ⁻² of visible light ($\lambda > 400$ nm).	188

CHAPTER VI

Figure VI. 1. Crystal structure (Ellipsoids 50 % probability level) of [Co ^I (PY5Me ₂)](BPh ₄) complex reported by J. Long and C. Chang groups. ¹⁰¹ . In purple, blue and grey there are the Co, N and C atoms, respectively; H atoms are omitted for clarity.	199
Figure VI. 2. Redox non-innocent nature of the L'Fe(pyridine) ₂ (L' = 2,4-bis(2,6-diisopropylimino)pentyl) complex and the reversible C-C bond formation at the para-position of the pyridine reduction.	201
Figure VI. 3. A, B and C) Paramagnetic ¹ H-NMR spectra measured at 235 K (500 MHz, CD ₃ CN) of the chemically synthesized compounds 1_{Co^ICl} , 1_{Co^{II}Cl} and 1_{Co^{II}CH₃CN} , respectively. D) ¹ H-NMR spectrum of 1_{Co^{III}Cl} in <i>d</i> ₆ -DMSO at 298 K. E) ¹ H-NMR spectrum of 1_{Co^{III}CH₃CN} in CD ₃ CN at 298 K.	204
Figure VI. 4. Crystal structures of the cobalt complexes 1_{Co^{II}CH₃CN} , 1_{Co^{II}Cl} and 1_{Co^{III}CH₃CN} . Ellipsoids are drawn at the 50 % probability level. Solvent molecules and hydrogen atoms are omitted for clarity. Color code: cobalt (blue), nitrogen (light blue), oxygen (red), fluor (yellow), carbon (grey) and sulfur (orange).	205
Figure VI. 5. ¹ H-NMR (CD ₃ CN, 500 MHz, 235 K) paramagnetic spectrum of 1_{Co^ICl}	206
Figure VI. 6. Photoreduction of 1_{Co^{II}Cl} to 1_{Co^ICl} . <i>Top</i> : ¹ H-NMR paramagnetic spectrum before irradiation. <i>Middle</i> : ¹ H-NMR paramagnetic spectrum after 15 min of irradiation. <i>Bottom</i> : ¹ H-NMR paramagnetic spectrum of the chemically synthesized 1_{Co^ICl} compound. Conditions: 1_{Co^{II}Cl} (20 mM), PS_{Ir} (20 mM), Et ₃ N (240 mM) in CD ₃ CN irradiating at 250 K ($\lambda = 447$ nm).	207
Figure VI. 7. Photoreduction of 1_{Co^{II}CH₃CN} to 1_{Co^ICH₃CN} . <i>Top</i> : ¹ H-NMR paramagnetic spectrum before irradiation. <i>Middle</i> : ¹ H-NMR paramagnetic spectrum after 15 min of irradiation. <i>Bottom</i> : ¹ H-NMR paramagnetic spectrum of the chemically synthesized 1_{Co^ICl} compound. Conditions: 1_{Co^{II}CH₃CN} (20 mM), PS_{Ir} (20 mM), Et ₃ N (240 mM) in CD ₃ CN irradiating at 250 K ($\lambda = 447$ nm).	208
Figure VI. 8. X-band EPR spectra (10 K) of butyronitrile solutions of 1 mM 1_{Co^{II}CH₃CN} (black), 1_{Co^{II}Cl} (blue) and 1_{Co^ICl} (red). Microwave frequency, 9.63 GHz; modulation frequency, 100 KHz.	209
Figure VI. 9. XANES spectra of chemically generated 1_{CoⁿCl} series (n = 1, 2, 3)	210
Figure VI. 10. XANES spectra of the photochemically generated 1_{Co^IMeCN} compound with the chemically synthesized 1_{CoⁿMeCN} (n = 2, 3).	212
Figure VI. 11. <i>Left</i> : XANES spectra of Me¹_{Co^{II}} and the photochemically generated Me¹_{Co^I} compound. <i>Right</i> : XANES spectra of 1_{Co^{II}CH₃CN} and Me¹_{Co^I}	214
Figure VI. 12. χ :T as a function of temperature from 300 to 2 K. The red dots correspond to 1_{Co^ICl} and the black ones to 1_{Co^{II}Cl}	215
Figure VI. 13. Protonation of 1_{Co^ICl} analyzed by ¹ H-NMR (CD ₃ CN, 500 MHz, 238 K). <i>Top</i> : ¹ H-NMR paramagnetic spectrum of 1_{Co^ICl} before the addition of TFA. <i>Middle</i> : ¹ H-NMR paramagnetic spectrum of 1_{Co^ICl} after the addition of 3 eq. TFA. <i>Bottom</i> : ¹ H-NMR spectrum of 1_{Co^ICl} after the addition of 3 eq. TFA.	216
Figure VI. 14. XANES spectra of the 1_{Co^ICl} precursor, the product derived from the reaction of 1_{Co^ICl} with TFA (1_{Co^ICl} + H ⁺), and the 1_{Co^{III}Cl} synthesized by one electron oxidation of 1_{Co^{II}Cl}	217

Figure VI. 15. XANES spectra of the photochemically generated 1_{Co}^I precursor, the product derived from the reaction of 1_{Co}^I with TFA ($1_{Co}^I + H^+$), and the 1_{Co}^{III} synthesized from 1_{Co}^I by one electron oxidation.	218
Figure VI. 16. Protonation of 1_{Co}^I with H_2O analyzed by 1H -NMR (CD_3CN , 500 MHz, 300 K). <i>Top:</i> 1H -NMR paramagnetic spectrum of 1_{Co}^I before the addition of H_2O . <i>Middle:</i> 1H -NMR paramagnetic spectrum of 1_{Co}^I after the addition of H_2O . <i>Bottom:</i> 1H -NMR spectrum of 1_{Co}^I after the addition of H_2O	219
Figure VI. 17. XAS analysis of 1_{Co}^I reactivity against water under anaerobic conditions.....	220
Figure VI. 18. <i>Left:</i> Fourier transformed spectra of $1_{Co}^I + H_2O$ (S) (no phase correction, FT, window= $2-12.5 \text{ \AA}^{-1}$). <i>Right:</i> Fourier transformed spectra of $1_{Co}^I + H_2O$ (no phase correction, FT, window= $2-12.5 \text{ \AA}^{-1}$) <i>Insets:</i> k^3 -weighted unfiltered EXAFS spectra. <i>Bottom tables:</i> selected path distances parameters for the various models from EXAFS analysis.	220
Figure VI. 19. Comparison between the XAS data obtained from the 1_{Co}^I reactivity against oxygen, oxygen and water, protons and the 1_{Co}^{III}	221
Figure VI. 20. <i>Left:</i> Fourier transformed spectra of $1_{Co}^I + O_2$ (no phase correction, FT, window= $2-12.5 \text{ \AA}^{-1}$). <i>Right:</i> Fourier transformed spectra of $1_{Co}^I + O_2 + H_2O$ (no phase correction, FT, window= $2-12.5 \text{ \AA}^{-1}$). <i>Insets:</i> k^3 -weighted unfiltered EXAFS spectra. <i>Bottom tables:</i> selected path distances parameters for the various models from EXAFS analysis.	221
Figure VI. 21. Spin density obtained for the DFT modelled 1_{Co}^I and 1_{Co}^II complexes.....	222
Figure VI. 22. Hypothetic redox non-innocent nature of the pyridine moiety in the 1_{Co}^I complex and the reversible C-C bond formation at the para-position of the pyridine reduction.	223
Figure VI. 23. On-line H_2 evolved versus time for 1_{Co}^I ($n = 1, 2, 3$) complexes (50 μM), PS_{Cu} (250 μM) in $CH_3CN:H_2O:NEt_3$ (4:6:0.2 mL) as solvent mixture and irradiated ($\lambda = 447 \text{ nm}$) at 25 $^\circ C$. The catalytic activity of the starting $Co(PPh_3)_3Cl$ salt with and without the presence of the $Py_2^{Ts}tacn$ ligand is also included.	224

CHAPTER VII

Figure VII. 1. Photoinduced 10a formation under varied light conditions. Green dots: formation of 9a under constant light irradiation. Red dots: formation of 10a under light-dark cycles: yellow area corresponds to irradiation at $\lambda = 447 \text{ nm}$, and grey corresponds to no irradiation of the sample. Conditions: 1_{Co} (3.8 μmol , 3 mol%), PS_{Ir} (2.5 μmol , 2 mol%), substrate 9a (0.126 mmol, 12.4 mM) in $MeCN:H_2O:Et_3N$ (2:8:0.2 mL) irradiated at $\lambda = 447 \text{ nm}$ and 30 $^\circ C$. The yield of 10a was determined by GC analysis after the workup using a calibrated internal standard.....	238
Figure VII. 2. 1H -NMR (400 MHz, 300 K) spectra recorded at different irradiation times. Conditions: 1_{Co} (0.32 μmol , 3 mol%), PS_{Ir} (1.2 μmol , 1.14 mol%), 9a (10.5 μmol , 20.6 mM) in $CD_3CN:D_2O:Et_3N$ (0.15:0.35:0.01 mL) irradiated ($\lambda = 447 \text{ nm}$) at 30 $^\circ C$, under N_2 . The amount of PS_{Ir} was reduced to 1.14 mol% in order to guarantee its solubilization in deuterated solvents. Each 1H -NMR spectrum corresponds to a different reaction in order to have continued irradiation.....	239
Figure VII. 3. 1H -NMR spectra (400 MHz, 300 K) in $CD_3CN:D_2O:Et_3N$ (0.15:0.35:0.01 mL) of A) 1H -NMR spectrum of a mixture of the meso forms of 2,3-diphenyl-2,3-butanediol (9a-pinacol). B) 1H -NMR of the pure 1-phenylethanol (10a). C) crude mixture after 41 h of irradiation ($\lambda = 447 \text{ nm}$) using 1_{Co} (0.32 μmol , 3 mol%), PS_{Ir} (1.2 μmol , 1.14 mol%), substrate (10.5 μmol , 20.6 mM) at 30 $^\circ C$, under N_2	240
Figure VII. 4. Selected cobalt complexes for the study. 1 $_{Co}$: $[Co^{II}(OTf)(Py_2^{Ts}tacn)](OTf)$, 2 : $[Co^{II}(OTf)(DPA-Bpy)](OTf)$, 3 : $[Co^{II}(OTf)(N4Py)](OTf)$, 4 : $[Co^{II}(OTf)(H-CDPy_3)](OTf)$, 5 : $[Co^{II}(OTf)_2(PDP)]$, 6 : $[Co^{II}(OTf)_2(TPA)]$, 7 : $[Co^{II}(Cl)_2(BpcMe)]$, and 8 : $[Co^{III}(Cl)(Py)(Glioxim)]$	242

Figure VII. 5. Photocatalytic activities of different cobalt-based complexes in H₂ and **10a** formation. Top: **10a** formation activities. Middle: H₂ formation activities in the presence of **9a**. Bottom: H₂ formation activities in the absence of **9a**. Reaction conditions: **9a** (0.168 mmol, 16.5 mM), **PS_{Ir}** (2.5 μmol, 1.5 mol%), **cobalt catalyst** (5 μmol, 3 mol%), MeCN:H₂O:Et₃N (2:8:0.2 mL), irradiating ($\lambda = 447$ nm) for 5 h at 30 °C under N₂. The initial reaction rates in **10a** formation have been determined at the first 15 min of irradiation. 243

Figure VII. 6. On-line monitoring of the photochemical H₂ production in the absence (solid line) and presence of acetophenone (dashed line) for complexes **1c_o-8**. Reaction conditions in the absence of substrate: **PS_{Ir}** (2.5 μmol), **cobalt catalyst** (5 μmol). Reaction conditions in the presence of substrate: [**9a**] (0.168 mmol, 16.5 mM), **PS_{Ir}** (2.5 μmol, 1.5 mol%), **cobalt catalyst** (5.04 μmol, 3 mol%). In all cases a solvent mixture of MeCN:H₂O:Et₃N (2:8:0.2 mL) was used, irradiating ($\lambda = 447$ nm) at 30 °C under N₂. The amount of H₂ was quantified by GC analysis when the hydrogen evolved reached a plateau. 244

Figure VII. 7. *Top:* Effect of the presence of the ligand Py₂^{Ts}tacn. Photocatalytic acetophenone reduction to **10a** using different cobalt salts in the absence (dark blue columns) and in the presence of 1 eq. of ligand (L=Py₂^{Ts}tacn) (blue columns). The addition of ligand give rise to a substantial improvement of yield. *Bottom:* Mmol of H₂ and **10a** produced with different cobalt salts in the presence of Py₂^{Ts}tacn. *Dark blue:* mmol of H₂ produced in the absence of **9a**. *Light blue:* mmol of H₂ produced in the presence of **9a**. *Green:* mmol of **10a** produced. Reaction conditions: [**9a**] (0.168 mmol, 16.5 mM), **PS_{Ir}** (2.5 μmol, 1.5 mol%), **cobalt salt** (5 μmol, 3 mol%), MeCN:H₂O: Et₃N (2:8:0.2 mL), irradiating at $\lambda = 447$ nm for 5 h at 30 °C under N₂. It should be noted that the total amount of mmol of products is similar in the presence and absence of substrate for each catalytic system..... 247

Figure VII. 8. Absorption (solid traces) and fluorescence (dashed traces) spectra of **PS_{Ir}** (red) and **PS_{Cu}** (black) in MeCN, 25 °C..... 253

Figure VII. 9. Optimization of the **1c_o** loading in the photocatalytic reduction of **9a** using **PS_{Cu}** as chromophore. 254

Figure VII. 10. Photocatalytic conversion of **9a** into **10a** catalyzed by **1c_o** using **PS_{Cu}** (black dots) compared with the reaction performed with **PS_{Ir}** (red dots) versus the reaction time (h). Conditions: **9a** (0.168 mmol, 16.5 mM), **PS** (2.5 μmol, 1.5 mol%), **1c_o** (5 μmol, 3 mol%) in MeCN:H₂O:Et₃N (4:6:0.2 mL) irradiated at $\lambda = 447$ nm at 30 °C under N₂. Each data point corresponds to a different reaction experiment. 255

Figure VII. 11. Left: Photocatalytic activities in **9a** reduction at different Et₃N loadings (equivalents versus **9a**). Right: Effect of the presence of O₂ in the photocatalytic **9a** reduction. 255

Figure VII. 12. Mmol of **10a**, **10b** and **10c** formed, H₂ generated and H₂ initial rates. Standard catalytic conditions (Table VII. 1) were used modifying the solvent mixture to MeCN:H₂O:Et₃N (3:7:0.2 mL) to guarantee the solubility of all of the components. 257

Figure VII. 13. A) Mmol of **10a** (blue dots) and H₂ (red dots) obtained and the sum of both (green dots) and B) initial rates of **10a** and H₂ formation versus [**9a**]. C) On-line monitoring of the photochemical H₂ production in the presence of increasing concentrations of **9a**. D) In-In plot of the initial rates for the **10a** formation versus [**9a**] showing the first-order dependence. Standard catalytic conditions (Table VII. 1) were used for the experiments A-B modifying the solvent mixture to MeCN:H₂O:Et₃N (3:7:0.2 mL) to guarantee the substrate solubility at 54 mM of **9a**. 258

Figure VII. 14. Photocatalytic H₂ production in the absence (black line) and presence (red-dotted line) of Hg(0) (>2000 eq.). Conditions: **1** (3.8 μmol, 3 mol%), **PS_{Ir}** (2.5 μmol, 2 mol%), substrate

(0.126 mmol, 12.4 mM) in MeCN:H ₂ O:Et ₃ N (2:8:0.2 mL) irradiated at $\lambda = 447$ nm and 30 °C. The yield of 10a was determined after the hydrogen evolved reached a plateau. Yield of 10a : 65 % in absence of Hg(0) and 61 % in the presence of Hg(0).	259
Figure VII. 15. Left: Isolated products using H ₂ O or D ₂ O (99.9 % in deuterium) in the solvent mixture: A) Reaction using H ₂ O, B) Blank experiment using D ₂ O, C) Reaction using D ₂ O and C) Reaction using D ₂ O under an atmosphere of hydrogen gas. Conditions: substrate (0.126 mmol, 12.4 mM), in MeCN:D ₂ O:Et ₃ N (2:8:0.2 mL) during 5h under irradiation at 447 nm. Right: Formation of 10a catalyzed by cobalt complex 1_{co} under H ₂ (blue squares) or N ₂ (red cycles) atmosphere. Conditions: 1_{co} (3.8 μ mol, 3 mol%), PS_{ir} (2.5 μ mol, 2 mol%), 9a (0.126 mmol, 12.4 mM) in MeCN:H ₂ O:Et ₃ N (2:8:0.2 mL) irradiated at $\lambda = 447$ nm and 30 °C. Each value of 10a yield is the result of an individual experiment. The yield of 10a was determined by GC analysis after the workup using a calibrated internal standard. Reaction rate for 9a \rightarrow 10a under N ₂ atmosphere 0.061 mmol·h ⁻¹ and under H ₂ atmosphere 0.060 mmol·h ⁻¹	260
Figure VII. 16. Molecular ion measured by EI GC-MS from the reduction of 9a when replacing the H ₂ O (C) by D ₂ O (A and B). Conditions: 1_{co} (3.8 μ mol, 3 mol%), PS_{ir} (2.5 μ mol, 2 mol%), substrate (0.126 mmol, 12.4 mM) in MeCN:H ₂ O(or D ₂ O):Et ₃ N (3:7:0.2 mL) irradiated at $\lambda = 447$ nm and 30 °C under N ₂ (A and C) or H ₂ (B) atmosphere.	261
Figure VII. 17. ¹ H-NMR spectrum (CDCl ₃ , 400 MHz, 300 K) of the isolated product 10a using H ₂ O (Top) or D ₂ O (99.9 % in deuterium) (Bottom) in the solvent mixture. Conditions: 1_{co} (3.8 μ mol, 3 mol%), PS_{ir} (2.5 μ mol, 2 mol%), substrate (0.126 mmols, 12.4 mM) in MeCN:H ₂ O(or D ₂ O):Et ₃ N (3:7:0.2 mL) irradiated at $\lambda = 447$ nm and 30 °C, under N ₂	262
Figure VII. 18. ¹³ C-NMR spectrum (CDCl ₃ , 101 MHz, 300 K) of the isolated product 10a using H ₂ O (Top) or D ₂ O (99.9 % in deuterium) (Bottom) in the solvent mixture. Conditions: 1_{co} (3.8 μ mol, 3 mol%), PS_{ir} (2.5 μ mol, 2 mol%), substrate (0.126 mmols, 12.4 mM) in MeCN:H ₂ O(or D ₂ O):Et ₃ N (3:7:0.2 mL) irradiated at $\lambda = 447$ nm and 30 °C, under N ₂	263
Figure VII. 19. Photocatalytic conversion during the irradiation time of acetophenone and 3-phenylbutanal in a (1:1) competition experiment. Red: acetophenone, green: 3-phenylbutanal, blue: 1-phenylethanol, orange: 3-phenylbutan-1-ol and purple: 3-phenylbut-2-en-1-ol isomers. The wide colored lines does not fit de data points but represent a general trend of the activity.	267
Figure VII. 20. DFT-modelled free-energy profiles for the reduction of cyclohexanone, water and acetophenone with the complex 1_{co} . The L ₅ level refers to the pentadentate Py ₂ ^T stacn ligand. Gibbs energies are in kcal·mol ⁻¹	269
Figure VII. 21. Log-Plot of the relative r of 10_R (R (bulky substituent) = Me, Et, nBu, ⁱ Pr, CH ₂ ⁱ Pr) relative to 10_a as a function of the Charton values (ν) using standard catalytic conditions. Charton values: ν (Me)= 0.52, ν (Et)= 0.56, ν (nBu)= 0.68, ν (ⁱ Pr)= 0.76, ν (CH ₂ ⁱ Pr)= 0.98. Reaction time: 15 min. For the substrate R= ^t Bu, no alcohol formation could be detected, and only the alcohol 10_a was produced.	272

CHAPTER VIII

Figure VIII. 1. Left: Representation of the effective magnetic moment of 1_{co}^{CO₂Et} , 1_{co} and 1_{co}^{DMM} as a function of temperature. μ_{eff} values were obtained in CD ₃ CN using the Evans' method. Right: UV/Vis absorption spectra of a 50 μ M solution of 1_{co}^{CO₂Et} (blue), 1_{co} (red) and 1_{co}^{DMM} (green) in MeCN at 298 K.	302
Figure VIII. 2. Crystal structures of the cobalt complexes 1_{co}^{DMM} (50 % probability) and ^{Me}1_{co}^{DMM} (30 % probability). Solvent molecules and hydrogen atoms are omitted for clarity. Color code:	

cobalt (blue), nitrogen (light blue), oxygen (red), fluor (yellow), carbon (grey) and sulfur (orange).	302
Figure VIII. 3. On-line hydrogen evolved versus time with the cobalt complexes (50 μM), PS_{Ir} (250 μM) using $\text{CH}_3\text{CN}:\text{H}_2\text{O}:\text{Et}_3\text{N}$ (2:8:0.2 mL) as solvent and irradiated ($\lambda = 447 \text{ nm}$) at 25 $^\circ\text{C}$. 1_{Co}^{CO2Et} (blue), 1_{Co} (red), Me¹1_{Co} (purple), 1_{Co}^{CO2Et} (green) and Me¹1_{Co}^{CO2Et} (orange). TON= $n(\text{H}_2)/n(\text{Cat})$.	303
Figure VIII. 4. Photocatalytic activities of the studied catalysts in 10a formation under standard catalytic conditions.	304
Figure VIII. 5. <i>Left:</i> Online monitoring of the photochemical H_2 production in the absence (solid line) and presence of 9a (dashed line) for 1_{Co}^{CO2Et} (blue), 1_{Co} (red) and 1_{Co}^{DMM} (green). Conditions in absence of 9a : PS_{Ir} (2.5 μmol), 1^R (5 μmol). Conditions in presence of 9a : [9a] (0.168 mmol, 16.5 mM), PS_{Ir} (2.5 μmol , 1.5 mol%), 1^R (5.04 μmol , 3 mol%). Solvent mixture: $\text{MeCN}:\text{H}_2\text{O}:\text{Et}_3\text{N}$ (2:8:0.2 mL), Irradiation $\lambda = 447 \text{ nm}$ at 30 $^\circ\text{C}$ under N_2 . <i>Right:</i> Photocatalytic activities of 1_{Co}^{CO2Et} (blue), 1_{Co} (red) and 1_{Co}^{DMM} (green) in H_2 and 10a formation in the presence (pale-colored columns) and absence (dark-colored columns) of substrate. The black columns are the photocatalytic activities in 9a reduction.	305
Figure VIII. 6. <i>Left:</i> Online monitoring of the photochemical H_2 production at different concentrations of 9a : 2.0 (blue), 4.1 (orange), 6.2 (black), 8.3 (green), 12.4 (red), 16.5 (grey), 24.7 (purple), 32.9-49.4 (brown colors). <i>Right:</i> mmol of 10a (blue dots) and H_2 (red dots) obtained at the end of the catalytic assay. Conditions: Cobalt catalyst (1.7 μmol), PS_{Cu} (250 μM , 2.5 μmol), in $\text{MeCN}:\text{H}_2\text{O}:\text{Et}_3\text{N}$ (4:6:0.2 mL), irradiating at $\lambda = 447 \text{ nm}$, 30 $^\circ\text{C}$.	307
Figure VIII. 7. Photocatalytic activities of the tetradentate $[\text{Co}(\text{OTf})_2(\text{Me},\text{X},\text{Y}\text{Pytacn})]$ systems in 10a formation using standard catalytic conditions.	308

CHAPTER IX

Figure IX. 1. Homolytic and heterolytic mechanisms for ketone reduction catalyzed by a molecular cobalt complex.	321
Figure IX. 2. Emission spectra of PS_{Ir} upon excitation at 450 nm in the presence of different concentrations Et_3N (A), 9a (C) and 1_{Co} (E). Stern-Volmer plot for photoluminescence quenching of PS_{Ir} by Et_3N (B), 9a (D) and 1_{Co} (F).	326
Figure IX. 3. UV/Vis spectra at different irradiation times (447 nm). A) In dark. After B) 10 s of irradiation, C) after 100 s irradiation. D) After the addition of 1_{Co} . E) At half regeneration of PS_{Ir}^{II} after the addition of 1_{Co} . F) At fully regeneration of PS_{Ir}^{II} after the addition of 1_{Co} .	329
Figure IX. 4. UV/Vis monitoring ($\lambda = 527 \text{ nm}$) of PS_{Ir}^{III} photoreduction with Et_3N to form PS_{Ir}^{II} at $\lambda = 447 \text{ nm}$ and subsequent addition of different amounts of 1_{Co}^{II} catalyst: 0 μM "self-decay" (black), 1.25 μM (blue), 2.5 μM (orange), 5 μM (green), 7.5 μM (red), 10 μM (purple), 12.5 μM (grey) and 20 μM (light green). Conditions: [PS_{Ir}^{III}] = 50 μM , Et_3N = 2000 eq., V_{total} = 2 mL, $\text{CH}_3\text{CN}:\text{H}_2\text{O}$ (0.8 : 1.2) at 5 $^\circ\text{C}$, under N_2 .	330
Figure IX. 5. Titration of the photogenerated PS_{Ir}^{II} species with 1_{Co} . Consumption extent (ΔAbs (at $\lambda = 527 \text{ nm}$)) of the PS_{Ir}^{II} species at different additions of 1_{Co} . Values are duplicate average.	330
Figure IX. 6. UV/Vis monitoring ($\lambda = 527 \text{ nm}$) of PS_{Ir}^{III} photoreduction with Et_3N to form PS_{Ir}^{II} at $\lambda = 447 \text{ nm}$ and subsequent addition of solvent alone (red trace), 10 μM of 9a (green trace) and 10 μM 1_{Co} (purple trace). Conditions: [PS_{Ir}^{III}] = 50 μM , Et_3N = 2000 eq., reaction volume = 2 mL, $\text{CH}_3\text{CN}:\text{H}_2\text{O}$ (0.6 : 1.4) at 5 $^\circ\text{C}$, under N_2 .	331
Figure IX. 7. Cyclic voltammograms of 1_{Co} (1 mM, red), PS_{Ir} (1 mM, orange), PS_{Cu} (1 mM, green) and acetophenone (9a) (1 mM, blue) were recorded using Bu_4NPF_6 (0.1 M) as a supporting	

electrolyte and glassy carbon as working electrode in dry acetonitrile. Scan rate= 100 mV/s. For the irreversible waves, the E values have been determined at the half intensity of the wave. ⁵²² E ($\mathbf{1Co}^{III/I}$) = -1.10 V ; E ($\mathbf{PS}_{Ir}^{III/II}$) = -1.38 V; E ($\mathbf{PS}_{Cu}^{I/0}$) = -1.64 V, E ($\mathbf{9a}^{0/-1}$) = -2.14 V.	335
Figure IX. 8. Cyclic voltammograms of $\mathbf{1Co}$ (1 mM), \mathbf{PS}_{Ir} (250 μ M), \mathbf{PS}_{Cu} (250 μ M) and acetophenone ($\mathbf{9a}$) (1 mM) in the solvent mixture MeCN:H ₂ O (4:6) (blue) and MeCN:H ₂ O:Et ₃ N (4:6:0.2) (red dashed) using KNO ₃ (0.1 M) as a supporting electrolyte and glassy carbon as working electrode. Scan rate= 100 mV/s. For the irreversible waves, the E values have been determined at the half intensity of the wave. ⁵²² E ($\mathbf{1Co}^{III/II}$) = -1.34 V, E ($\mathbf{PS}_{Ir}^{III/II}$) = -1.47 V, E ($\mathbf{9}^{0/-1}$) = -1.65 V.	335
Figure IX. 9. Theoretical estimation of the pinacol yield (%) versus the percentage of \mathbf{PS}_{Ir}^{II} in solution for $\mathbf{9a}$ (E = - 1.65 V, left) and $\mathbf{9m}$ (E = - 1.74 V, right).	336
Figure IX. 10. Correlation between A) Yield pinacol-redox potential substrate B) Yield alcohol-redox potential substrate C) Yield alcohol – yield pinacol.	337
Figure IX. 11. Cyclic voltammetry of 3-phenylbutanal (5 mM) in the solvent mixture MeCN:H ₂ O (4:6) with KNO ₃ (0.1 M) as a supporting electrolyte, using glassy carbon working electrode and at scan rate of 100 mV/s.	339
Figure IX. 12. Effect of TEMPO in the formation of H ₂ and ketone reduction. <i>Top</i> : No TEMPO. <i>Bottom</i> : Presence of TEMPO (1 eq. versus $\mathbf{9a}$). Solid blue traces: H ₂ evolved versus time in the absence of $\mathbf{9a}$. Dashed orange traces: H ₂ evolved versus time in the presence of $\mathbf{9a}$. Dark dots: Formation of alcohol $\mathbf{10a}$ versus time. Reaction conditions: $\mathbf{9a}$ (0.126 mmol, 12.4 mM), \mathbf{PS}_{Ir} (2.5 μ mol, 2 mol%), $\mathbf{1Co}$ (3.8 μ mol, 3 mol%), MeCN:H ₂ O: Et ₃ N (3:7:0.2 mL), irradiating (λ = 447 nm) for 5 h at 30 °C under N ₂ . The red region corresponds to the time (0.5 h) that the activity was completely suppressed.	341
Figure IX. 13. Hammett plot analysis of the light-driven ketone reduction.	343
Figure IX. 14. Correlation between the relative reaction rates in the reduction of ring-substituted acetophenones and the redox potential of the substrate.	344
Figure IX. 15. <i>Top</i> : online MS-monitoring of the formation of H ₂ , HD and D ₂ (Ion current) versus time. Black traces: H ₂ evolved in the absence (black line) and presence of $\mathbf{9a}$ (dashed black line). Blue traces: HD evolved in the absence (blue line) and presence of $\mathbf{9a}$ (dashed blue line). Red traces: D ₂ evolved in the absence (red line) and presence of $\mathbf{9a}$ (dashed red line). <i>Bottom</i> : H ₂ /D ₂ , HD/D ₂ and H ₂ /HD ratios determined by the online MS-measurements versus the reaction time. Only ratios after the first 100 seconds are represented since measure errors in the beginning are larger. Ratios in presence (traces A, C, E) and absence of $\mathbf{9a}$ (traces B, D, F). Conditions: \mathbf{PS}_{Ir} (250 μ M), $\mathbf{1Co}$ (1 μ mol), MeCN:H ₂ O:D ₂ O: Et ₃ N (0.6:0.7:0.7:0.04), reaction volume= 2 mL, irradiated at λ = 447 nm at room temperature.	345
Figure IX. 16. (a) ¹³ C isotopic composition of the acetophenone recovered from a reaction taken at to 89.5% completion, relative to the starting acetophenone (b) ¹³ C KIEs (k_{12C}/k_{13C}) calculated from the results in (a). (c, d, e) Modelled ¹³ C KIEs (k_{12C}/k_{13C} , 25 °C) for the postulated mechanisms.	348
Figure IX. 17. ¹ H-NMR spectrum (CDCl ₃ , 500 MHz) of the benzylic CH ₂ :CHD signals. The ratio of the labelled:unlabelled products for the 4-Me-PhCHO:4-Me-PhCDO (1:1) reduction products was found to be 1.17. SDKIE= ^{Me} k _H / ^{Me} k _D = 1.17	351
Figure IX. 18. Reaction order versus $\mathbf{1Co}$ (A), \mathbf{PS}_{Ir} (B) and substrate (D). C) Initial rates in the reduction of $\mathbf{9s}$ (red), $\mathbf{9a}$ (green), $\mathbf{9i}$ (orange) and $\mathbf{9m}$ (blue).	352
Figure IX. 19. Calculated hydride donor abilities for selected main group hydrides in acetonitrile reported in the literature. ⁵⁵² Our calculated Co ^{III} -H and Co ^{II} -H intermediates are included in the diagram for comparison reasons. Figure adapted with permission from reference ⁵⁵² . Copyright (2015) American Chemical Society.....	355

Figure IX. 20. Global free energy profiles of the Co ^{II} -H heterolytic (green profile), Co ^{III} -H homolytic (black profile) and Co ^{II} -H homolytic (blue profile) mechanisms for the acetophenone reduction reaction. The L ₅ label refers to the Py ₂ ^{Ts} tacn ligand. Gibbs energies are in kcal·mol ⁻¹	356
Figure IX. 21. Heterolytic reduction performed by L ₅ Co ^{II} -H. Comparison between the free energy profiles for the reduction reaction of different organic substrates and water. The L ₅ label refers to the pentadentate Py ₂ ^{Ts} tacn ligand. Gibbs energies are in kcal·mol ⁻¹	357
Figure IX. 22. Setup for the online measurement of the H ₂ , HD and D ₂ ratios formed under light-driven conditions.	360
Figure IX. 23. ¹³ C enrichment after the reaction. Integration values of the C _B carbon compared to the para carbon set at 1000 before (Top) and after the recovery of the acetophenone at 89.5% of conversion (Bottom).	363
Figure IX. 24. <i>Left:</i> Simulated R/R ₀ values versus the conversion for a KIE value of 1.05. <i>Right:</i> Simulated KIE uncertainties versus the conversion. Uncertainties calculated with the Equation 6.	364

ANNEX

Figure A. 1. 1. ¹ H NMR (CDCl ₃ , 400 MHz, 300 K) spectrum of Py ₂ ^{Ts} tacn.	399
Figure A. 1. 2. ¹³ C{ ¹ H} NMR (CDCl ₃ , 101 MHz, 300 K) spectrum of Py ₂ ^{Ts} tacn.	399
Figure A. 2. 1. ¹ H-NMR spectra (500 MHz) of 1 ^{NMe₂} in CD ₃ CN at different temperatures.	402
Figure A. 2. 2. ¹ H-NMR spectra (500 MHz) of 1 ^{DMM} in CD ₃ CN at different temperatures.	403
Figure A. 2. 3. ¹ H-NMR spectra (500 MHz) of 1 ^{CO₂Et} in CD ₃ CN at different temperatures.	404
Figure A. 2. 4. ¹ H-NMR spectra (500 MHz) of 1 ^{CF₃} in CD ₃ CN at different temperatures.	405
Figure A. 2. 5. ¹ H-NMR spectra (500 MHz) of 1 ^{NO₂} in CD ₃ CN at different temperatures.	406
Figure A. 2. 6. ¹⁹ F-NMR spectra (500 MHz) of 1 ^H in CD ₃ CN at different temperatures.	407
Figure A. 2. 7. FT-IR spectra of 1 ^R complexes.	408
Figure A. 2. 8. Successive cyclic voltammograms obtained at different concentrations of TFA with different 1 ^R complexes (1 ^{NMe₂} (green), 1 ^{DMM} (red), 1 ^H (grey), 1 ^{Cl} (orange), 1 ^{CO₂Et} (blue) and 1 ^{CF₃} (black)). Conditions: 1 ^R (1 mM) in acetonitrile containing Bu ₄ NPF ₆ (0.1 M) in the presence of TFA (1 – 100 mM, as indicated in each case). Scan rate of 100 mV·s ⁻¹	414
Figure A. 3. 1. ¹ H-NMR spectra (500 MHz) of 1 _{Co^{II}Cl} in CD ₃ CN at different temperatures.	415
Figure A. 3. 2. ¹ H-NMR spectra (500 MHz) of 1 _{Co^{II}CH₃CN} in CD ₃ CN at different temperatures. ..	416
Figure A. 3. 3. ¹ H-NMR spectra (500 MHz) of 1 _{Co^ICl} in CD ₃ CN at different temperatures.	417
Figure A. 4. 1. ¹ H-NMR (CD ₃ CN, 400 MHz, 260 K) spectrum of [Co(OTf)(DPA-Bpy)](OTf).	420
Figure A. 4. 2. ¹ H-NMR (CD ₃ CN, 400 MHz, 260 K) spectrum of [Co(N4Py)(OTf)](OTf).	420
Figure A. 4. 3. ¹ H-NMR (CD ₃ CN, 400 MHz, 260 K) spectrum of [Co(OTf) ₂ ((S,S)-PDP)].	421
Figure A. 4. 4. ¹ H-NMR (CD ₃ CN, 500 MHz, 260 K) spectrum of [Co(Cl) ₂ (BpcMe)].	421
Figure A. 4. 5. ¹ H-NMR (CD ₃ CN, 500 MHz, 260 K) spectrum of [Co(OTf)(H-CDPy ₃)](OTf).	422
Figure A. 4. 6. Photocatalytic reduction of 9a into 10a with PS _{Co} at different ratios of MeCN:H ₂ O.	423
Figure A. 4. 7. Photocatalytic reduction of 9a into 10a with PS _{Co} at different ratios of MeCN:H ₂ O.	424
Figure A. 4. 8. ¹ H-NMR spectrum (CDCl ₃ , 400 MHz, 300 K) of the isolated product 10b using H ₂ O (Top) or D ₂ O (99.9 % in deuterium) (Bottom) in the solvent mixture. Conditions: 1 _{Co} (3.8 μmol, 3	

mol%), PS_{ir} (2.5 μmol, 2 mol%), substrate (0.126 mmol, 12.4 mM) in MeCN:H ₂ O(or D ₂ O):Et ₃ N (3:7:0.2 mL) irradiated at λ= 447 nm and 30 °C, under N ₂	426
Figure A. 4. 9. ¹³ C-NMR spectrum (CDCl ₃ , 101 MHz, 300 K) of the isolated product 10b using H ₂ O (Top) or D ₂ O (99.9 % in deuterium) (Bottom) in the solvent mixture. Conditions: 1_{co} (3.8 μmol, 3 mol%), PS_{ir} (2.5 μmol, 2 mol%), substrate (0.126 mmol, 12.4 mM) in MeCN:H ₂ O(or D ₂ O):Et ₃ N (3:7:0.2 mL) irradiated at λ= 447 nm and 30 °C, under N ₂	427
Figure A. 4. 10. ¹ H-NMR spectrum (CDCl ₃ , 400 MHz, 300 K) of the isolated product 10g using H ₂ O (Top) or D ₂ O (99.9 % in deuterium) (Bottom) in the solvent mixture. Conditions: 1_{co} (3.8 μmol, 3 mol%), PS_{ir} (2.5 μmol, 2 mol%), substrate (0.126 mmol, 12.4 mM) in MeCN:H ₂ O(or D ₂ O):Et ₃ N (3:7:0.2 mL) irradiated at λ= 447 nm and 30 °C, under N ₂	428
Figure A. 4. 11. ¹ H-NMR spectrum (CDCl ₃ , 400 MHz, 300 K) of the isolated product 10g using H ₂ O (Top) or D ₂ O (99.9 % in deuterium) (Bottom) in the solvent mixture. Conditions: 1_{co} (3.8 μmol, 3 mol%), PS_{ir} (2.5 μmol, 2 mol%), substrate (0.126 mmol, 12.4 mM) in MeCN:H ₂ O(or D ₂ O):Et ₃ N (3:7:0.2 mL) irradiated at λ= 447 nm and 30 °C, under N ₂	429
Figure A. 4. 12. ¹ H-NMR (CDCl ₃ , 400 MHz, 300 K) spectrum of the isolated product 5-Hydroxy-5-phenylpentan-2-one	430
Figure A. 4. 13. ¹ H- ¹ H COSY (CDCl ₃ , 400 MHz, 300 K) spectrum of the isolated product 5-Hydroxy-5-phenylpentan-2-one	430
Figure A. 4. 14. ¹³ C{ ¹ H}-NMR (CDCl ₃ , 101 MHz, 300 K) spectrum of the isolated product 5-Hydroxy-5-phenylpentan-2-one	431
Figure A. 4. 15. DEPTQ135 (CDCl ₃ , 400 MHz, 300 K) spectrum of the isolated product 5-Hydroxy-5-phenylpentan-2-one	431
Figure A. 4. 16. ¹ H- ¹³ C HSQC (CDCl ₃ , 400 MHz, 300 K) phase sensitive spectrum of the isolated product 5-Hydroxy-5-phenylpentan-2-one	432
Figure A. 4. 17. ¹ H- ¹³ C HMBC (CDCl ₃ , 400 MHz, 300 K) phase sensitive spectrum of the isolated product 5-Hydroxy-5-phenylpentan-2-one	432
Figure A. 4. 18. ¹ H-NMR (CDCl ₃ , 400 MHz, 300 K) spectrum of the isolated product 1-Phenyl-4-penten-1-ol	433
Figure A. 4. 19. ¹ H- ¹ H COSY (CDCl ₃ , 400 MHz, 300 K) spectrum of the isolated product 1-Phenyl-4-penten-1-ol	433
Figure A. 4. 20. ¹³ C{ ¹ H}-NMR (CDCl ₃ , 101 MHz, 300 K) spectrum of the isolated product 1-Phenyl-4-penten-1-ol	434
Figure A. 4. 21. DEPTQ135 (CDCl ₃ , 400 MHz, 300 K) spectrum of the isolated product 1-Phenyl-4-penten-1-ol	434
Figure A. 4. 22. ¹ H- ¹³ C HSQC (CDCl ₃ , 400 MHz, 300 K) phase sensitive spectrum of the isolated product 1-Phenyl-4-penten-1-ol	435
Figure A. 4. 23. ¹ H- ¹³ C HMBC (CDCl ₃ , 400 MHz, 300 K) phase sensitive spectrum of the isolated product 1-Phenyl-4-penten-1-ol	435
Figure A. 4. 24. ¹ H-NMR (CDCl ₃ , 400 MHz, 300 K) spectrum of the isolated product 1-Phenyl-4-pentyn-1-ol	436
Figure A. 4. 25. ¹ H- ¹ H COSY (CDCl ₃ , 400 MHz, 300 K) spectrum of the isolated product 1-Phenyl-4-pentyn-1-ol	436
Figure A. 4. 26. ¹³ C{ ¹ H}-NMR (CDCl ₃ , 101 MHz, 300 K) spectrum of the isolated product 1-Phenyl-4-pentyn-1-one	437
Figure A. 4. 27. DEPTQ135 (CDCl ₃ , 400 MHz, 300 K) spectrum of the isolated product 1-Phenyl-4-pentyn-1-ol	437

Figure A. 4. 28. ^1H - ^{13}C HSQC (CDCl_3 , 400 MHz, 300 K) phase sensitive spectrum of the isolated product 1-Phenyl-4-pentyn-1-ol	438
Figure A. 4. 29. ^1H - ^{13}C HMBC (CDCl_3 , 400 MHz, 300 K) phase sensitive spectrum of the isolated product 1-Phenyl-4-pentyn-1-ol	438
Figure A. 5. 1. ^1H - ^1H COSY (CDCl_3 , 400 MHz, 300 K) spectrum of $^{\text{H,CO}_2\text{Et}}\text{Py}_2^{\text{Ts}}\text{tacn}$	439
Figure A. 5. 2. $^{13}\text{C}\{^1\text{H}\}$ -NMR (CDCl_3 , 101 MHz, 300 K) spectrum of $^{\text{Me,OMe}}\text{Py}_2^{\text{Ts}}\text{tacn}$	439
Figure A. 5. 3. ^1H - ^1H COSY (CDCl_3 , 400 MHz, 300 K) spectrum of $^{\text{Me,OMe}}\text{Py}_2^{\text{Ts}}\text{tacn}$	440
Figure A. 5. 4. $^{13}\text{C}\{^1\text{H}\}$ NMR (CDCl_3 , 101 MHz, 300 K) spectrum of $^{\text{Me,OMe}}\text{Py}_2^{\text{Ts}}\text{tacn}$	440
Figure A. 5. 5. ^1H -NMR spectra (500 MHz) of $\mathbf{1}_{\text{Co}}^{\text{DMM}}$ in CD_3CN at different temperatures.....	441
Figure A. 5. 6. ^1H -NMR spectra (500 MHz) of $\mathbf{1}_{\text{Co}}^{\text{CO}_2\text{Et}}$ in CD_3CN at different temperatures.	442
Figure A. 6. 1. ^1H -NMR (400 MHz, 300 K) recorded at variable irradiation times (2.5-18 min) using $\text{CH}_3\text{CN}:\text{H}_2\text{O}:\text{Et}_3\text{N}$ (0.15:0.35:0.01 mL) as solvent mixture. Conditions: $\mathbf{1}_{\text{Co}}$ (0.189 μmol , 3 mol%), PS_{Ir} (0.076 μmol , 1.2 mol%) and $\mathbf{9a}$ (6.30 μmol , 12.6 mM) irradiated at $\lambda = 447$ nm in a NMR tube.	445
Figure A. 6. 2. ^1H -NMR (400 MHz, 300 K) recorded at variable irradiation times (2.5-18 min) using $\text{CH}_3\text{CN}:\text{D}_2\text{O}:\text{Et}_3\text{N}$ (0.15:0.35:0.01 mL) as solvent mixture. Conditions: $\mathbf{1}_{\text{Co}}$ (0.189 μmol , 3 mol%), PS_{Ir} (0.076 μmol , 1.2 mol%) and $\mathbf{9a}$ (6.30 μmol , 12.6 mM) irradiated at $\lambda = 447$ nm in a NMR tube.	446
Figure A. 6. 3. Determination of KIE by NMR. Formation of $\mathbf{10a}$ (μmol) versus time (min) in $\text{CH}_3\text{CN}:\text{H}_2\text{O}:\text{Et}_3\text{N}$ (3:7:0.2 mL) (blue dots, derived from Figure A. 6. 1) and $\text{CH}_3\text{CN}:\text{D}_2\text{O}:\text{Et}_3\text{N}$ (3:7:0.2 mL) (red squares, derived from Figure A. 6. 2), $\mathbf{1}_{\text{Co}}$ (0.189 μmol , 3 mol%), PS_{Ir} (0.076 μmol , 1.2 mol%) and $\mathbf{9a}$ (6.30 μmol , 12.6 mM) irradiated at $\lambda = 447$ nm in a NMR tube. The amount of $\mathbf{10a}$ was determined by ^1H -NMR (400 MHz, 300 K) using 4-nitroacetophenone as internal standard. $\text{KIE} = \text{rate in H}_2\text{O} / \text{rate in D}_2\text{O}$	447
Figure A. 6. 4. Plot $\mathbf{10a}$ (mmol) produced versus time (min) in $\text{CH}_3\text{CN}:\text{H}_2\text{O}:\text{Et}_3\text{N}$ (3:7:0.2 mL) (blue dots) and $\text{CH}_3\text{CN}:\text{D}_2\text{O}:\text{Et}_3\text{N}$ (3:7:0.2 mL) (red squares). Conditions: $\mathbf{1}_{\text{Co}}$ (3.8 μmol , 3 mol%), (PS_{Ir} (2.5 μmol , 2 mol%), substrate (0.126 mmol, 12.4 mM) under irradiation ($\lambda = 447$ nm). The amount of $\mathbf{10a}$ was determined by GC using 1,3,5-trimethoxybenzene as an internal standard. $\text{KIE} = \text{rate in H}_2\text{O} / \text{rate in D}_2\text{O}$	447
Figure A. 6. 5. UV/Vis monitoring ($\lambda = 527$ nm) of $\text{PS}_{\text{Ir}}^{\text{III}}$ photoreduction with Et_3N to form $\text{PS}_{\text{Ir}}^{\text{II}}$ at $\lambda = 447$ nm and subsequent addition of different amounts of $\mathbf{1}_{\text{Co}}^{\text{II}}$ catalyst (0, 1.25, 2.5, 5, 7.5, 10, 12.5 and 20 μM). Conditions: $[\text{PS}_{\text{Ir}}^{\text{III}}] = 50 \mu\text{M}$, $\text{Et}_3\text{N} = 2000$ eq., reaction volume = 2 mL, $\text{CH}_3\text{CN}:\text{H}_2\text{O}$ (0.6 : 1.4) at 5°C , under N_2 . Dark trace corresponds to the self-decay of the photogenerated $\text{PS}_{\text{Ir}}^{\text{II}}$ in the absence of $\mathbf{1}_{\text{Co}}^{\text{II}}$	448
Figure A. 6. 6. Cyclic voltammograms obtained with different substituted acetophenones (5 mM) in the solvent mixture $\text{MeCN}:\text{H}_2\text{O}:\text{Et}_3\text{N}$ (4:6:0.2 mL) using KNO_3 (0.1 M) as a supporting electrolyte. Scan rate = 100 mV/s, glassy carbon working electrode. Potentials are referenced versus SCE.....	449
Figure A. 6. 7. ^1H - ^1H COSY (CDCl_3 , 400 MHz, 300 K) spectrum of the isolated product 1,4-diphenylbutan-1-one (10ap)	450
Figure A. 6. 8. ^{13}C DEPT135 (CDCl_3 , 101 MHz, 300 K) spectrum of 1,4-diphenylbutan-1-one (10ap)	450
Figure A. 6. 9. ^1H -NMR (CDCl_3 , 400 MHz, 300 K) spectrum of p-tolylmethan- d_2 -ol ([D]-10v)..	451
Figure A. 6. 10. $^{13}\text{C}\{^1\text{H}\}$ -NMR (CDCl_3 , 101 MHz, 300 K) spectrum of p-tolylmethan- d_2 -ol ([D]-10v).	451

Figure A. 6. 11. ^1H -NMR (CDCl_3 , 400 MHz, 300 K) spectrum of 4-methyl-1-d₁-benzaldehyde ([D]-9v)	452
Figure A. 6. 12. $^{13}\text{C}\{^1\text{H}\}$ -NMR (CDCl_3 , 400 MHz, 300 K) spectrum of 4-methyl-1-d₁-benzaldehyde ([D]-9v)	452
Figure A. 6. 13. ^1H -NMR spectrum (CDCl_3 , 500 MHz) of the benzylic CH_2 :CHD signals. The ratio of the labelled:unlabelled products for the 4-OMe-PhCHO:4-OMe-PhCDO (1:1) reduction products was found to be 1.07. $\text{SDKIE} = \text{}^{\text{OMe}}\text{k}_\text{H}/\text{}^{\text{OMe}}\text{k}_\text{D} = \mathbf{1.07}$	453
Figure A. 6. 14. ^1H -NMR spectrum (CDCl_3 , 500 MHz) of the benzylic CH_2 :CHD signals. The ratio of the labelled:unlabelled products for the 3,5-Di- ^t Bu-PhCHO: 3,5-Di- ^t Bu-PhCDO (1:1) reduction products was found to be 1.19. $\text{SDKIE} = \text{}^{\text{tBu}}\text{k}_\text{H}/\text{}^{\text{tBu}}\text{k}_\text{D} = \mathbf{1.19}$	453

List of Schemes

CHAPTER I

- Scheme I. 1.** Schematic illustration of the natural photosynthetic energy transference chain (Z-scheme) and dark reaction (Calvin cycle). During the photosynthetic process, the photon energy is absorbed by the PS II and PS I, and the electrons generated from the oxidation of water by the oxygen-evolving complex are transferred to NADP⁺ reductase by means of an electron-transport chain comprised of pheophytin (Ph), plastoquinone (PQ), cytochrome b₆f (b₆f), plastocyanin (PC) and ferredoxin (FN). P680 and P700 = light-harvesting complexes containing reaction centers, located in PS II and PS I, respectively. 8
- Scheme I. 2.** Visible light-driven chemical synthesis in natural photosynthesis and biocatalyzed artificial photosynthesis. 35
- Scheme I. 3.** General scheme for biocatalyzed light-driven reactions. 36
- Scheme I. 4.** Plausible mechanism of asymmetric reduction of acetophenones based on multianthroquinone porphyrin as a visible-light harvester, promoting the reduction of NADP⁺ to NADPH. LKADH: alcohol dehydrogenase from *Lactobacillus kefir*. ET = Electron transfer. Adapted with permission from ref ²⁶¹. Copyright 2015 John Wiley and Sons. 37
- Scheme I. 5.** Schematic diagram of photochemical cofactor regeneration using an inorganic photosensitizer and their connection with L-glutamate dehydrogenase for the synthesis of L-glutamate from α -ketoglutarate. Reprinted with permission from ref 273. Copyright 2012 John Wiley and Sons. 38
- Scheme I. 6.** Schematic diagram of photochemical cofactor regeneration using H-SiNWs as photosensitizer and their connection with L-glutamate dehydrogenase for the synthesis of L-glutamate from α -ketoglutarate. Reprinted with permission from ref 276. Copyright 2016 Royal Society of Chemistry. 39
- Scheme I. 7.** Photobiocatalytic enantioselective reduction of ketoisophorone to (R)-levodione by an oxidoreductase enzyme mediated by FADH₂ using Au/TiO₂ as a semiconductor and water as a sacrificial electron donor. Reprinted with permission from ref 278. Copyright 2014 Nature Publishing Group. 39
- Scheme I. 8.** General scheme for light-driven reductions reactions using a synthetic catalyst. 41
- Scheme I. 9.** Reduction of carbonyl compounds catalyzed by Ir or Ru complexes and using CdS as photoredox catalyst. For **Ir cat**: $\lambda > 400$, 300 W Xe lamp. **Ru cat**: $\lambda > 420$, Xe lamp. 42
- Scheme I. 10.** Top: Proposed mechanism for the photocatalytic reduction of carbonyl compounds involving PF as photocatalyst and [Cp*Rh^{III}(bpy)Cl]Cl. Bottom: Chemoselective reduction of benzaldehyde in the presence of acetophenone. Reprinted with permission from ref 286. Copyright 2015 The Royal Society of Chemistry. 43
- Scheme I. 11.** Proposed mechanism for semihydrogenation of alkynes. 45

CHAPTER III

- Scheme III. 1.** Synthesis of ligand Py₂^{Ts}tacn and complexes **1_{Fe}**, **1_{Co}** and **1_{Ni}**. The ORTEP structure with ellipsoids set at the 50% probability level of Py₂^{Ts}tacn ligand from the X-Ray diffraction analysis is also depicted. Hydrogen atoms have been omitted for clarity. 57
- Scheme III. 2.** Differences in reactivity among **1_{Fe}**, **1_{Co}** and **1_{Ni}** in single electron reduction process to M^I species and the subsequent protonation to yield the M^{III}-H species under photochemical conditions. pK_a values have been obtained by DFT calculations. 81
- Scheme III. 3.** Synthesis of Py₂^{Ts}tacn. 86
- Scheme III. 4.** Synthesis of [Fe(OTf)(Py₂^{Ts}tacn)](OTf). 87

Scheme III. 5. Synthesis of $[\text{Co}(\text{OTf})(\text{Py}_2^{\text{Tstacn}})](\text{OTf})$	87
Scheme III. 6. Synthesis of $[\text{Ni}(\text{OTf})(\text{Py}_2^{\text{Tstacn}})](\text{OTf})$	88

CHAPTER IV

Scheme IX. 1. Oxidative and reductive quenching cycle of PS_{Ir}	324
Scheme IX. 2. Plausible oxidative quenching pathway of $\text{PS}_{\text{Ir}}^{\text{III}^*}$ through Et_3N as electron donor.	327
Scheme IX. 3. Plausible reductive quenching pathway operating under photocatalytic conditions for PS_{Ir} through Et_3N as electron donor and the subsequent oxidation of the $\text{PS}_{\text{Ir}}^{\text{II}}$	332
Scheme IX. 4. Reactivity of ketones in the presence and absence of cobalt catalyst under photocatalytic conditions.....	334
Scheme IX. 5. Conversion of 9y into 3-phenylbutan-1-ol (10y) and 3-phenyl-2-en-1-ol (9ak). 338	
Scheme IX. 6. Heterolytic and homolytic pathway for the reduction of aryl cyclopropyl ketones.	340
Scheme IX. 7. Two possible mechanistic pathways with their corresponding kinetic isotopic effect.	347
Scheme IX. 8. Two possible mechanistic pathways with their corresponding expected SDKIE.	349
Scheme IX. 9. General scheme of the reduction of labelled aldehydes [D]-9v-x	350
Scheme IX. 10. Strategy followed for the SDKIE determination.....	350
Scheme IX. 11. Proposed mechanism for the photocatalytic ketone reduction catalyzed by cobalt complexes.	354

CHAPTER V

Scheme V. 1. Synthesis of the biotinylated complexes 1^{Biotin} and 1^{Spacer-Biotin} employed in this work.	164
Scheme V. 2. Synthesis of the basic structure Py_2tacnH	192
Scheme V. 3. Synthesis of $\text{Py}_2\text{tacn-Biotin}$	193
Scheme V. 4. Synthesis of 4- NO_2 -spacer- Py_2tacn	193
Scheme V. 5. Synthesis of 4- NH_2 -spacer- Py_2tacn	194
Scheme V. 6. Synthesis of $\text{Py}_2\text{tacn-spacer-Biotin}$	194

CHAPTER VI

Scheme VI. 1. Synthesis of compounds $\mathbf{1}_{\text{Co}^n\text{L}}$ ($n = \text{II or III}$ and $\text{L} = \text{NCCH}_3$ or Cl).	203
Scheme VI. 2. Synthesis of $\mathbf{1}_{\text{Co}^{\text{I}}\text{Cl}}$ and their reactivity with $\text{Na}(\text{BPh}_4)$	206
Scheme VI. 3. Synthesis of compounds $\text{Me}^n\mathbf{1}_{\text{Co}^n}$ ($n = \text{I or II}$).	213
Scheme VI. 4. Synthesis of $[\text{Co}^{\text{I}}(\text{Cl})(\text{Py}_2^{\text{Tstacn}})](\mathbf{1}_{\text{Co}^{\text{I}}\text{Cl}})$	227
Scheme VI. 5. Synthesis of $[\text{Co}^{\text{II}}(\text{Cl})(\text{Py}_2^{\text{Tstacn}})](\text{Cl})$ ($\mathbf{1}_{\text{Co}^{\text{II}}\text{Cl}}$).	228
Scheme VI. 6. Synthesis of $[\text{Co}^{\text{II}}(\text{Py}_2^{\text{Tstacn}})(\text{CH}_3\text{CN})](\text{OTf})_2$ ($\mathbf{1}_{\text{Co}^{\text{II}}\text{CH}_3\text{CN}}$).	228
Scheme VI. 7. Synthesis of $[\text{Co}^{\text{II}}(\text{Py}_2^{\text{Tstacn}})(\text{CH}_3\text{CN})](\text{OTf})_2(\text{BF}_4)$ ($\mathbf{1}_{\text{Co}^{\text{II}}\text{CH}_3\text{CN}}$).	229
Scheme VI. 8. Synthesis of $[\text{Co}^{\text{II}}(\text{Cl})(\text{Py}_2^{\text{Tstacn}})](\text{Cl})(\text{BF}_4)$ ($\mathbf{1}_{\text{Co}^{\text{II}}\text{Cl}}$).....	229
Scheme VI. 9. Synthesis of $[\text{Co}^{\text{II}}(\text{Py}_2^{\text{Metacn}})(\text{CH}_3\text{CN})](\text{OTf})_2$ ($\text{Me}^n\mathbf{1}_{\text{Co}^{\text{II}}}$).	230

CHAPTER VII

Scheme VII. 1. General scheme for the synthesis of M-H and the reduction of carbonyl compounds.....	234
Scheme VII. 2. A) Stability of 9a-Pinacol under standard catalytic conditions. 9a-Pinacol was fully recovered without formation of traces of other products. B) Reduction of 9a to 10a in the presence of 1 eq. of 9a-Pinacol . C) Reduction of 9a in the presence of 1 eq. of 10a	241

Scheme VII. 3. Synthesis of the Cu ^I -based photoredox catalyst PS_{Cu} .	252
Scheme VII. 4. Synthesis of the deuterium-labeled alcohols [D]-10a, [D]-10b, [D]-10g .	264
Scheme VII. 5. Selective reduction of aromatic ketones in the presence of aliphatic ketones, aldehyde, alkene and alkyne. The conditions employed using PS_{Ir} and PS_{Cu} are described in Table VII. 3.	266
Scheme VII. 6. Analysis of the steric effects by competition experiments.	270
Scheme VII. 7. General proposed mechanism for the reduction of ketones, aldehydes and H ₂ involving a common cobalt intermediate.	272
Scheme VII. 8. Asymmetric reduction of 9c, 9b, 9a and 9j catalyzed by [Co(OTf) ₂ ((S,S)-PDP)].	273
Scheme VII. 9. General scheme for the chiral reduction of ketones using H ₂ O and light catalyzed by a homogeneous chiral cobalt catalyst.	273
Scheme VII. 10. Synthesis of [Co(OTf)(DPA-Bpy)](OTf).	279
Scheme VII. 11. Synthesis of [Co(OTf)(N4Py)](OTf).	281
Scheme VII. 12. Synthesis of [Co(OTf) ₂ ((S,S)-PDP)].	282
Scheme VII. 13. Synthesis of [Co(BpcMe)Cl ₂] and [Co(OTf)(H-CDPy ₃)](OTf).	284
Scheme VII. 14. Synthesis of 1-phenyl-4-en-1-one (9ah).	292
Scheme VII. 15. Synthesis of 1-Phenyl-4-pentyn-1-one (9ai).	293

CHAPTER VIII

Scheme VIII. 1. General scheme for the preparation of the ligands and complexes employed in this study.	300
Scheme VIII. 2. Synthesis of ^{Me,OMe} Py ₂ ^{Ts} tacn.	312
Scheme VIII. 3. Synthesis of ^{H,CO₂Et} Py ₂ ^{Ts} tacn.	313
Scheme VIII. 4. Synthesis of ^{Me,OMe} Py ₂ ^H tacn.	313
Scheme VIII. 5. Synthesis of ^{Me,OMe} Py ₂ ^{Me} tacn.	314
Scheme VIII. 6. Synthesis of 1_{Co}^{CO₂Et} .	315
Scheme VIII. 7. Synthesis of 1_{Co}^{DMM} .	315
Scheme VIII. 8. Synthesis of ^{Me} 1_{Co}^{DMM} .	316

CHAPTER IX

Scheme IX. 1. Oxidative and reductive quenching cycle of PS_{Ir} .	324
Scheme IX. 2. Plausible oxidative quenching pathway of PS_{Ir}^{III*} through Et ₃ N as electron donor.	327
Scheme IX. 3. Plausible reductive quenching pathway operating under photocatalytic conditions for PS_{Ir} through Et ₃ N as electron donor and the subsequent oxidation of the PS_{Ir}^{II} .	332
Scheme IX. 4. Reactivity of ketones in the presence and absence of cobalt catalyst under photocatalytic conditions.	334
Scheme IX. 5. Conversion of 9y into 3-phenylbutan-1-ol (10y) and 3-phenyl-2-en-1-ol (9ak).	338
Scheme IX. 6. Heterolytic and homolytic pathway for the reduction of aryl cyclopropyl ketones.	340
Scheme IX. 7. Two possible mechanistic pathways with their corresponding kinetic isotopic effect.	347
Scheme IX. 8. Two possible mechanistic pathways with their corresponding expected SDKIE.	349
Scheme IX. 9. General scheme of the reduction of labelled aldehydes [D]-9v-x .	350
Scheme IX. 10. Strategy followed for the SDKIE determination.	350
Scheme IX. 11. Proposed mechanism for the photocatalytic ketone reduction catalyzed by cobalt complexes.	354

List of Tables

CHAPTER III

Table III. 1. Selected bond lengths [Å] and angles [°] for 1_{Co} and 1_{Ni}	59
Table III.2. Redox potentials for the studied complexes 1_{Fe} , 1_{Co} and 1_{Ni} in anhydrous CH ₃ CN, and CH ₃ CN/H ₂ O mixtures.	72
Table III. 3. Computed free energy (ΔG) for coordination of CH ₃ CN and H ₂ O to 1_M and for ligand exchange reactions: ^a	80
Table III. 4. DFT computed reduction potentials (V) and pK _a values of the proposed cobalt, nickel and iron intermediates. ^a	80

CHAPTER IV

Table IV. 1. Experimentally observed transition energies and absorption coefficients.	106
Table IV. 2. Redox potentials for the studied complexes in anhydrous CH ₃ CN.....	109
Table IV. 3. Photochemical activities of 1^R complexes in H ₂ production.	112
Table IV. 4. Summary of the KIE^g and KIE^{sel} measured.	124
Table IV. 5. Summary of the experimental and theoretical E(Co ^{II/I}) and E(Co ^{III/II}) redox values vs. SCE and the theoretical pK _a (Co ^{III} -H) values of 1^R complexes.....	132

CHAPTER V

Table V. 1. Redox potentials (V) and overpotentials (η) of 1^{Biotin} and 1^{Biotin} C SA measured in aqueous solution at different pH values.	181
Table V. 2. Redox potentials (V) and overpotentials (η) of 1^{Spacer-Biotin} and 1^{Spacer-Biotin} C SA measured in aqueous solution at different pH values.	181
Table V. 3. Light-driven water reduction to H ₂ of 1^{Spacer-Biotin} and 1^{Spacer-Biotin} C SA at different pH.	185
Table V. 4. Photocatalytic activities in H ₂ evolution using PS_{Cu} as photoredox catalyst.....	188

CHAPTER VI

Table VI. 1. Selected theoretical and experimental distances (Å) obtained by EXAFS and X-ray.	211
---	-----

CHAPTER VII

Table VII. 1. Screening conditions for the light-driven acetophenone reduction.	237
Table VII. 2. Cobalt salts screened in presence and absence of Py ₂ ^T tacn ligand and substrate 9a	246
Table VII. 3. Light-driven reduction of selected carbonyl compounds.....	249
Table VII. 4. Yields of 9-pinacols obtained in the control experiments in the absence of cobalt catalyst.	251
Table VII. 5. Control experiments when using PS_{Cu} as chromophore.....	256
Table VII. 6. Log-Plot of the mmol produced of 10_R (R (bulky substituent)= Me, Et, <i>n</i> Bu, ⁱ Pr or CH ₂ ⁱ Pr) relative to 10a as a function of the Charton values (ν) using standard catalytic conditions. Reaction time: 30 min. Charton values: ν (Me)= 0.52, ν (Et)= 0.56, ν (<i>n</i> Bu)= 0.68, ν (ⁱ Pr)= 0.76, ν (CH ₂ ⁱ Pr)= 0.98.	271

CHAPTER IX

Table IX. 1. Formation of 9-pinacol for selected substrates in the absence of cobalt catalyst.	333
---	-----

Table IX. 2. Effects of the ring-substitution on rates of acetophenone reduction by 1_{Co} under photochemical conditions.....	342
Table IX. 3. SDKIEs for the reduction of substituted aldehydes.	351
Table IX. 4. Average ¹³ C integration values for acetophenone.....	362
Table IX. 5. <i>R/R_o</i> calculated values for acetophenone.	364
Table IX. 6. ¹³ C KIEs values calculated from Table IX. 5 and Eq. IX. 4.	365

Table IX. 1. Formation of 9-pinacol for selected substrates in the absence of cobalt catalyst.	333
---	-----

Table IX. 2. Effects of the ring-substitution on rates of acetophenone reduction by 1_{Co} under photochemical conditions.....	342
Table IX. 3. SDKIEs for the reduction of substituted aldehydes.	351
Table IX. 4. Average ¹³ C integration values for acetophenone.....	362
Table IX. 5. <i>R/R_o</i> calculated values for acetophenone.	364
Table IX. 6. ¹³ C KIEs values calculated from Table IX. 5 and Eq. IX. 4.	365

ANNEX

Table A. 1. 1. Crystal data and refinement details for Py₂^{Ts}tacn , 1_{Co} and 1_{Ni}	400
--	-----

Table A. 1. 2. Screening catalytic conditions of photochemical water reduction of 1_{Co}	401
---	-----

Table A. 2. 1. Selected Bond Lengths (Å) and Angles (°) for 1^{NO2} , 1^{CO2Et} and 1^{Cl}	409
--	-----

Table A. 2. 2. Selected Bond Lengths (Å) and Angles (°) for 1^H , 1^{DMM} and 1^{NMe2}	410
--	-----

Table A. 2. 3. Crystal Data for 1^{NO2} , 1^{CO2Et} and 1^{Cl}	411
---	-----

Table A. 2. 4. Crystal Data for 1^H , 1^{DMM} and 1^{NMe2}	412
--	-----

Table A. 2. 5. Crystal Data for Co^{(H,NO2)Py^{Me}tacn}(MeCN)₂(OTf)₂	413
---	-----

Table A. 3. 1. Crystal Data for 1_{Co^{II}}^{CH3CN} , 1_{Co^{II}}^{Cl} and 1_{Co^{III}}^{CH3CN}	418
--	-----

Table A. 3. 2. Selected Bond Lengths (Å) and Angles (°) for 1_{Co^{II}}^{CH3CN} , 1_{Co^{II}}^{Cl} and 1_{Co^{III}}^{CH3CN}	419
--	-----

Table A. 4. 1. Photocatalytic reduction of 9a with PS_{Cu} at different ratios of MeCN:H ₂ O.....	423
---	-----

Table A. 4. 2. Photocatalytic reduction of 9a using different PS_{Cu} loadings.	424
---	-----

Table A. 4. 3. Photocatalytic reduction of 9a using different 1_{Co} loadings.	425
--	-----

Table A. 5. 1. Crystal Data for 1_{Co^{II}}^{MeCN} , 1_{Co^{II}}^{Cl} and 1_{Co^{III}}^{MeCN}	443
---	-----

Table A. 5. 2. Selected Bond Lengths (Å) and Angles (°) for 1_{Co^{II}}^{MeCN} , 1_{Co^{II}}^{Cl} and 1_{Co^{III}}^{MeCN}	444
--	-----

Agraïments

Estic a punt de tancar una etapa molt important de la meua vida que, sense cap dubte, ha estat una època inoblidable no només per tot el que he après sinó que també per la gent que he conegut.

Voldria dedicar aquestes primeres línies per mostrar el més sencer agraïment al Dr. Julio Lloret, el meu director de tesi. Julio, m'és molt difícil expressar el meu agraïment escrivint quatre paraules. M'ha encantat treballar amb tu ja que m'has transmès el teu entusiasme per la química, la teua implicació amb la recerca i sobretot el teu afany per descobrir coses noves i intentar entendre la química fins a l'últim detall, que tots sabem que no és gens fàcil. Gràcies per la teua plena disposició a ajudar-me en tot moment, per transmetre'm aquest esperit de superació amb mi mateix, per tot el que m'has ensenyat i per fer-me creure que un no es pot rendir davant les dificultats. T'agraeixo també la teua paciència, els teus consells i els teus ànims que m'han fet falta en els moments més durs. Per últim, estic molt content que m'hagis donat la oportunitat de poder-me incorporar en el teu grup de recerca a l'Institut Català d'Investigació Química (ICIQ). Ha estat una última etapa de la tesi molt enriquidora i que no oblidaré mai.

També vull donar especial agraïment al Dr. Miquel Costas, per haver-me ajudat quan ho he necessitat, per els seus consells i per les seves aportacions durant el transcurs de la Tesi. Miquel, moltes gràcies per la confiança que amb en Xavi vàreu dipositar en mi, i per permetre'm iniciar el doctorat en el vostre grup de recerca.

Mirant ara la tesi ja acabada, em sembla que hem fet una bona feina tenint en compte que fa 4 anys vàrem començar des de "zero". Estic molt orgullós de tot el que hem fet i de tot el que hem après. Moltes gràcies per tot!

També vull fer extensible el meu agraïment a tots els companys del QBIS, especialment a en Xavi Ribas i a l'Anna Company, els quals sempre m'han ajudat quan ho he necessitat i per ser tant bona gent. Tampoc em vull oblidar de tots els altres membres del QBIS, en concret els meus companys de Màster i laboratori (Gerard, Joan i Olaf) per tots els bons moments que hem compartit i per l'ajuda que ens hem prestat mútuament, com també a la Mireia, Mercè, Irene, Raquel, Mònica, Oriol, Cristina, Jordi....

Gràcies també a tots els companys del grup de recerca de l'ICIQ (Federico, Alicia, Noufal, Miguel, Katia, Klaudia, Suvendu i Felix) per ser tant bons companys i per ajudar-me quan ho he necessitat. Voldria fer especial èmfasi a la Carla. Carla, amb tu vaig començar aquí a l'ICIQ. No et negaré que els començaments sempre són difícils i sense tu hagués estat tot més complicat. Ha estat un plaer compartir laboratori amb tu. Moltes gràcies per la teua ajuda i per ser-hi en tot moment.

També valoro especialment l'oportunitat que em va donar la Dr. Giovanna Ghirlanda per realitzar l'estada doctoral a la Arizona State University (EUA). Va ser una gran experiència poder desenvolupar les metal·loproteïnes de cobalt en aquesta universitat a on hi treballen científics de primer nivell.

Vull destacar que el treball inclòs en aquesta memòria no hagués estat possible sense les aportacions i el treball de diverses persones. En primer lloc, els càlculs teòrics han estat realitzats pel Dr. Ferran Acuña i per en Sergi Fernández, sota la supervisió del Dr. Josep M^a Luis (Universitat de Girona) i el Dr. Julio Lloret. Han fet una gran feina per poder calcular estructures i camins de reacció que no són gens fàcils de modelar. Gràcies a la seva aportació hem pogut obtenir dades

mecanístiques molt interessants i estic segur que ens serviran per futurs treballs. Moltes gràcies. Vull fer extensible el meu agraïment al Dr. Vlad Martin (Universitat de Girona) per els seus extraordinaris anàlisis de EXAFS, els quals han estat clau per entendre la naturalesa de l'intermedi de Co^I. També han col·laborat la Dr. Cristina Sáenz (ICIQ) i el Dr. José Ramón Galan (ICIQ) per fer les mesures de magnetisme a l'SQUID i Dr. Noufal Kandoth (ICIQ) per experiments a l'UV.

Voldria expressar el més sincer agraïment a la Universitat de Girona i al Ministerio de Educación i Ciencia per les beques predoctorals BRGR-07 i AP2012-6436, així com els projectes de financiació FP7-PEOPLE-2010-ERG-268445, ERC-2009-StG-239910, ERC-2014-CoG-648304, CTQ2012-37420-C02-01/BQU i INP-2011-0059-PCT-420000-ACT1.

També, com no, a la colla de Vidreres perquè malgrat que moltes vegades no podem quedar, sé que us tinc pel que faci falta. Sou una part una part molt important a la meua vida. Per suposat, tampoc en vull oblidar d'esmentar la colla del Ranxo de Vidreres que, per mi, sou com una família. No canvieu mai.

I finalment, un agraïment molt especial a la meua família i sobretot als meus pares que estimar-me tant, per ajudar-me el dia a dia i per recolzar-me sempre en les decisions que he pres i per entendre quin és el camí que vull seguir. M'heu demostrat que treballant es pot arribar lluny i gràcies a vosaltres avui sóc on sóc. Al meu germà, en Jaume, i a l'Estefania, els hi vull donar les gràcies per ser com són, i per aguantar les bromes i rampells que tinc a vegades. Voldria també fer un record molt especial al meu avi, a qui sempre tindrè present i que hauria estat molt orgullós de veure aquesta tesi. I, per acabar, voldria dedicar aquestes últimes paraules a la Marina, qui ha estat al meu costat en aquests últims anys. Gràcies per estimar-me tant, per aguantar a vegades algunes situacions i per recolzar-me en tot moment. Gràcies per fer-te imprescindible en la meua vida, per tots els moments que hem viscut i per tots els que viurem, tant si estem aprop com lluny.

Moltes gràcies a tots!

Arnau

Table of Contents

Abstract.....	1
Resum.....	2
Resumen.....	3
CHAPTER I. GENERAL INTRODUCTION.....	5
I.1. WORLD ENERGY PROBLEM	7
I.2. NATURAL PHOTOSYNTHESIS	8
I.3. TOWARDS ARTIFICIAL PHOTOSYNTHESIS.....	9
I.4. HYDROGEN PRODUCTION IN THE NATURE: HYDROGENASE ENZYMES.....	10
I.5. MOLECULAR COMPLEXES FOR H ₂ EVOLUTION	12
I.5.1. Catalytic Systems Based on Iron	12
I.5.2. Catalytic Systems Based on Nickel	13
I.5.3. Catalytic Systems Based on Cobalt.....	17
I.5.4. Hydrogen Evolution Mechanisms in Cobalt-Based Catalysts.....	24
I.6. ARTIFICIAL BIOMOLECULAR SYSTEMS FOR HYDROGEN PRODUCTION	25
I.6.1. Peptide-Catalyst Assemblies	26
I.6.2. Protein-Catalyst Hybrids.....	27
I.6.3. Biocatalytic Systems Made by Metal-Substitution	30
I.7. CATALYTIC SYSTEMS FOR THE REDUCTION OF ORGANIC MOLECULES WITH LIGHT	33
I.7.1. Use of Light for Challenging Organic Chemical Transformations.....	33
I.7.2. Coupling Visible-Light Photoredox Catalysis with Biocatalytic Systems for the Reduction of Organic Molecules	35
I.7.3. Light-Driven Reduction of Organic Molecules Catalyzed by Non-Biological Systems....	41
I.7.3.1. Photocatalytic reduction of ketones and aldehydes.....	42
I.7.3.2. Photocatalytic reduction of alkenes.....	43
I.7.3.3. Photocatalytic reduction of alkynes.....	45
CHAPTER II. MAIN OBJECTIVES.....	47
CHAPTER III. PHOTO- AND ELECTROCATALYTIC H₂ PRODUCTION BY NEW FIRST-ROW TRANSITION-METAL COMPLEXES BASED ON AN AMINOPYRIDINE PENTADENTATE LIGAND.....	53
III.1. STATE-OF-THE ART	55
III.2. RESULTS AND DISCUSSION.....	57
III.2.1. Synthesis and Characterization of the Py₂^{Ts}tacn Co, Ni and Fe Complexes	57
III.2.2. Photocatalytic Water Reduction to H ₂	60
III.2.2.1. Effect of the metal.....	60
III.2.2.2. Effect of the photosensitizer	61

III.2.2.3. Effect of the sacrificial electron donor and the solvent mixture	62
III.2.2.4. Effect of the photosensitizer and catalyst concentration	63
III.2.2.5. Regeneration of the catalytic activity	64
III.2.2.6. Effect of the O ₂ presence in the catalytic activity	65
III.2.2.7. Mechanistic studies.....	66
III.2.2.8. Study of the formation of nanoparticles during catalysis	69
III.2.3. Electrochemical Proton Reduction to H ₂	71
III.2.4. Mechanistic Considerations	78
III.3. EXPERIMENTAL SECTION.....	83
III.3.1. General Methods	83
III.3.2. Instrumentation	83
III.3.3. X-ray Crystallography	83
III.3.4. Gas-Evolution Monitoring Studies	84
III.3.5. Gas-Evolution Studies Performed in the Presence of Hg ⁰	84
III.3.6. Parallel Pressure Transducer Hardware.....	85
III.3.7. Gas Chromatography Identification and Quantification of Gases	85
III.3.8. Acid Concentration Dependence Study	86
III.3.9. Catalyst Concentration Dependence Study	86
III.3.10. Synthesis of Complexes and Characterization	86
III.3.10.1. Synthesis of 1,4-di(picolyl)-7-(p-toluenesulfonyl)-1,4,7-triazacyclononane, (Py ₂ ^{Ts} tacn).....	86
III.3.10.2. Synthesis of [Fe(OTf)(Py ₂ ^{Ts} tacn)](OTf) (1_{Fe})	87
III.3.10.3. Synthesis of [Co(OTf)(Py ₂ ^{Ts} tacn)](OTf) (1_{Co})	87
III.3.10.4. Synthesis of [Ni(OTf)(Py ₂ ^{Ts} tacn)](OTf) (1_{Ni}).....	88
III.3.11. Electrochemical Reduction of Protons.....	89
III.3.11.1. Determination of the E _{1/2} , overpotential and reaction orders.....	89
III.3.12. Theoretical Studies.....	90
III.3.12.1. Computational details	90
III.3.12.2. Redox potentials and pK _a values	90
CHAPTER IV. INFLUENCE OF THE ELECTRONIC EFFECTS ON THE H₂ EVOLUTION CATALYZED BY COBALT COMPLEXES BASED ON N-TETRADENTATE PYTACN TYPE LIGANDS.....	93
IV.1. STATE-OF-THE-ART.....	95
IV.2. RESULTS AND DISCUSSION.....	97
IV.2.1. Synthesis and Characterization of the Cobalt Complexes	97
IV.2.1.1. ¹ H-NMR spectroscopy	98
IV.2.1.2. Effective magnetic moment.....	104

IV.2.1.3. UV/Vis spectroscopy	105
IV.2.1.4. Solid-state characterization	107
IV.2.1.5. Cyclic voltammetry studies	108
IV.2.2. Photocatalytic water reduction to H ₂	111
IV.2.2.2. Dependence of cobalt concentration in light-driven water reduction	115
IV.2.2.3. Reactivity of photogenerated [Ir ^{II} (ppy) ₂ (bpy)] (PS _{Ir^{II}}) with 1^R	118
IV.2.2.4. Labelling experiments with D ₂ O	120
IV.2.2.5. Eyring plot with 1^{CO₂Et}	126
IV.2.2.6. Study of the effect of the presence of O ₂ in the photochemical catalytic activity	127
IV.2.2.7. Mechanistic considerations and DFT calculations	129
IV.2.3. Electrocatalytic Proton Reduction to H ₂	135
IV.3. EXPERIMENTAL SECTION	141
IV.3.1. General Methods	141
IV.3.2. Physical Methods	141
IV.3.3. Gas-Evolution-Monitoring Studies	143
IV.3.4. Gas-Evolution Studies Performed in the Presence of Hg ⁰	143
IV.3.5. UV/Vis Measurements with On-line Irradiation	144
IV.3.6. Calibration of the on-line MS monitoring formation of H ₂ , HD and D ₂	144
IV.3.7. Acid Concentration Dependence Study	145
IV.3.8. Synthesis of Ligands	145
IV.3.8.1. Synthesis of 1,4-dimethyl-1,4,7-triazacyclononane trihydrobromide, Me ₂ tacn·3HBr	145
IV.3.8.2. Synthesis of the ligand 1,4-dimethyl-7-(4-nitro-2-pyridylmethyl)-1,4,7-triazacyclononane, ^{H,NO₂} Py ^{Me} tacn	147
IV.3.8.3. Synthesis of the ligand 1,4-dimethyl-7-(4-trifluoromethyl-2-pyridylmethyl)-1,4,7-triazacyclononane, ^{H,CF₃} Py ^{Me} tacn	149
IV.3.8.4. Synthesis of the ligand 1,4-dimethyl-7-(4-ethoxycarbonyl-2-pyridylmethyl)-1,4,7-triazacyclononane, ^{H,CO₂Et} Py ^{Me} tacn	151
IV.3.8.5. Synthesis of the ligand 1,4-dimethyl-7-(4-chloro-2-pyridylmethyl)-1,4,7-triazacyclononane, ^{H,Cl} Py ^{Me} tacn	153
IV.3.8.6. Synthesis of the ligand 1,4-dimethyl-7-(2-pyridylmethyl)-1,4,7-triazacyclononane, ^{H,H} Py ^{Me} tacn	155
IV.3.8.7. Synthesis of the ligand 1,4-dimethyl-7-(3,5-dimethyl-4-methoxy-2-pyridylmethyl)-1,4,7-triazacyclononane, ^{Me,OMe} Py ^{Me} tacn	156
IV.3.8.8. Synthesis of the ligand 1,4-dimethyl-7-(4-dimethylamino-2-pyridylmethyl)-1,4,7-triazacyclononane, ^{H,NMe₂} Py ^{Me} tacn	156
IV.3.9. Synthesis of Complexes	158

CHAPTER V. IMPROVED ACTIVITY AND STABILITY OF A COBALT REDUCTION CATALYST BY SUPRAMOLECULAR CONFINEMENT IN STREPTAVIDIN..... 161

V.1. STATE-OF-THE-ART.....	163
V.2. RESULTS AND DISCUSSION.....	164
V.2.1. Synthesis of Ligands and Cobalt Complexes	164
V.2.2. Synthesis, Purification and Characterization of the 1^{Biotin} C SA and $1^{\text{Spacer-Biotin}}$ C SA metalloenzymes	167
V.2.2.1 Interaction of Streptavidin with 1^{Biotin} and $1^{\text{Spacer-Biotin}}$	167
V.2.2.2 Synthesis and Purification.....	172
V.2.2.3 Characterization.....	173
V.2.3. Electrocatalytic Water Reduction to Hydrogen	176
V.2.4. Photoinduced Water Reduction to Hydrogen	184
V.3. EXPERIMENTAL SECTION	190
V.3.1. Materials	190
V.3.2. Instrumentation and Experimental Procedures	190
V.3.3. Synthesis of Ligands	191

CHAPTER VI. SYNTHESIS, CHARACTERIZATION AND REACTIVITY OF COBALT INTERMEDIATES IN LOW-OXIDATION STATE..... 197

VI.1. STATE-OF-THE-ART	199
VI.2. RESULTS AND DISCUSSION	203
VI.2.1. Synthesis and Characterization of Cobalt Complexes $1_{\text{Co}^{\text{I}}}\text{Cl}$, $1_{\text{Co}^{\text{II}}}\text{L}$ and $1_{\text{Co}^{\text{III}}}\text{L}$	203
VI.2.1.1. X-ray Absorption Fine Structure Characterization (XAS and EXAFS) of $1_{\text{Co}^{\text{I}}}\text{L}$, $1_{\text{Co}^{\text{II}}}\text{L}$ and $1_{\text{Co}^{\text{III}}}\text{L}$ (L = Cl or CH ₃ CN)	209
VI.2.1.3. Magnetic measurements by SQUID magnetometry.....	214
VI.2.2. Reactivity of Co ^I Species.....	215
VI.2.3. Photocatalytic Activity in H ₂ Evolution.....	223
VI.3. EXPERIMENTAL SECTION	225
VI.3.1. Physical Methods	225
VI.3.2. General Procedure for the Photogeneration of $1_{\text{Co}^{\text{I}}}\text{Cl}$ and $1_{\text{Co}^{\text{I}}}\text{MeCN}$ Species.....	226
VI.3.3. Synthesis of the Complexes and Characterization.....	227
VI.3.3.1. Synthesis of Co(PPh ₃) ₃ Cl.....	227
VI.3.3.2. Synthesis of [Co ^I (Cl)(Py ₂ ^{Ts} tacn)] ($1_{\text{Co}^{\text{I}}}\text{Cl}$).....	227
VI.3.3.3. Synthesis of [Co ^{II} (Cl)(Py ₂ ^{Ts} tacn)]Cl ($1_{\text{Co}^{\text{II}}}\text{Cl}$).....	228
VI.3.3.4. Synthesis of [Co(Py ₂ ^{Ts} tacn)(CH ₃ CN)](OTf) ₂ ($1_{\text{Co}^{\text{II}}}\text{CH}_3\text{CN}$).....	228
VI.3.3.5. Synthesis of [Co(Py ₂ ^{Ts} tacn)(CH ₃ CN)](OTf) ₂ (BF ₄) ($1_{\text{Co}^{\text{II}}}\text{CH}_3\text{CN}$)	229
VI.3.3.6. Synthesis of [Co(Py ₂ ^{Ts} tacn)(Cl)](Cl)(BF ₄) ($1_{\text{Co}^{\text{III}}}\text{Cl}$)	229

VI.3.3.7. Synthesis of $[\text{Co}(\text{Py}_2^{\text{Me}}\text{tacn})(\text{CH}_3\text{CN})](\text{OTf})_2$ (Me¹Co^{II})	230
CHAPTER VII. COBALT COMPLEXES CATALYZED LIGHT-DRIVEN REDUCTION OF KETONES AND ALDEHYDES USING WATER AND Et_3N AS SOURCE OF HYDRIDE.....	231
VII.1. STATE-OF-THE-ART.....	233
VII.2. RESULTS AND DISCUSSION.....	236
VII.2.1. Screening of the Conditions.....	236
VII.2.2. Influence of the Structure of the Cobalt Catalyst.....	241
VII.2.3. <i>In-situ</i> formation of the cobalt catalyst. Anion effect.....	245
VII.2.4. Substrate screening	248
VII.2.5. Formation of pinacols	250
VII.2.6. Catalytic Reactions Using PS_{Co}	252
VII.2.7. Preliminary Mechanistic Studies.....	257
VII.2.8. Molecularity of the Catalytic System: Hg^0 Poisoning Experiments.....	258
VII.2.9. Evaluation of the Hydrogen Source: Deuterium Incorporation Studies.....	259
VII.2.10. A new straightforward Way for the Synthesis of Deuterium-Labelled Alcohols....	264
VII.2.11. Selectivities	265
VII.2.12. Analysis of the Steric Effects.....	270
VII.2.13. Chiral Induction.....	272
VII.3. EXPERIMENTAL SECTION	275
VII.3.1. Material and Reagents.....	275
VII.3.2. Instrumentation	275
VII.3.3. Experimental Procedures.....	277
VII.3.3.1. General procedure employed in reaction screening conditions for the light-driven reduction of compounds.....	277
VII.3.3.2. General procedure for the alcohol isolation.....	277
VII.3.3.3. Gas-evolution monitoring studies.....	277
VII.3.3.4. Poisoning studies with Hg^0	278
VII.3.4. Synthesis of cobalt complexes	279
VII.3.4.1. Synthesis of $[\text{Co}(\text{OTf})(\text{DPA-Bpy})](\text{OTf})$ (2)	279
VII.3.4.2. Synthesis of $[\text{Co}(\text{OTf})(\text{N4Py})](\text{OTf})$ (3).....	281
VII.3.4.3. Synthesis of $[\text{Co}(\text{OTf})_2((\text{S,S})\text{-PDP})]$ (5)	282
VII.3.4.4. Synthesis of $[\text{Co}(\text{Cl})_2(\text{BpcMe})]$ (7) and $[\text{Co}(\text{OTf})(\text{H-CDPy}_3)](\text{OTf})$ (4).	284
VII.3.5. Characterization of the Isolated Alcohols.....	287
VII.3.6. Characterization of the Deuterated Alcohols	291
VII.3.7. Selectivities	292
VII.3.7.1. Synthesis of the substrates	292

VII.3.7.2. NMR characterization of the reduced products 10ag , 10ah and 10ai	293
CHAPTER VIII. INFLUENCE OF THE ELECTRONIC EFFECTS IN COBALT CATALYSTS ON PHOTOCATALYTIC KETONE REDUCTION.....	297
VIII.1. STATE-OF-THE-ART.....	299
VIII.2. RESULTS AND DISCUSSION.....	300
VIII.2.1. Synthesis and Characterization of Cobalt Complexes.....	300
VIII.2.2. Activities of the Complexes Based on Pentadentate Aminopyridine Ligands	303
VIII.2.3. Activities of Complexes Based on Tetradentate Aminopyridine Ligands	307
VIII.2.4. General Discussion.....	308
VIII.3. EXPERIMENTAL SECTION	309
VIII.3.1. Material and Reagents.....	309
VIII.3.2. Instrumentation	309
VIII.3.3. Experimental Procedures.....	310
VIII.3.3.1. General procedure employed in reaction screening conditions for the light-driven reduction of compounds.....	310
VIII.3.3.2. Gas-evolution monitoring studies.....	311
VIII.3.4. Synthesis of the Ligands and Complexes	312
VIII.3.4.1. Synthesis of 4,7-bis(4-methoxy-3,5-dimethyl-pyridine-2-ylmethyl)-7-(p-toluenesulfonyl)-1,4,7-triazacyclononane, (^{Me,OMe} Py ₂ ^{Ts} tacn)	312
VIII.3.4.2. Synthesis of 4,7-bis(4-ethoxycarbonyl-2-pyridylmethyl)-7-(p-toluenesulfonyl)-1,4,7-triazacyclononane, (^{H,CO₂Et} Py ₂ ^{Ts} tacn)	313
VIII.3.4.3. Synthesis of 4-bis(4-methoxy-3,5-dimethyl-pyridine-2-ylmethyl)-1,4,7-triazacyclononane (^{Me,OMe} Py ₂ ^H tacn).....	313
VIII.3.4.4. Synthesis of 1-methyl-4,7-bis(4-methoxy-3,5-dimethyl-pyridine-2-ylmethyl)-1,4,7-triazacyclononane (^{Me,OMe} Py ₂ ^H tacn)	314
VIII.3.4.5. Synthesis of [Co(OTf)(^{H,CO₂Et} Py ₂ ^{Ts} tacn)](OTf).....	315
VIII.3.4.6. Synthesis of [Co(OTf)(^{Me,OMe} Py ₂ ^{Ts} tacn)](OTf)	315
VIII.3.4.7. Synthesis of [Co(OTf)(^{Me,OMe} Py ₂ ^H tacn)](OTf).....	316
CHAPTER IX. MECHANISTIC STUDIES ON PHOTOCHEMICAL REDUCTION OF KETONES CATALYZED BY COBALT COMPLEXES.....	317
IX.1. STATE-OF-THE ART	319
IX.2. RESULTS AND DISCUSSION.....	323
IX.2.1. Studies on the [Ir(ppy) ₂ (bpy)](PF ₆) Photoredox Cycle.....	323
IX.2.1.1. Fluorescence quenching studies	324
IX.2.1.2. In-Situ Synthesis and Reactivity of PS_{Ir}^{II} with 1_{Co} and 9a	327
IX.2.2. Reactivity Studies	332
IX.2.2.1. Formation of pinacols	332

IX.2.2.2. Radical clocks and probes	340
IX.2.3. Studies to Characterize the Transition State in Ketone Reduction.....	342
IX.2.3.1. Hammett plot analysis	342
IX.2.3.2. Kinetic isotopic studies.....	344
IX.2.3.3. Kinetics: reaction orders	352
IX.2.4. General Mechanistic Discussion.....	353
IX.4. EXPERIMENTAL SECTION.....	359
IX.4.1. Material and Reagents	359
IX.4.2. Instrumentation	359
IX.4.3. General procedure for KIE determination using H ₂ O and D ₂ O	361
IX.4.4. General Procedure of NMR Measurements for ¹³ C KIE Determination.....	362
IX.4.5. SDKIE Determination.....	365
IX.4.5.1. General procedure	365
IX.4.5.2. Synthetic procedures	365
IX.4.6. Theoretical Studies.....	367
IX.4.6.1. Computational details	367
IX.4.6.2. Redox potentials, pK _a values and hydricities	368
CHAPTER X. GENERAL CONCLUSIONS.....	371
REFERENCES.....	377
ANNEX.....	397
A.1. ANNEX CHAPTER III	399
A.1.1. Characterization of Py₂^{Ts}tacn by NMR	399
A.1.2. Solid State Characterization Py₂^{Ts}tacn , 1_{Co} and 1_{Ni}	400
A.1.3. Photochemical Hydrogen Generation Studies.....	401
A.2. ANNEX CHAPTER IV	402
A.2.1. Characterization of Complexes	402
A.2.1.1. Paramagnetic NMR spectra	402
A.2.1.2. FT-IR characterization of the 1^R complexes	408
A.2.1.3. Solid state characterization of complexes	409
A.2.2. Electrochemical Studies	414
A.3. ANNEX CHAPTER VI.....	415
A.3.1. Characterization of Complexes.....	415
A.3.1.1. Paramagnetic NMR spectra	415
A.3.1.2. Solid state characterization of the complexes.....	418
A.4. ANNEX CHAPTER VII.....	420

A.4.1. Characterization of Complexes	420
A.4.1.1. Paramagnetic NMR spectra	420
A.4.2. Catalytic Studies Using PS_{Cu} as Photoredox Catalyst.....	423
A.4.2.1. Optimization of the solvent mixture.....	423
A.4.2.2. Optimization of the PS_{Cu} loading	424
A.4.2.3. Optimization of the cobalt catalyst 1_{Co} loading.	425
A.4.3. NMR Spectra of the deuterated alcohols	426
A.4.4. NMR Spectra of the isolated alcohols 10ah , 10ai and 10aj	430
A.5. ANNEX CHAPTER VIII	439
A.5.1. NMR spectra	439
A.5.1.1. NMR spectra of the ligands ^{H,CO₂Et} Py₂^{Ts+}tacn and ^{Me,OMe} Py₂^{Ts+}tacn	439
A.5.1.2. Paramagnetic NMR spectra	441
A.5.1.2. Solid state characterization	443
A.6. ANNEX CHAPTER IX	445
A.6.1. KIE determination	445
A.6.1.1. KIE determined by NMR.....	445
A.6.1.2. KIE determined by GC	447
.....	447
A.6.2. Oxidation of the In-situ Photogenerated PS_r Species with Different Amounts of 1_{Co}	448
A.6.3. Cyclic Voltammograms of the Substrates Under Reaction Solvent Mixture	449
A.6.4. NMR data of 1,4-diphenylbutan-1-one (10ap)	450
A.6.5. NMR spectra of the labelled products p-tolylmethan-d ₂ -ol and 4-methyl-1-d ₁ - benzaldehyde	451
A.6.6. Determination of the SDKIE in the substrates [D]-9v and [D]-9x	453

ABSTRACT

The increasing need for more efficient synthetic methods and sustainable processes for fuel and high-value organic molecules production can be seen as one of the major challenging goals for the future. Nature has developed a sophisticated system to store the light energy into chemical bonds. The mimicking of the natural systems through the development of artificial photosynthetic schemes is extremely interesting since it could effort green reduction alternatives.

Toward this end, in this thesis we describe a new family of cobalt complexes based on aminopyridine ligands able to reduce protons and ketones under photochemical conditions. Additionally, the same catalytic systems were found active for the electrocatalytic proton reduction to H₂.

Ligand availability, modularity and versatility of this type of coordination complexes let us to tune the first coordination sphere of the metal by changing the electronic and structural features of the ligand. This allows us to pinpointing preferred ligand structures to sustain efficient H₂ and alcohol production. In addition, the straightforward tuning of the ligand nature let to modulate or even alter the selectivity proton-ketone reduction.

The high modularity of these systems also allows to modify the secondary coordination sphere of metal center. In this way, the functionalization of cobalt systems with a biotin moiety bring us to encapsulate the cobalt catalyst system into a protein environment. We prove that the natural pocket enhances the reactivity in water reduction to H₂.

Mechanistic studies and characterization of the intermediates have been pursued, with the aim of understanding the requirements for a better design of cobalt-based catalysts. Spectroscopic, magnetic and NMR experiments, along with DFT calculations suggest that the Co^I intermediate with the Py₂^Ttacn ligand shows an important electron density over the pyridine moiety, leading to a formal Co^{II} metal center.

Finally, using fluorescence quenching, UV/Vis, electrochemical, kinetic and isotope labelling experiments the mechanism in the photocatalytic ketone reduction is constructed. Supported by DFT calculations, a heterolytic pathway for ketone reduction seems to be preferred, although the contribution of a homolytic pathway could not be fully ruled out.

This thesis paves the way for the construction of more active cobalt based catalytic systems for light-driven reduction reactions.

RESUM

La creixent necessitat de sistemes sintètics més eficients i processos sostenibles per la producció de combustibles i molècules orgàniques d'alt valor afegit, pot ser vist com una de les principals fites més desafiantes pel futur. La natura ha desenvolupat un sofisticat sistema per emmagatzemar l'energia llumínica en forma d'enllaços químics. La imitació dels sistemes naturals mitjançant el desenvolupament d'esquemes artificials és summament interessant, que ja podria proporcionar alternatives ecològiques de reducció.

Amb aquesta finalitat, en aquesta tesi descrivim una nova família de complexos de cobalt basats en lligands aminopiridinics capaços de reduir els protons i cetones en condicions fotoquímiques. A més, el mateixos sistemes catalítics també són actius en la formació d'hidrogen electrocatalítica.

La disponibilitat del lligand, la modularitat i la versatilitat d'aquesta família de complexos de coordinació ens permeten també tunejar la primera esfera de coordinació del metall a través de la modificació de les característiques electròniques i estructurals del lligand. Això ens permet la identificació de les estructures del lligand preferides per a dur a terme de producció eficient d'hidrogen i alcohol. A més a més, la modificació directa de la naturalesa del lligand permet modular o fins i tot alterar la selectivitat protó-cetona en la reducció.

L'alta modularitat d'aquests sistemes també permet modificar la segona esfera de coordinació del centre metàl·lic. En aquest sentit, la funcionalització de sistemes de cobalt amb un fragment de biotina ens concedeix la possibilitat d'encapsular el sistema catalític en un entorn proteic. Es demostra que la presència de la cavitat proteica proporciona una millora en l'eficiència de reducció de l'aigua a H₂.

S'han realitzat estudis mecanístics i s'han caracteritzat els intermedis de reacció amb el propòsit d'entendre els requisits principals per un millor disseny de catalitzadors. Experiments basats en espectroscòpia, magnetisme i de ressonància magnètica nuclear, juntament amb càlculs DFT han suggerit que l'intermedi de Co^I amb el lligand Py₂^Tta_{cn} presenta una densitat electrònica important en la piridina del lligand, fet que condueix a un centre formal de Co^{II}.

Finalment, utilitzant experiments de mesura de fluorescència, UV/Vis, electroquímica i experiments de marcatge isotòpic hem pogut construir el mecanisme de reducció de cetones impulsat per la energia llumínica. Amb el suport de càlculs teòrics, sembla ser que el mecanisme heterolític és el preferit, i tot que no es pot descartar la contribució d'una via homolítica.

Aquesta tesi aplanar el camí per a la construcció de sistemes catalítics basats en cobalt més actius en reaccions de reducció impulsades per l'energia llumínica.

RESUMEN

La creciente necesidad de sistemas sintéticos más eficientes y procesos sostenibles por la producción de combustibles y moléculas orgánicas de alto valor añadido, puede ser visto con una de las principales metas más desafiantes para el futuro. La naturaleza ha desarrollado un sofisticado sistema para almacenar la energía lumínica en forma de enlaces químicos. La imitación de los sistemas naturales mediante el desarrollo de esquemas artificiales es sumamente interesante, que ya podría proporcionar alternativas ecológicas de reducción.

Con esta finalidad, en esta tesis describimos una nueva familia de complejos de cobalto basados en ligandos aminopiridina capaces de reducir los protones y cetonas en condiciones fotoquímicas. Además, los mismos sistemas catalíticos también son activos en la formación de hidrógeno electrocatalítica.

La disponibilidad del ligando, la modularidad y la versatilidad de este familia de complejos de coordinación nos permiten también tunear la primera esfera de coordinación del metal a través de la modificación de las características electrónicas y estructurales del ligando. Esto nos permite la identificación de las estructuras del ligando favoritas para llevar a cabo de producción eficiente de hidrógeno y alcohol. Además, la modificación directa de la naturaleza del ligando permite modular o incluso alterar la selectividad protón-cetona en la reducción.

La alta modularidad de estos sistemas también permite modificar la esfera segunda esfera de coordinación del centro metálico. En este sentido, la funcionalización de sistemas de cobalto con un fragmento de biotina nos concede la posibilidad de encapsular el sistema catalítico en un entorno proteico. Se demuestra que la presencia de la cavidad proteica proporciona una mejora en la eficiencia de reducción del agua a H_2 .

Se han realizado estudios mecanísticos y se han caracterizado los intermedios de reacción con el propósito de entender los requisitos principales para un mejor diseño de catalizadores. Experimentos basados en espectroscopía, magnetismo y de resonancia magnética nuclear, junto con cálculos DFT han sugerido que el intermedio de Co^I con el ligando $Py_2^{Tst}acn$ presenta una densidad electrónica importante en la piridina del ligando, lo que conduce a un centro formal de Co^{II} .

Finalmente, utilizando experimentos de medida de fluorescencia, UV/Vis, electroquímica y experimentos de marcaje isotópico hemos podido construir el mecanismo de reducción de cetonas impulsado por la energía lumínica. Con el apoyo de cálculos teóricos, parece ser que el mecanismo heterolítico es el preferido, aunque no se puede descartar la contribución de una vía homolítica.

Esta tesis allana el camino para la construcción de sistemas catalíticos más activos basados en cobalto para reacciones de reducción impulsadas por la energía lumínica

CHAPTER I

General Introduction

I. GENERAL INTRODUCTION

I.1. WORLD ENERGY PROBLEM

The current growth of a society based on the massive use of fossil fuels as a cheap energy source does not have precedents in the human evolution. The world energy consumption is expected to double by 2050 which, if sustained by fossil fuels, will lead to an unparalleled increase in the atmospheric CO₂ levels.^{1,2} This increase in the CO₂ concentration is behind the raise of the global surface temperature during the last century (0.74 ± 0.18 °C), which is manifested in the new extreme climate patterns, the rise of the sea level, the expansion of deserts and the retreat of glaciers. The increase of the energy demand led by the fast expansion of population and emerging economies is going to aggravate the problem.

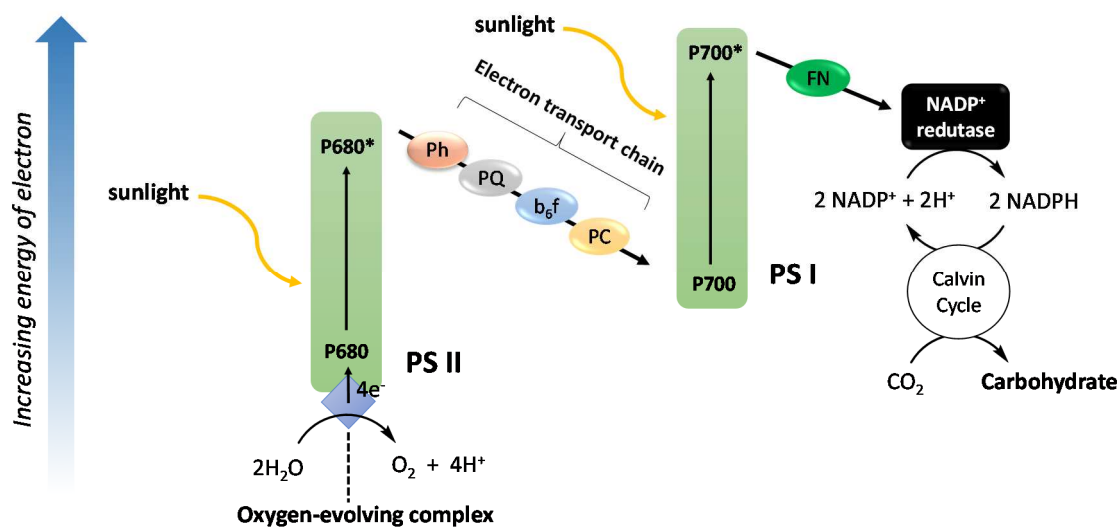
The current energetic and environmental scenario forces to replace the carbon-based energy fuels for more sustainable ones. Therefore, it is mandatory to find non-polluting, clean, inexhaustible and economic energetic alternatives. Solar energy is an optimum energy source due to its availability and density. Indeed, it exceeds all other renewable energy sources combined and it is widely exploitable in almost all of the regions of the planet. Interestingly, the total solar irradiation that arrives to the Earth surface *per* hour represents the total energy consumption that humans need *per* year.³ Therefore, sunlight energy is very appealing since it is unlimited and it can undoubtedly satisfy the world energy demand. However, the intermittency of day/night cycles causes a drawback in its permanent supply.⁴ To overcome this issue a convenient energy storage system is required. Among the different options, the conversion of solar energy into chemical bonds awakes great interest for the easy transport and high energy storage densities of the chemical fuel, being the natural photosynthesis a mechanism to reflect on.

One promising chemical energy carrier is hydrogen, which has the highest specific enthalpy (140 MJ/Kg) of any chemical fuel. The oxidation of hydrogen, by either fuel cells or combustion, yields water as its only byproduct, making it environmentally benign. So, it represents one of the most promising approaches regarding sustainability

and energy security, avoiding undesirable emissions if its generation comes from water, the most abundant hydrogen source in the world.

I.2. NATURAL PHOTOSYNTHESIS

Nature has created a very sophisticated system to store sunlight energy into chemical bonds. It is achieved through the so-called photosynthesis in which the light energy is harvested and stored into carbohydrates by reducing carbon dioxide and using water as the primary source of electrons and protons. Photosynthesis in green plants occurs through a complex cascade of photoinduced energy-transfer steps that trigger light (Kok cycle) and dark reactions (Calvin Cycle), forming together a very complex machinery (Scheme I. 1). In the light reactions, mainly three types of proteins embedded in the thylakoid membrane of chloroplasts of higher green plants, algae and cyanobacteria are involved; Photosystem II (PS II), Cytochrome b_6f and Photosystem I (PS I).^{5,6} The energy transference occurs through the Z-scheme, involving photosystems PS I and PS II, which contain an oxygen-evolving complex, light-harvesting antennae, and different redox-active proteins.



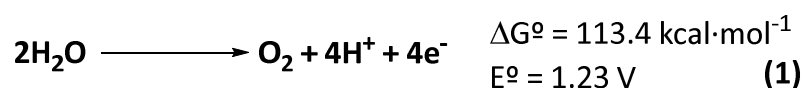
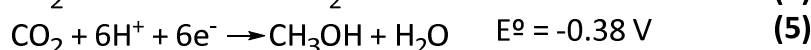
Scheme I. 1. Schematic illustration of the natural photosynthetic energy transference chain (Z-scheme) and dark reaction (Calvin cycle). During the photosynthetic process, the photon energy is absorbed by the PS II and PS I, and the electrons generated from the oxidation of water by the oxygen-evolving complex are transferred to $NADP^+$ reductase by means of an electron-transport chain comprised of pheophytin (Ph), plastoquinone (PQ), cytochrome b_6f (b_6f), plastocyanin (PC) and ferredoxin (FN). $P680$ and $P700$ = light-harvesting complexes containing reaction centers, located in PS II and PS I, respectively.

The sunlight energy collected by the light-harvesting antennae in PS II leads to the excitation of chlorophyll molecules ($P680 \rightarrow P680^*$), and this promotes the oxidation of water ($H_2O \rightarrow 0.5 O_2 + 2H^+ + 2e^-$). The excited electrons in PS II are transferred through the electron-transport chain to the PS I and re-excited by the light-harvesting complex ($P700 \rightarrow P700^*$). Ultimately, the sunlight energy is efficiently stored in energy-rich molecules, such as ATP and NAD(P)H reduced cofactors. The cofactors are further used as reducing agents in the CO_2 reduction to carbohydrates in the light-independent redox enzymatic reactions of the Calvin Cycle. Thus, natural photosynthesis serves as an elegant example of how to merge light harvesting systems with catalytic system for the synthesis of energy-rich molecules.

I.3. TOWARDS ARTIFICIAL PHOTOSYNTHESIS

Fascinated by natural photosynthesis, one of the most ambitious and challenging goals is to reproduce it artificially.^{1,7,8} In this regard, many efforts have been devoted to mimic the photovoltaic effect in nature. Therefore, the use of solar energy, through promoting photoinduced electron-transfer reactions, represents an appealing sustainable and environmental benign tool for the development of artificial photosynthetic schemes. However, it requires a tremendous effort in order to understand and improve the issues related with i) the light harvesting, ii) charge separation, and iii) light-driven water oxidation to O_2 (Equation 1), which can be seen as the most convenient source of electrons, iv) the reduction of water to H_2 (Equation 2) and v) the CO_2 reduction either to CO , formic acid or methanol (Equations 3-5) using the electrons obtained from water oxidation.⁹

Since multiple electronic and protonic stages are required for the CO_2 reduction and the H_2O oxidation, these charge-transfer steps are considered the bottlenecks in the development of efficient artificial photosynthesis. Indeed, the production of H_2 or $CO/CH_3OH/CH_4$ from H^+ or CO_2 as energy storage molecules provides a simple alternative to the dark process in the photosynthetic scheme, being the proton reduction the easier process to achieve. Due to the inherent complexity of these processes, it is important to study separately the water oxidation, proton and CO_2 reduction in order to achieve better efficiencies.

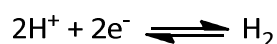
Water oxidation half reaction: an energetic "uphill" reaction**Proton and selected CO₂ reduction half reactions**

Light-driven proton reduction to H₂ in highly efficient manner is not still solved. This challenge can be addressed either by designing new catalysts or light-harvesting systems able to promote this transformation by photoinduced electron transfer events.

An alternative way is the electrocatalytic reduction of water to generate H₂. In this case, the electrons are provided by the electrode rather than by the photoredox system.

I.4. HYDROGEN PRODUCTION IN THE NATURE: HYDROGENASE ENZYMES

The most efficient mechanisms for molecular hydrogen formation and consumption are found in nature. These biological processes are catalyzed by a family of enzymes called *hydrogenases*, in which three different active sites formed by organometallic structures are known: [NiFe]-hydrogenases, [FeFe]-hydrogenases, and [Fe]-hydrogenase. These enzymes are considered as metalloproteins because they can contain iron or nickel-iron in their active center surrounded by an aminoacid chain rich in sulfur. Although, their exactly role is still not well understood, it seems that all of these types of enzymes are involved in the metabolism of dihydrogen.^{10,11}



Despite the simplicity of the H₂ redox equilibrium reaction, hydrogenase enzymes are complex multi-metal domain proteins of high molecular weight. The elucidation of the structures, through X-ray crystallography, has shown that the octahedral coordination sphere of each iron core catalytically active is completed with CO, CN and bridged thiolates.¹²⁻¹⁶

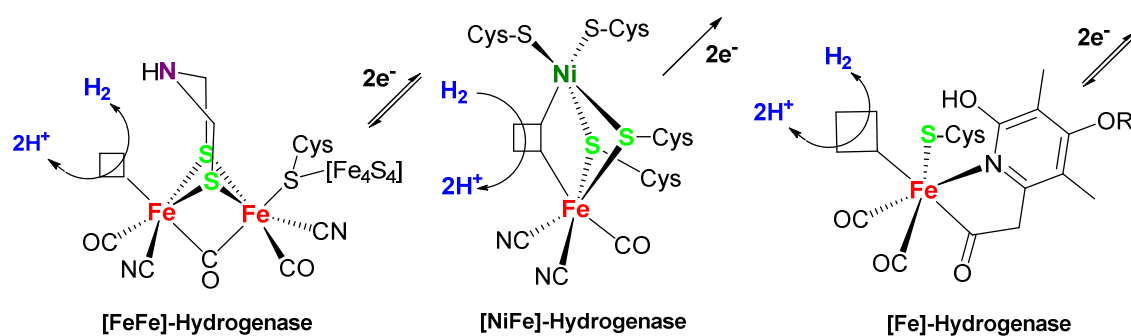


Figure I. 1. Structure of the active centers of the dinuclear and mononuclear hydrogenases.

Typical activities for mono-[Fe] hydrogenases are highly evolved for catalysis and are 50-100 times more active than [NiFe] hydrogenases.¹⁶ The hydrogenases activities range from 100-1000 molecules of H_2 per s^{-1} (Turnover frequency: TOF) for the [NiFe] to 6000-60000 TOF for the mono-[Fe] hydrogenase. Compared with [FeFe]-hydrogenases, [NiFe]-hydrogenases have 100 times more affinity for hydrogen and are less sensitive to oxygen and carbon monoxide.

One of the most important features in natural hydrogenases is the presence of a pendant amine, a base situated in proximity to the metal, yet too distant to form a strong bond with the metal. This base has often been proposed to function as a proton relay, a therefore approaching to protons to the metal center.¹⁷ By DFT modelling studies it has been proposed that its presence lead to an energetic enhancement in the protonation event of the metal core.¹⁸

The outstanding catalytic activity of hydrogenases awakes special attention to solve the energy demands. The synthesis of hydrogenase biomimetic systems may aid to understand the role of the components involved in the active site of natural enzymes and, additionally, may help in the development of artificial robust and efficient catalysts for H_2 evolution that operate in H_2O and stable in O_2 .¹⁹ In the following sections we will summarize some selected catalysts for the electro- and photocatalytic H_2 production based on first-row transition metal complexes.

I.5. MOLECULAR COMPLEXES FOR H₂ EVOLUTION

I.5.1. Catalytic Systems Based on Iron

Iron is the most abundant transition metal in nature and, from a biologic point of view, the most important. To mimic the function of hydrogenases enzymes the most logical way is to develop artificial biomimetic systems containing iron at the active site. Therefore, scientists have developed and studied iron-based biomimetic model systems of the hydrogenases for the electrochemical and photochemical²⁰⁻²⁵ proton reduction (Figure I. 2). There is a large number of examples proving the capacity of these artificial systems to undergo the reduction of protons at an applied potential.²⁶⁻³⁰ Despite the significant achievements in the structural modelization of iron hydrogenases, the biomimetic systems show very little activity and the H₂ formation occurs at a significantly more negative than the potential in which the protons are reduced in the natural systems.^{27,28}

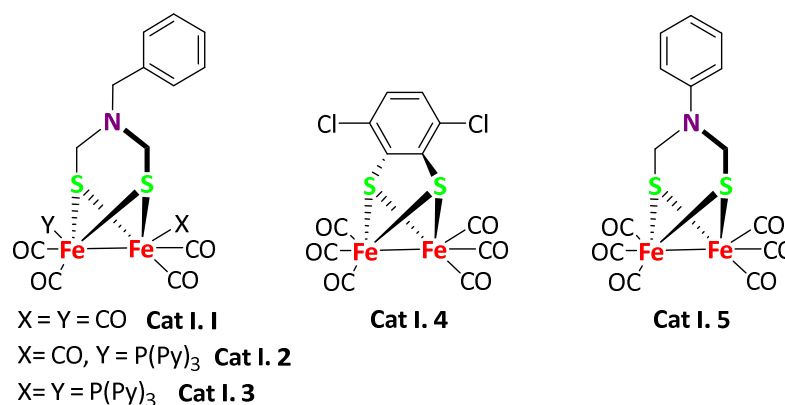


Figure I. 2. Selected biomimetic iron complexes used in proton reduction.

Another approach is to develop completely new H₂ generation catalyst from potentially active non-biomimetic system (different ligands and metals) and introducing new structural and electronic properties inspired by the structure of the active sites of the enzymes. These systems can be called bioinspired and non-bioinspired models approach, depending on the similarity with the natural structure. In this sense, in the last years iron catalysts based on polypyridyl³¹⁻³³ and amine-bis(phenolate)³⁴⁻³⁷ ligands have been developed.

I.5.2. Catalytic Systems Based on Nickel

Nickel is another interesting element to develop water reduction catalysts. Inspired by nature, scientists have mimicked the active site of the natural enzymes by creating [NiFe] hydrogenase model complexes.³⁸ However, despite the many efforts devoted to this field, the activities provided by these model systems are insignificant to those obtained with the natural enzymes. A review of [NiFe] hydrogenase mimics²⁷ shows that they function only in pure organic solvents, and no model complex of [NiFe] has been reported for hydrogen production when water is the proton source. Figure I. 3 depicts some selected NiFe biomimetic systems for H₂ evolution reported by Rauchfuss and co-workers (**Cat I. 6** and **7**)³⁹ and Ogo and co-workers (**Cat I. 8**).⁴⁰

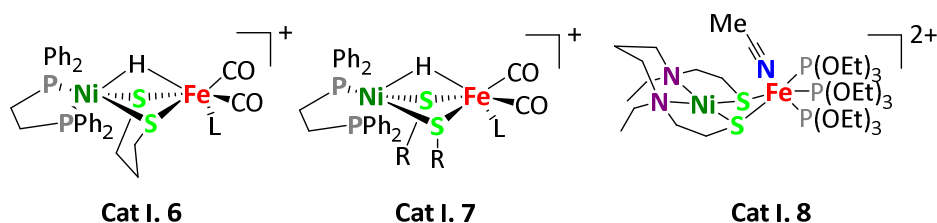


Figure I. 3. Selected NiFe biomimetic systems

Dubois and co-workers designed a series of nickel-based molecular catalysts, in which each ligand contains two phosphine coordination sites and two non-coordinating basic sites (amino groups), for the electrocatalytic hydrogen production. It was thought that these basic sites, inspired by a similar pendant amine in [FeFe] hydrogenases, could play a very important role to achieve high catalytic activity. In the literature there is an enormous amount of studies in which the influence of the catalyst structure as well as the nature of the pendant arm are studied.^{17,41-53} Figure I. 4 shows the relation the pendant arm structure with respect the activity of the catalytic system.

Complex **Cat I. 9** (TOF < 0.2 s⁻¹, overpotential = 1.2 V) constituted the first generation catalyst for H₂ oxidation, and the use of an external base was required for the heterolytic cleavage of H₂.⁵⁴ The introduction of pendant amine arms (**Cat I. 10**),⁵⁴ and their positioning (**Cat I. 11**),^{55,56} led to an enhancement in the overpotentials as well as in the reaction rate, respectively. Then, by controlling the thermodynamic driving force for H₂ addition, it could be possible to design catalysts for H₂ elimination (**Cat I. 12 and 13**) or H₂ oxidation.⁵⁵⁻⁵⁸ Thanks to this structure-activity correlation, huge turnover

frequencies of 100.000 s^{-1} could be achieved through using the nickel catalyst **Cat I. 13** with two pendant amine arms.⁵⁹

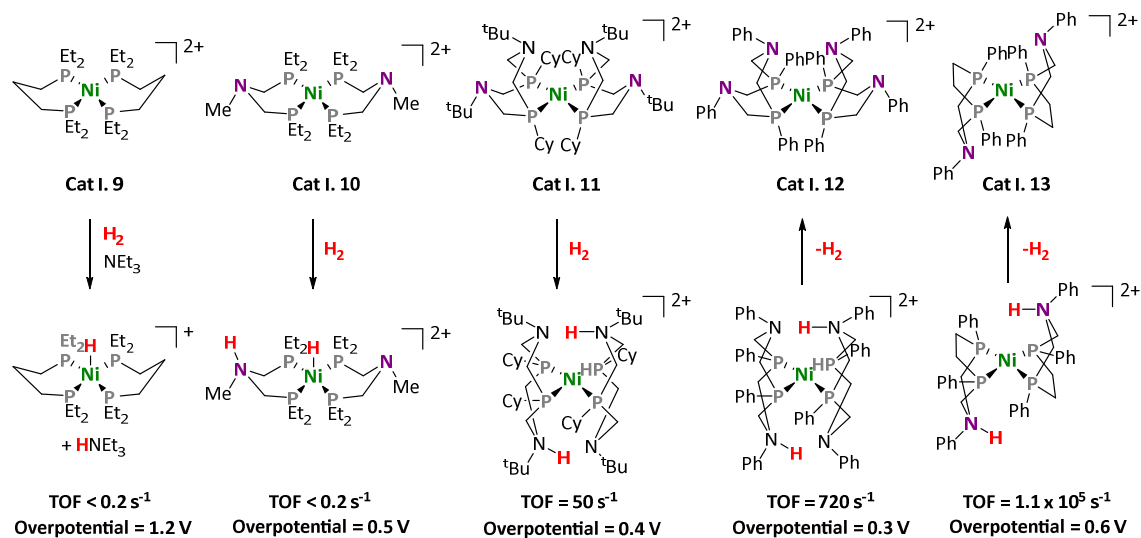


Figure I. 4. Evolution of H_2 oxidation and production catalysts containing amine pendant arms.

Due to the well behave of this systems, several works has been performed in order to extent their applicability and performance. For instance, Artero and co-workers functionalized carbon nanotube electrodes with Dubois' nickel catalysts for electrocatalytic hydrogen production.⁶⁰ High catalytic activity (100.000 TON) were observed under strongly acidic conditions. Additionally, the same catalytic systems have also been tested for the photochemical H_2 generation. Such as, **Cat I. 12** depicted 2700 TON when paired with a photoredox catalyst such as Eosin Y or $[\text{Ru}(\text{bpy})_3]^{2+}$ in the presence of ascorbic acid as electron donor.⁶¹

Inspired by the active core of $[\text{NiFe}]$ hydrogenases, a family nickel thiolene complexes has been developed.⁶² Holland and Eisenberg were the first to develop such nickel complexes $[\text{Ni}(\text{pyS})_3]^-$ (pyS = pyridine-2-thiolate) (**Cat I. 14**). It was found to be an excellent catalyst for light-driven H_2 production ($\lambda = 520\text{ nm}$) employing fluorescein as chromophore and Et_3N as sacrificial electron donor in basic 1:1 $\text{EtOH}/\text{H}_2\text{O}$ mixture.⁶³ Over 5000 TON were obtained, and the activity could be recovered with periodic addition of Et_3N . In order to understand this system more deeply, closely related pyridyl- and pyrimidylthiolate Ni^{II} complexes (**Cat I. 19** and **20**) were examined for both photo and electrocatalytic H_2 production (Figure I. 5, left).^{64,65} After several mechanistic studies it was concluded that Ni^{II} thiolene complexes catalyzed the formation of H_2 involving the

protonation of the pyridine, which then assisted the protonation of the Ni-H intermediate, leading the formation of H₂ (Figure I. 5, right). This resembles the mechanism in [FeFe] and [NiFe] hydrogenases.^{10,41,66,67}

Finally, bis chelated nickel complexes of square planar coordination have also been explored (**Cat I. 24-27**).⁶⁸⁻⁷⁰ All of them were found active under photochemical conditions (up to 6000 TON) depicting a surprising stability of more than 100 hours under irradiation. Additionally, excellent electrocatalytic activities were observed in neutral pH achieving Faradaic yields close to 100 % under anaerobic conditions and 80 % under aerobic conditions. From these square planar Ni thiolene complexes, several S₂P₂ coordinated nickel complexes for the electrocatalytic hydrogen production have been developed through exchanging one thiolene ligand by one bidentate phosphine ligand.⁷¹

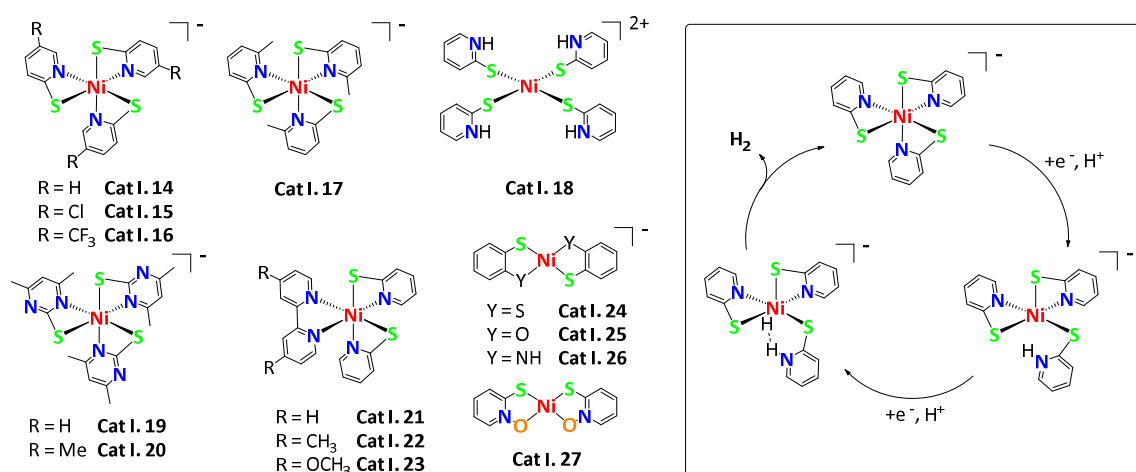


Figure I. 5. Left: Selected nickel thiolene complexes. Right: Proposed mechanism of hydrogen formation by thiolene complexes.

The scope of Ni complexes with nitrogen-based ligands is quite limited, however in the literature there are some examples that prove the chance of using nitrogen-based ligands (Figure I. 6). Following the initial report by Fisher and Eisenberg of homogeneous Ni^{II} macrocyclic catalysts for the electrocatalytic CO₂ and water reduction to H₂,⁷² Collin and Sauvage described two related Ni^{II} macrocyclic complexes, [Ni(cyclam)]²⁺ (**Cat I. 28** and **29**), and [Ni₂(biscyclam)₂]⁴⁺ (**Cat I. 30**) for the electrocatalytic reduction of water to H₂.⁷³ The activity of the complexes was compared at fixed potential (-1.25 V vs. SCE), showing that **Cat I. 30** was the most active catalyst of the series presumably due to the

close proximity of the two Ni centers. Turnover numbers up to 100 were reached, and a Ni-H intermediate was proposed as active intermediate. From these initial reports, the growing interest on the use of polypyridine ligands led to the creation of several Ni complexes containing pyridine moieties.⁷⁴ For instance, Licheng Sun and co-workers (2014) reported the Ni complex **Cat I. 31** based on bipyridine-derivative ligands containing internal bases.⁷⁵ It was found to be an excellent catalyst for light-driven H₂ production (3230 TON) when coupled with fluorescein as chromophore and Et₃N as electron donor. Neutral Ni^{II} phthalocyanine complex **Cat I. 32** was found also active (680 TON) for visible-light driven H₂ production when paired with [Ir(dfppy)₂(Hdcbpy)] as photosensitizer in the presence of TEOA as sacrificial electron donor.⁷⁶

Robert and Lau studied the photo and electrocatalytic activities of a series of Ni^{II} complexes bearing tetradentate macrocyclic N₃X (X = NH, P-Ph or S) ligands (**Cat I. 33 – 38**).⁷⁷ They found that the complex **Cat I. 34** bearing a phosphorous atom, showed the highest efficiency (5000 TON) under photochemical conditions. However, they noted that under irradiation conditions nickel nanoparticles were formed, being the real catalytic species. However, this behavior was not observed under electrocatalytic conditions.

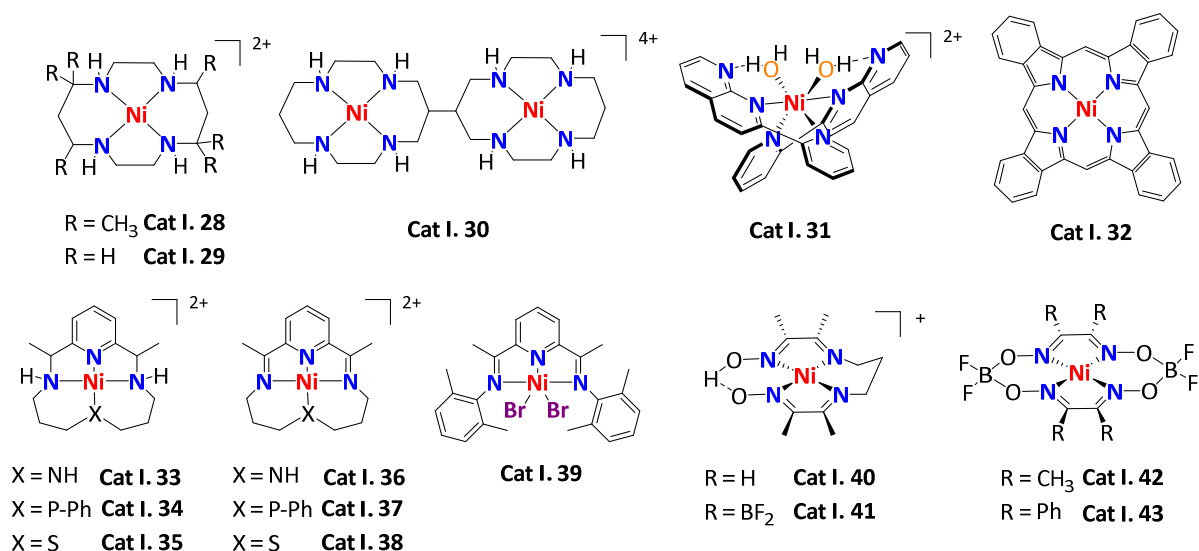


Figure I. 6. Selected Ni complexes for H₂ production containing nitrogen ligands.

Likewise, the use of imine-based ligands is very challenging since it provides the reduction of protons at low overpotentials. The tridentate Ni^{II} with a redox-active pincer ligand (**Cat I. 39**) reduced the protons in aqueous acid solutions with a rate of 105 s⁻¹ at

low overpotential (140 mV).⁷⁸ Related organometallic Ni complexes with phosphine pincer ligands have also been explored for the electrocatalytic proton reduction.⁷⁹ In the same way, nickel glyoxime complexes **Cat I. 40-43** have presented efficient electrocatalytic activities in acidic nonaqueous solutions and at low overvoltages.⁸⁰⁻⁸² Interestingly, the use of Ni instead of Co let to work at slightly lower overpotentials together with larger stabilities towards hydrolysis.

I.5.3. Catalytic Systems Based on Cobalt

Although cobalt has no biological relevance for the catalytic reduction of protons to hydrogen, and truly it is significant less abundant (20-30 ppm) than Fe (63000 ppm) and Ni (90 ppm), it has emerged as an interesting metal for the development of water reduction catalytic systems.^{83,84} In this Chapter, we will discuss selected examples of homogeneous cobalt complexes for the electro and photocatalytic hydrogen production.

Among the earliest report of cobalt systems, there are the complexes based on azamacrocycles (Figure I. 7). For instance, [14]diene-N₄ macrocyclic cobalt complexes **Cat I. 44-45**, [14]tetraene-N₄ analogues **Cat I. 46-49** and cobalt porphyrin derivatives **Cat I. 50-53** were found to be catalytically active in the electrochemical reduction of protons from neutral aqueous solutions.⁸³ Good activities were observed in the case of the porphyrin systems. As an example, a turnover frequency of 1.83 s⁻¹ was observed using **Cat I. 52** at nearly quantitative Faradaic yield at applied potential of -1.29 V vs. SCE.⁸⁵ However, this kind of systems are prone to absorb at the electrode surface. Peters and co-workers established that a Co^{II} tetrazamacrocycle containing pyridine donor (**Cat I. 54**) catalyzed hydrogen evolution at -0.69 V vs. SCE with 92 % Faradaic efficiency. The catalytic wave showed strong pH dependence consistent with an equilibrium protonation of the ligand, involving an initial one-electron, one-proton reduction to form a protonated Co^{II} complex followed by a subsequent catalytic reduction by two electrons and one proton to generate H₂.⁸⁶

On the other hand, in the literature there is a large number of studies based on imine/oxime cobalt systems (**Cat I. 55-56**)^{80,87} and cobaloximes (**Cat I. 57-64**)^{88,89} that able to reduce protons under electrochemical conditions (Figure I. 7). The interest of

these compounds is based on the fact that due to the weak donor character of the ligand, the reduction of the cobalt system is very favoured and therefore it provides the reduction of protons at very low overpotentials (100-300 mV) close to the thermodynamic equilibrium over a wide range of acid–base conditions in nonaqueous solutions. In general, the H₂ evolution proceeds *via* proton-coupled electron transfer steps involving the oxime bridge as a protonation site, reproducing the mechanism in the active sites of hydrogenase enzymes. In contrast, this is not observed with the systems containing BF₂ groups on the ligand, since the proton relay is absent.⁸⁷

Cobaloximes and imine/oxime cobalt systems have also shown their potential in light-driven H₂ generation in both water/organic solvent mixtures and in fully aqueous solutions. However, one of the drawbacks of these systems is the low stability in water due to the hydrolysis of the ligand, limiting their applicability. This was quite prevented by using the imine/oxime systems, which conferred more stability towards hydrolysis due to the carbon bridge.

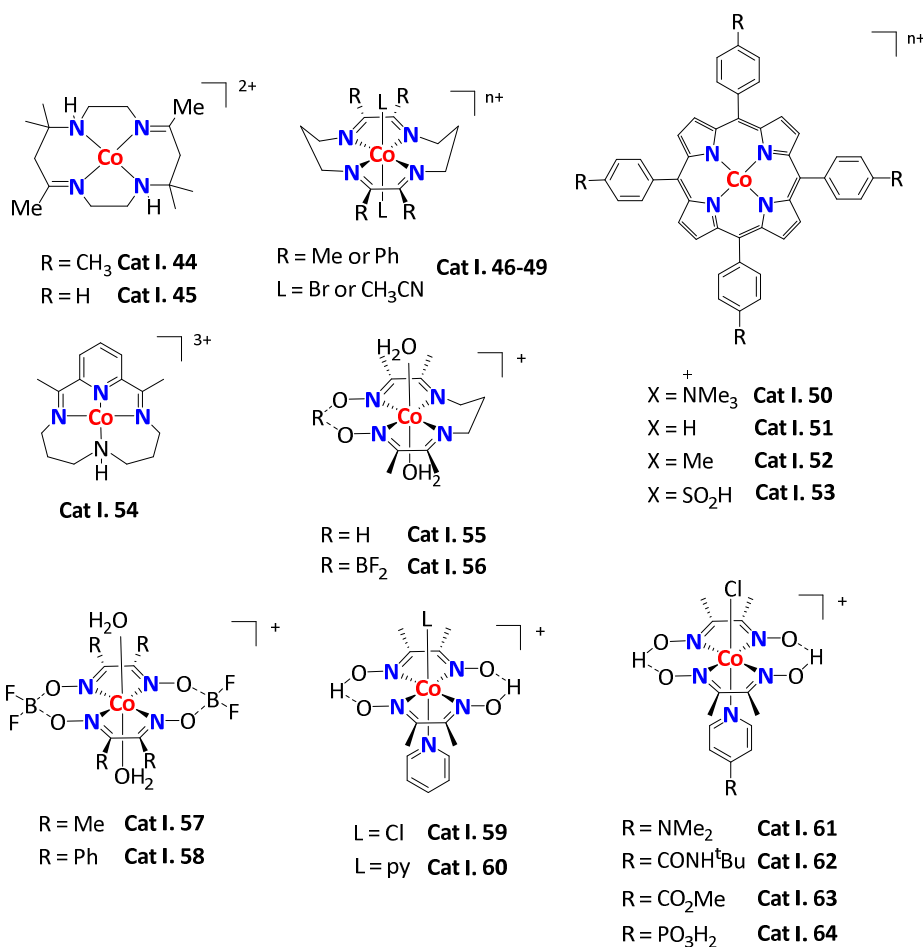


Figure I. 7. Selected cobalt macrocyclic platforms for H₂ evolution.

A series of boron-capped tris(glioximato) cobalt complexes have also been reported. However, as reported by Savéant and co-workers, the catalytic activity towards H₂ evolution can result from an electro-deposition of cobalt containing nanoparticles on the electrode surface at a modest cathodic potential.⁹⁰

The molecular and modular character of cobaloxime systems let to their attachment to homogenous⁸³ or heterogeneous⁹¹ photoredox systems, as well as to electrodes.^{92,93} This supramolecular assemblies in most of the cases are more active than the corresponding multicomponent systems.

In an attempt to design more efficient and robust cobalt catalysts for proton reduction, cobalt catalysts based on aminopyridine and polypyridyl ligands were tested (Figure I. 8). These ligands took inspiration from the work of Sutin and co-workers (1980) with the [Co(bpy)₃]²⁺ system.^{94,95} Polypyridyl catalysts display an increased stability under reductive conditions compared with [Co(bpy)₃]²⁺ and cobaloximes, and therefore they allow a more systematic evaluation of their activity in fully aqueous media. Moreover, the use of these ligands let to a straightforward modification of the structural and electronic properties of the ligand, allowing a tuning of the catalytic activity.

The first electrocatalytic hydrogen evolution using a Co^{II}-polypyridyl system (**Cat I. 65**) was reported in 2010 by Chang and co-workers.⁹⁶ They designed a tetradentate ligand able to stabilize the cobalt in its reduced state, with two free cis positions in which the catalysis occurred. The addition of trifluoroacetic acid (TFA) to an organic solution of **Cat I. 65** triggered the appearance of a catalytic wave (at -1.0 V vs. SCE) attributed to the reduction protons near to the Co^{II/I} redox couple, with an overpotential of 400 mV. The estimated turnover frequency (TOF) was 40 mol H₂/mol catalyst at 60 mM TFA. Importantly, these authors also demonstrated that the generation of H₂ was also compatible in the presence of water (at -1.2 V vs. SCE), and thus paving the way for future catalytic systems with similar ligands operating in aqueous media.

From this initial study, several works have been devoted to develop cobalt-polypyridyl systems in order to achieve better activities in the electro and photocatalytic water reduction. For instance, catalysts **Cat I. 68** and **Cat I. 69** where electronically modified replacing OMe by Me (**Cat I. 68**) and bearing a CF₃ substituent on the pyridine

(**Cat I. 69**).⁹⁷ This modification let them to modulate the redox potential of the Co^{II/I} couple and therefore the onset potential in proton reduction. It is important to note that the introduction of the electron withdrawing CF₃ substituent significantly decreased the electrocatalytic current due to a diminished activity of the Co^I species.⁹⁸ Such behavior was also confirmed by the photocatalytic experiments.

In a related strategy, the same group reported the pentadentate pyridine platform Py5Me₂ tuned with different electronic groups on the central pyridine (**Cat I. 70-72**). Under electrocatalytic conditions all three complexes displayed high stability and activity in neutral water with 100 % Faradaic efficiency and achieving 55.000 TON in the case of **Cat I. 71**. Additionally, the catalyst **Cat I. 70** was proved to be the best catalyst of the series under photocatalytic conditions, providing twice the amount of H₂ of **Cat I. 72**, after 8 h of visible-light irradiation ($\lambda = 452$ nm).⁹⁷⁻¹⁰⁰ Electrochemical mechanistic studies centered on these cobalt pentadentate systems revealed an anation of the complex by the conjugate base of the acid used in the experiments. This was demonstrated by the shift in the catalytic wave upon addition of acid.¹⁰¹

Long, Chang and Castellano expanded the family of cobalt complexes and constructed complexes **Cat I. 73-75** which are structurally related with complexes **Cat I. 70-72** but with the single pyridine moiety removed. This let them directly compare the activity between penta and tetradentate cobalt structures.⁹⁷ It was established that tetradentate ligands led to significantly more active catalysts (1550 TON with **Cat I. 73** versus 330 TON with **Cat I. 71**) under the same experimental conditions. However, it is not possible to demonstrate a clear advantage of tetradentate ligands over pentadentate ones, since a clear trend has not been observed in other related systems.^{102,103} It is important to remark that some closely related pentadentate systems undergo decoordination of one pyridine arm during the catalysis, and therefore giving rise to a “tetradentate” systems.^{104,105}

Complexes **Cat I. 76-79** which accommodate a bipyridine as redox active moiety in the ligand backbone, have been proposed to undertake ligand-centered redox processes.^{100,103,106} This was proposed on the basis of additional reversible reductive waves observed slightly more negative than the Co^{II/I} redox couple, which are likely attributed to ligand reduction. These results demonstrated that the ligand-assisted

catalytic processes can occur at relatively positive potentials and can play an important role even under photocatalytic conditions. The presence of non-metal centered catalytic processes contrasts with the related pentadentate catalysts **Cat I. 70-72**, in which a redox-active ligand is lacking.

The use of bipyridyl moieties has also been extended in other ligand-type backbones. In 2012, Lau and co-workers reported the complex $[\text{Co}(\text{qpy})(\text{OH}_2)_2]^{2+}$ (**Cat I. 80**)¹⁰⁷ (qpy 2,2':6',2'':6'',2'''-quaterpyridine) as an efficient visible-light driven catalyst for both water reduction and water oxidation. It was able to produce H₂ (1730 TON) when it was paired with an iridium photoredox catalyst ($\lambda = 420 \text{ nm}$) and TEOA as sacrificial electron donor.

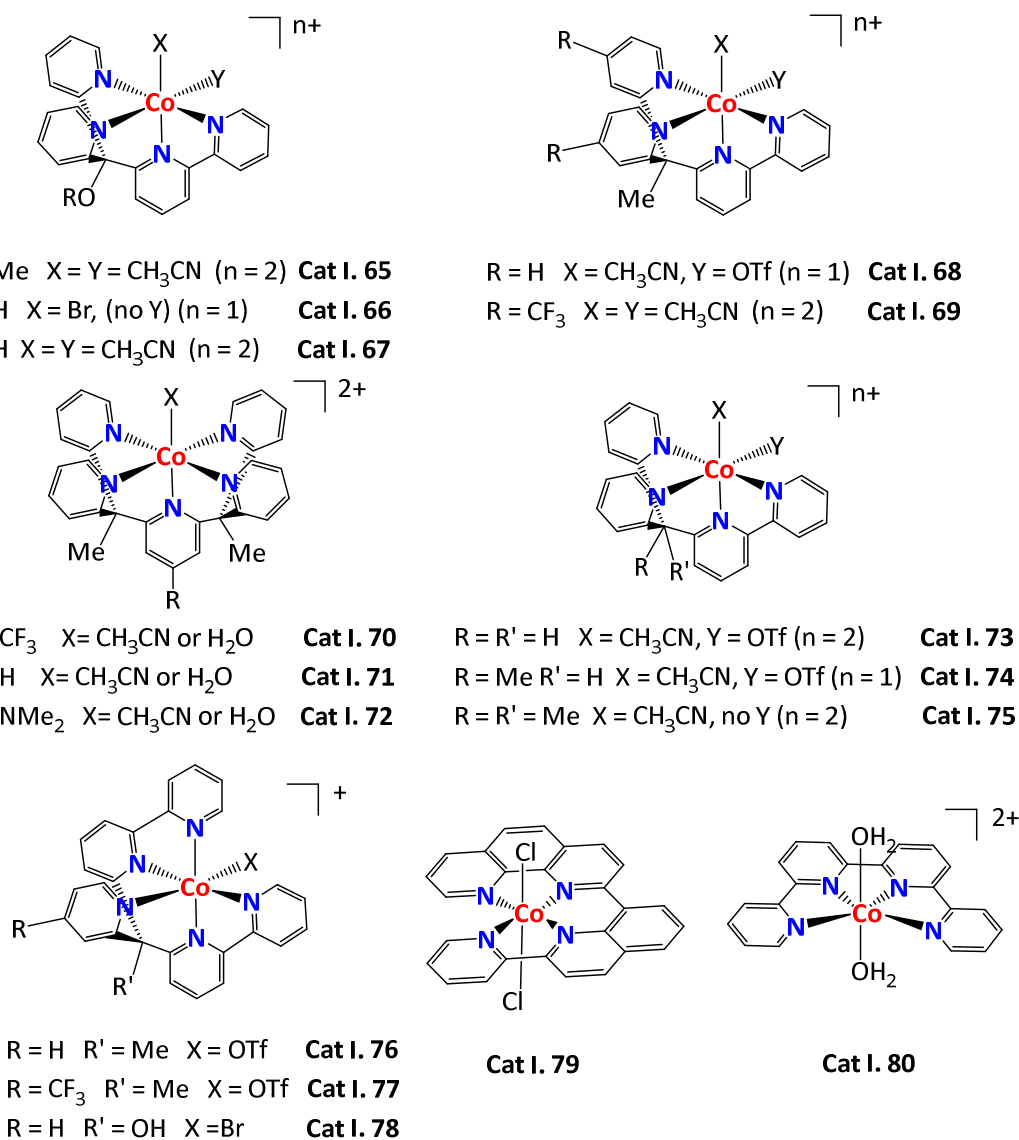


Figure I. 8. Selected cobalt polypyridyl catalysts for H₂ evolution.

In the same year, Wester, Zaho and co-workers developed the mononuclear pentadentate cobalt complex $[\text{Co}(\text{DPA-Bpy})(\text{OH}_2)]^{3+}$ (**Cat I. 81**)¹⁰⁸ (DPA-bpy = N,N-bis(2-pyridinylmethyl)-2,2'-bipyridine-6-methanamine) that efficiently catalyzed the production of H_2 in purely aqueous solution in both electrochemical (overpotential of 600 mV) and photochemical approaches (TON = 2100, TOF up to 1900 h^{-1}) (Figure I. 9). In a more recent report,¹⁰⁹ the same authors replaced the two pyridine moieties by isoquinoline groups (**Cat I. 82**). The modification of the electronic nature of the ligand let them reduce the overpotential (530 mV) and improve around 2 fold the photocatalytic efficiency (5400 TON). Meanwhile, the bipyridine moiety was modified to create the $[\text{Co}(\text{DPA-Dmphen})(\text{OH}_2)]^{2+}$ complex (Dmphen = 9-methyl-1,10-phenanthroline-2-yl)methyl]bis-(pyridin-2-ylmethyl)amine) (**Cat I. 83**).¹¹⁰ Under visible-light irradiation, **Cat I. 83** showed photocatalytic activity (210 TON) in combination with $[\text{Ir}(\text{ppy})_2(\text{bpy})](\text{PF}_6)$ as chromophore and Et_3N as sacrificial electron donor. Additionally, it showed electrocatalytic proton reduction from acetic acid at an overpotential of 480 mV.

Inspired by the good performance of cobalt aminopyridine ligands, a cobalt tripyridine-diamine complex (**Cat I. 84**) was evaluated. It was found to be a stable and highly active electrocatalyst for H_2 production in neutral water showing an activity of $860 \text{ mol H}_2 \cdot (\text{mol cat})^{-1} (\text{cm} \cdot \text{Hg})^{-1}$ over 60 h of controlled potential.¹¹¹

During the irradiation time, the formation of $\text{Co}^{\text{III}}\text{-H}$ intermediate is expected to occur with the displacement of one monodentate ligand (solvent or anion), and then it can be recovered at the end of the hydrogen evolution cycle. The situation could be a bit different for catalysts based on pentadentate ligands. Two recent works related with the N4Py platform (**Cat I. 85-88**) suggested that the formation of $\text{Co}^{\text{III}}\text{-H}$ intermediate occurs *via* decoordination of one pyridine arm of the ligand, rather than by removal of the monodentate anion from the cobalt center,^{104,112} as proposed for **Cat I. 81**.¹⁰⁵

Finally, dinuclear cobalt systems made of pyridine ligands have also been found to be active under both photo and electrochemical conditions.^{113,114}

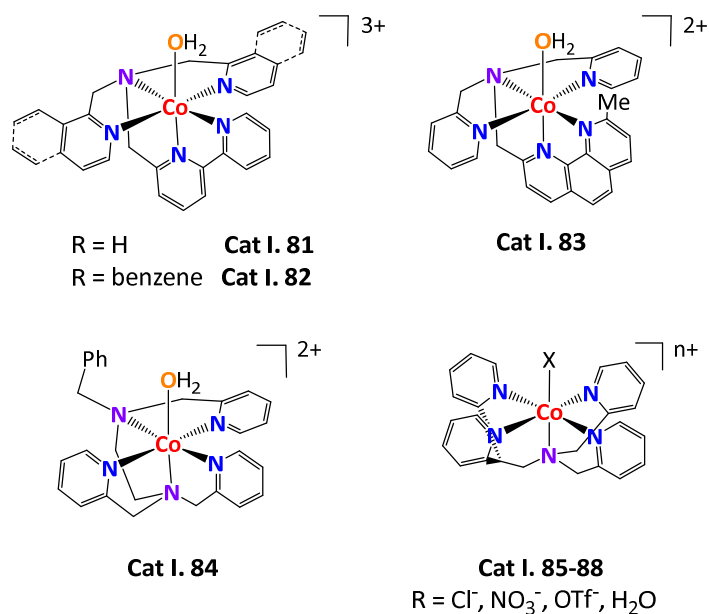


Figure I. 9. Selected cobalt catalysts based on aminopyridine ligands for H₂ evolution.

Inspired by the structural design of thiolene ligands, a series of cobalt dithiolene complexes have been developed.¹¹⁵ All of them have been found active in the electro- and photoreduction of water. These complexes are exceptionally active for the catalytic reduction of protons when paired with [Ru(bpy)₃]²⁺ as photosensitizer and ascorbic acid as electron donor, affording a highest activity up to 9000 TON. The photocatalytic activity of these systems can be significantly improved by the introduction of electron withdrawing groups on the ligand backbone (Figure I. 10).

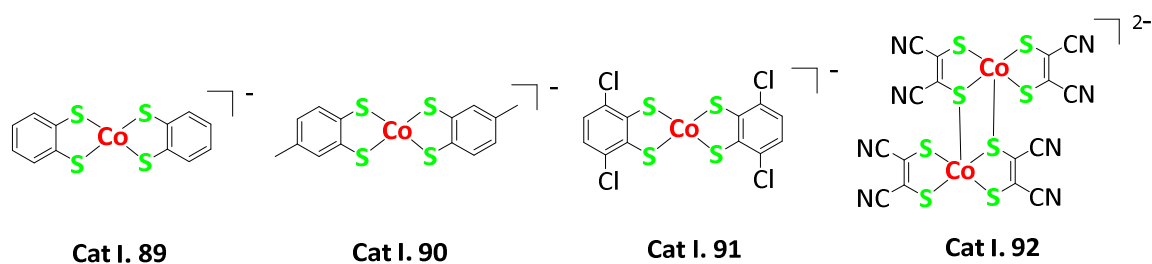


Figure I. 10. Structures of some selected cobalt dithiolene catalysts.

Finally, the reduction of water has been also explored with homogeneous systems based on other metals such as Cu,¹¹⁶ Al,¹¹⁷ Mo,^{118,119} Ru,¹²⁰ Rh¹²¹ and Pt.¹²²⁻¹²⁵

I.5.4. Hydrogen Evolution Mechanisms in Cobalt-Based Catalysts

Hydrogen evolution catalyzed by molecular complexes may occur through two distinct mechanisms. All of them imply the formation of cobalt hydride species by protonation of a Co^{I} intermediate.⁸³ In the heterolytic mechanism, the metal hydride intermediate, either $\text{Co}^{\text{III}}\text{-H}$ or $\text{Co}^{\text{II}}\text{-H}$, suffers a proton attack and evolves H_2 . During the catalytic cycle, two electrons are transferred to the complex either consecutively (Figure I. 11, heterolytic A), or alternating in two protonation steps (Figure I. 11, heterolytic B). The distinction between these two mechanisms is difficult to establish, however DFT-supported studies in cobaloxime systems favor the heterolytic mechanism involving a $\text{Co}^{\text{II}}\text{-H}$ as intermediate species from which hydrogen is evolved.¹²⁶⁻¹²⁸ In the alternative mechanism, two metal hydride complexes evolve hydrogen through the involvement of the homolytic cleavage of two Co-H (Figure I. 11, homolytic pathway). Therefore, in the course of the reaction, each cobalt center undergoes a single electron reduction, either before the protonation (Figure I. 11, homolytic A) or after the formation of the $\text{Co}^{\text{III}}\text{-H}$ species (Figure I. 11, homolytic B).^{88,129,130}

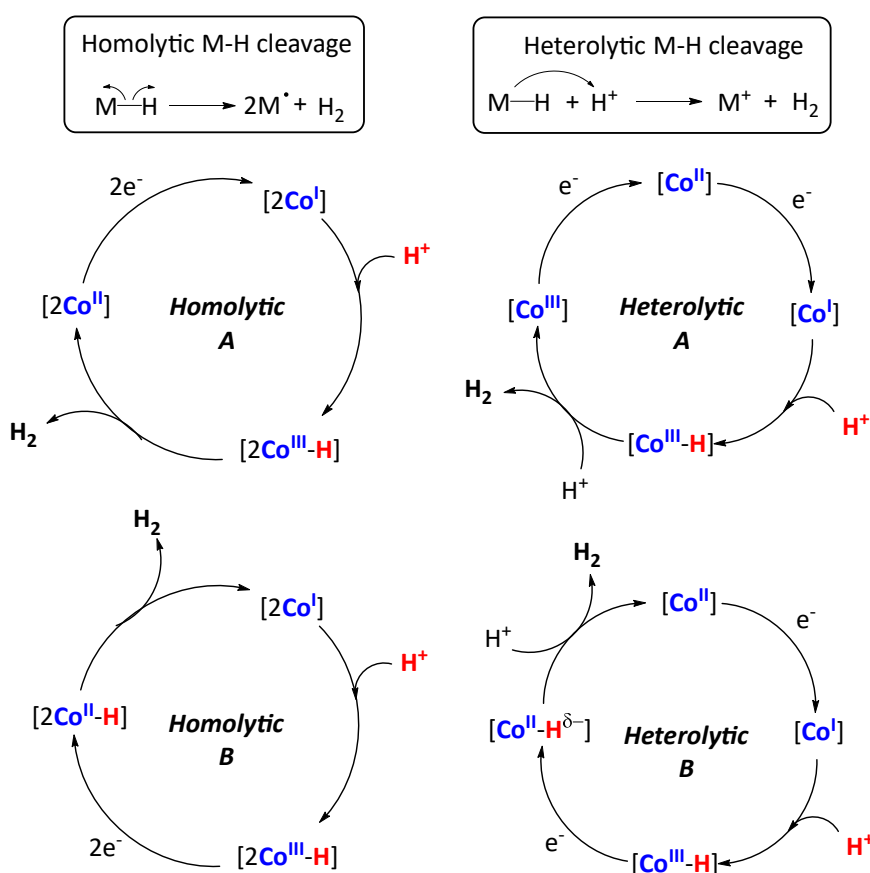


Figure I. 11. Homolytic and heterolytic mechanisms for H_2 evolution catalyzed by molecular cobalt complexes. The electrons can be provided by a photoredox catalyst or from an electrode.

It is important to remark that the electrons injected into the system can be provided by a photoredox catalyst combined with a sacrificial electron donor (photochemical H₂ production) or by an electrode (electrochemical H₂ production).

Despite the extensive mechanistic studies, some mechanistic details are still not solved, mainly due to the difficulty to detect the key reactive intermediates such as Co-H species.¹³¹⁻¹³⁵ On the other hand, both pathways can coexist,¹³⁶ and switching from an heterolytic to a homolytic pathway can be simply be a matter of experimental conditions.^{89,137}

In comparison to cobaloxime complexes,^{88,130,135,136,138,139} Co-polypyridyl systems have been mechanistically investigated in less extent. Few studies of electrocatalytic or photocatalytic H₂ evolution with Co-polypyridyl based catalysts focused on the mechanistic and kinetic details, have been performed.^{97,133,140-142} It is proposed that the heterolytic pathway involving Co^{II}-H species is the most favorable pathway, although the contribution of the homolytic pathway cannot be discarded.

I.6. ARTIFICIAL BIOMOLECULAR SYSTEMS FOR HYDROGEN PRODUCTION

The use of hydrogenases for bulk production of hydrogen is mainly hampered for their high oxygen sensitivity.¹⁴³ As depicted above, a complementary approach relies on the use of organometallic complexes including non-biomimetic^{62,83,87,88,144-148} and biomimetic systems.²⁷ The aim for structural mimicking of enzymatic natural cores rely on the development of equivalent ligand frameworks, including the challenging control of the second coordination sphere to facilitate proton shuttling to the metal active site.^{48,50,59,149-152} However, their real application in technological devices is impeded by the current activity rates which are slower than the ones achieved by the natural enzymes. In addition, high overpotentials are still required together with harsh conditions (strong acids and/or organic solvents). Therefore, considering the attractive features of biomolecular structures, an attractive approach for H₂ evolution is to assemble a synthetic catalyst with a biomolecule. The biomolecule can have a binding pocket to accommodate the synthetic catalyst and provide a specific environment that could facilitate the electron delivery and/or protect the active catalyst against undesired side-reactions and thus improving the overall stability. This concept has also been

exploited by introducing inorganic complexes into simple hydrophobic environments, such as chitostan,¹⁵³ cyclodextrine,¹⁵⁴ micelles,¹⁵⁵ metal-organic frameworks¹⁵⁶ and dendrimers.¹⁵⁷ These alternatives based on non-proteic environments also let to the increase of the stability as well as the activity of the inorganic catalytic system in photoinduced H₂ production. However, these works are outside of the scope of this thesis, and we will display some selected examples of synthetic biomolecular systems for H₂ evolution. We emphasize that nature's hydrogenase systems in assemblies for H₂ evolution^{143,158-165} will not be include in this brief summary.

I.6.1. Peptide-Catalyst Assemblies

The simplest way to emerge metal-ligand complexes with biomolecular structures is to introduce an active catalyst site into a simple peptide. Inspired on the structure of natural hydrogenases, biomimetic systems based on a [FeFe] core have received a lot of attention for their consecutive binding into peptide structures.^{166,167} This goal was pioneered by Jones and co-workers in 2007,¹⁶⁸ when it was demonstrated that a [FeFe] biomimetic complex could be bound to a designed helical peptide, and thus constructing a first generation of artificial [FeFe] hydrogenases. This work triggered the creation of more sophisticated peptides containing second coordination sphere residues designed to modulate the properties of the diiron site. These emerged systems showed their ability for the electro and photocatalytic H₂ production.

An elegant example was reported by Ghirlanda and co-workers when a diiron cluster was anchored to a synthetic α -helical peptide (Figure I. 12, A).¹⁶⁹ Interestingly, the combination of this system with [Ru(bpy)₃]²⁺ and ascorbic acid yielded 84 TON in H₂ evolution upon irradiation for 2.3 h. Moreover, an irreversible reduction wave at -1.1 V vs. SHE was observed by cyclic voltammetry. The intensity of the catalytic current depicted an interesting pH dependence (measured from 3.6 to 5.5), being more significant at decreased pH values. Similar to this work, Hayashi and coworkers developed a diiron hydrogenase model based on a peptide fragment of cytochrome C₅₅₆ with an attached diiron carbonyl cluster.¹⁷⁰ This system was found to be active in the photocatalytic H₂ production using [Ru(bpy)₃]²⁺ as chromophore (Figure I. 12, B). In a related strategy, the chromophore was attached to the same peptide giving rise an active unimolecular catalytic system for light-driven H₂ production (Figure I. 12, C).¹⁷¹

These peptide-based systems represent the initial steps for the construction of designed enzymes that mimic the structure and activity of [FeFe] hydrogenases.

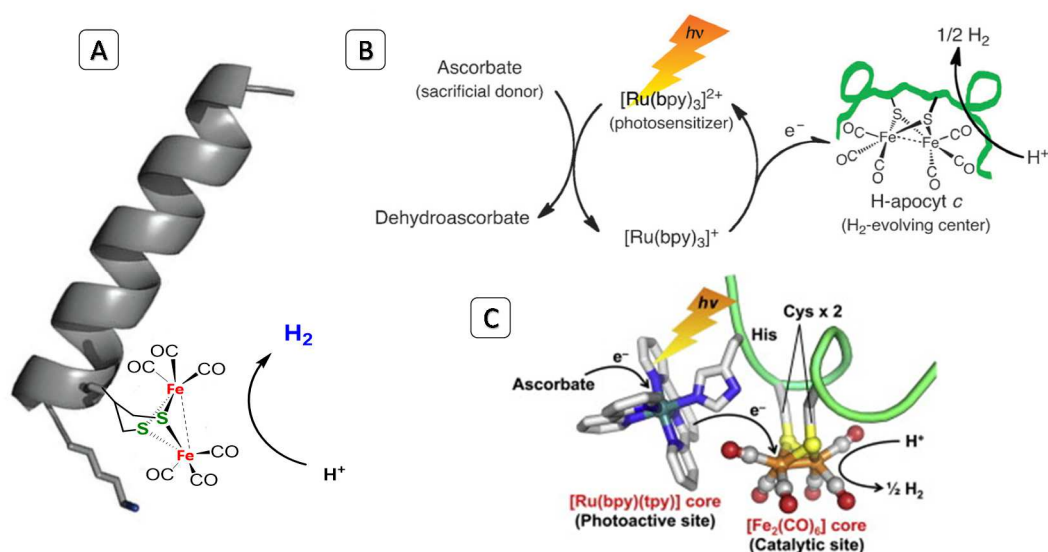


Figure I. 12. Artificial hydrogenases based on diiron-complexes and a peptide chain. A) Synthetic α -helical peptide containing $[\text{Fe}_2(\text{CO})_6]$ developed by Ghirlanda and co-workers. B) Proposed mechanism for proton reduction catalyzed by H-apocyt c containing the iron carbonyl cluster. Reprinted with permission from ref 169 Copyright 2011 Royal Society of Chemistry. C) Scheme of the photocatalytic reduction reaction of protons by [FeFe][Ru]Pep-18 in aqueous media. Reprinted with permission from ref 171. Copyright 2012 Elsevier.

I.6.2. Protein-Catalyst Hybrids

Another approach to prepare artificial hydrogenases is through the use of biomolecules. The advantage is that those biomolecules can be structurally engineered and modified providing the potentiality of rational tuning of the second coordination sphere by manipulating the protein pocket structure. The synthetic catalyst can be incorporated into a specified site of the protein. This can lead to understanding the effect of the protein environment into the catalytic activity of the metal core. One interesting example is the introduction the hydrogen evolving complex $(\mu\text{-S})_2\text{Fe}_2(\text{CO})_6$ into the cavity of the protein nitrobindin.¹⁷² The catalyst was linked through coupling a maleimide moiety to a cysteine residue within the rigid β -barrel protein matrix (Figure I. 13, A). The diiron complex embedded within the cavity depicted a photocatalytic activity in H₂ evolution of 130 TON in 6 h by using $[\text{Ru}(\text{bpy})_3]^{2+}$ as photosensitizer in a solution of 100 mM ascorbate and 50 mM Tris/HCl buffer at pH 4.0 and 25 °C. It is important to remark that the activities obtained are higher to that compared using

simple peptides and FeFe mimics. Photosystem I (PSI) is an attractive protein for converting light-energy and it was coupled by Uttischig, Teide and co-workers (2011) with a synthetic cobaloxime catalyst ($\text{Co}(\text{dmgH})_2\text{pyCl}$, $\text{dmgH}_2 = \text{dimethylglyoxime}$) for the application in light-driven hydrogen production.¹⁷³ A TON of 5200 mol H_2/mol PSI and a TOF of 170 mol H_2/mol PS I-min were obtained upon light irradiation (500 nm) for 1.5 h in the presence of sodium ascorbate as sacrificial electron donor and cytochrome c_6 as an electron mediator. The H_2 production activities were in the range of the typical activities obtained with cobaloxime catalysts (38 to 9000 TON).^{88,174} Although the authors do not study the electrocatalytic proton reduction with this biocatalytic system, they note that the $\text{Co}^{\text{II/I}}$ potential of $\text{Co}(\text{dmgH})_2\text{pyCl}$ was shifted toward negative potentials when introducing the catalyst inside the protein (from -740 to -880 mV). They attribute the shift of ~ 140 mV due to the hydrophobic interior of PSI.

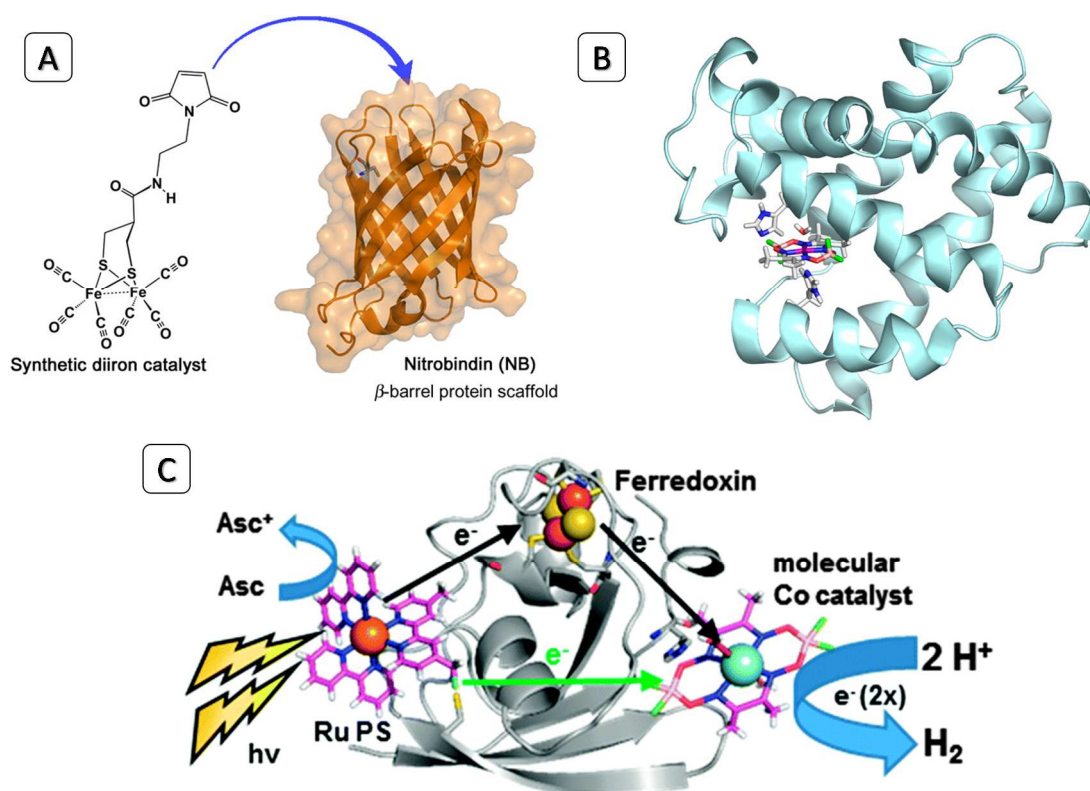


Figure I. 13. The modified hydrogen evolving complex $(\mu\text{-S})_2\text{Fe}_2(\text{CO})_6$ reacts with a cysteine residue located inside of the protein nitrobindin cavity. B) Structure of SwMb-cobaloxime computed at the QC-MM level. C) Photocatalytic H_2 production scheme in Ru-Fd-Co biohybrids with two possible pathways for electron transfer from PS to catalyst. Reprinted with permission from (A) ref 172, (B) ref 173 and (C) ref 179. Copyright 2014 American Chemical Society.

Despite everything, the limiting factor of this catalytic system is the low longevity (up to 1.5 h) mainly attributed to the catalyst dissociation from PSI during photocatalysis.

The assemble of the PSI with a synthetic nickel catalyst ($[\text{Ni}(\text{P}_2\text{PhN}_2\text{Ph})_2](\text{BF}_4)_2$)^{59,175} has been also reported (2013). Under photocatalytic conditions using ascorbic acid and cytochrome c_6 , a total TON of 1870 mol H_2 /mol PSI were obtained.¹⁷⁶ This value was lower to that obtained with the free catalyst under comparable conditions (2700 TON).⁶¹ However, although the TON of the Ni-PSI complex was lower, the rate in H_2 evolution was 10 times greater.¹⁷⁶

Artero and co-workers developed in 2014 two well-defined biohybrid systems for H_2 production operating in neutral aqueous solution. In particular, they inserted the synthetic cobaloxime derivatives $\text{Co}(\text{dmgH})_2$ and $\text{Co}(\text{dmgBF}_2)_2$ into the heme pocket of apo *Sperm-whale* myoglobin (*SwMb*) (Figure I. 13, B).¹⁷⁷ Spectroscopic measurements and modelling studies demonstrated that the protein provides an axial histidine imidazole His93 to bind the cobalt catalyst inside the protein pocket. Interestingly, electrochemical studies revealed that the cobaloxime-Mb complex evolved H_2 in neutral aqueous solution at low overpotential (200 mV). In addition, the cyclic voltammogram of the cobaloxime-Mb complex recorded in Tris-HCl (pH 7.5) buffer displayed a $\text{Co}^{\text{II/I}}$ redox couple at -0.58 V vs. SCE. This value is significantly more negative (about 100 mV), compared to the free catalyst alone, which is -0.38 V vs. SCE. The authors attributed this shifts not only to the coordination of the His93 ligand but also to the modulation of the second-coordination sphere interactions or the specific dielectric constant experienced by the complex within the protein framework. These results are equivalent to the negative shift observed in the PSI-cobaloxime system previously mentioned.¹⁷³ Additionally, these biohybrids also provide photocatalytic activity in H_2 evolution showing up to 10 TON, with a very short lifetime (around 5 min). The authors proposed that the decomposition of the catalytic system could be attributed to the hydride transfer event from an active $\text{Co}^{\text{III}}\text{-H}$ species to the glyoximate ligand. This transfer could take place before the second electron transfer yielding $\text{Co}^{\text{II}}\text{-H}$, which is then responsible for H_2 production. On the other hand, it can also be possible that the protonation of $\text{Co}^{\text{II}}\text{-H}$ is significantly slower than the deactivation pathway, which then magnifies the

deactivation of the catalytic system. The use of stable ligands against reduction is highly important to develop robust and efficient artificial metalloenzymes.

With the aim to control the electron transfer pathways,¹⁷⁸ Utschig and co-workers assembled in the ferredoxin protein the photoredox catalyst $[\text{Ru}(\text{bpy})_2]^{2+}$ as a donor and the metal complex $\text{Co}(\text{dmgBF}_2)_2$ as an acceptor (Figure I. 13, C).¹⁷⁹ The iron-sulfur cluster (Fd [2Fe-2S]) of the ferredoxin protein provides an electron relay between an attached units. This biohybrid system is capable of producing H_2 from water up to 210 ± 60 TON with respect to the photosensitizer. By several spectroscopic techniques it was demonstrated that the Fd [2Fe-2S] cluster is necessary for the activity, indicating that the electron-transfer site connects the donor and the acceptor allowing the formation of a long-lived (> 1.5 ns) $\text{Ru}(\text{III})\text{-Fd-Co(I)}$ charge separated state.¹⁸⁰

I.6.3. Biocatalytic Systems Made by Metal-Substitution

The construction of protein-catalyst hybrids is a conceptual easy manner to create a desired active-site structure inside the protein pocket. However, one of the main problems is that proteins have not evolved to accommodate the synthetic catalysts, and in some cases the inclusion of a catalyst it can derive in their inactivation. An alternative approach is the modification of natural enzymes using metal substitution and/or mutation. This method enables to obtain more well-defined structures at the active site compared to the synthetic catalyst-protein hybrids, facilitating characterization, mechanistic studies and active-site engineering. A first demonstration of this strategy was carried out in 1988 by constructing a nickel tetrahedral sulfur-coordinated core formed by replacing the native iron in *Desulfovibrio* species rubredoxins (non-hydrogenase protein) by nickel.¹⁸¹ This metal substitution led to obtain of a nickel rubredoxin (NiRd) with an active site similar to the nickel site of [NiFe] hydrogenases.¹⁸² More recently, the nickel-substituted rubredoxin was studied in the electro and photocatalytic proton reduction to hydrogen.¹⁸³ The authors demonstrated that these systems are able to generate H_2 with an overpotential of 540 mV (similar to some synthetic catalysts reported in the literature¹⁴⁸) showing maximum turnover frequencies of $20\text{-}200\text{ s}^{-1}$ at $4\text{ }^\circ\text{C}$. These rates as well the electrocatalytic mechanism (PCET) are directly comparable to those obtained for [NiFe] hydrogenases under similar conditions. In addition, photoinduced hydrogen production was also observed with an

initial TOF of 0.5 min^{-1} ($80.6 \pm 14.4 \text{ nmol/min/mg protein}$) reaching a maximum TON of 100 at decreased protein concentrations. These engineered rubredoxin-based enzyme are chemically and thermally robust, easily accessible and highly tunable.

In the same line, Ghirlanda and co-workers showed for the first time that cobalt myoglobin (CoMyo) catalyzed hydrogen production in mild conditions with a TON of 520 over 8 h of irradiation.¹⁸⁴ The CoMyo was constructed by replacing the native iron protoporphyrin IX with cobalt protoporphyrin IX (CoP) (Figure I. 14, A). Compared to free CoP, the incorporation into myoglobin resulted in a 4-fold increase in the photoinduced hydrogen production activity. Additionally, engineered variants in which specific histidine residues in proximity to the active site were mutated to alanine resulted in modulation of the catalytic activity, improving up to 2.5-fold times the activity using the H64A/H97A mutant. On the other hand, the electrocatalytic activity of these system was found to be also dependent on the mutant nature. This study illustrated that the activity could be modulated by mutating the protein. Surprisingly, a decrease in the activity of CoMyo was seen below neutral pH, and it was attributed to the protonation of the His proximal to the active site. Encouraged by these promising results, the same group swapped the Fe-protoporphyrin for CoP in cytochrome b_{562} , and it resulted in an efficient catalyst for the photoinduced proton reduction to hydrogen.¹⁸⁵ The activity of wild type Co-cyt b_{562} could be modulated by a factor of 2.5 by exchanging the coordinating methionine axial ligand with alanine or aspartic acid. The observed TON were between 125 and 305, and correlated well with the redox potential of the Co-cyt b_{562} mutants. Finally, photocatalytic activity could be observed even under aerobic atmosphere. This cobalt-porphyrin protein depicted similar activity to that obtained with CoMyo.

Inspired by cobalt substitution, Bren and co-workers developed a biomolecular catalyst made from the cobalt substitution of microperoxidase-11 (MP-11), a water-soluble heme-undecapeptide derived from the horse protein cytochrome c .¹⁸⁶ MP-11 consists in a heme attached to an 11-mer peptide through a Cys-X-X-Cys-His motif in which the two Cys residues form covalent bonds to the porphyrin and His coordinates to iron. The authors obtained the final biomolecular catalyst by substituting the iron with cobalt, and the free amino groups were acetylated to give the acetylated cobalt

microperoxidase-11 (CoMP11-Ac) (Figure I. 14, B). One axial position of the complex is occupied by one His.¹⁸⁷ In aqueous solution at pH 7.0, this catalytic system was able to reduce protons to H₂ electrocatalytically under aerobic conditions. Additionally, it operates near quantitative Faradaic efficiency, with a TOF ~6.7 s⁻¹ measured over at 10 min at an overpotential of 852 mV. The total TON obtained with the biomolecule were 2.5x10⁴ over 4 h of controlled potential electrolysis, showing low sensitivity to oxygen. Interestingly, they found a significant enhanced catalytic activity (measured by TOF) relative to that reported for other water-soluble cobalt porphyrin electrocatalysts.¹⁸⁸⁻¹⁹⁰ However, an important limitation of this system is its poor stability under electrocatalytic conditions due to degradation after 15 min.

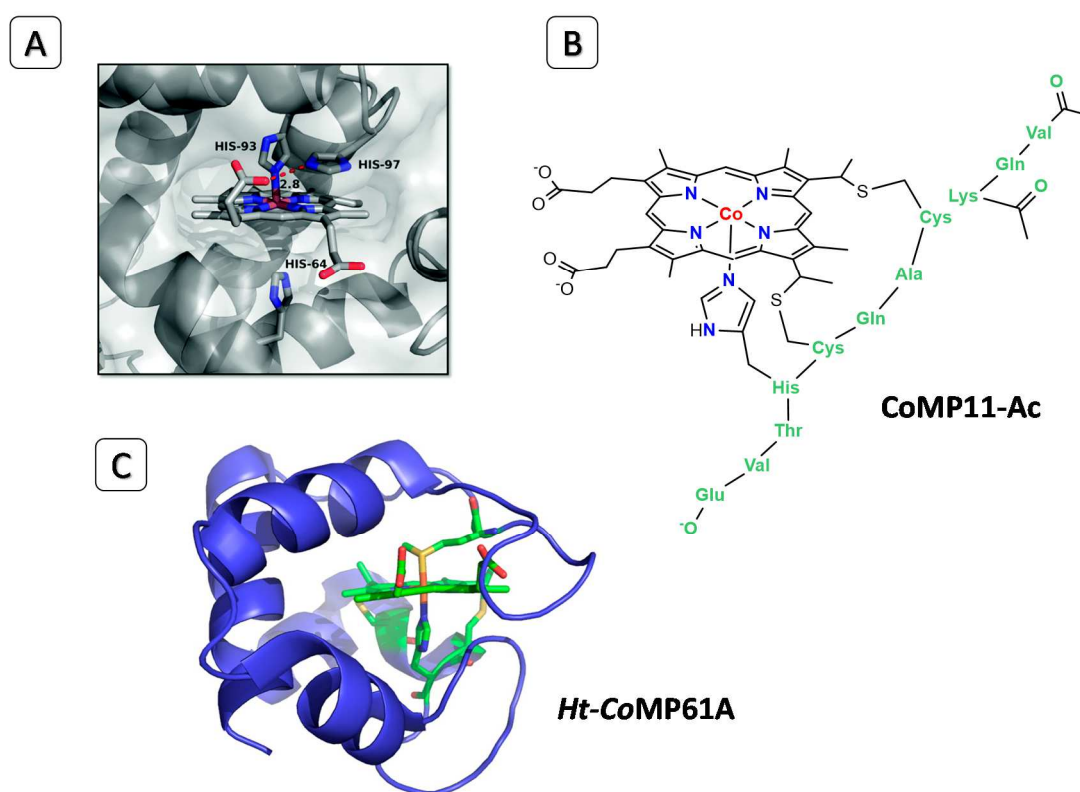


Figure I. 14. Biocatalytic systems for H₂ evolution based on cobalt. A) Synthetic CoMyo system developed by Ghirlanda and co-workers. Reprinted with permission from ref 184. Copyright 2014 Royal Society of Chemistry. B) Structure of the synthetic CoMP11-Ac system. C) Biocatalytic system *Ht*-CoM61A developed by Bren and co-workers. Reprinted with permission from ref 187. Copyright 2016 American Chemical Society.

Very recently, with the aim to enhance the catalytic stability and activity of CoMP11-Ac, the same group prepared a biomolecular catalyst with an active site similar to that of CoMP11-Ac but the porphyrin contained within a heme pocket.¹⁹¹ To achieve

these goals, they enhance the activity by manipulating the active site environment¹⁹²⁻¹⁹⁴ and the longevity of the system was improved by changing the polypeptide matrix.¹⁸⁴ Therefore, they developed a cobalt-substituted M61A mutant of *Ht c-552* (*Ht-CoM61A*) (Figure I. 14, C), which was found to be an excellent electrocatalysts for H₂ evolution capable to produce up to TON > 270000, which is more than 10-fold fold increase than CoMP11-Ac. The electrocatalytic activity of this biocatalytic system was observed at -1.45 V vs. Ag/AgCl (1 M AgCl), corresponding to an overpotential of 800 mV for proton reduction at pH 7.0. In addition, cyclic voltammograms of *Ht-CoM61A* were found to exhibit a pH-dependence catalytic wave, with an onset of ~1.30 V. The current increased at lower pH, as expected for proton reduction. The lifetime of the catalytic system was also improved up to 24 h, which demonstrated that surrounding the cobalt porphyrin active site with the polypeptide chain significantly enhanced its robustness in electrocatalysis.

I.7. CATALYTIC SYSTEMS FOR THE REDUCTION OF ORGANIC MOLECULES WITH LIGHT

I.7.1. Use of Light for Challenging Organic Chemical Transformations

The use of light, generally visible light, as driving force for chemical reactions has attracted much attention in organic chemistry.^{195,196} In the last years, photoredox catalysis has emerged as a powerful tool to activate and transform organic molecules.¹⁹⁷⁻²⁰¹ In a general sense, this approach relies on the ability of metal complexes, semiconductors or organic dyes to engage single-electron transfer with organic substrates upon excitation by visible-light. Nevertheless, the capacity of some substrates to generate radicals allows the extension of the photochemical reactivity beyond the substrate reduction, such as dehalogenation,^{200,202,203} cross-coupling,²⁰⁴ radical cyclizations,²⁰⁵ C-H functionalization,^{206,207} arylations, hydroaminations,²⁰⁸ cycloadditions,²⁰⁹ C-C bond formation,²¹⁰ amine functionalization,²¹¹ etc.... In addition, the own reductive power of the photoredox system has also been employed to undergo the reduction of organic substrates by single-electron transfer. For instance, NO₂ groups have been efficiently reduced into the corresponding amino groups using TiO₂,²¹²⁻²¹⁹ CdS,^{220,221} ZnO,²²² Au nanoparticles,²²³⁻²²⁶ Ag nanoparticles,²²⁵ Cu nanoparticles,²²⁷

SrBi₂Nb₂O₉,²²⁸ PbBi₂Nb₂O₉,²²⁹ In₂S₃,²³⁰ WO₃-Ag nanowires,^{231,232} organic dyes,^{233,234} metal-organic frameworks²³⁵ and [Ru(bpy)₃]²⁺.^{236,237} In the same way, ketones have been reduced by single electron transfer to the corresponding alcohols by TiO₂,²³⁸⁻²⁴¹ dye-sensitized-TiO₂,^{242,243} CdS,^{244,245} Au nanoparticles^{223,224} and organic polypyridinic systems.^{246,247} On the other hand, activated olefins have been reduced on CdS²⁴⁵ and [Ru(bpy)₃]²⁺.²⁴⁸

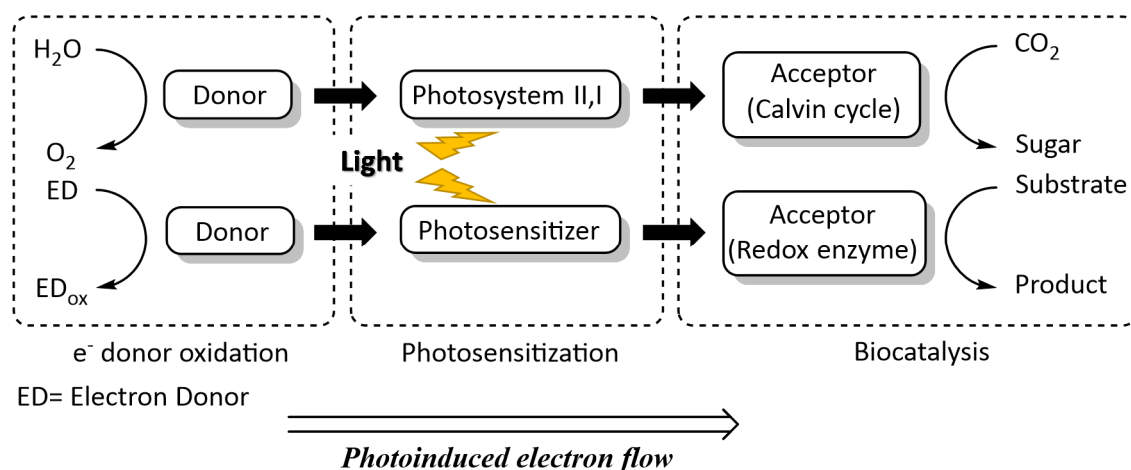
Despite these advances, the direct reduction of the functional group by single electron transfer from the photoredox catalyst is often limited to the redox potential of the chromophore. Actually, the use of high-energy light (UV) is often needed. Moreover, one of the major impediments for the direct application is the formation of undesired by-products such as dimers.^{244,245} Indeed, the photoredox-catalyzed reductive coupling of ketones and aldehydes is well-known through the formation of ketyl radical intermediates.²⁴⁹

One strategy to address this drawback is the modification of the properties of the photoredox catalysts. This implies the appropriate tuning of the redox potential of the chromophore system. However, this is a difficult task, especially considering the control of selectivity. An alternative solution is the introduction of functionalized molecules, such as organometallic complexes or biocatalytic systems, as electron mediators or hydride donors between reactants and photosensitizers/semiconductors. These catalytic systems can act as co-catalysts, activated by photoexcited electron-transfer processes and then trigger catalytic reactions. This strategy has inherent advantages: (1) it facilitates the charge separation process in space, (2) reduces the energy barrier of reactants by multistep electron-transfer, (3) lets to control the selectivity through the active sites of the (bio)catalysts, and (4) lets to rationally design the reactions according to the activity of the catalyst. The cooperation between photoredox catalysis and other domains in catalysis such as transition-metal catalysis, biocatalysis or electrocatalysis, for the catalytic organic transformation has been explored in the recent years.²⁵⁰ Cooperative photoredox catalysis merges the best of both a light-dependent cycle and a light-independent cycle in order to achieve a synergic photochemical system for the organic substrate transformation. In the following

sections we will discuss some selected examples of this field using (bio)catalytic systems for substrate reduction.

I.7.2. Coupling Visible-Light Photoredox Catalysis with Biocatalytic Systems for the Reduction of Organic Molecules

The ultimate goal is the use of solar energy for the synthesis of fine chemicals and fuels (Scheme I. 2). In this line, biocatalyzed light-driven reactions have emerged by coupling photocatalysis with biocatalytic systems. As it occurs in natural photosynthesis, these transformations are based on photoinduced electron-transfer processes, which finally trigger enzymatic chemical synthesis. Although natural photosystems are highly efficient in the solar energy storage, they are too complex to be directly coupled with synthetic biocatalyzed transformations. Therefore, the direct use of biocatalytic systems in combination with photoredox catalysts lets the transformation of organic molecules under mild conditions.



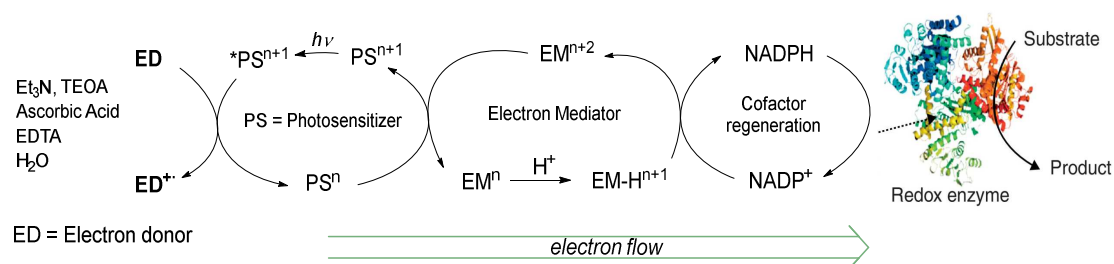
Scheme I. 2. Visible light-driven chemical synthesis in natural photosynthesis and biocatalyzed artificial photosynthesis.

This process is accomplished by regenerating biochemical cofactors, such as nicotinamide cofactors (i.e. NAD(P)H) or FADH₂, through photosensibilization by organic dyes, metal complexes or inorganic semiconductors.²⁵¹ The electrochemical reduction of NAD(P)⁺ into NAD(P)H takes place through a two-step electron transfer (-1.1 and -1.7 V vs. SCE) from an electron donor, followed by protonation.²⁵² In order to avoid the formation of NAD(P)H isomers and dimers²⁵³ (which are enzymatically inactive), an

electron mediator is needed and thus adding another catalytic cycle in the whole process.

Electron mediators obtain electrons from high-energy electron sources (i.e. photoredox catalysts) (in natural systems it would be Ferredoxin, which reacts with ferredoxin-NADP reductase (FNR)). The most commonly used synthetic ones are methyl viologen (MV)^{254,255} and a rhodium-based organometallic mediator, $[\text{Rh}(\text{bpy})(\text{Cp}^*)\text{H}_2\text{O}]^{2+}$ (bpy = bipyridine, Cp* = pentamethylcyclodienyl), developed by Steckhan and co-workers.²⁵⁶⁻²⁵⁸ The rhodium-based mediator has been widely used since it exhibits high robustness over pH and temperature, and transfers two electrons and one proton to the NAD(P)^+ cofactor through the formation of a hydride-intermediate $[\text{Rh}(\text{bpy})(\text{Cp}^*)\text{H}]^+$.^{259,260}

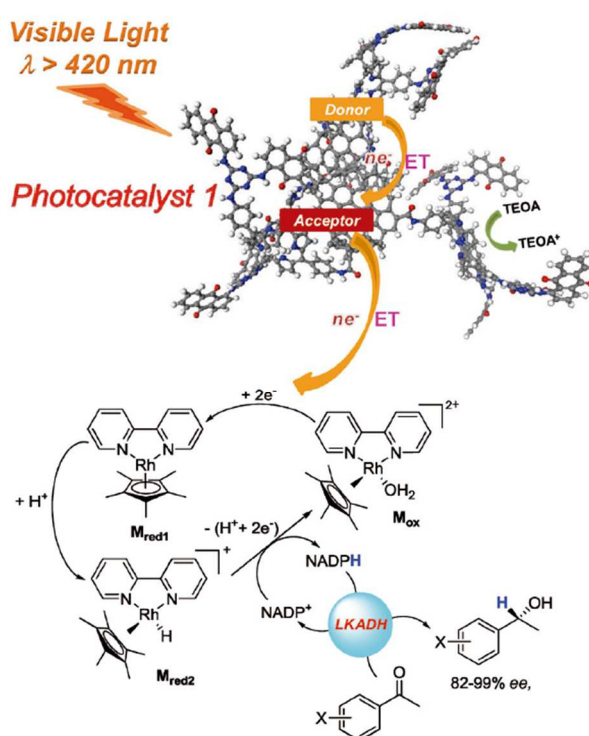
The process starts when the electrons are transferred from an electron donor (typically TEOA, Et₃N, ascorbic acid, EDTA, and more rarely H₂O) to the light-harvesting system, which are then used to activate the electron mediator responsible to regenerate the biochemical cofactor. Finally, this is stoichiometrically consumed by the enzymatic system generating again the oxidized form of the biochemical cofactor and therefore closing the catalytic cycle (Scheme I. 3).



Scheme I. 3. General scheme for biocatalyzed light-driven reactions.

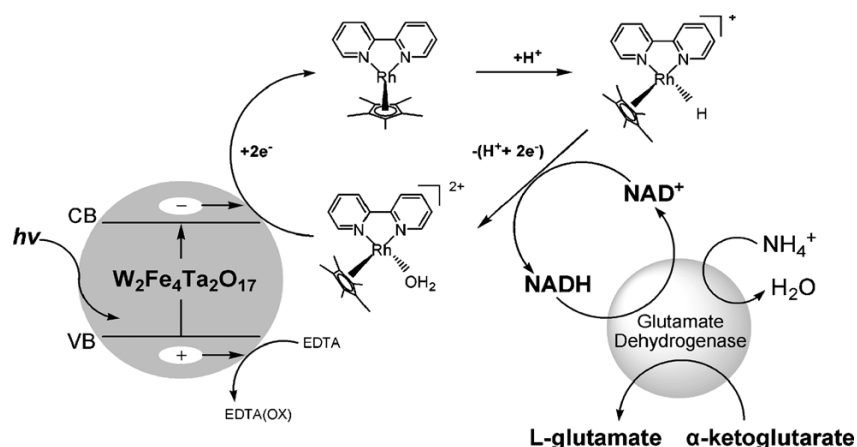
Biocatalyzed artificial photosynthesis is still in its infancy. However there are few systems based on redox enzymes that have demonstrated the viability of selective light-driven reduction of substrates using water as the source of hydrogen, for the production high-value chemicals or fuels. In this Chapter we will only discuss the examples based on the photochemical reduction of organic molecules induced by a biocatalytic process. Nevertheless, other applications such as oxidation of organic substrates have been reported.^{250,251,253}

Encouraged and fascinated by the merge between photocatalysis and biocatalysis, Baeg and co-workers (2012) developed a graphene-based photocatalyst, composed of chemically converted graphene coupled with the organic dye multianthraquinone-substituted porphyrin (CCGMAQSP), which was used as visible-light ($\lambda > 420$ nm) photoredox catalyst for the chiral biocatalytic reduction of ketones using an enzyme (alcohol dehydrogenase from *Lactobacillus kefir*, LKADH) (Scheme I. 4).²⁶¹ The reaction started with the reductive quenching of visible-light-excited CCGMAQSP by TEOA, resulting in the oxidation of TEOA and the transfer of electrons to the Rh complex, which regenerates the NADPH cofactor. Then, the enzyme LKADH consumes the reduced NADPH to perform the chiral synthesis of alcohols. Both enzymatic and photoredox catalysis occur at the buffered aqueous phase, while the chiral alcohol products are formed in the organic one. Although this is a very complicated scheme, it is one of the best schemes to demonstrate the concept of biocatalytic reactions for challenging synthesis fine chemicals.²⁶²



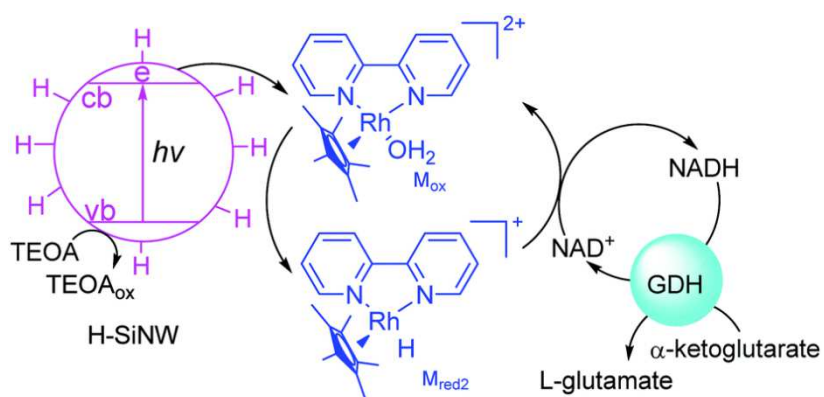
Scheme I. 4. Plausible mechanism of asymmetric reduction of acetophenones based on multianthroquinone porphyrin as a visible-light harvester, promoting the reduction of NADP⁺ to NADPH. LKADH: alcohol dehydrogenase from *Lactobacillus kefir*. ET = Electron transfer. Adapted with permission from ref ²⁶¹. Copyright 2015 John Wiley and Sons.

Organic dyes can be replaced by inorganic semiconductors.²⁶³ Many different types of semiconducting materials such as metal oxides,^{254,264-267} quantum dots,^{254,268-270} metal nanoparticles²⁷¹ and their composite materials,^{270,272} have been reported for the heterogeneous photocatalytic regeneration of NAD(P) cofactors. The use of the inorganic photocatalyst $W_2Fe_4Ta_2O_{17}$ combined with $[Rh(bpy)(Cp^*)H_2O]^{2+}$ as electron and proton shuttle selectively regenerates the NADH cofactor. In the final step, NADH is consumed by α -ketoglutarate substrate for its enzymatic (L-glutamate dehydrogenase) conversion to L-glutamate in the biocatalytic cycle (Scheme I. 5).²⁷³ Therefore, as in the previous example, the catalytic cycles couples integrally the work of an inorganic system with an enzyme yielding ultimately the amino acid. In this case, the electrons are provided by EDTA which acts as sacrificial electron donor.



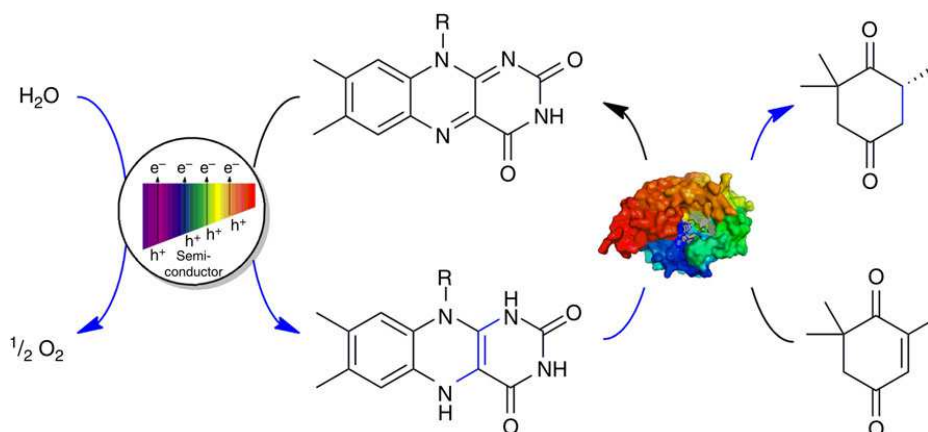
Scheme I. 5. Schematic diagram of photochemical cofactor regeneration using an inorganic photosensitizer and their connection with L-glutamate dehydrogenase for the synthesis of L-glutamate from α -ketoglutarate. Reprinted with permission from ref 273. Copyright 2012 John Wiley and Sons.

An analogous system has been developed for the asymmetric reduction of α -ketoglutarate by L-glutamate dehydrogenase but through the use of hydrogen-terminated silicon nanowires (H-SiNWs) that act as photoredox catalysts.^{274,275} In this system,²⁷⁶ visible-light ($\lambda > 420$ nm) promotes the excitation of the H-SiNWs electrons transferring them to NAD^+ via the rhodium-based mediator ($[Rh(bpy)(Cp^*)H_2O]^{2+}$), followed by biocatalytic conversion of α -ketoglutarate to L-glutamate (Scheme I. 6). Light-harvesting H-SiNWs systems are very promising since they enhance the electron transfer to the mediator and amplify the photocatalytic conversion efficiency.²⁷⁷



Scheme I. 6. Schematic diagram of photochemical cofactor regeneration using H-SiNWs as photosensitizer and their connection with L-glutamate dehydrogenase for the synthesis of L-glutamate from α -ketoglutarate. Reprinted with permission from ref 276. Copyright 2016 Royal Society of Chemistry.

An step forward was done by Hollmann and Corma.²⁷⁸ By combining the photocatalytic activity of Au nanoparticles (NPs) supported on TiO_2 with the enzymatic activity of oxidoreductases by means of FAD^+ as mediator and cofactor, they were able to achieve the stereospecific hydrogenation of conjugated C=C bonds of ketoisophorone to (*R*)-levodione (Scheme I. 7).



Scheme I. 7. Photobiocatalytic enantioselective reduction of ketoisophorone to (*R*)-levodione by an oxidoreductase enzyme mediated by FADH_2 using Au/ TiO_2 as a semiconductor and water as a sacrificial electron donor. Reprinted with permission from ref 278. Copyright 2014 Nature Publishing Group.

Interestingly, water was used as electron donor generating O₂ as by-product in the process (under UV and visible-light irradiation). This represented a first step to mimic the enzymatic conditions in PSII, and therefore increased the interest of the process. The electrons in the conduction band of TiO₂ reduced the FAD⁺ to the corresponding FADH₂ that was the needed cofactor to activate the oxidoreductase (*E. Coli BL21*, DE3.), which catalyzes the enantioselective reduction of the conjugated C=C bonds.

They found that the rate-determining step of the reaction was the regeneration of FADH₂ due to the difficulty to achieve the water oxidation step. This bottleneck could be overcome by using more efficient electron donors as well as by introducing electron mediators as electron relays between the semiconductor and FAD⁺. However, this work is an elegant example that demonstrates the potential of using water for photocatalytic synthesis of fine chemicals under UV and/or visible-light irradiation conditions.

From this pioneer work, Park and co-workers developed a homogeneous molecular photocatalytic system based on [Ru(bpy)₃]²⁺ as light harvester merged with a cobalt polyoxometalate as co-catalyst and ([Rh(bpy)(Cp*)H₂O]²⁺ as electron mediator, for the photoregeneration of NADPH using water as electron source.²⁷⁹

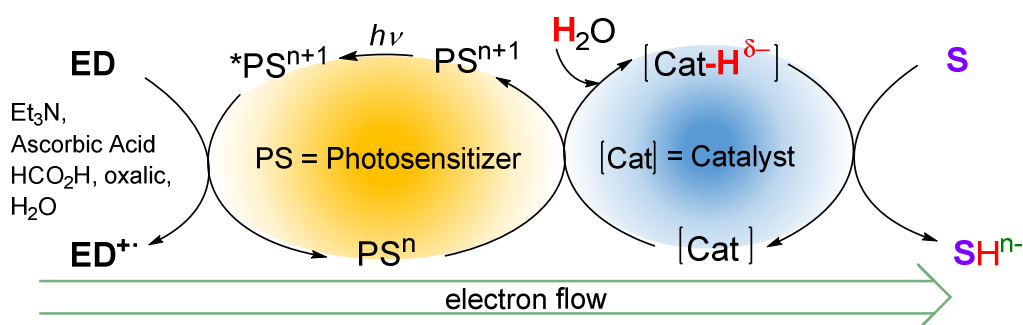
An extension of the applicability of cooperating photoredox systems is the reduction of CO₂. Baeg employed the same functionalized graphene-based photocatalyst (CCGCMAQSP) employed in the asymmetric reduction of ketones, for the photosynthetic production of formic acid from CO₂.²⁸⁰ It was achieved by coupling the light-harvesting system with the enzyme formate dehydrogenase through the use of NADPH cofactor chemically regenerated with [Rh(bpy)(Cp*)H₂O]²⁺ under visible-light irradiation ($\lambda > 420$ nm). Another related example was reported by Armstrong (2011), in which the use of CO₂ dehydrogenase I (CODHI) let the reduction of CO₂ to CO, through the use of TiO₂ nanoparticles and mercaptoethylsulphonate as sacrificial electron donor.²⁸¹

The biocatalytic systems here described are very interesting since they are elegant models that mimic natural systems, showing the viability of selective light-driven reduction of substrates using water as the hydrogen source. However, from an economic point of view, the high cost of enzymes limits their applicability in bulk synthesis. On the

other hand, the long-term chemical stability of the components^{282,283} is still an unsolved issue. Moreover, the final limited outcome (low TON and TOF) of these systems mainly attributed to the difficulty to regenerate the cofactors, requires many efforts in order to maximize the overall efficiency of the process. In addition, from an academic point of view, such systems are very difficult to study and improve due to their inherent complexity.

I.7.3. Light-Driven Reduction of Organic Molecules Catalyzed by Non-Biological Systems

To overcome the drawbacks of biocatalytic reactions, an appealing approach is the combination of synthetic catalysts and photoredox systems. Indeed this combination has been widely exploited in light-driven water reduction processes. Therefore, the synthetic catalyst would replace the role of the redox enzyme without the use of an electron mediator and natural cofactor. On the one hand this could simplify the general scheme facilitating the modulation of the activity by just changing the structural and electronic features of the synthetic catalyst (Scheme I. 8). In addition, it could facilitate the enhancement of the efficiency and longevity of the overall catalytic system. Finally, as it merges two different cycles, it opens up the opportunity to explore new reactivities/selectivities through changing the nature of the light-independent cycle.

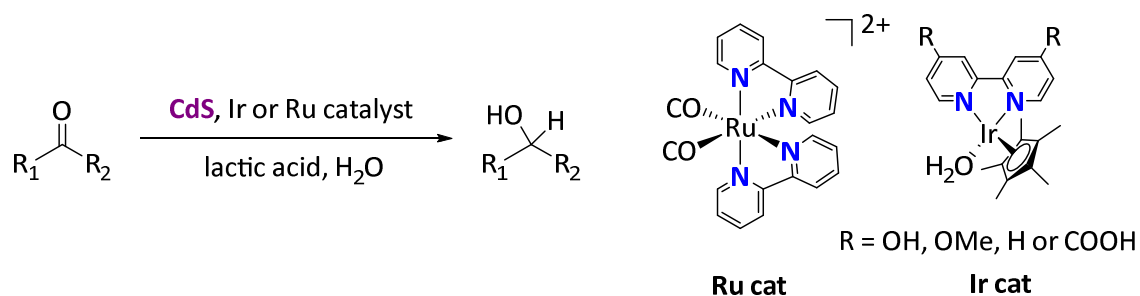


Scheme I. 8. General scheme for light-driven reductions reactions using a synthetic catalyst.

In the literature there are few examples based on the use of metal-catalytic systems that prove this idea.

1.7.3.1. Photocatalytic reduction of ketones and aldehydes

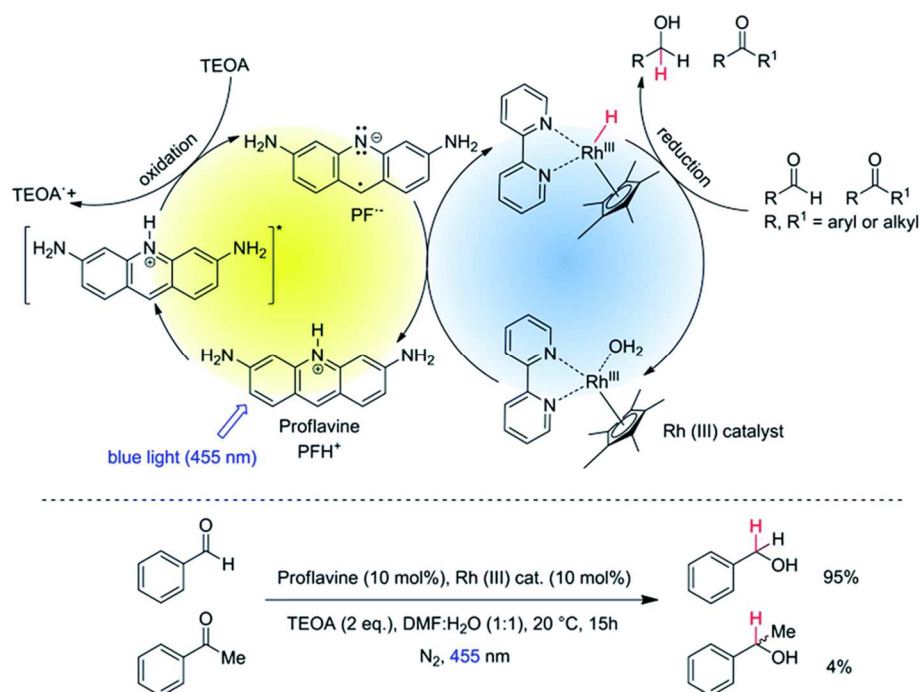
The reduction of ketones and aldehydes to alcohols promoted by visible light, was first reported employing the semiconductor photoredox catalyst CdS coupled with Ir²⁸⁴ or Ru-metal²⁸⁵ complexes (Scheme I. 9). In both systems, CdS nanoparticles harvested the visible-light energy ($\lambda > 400$ nm) and activated the homogeneous metal complex by electron transfer, which then reduced the substrate. Lactic acid was used as reductant. Despite the substrate scope was limited, the catalytic system was capable to reduce aromatic and aliphatic carbonyl compounds, conferring excellent selectivity. For instance, when 4-phenyl-3-buten-2-one was used, the reduction of the C=C bond occurred rather than the reduction of the ketone. In the case of the Ru complex, a Ru^{III}-H was proposed as active species for ketone reduction.



Scheme I. 9. Reduction of carbonyl compounds catalyzed by Ir or Ru complexes and using CdS as photoredox catalyst. For **Ir cat**: $\lambda > 400$, 300 W Xe lamp. **Ru cat**: $\lambda > 420$, Xe lamp.

Recently, an elegant combination of two catalytic cycles was discovered by König and co-workers for the chemoselective photoreduction ($\lambda = 455$ nm) of aldehydes into alcohols in the presence of ketones.²⁸⁶ It was achieved by coupling proflavine (PF) as photocatalyst with [Cp*Rh^{III}(bpy)Cl]Cl in the presence of TEOA as sacrificial electron donor. Mechanistic studies revealed that the photoreduced PF reacted with the rhodium catalyst leading to the formation of a Rh^{III}-H specie, which is the active intermediate for substrate reduction (Scheme I. 10, *Top*). Moreover, the photoredox catalytic production of Rh^{III}-H is very slow, which could kinetically distinguish between aldehydes and ketones (Scheme I. 10, *Bottom*). However, in the absence of the aldehyde compound, the catalytic system was not able to reduce ketones efficiently. For instance, acetophenone was reduced only in 7 % yield after 15 hours of irradiation. This is

attributed to the low reactivity of the rhodium organometallic complex towards the substrate reduction.



Scheme 1.10. *Top:* Proposed mechanism for the photocatalytic reduction of carbonyl compounds involving PF as photocatalyst and [Cp*Rh^{III}(bpy)Cl]Cl. *Bottom:* Chemoselective reduction of benzaldehyde in the presence of acetophenone. Reprinted with permission from ref 286. Copyright 2015 The Royal Society of Chemistry.

1.7.3.2. Photocatalytic reduction of alkenes

The photoreduction of alkenes to alkanes without the use of H₂ has been achieved in alcoholic suspension of TiO₂ with Pd as co-catalyst.²⁸⁷ Under these conditions, the UV irradiation ($\lambda_{\text{max}} = 366 \text{ nm}$) absorbed by TiO₂ promotes the reduction of H⁺ over the Pd surface to give Pd-H species, which are then inserted to a C=C bond.

In 2015 Xiong and co-workers developed a metallic nanostructure composed by a Ag-Pd alloy able to reduce styrene to ethylbenzene under visible-light irradiation ($\lambda > 400 \text{ nm}$).²⁸⁸ Without the involvement of a metal oxide support, the plasmonic metal Ag harvested light-energy into heat to drive the catalytic sites of Pd in the nanocages for the hydrogenation process, using H₂ as reductant. Although it is an example that can be hardly related to a water splitting process, it makes evident the potential of cooperative photocatalysis to accomplish organic reduction through the use of light energy.

The synergy between a photoredox material with an homogeneous system for the photocatalytic reduction of olefins was demonstrated by Shimakoshi and Hisaeda (2014).²⁸⁹ They embedded the B₁₂ complex (cyanoaquacobyrinic acid) on the surface of TiO₂ for the construction of a B₁₂-TiO₂ hybrid heterogeneous catalyst (Figure I. 15). During the UV irradiation ($\lambda = 365$ nm), and in the presence of EDTA as electron donor, the semiconductor material absorbed light facilitating the reduction of the cobalt system to Co^I intermediate. As proposed for H₂ evolution using cobalt complexes, the Co^I intermediate reacted with a proton forming a cobalt-hydride intermediate, Co^{III}-H.^{83,88,130,136} The likely radical character of Co^{III}-H, let to a hydrogen radical attack at the β -position of the alkene, in order to minimize the steric effects imposed by the α -position substituents. However, it is important to remark that the reduced product was accompanied by an important generation of dimeric products derived from the radical coupling between olefins. For instance, styrene was reduced to ethylbenzene in 10 % yield with 82 % yield of 2,3-diphenylbutane as dimeric byproduct. The authors also noted that during the irradiation time H₂ was evolved from the solution at 1 TON·h⁻¹, and the amount of H₂ was more significant in the absence of olefin, suggesting the competitiveness between water and olefin reduction promoted by UV light.

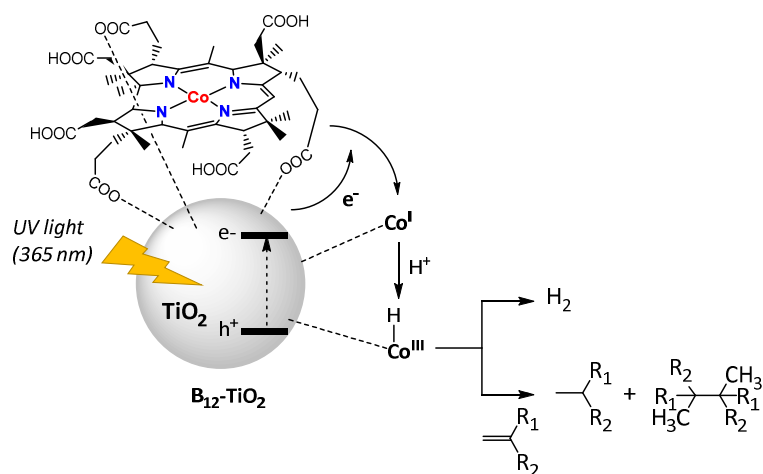


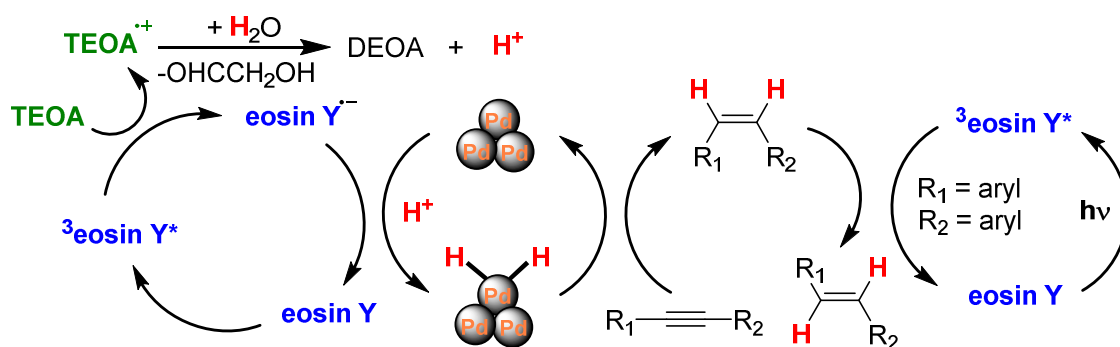
Figure I. 15. Photocatalytic reduction of water to hydrogen and alkenes catalyzed by B₁₂-TiO₂ hybrid system.

Despite the formation of dimeric products and the mandatory use of UV light, it is an important precedent since it demonstrates the possibility of triggering photoreductive reactions of organic molecules by using first-row transition metal

complexes. It could be interesting to develop alternative catalytic systems to be able to reduce more efficiently and selectively olefins employing visible-light.

1.7.3.3. Photocatalytic reduction of alkynes

Very recently, Wu and co-workers have demonstrated the potential of cooperative catalysis for the semihydrogenation of alkynes to alkenes using visible-light energy ($\lambda = 525 \text{ nm}$).²⁹⁰ The catalytic system was comprised by the organic dye eosin Y as photosensitized combined with colloidal Pd nanoparticles, taking use of TEOA as sacrificial electron donor. The catalytic transfer hydrogenation could be coupled to a photoisomerization reaction to produce *E*-alkenes or *Z*-alkenes exclusively depending on the aryl or alkyl substituted alkynes (Scheme I. 11).



Scheme I. 11. Proposed mechanism for semihydrogenation of alkynes.

These examples based on cooperative catalysis probe the possibility of transition metal complexes to undergo the reduction of organic substrates under photochemical conditions. In some cases, H₂O is used as proton source which is desirable in order to implement this process in a water splitting device.

Since transition metal hydride complexes (M-H) are postulated intermediates in hydrogen evolution catalysis, and our target organic transformations are basically related to the M-H heterolytical (H⁻ transfer) or homolytical (H[•] transfer) cleavage, we can envision that photogenerated M-H species from well-defined complexes in water, could be engaged in new challenging transformations. Therefore, hydrogens from water could be inserted to organic substrates by H⁻ or H[•] transfer, depending on the organic substrate, catalyst and conditions. In addition, the use of modular and tunable ligands could lead to new patterns of selectivity. As observed in some of these cases, the use of water as hydrogen source would avoid the use of stoichiometric chemical reductants,

such as metal hydrides and silanes or using alcohol as solvent or H₂ gas. Therefore, many efforts can be devoted to develop robust and efficient homogeneous catalysts operating at milder conditions (and using visible-light energy). These could have an important impact on many processes that are widely used in the multimillion-dollar industry of pharmaceuticals and agrochemicals.

CHAPTER II

Main Objectives

II. MAIN OBJECTIVES

The main aim of this thesis is the development and study of molecular systems capable to photo-(electro)catalytically reduce protons to H₂ and/or high-value organic molecules. To this end, it is important to rational design the catalyst architecture and to study the mechanism understand the basic parameters that controls these transformations. The knowledge acquired will aid to advance the state-of-the-art of light-driven catalyzed reduction reactions.

To date, earth-abundant homogeneous water reduction catalysts have been developed, however the structural and electronic factors that control the activity are still not well understood. On the other hand, the photoreduction of organic molecules under mild conditions is still limited and usually catalyzed by expensive, toxic and scare second and third-row transition metals. Therefore, the development of robust, modular and efficient systems based on readily available metals is needed.

In this regard, we will focus the first two parts of this thesis on the development of aminopyridine first-row transition metal complexes for the electro and photocatalytic hydrogen production. The effect of the metal (Chapter III) as well as the electronic modification of the ligand (Chapter IV) will aid towards the understanding of key aspects on the catalysis. To achieve this aim we planned to use of two different structures derived from the tacn (1,4,7-triazacyclononane) backbone (Figure II. 1). These systems will be synthesized, characterized and the catalytic activity in H₂ evolution will be evaluated.

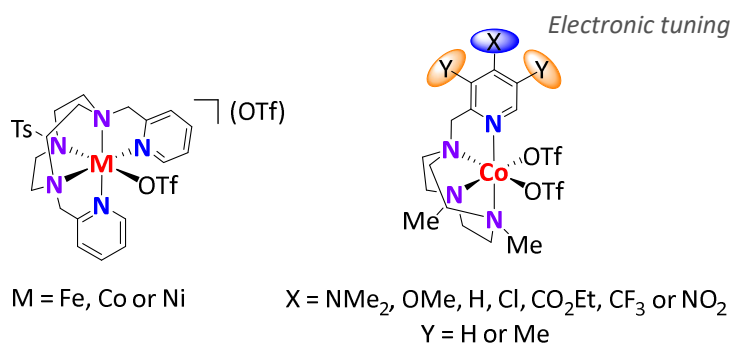


Figure II. 1. Promising first-row transition metal complexes based on penta and tetradentate aminopyridine ligands for catalytic proton reduction to H₂.

In the next part of the thesis (Chapter V) we seek to modify the secondary coordination sphere of the catalytic system. We propose to introduce a synthetic cobalt catalyst into a protein since these natural supramolecular structures provides a well-defined cavity. Taking advantage of the biotin-streptavidin interaction we plan to introduce the cobalt catalyst tuned with a biotin moiety, into the streptavidin. The photo and electrocatalytic water reduction activity of the resulting artificial metalloenzyme will be tested.

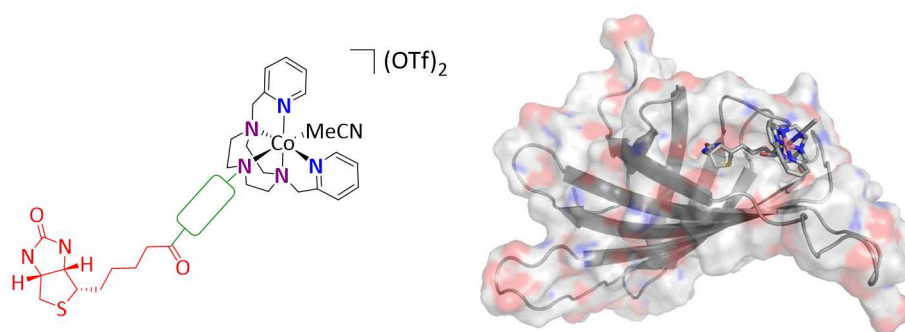


Figure II. 2. General selected cobalt biotinylated complexes for the construction of cobalt metalloenzymes.

An important objective is to study the key intermediates involved in the catalytic cycle. We aim to characterize and study the reactivity towards protons of cobalt intermediates with low oxidation state. To achieve this goal we select as model system the cobalt pentadentate structure developed in Chapter III.

In the next main objective of the thesis (Chapters VII, VIII and IX) is to explore the reduction of ketones and aldehydes using equivalent conditions used in photoinduced H_2 production. Our hypothesis is that the same catalytic systems could be employed for developing a methodology for photocatalytic organic reductions.

First, we seek to explore the basic reactivity of selected aminopyridine systems for ketone and aldehyde reduction. This also includes the optimization of the system in order to achieve better activities (Chapter VII). The use of these ligands, is very promising since it affords the possibility to easy tune the properties of the ligand. We envision that the appropriate tuning of catalyst will lead to achieve better activities (Chapter VIII).

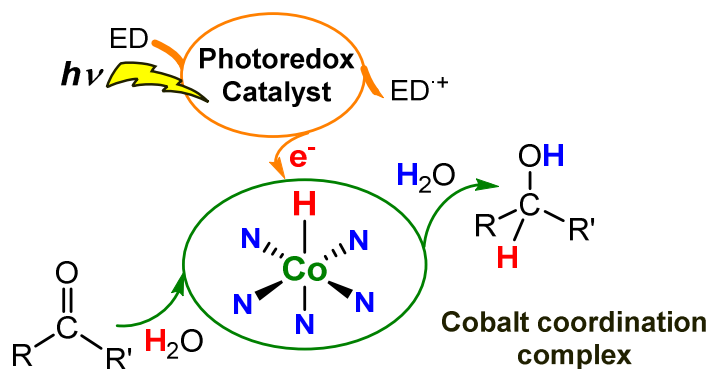
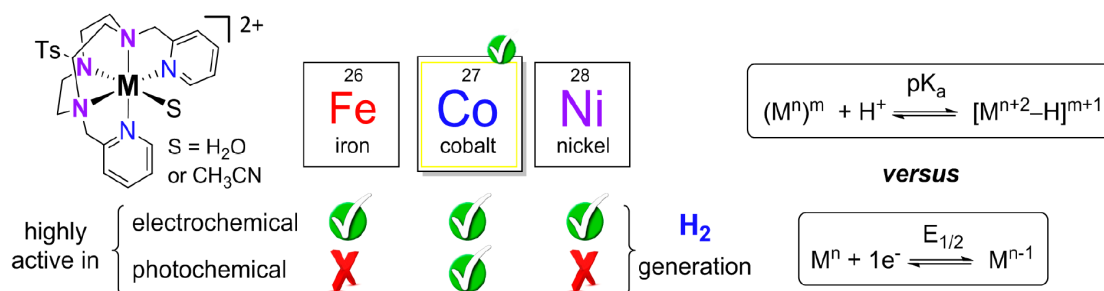


Figure II. 3. Reduction of ketones using aminopyridine cobalt complexes.

Finally, due to the finding of an efficient family of ketone reduction catalysts, the last part of the thesis (Chapter IX) is to thoroughly study the mechanism responsible for the reduction ketones and aldehydes. This understanding together with the basic reactivity explored in Chapters VII and VIII could gain insight towards the rational development of more efficient and robust ketone reduction systems.

CHAPTER III

Photo- and Electrocatalytic H₂ Production by New First-Row Transition-Metal Complexes Based on an Aminopyridine Pentadentate Ligand



III. PHOTO- AND ELECTROCATALYTIC H₂ PRODUCTION BY NEW FIRST-ROW TRANSITION-METAL COMPLEXES BASED ON AN AMINOPYRIDINE PENTADENTATE LIGAND

III.1. STATE-OF-THE ART

In the last years an intense search has been dedicated to find earth-abundant transition-metal complexes able to catalyze the reduction of protons to hydrogen at low overpotentials or by using light as a source of energy.^{27,83,88,144,146-148} Polypyridyl and aminopyridine-based catalysts has been emerged as promising catalytic systems for H₂ production, since these ligands lead to increased stabilities towards hydrolysis. This allows a more systematic evaluation of their catalytic activity in fully aqueous media. The potential of these ligands in water reduction has mainly been demonstrated through their combination with cobalt centers, since it offers the construction of very active catalysts under both photo- and electrocatalytic conditions.¹⁴⁵ Several comparative studies have been devoted to construct a series of complexes based on different metals with the same ligand,^{100,103} however the understanding of the factors that affect the reactivity has not been exploited so far.

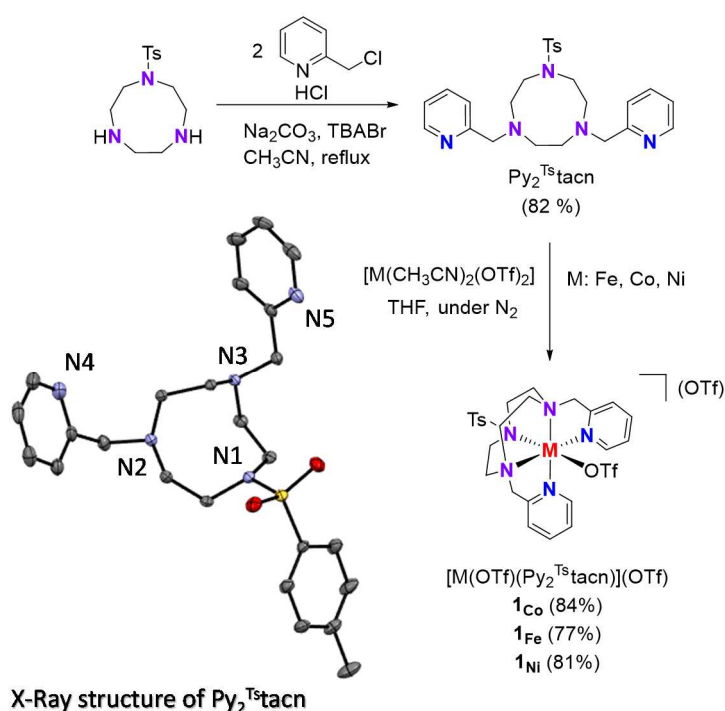
It is known that the triazacyclononane (tacn) moiety is a highly electron-donating, redox-innocent, and robust ligand moiety that stabilizes high oxidation states at metal centers. In principle, the application of ligands derived from this unit to water reduction are counterintuitive considering the mechanisms proposed for molecular complexes with polypyridine ligands that usually require reduction of the metal center to M^I or even M⁰.^{88,136} In this regard, the introduction of electron-withdrawing substituents could decrease the ligand stabilization and favour the low oxidation states,²⁹¹ but preserve the high chelating nature of the moiety. More interestingly is to explore catalysts for both water oxidation (WO) and water reduction (WR) reactions based on analogous ligand structures. To date, only a few examples of catalysts have been reported that can carry out both WO and WR catalysis.¹⁰⁷ Water splitting devices could be favoured by the use of both WO and WR catalysts build from comparable structural motifs in order to achieve compatibilities and synergies among homogeneous systems.

With this aim, we decided to construct a robust platform assembled by appending on the N atoms of the tacn ring with one electron-withdrawing tosyl group and two methylpyridine arms, giving a pentadentate ligand. The corresponding iron, cobalt and nickel complexes were synthesized in order to study the differences in reactivity in both photo and electrocatalytic conditions. This comparative study among complexes with the same ligand framework allows us to establish the basic principles for water reduction catalysts based on aminopyridine ligands.

III.2. RESULTS AND DISCUSSION

III.2.1. Synthesis and Characterization of the Py₂^{Ts}tacn Co, Ni and Fe Complexes

The synthesis of the 1,4-di(picolyl)-7-(p-toluenesulfonyl)-1,4,7-triazacyclononane (Py₂^{Ts}tacn) ligand was achieved straightforward in excellent yield (82%) from a direct dialkylation of the monotosylated 1,4,7-triazacyclononane with two equivalents of 2-(chloromethyl)pyridine hydrochloride. The ligand was characterized by NMR (See section III.3.10.5), ESI-MS, elemental analysis and X-ray diffraction.



Scheme III. 1. Synthesis of ligand Py₂^{Ts}tacn and complexes **1_{Fe}**, **1_{Co}** and **1_{Ni}**. The ORTEP structure with ellipsoids set at the 50% probability level of Py₂^{Ts}tacn ligand from the X-Ray diffraction analysis is also depicted. Hydrogen atoms have been omitted for clarity.

The reaction of the Py₂^{Ts}tacn ligand with one equivalent of [M(CH₃CN)₂(OTf)₂] (M = Co, Fe and Ni) in THF at room temperature afforded the M^{II} five-coordinated monocationic complexes of general formula [M(CF₃SO₃)(Py₂^{Ts}tacn)][CF₃SO₃], (M = Co (**1_{Co}**), Fe (**1_{Fe}**) and Ni (**1_{Ni}**)) (Scheme III. 1).

The ¹H-NMR of the synthesized complexes at room temperature are collected in the Figure III. 1. The three M^{II} complexes exhibit a paramagnetic spectra expanded from -10 to 210 ppm, which is in agreement with octahedral M^{II} paramagnetic species.

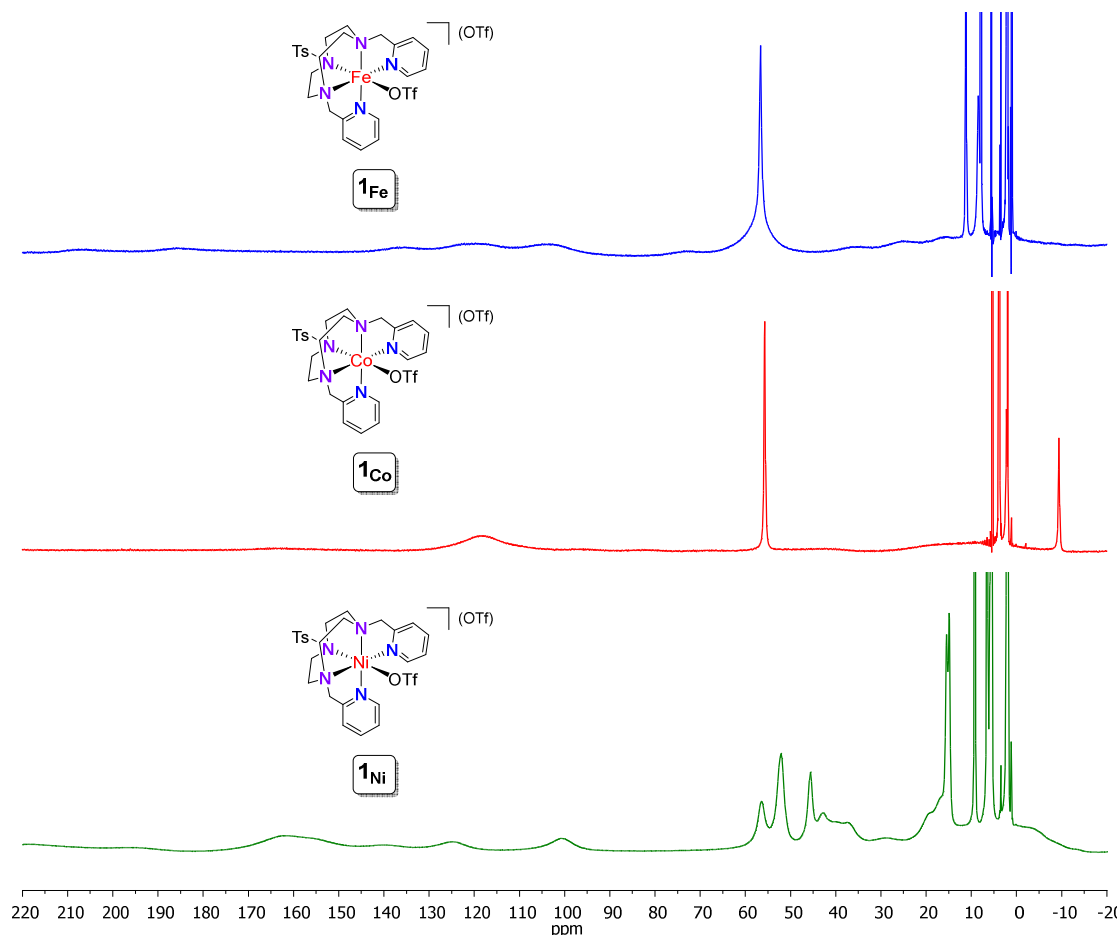


Figure III. 1. ¹H-NMR (CD₃CN, 400 MHz, 300 K) spectrum of **1_{Fe}**, **1_{Co}** and **1_{Ni}**.

High-resolution electrospray ionization mass spectrometry (HR-ESI-MS) shows the monocharged molecular peak (673.1054 m/z for [**1_{Co}**-OTf]⁺, 670.1069 m/z for [**1_{Fe}**-OTf]⁺ and 672.1058 m/z for [**1_{Ni}**-OTf]⁺) and the double charged molecular peak of the complexes without the triflates (262.0766 m/z for [**1_{Co}**-2OTf]²⁺, 260.5804 m/z for [**1_{Fe}**-2OTf]²⁺ and 261.5797 m/z for [**1_{Ni}**-2OTf]²⁺).

The solid state structure of **1_{Co}** and **1_{Ni}** could be established by X-Ray diffraction analysis. Crystals of **1_{Co}** and **1_{Ni}** were grown by layering a solution of dichloromethane with ethyl ether. The analysis of monocrystals from **1_{Co}** and **1_{Ni}** confirm the formation of distorted octahedral complexes formed by a pentacoordinate ligand bonded to the metal by the three amines of the triazacyclononane unit and two different pyridines; the

last coordination site occupied by a labile triflate anion (Figure III.2). Both complexes crystallize in a triclinic crystal system.

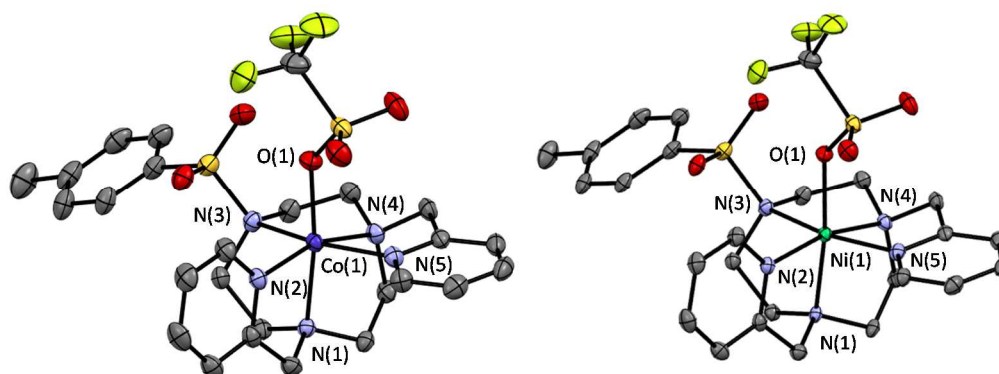


Figure III.2. ORTEP structures with ellipsoids set at the 50% probability level of **1_{Co}** (Left) and **1_{Ni}** (Right) from the X-ray diffraction analysis. Hydrogen atoms have been omitted for clarity.

Experimental details of their crystal structure are summarized in Table A. 1. 1 (Annex A.1.2), and the selected bond distances and angles are collected in . M-N bond lengths are in the range of the expected values for the two pyridines (ca. 2.10 and 2.05 Å for **1_{Co}** and **1_{Ni}**, respectively) and the alkyl amines (ca. 2.14 and 2.07 Å for **1_{Co}** and **1_{Ni}**, respectively), but considerably larger for the tosylated amine (2.320 and ca. 2.264 Å for **1_{Co}** and **1_{Ni}**, respectively). The averaged Co-N bond lengths for these complexes are 2.0-2.2 Å, characteristic of high-spin Co^{II} complexes with $S = 3/2$.^{97,292}

Table III. 1. Selected bond lengths [Å] and angles [°] for **1_{Co}** and **1_{Ni}**.

1_{Co}		1_{Ni}	
Co-N1	2.141(2)	Ni-N1	2.071(2)
Co-N2	2.093(2)	Ni-N2	2.042(2)
Co-N3	2.320(2)	Ni-N3	2.264(2)
Co-N4	2.130(2)	Ni-N4	2.076(2)
Co-N5	2.133(2)	Ni-N5	2.066(2)
Co-O1	2.034(1)	Ni-O1	2.0488(17)
N1-Co-N2	80.05(6)	N1-Co-N2	82.18(8)
N1-Co-N3	81.61(6)	N1-Co-N3	83.67(8)
N1-Co-N4	82.20(6)	N1-Co-N4	84.51(8)
N1-Co-N5	96.47(6)	N1-Co-N5	96.52(8)
N2-Co-N3	101.95(6)	N2-Co-N3	100.46(7)
N2-Co-N4	161.67(7)	N2-Co-N4	166.31(8)
N3-Co-N5	159.09(6)	N3-Co-N5	161.82(7)
N4-Co-N5	79.31(7)	N4-Co-N5	80.75(8)
N1-Co-O1	172.39(6)	N1-Co-O1	173.15(7)

The UV/Vis spectra of the **1**_M complexes (100 μM) in acetonitrile are characterized by intense transitions from 200 to 400 nm: **1**_{Fe} (232 nm; ε = 20151 M⁻¹·cm⁻¹, 257 nm (*shoulder*); ε = 11645 M⁻¹·cm⁻¹, 351 nm; ε = 1492 M⁻¹·cm⁻¹), **1**_{Co} (229 nm; ε = 22386 M⁻¹·cm⁻¹, 263 nm (*sh*); ε = 10542 M⁻¹·cm⁻¹), **1**_{Ni} (235 nm; ε = 21688 M⁻¹·cm⁻¹, 262 nm (*sh*); ε = 9828 M⁻¹·cm⁻¹) (Figure III. 3). By analogy to the UV/Vis spectra of other cobalt(II) complexes by aminopyridine ligands, the higher intensive bands in the UV region can be assigned to a MLCT or π-π* transitions.^{293,294}

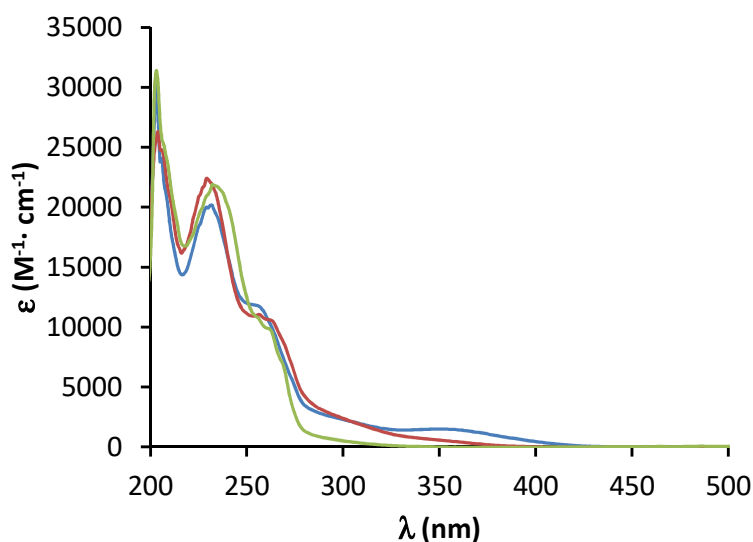


Figure III. 3. UV/Vis absorption spectra of **1**_{Fe} (0.1 mM, Blue), **1**_{Co} (0.1 mM, red) and **1**_{Ni} (0.1 mM, green) in MeCN at 298 K.

III.2.2. Photocatalytic Water Reduction to H₂

III.2.2.1. Effect of the metal

First, we tested the catalytic activity of **1**_{Fe}, **1**_{Co} and **1**_{Ni} under light-driven conditions by using a photosensitizer and a sacrificial electron-donor under irradiation (λ = 447 nm). Hydrogen evolution was monitored online by the difference of pressure between the reaction vessel containing the mixture of the reaction and a blank sample under the same conditions, but lacking the metal complex. Reactions were carried out by using an acetonitrile/water mixture; acetonitrile was used to ensure the complete solubilization of the photosensitizer. The amount of hydrogen obtained at the end of the reaction was established in every case by analyzing an aliquot of the headspace using gas chromatography with a thermal conductivity detector (GC-TCD).

The comparison among the activity of the three complexes was carried out by irradiation of a mixture containing the complex **1_M** (50 μM), [Ir(ppy)₂(bpy)]PF₆ (**PS_{Ir}**, 250 μM, ppy: phenyl pyridine) as photosensitizer and Et₃N (200 μL) as a source of electrons, in water/acetonitrile (7:3 mL) mixture. Under these conditions complex **1_{Co}** is highly active, producing 3.2 mL of H₂ after 1.5 h of reaction with a TON_{cat} ($n_{H_2}/n_{complex}$) and TOF_{cat} (TON_{cat}·h⁻¹) values of 260 and 174 h⁻¹ (2.1 mL(H₂)·h⁻¹), respectively. In contrast, complex **1_{Ni}** produces small amounts of hydrogen (6 TON_{cat}) and **1_{Fe}** does not show any photocatalytic activity (Figure III. 4, left). This is a very interesting result, but the difference among the activities of the complexes is difficult to rationalize at this point and will be discussed in more detail in the following sections. Control experiments show that the three components (catalyst, photosensitizer and electron donor) are needed for the photocatalytic H₂ evolution. Furthermore, when the reaction was performed in the dark, no gas production could be detected. Finally, only negligible amounts of H₂ were measured when using [Co(OTf)₂(CH₃CN)₂], [Ni(OTf)₂(CH₃CN)₂] and [Fe(OTf)₂(CH₃CN)₂] (< 15 TON) under analogous photochemical conditions. Therefore, these results provide strong evidence that the H₂ obtained in our experiments cannot be attributed to the activity of free metal in solution, and therefore we conclude that the catalytic activity arises from the metal complex.

III.2.2.2. Effect of the photosensitizer

H₂ production by **1_{Co}** was drastically reduced when photosensitizers such as [Ru(bpy)₃]²⁺ (**PS_{Ru}**) or erythrosine B (**PS_{EB}**) were used instead of **PS_{Ir}** (TON_{cat}=20 with an initial TOF_{cat} of 26 h⁻¹ and negligible, respectively) (Figure III. 4, right). This can be rationalized by the reduction potentials of the photosensitizer (**PS_{Ir}**: -1.38,²⁹⁵ **PS_{Ru}**: -1.34,²⁹⁶ and **PS_{EB}**: -1.05 V⁶⁹ vs. SCE). The redox potential E (**1_{Co}^{II/I}**), measured by cyclic voltammetry, was found -1.10 V versus SCE. Therefore **PS_{Ir}** has a higher reduction potential, and it is appropriate to account for the catalytic activity.

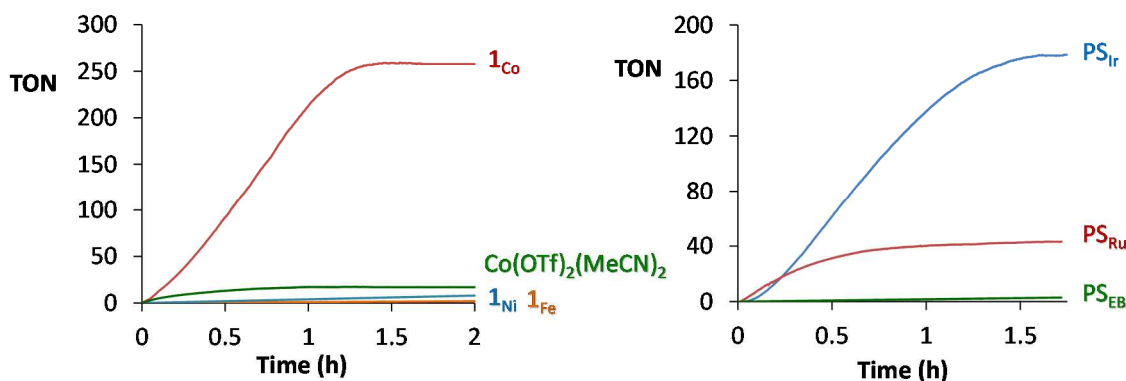


Figure III. 4. *Left:* On-line time dependent traces of photochemical H₂ generated (TON) by **1**_{Co} (50 μM, red), **1**_{Fe} (50 μM, orange), **1**_{Ni} (50 μM, blue) and [Co(OTf)₂(MeCN)₂] (50 μM, green) with **PS**_{Ir} (250 μM) in CH₃CN:H₂O:Et₃N (3:7:0.2 mL) solvent mixture, irradiated at 447 nm, under N₂. *Right:* On-line time dependent traces of photochemical H₂ generated (TON) by **1**_{Co} (50 μM) with **PS**_{Ir} (250 μM, blue), **PS**_{Ru} (250 μM, red) or **PS**_{EB} (250 μM, green) in CH₃CN:H₂O:Et₃N (2:8:0.2 mL) solvent mixture, irradiated at 447 nm, under N₂.

III.2.2.3. Effect of the sacrificial electron donor and the solvent mixture

The light-driven hydrogen production catalyzed by **1**_{Co} is also dependent on the amount of sacrificial electron donor and the solvent mixture. For instance, the yield of H₂ production is lower at higher Et₃N loadings than 2% in volume of the reaction mixture (Figure III.5). This reduction in activity can be rationalized by the increase in pH due to the increase on concentration of Et₃N (from pH 11.9 using 1% of Et₃N to pH 12.6 using 15% of Et₃N), which may hinder either the formation of the Co-H intermediate or the reaction of Co-H with protons to form H₂. Likewise, the ratio water/CH₃CN modifies the catalytic activity due to the need of the presence of protons and to adjust the polarity of the medium to have all the components well solubilized. The highest activity was found at 70% (v/v) of water in acetonitrile (TON: 260, TOF: 174 h⁻¹) (Figure III.5).

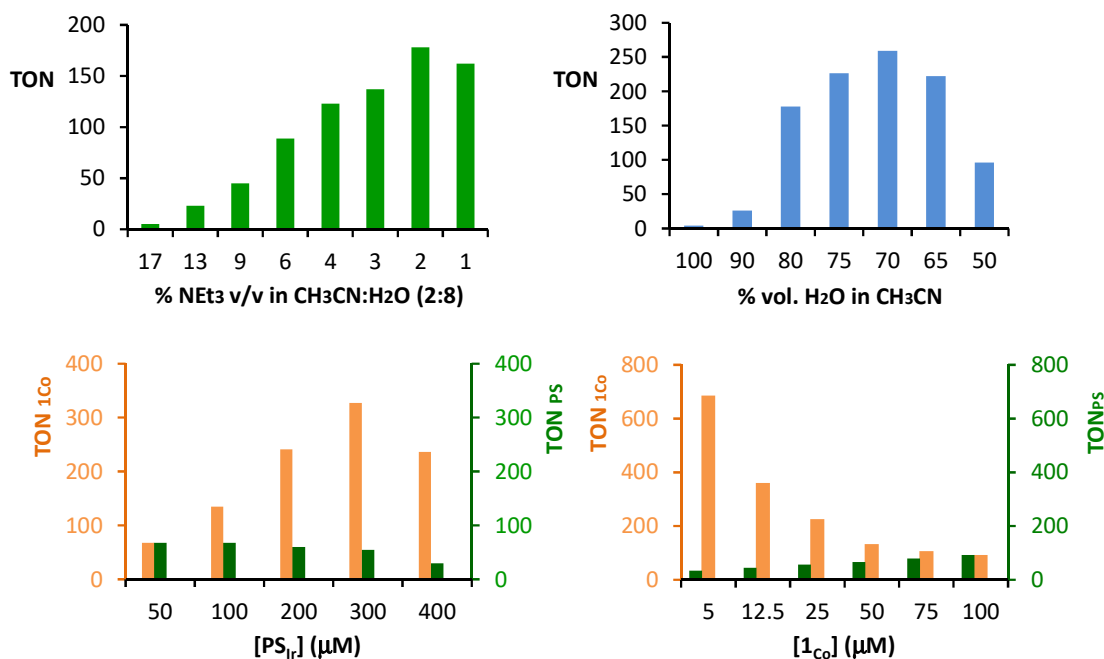


Figure III.5. Study of the effect of solvent mixture, [Et₃N], [PS_{Ir}] and [1_{Co}] in the photocatalytic H₂ formation by 1_{Co}. Top left: effect of Et₃N% v/v in the solvent mixture, CH₃CN/H₂O (2:8 mL), 1_{Co} (50 μM) and PS_{Ir} (250 μM). Top right: effect of the CH₃CN/H₂O solvent mixture (total volume 10 mL), Et₃N (0.2 mL), 1_{Co} (50 μM), PS_{Ir} (250 μM). Bottom left: TON_{1Co} and TON_{PS} as a function of [PS_{Ir}] in CH₃CN/H₂O/Et₃N (2:8:0.2 mL), 1_{Co} (50 μM). Bottom right: TON_{1Co} and TON_{PS} as a function of [1_{Co}], CH₃CN/H₂O/Et₃N (2:8:0.2 mL), PS_{Ir} (100 μM). TON_{cat}= n_{H_2}/n_{cat} , TON_{PS}= n_{H_2}/n_{PSIr} .

III.2.2.4. Effect of the photosensitizer and catalyst concentration

The increase of the concentration of PS_{Ir} had a positive impact in the total amount H₂ obtained. The TON_{cat} increases linearly with the concentration of the chromophore; however, the TON_{PS} (n_{H_2}/n_{PS}) is almost independent of the photosensitizer concentration. For instance, TON_{cat} values of 68 and 327 and TON_{PS} values of 68 and 55 were found when using 50 and 300 μM of PS_{Ir}, respectively (Figure III.5). The loss of activity at PS_{Ir} concentrations higher than 300 μM can be attributed to the limited PS_{Ir} solubility under these conditions. Initial reaction rates calculated at 10% of conversion versus the [PS_{Ir}] revealed first-order dependence (Figure III.5), which is an indication that the reduction of the cobalt complex by the photoreduced PS_{Ir}^{II} controls the H₂ production rate.

Afterwards, we studied the dependence of the H₂ production versus the concentration of 1_{Co}. Experiments were carried out varying the concentration of catalyst (5–100 μM) and fixing the concentration of PS_{Ir} (100 μM) with CH₃CN/H₂O/Et₃N (2:8:0.2)

as solvent mixture (Figure III.5 and Figure III.6). The activity clearly increases with the decrease of the **1**_{Co} concentration. At low catalyst concentrations (**1**_{Co}=5 μM, **PS**_{Ir} =100 μM) a TON_{**1**_{Co}} of 690 and a TOF_{**1**_{Co}} of 703 h⁻¹ were obtained. At lower catalyst concentrations, higher TON are clearly produced; however, the inaccuracy of the measurements under these conditions avoids further analysis. On the other hand, at higher catalyst concentrations (100 μM) the hydrogen production rate is still remarkable (1.46 mL·h⁻¹ of H₂). Initial reaction rates shows that the reaction becomes faster at lower **1**_{Co} concentration. The double ln plot of the *k*_i versus **1**_{Co} concentration shows an inverse catalytic-activity/metal-complex concentration correlation (Figure III.6, left, inset). This might suggest the formation of inactive dimers or oligomeric species, but also cobalt nanoparticles, although the mononuclear species may have the higher activity and increase in number when the concentration is decreased.

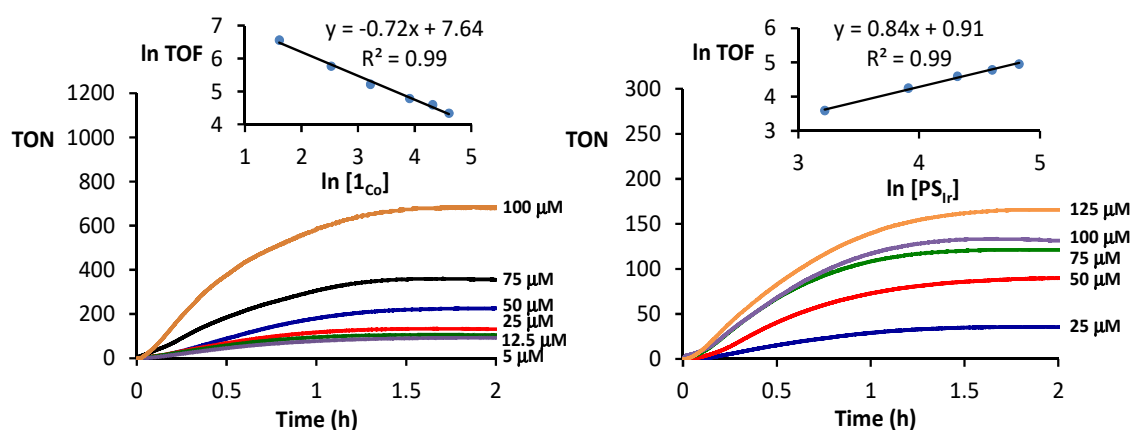


Figure III.6. Plots of on-line pressure monitored versus time for reactions using CH₃CN/H₂O/Et₃N (2:8:0.2) as solvent mixture under irradiation at λ=447 nm. Top: **PS**_{Ir} (100 μM) and [**1**_{Co}] from 5 μM to 100 μM. Inset: double-ln plot of initial H₂ evolution rates versus [**1**_{Co}]. Bottom: **1**_{Co} (50 μM) and [**PS**_{Ir}] from 25 μM to 125 μM. Inset: double-ln plot of initial H₂ evolution rates versus [**PS**_{Ir}].

III.2.2.5. Regeneration of the catalytic activity

All efforts to regenerate the catalytic activity at the end of the reaction were unsuccessful. Indeed, further addition of any of the reaction components (**PS**_{Ir}, **1**_{Co} or Et₃N) at the end of the reaction did not restart the catalytic activity. Furthermore, the combined addition of catalyst and Et₃N or **PS**_{Ir} and Et₃N results in negligible H₂ evolved. Only 25% of the catalytic activity could be restored upon addition of more catalyst and PS and 40% when all three components were added at the same time (Figure III. 7).

Altogether, these results suggest that the catalytic activity degradation over time may be due to a poisoning of the catalytic system by decomposition products formed during the H₂ evolution.

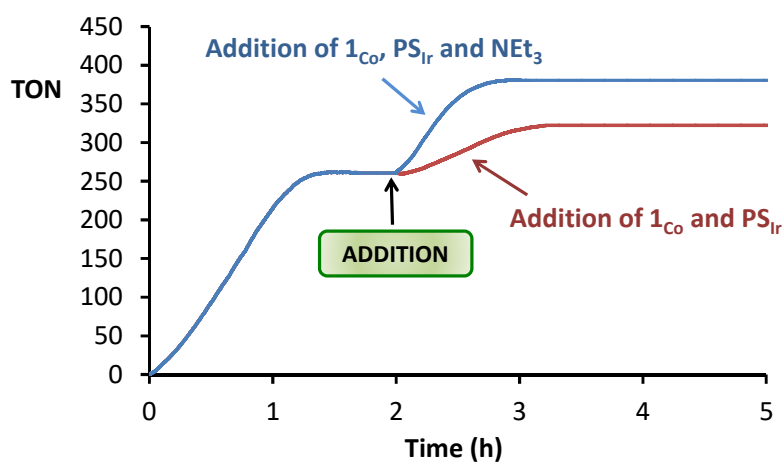


Figure III. 7. Photochemical H₂ production experiments after a 1st H₂ photogeneration run. 1st run (from t = 0 to 2h, blue dark line) **1**_{Co} (50 μM) and **PS**_{Ir} (250 μM) in MeCN:H₂O:Et₃N (3:7:0.2 mL). t = 2 - 5h, red line) H₂ produced after addition of an extra **1**_{Co} (50 μM) and **PS**_{Ir} (250 μM) at t = 2h. t = 2 - 5h, blue pale line). H₂ produced after addition of an extra **1**_{Co} (50 μM) and **PS**_{Ir} (250 μM) and Et₃N (0.2 mL) at t = 2h.

III.2.2.6. Effect of the O₂ presence in the catalytic activity

One of the main problems of the water reduction catalysts is that for most catalysts the presence of O₂ inhibits completely the H₂ formation.^{108,297} Interestingly, the reactions of **1**_{Co} under air retain a significant amount of photoinduced H₂-evolution activity. For instance, a reaction carried out with **1**_{Co} (50 μM) and **PS**_{Ir} (25 μM) under air in a solvent mixture of CH₃CN/H₂O/Et₃N (3:7:0.2) gives a TON_{cat} value of 63, and a TOF value of 44 h⁻¹. Nevertheless, the same reaction carried out under strict inert conditions produce a total TON_{cat} value of 259 and a TOF value of 147 h⁻¹. Despite the fact that O₂ clearly reduces the evolution of H₂, up to 25% of the activity is maintained (Figure III. 8). Recently, Reisner et al. reported the first first-row transition-metal catalyst that can produce hydrogen in presence of high levels of O₂.²⁹⁸ This was achieved by using a homogeneous catalytic system based on a cobaloxime type of catalyst and eosin Y as photosensitizer. Nevertheless, our system operates under distinct conditions.

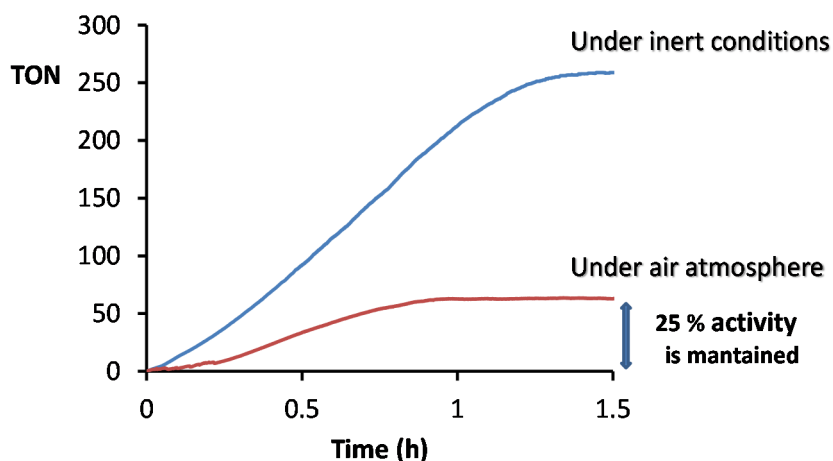


Figure III. 8. Photocatalytic H₂ production under inert conditions (blue curve) and in the presence of 21 % of O₂. Reaction conditions: **1**_{Co} (50 μM) and **PS**_{Ir}^{II} (250 μM) in MeCN:H₂O:Et₃N (3:7:0.2 mL) solvent mixture irradiated at λ = 447 nm.

III.2.2.7. Mechanistic studies

To get insight into the first steps of the mechanism we studied the reaction of the reduced photosensitizer (**PS**_{Ir}^{II} = [Ir^{II}(ppy)₂(bpy)][PF₆]; ppy=2-phenylpyridine) with **1**_M (M=Co, Ni and Fe) by UV/Vis spectroscopy. **PS**_{Ir}^{II} was generated *in situ* by irradiation of a solution containing **PS**_{Ir}^{III} (0.1 μM) and Et₃N (1000 eq.) in anhydrous CH₃CN under N₂ atmosphere. Reactions were performed at 20°C to minimize the decomposition of **PS**_{Ir}^{II}, which occurs fast at 25°C. Upon irradiation, three bands located at 385, 495 and 527 nm belonging to the **PS**_{Ir}^{II} raised (Figure III.9). After quantitative formation of **PS**_{Ir}^{II} (ca. 30 s) one equivalent of **1**_M was added. At this point, the addition of **1**_{Co} (1 eq.) produced the vanishing of the spectral features corresponding to **PS**_{Ir}^{II} in approximately 1.5 s with a concomitant recovery of **PS**_{Ir}^{III}, as judged by UV/Vis changes. Therefore, this implies the reduction of **1**_{Co} by **PS**_{Ir}^{II} is a one-electron process. Continuous irradiation of the solution produced the recovery of **PS**_{Ir}^{II}. In the case of the addition of **1**_{Ni} (1 eq.), again the UV/Vis features of **PS**_{Ir}^{II} vanished with a concomitant rising of a new broad band with a λ_{max} at 523 nm, which was attributed to the reduction of the **1**_{Ni} complex by one electron. However, in the case of the addition **1**_{Fe} (1 eq.) only partial loss and then only partial recovery of **PS**_{Ir}^{II} occurs under continuous irradiation. This clearly indicates that **PS**_{Ir}^{II} do not have enough potential to reduce **1**_{Fe}. The extent of the reactivity with the **PS**_{Ir}^{II} follows the order **1**_{Co} ≈ **1**_{Ni} < **1**_{Fe}, which is in agreement with the redox potentials measured in CH₃CN (E (**1**_{Co}^{III/I})=-1.10, E (**1**_{Ni}^{III/I})=-1.07 and E (**1**_{Fe}^{III/I})=-1.38 V vs. SCE). This

behavior infers that under catalytic conditions the formation of reducing species in case of **1**_{Co} and **1**_{Ni} is favoured, while is unlikely for **1**_{Fe}. Consequently, one of the reasons of photochemical inactivity in H₂ production of **1**_{Fe} is the inability of **PS**_{Ir}^{II} to generate the necessary reduced species of **1**_{Fe}.

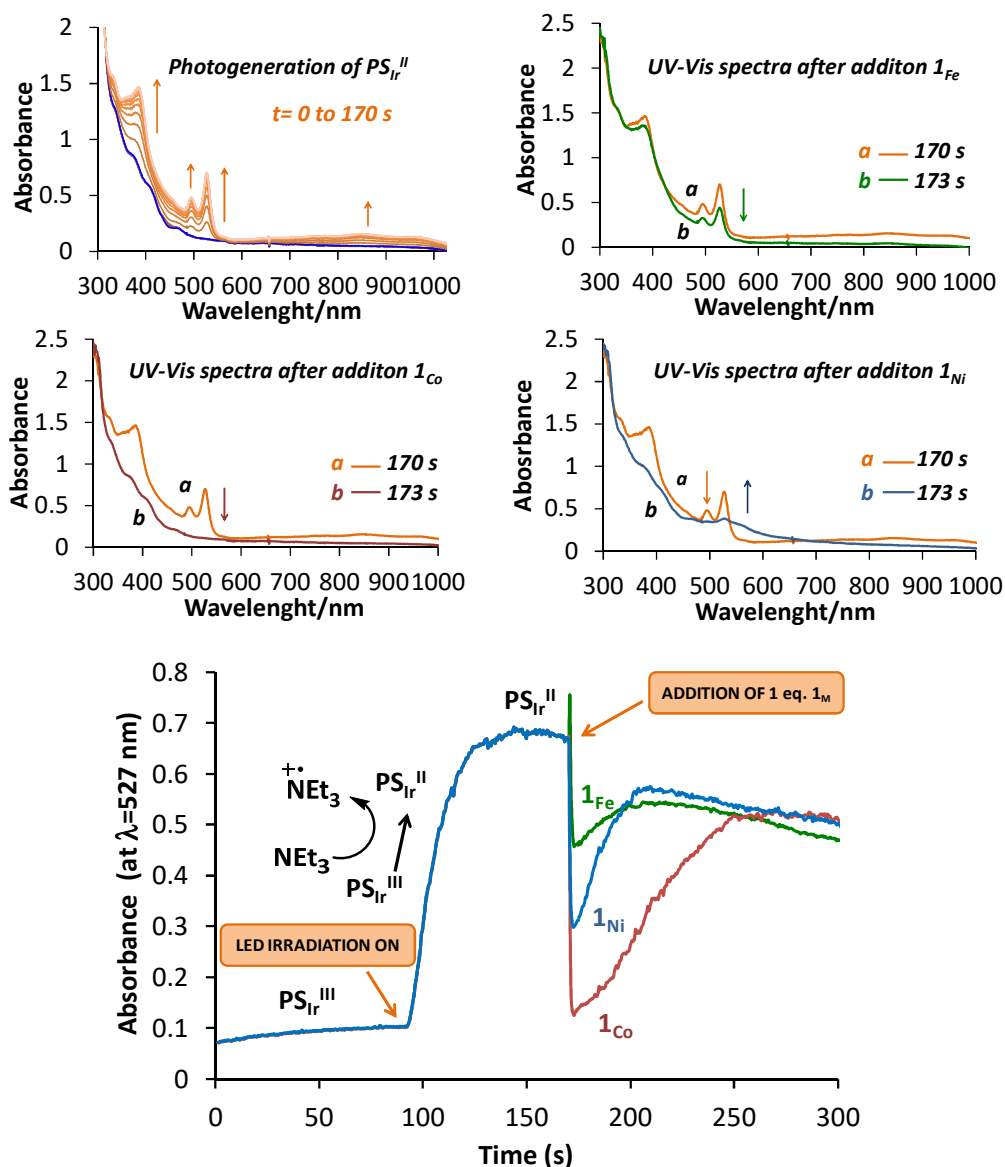


Figure III.9. UV/Vis monitoring of **PS**_{Ir}^{III} (0.1 mM) reductive quenching with Et₃N (1000 eq.) to form **PS**_{Ir}^{II} at $\lambda=447$ nm, and subsequent addition of one equivalent of **1**_{Fe}, **1**_{Co} or **1**_{Ni} in anhydrous CH₃CN at -20°C, under N₂ atmosphere.

Additional UV/Vis spectroscopic experiments were performed monitoring the amount of H₂ produced under catalytic conditions (CH₃CN/H₂O (3:7) at 25°C). The irradiation of the sample ($\lambda=447$ nm) forms **PS**_{Ir}^{II}. Further stoichiometric addition of **1**_{Co} produced a clear consumption of the reduced photosensitizer (**PS**_{Ir}^{II}) with a concomitant

formation of H₂, up to 170 mL H₂ were formed after 1.5 h of irradiation. Most importantly no induction time was observed (Figure III.10, bottom/inset). This is very relevant, since it is an indication that **1**_{Co} is the competent catalytic species. In contrast, when **1**_{Ni} was added, 20 mL H₂ were formed, while in case of **1**_{Fe} no H₂ was detected (Figure III.10), which qualitatively correlates with the [PS_{Ir}^{II}] decay in each case, as judged by the UV/Vis.

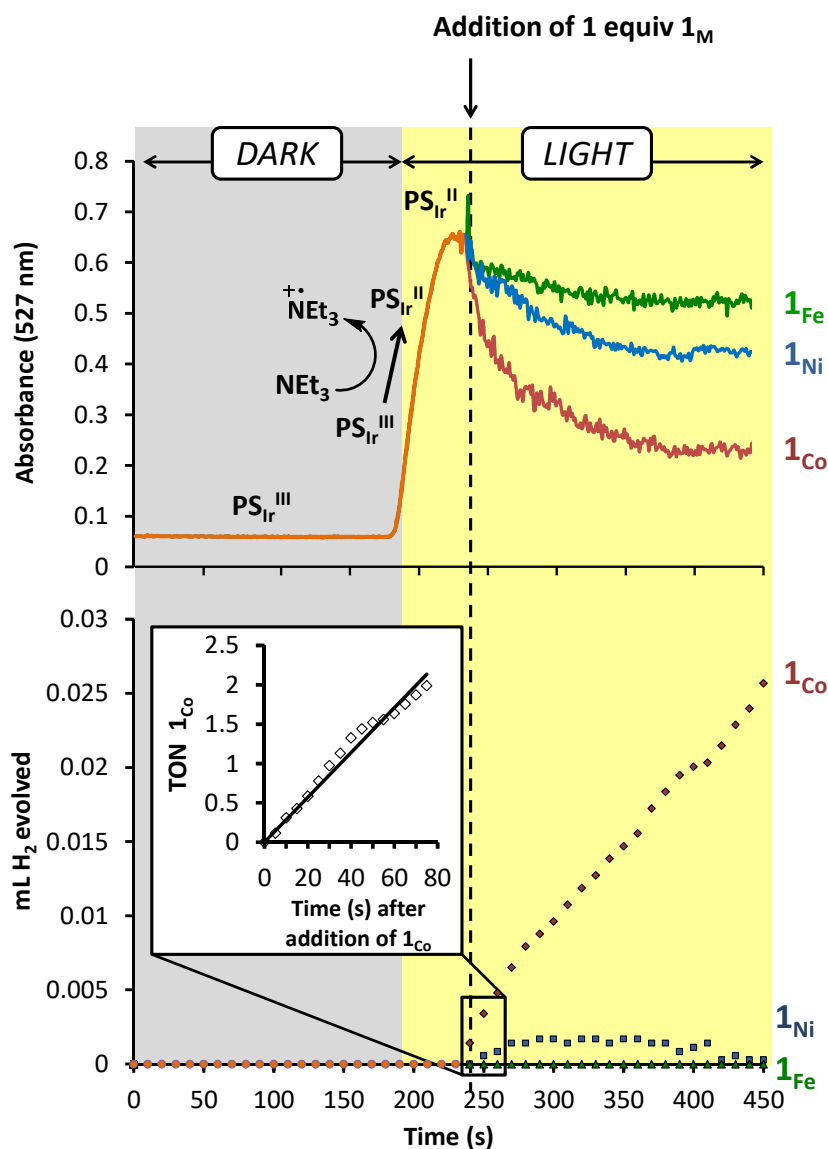


Figure III.10. Top: UV/Vis monitoring of the reductive quenching of PS_{Ir}^{II} species generated by irradiating at $\lambda=447$ nm, upon addition of one equivalent of **1**_{Fe}, **1**_{Co} and **1**_{Ni}. Conditions: [PS_{Ir}]=0.1 mM, Et₃N=1000 eq., reaction volume= 2 mL, CH₃CN/H₂O (0.6:1.4) at 25°C. Bottom: Time-dependent photocatalytic H₂ evolution activities measured in the UV/Vis cell upon addition of one equivalent of **1**_{Fe} (green triangles), **1**_{Co} (red diamonds) and **1**_{Ni} (blue squares). Inset: Magnification in the case of **1**_{Co}.

III.2.2.8. Study of the formation of nanoparticles during catalysis

Dynamic light scattering (DLS) experiments and tracking analysis of nanoparticles (NTA) were performed during the reaction to ascertain whether catalyst degradation could result in nanoparticle formation during the irradiation time.²⁹⁹ DLS analysis on catalytic reactions of **1**_{Co} (50 and 200 μM), in which **PS**_{Ir} (200 μM) is used as a chromophore and Et₃N (2% v/v) as a sacrificial electron-donor reagent, reveal the formation of nanoparticles that increase in size during the reaction (from 1 nm at 30 min irradiation to 100 nm after 3 h of irradiation) (Figure III. 11, left). Since no clear evidence of nanoparticles were found during the first 30 min of the reaction and no induction time is observed under the same conditions, we conclude that the H₂ production activity is molecular. Moreover, we found that the concentration of nanoparticles in solution was very low, usually at the limit of detection for this instrument (the lowest nanoparticle concentration that can be detected for a reliable measurement >0.1 ppm), and it was not always possible to have a reliable size distribution measurement.

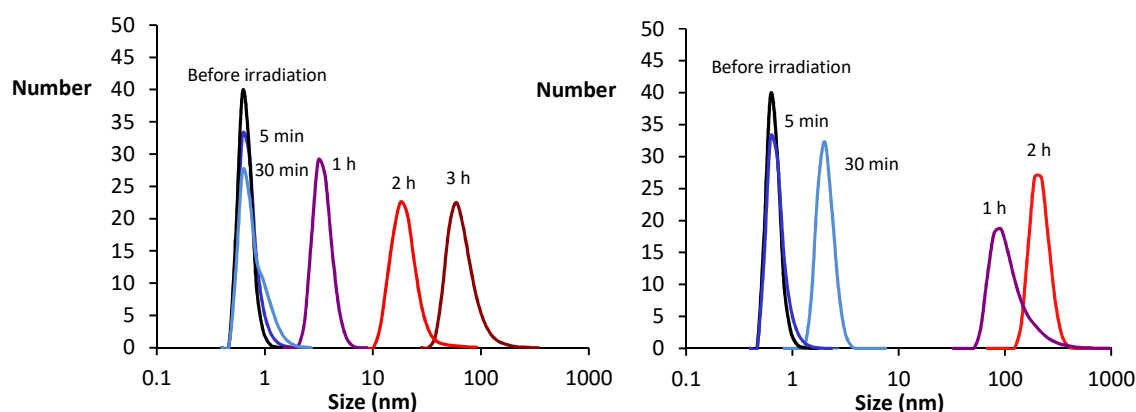


Figure III. 11. Number of nanoparticles distribution after different irradiation times: before irradiation (black line), 5 min (dark-blue line), 30 min (light-blue line), 1 h (purple line), 2 h (red line) and 3 h (brown line). Conditions: *Left*) **1**_{Co} (50 μM), **PS**_{Ir} (200 μM), CH₃CN:H₂O:Et₃N (5:5:0.2 mL) as solvent mixture irradiated at 447 nm. *Right*) **1**_{Co} (500 μM), **PS**_{Ir} (200 μM), CH₃CN:H₂O:Et₃N (5:5:0.2 mL) as solvent mixture irradiated at 447 nm.

The same conclusions were reached by studying the same experimental conditions by using nanoparticle tracking analysis (NTA). NTA showed values of nanoparticles·mL⁻¹ in the 1x10⁸-1x10⁹ range. We note that nanoparticle concentration did not significantly vary before and after irradiation (ca. 1.5- to 2-fold increase), with oscillations under the same order of magnitude. Moreover, the same experiments conducted in the presence of Hg⁰ reduce the nanoparticle concentration by a similar

proportion. Furthermore, if we consider the obtained concentration of 1×10^8 - 1×10^9 particles mL⁻¹ by NTA as being responsible for the catalytic water reduction, a TOF value of 10^6 - 10^7 s⁻¹ is obtained. This value is evidently unrealistic and hence the low concentration of nanoparticles formed can be excluded as being responsible for the observed catalytic activity.

DLS analysis on catalytic reactions of **1_{Co}** under high concentration conditions (500 μM) and typical concentrations of **PS_{Ir}** (200 μM) and Et₃N (2% v/v), reveal more clearly the formation of nanoparticles, which again increase in size during the reaction (Figure III. 11). NTA under these conditions reveal nanoparticle concentrations in the 10⁹ order of magnitude, which again imply an unrealistic TOF. DLS and NTA experiments suggest that the loss of the catalytic activity overtime may be related with the decomposition of the molecular system to form nanoparticles, which is in agreement with the -0.7 reaction order obtained for the **1_{Co}**.

Finally we investigated the effect on the catalytic activity of possible nanoparticles formed during the reaction by poisoning experiments with a large excess of Hg⁰ (1000 eq. or even 1.5 mL which corresponds to the 15% of the total reaction volume) added 5 min before starting the irradiation. Experiments in triplicate were carried out under standard conditions (**1_{Co}** (50 μM), **PS_{Ir}** (250 μM), CH₃CN/H₂O/Et₃N (3:7:0.2 mL)) and with and without Hg⁰ for comparison reasons (Figure III. 12, *left*). The results evidenced the same catalytic behavior of H₂ production independently of the amount of Hg⁰ used, within the experimental error. Furthermore, we also examined the effect of addition of Hg⁰ during the reaction (2x0.5 mL, 10% v/v), which did not produce any significant effect on the time-profile nor on the hydrogen production TOF (Figure III. 12, *right*). Arguably, nanoparticles are unlikely to be responsible for the observed hydrogen evolution activity; however, these results could also indicate that the formation of nanoparticles may be related with the catalyst decomposition and should be considered.

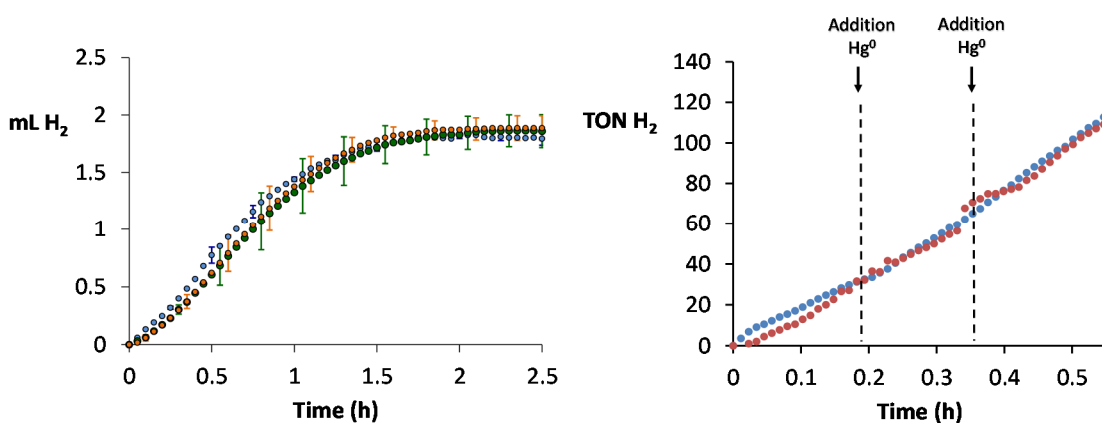


Figure III. 12. Hg⁰ poisoning experiments. Effect of the addition of Hg⁰ to photochemical H₂ production carried out using **1**_{Co} (50 μM), **PS**_r (250 μM), Et₃N (2% v/v) and irradiated at 447 nm in CH₃CN:H₂O (3:7 mL). *Left*) Reactions: without Hg⁰ (green dots), with the presence of 1000 eq. of Hg⁰ (Orange dots) and with the presence of 1.5 mL (15% of the total volume of the reaction) of Hg⁰ (blue dots) from the 5 min before irradiation. Bars represent the errors (usually below 10%) of reactions in triplicate. *Right*) Reactions: without Hg⁰ (blue dots) and with the addition of 0.5 mL Hg⁰ after t = 0.23 h and t = 0.37 h (red dots) from the beginning of irradiation.

III.2.3. Electrochemical Proton Reduction to H₂

To get further insight into the capacity of metal complexes **1**_{Fe}, **1**_{Co} and **1**_{Ni} in the production of H₂, we explored the reduction of protons under electrochemical conditions. First, redox potentials were determined for **1**_{Fe}, **1**_{Co} and **1**_{Ni} (Figure III. 13) by using a glassy carbon as working and a saturated calomel (SCE) as reference electrode in CH₃CN containing Bu₄NPF₆ (0.1 M) as supporting electrolyte. A summary of the M^{I/0}, M^{II/I} and M^{III/II} reduction potentials is presented in Table III.2.

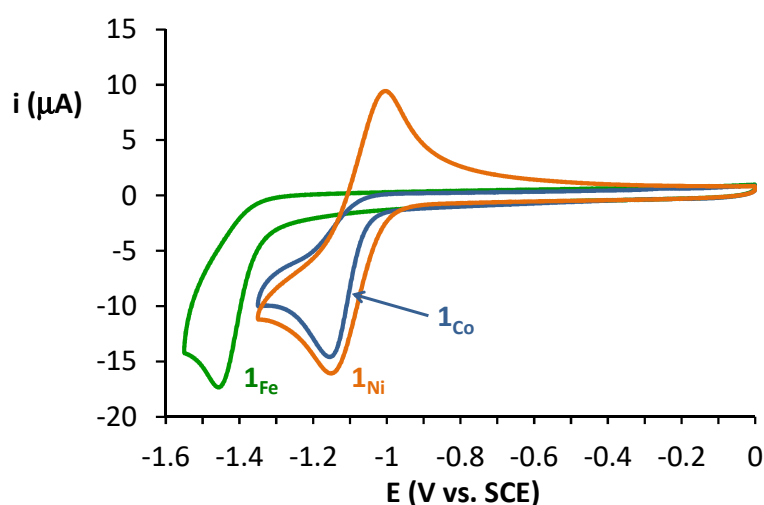


Figure III. 13. CVs of **1**_{Fe}, **1**_{Co} and **1**_{Ni}. Experimental conditions: Bu₄NPF₆ (0.1 M) as supporting electrolyte in acetonitrile, using a glassy carbon as working and SCE as reference electrodes. Scan rate of 100 mV·s⁻¹.

Complex **1_{Fe}** presents the lowest reduction potential $M^{II/I}$ from the series (-1.38 V), and therefore it is the less favoured to be reduced to oxidation state (I). In both cases **1_{Co}** and **1_{Ni}** showed similar reduction potentials for the $M^{II/I}$ couple (-1.10 and -1.07 V, respectively). The CV of the same complexes in the solvent mixture used in the photocatalyzed H₂ formation (CH₃CN/H₂O 3:7) experiments exhibit a reduction in the redox potentials for the $M^{II/I}$ couple in the range of 100-200 mV. This is slightly accentuated by the basification of the media after the addition of Et₃N. We note that the ligand alone does not show any reduction wave above -1.8 V. The trend found in the relative reduction potential $M^{II/I}$ among the three complexes is the expected and can be understood from the general increase in ionization energies from left to right across a period in the d block.

Table III.2. Redox potentials for the studied complexes **1_{Fe}**, **1_{Co}** and **1_{Ni}** in anhydrous CH₃CN, and CH₃CN/H₂O mixtures.

1_M	CH ₃ CN ^[a]				CH ₃ CN:H ₂ O	CH ₃ CN:H ₂ O:Et ₃ N
					(3:7) ^[c]	(3:7:0.2) ^[d]
	E (V)	E (V)	E (V)	η_{TFA}	E (V) $M^{II/I}$	E (V) $M^{II/I}$
	$M^{I/0}$	$M^{II/I}$	$M^{III/II}$	(V) ^[b]		
1_{Fe}	-1.68	-1.38	1.14	0.87	-1.58	-1.63
1_{Co}	-1.49	-1.10	0.72	0.59	-1.23	-1.34
1_{Ni}	-	-1.07	1.75	0.56	-1.20	-1.21

Glassy carbon and SCE were the working and reference electrodes, scan rate = 100 mV·s⁻¹. Potentials are quoted versus SCE. [a] CV measured in CH₃CN containing Bu₄NPF₆ (0.1 M) as supporting electrolyte (SE). [b] H₂ reduction overpotentials (η) has been calculated considering the protons reduction of TFA as proton source, which is E^o (TFA/H₂) = -0.51 V (See Experimental Section III.3.12.1 for detailed information). [c] CVs measured in CH₃CN:H₂O (3:7) containing KNO₃ (0.1 M) as supporting electrolyte. [d] CVs measured in CH₃CN:H₂O:Et₃N (3:7:0.2) containing KNO₃ (0.1 M) as supporting electrolyte.

The electrocatalytic proton reduction capacity of the three complexes was studied in acetonitrile after addition of increasing amounts of trifluoroacetic acid (TFA, pKa=12.7 in acetonitrile)³⁰⁰ as the proton source. The CV of all three **1_M** complexes presents the appearance of new irreversible cathodic waves upon the addition of increasing amounts of TFA triggers (Figure III.14). The grown of the reduction peak

versus increase of acid concentration is a clear indication of electrocatalytic behaviour of proton reduction to H₂. At low acid concentrations the shape of the catalytic wave was similar to the wave of the respective complex in the absence of acid; however, at higher acid concentrations the electrocatalytic wave becomes broader and more intense.

In all cases the onset of the catalytic wave matches the potential of the M^{II/I} redox couple, and therefore this is consistent with M^I species as the active ones in electrocatalysis through the formation of M^{III}-H by protonation.^{81,96} The proton reduction overpotential (η) for complexes **1_{Co}** (590 mV) and **1_{Ni}** (560 mV) turned to be considerable lower than for **1_{Fe}** (870 mV) (Table III.2).

The dependence of the peak intensity versus the concentration of acid gives valuable information about the H₂ formation mechanism. In this regard, we studied the i_{cat}/i_p ratio as a function of the TFA concentration in a 1 mM solution of **1_{Co}**, **1_{Fe}** and **1_{Ni}** in acetonitrile, (in which i_{cat} stands for the peak current in the presence of acid and i_p for the peak current in the absence of acid). As shown in Figure III.15, the i_{cat}/i_p ratio of currents of **1_{Co}** increases with the acid concentration until it becomes independent versus the concentration of protons. Below a TFA concentration of 100 mM the i_{cat}/i_p versus [TFA] is linear and consistent with a second-order process on [H⁺] (Figure III.14). At a TFA concentration higher than 100 mM, i_{cat}/i_p it is independent of the [TFA] (Figure III.15), suggesting that under these conditions the rate-limiting step is an intramolecular proton transfer or an elimination of H₂.

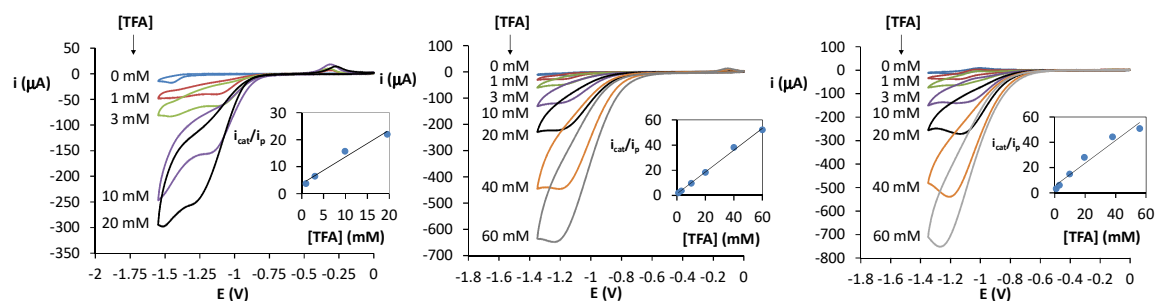


Figure III.14. Successive CVs of **1_{Fe}** (top), **1_{Co}** (middle) and **1_{Ni}** (bottom) (1 mM) in acetonitrile containing Bu₄NPF₆ (0.1 M) in the presence of TFA (0–60 mM). Scan rate=100 mV·s⁻¹, glassy carbon as working electrode. Insets: i_{cat}/i_p versus [TFA].

On the other hand, complexes **1**_{Fe} and **1**_{Ni} have similar behaviors at low acid concentration (up to 40 mM for **1**_{Fe}, and 60 mM for **1**_{Ni}), while at higher acid concentration the i_{cat}/i_p dramatically decreases, which may be due to catalyst degradation provoked by the high concentration of protons in the reaction medium.

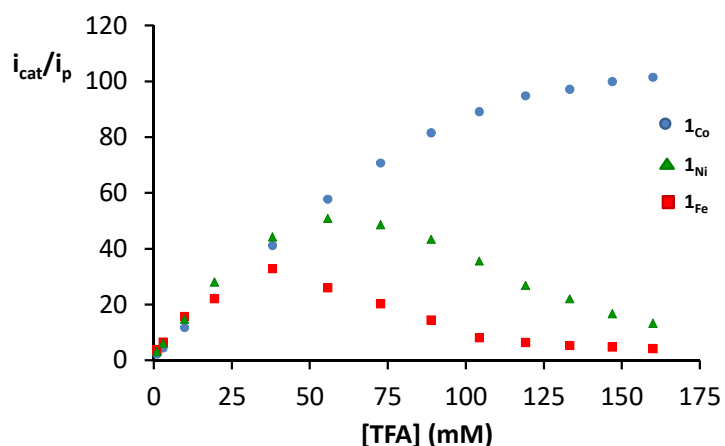


Figure III.15. i_{cat}/i_p ratio as a function of the [TFA] in a 1 mM concentration solution of **1**_{Fe}, **1**_{Co} or **1**_{Ni}. Scan rate=100 mV·s⁻¹. Glassy carbon working electrode and SCE as reference. i_{cat}/i_p values were measured at the M^{II/I} redox potential.

To ensure that the electrocatalytic behavior of **1**_{Co} corresponds to a molecular catalytic activity and thus discarding an electrodeposition process over the surface of the glassy carbon electrode, we first measured the CV of **1**_{Co} (1 mM) in the presence of TFA (100 mM), and then after rinsing the surface of the working electrode, a new CV

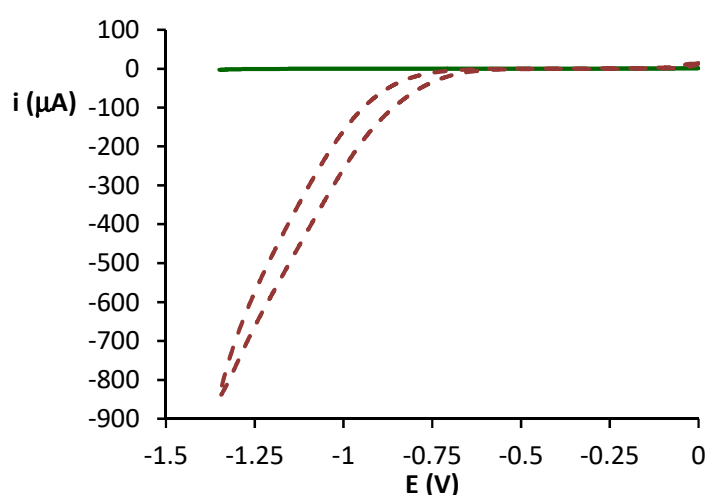


Figure III. 16. Cyclic voltammetry in acetonitrile using 0.1 M Bu₄NPF₆ as supporting electrolyte at scan rate of 100 mV/s using a glassy carbon working electrode: a) of **1**_{Co} (1 mM) and TFA (100 mM, red) and b) after CV after (a) without **1**_{Co} but under the same condition using the same glassy carbon working electrode without polishing.

was recorded from a freshly prepared TFA (100 mM) solution, which did not contained **1**_{Co} (Figure III. 16). In this case, the electrocatalytic wave completely disappeared. Consequently, the i_{cat}/i_p values obtained cannot be attributed to electrodeposition of cobalt species.

The good electrochemical behavior of **1**_{Co} facilitates the calculation of the electrocatalytic rate constant for hydrogen production, k_e (95 M⁻² s⁻¹) and the corresponding turnover frequency (TOF= $k[H^+]^2=3420 \text{ mol(H}_2\text{)mol(1Co)}^{-1} \text{ h}^{-1}$) by plotting the slopes obtained of i_{cat}/i_p versus [TFA] at different scan rates (v) as a function of $v^{-1/2}$ (Figure III. 17 and Figure III. 18).⁹⁶

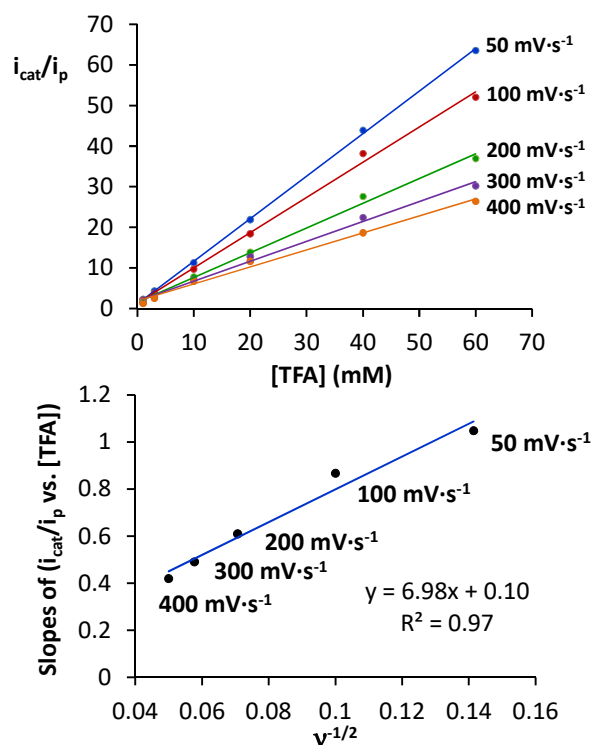


Figure III. 17. Top: plots of i_{cat}/i_p versus [TFA] for a 1 mM solution of **1**_{Co} at different scan rates. Bottom: Plot of the i_{cat}/i_p slopes at different scan rates versus [TFA] as function of the $v^{-1/2}$.

In addition, the dependence of the catalytic current on the concentration of catalyst at sufficiently high TFA concentration (100 mM) was found to be first-order (Figure III. 19). In summary, these studies lead us to formulate an overall rate law for the production of hydrogen of $v=k_e[H^+]^2[1Co]$.

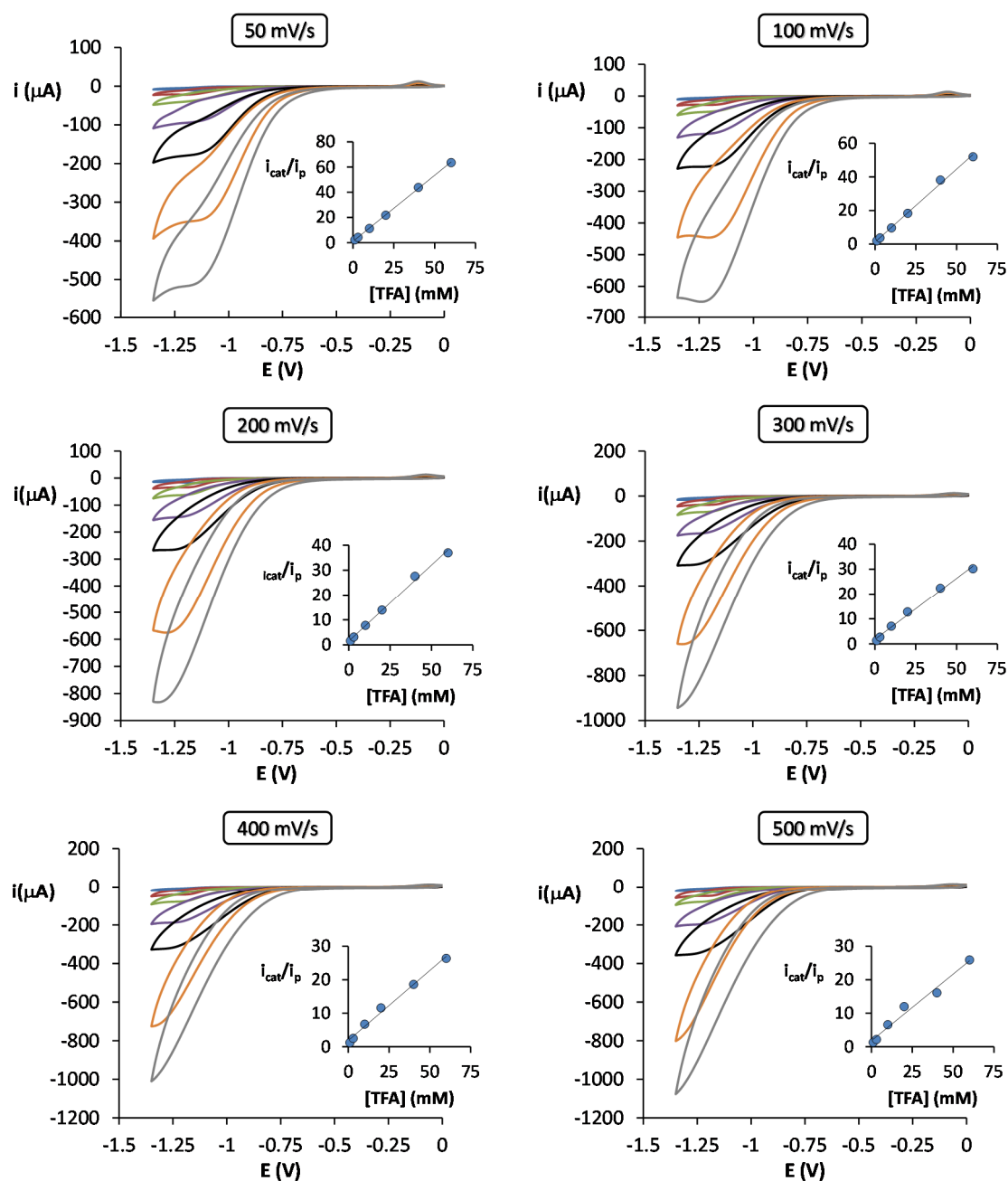


Figure III. 18. Successive cyclic voltammograms of **1**_{Co} (1 mM) in acetonitrile containing Bu₄NPF₆ (0.1 M) in the presence of acid: TFA (blue: 0 mM, red: 1 mM, green: 3 mM, purple: 10 mM, black: 20 mM, orange: 40 mM and grey: 60 mM), measured at different scan rates (50, 100, 200, 300, 400 and 500 mV/s). Glassy carbon electrode and SCE electrodes were used as working and reference electrodes, respectively.

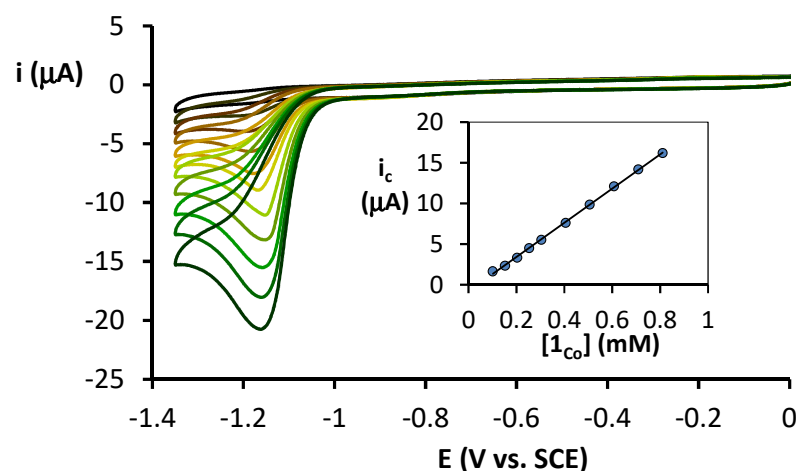


Figure III. 19. Successive CVs at increasing $[\mathbf{1}_{\text{Co}}]$. Conditions: $[\text{TFA}] = 100$ mM, Supporting electrolyte: Bu_4NPF_6 (0.1 M), scan rate = $100 \text{ mV}\cdot\text{s}^{-1}$, Glassy Carbon working electrode. Inset: Electrocatalytic current versus $[\mathbf{1}_{\text{Co}}]$ (0.1–0.8 mM) showing a first order kinetics.

Finally, complex **1**_{Co} was soluble and stable in pure aqueous solution. The cyclic voltammograms in water showed a redox couple $\text{Co}^{\text{II/I}}$ at -1.29 V versus SCE. This is slightly shifted to lower potentials in comparison with the one obtained in CH_3CN (-1.10 V vs. SCE). The addition of TFA to a 1 mM solution of **1**_{Co} causes an increase of the electrocatalytic current near the $\text{Co}^{\text{II/I}}$ couple (Figure III. 20) comparable to the previously observed in CH_3CN . Remarkably, the i_{cat}/i_p in water (65 at 60 mM) was found to be significantly higher than in acetonitrile (48 at 60 mM). The i_p was measured in a non-pH-buffered aqueous solution of KNO_3 (0.1 M, pH 6) and therefore a part of the i_p value could be partly associated with H₂ generation activity. Consequently, **1**_{Co} is not only

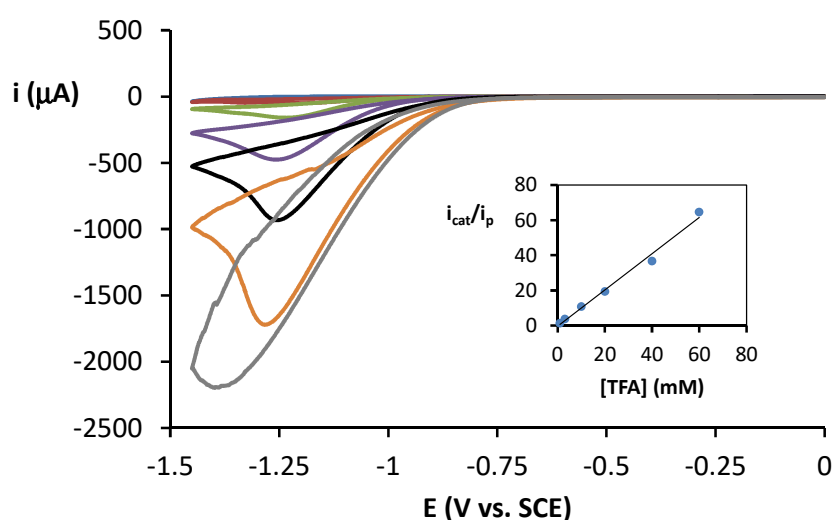


Figure III. 20. Successive CVs of **1**_{Co} (1 mM) in water containing KNO_3 (0.1 M) and TFA acid: from bottom to top 0, 1, 3, 10, 20, 40, and 60 mM. Scan rate = $100 \text{ mV}\cdot\text{s}^{-1}$, glassy carbon as working electrode.

stable in water, but also is more electrocatalytically active for proton reduction to H₂ than in pure acetonitrile.

III.2.4. Mechanistic Considerations

Complexes **1_M** (M = Co, Ni and Fe) are all electrocatalysts for H₂ production, while only **1_{Co}** is highly active under photochemical conditions. Under the latter conditions, **1_{Ni}** presents much reduced activity and **1_{Fe}** is completely inactive. The inactivity of **1_{Fe}** under photochemical conditions could be attributed to the low redox potential observed that it is needed for the formation of the Fe^I species. This was shown by the reaction of the in situ generated **PS_{Ir}^{II}** with **1_M** complexes. Complexes **1_{Ni}** and **1_{Co}** instantaneously react with **PS_{Ir}^{II}**, while **1_{Fe}** apparently is mainly inert to **PS_{Ir}^{II}**. This was also consistent with the M^{III/I} reduction potential of **1_{Fe}** in acetonitrile and the observed electrocatalytic H₂ production, which only occurs at very low potentials. However, **1_{Ni}** presents similar M^{III/I} reduction potential and overpotential in electrocatalytic H₂ formation as **1_{Co}** and moreover reacts instantaneously with in situ generated **PS_{Ir}^{II}**. Therefore, other limitations should be considered for the low H₂ production under photochemical conditions exhibited by **1_{Ni}**. One must consider that electro- and photochemical conditions are rather different. For instance, the electrochemical studies were performed in organic solvents or water, but evaluating the electrocatalytic current based on the [H⁺], usually provided by the addition of a strong acid (TFA in our case). This acid supply sets up the medium to a low pH. In contrast, in photochemical reactions the electrons are provided by the incorporation of a sacrificial agent (Et₃N in our case). This makes the reaction medium highly basic (pH≈12). The large pH differences between electro- and photochemical conditions, makes pH as one of the factor which diverged the H₂ formation activity among complexes and conditions (**1_{Ni}** and **1_{Co}**). Electro- and photochemical experiments provided evidence that under these conditions both **1_{Ni,Co}** are reduced by one electron to form M^I species. Then, subsequent protonation of those species will generate M^{III}-H intermediates and further protonation will produce H₂. Alternatively, under certain conditions M^{III}-H intermediates may not be enough reactive to produce H₂ (for instance under basic conditions) and will first require an additional reduction by one electron to form M^{II}-H, which then by protonation produce H.⁹⁸

To provide some light on the reactivity differences among the **1_M** series of complexes, structures of M^I, M^{II}, M^I-L, M^{II}-L (L=H₂O or CH₃CN) and M^{III}-H species were DFT modelled with the Gaussian 09 program³⁰¹ using the B3LYP hybrid exchange correlation functional and taking into account the effect of water solvation and London dispersion effects (See section III.3.12) for complete details of the employed methodology). Theoretical efforts focused on the evaluation of the solvent coordination, the M^{II/I} reduction potentials and the pK_a values of hydride species to explore the energetic accessibility of the proposed intermediates as well as their relative stability. The results are summarized in Tables III.3 and III.4.

Under photochemical conditions (CH₃CN:H₂O 3:7 solvent mixture) the metal centre may interact with both solvent molecules and the redox activity of the resulting aqua or acetonitrile complexes could be substantially different. Therefore, the identification of the most stable aqua, acetonitrile or solvent-free intermediate for each metal oxidation state is necessary to ensure a correct description of the initial redox step. In general, the energies gained by coordination of water or acetonitrile to the metal complexes in oxidation II were only small or even disfavoured for **1_{Fe}**. Binding of water to **1_{Co}** was also energetically disfavoured. This trend is clearer for the oxidation state I. But with some exceptions energies fall in the limits of the average error of the used methodology (Table III. 3). Concluding therefore that the absence of solvent ligand coordinated is generally favoured for oxidation state I in both, water or acetonitrile and also favoured for oxidation state II in water.

The reduction potentials M^{II/I} for **1_{Co}**, **1_{Ni}** and **1_{Fe}** without solvent bonded were calculated -0.86 V, -0.97 V and -1.42 V (SCE) respectively, in qualitative agreement with the experimental reduction potentials of -1.23 V, -1.20 V and -1.58 V (SCE). Although these values are 150-250 mV lower than the experimental results, they still fall in the usual range of the method accuracy.

Table III. 3. Computed free energy (ΔG) for coordination of CH₃CN and H₂O to **1**_M and for ligand exchange reactions:^a

ΔG (kcal/mol)	M = Fe		M = Co		M = Ni	
	Fe ^I	Fe ^{II}	Co ^I	Co ^{II}	Ni ^I	Ni ^{II}
$(\text{Py}_2^{\text{Tstacn}})\text{M}^{\text{II/I}} + \text{L} \rightarrow (\text{Py}_2^{\text{Tstacn}})\text{M}^{\text{II/I}} - \text{L}$						
L = CH ₃ CN	2.9	3.4	-0.2	-1.1	5.5	-5.1
L = H ₂ O	2.2	1.8	3.9	4.1	9.6	-1.9
$\text{CH}_3\text{CN} + (\text{Py}_2^{\text{Tstacn}})\text{M}^{\text{II/I}} - \text{OH}_2$ $\leftrightarrow (\text{Py}_2^{\text{Tstacn}})\text{M}^{\text{II/I}} - \text{NCCH}_3 + \text{H}_2\text{O}$						
	-0.6	1.6	-3.8	-5.1	-4.1	-3.2

^aAll values have been obtained using the ground spin state for each structure.

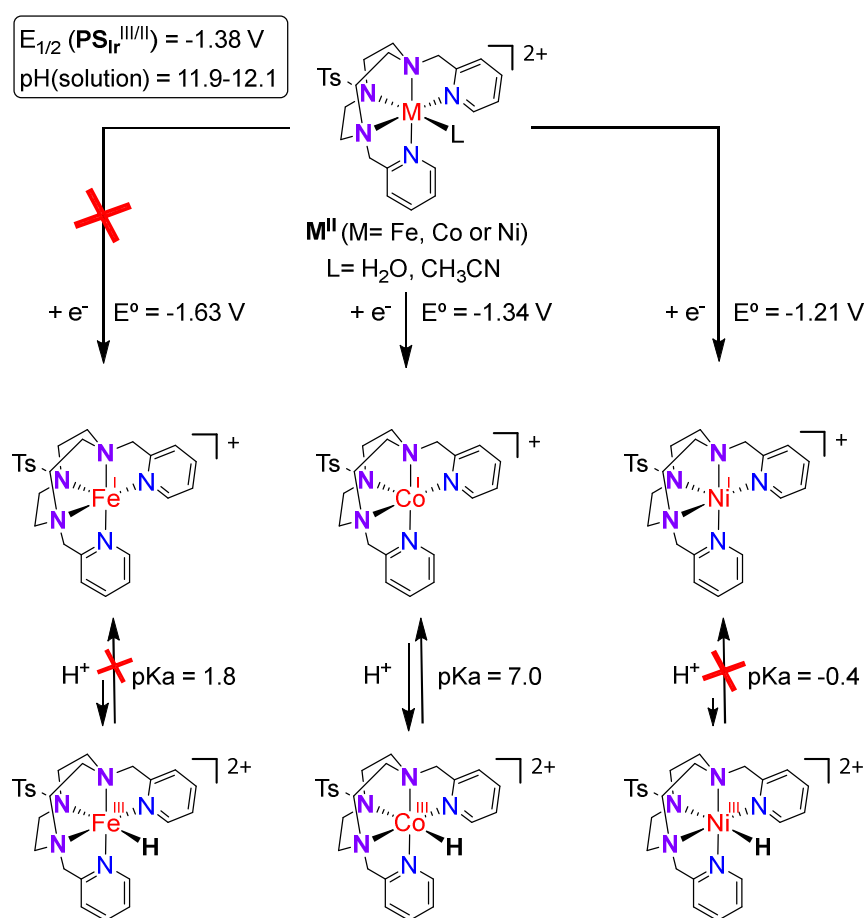
Table III. 4. DFT computed reduction potentials (V) and pK_a values of the proposed cobalt, nickel and iron intermediates.^a

	M = Fe	M = Co	M = Ni
E (M ^{II/I}) ^b	-1.42	-0.86	-0.97
pK _a (M ^{III} -H) ^c	1.8	7.0	-0.4

[a] All values have been obtained using the ground spin state for each structure. E^o values correspond to the standard reduction potentials relative to the SCE electrode. [b] Complexes without solvent coordination were employed for the calculation. [c] pK_a values have been calculated at 298 K.

Experimental and computational results determine that both **1**_{Co} and **1**_{Ni} complexes form species with a M^I oxidation state upon reacting with the reduced **PS**_{Ir}. Consequently, the origin of the photochemical inactivity of nickel species for H₂ production may be due to other factor such as the inaccessibility of the [Ni^{III}-H] species under basic pH, since under electrocatalytic acidic pH conditions the H₂ evolution reaction take place. In this regard, the DFT calculated pK_a values for [Co^{III}-H] and [Ni^{III}-H] were 7.0 and -0.4, respectively. This clearly underlines the more acidic character of the [Ni^{III}-H]. We should note that under photocatalytic conditions the pK_a of the mixture is in the range of 11-12. Therefore, these suggests that the protonation is disfavoured, thus blocking the H₂ production. In contrast, the reduction potential of -1.42 V for the Fe^{II/I} couple agree with the electrochemically observed of -1.58 V, revealing that the Fe^I species may not be photochemically generated. This situation bans the possible

formation of Fe^{III}-H species (pK_a 1.8, also disfavoured), and then the capacity to photo-produce H₂ when using **PS**_{Ir} as photosensitizer (Scheme III. 2).



Scheme III. 2. Differences in reactivity among **1**_{Fe}, **1**_{Co} and **1**_{Ni} in single electron reduction process to M^I species and the subsequent protonation to yield the M^{III}-H species under photochemical conditions. pK_a values have been obtained by DFT calculations.

In summary, we synthesised and characterized a new ligand 1,4-di(picoly)-7-(*p*-toluenesulfonyl)-1,4,7-triazacyclononane (Py₂^{Ts}tacn) and the corresponding metal complexes **1**_{Fe}, **1**_{Co} and **1**_{Ni}. All showed to be good electrochemical catalysts for proton reduction to H₂. However, only **1**_{Co} is an efficient catalyst for water reduction when using [Ir(ppy)₂(bpy)]PF₆ as photosensitizer and Et₃N as electron donor. In contrast, under the same conditions **1**_{Ni} presents low photochemical water reduction activity and **1**_{Fe} is inactive. More interestingly, to some extent the catalyst **1**_{Co} can operate as photocatalyst for H₂ production in presence of O₂.

The active species during the photocatalytic water reduction are molecular. This was clear by the lack of lag time in the H₂ evolution, and the absence of nanoparticles during the first minutes of the reaction, when the system was most active. Moreover, the formation of nanoparticles is ascribed to the reduction of catalytic activity.

Mechanistic investigations, electrochemical studies and DFT calculations allowed us to elucidate the factors that control the activity among the three complexes with the same aminopyridine ligand. The Py₂^Ttacn ligand not only controls the relative stabilization of the metal oxidation state, but also the basicity. Both factors are important and should be considered for the boundary reaction conditions imposed by the photosensitizer, electron donor and pH. Indeed, the use of [Ir(ppy)₂(bpy)]PF₆ as photosensitizer allows the one-electron reduction of **1_{Co}^{II}** and **1_{Ni}^{II}**, but not in the case of **1_{Fe}^{II}**. On the other hand, the use of Et₃N as electron donor basifies the media making the protonation of the M^I metal centre for **1_{Ni}** difficult and, therefore, the H₂ evolution. Altogether, this study gives light on important factors to be considered for the development of more efficient first-row transition-metal catalysts for water reduction.

III.3. EXPERIMENTAL SECTION

III.3.1. General Methods

All procedures were carried out under N₂ using standard vacuum line, Schlenk, and inert atmosphere glovebox techniques. Reagents and solvents were purchased from commercial sources as used as received unless otherwise stated. Triethylamine (Et₃N) ≥ 99 % purity and ascorbic acid (≥ 99 %) were purchased from Sigma-Aldrich® and used without further purification. Compounds 1-(*p*-toluensulfonyl)-1,4,7-triazacyclononane (^{Ts}tacn),³⁰² and [Ir(ppy)₂(bpy)]PF₆³⁰³ were synthesized according to the literature procedures. Anhydrous acetonitrile was purchased from Scharlab. Water (18.2 MΩ·cm) was purified with a Milli-Q Millipore Gradient AIS system. All the solvents were strictly degassed and stored in anaerobic conditions. All water reduction catalytic reactions were performed under N₂ otherwise notified.

III.3.2. Instrumentation

NMR spectra were recorded on Bruker spectrometers operating at 300 or 400 MHz as noted at 300 K. All ¹H chemical shifts are reported in ppm and were internally calibrated to the monoprotonic impurity of the deuterated solvent. The coupling constants are measured in Hz. The ¹³C chemical shifts were internally calibrated to the carbon atoms of the deuterated solvent. All experimental procedures were conducted at ambient temperature under nitrogen atmosphere and using degassed acetonitrile. A standard three-electrode configuration was employed in conjunction with CH Instruments potentiostat interfaced to a computer with CH Instruments 600D software. Using a one-compartment cell, all voltammetric scans were recorded using glassy carbon working electrode, which was treated between experiments by means of a sequence of polishing with MicroPolish Powder (0.05 micron) before washing and sonification. A saturated calomel electrode (SCE) and Pt wire were used as reference and counter electrodes, respectively. All materials for electrochemical experiments were dried at room temperature before use. UV/Vis spectra were recorded on an Agilent 8453 diode array spectrophotometer (190–1100 nm range) in 1 cm quartz cells. A cryostat from Unisoku Scientific Instruments was used for the temperature control. Electrospray ionization mass spectrometry (ESI-MS) experiments were performed on Bruker Daltonics Esquire 3000 Spectrometer, by introducing samples directly into the ESI-source using a syringe. DLS and NTA experiments were performed on a Zetasizer Nano ZS, Malvern Instruments (particle-size distribution from 0.6 to 6.000 nm) and Nanosight LM20 (particle-size distribution from 1 to 2000 nm). The analyses were carried out in the Institut de Ciència dels Materials de Barcelona.

III.3.3. X-ray Crystallography

Single crystals of **1_{Co}** and **1_{Ni}** were mounted on a nylon loop for X-ray structure determination. The measurements were carried out on a BRUKER SMART APEX CCD diffractometer using graphite-monochromated MoK_α radiation (λ=0.71073 Å). Programs

used: data collection, Smart version 5.631 (Bruker AXS 1997-02); data reduction, Saint+ version 6.36A (Bruker AXS 2001); absorption correction, SADABS version 2.10 (Bruker AXS 2001). Structure solution and refinement was done using SHELXTL Version 6.14 (Bruker AXS 2000–2003). The structure was solved by direct methods and refined by full-matrix least-squares methods on F². The non-hydrogen atoms were refined anisotropically. The hydrogen atoms were placed in geometrically optimized position and forced to ride on the atom to which they are attached.

CCDC-957199 (**1_{Co}**) and CCDC-957198 (**1_{Ni}**) contain the supplementary crystallographic data for this work. These data can be obtained free of charge from The Cambridge Crystallographic Data Centre via www.ccdc.cam.ac.uk/data_request/cif.

III.3.4. Gas-Evolution Monitoring Studies

All catalytic reactions were performed in a 15 mL vial capped with a septum. Each experiment was conducted in a volume-calibrated-vial equipped with stir-bars and containing the solvent mixture with the reagents, and then was connected to one port of a differential pressure transducer sensor (Honeywell-ASCX15DN, ±15 psi). Each reaction had its own reference reaction, which was conducted at the other port of the differential pressure transducer sensor. The reaction and reference vials were kept under the same experimental conditions to minimize the system noise due to temperature– pressure fluctuations. In this sense, each vial was submitted and located just over a LED radiation source. Furthermore, in order to ensure a constant and stable irradiation, the LED sources were equipped with a water refrigeration system. Just before starting the reaction, the corresponding catalyst was added by syringe through the septum from a stock solution prepared in acetonitrile. The reaction began when the LEDs were turned on. At this point, the hydrogen evolved from the reactions was monitored by recording the increase in pressure of the headspace (1 s interval). The pressure increment was the result of the difference in pressure between the reaction and reference vials. After the hydrogen evolution reached a plateau the amount of the formed gas was captured and measured, equilibrating the pressure between reaction and reference vials. The hydrogen contained in each of the reactions was measured by analyzing an aliquot of gas of the headspace (0.2 mL) by gas chromatography. GC measurements of H₂ corroborated the values obtained by pressure increments.

III.3.5. Gas-Evolution Studies Performed in the Presence of Hg⁰

Catalytic reactions performed in the presence of Hg⁰ were carried out in a 15 mL vial capped with a septum. Each experiment was conducted in a volume-calibrated-vial equipped with stir-bars and containing the CH₃CN/H₂O (3:7) as the solvent mixture with all the reagents under N₂. The experiments were conducted in one port of a differential pressure transducer sensor, with a reference reaction at the other port. The reaction and reference vials were kept under the same experimental conditions to minimize the System noise due to temperature-pressure fluctuations. Before starting the reaction Hg⁰

was added in large excess (1000 eq. or 1.5 mL; 15% of the total reaction volume) by syringe through the septum. The solution was stirred for 5 min under and then the solution was submitted to LED irradiation at 447 nm. Hg⁰ was left in contact with the solution during the whole catalytic assay in order to poison the heterogeneous catalyst formed during the irradiation time. The hydrogen evolved from the reaction was monitored in real time by recording the increase in pressure of the headspace (1 s interval). The pressure increment was the result of the difference in pressure between the reaction and reference vials. After the hydrogen evolution reached a plateau the amount of the formed gas was captured and measured, equilibrating the pressure between reaction and reference vials. The hydrogen contained in each of the reactions was measured by analyzing an aliquot of gas of the headspace (0.2 mL) by gas chromatography. GC measurements of H₂ corroborated the values obtained by pressure increments.

III.3.6. Parallel Pressure Transducer Hardware

The parallel pressure transducer that we used for these studies is the same that previously was developed and described for water oxidation studies.³⁰⁴ This is composed by 8 differential pressure transducers (Honeywell-ASCX15DN, ± 15 psi) connected to a hardware data-acquisition system (base on Atmega microcontroller) controlled by a home-developed software program. The differential pressure transducer Honeywell-ASCX15DN is a 100 microseconds response, signal-conditioned (high level span, 4.5 V) output, calibrated and temperature compensated (0 °C to 70 °C) sensor. The differential sensor has two sensing ports that can be used for differential pressure measurements. The pressure calibrated devices to within ± 0.5 matm was offset and span calibrated *via* software with a high precision pressure transducer (PX409-030GUSB, 0.08% Accuracy). Each of the 8 differential pressure transducers (Honeywell-ASCX15DN, ±15 psi) produce a voltage outputs that can directly transformed to a pressure difference between the two measuring ports. The voltage outputs were digitalized with a resolution of 0.25 matm from 0 to 175 matm and 1 matm from 176 to 1000 matm using an Atmega microcontroller with an independent voltage auto-calibration. Firmware Atmega microcontroller and control software were home-developed. The sensitivity of H₂ analytics allows quantifying the gas formed when low H₂ volumes are generated. Therefore, it could not be discarded that small amounts of H₂ were produced by inactive complexes.

III.3.7. Gas Chromatography Identification and Quantification of Gases

Hydrogen at the headspace was analyzed with an Agilent 7820A GC System equipped with columns Washed Molecular Sieve 5A, 2m x 1/8" OD, Mesh 60/80 SS and Porapak Q, 4m x 1/8" OD, SS. Mesh: 80/100 SS and a Thermal Conductivity Detector. The H₂ amount obtained was calculated through the interpolation of the previous calibration using different H₂/N₂ mixtures.

III.3.8. Acid Concentration Dependence Study

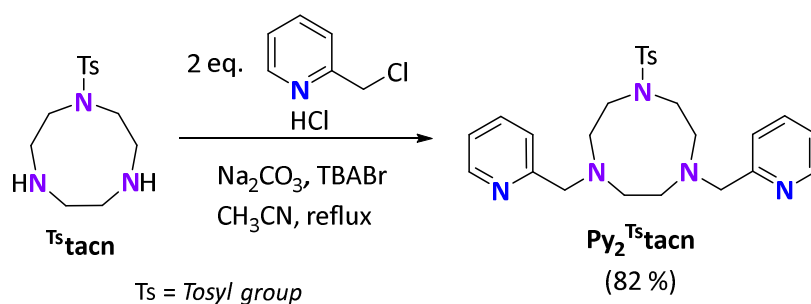
A 0.8 M stock solution of TFA was prepared in a CH₃CN solution of 0.1m Bu₄NPF₆. Aliquots of this solution were added to a degassed solution of 1 mM catalyst in CH₃CN. After the addition the solution was purged with N₂ before carrying out the cyclic voltammetry. The order with respect to [acid] was determined by plotting the current at the potential M^{I/I} versus the concentration of acid.

III.3.9. Catalyst Concentration Dependence Study

TFA was added to a solution of 0.1 M Bu₄NPF₆ in CH₃CN in an electrochemistry cell to provide an acid concentration of 100 mM. To this solution, aliquots of 20 mM stock solution of **1**_{Co} were added and CVs were collected. The order of the proton reduction with respect to [catalyst] was determined by plotting the current at the potential M^{I/I} versus the concentration of catalyst.

III.3.10. Synthesis of Complexes and Characterization

III.3.10.1. Synthesis of 1,4-di(picoly)-7-(p-toluenesulfonyl)-1,4,7triazacyclononane, (Py₂^{Ts}tacn)

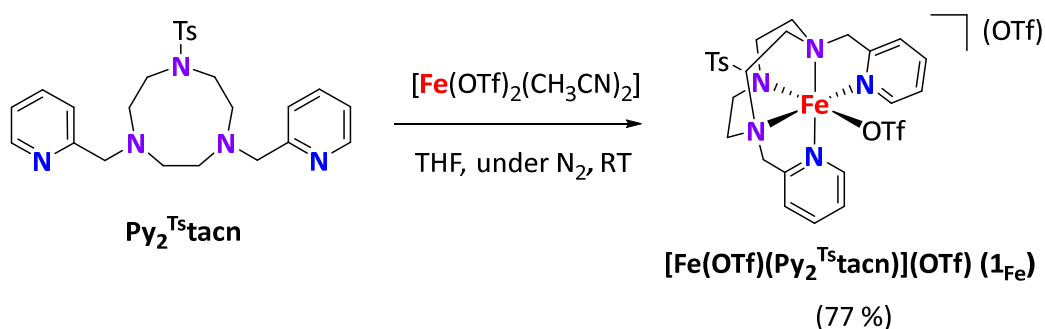


Scheme III. 3. Synthesis of Py₂^{Ts}tacn.

2-Picolyl chloride hydrochloride (1.16 g, 7.04 mmol), ^{Ts}tacn (1 g, 3.53 mmol) and anhydrous acetonitrile (40 mL) were mixed in a 100 mL flask. Na₂CO₃ (2.05 g) and tetrabutylammonium bromide, TBABr (80 mg) were added directly as solids and the resulting mixture was heated at reflux under N₂ for 22 hours. After cooling to room temperature, the resulting orange mixture was filtered and the filter cake was washed with CH₂Cl₂. The combined filtrates were evaporated under reduce pressure. To the resulting residue, 2 M NaOH (15 mL) was added and the mixture was extracted with CH₂Cl₂ (4 x 40 mL). The combined organic layers were dried over MgSO₄ and the solvent was removed under reduced pressure. The resulting residue was treated with *n*-hexane (100 mL) and stirred for 12 hours. A fine white solid appeared which was filtered off and dried under vacuum to yield 1.34 g of the desired product (2.88 mmols, 82 %). ¹H-NMR (CDCl₃, 300 MHz, 300 K) δ, ppm: 8.50 (d, *J* = 4.8 Hz, 2H, **H**₂ of py), 7.66-7.60 (m, 4H, **H**_{7S} and **H**₄ of py), 7.47 (d, *J* = 7.8 Hz, 2H, **H**_{7S}), 7.26 (d, 2H, *J* = 8.4 Hz, **H**₅ of py), 7.15-7.11 (m, 2H, **H**₃ of py), 3.86 (s, 4H, **CH**₂-py), 3.22 (m, 4H, N-**CH**₂-CH₂), 3.12 (m, 4H, N-**CH**₂-CH₂),

2.79 (s, 4H, N-CH₂-CH₂), 2.40 (s, 3H, CH₃). ¹³C-NMR (CDCl₃, 75 MHz, 300 K) δ, ppm: 159.75 (C₁₀), 149.00 (C₁₄), 142.99 (C₅), 136.40 (C₁₂), 135.94 (C₂), 129.60 (C₁₁), 127.12 (C₄), 123.23 (C₃), 121.94 (C₁₃), 63.84 (C₉), 55.85 (C_{7,8}), 50.87 (C₆), 21.47 (C₁). ESI-MS (m/z): 466.2 [M+H]⁺. Anal. Calcd for C₂₅H₃₁N₅O₂S·1/2H₂O: C, 63.27; H, 6.80; N, 14.76 %. Found: C, 63.47; H, 6.68; N, 13.91 %.

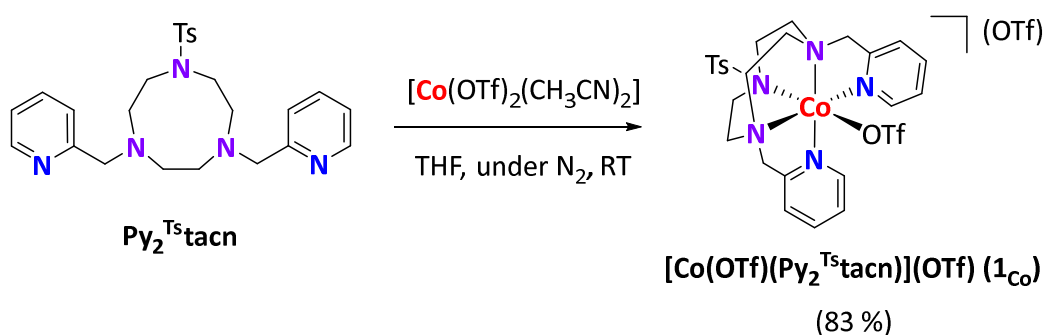
III.3.10.2. Synthesis of [Fe(OTf)(Py₂^{Ts}tacn)](OTf) (**1_{Fe}**)



Scheme III. 4. Synthesis of [Fe(OTf)(Py₂^{Ts}tacn)](OTf).

In a glovebox, a solution of [Fe(OTf)₂(CH₃CN)₂] (235 mg, 0.539 mmol) in anhydrous THF (1 mL) was added dropwise to a vigorously stirred solution of Py₂^{Ts}tacn (251.2 mg, 0.539 mmol) in THF (1 mL). After few minutes, the solution became cloudy and a pale yellow precipitate appeared. After stirring for an additional 5 hours the solution was filtered off and the resulting solid dried under vacuum. This solid was dissolved with CH₂Cl₂, and the slow diffusion of diethyl ether over the resultant solution afforded, in few days, 340 mg of a pale yellow solid (0.414 mmol, 76.9 %). ¹H-NMR (CD₃CN, 400 MHz, 300 K) δ, ppm: 56.62, 11.18, 8.42, 7.88, 3.45, 2.17, 1.12. Anal. Calcd for C₂₇H₃₁F₆FeN₅O₈S₃·1/2CH₂Cl₂: C, 38.21; N, 8.21; H, 3.74 %. Found: C, 38.54; N, 8.27; H, 3.73 %. HR-ESI-MS (m/z): 670.1069 [M-OTf]⁺, 260.5804 [M-2·OTf]²⁺.

III.3.10.3. Synthesis of [Co(OTf)(Py₂^{Ts}tacn)](OTf) (**1_{Co}**)

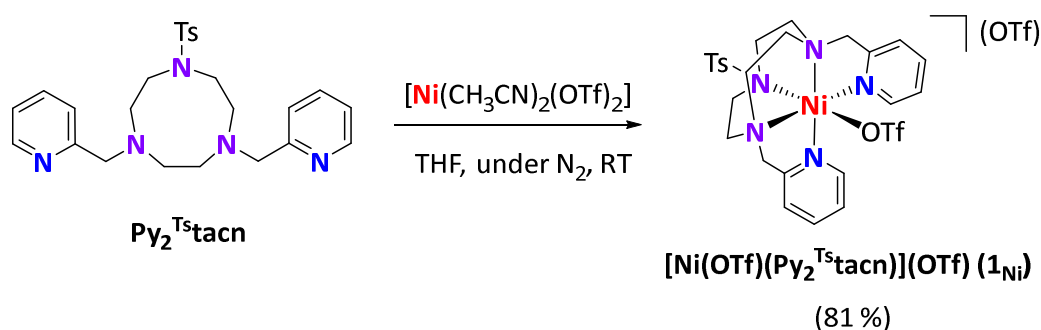


Scheme III. 5. Synthesis of [Co(OTf)(Py₂^{Ts}tacn)](OTf).

In a glovebox, a solution of [Co(OTf)₂(CH₃CN)₂] (236 mg, 0.537 mmol) in anhydrous THF (1 mL) was added dropwise to a vigorously stirred solution of Py₂^{Ts}tacn (250 mg, 0.537

mmol) in THF (1 mL). After few minutes, the solution become cloudy and a pale pink precipitate appeared. After stirring for an additional 2 hours the solution was filtered off and the resulting solid dried under vacuum. This solid was dissolved in CH₂Cl₂ and the slow diffusion of diethyl ether into this solution produced 355 mg of pink crystals (0.432 mmol, 83%). ¹H-NMR (CD₃CN, 300 MHz, 300K) δ, ppm: 118.28, 55.72, 3.92, 3.76, 2.22, 9.42. Anal. Calcd for C₂₇H₃₁F₆CoN₅O₈S₃: C, 39.42; N, 8.51; H, 3.80 %. Found: C, 39.23; N, 8.56 ; H, 3.68 %. HR-ESI-MS (m/z): 673.1054 [M - OTf]⁺, 262.0766 [M-2·OTf]²⁺.

III.3.10.4. Synthesis of [Ni(OTf)(Py₂^{Ts}tacn)](OTf) (**1_{Ni}**)



Scheme III. 6. Synthesis of [Ni(OTf)(Py₂^{Ts}tacn)](OTf).

In a glovebox, a solution of [Ni(OTf)₂(CH₃CN)₃] (205.9 mg, 0.429 mmol) in anhydrous THF (1 mL) was added dropwise to a vigorously stirred solution of Py₂^{Ts}tacn (200 mg, 0.429 mmol) in THF (1 mL). After few minutes, the solution become cloudy and a purple precipitate appeared. After stirring for an additional 4 hours the solution was filtered off and the resulting solid dried under vacuum. This solid was dissolved in CH₂Cl₂ and the slow diffusion of diethyl ether into this solution produced 285 mg of purple crystals (0.346 mmol, 80.65 %). ¹H-NMR (CD₃CN, 400 MHz, 300 K) δ, ppm: 56.41, 52.13, 45.61, 15.46, 14.89, 9.21, 6.46, 5.70, 2.17. Anal. Calcd for C₂₇H₃₁F₆NiN₅O₈S₃·1/2CH₂Cl₂: C, 38.19; N, 8.10; H, 3.73 %. Found: C, 38.17; N, 8.15; H, 3.51 %. HR-ESI-MS (m/z): 672.1058 [M - OTf]⁺, 261.5797 [M - 2·OTf]²⁺.

III.3.11. Electrochemical Reduction of Protons

III.3.11.1. Determination of the $E_{1/2}$, overpotential and reaction orders

For the calculation of $E_{1/2}$, overpotential and TOF it has been considered the current at half $M^{II/I}$ reduction wave, according to the procedures previously described by Artero, Fontecave and coworkers.⁸³ The determination of the overpotential has been carried out based on the lowest potential at which TFA can be reduced to dihydrogen in the employed conditions, which is: $E^{\circ}(H^+/H_2) = 0.24$ V vs. SCE in CH₃CN. Taking into consideration the acid dissociation constant ($K_{a,HA}$) it can be obtain the reduction potential as function of the $pK_{a,HA}$ (Eq. III. 1).

$$E^{\circ}_{HA} = E^{\circ}(H^+/H_2) - (2.303RT/F)pK_{a,HA} \quad (\text{Eq. III.1})$$

In the case of TFA, the acidity in acetonitrile is $pK_{a,TFA} = 12.7$ and therefore $E^{\circ}(TFA/H_2) = -0.51$ V. For **1**_{Co} the $Co^{II/I}$ redox potential at the half of reduction wave is -1.10 V and therefore the overpotential estimated for reduction of protons is 590 mV.

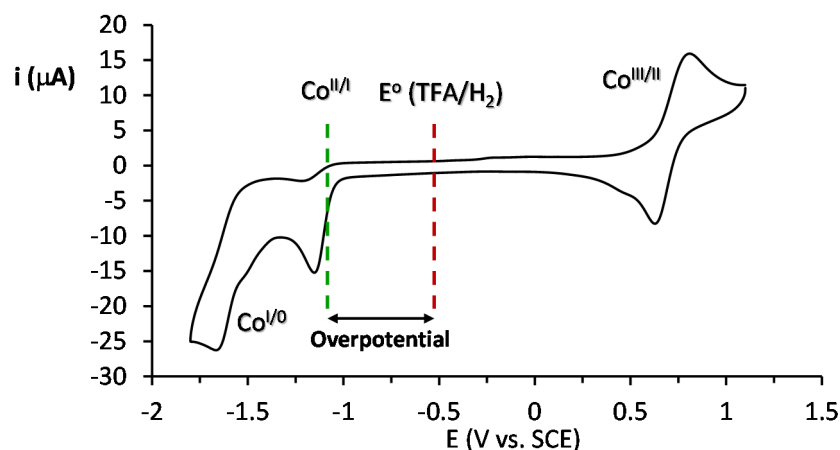


Figure III. 21. Determination of the overpotential in the case of **1**_{Co} using TFA.

When electrochemical measurements of **1**_{Co} were carried out in the presence of acid, a large increase in the cathodic peak current was observed. This current enhancement (i_{cat}) caused by the catalytic production of hydrogen, was found first order respect to the catalyst, second order in $[H^+]$ and independent of scan rate (Eq. III. 2)

$$i_{cat} = nFA[cat]\sqrt{Dk[H^+]^2} \quad (\text{Eq. III. 2})$$

Where n is the number of electrons involved in the catalytic reaction and k is the second order rate constant. The TOF was calculated by using equation III.3. Where the i_p (current measured in the absence of acid) and i_{cat} (catalytic current, in presence of acid) for each acid concentration was measured at the half $Co^{II/I}$ reduction wave potential, n is the number of electrons involved in the catalytic reaction, $k_{obs} = k[H^+]^2$ is the observed first-order rate constant, R is the universal gas constant, T is the temperature in Kelvin,

F is Faraday's constant, ν is the scan rate (Eq. III. 3). A linear correlation between i_{cat}/i_p vs [acid] means a second-order process with respect the acid.

$$\frac{i_{cat}}{i_p} = \frac{n}{0.4463} \sqrt{\frac{RT(k[H^+]^2)}{F\nu}} \quad (\text{Eq. III. 3})$$

III.3.12. Theoretical Studies

III.3.12.1. Computational details

The DFT calculations were performed by Dr. F. Acuña. The methodology is here described to merely informative reasons. DFT calculations were carried out using the Gaussian09 program³⁰¹ with B3LYP hybrid exchange-correlation functional.³⁰⁵⁻³⁰⁷ X-ray structures **1_{Co}** and **1_{Ni}** were used as starting point for the geometry optimizations, using 6-31G* basis set for all atoms. Solvating and Van der Waals dispersion effects were included in geometry optimizations through the SMD polarizable continuum model³⁰⁸ and the Grimme DFT-D₂ method,³⁰⁹ respectively. The nature of stationary points was established by vibrational frequency calculations in condensed phase, where minima have no imaginary frequencies. Free energies values (G) were obtained by including solvent and Grimme corrections to energy computed with 6-311+G** basis set on the equilibrium geometries:

$$G = E_{6-311+G^{**}} + G_{corr.} + G_{solv.} + E_{VW} \quad (\text{Eq. III. 4})$$

where the Gibbs correction ($G_{corr.}$) was obtained from gas phase frequency calculations at UB3LYP/6-31G* level, the solvation energy ($G_{solv.}$) was calculated as the difference of the total free energy in gas phase and in water at the same level of theory and geometry and E_{VW} was the Grimme dispersion correction.

All calculations employ the spin-unrestricted formalism and spin-contaminated 6-311+G** electronic energies were systematically corrected using the methodology described in the literature.³¹⁰

III.3.12.2. Redox potentials and pK_a values

The pK_a can be quantified by:

$$pK_a = \frac{\Delta G^{\circ}}{RT \ln(10)} \quad (\text{Eq. III. 5})$$

where R is the universal gas constant and T is the temperature.³¹¹ The ΔG° (standard dissociation free energy change between an acid (AH) and its conjugate base (A⁻) in aqueous phase) may be expressed using the following equations:

$$\Delta G^{\circ} = G(A_{aq}^{-}) + G(H_{aq}^{+}) - G(AH_{aq}) + \Delta G^* \quad (\text{Eq. III. 6})$$

$$G(\text{H}_{\text{aq}}^+) = G(\text{H}_{\text{gas}}^+) + \Delta G_{\text{solv}}^{\text{H}^+} \quad (\text{Eq. III. 7})$$

where $G(\text{AH}_{\text{aq}})$ and $G(\text{A}_{\text{aq}}^-)$ are standard free energies of the acid and its conjugate base, respectively. The $G(\text{H}_{\text{aq}}^+)$ is the free energy of the proton in water, obtained from the experimental solvation free energy of a proton ($\Delta G_{\text{solv}}^{\text{H}^+} = -265.9 \text{ kcal} \cdot \text{mol}^{-1}$) and its gas-phase free energy ($G(\text{H}_{\text{gas}}^+) = -6.3 \text{ kcal} \cdot \text{mol}^{-1}$).³¹² ΔG^* is the free energy change associated with the conversion from a standard-state of 1 M in the aqueous phase and 1 atm in gas phase, to 1 M in both phases. Its value is $1.89 \text{ kcal} \cdot \text{mol}^{-1}$ at 298 K.

The standard one electron redox potentials relative to the SCE electrode were calculated by:

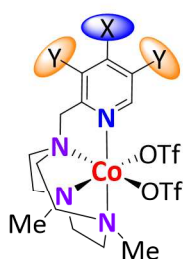
$$E^{\circ} = -\frac{\Delta G^* - \Delta G_{\text{SHE}}^*}{F} + \Delta E_{\text{SCE}}^{\circ} \quad (\text{Eq. III. 8})$$

where ΔG^* is the standard free energy change associated with the reduction reaction, F is the Faraday constant ($23.06 \text{ kcal} \cdot \text{mol}^{-1} \text{ V}^{-1}$) and ΔG_{SHE}^* is the free energy change associated with the proton reduction ($-100.64 \text{ kcal} \cdot \text{mol}^{-1}$).⁷ The parameter $\Delta E_{\text{SCE}}^{\circ} = 0.24 \text{ V}$ is a correction to make the redox values relative to the saturated calomel electrode (SCE).

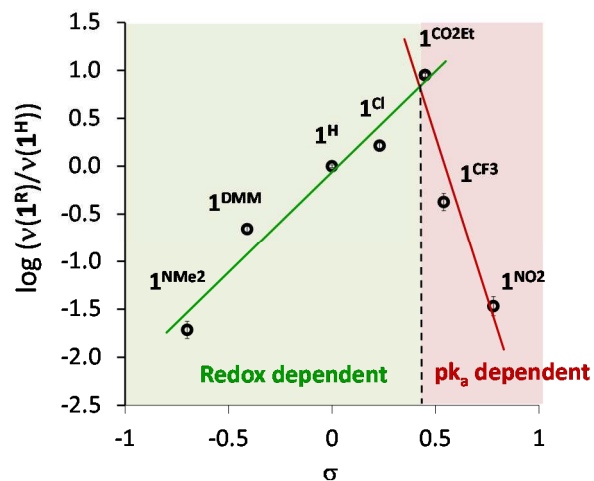
CHAPTER IV

Influence of the Electronic Effects on the H₂ Evolution Catalyzed by Cobalt Complexes Based on *N*-tetradentate Pytacn type Ligands

Electronic modulation



X = NMe₂, OMe, H, Cl, CO₂Et, CF₃ or NO₂
Y = H or Me



IV. INFLUENCE OF THE ELECTRONIC EFFECTS ON THE H₂ EVOLUTION CATALYZED BY COBALT COMPLEXES BASED ON *N*-TETRADENTATE PYTACN TYPE LIGANDS

IV.1. STATE-OF-THE-ART

To study the effect of the electronic nature of metals complexes in catalysis can be a very powerful strategy to interrogate reaction mechanisms. In this regard, the catalytic proton reduction to H₂ mediated by homogeneous metal complexes has been also investigated by means of electronic effects.^{51,57,83,144-148} However, the inherent complexity of the mechanism and the lack of a broad library of metal complexes with ligands imposing monotonic electronic effects limited the conclusions of these studies.

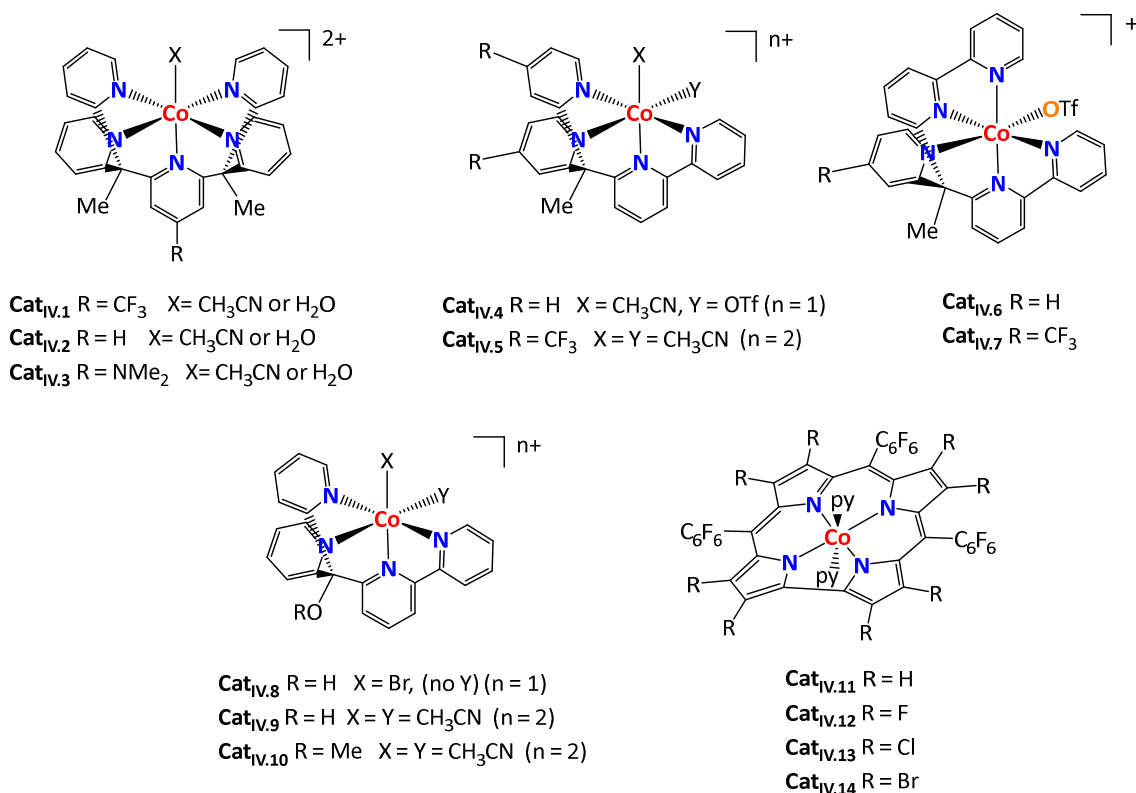


Figure IV. 1. Selected cobalt complexes based containing different electronic substituents studied in catalytic hydrogen production.

Cobalt complexes based on polypyridine ligands are easily tunable and therefore excellent candidates to carry out these studies. Indeed, the first study focused on how the electronic properties of the ligand influence the catalytic activity was performed by Chang and co-workers (2013).⁹⁸ They developed three new cobalt complexes base on pentadentate ligands differing only in the *para*-substituent of the central pyridine; with

p-CF₃ (**Cat_{IV.1}**), *p*-H (**Cat_{IV.2}**) and *p*-NMe₂ (**Cat_{IV.3}**) groups (Figure IV. 1). In agreement with electrocatalytic studies, the most efficient light-driven H₂ evolution catalyst had the electron withdrawing CF₃ group and 2-fold TON than the catalyst containing the *p*-NMe₂ group. Later on, the same authors designed two new set of cobalt complexes based on tetra- (**Cat_{IV.4-5}**⁹⁷) and pentadentate (**Cat_{IV.6-7}**¹⁰⁰) polypyridine ligands (Figure IV. 1). In contrast with the previous system the new complexes containing the strong electron withdrawing CF₃ group (**Cat_{IV.5}** and **Cat_{IV.7}**) presented lower catalytic activities.^{97,100}

The electronic effects has been also evaluated in cobalt corroles by means of introducing different halide substituents at the aryl groups (H, F, Cl and Br, **Cat_{IV.11-14}** respectively)³¹³ (Figure IV. 1). The halide substituents affect not only the reduction potentials but also the catalytic activity. The electrocatalytic activity was significantly enhanced by reducing the electron density over the metal center through the π -system of the corrole (higher activity was obtained with **Cat_{IV.12}**).

Despite the important efforts devote to rationalize the electronic effects this has been probed very challenging and the conclusions are limited only to specific aspects. Therefore, it could be interesting to approach the problem in a more systematic manner. In particular, we propose to study the electro- and photochemical catalytic activity of a broad series of cobalt complexes sharing the same ligand architecture but tuned with different substituent to allow the fine tuning of the electronic effects. We hypothesize that by the combination of the results is catalysis with a theoretical modelling of basic thermodynamic parameters will guide us to identify the key factors that controls the catalytic activity. This information will be of value for the design of more active water reduction catalysis.

The fine tuning of the electronic properties of the ligand can be obtained by straightforward introduction of substituents at the γ -position (X = NO₂, CF₃, CO₂Et, Cl, H, OMe and NMe₂) and β (Y = MeO when X = Me) of the pyridine (Scheme IV. 1).^{323,324} Moreover, this ligand derivatization do not introduce significant steric effects. ^{Y,X}Py^{Me}tacn ligands were synthesized according to literature procedures by the alkylation of the 1,4-dimethyl-1,4,7-triazacyclononane (tacnMe₂) moiety with the appropriate functionalized pycolyl chloride arm in dry acetonitrile, in yields up to 97 %.^{315,325,326}

Seven well-defined Co^{II} complexes (**1^R**) were synthesized by reaction of tetradentate ligands ^{Y,X}Py^{Me}tacn with an equimolar amount of [Co(OTf)₂(MeCN)₂] (OTf = trifluoromethanesulfonate anion) in dry THF under strict anaerobic conditions at room temperature. The desired bis-triflate complexes [Co^{II}(OTf)₂(^{Y,X}Py^{Me}tacn)] were purified by slow diffusion of diethylether in a CH₂Cl₂ solution of **1^R**, affording crystalline material in yields between 61-86 %. All complexes have been characterized by UV/Vis absorption spectroscopy, ESI-MS, FT-IR, cyclic voltammetry, elemental analysis, ¹H-NMR and the spin state has also been determined. Additionally, except for **1^{CF3}** all complexes have also been characterized by single crystal X-Ray diffraction crystallography.

IV.2.1.1. ¹H-NMR spectroscopy

The structure of complexes **1^R** was studied in solution by means of ¹H-NMR spectroscopy. Since Co^{II} complexes are paramagnetic species present a fast nuclear relaxation (short T₁) with a line broadening around 2-50 Hz consistent with Co^{II} high spin complexes, which as expected is larger than the spin-spin coupling constant.³²⁷ The ¹H-NMR spectra at room temperature of complexes **1^R** are collected in the Figure IV. 4. All of the **1^R** complexes exhibit spectra windows ranged from -14 to 240 ppm, which is in agreement with t_{2g}⁵ e_g² or t_{2g}⁶ e_g¹ configuration of Co^{II} paramagnetic species.

The assignment of protons have been done on the basis of their relative integration, relative peak width ($\Delta\delta$, measured at half-peak intensity) and the comparison of the ¹H-NMR spectra within the **1^R** series. The integration of peaks for **1^H** (280 K) at 242.9 ($\Delta\delta = 0.60$), 91.9 ($\Delta\delta = 0.10$), 65.6 ($\Delta\delta = 0.12$) and 28.9 ($\Delta\delta = 0.04$) have about the same relative intensity (Figure IV. 2), which can be set up to 1 and likely

correspond to the aromatic hydrogens of the pyridine moiety. Signal at 242.9 ppm with the highest $\Delta\delta$ value ($\Delta\delta = 0.60$, $d(\text{Co-H}_\alpha) = 3.1900 \text{ \AA}$) can be assigned to the H_α, since this is the hydrogen closest to the paramagnetic Co^{II} center. This is in agreement with the characteristic field upshift behavior of H_α^{315,328} derived from Fermi contact interactions with the metal center.³²⁹ The narrow signals at 91.9 ($\Delta\delta = 0.10$, $d(\text{Co-H}_\beta) = 5.1312 \text{ \AA}$) and 65.6 ($\Delta\delta = 0.12$, $d(\text{Co-H}_{\beta'}) = 4.923 \text{ \AA}$) can be attributed to the H_β and H_{β'} according to the integration and similar $\Delta\delta$ values. The distinction between H_β and H_{β'} protons was done on the basis of the cobalt-H_β distances obtained by X-Ray crystallography and $\Delta\delta$ compared with the $\Delta\delta$ values. The assignment of H_β was confirmed by their absent in the β substituted **1^{DMM}**, but present in the other *para*-substituted cobalt complexes (Figure IV. 4). Finally, according to the lowest $\Delta\delta$ value, the peak at 28.9 ($\Delta\delta = 0.04$) can be attributed to the γ proton since is located at the longest distance from the paramagnetic center and is absent in all *para*-substituted complexes.

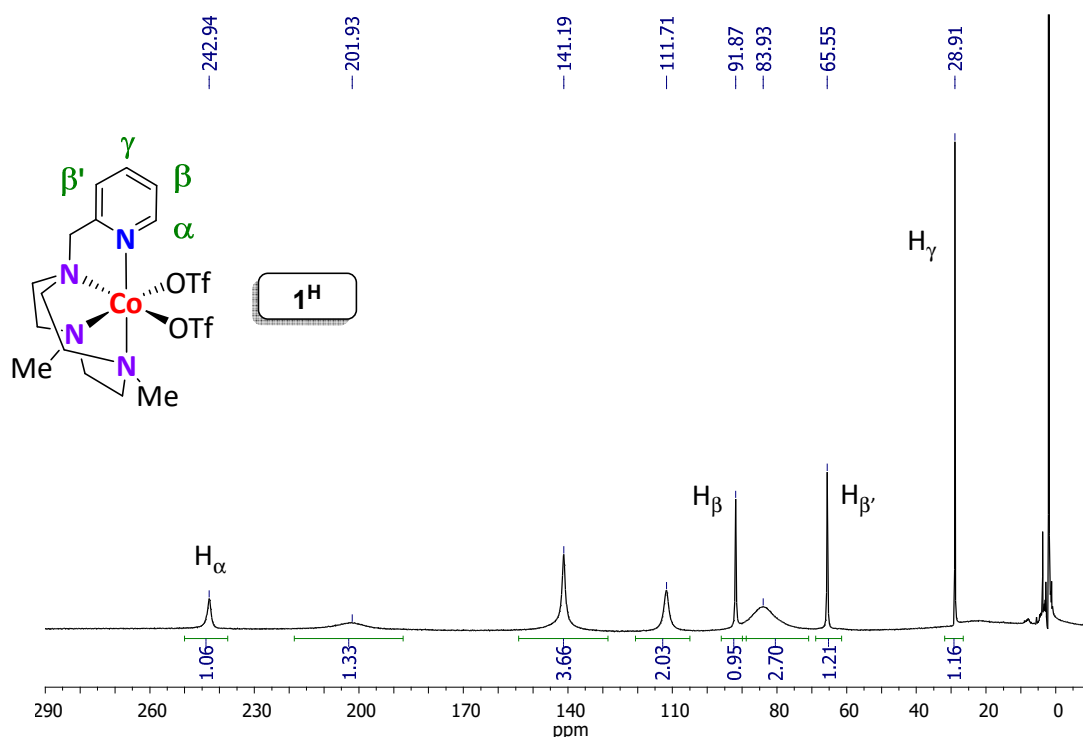


Figure IV. 2. Paramagnetic ¹H-NMR spectrum of **1^H** complex in CD₃CN at 280 K. Peak width measured at half peak intensity ($\Delta\delta$, in ppm): 242.9 (0.6), 201.9 (4.3), 141.1 (0.61), 111.7 (0.81), 91.9 (0.10), 83.93 (4.24), 65.55 (0.12), 28.91 (0.04).

The remaining paramagnetic ¹H-NMR signals appeared downfield shifted (between 90 and 200 ppm) compared with the H_β protons, and as broad signals. In general, proton assignment is consistent with the typical ¹H-NMR patterns of related Co^{II} polypyridyl complexes described in the literature.³²⁸

Interestingly, the ¹H-NMR shift of the α and β hydrogen atoms correlates with the electric properties of the *para*-substitution at the pyridine (Figure IV. 3), which also correlates with the Co-N_{py} bond length. As is observed in the molecular structures obtained by X-Ray crystallography, the electronic nature of substituent group at the *para*-pyridine ring significantly modify the Co-N_{py} bond length (Table A. 2. 1 and Table A. 2. 2) Thus, higher the electron donating properties of the ligand, shorter the Co-N_{py} bond and lower the ¹H-NMR signal corresponding to the H_α and H_β atoms since the distance to the paramagnetic center is shorter. Moreover, ¹H-NMR shifts of H_α correlates with the σ Hammett parameter for the **1^R** family (Figure IV. 3).

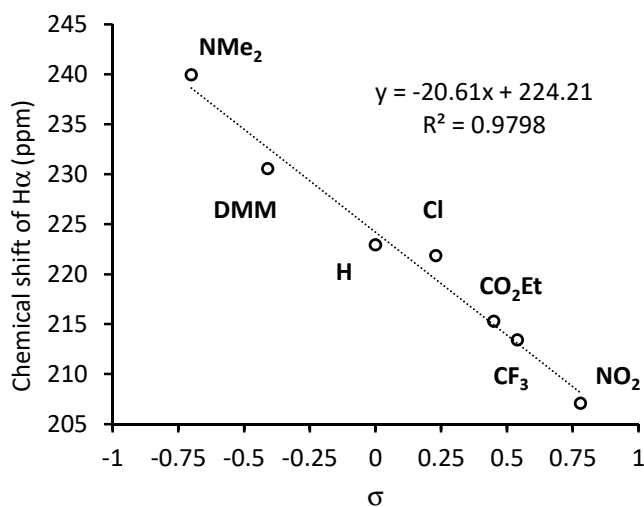


Figure IV. 3. Linear plot of H_α chemical shift (T = 298 K) of the **1^R** complexes versus the Hammett σ parameter.

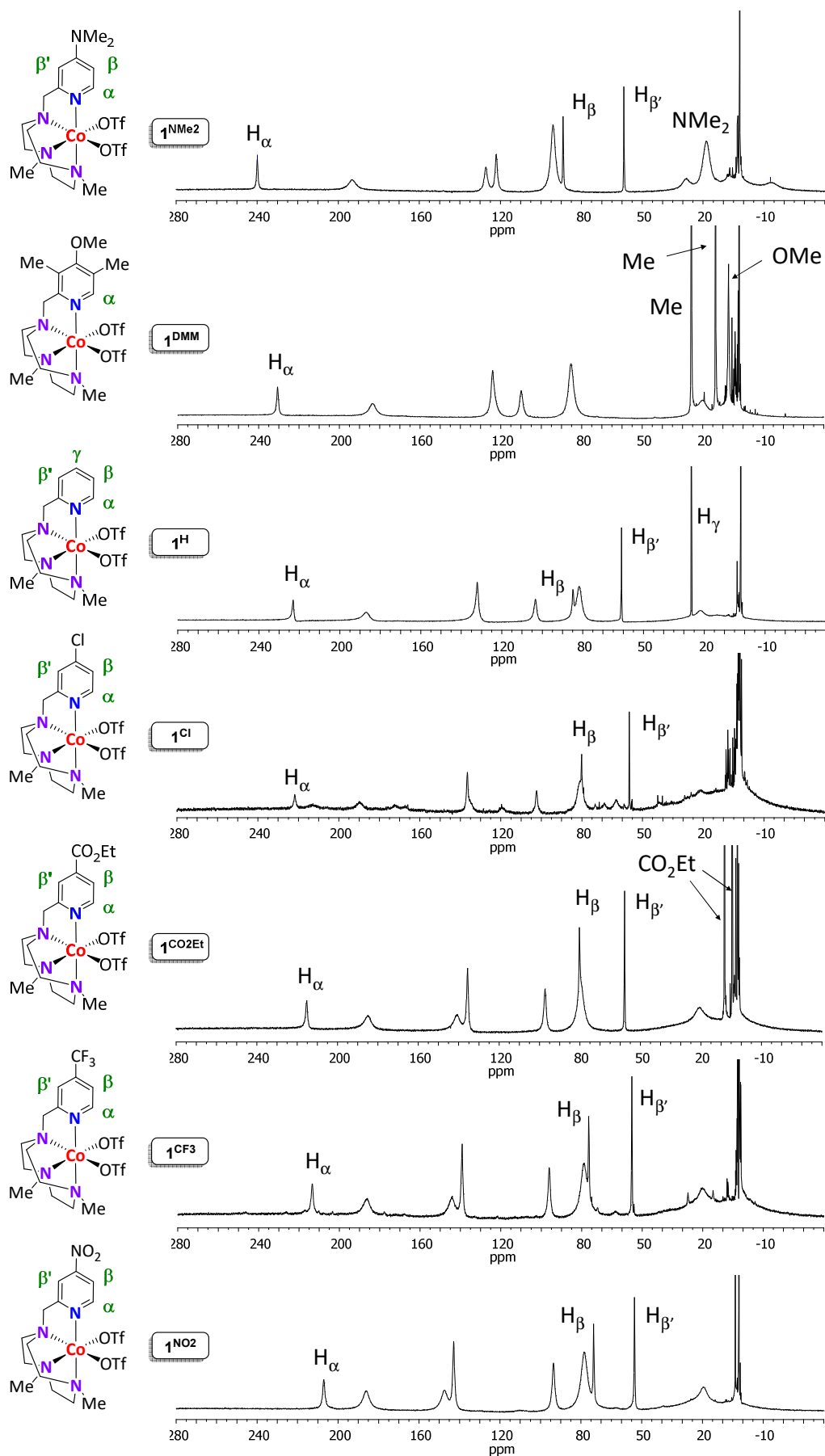


Figure IV. 4. Paramagnetic ¹H-NMR spectra of **1^R** complexes in CD₃CN at 298 K

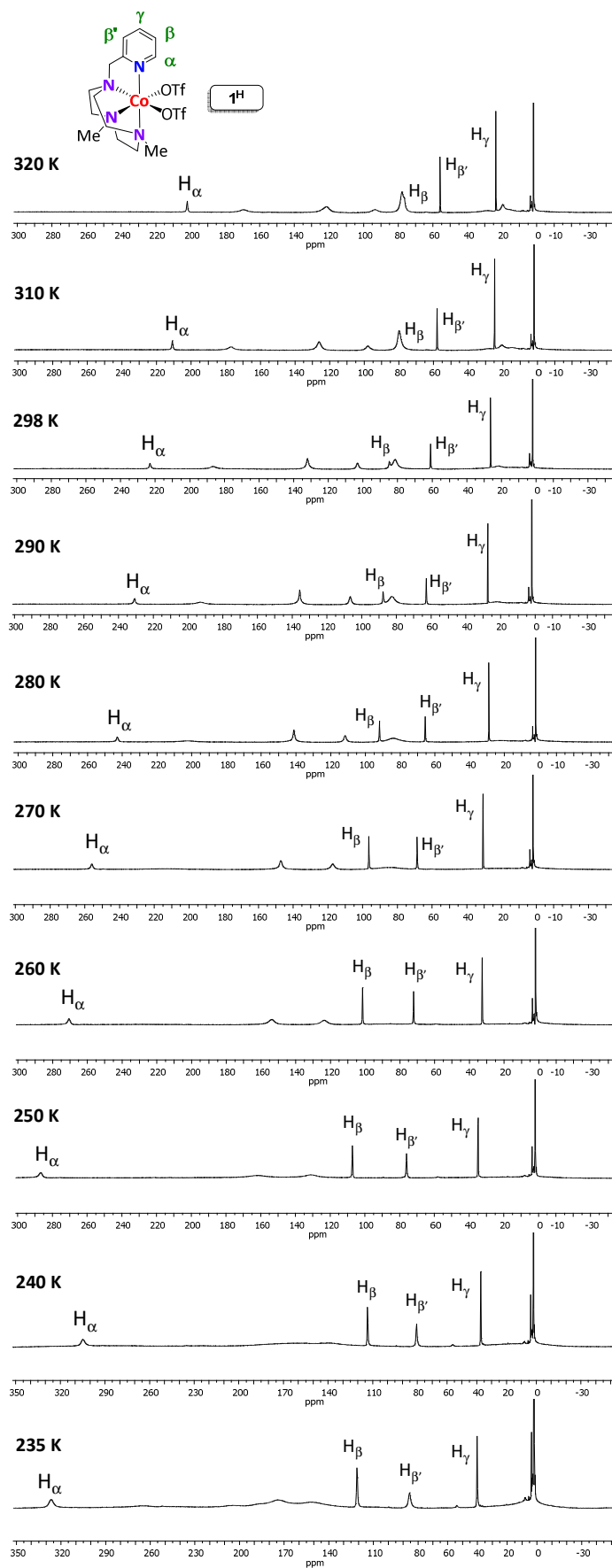


Figure IV. 5. ¹H-NMR spectra (500 MHz) of **1^H** in CD₃CN at different temperatures.

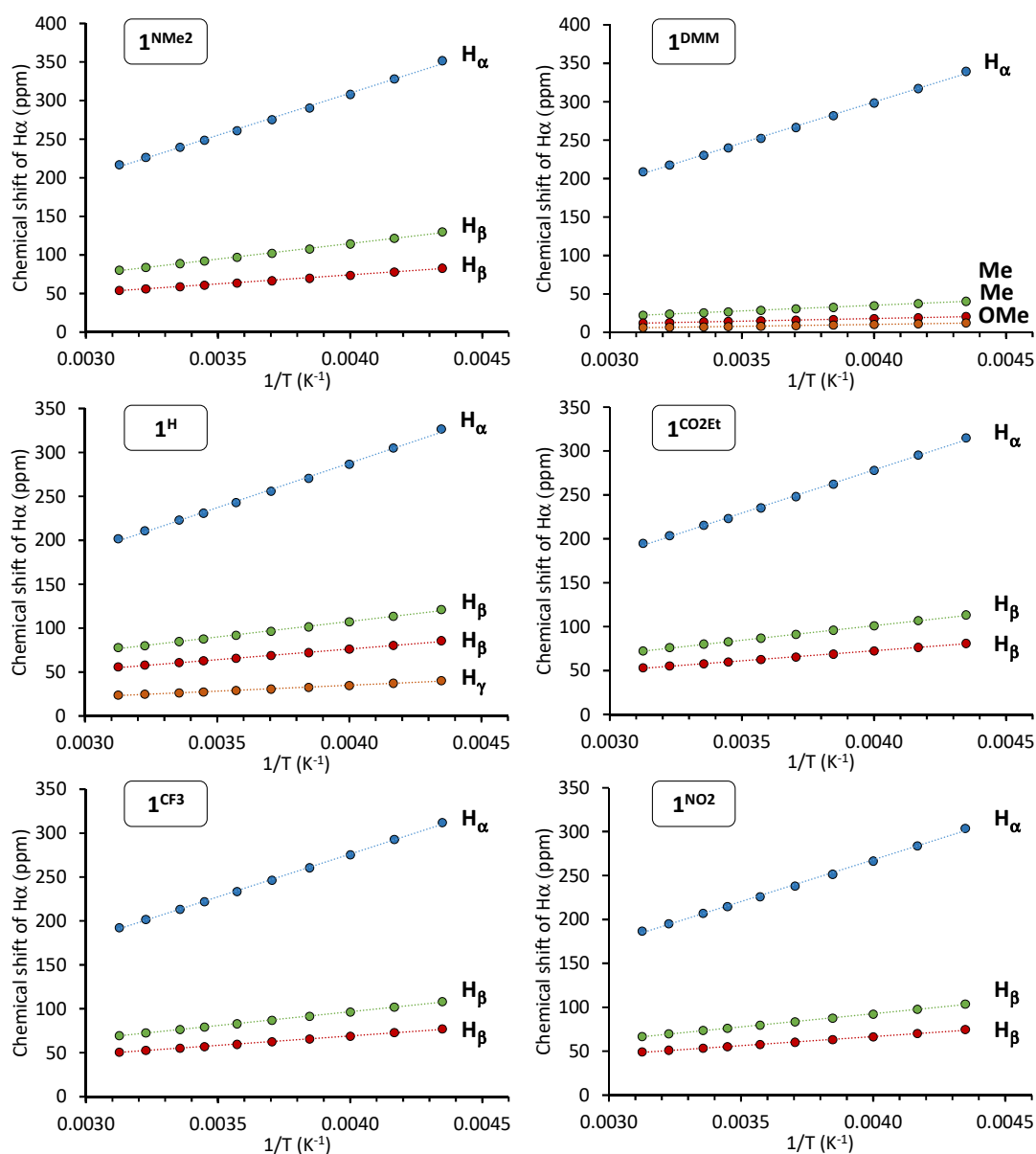


Figure IV. 6. Representation of the chemical shift of aromatic protons of **1^R** complexes (in CD₃CN) in front of temperature in the ¹H-NMR spectrum in CD₃CN

Afterwards, we studied the temperature dependence paramagnetism of the **1^R** complexes (230 – 320 K). Signals assigned to CH₂ fragments and N-Me groups become significantly broader when decreasing the temperature and basically disappear at 235 K. However, pyridine signals does not significantly change with the temperature. In general terms, all of the protons assigned to the **1^R** cobalt complexes exhibit a chemical shift linearly dependent on 1/T, consistent with Curie's law, which indicates that there is not a spin change in this temperature range (Figure IV. 6).³³⁰

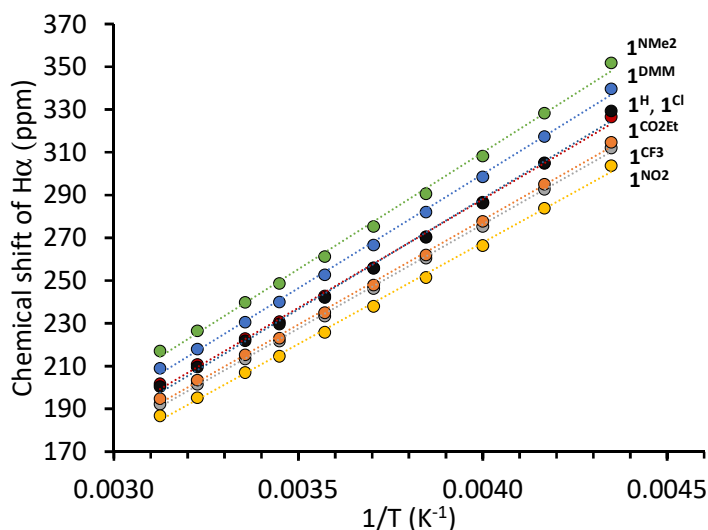


Figure IV. 7. Left: Representation of the chemical shift of H_α signals in front of temperature in the ¹H-NMR spectrum of **1^R** complexes in CD₃CN.

IV.2.1.2. Effective magnetic moment

The μ_{eff} values were measured following the Evans' NMR method³³¹⁻³³³ in the 235 - 330 K temperature range in steps of 10 K. As shown in Figure IV. 8, all **1^R** complexes present reasonably constant μ_{eff} values (3.6-4.3 BM) between 235 and 330 K, in good agreement with d⁷ high-spin Co^{II} complexes reported in the literature.^{96,334,335} For high-spin d⁷ (S=3/2) Co^{II} complexes with an octahedral, trigonal bipyramidal or pentagonal bipyramidal the expected μ_{eff} value is about 3.9 BM. However, for the corresponding low-spin (S= 1/2) Co^{II} complexes, the μ_{eff} value is 1.7 BM.

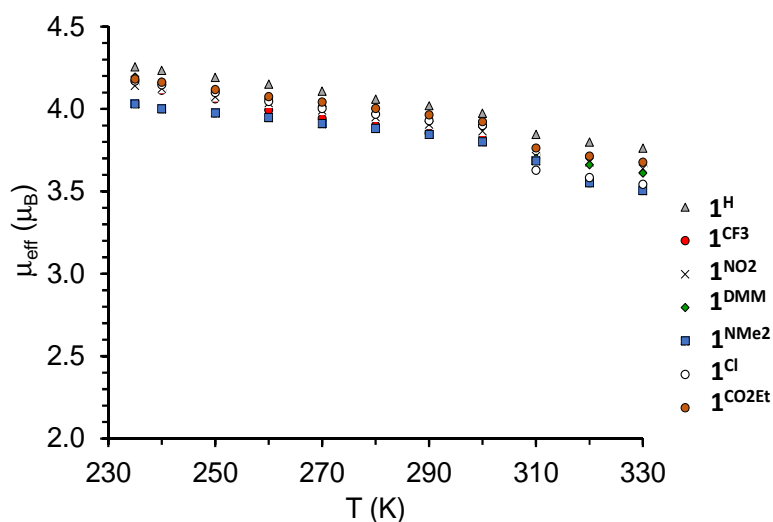


Figure IV. 8. Representation of the effective magnetic moment of **1^R** complexes as a function of the temperature. μ_{eff} values were obtained in CD₃CN using the Evans' method

The ¹⁹F-NMR of complex **1^H** shows a single around -80 ppm, which is characteristic to a free triflate anion in CD₃CN solution in diamagnetic species.^{315,336,337} The temperature dependent ¹⁹F-NMR shows a signal broadening and shifting to higher field that can be attributed to the triflate anion ligand exchange with the metal center (Figure A. 2. 6). The replacement of triflate anions by CH₃CN is also demonstrated by the X-Ray diffraction analysis of single crystals obtained from an acetonitrile solution containing **1^{NO2}** (Figure IV. 9). We note that a change in color was observed when CH₃CN was added to a solution of the triflate **1^{NO2}** complex in CH₂Cl₂ (from pale red to dark red). This change in color could be attributed to the CH₃CN coordination. The behavior is observed for the whole series of **1^R** complexes.

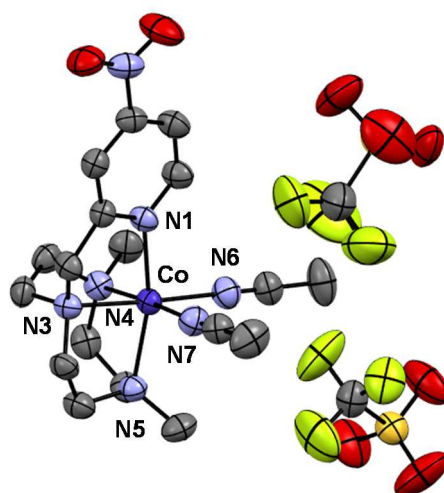


Figure IV. 9. Thermal ellipsoid plots of complex [Co(^{H,NO2}Py^{Me,tacn})(MeCN)₂](OTf)₂ (50% probability) measured at 298 K. Hydrogen atoms have been omitted for clarity. The crystal data and the selected bond and angles are collected in the section IV.3.12.3.

IV.2.1.3. UV/Vis spectroscopy

The UV/Vis spectra of the bis-acetonitrile complexes, formed by dissolving the corresponding bis-triflate **1^R_{OTf}** complexes (100 μM) in acetonitrile, were analyzed to obtain further information about the electronic structure of the complexes. The UV/Vis spectra of **1^R** complexes are characterized by several intense transitions from 200 to 400 nm: 270 (**1^{NMe2}**, ε = 17950 M⁻¹·cm⁻¹), 260 (**1^{DMM}**, ε = 5400 M⁻¹·cm⁻¹), 256 (**1^H**, ε = 5500 M⁻¹·cm⁻¹).

$1 \cdot \text{cm}^{-1}$), 217 (**1^{Cl}**, $\epsilon = 13800 \text{ M}^{-1} \cdot \text{cm}^{-1}$), 281 (**1^{CO2Et}**, $\epsilon = 6845 \text{ M}^{-1} \cdot \text{cm}^{-1}$), 268 (**1^{CF3}**, $\epsilon = 6250 \text{ M}^{-1} \cdot \text{cm}^{-1}$) and 223 (**1^{NO2}**, $\epsilon = 16650 \text{ M}^{-1} \cdot \text{cm}^{-1}$) (Figure IV. 10).

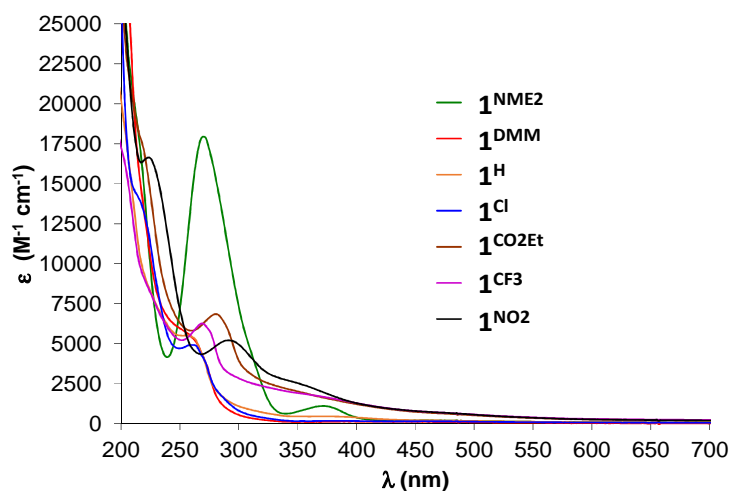


Figure IV. 10. UV/Vis spectra of 100 mM solution of **1^{NMe2}** (green), **1^{DMM}** (red), **1^H** (orange), **1^{Cl}** (blue), **1^{CO2Et}** (brown), **1^{CF3}** (purple) and **1^{NO2}** (black), in MeCN at 298 K.

By analogy to the UV/Vis spectra of other cobalt(II) complexes by aminopyridine ligands, the higher intensive bands in the UV region could correspond to a ligand-centered charge transfer (LLCT) or alternately a π - π^* transition.^{293,294} The complexes **1^{NMe2}** and **1^{NO2}** show two bands located at 372 ($\epsilon = 1090 \text{ M}^{-1} \cdot \text{cm}^{-1}$) and 356 ($\epsilon = 2390 \text{ M}^{-1} \cdot \text{cm}^{-1}$), respectively, which could be attributed to a metal-to-ligand charge transfer (MLCT) (Table IV. 1).

Table IV. 1. Experimentally observed transition energies and absorption coefficients.

Complex	$\lambda_{\text{max}} \text{ nm } (\epsilon, \text{ M}^{-1} \cdot \text{cm}^{-1})^{\text{a}}$	
	LLCT or π - π^*	MLCT
1^{NMe2}	270 (17950)	372 (1090)
1^{DMM}	260 (5400)	
1^H	256 (5500)	
1^{Cl}	217 (13800)	
1^{CO2Et}	261 (4900)	
	281 (6845)	
1^{CF3}	268 (6250)	
1^{NO2}	223 (16650)	356 (2390)
	291 (5200)	

^a Physical data measured in CH₃CN, T = 298 K.

IV.2.1.4. Solid-state characterization

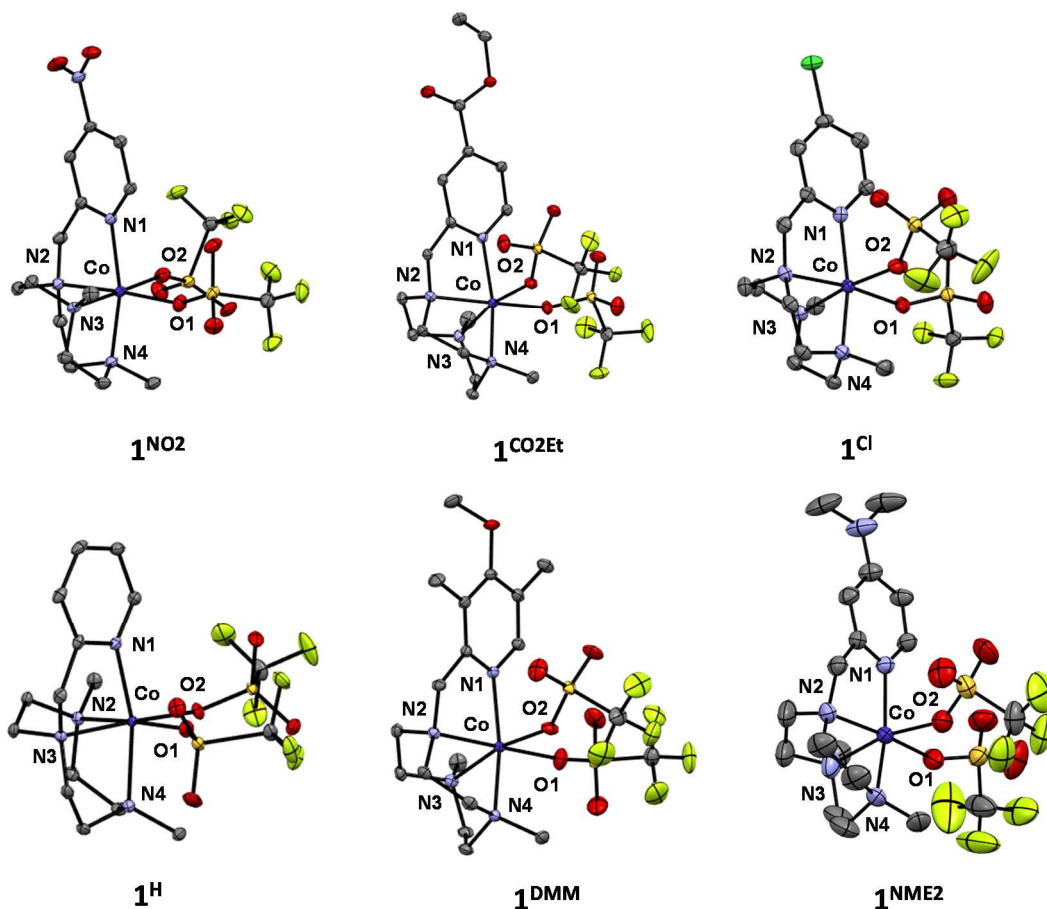


Figure IV. 11. Thermal ellipsoid plots of $\mathbf{1}^{\text{NO}_2}_{\text{OTf}}$, $\mathbf{1}^{\text{CO}_2\text{Et}}_{\text{OTf}}$, $\mathbf{1}^{\text{Cl}}_{\text{OTf}}$, $\mathbf{1}^{\text{H}}_{\text{OTf}}$, $\mathbf{1}^{\text{DMM}}_{\text{OTf}}$ (50% probability) and $\mathbf{1}^{\text{NME}_2}$ (30% probability). Solvent molecules and hydrogen atoms are omitted for clarity. Color code: cobalt (blue), nitrogen (light blue), oxygen (red), fluor (yellow), carbon (grey) and sulfur (orange).

The solid state molecular structure of the series of $\mathbf{1}^{\text{R}}_{\text{OTf}}$ complexes were determined by X-ray diffraction analysis. Crystals of the cobalt complexes $\mathbf{1}^{\text{NO}_2}_{\text{OTf}}$, $\mathbf{1}^{\text{CO}_2\text{Et}}_{\text{OTf}}$, $\mathbf{1}^{\text{Cl}}_{\text{OTf}}$, $\mathbf{1}^{\text{H}}_{\text{OTf}}$, $\mathbf{1}^{\text{DMM}}_{\text{OTf}}$ and $\mathbf{1}^{\text{NME}_2}_{\text{OTf}}$ were grown by layering a solution of dichloromethane with ethyl ether. Compound $\mathbf{1}^{\text{CF}_3}_{\text{OTf}}$ crystallizes as very thin needles not suitable for X-Ray diffraction analysis. Complexes $\mathbf{1}^{\text{NO}_2}_{\text{OTf}}$, $\mathbf{1}^{\text{CO}_2\text{Et}}_{\text{OTf}}$, $\mathbf{1}^{\text{Cl}}_{\text{OTf}}$, $\mathbf{1}^{\text{H}}_{\text{OTf}}$ and $\mathbf{1}^{\text{DMM}}_{\text{OTf}}$ were measured at 100 K, whereas $\mathbf{1}^{\text{NME}_2}_{\text{OTf}}$ was measured at 298 K due to the low stability of the crystal at low temperature. Experimental details of their crystal structure are summarized in Section A.2.1.3 $\mathbf{1}^{\text{R}}$ complexes crystallize in a monoclinic (for $\mathbf{1}^{\text{NO}_2}$, $\mathbf{1}^{\text{CO}_2\text{Et}}$, $\mathbf{1}^{\text{Cl}}$, $\mathbf{1}^{\text{DMM}}$ and $\mathbf{1}^{\text{NME}_2}$) or orthorhombic (for $\mathbf{1}^{\text{H}}$) crystal system.

The crystal structures of the bis-triflate complexes (Figure IV. 11) show the expected slightly distorted octahedral coordination geometries for Co^{II} with four coordination sites occupied by the three N atoms of the triazacyclononane (tacn) moiety. Moreover, the pyridine arm coordinates *trans* to one of the *N*-methyl groups of the tacn ligand. This provides two accessible coordination sites in a relative *cis* configuration that are occupied by the two triflate anions. The averaged Co–N bond lengths for these complexes are 2.0–2.2 Å, characteristic of high-spin Co^{II} complexes with $S = 3/2$.^{97,292}

More interestingly, the electronic properties of the substituted pyridine ligand, give rise a systematic differences in the Co^{II} coordination environment. For instance, the Co–N_{py} bond length changes depending on the electronic substitution of the pyridine ring. Thus, the Co–N_{py} value becomes smaller when the electron-donating character of R substituent increases; 2.1325 ± 13 Å for **1**^{NO₂}_{OTf}, 2.1175 ± 17 Å for **1**^{CO₂Et}_{OTf}, 2.116 ± 2 Å for **1**^{Cl}_{OTf}, 2.0969 ± 12 Å for **1**^H_{OTf}, 2.0883 ± 13 Å for **1**^{DMM}_{OTf} and 2.088 ± 4 Å for **1**^{NMe₂}_{OTf} (Table A. 2. 1 and Table A. 2. 2). This observation strongly suggests that the introduction of electron-withdrawing groups into the ligand weakness the pyridine-cobalt interactions significantly.⁹⁷ Being isostructural to the previously reported Fe^{II} complexes,³¹⁵ similar distortions from the ideal octahedral geometry are observed. These distortions are probably the result of ligand constraints with only one carbon atom between tacn moieties with the pyridine ring. The N^{CH₂Py}_{tacn}–Co–N_{Py} angles are in the range of 78.0–80.2°, causing a decreasing in the N^{Me}_{tacn}–Co–N_{Py} angle (155.7–163.3°) with respect the ideal 180° (Table A. 2. 1 and Table A. 2. 2).

IV.2.1.5. Cyclic voltammetry studies

Cyclic voltammetry provides relevant information for assessing the catalytic activity of the water reduction catalysts.³³⁸ The redox potential of **1**^R complexes were determined by cyclic voltammetry using glassy carbon working and a saturated calomel (SCE) as reference electrode in dry CH₃CN containing Bu₄NPF₆ (100 mM) as supporting electrolyte. A summary of the Co^{I/0}, Co^{II/I} and Co^{III/II} reduction potentials is presented in the Table IV. 2. The cyclic voltammograms obtained for all the studied complex are included in Figure IV. 13. In general, Co^{III/II} redox couples are reversible but Co^{II/I} and Co^{I/0} are not, except for some specific cases, which are pseudo reversible. This lack of

reversibility complicates the characterization of the redox processes. For this reason, we have chosen to measure the redox potential at half-peak intensity as a practical criteria for the Co^{II/I} and Co^{I/0} redox couples. The more relevant redox process regarding the catalytic proton reduction performance is the Co^{II/I}. This redox process is clearly influenced by the electronic nature of the substituents at the pyridine, being able to modify the Co^{II/I} redox event in up to 270 mV (Figure IV. 12). This influence of the redox processes by the electronic effects of the ligand has been theoretically proposed in cobalt diglyoxime systems.³³⁹

Table IV. 2. Redox potentials for the studied complexes in anhydrous CH₃CN.

Complex	σ	E Co ^{I/0} (V)	E Co ^{II/I} (V)	E Co ^{III/II} (V)
1 ^{NMe2}	-0.70	-1.75	-1.40	0.35
1 ^{DMM}	-0.41	-1.65	-1.34	0.37
1 ^H	0	-1.55	-1.29	0.45
1 ^{Cl}	0.23	-1.56	-1.26	0.50
1 ^{CO2Et}	0.45	-1.70	-1.13	0.49
1 ^{CF3}	0.54	-1.74	-1.19	0.51
1 ^{NO2}	0.78	-	-0.50	0.57

Conditions: CV measured in CH₃CN containing Bu₄NPF₆ (100 mM) as supporting electrolyte, glassy carbon and SCE were the working and reference electrodes, scan rate = 100 mV · s⁻¹. Potentials are quoted vs SCE.

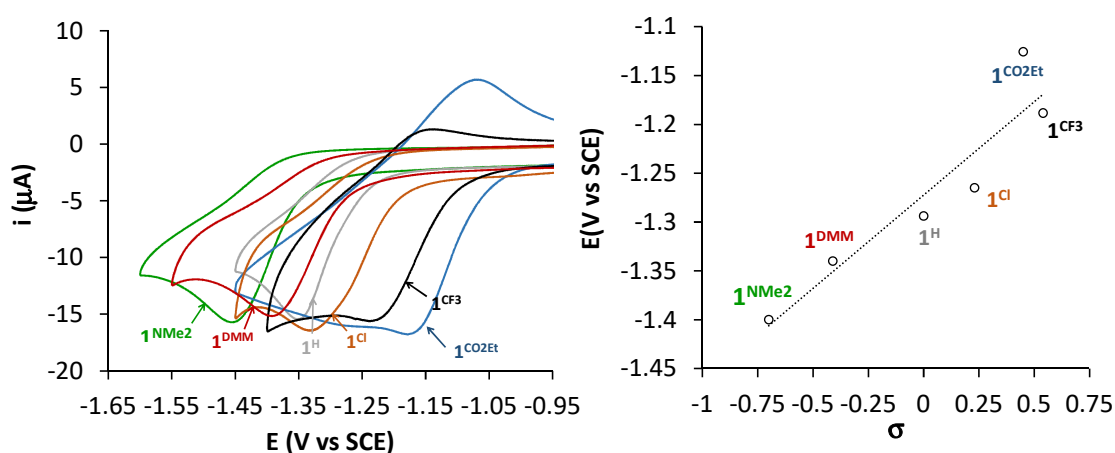


Figure IV. 12. Left: Electrochemical wave of **1**^{NMe2} (green), **1**^{DMM} (red), **1**^H (grey), **1**^{Cl} (orange), **1**^{CO2Et} (blue) and **1**^{CF3} (black). Right: Redox potentials of Co^{II/I} versus the Hammett constant ($\sigma_p + \sigma_m$) for the R substituents. Experimental conditions: **1**^R (1 mM), Bu₄NPF₆ (100 mM) as supporting electrolyte in dry acetonitrile, using glassy carbon as working and SCE as reference electrodes. Scan rate: 100 mV · s⁻¹. Potentials are quoted versus SCE.

Interestingly, cobalt complexes with the strongest electron withdrawing groups on the pyridine (**1**^{CO₂Et}, **1**^{CF₃} and **1**^{NO₂}) showed additional reduction wave close to the redox wave attributed to the Co^{II/I} pair, which could be attributed to a ligand centered redox process (Figure IV. 13). This hypothesis will be discussed in further detail in section IV.2.2.7.

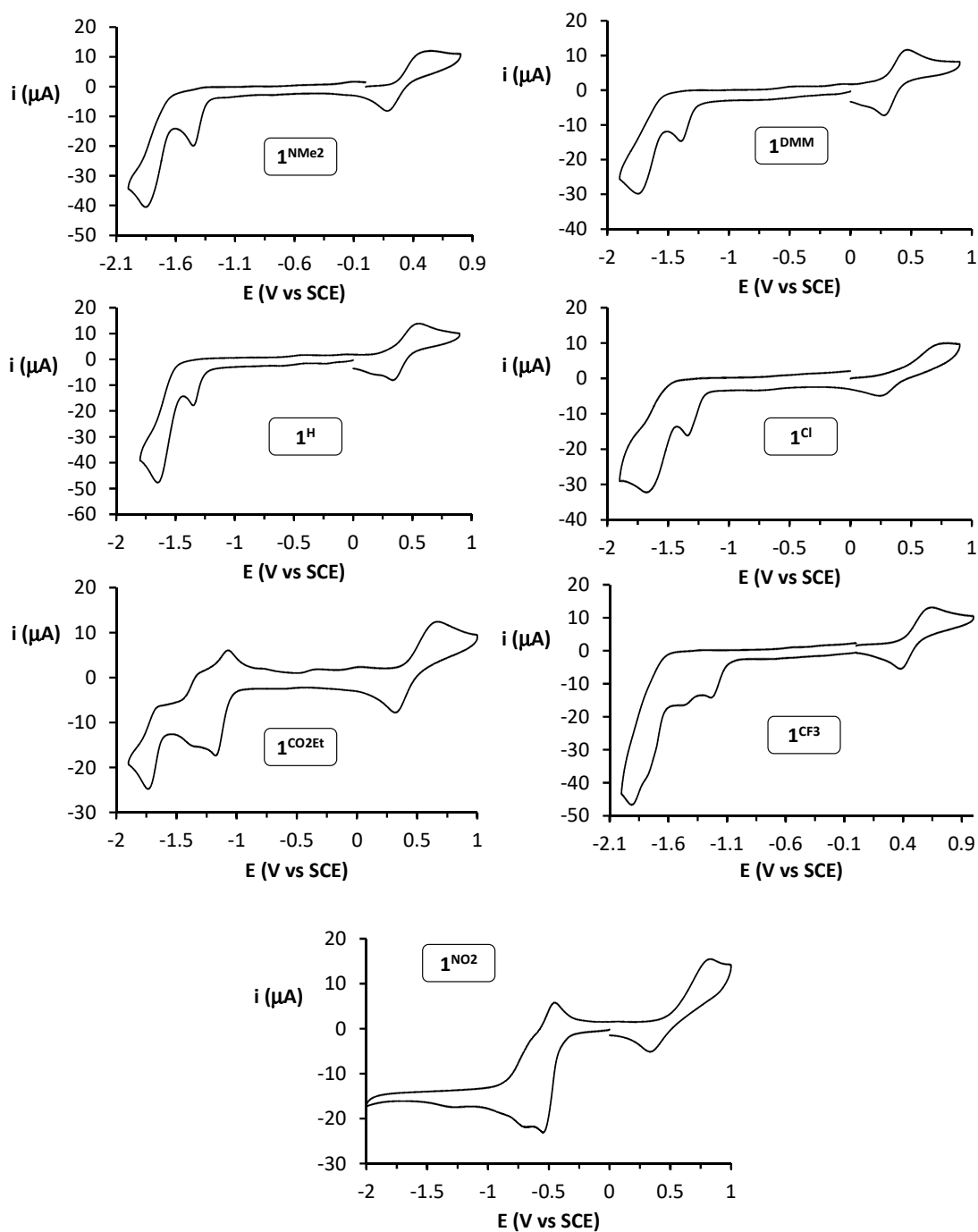


Figure IV. 13. Cyclic voltammograms of **1**^R (1 mM) complexes measured in MeCN containing Bu₄NPF₆ (100 mM) as supporting electrolyte, using glassy carbon as working and SCE as reference electrodes. Scan rate: 100 mV·s⁻¹. Potentials are quoted versus SCE.

The Co^{III/I} redox event of **1^R** complexes correlates with the corresponding σ parameters of substituents as shown in the Hammett plot (Figure IV. 12). However, there are two clear exceptions from the linearity, complexes **1^{CO2Et}** and **1^{NO2}** which shows the second redox wave. The second redox process for **1^{CO2Et}** is very close to the first one, which could be reason for the deviation (Figure IV. 12, *right*). In the case of **1^{NO2}** the deviation is much higher, and could be related with a single electron reduction of the NO₂ group (~ 0.50 V vs. SCE) (Figure IV. 13). Since the first redox process of **1^{NO2}** is most probably due to a -NO₂ redox event this complex was not included in the electrocatalytic studies.

IV.2.2. Photocatalytic water reduction to H₂

Light-driven H₂ evolution studies were performed with the aim of evaluating the influence of the ligand on the catalytic activity. Our initial photocatalytic water reduction studies were performed with 50 μ M of **1^R** and 150 μ M of [Ir(ppy)₂(bpy)](PF₆) (**PS_{Ir}**) in order to facilitate the study. Et₃N was used as sacrificial electron donor and MeCN:H₂O (4:6) solvent mixture was used to guarantee the complete solubility of all compounds. The catalytic assays were conducted by irradiating the reaction mixture at $\lambda=447\pm 20$ nm (T= 25 °C). Hydrogen evolution was monitored on-line and quantified as previously detailed in Chapter III. Control experiments show that all of the components including light are needed for the photocatalytic hydrogen production. We tested [Co(OTf)₂(MeCN)₂] as a control for the possible hydrolysis and negligible amounts of H₂ were detected. Finally, we have performed Hg⁰ poisoning experiments to test possible formation of active nanoparticles. It is well-known that metal(0) nanoparticles are amalgam to Hg⁰.³⁴⁰ The presence of large amount Hg⁰ (1.5 mL which corresponds to 15 % of the total reaction volume) do not had any effect on the quantity nor in the kinetics of the catalytic hydrogen formation. As a consequence, it can be argued that nanoparticles are unlikely to be responsible for the observed photocatalytic activity. The molecularity of the system is also corroborated by the absence of induction time at the beginning of irradiation. However, it should be noted that the absence of such a kinetic behavior does not rule out the transformation of the molecular complex into a different active species if the process is very fast.

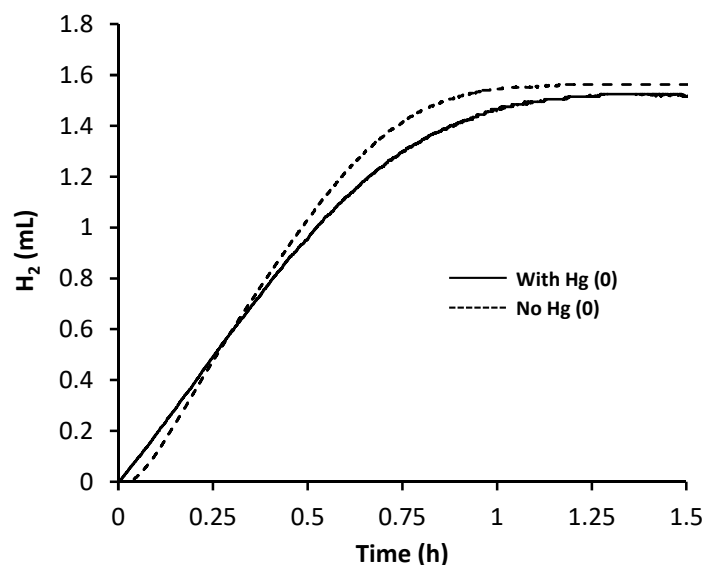


Figure IV. 14. Photocatalytic hydrogen production in the presence (dashed line) and absence (solid line) of Hg⁰. Conditions: **1^H** (50 μM), **PS_{Ir}** (250 μM) using CH₃CN:H₂O:Et₃N (4:6:0.2 mL) as solvent and irradiated (λ = 447 nm) at 25 °C. The reaction using Hg⁰ was performed using 1.5 mL of Hg⁰ (15 % of the total volume of the reaction).

Under standard conditions we monitored in real time the hydrogen evolved by **1^R** complexes, being all very active. Interestingly, the substituents at the pyridine had a significant effect on the turnover numbers (TON = $n(\text{H}_2)/n(\mathbf{1}^{\text{R}})$), the initial reaction rate (TOF = TON/t) and also in the stability of the catalytic system. For instance, hydrogen evolved expands from 0.3 to 6.1 mL and the initial reaction rate between 50 and 711 h⁻¹ for the **1^R** series (Table IV. 3).

Table IV. 3. Photochemical activities of **1^R** complexes in H₂ production.

Complex	σ	TON ^b	H ₂ (mL)	TOF ^c	TOF _{max} ^d
1^{NMe2}	-0.70	26 ± 4	0.3 ± 0.1	50 ± 4	80 ± 10
1^{DMM}	-0.41	37 ± 3	0.45 ± 0.03	14 ± 5	240 ± 20
1^H	0	85 ± 3	1.00 ± 0.04	275 ± 4	445 ± 5
1^{Cl}	0.23	100 ± 10	1.3 ± 0.1	340 ± 20	510 ± 20
1^{CO2Et}	0.45	500 ± 20	6.1 ± 0.3	710 ± 20	790 ± 10
1^{CF3}	0.54	60 ± 10	0.7 ± 0.1	190 ± 30	310 ± 10
1^{NO2}	0.78	34 ± 2	0.40 ± 0.03	65 ± 2	86 ± 3

Light-driven H₂ production of the series of **1^R** complexes. Conditions: 50 μM **1^R**, 150 μM **PS_{Ir}**, CH₃CN:H₂O:Et₃N (4:6:0.2 mL), irradiation (λ = 447 nm) at 25 °C. ^aHammett value of σ_p + σ_m. ^bTON = $n(\text{H}_2)/n(\mathbf{1}^{\text{R}})$. ^cInitial reaction rate: TOF (h⁻¹). ^dTOFs calculated at maximum TON/h ratio.

Time traces depicted in the Figure IV. 15 demonstrate that H₂ formation started immediately upon light irradiation without induction. In addition, it can be observed that photoinduced hydrogen evolution stops around 0.5 h for the complexes **1**^{Cl}, **1**^H, **1**^{CF₃} and **1**^{DMM} despite the large excess of Et₃N. In the case of **1**^{NO₂} and **1**^{NMe₂} the catalytic activity is reduced at longer reaction times (1 h). The lifetime of the catalytic system is maximized with **1**^{CO₂Et} in which the hydrogen evolution is prolonged for 2 h (Figure IV. 15). We hypothesize that the deactivation of the catalytic system is in part attributed to degradation products derived from the Et₃N.

Interestingly, for complexes **1**^{NMe₂}, **1**^{DMM}, **1**^H, **1**^{Cl} and **1**^{CO₂Et} the light-driven H₂ production increases by increasing the electro-withdrawing character of the group present at the pyridine, being **1**^{CO₂Et} the most active catalyst of the series (TON = 500 ± 24). Surprisingly, further increase of the electron-withdrawing character of the substituents (TON values of **1**^{CF₃} and **1**^{NO₂} are 60 ± 10 and 34 ± 2, respectively) exhibit a drastic decrease in the catalytic activity compared with **1**^{CO₂Et} (TON = 500 ± 20, Table IV. 3 and Figure IV. 15).

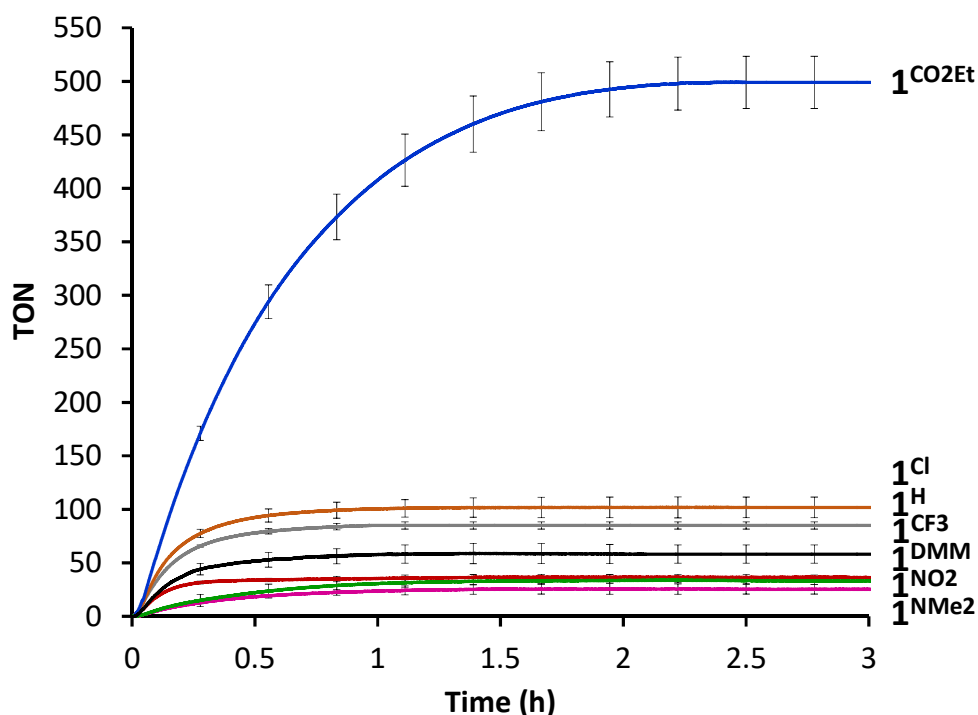


Figure IV. 15. On-line H₂ evolved vs time for **1**^R complexes (50 μM), **PS**_{Ir} (150 μM) in CH₃CN:H₂O:Et₃N (4:6:0.2 mL) as solvent mixture and irradiated (λ = 447 nm) at 25 °C. **1**^{CO₂Et} (blue), **1**^{Cl} (orange), **1**^H (grey), **1**^{CF₃} (black), **1**^{DMM} (red), **1**^{NO₂} (green) and **1**^{NMe₂} (purple). TON = n(H₂)/n(**1**^R).

Likewise, reaction rates are strongly dependent on the electronic nature of the ligand. The H₂ production rate follows the same trend as the observed in the H₂ yield. Thus, the initial rate increase from **1**^{NMe₂} (TOF = 50 ± 4) to **1**^{CO₂Et} (TOF = 711 ± 15) (Table IV. 3) and then is reduced with stronger electron-withdrawing substituents such as **1**^{CF₃} and **1**^{NO₂} (TOF_{1CF₃} = 190 ± 30, TOF_{1NO₂} = 65 ± 2) (Table IV. 3)

Rate profiles represented in the Figure IV. 16 showed that in all of the **1**^R complexes the rates increased sharply upon light irradiation, until reaching the maximum rate value (TOF_{max}) that is located around 0.06-0.08 h. The trend observed in the TOF_{max} values is in agreement with the general trend observed in the electronic effects.

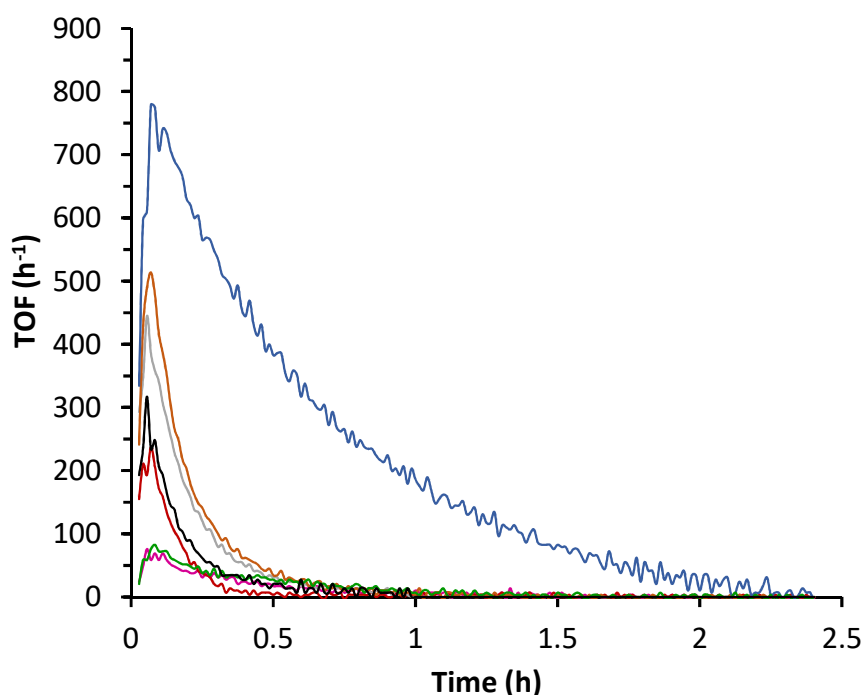


Figure IV. 16. Top: Rate profiles in H₂ evolution for **1**^{CO₂Et} (blue), **1**^{Cl} (orange), **1**^H (grey), **1**^{CF₃} (black), **1**^{DMM} (red), **1**^{NO₂} (green) and **1**^{NMe₂} (purple). Conditions: **1**^R (50 μM), **PS**_r (150 μM) using CH₃CN:H₂O:Et₃N (4:6:0.2 mL) as solvent and irradiated (λ = 447 nm) at 25 °C.

This interesting behavior is clearly illustrated in the excellent linear correlations observed in the Hammett analysis of reaction rates ($\log(v(\mathbf{1}^R)/v(\mathbf{1}^H))$) versus Hammett values of substituents (σ), showing two different regimens. In the first region, the catalysis is enhanced by increasing the electron deficiency nature of the ligand while in the second is clearly reduced (Figure IV. 17). This can be rationalized by two opposing effects (such as E (Co^{II/I}) and pK_a of the Co^{III}-H species) induced by the pyridine

substituents which determine the overall rate process. At this point it is difficult to rationalize further these two trends and we will discuss in more detail in the following sections.

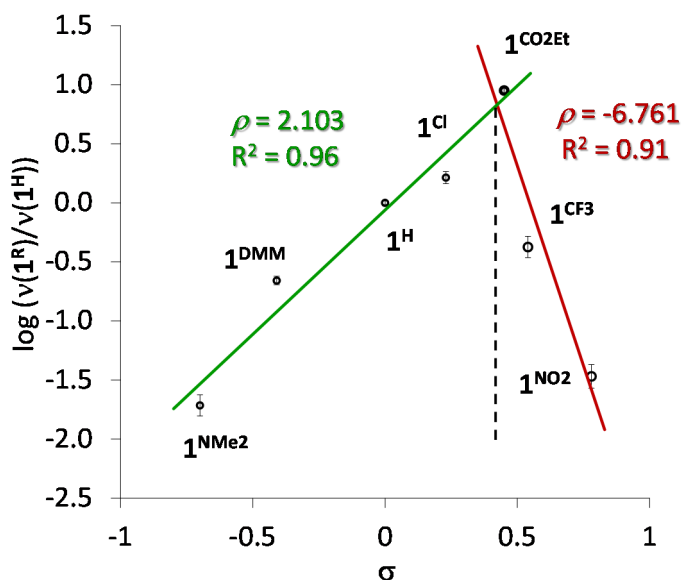


Figure IV. 17. Hammett plot of the relative reaction rates versus the Hammett substituent value (σ). v : Initial reaction rate determined at 10% conversion.

Altogether, the electronic effects play an important role in the catalytic water reduction to hydrogen in the studied systems. However, more studies are deserved to further understand the mechanism. These data also suggests the molecularity of the catalytic system.

IV.2.2.2. Dependence of cobalt concentration in light-driven water reduction

Previous studies of aminopyridine cobalt complexes demonstrated that the activity (TON) is enhanced at low catalyst concentrations.¹⁰³ This was attributed to the formation of inactive aggregates of the cobalt complex. In this regard at lower concentrations linearity should be observed. However, H₂ analysis is very challenging at lower concentration. Since catalyst **1^{CO2Et}** is highly active we now can study catalyst concentrations in the 0.25 - 100 μ M range. As expected, increasing the amount of catalyst from 0.25 to 100 μ M increase of total amount of H₂ produced (Figure IV. 18) although is not linear as previously observed for other cobalt aminopyridine complexes.¹⁰³

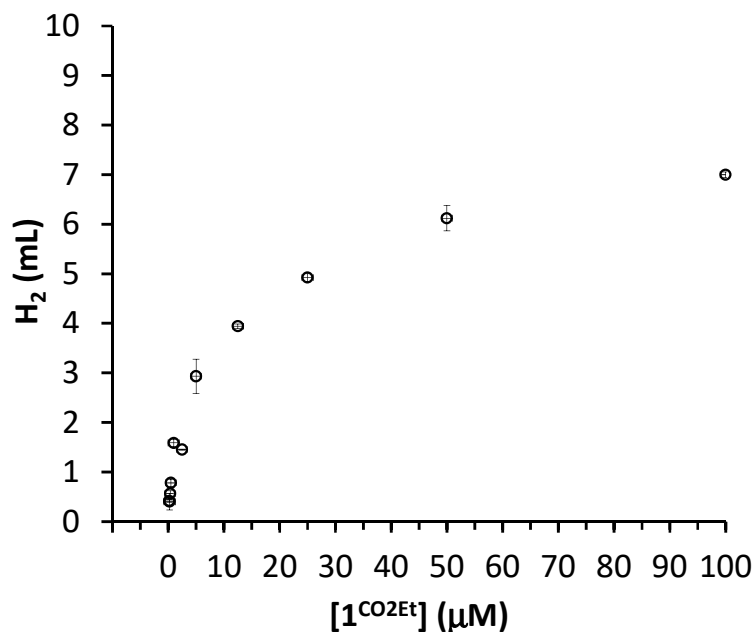


Figure IV. 18. Hydrogen production (mL H₂) versus the concentration of **1^{CO2Et}**. Conditions: **1^{CO2Et}** (0.25-100 μM), **PS_{ir}** (150 μM) using CH₃CN:H₂O:Et₃N (4:6:0.2 mL) as solvent and irradiated (λ = 447 nm) at 25 °C.

Remarkably, the double ln-plot of the reaction rate (mmol H₂·h⁻¹) versus **1^{CO2Et}** concentration shows a first order dependence at concentrations below 1 μM (Figure IV. 19, *bottom right*). The initial reaction rates were measured at 10% of the overall H₂ produced. At higher cobalt concentrations (range of 1-100 μM) a saturation of the initial rate is observed, leading to a zero order dependence. It was proposed that formation of inactive dimers or oligomeric species, or cobalt nanoparticles, are responsible for the reduction of catalytic activity at high concentration.³⁴⁰ An alternative explanation of the saturation in reaction rate is that the reduction of the cobalt catalyst is limited by the reduced **PS_{ir}** available in the reaction media. The reaction order at higher **PS_{ir}** concentration is needed to confirm the later hypothesis. At low concentration of cobalt complex the lifetime of the catalytic system is significantly reduce. For instance, at 100 μM hydrogen evolution last for 2 h while for 0.25 μM only 0.5 h. This could indicate that formation of dimeric or oligomeric species could protect from catalyst deactivation.

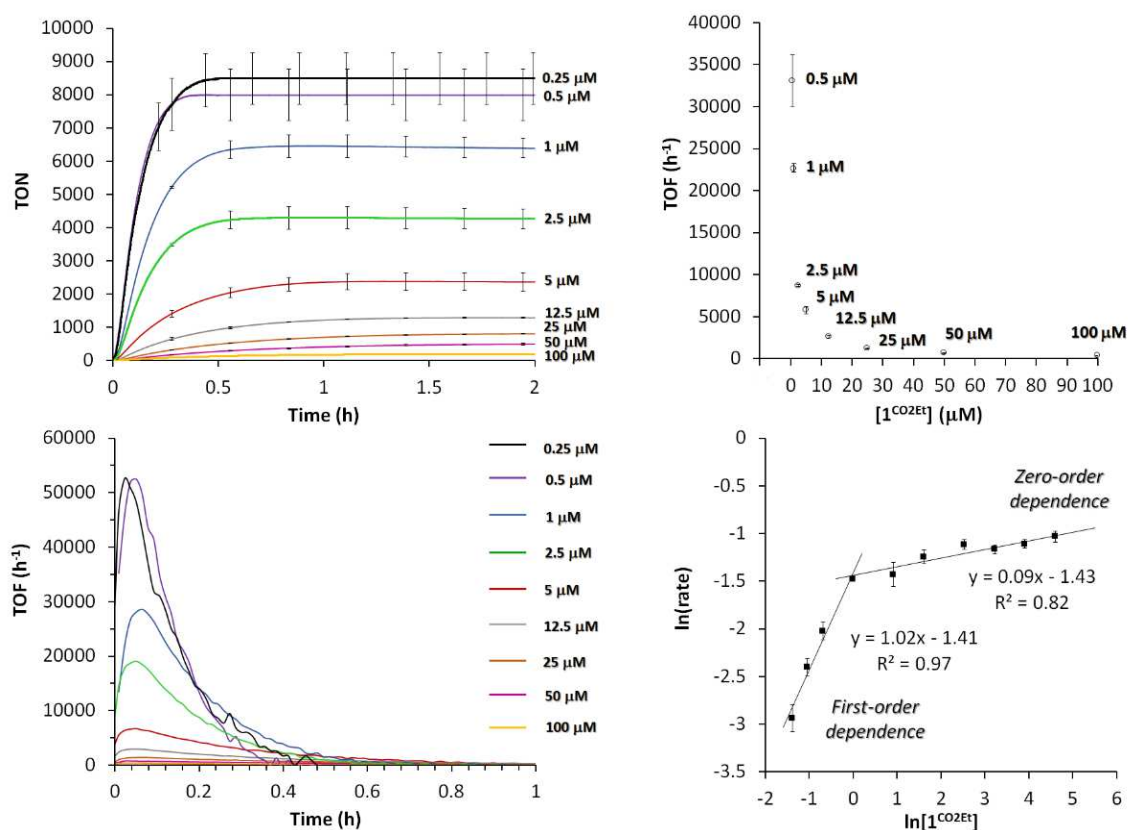


Figure IV. 19. Study of the dependence of the cobalt concentration. *Top left:* On-line hydrogen evolution traces with different concentrations of $\mathbf{1}^{\text{CO}_2\text{Et}}$ (0.25 – 100 μM). *Top right:* Initial reaction rates (TOF) vs $[\mathbf{1}^{\text{CO}_2\text{Et}}]$. *Bottom left:* Rate profiles in H₂ evolution at different concentrations of $\mathbf{1}^{\text{CO}_2\text{Et}}$: TOF_{max} (h^{-1}): 425 (100 μM), 780 (50 μM), 1420 (25 μM), 2965 (12.5 μM), 6720 (5 μM), 19075 (2.5 μM), 28610 (1 μM), 52485 (0.5 μM) and 52570 (0.25 μM). *Bottom right:* Double-ln plot of initial H₂ evolution rates vs [Co]. Conditions: $\mathbf{1}^{\text{CO}_2\text{Et}}$ (0.25-100 μM), PS_{Ir} (150 μM) using $\text{CH}_3\text{CN}:\text{H}_2\text{O}:\text{Et}_3\text{N}$ (4:6:0.2 mL) as solvent and irradiated ($\lambda = 447 \text{ nm}$) at 25 $^\circ\text{C}$.

Interestingly, the TON for $\mathbf{1}^{\text{CO}_2\text{Et}}$ increases from 200 at 100 μM to about 9000 at 0.25 μM and the TOF maximum (TOF_{max}) increase from 425 (100 μM) to more than 52000 (0.25 μM) (Figure IV. 19). Although by reducing the catalyst concentration the TON is maximized the total amount of hydrogen produced is very low (Figure IV. 18). Nevertheless, both the high TONs and TOFs, corroborate the excellent performance of $\mathbf{1}^{\text{CO}_2\text{Et}}$, which is comparable with the highest light-driven H₂ production catalysts based on polypyridyl ligands.^{17,34-37} The TON value reported for the **[CoBr(aPPy)]Br** catalyst (**aPPy** = Di-2,2'-bipyridiyl-6-yl(pyridin-2-yl)methanol) (TON = 33300 in 70 h of irradiation),³⁴¹⁻³⁴³ developed by Alberto and co-workers, is higher than for $\mathbf{1}^{\text{CO}_2\text{Et}}$, but the TOF_{max} is significantly lower (TOF_{max} = 5880 h^{-1} vs 52570 h^{-1}). To the best of our knowledge the TOF_{max} obtained with $\mathbf{1}^{\text{CO}_2\text{Et}}$ are the highest reported in the literature.

IV.2.2.3. Reactivity of photogenerated [Ir^{II}(ppy)₂(bpy)] (PS_{Ir}^{II}) with **1^R**

To obtain further information about the water reduction mechanism we have studied the reaction between the *in-situ* generated [Ir^{II}(ppy)₂(bpy)](PF₆) (PS_{Ir}^{II}) and **1^R** complexes, in a similar manner than in chapter III. The experimental set-up is illustrated in Figure IV. 37. The irradiation source ($\lambda = 447$ nm) was located at 90 degrees respect to the source/detector of the UV/Vis spectrometer. In addition we located at pressure transducer sensor at the top of the UV/Vis cuvette. This special set up allow us monitor at the same time both the UV/Vis Spectra (0.5 s temporal resolution) during irradiation and the amount of gas evolved (H₂, 0.1 s temporal resolution). The total amount of H₂ evolved was quantified by GC-TDC.

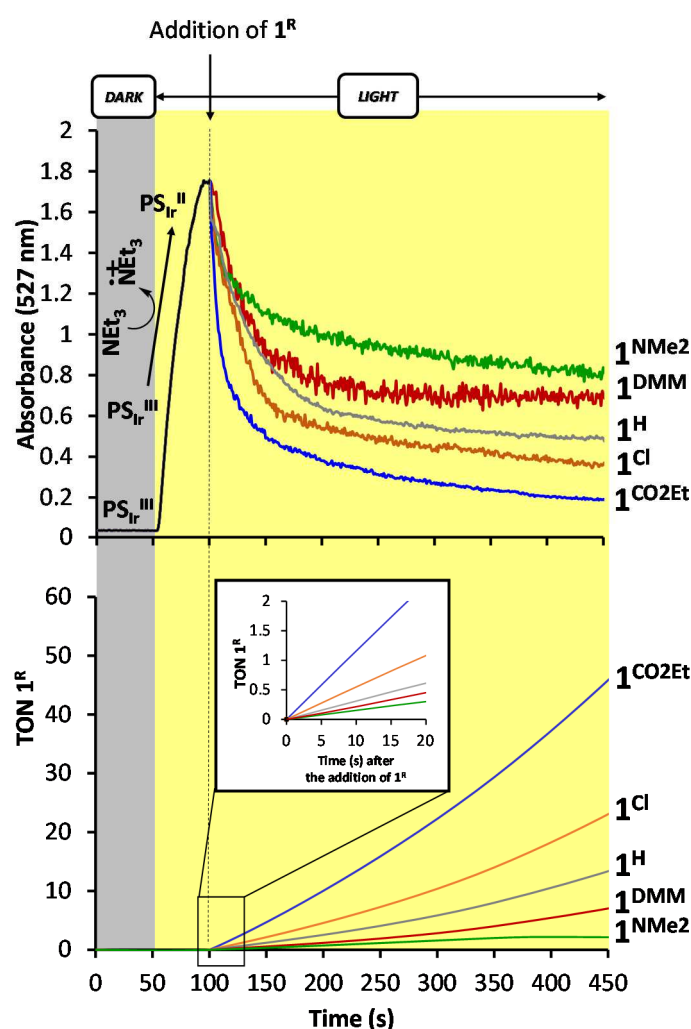


Figure IV. 20. Top: UV/Vis monitoring at 527 nm associated with the formation of PS_{Ir}^{II} species by irradiating at $\lambda = 447$ nm, upon addition of **1^R** complex (0.1 eq. vs. PS_{Ir}). Conditions: [PS_{Ir}] = 0.25 mM, [Et₃N] = 100 mM, CH₃CN:H₂O (0.8:1.2 mL) at 25 °C. Bottom: Time-dependent photocatalytic H₂ evolution. Inset: Magnification in the first seconds after the addition of **1^R**.

The typical conditions were [Ir^{III}(ppy)₂(bpy)](PF₆) (**PS**_{Ir}^{III}, 0.25 mM) and Et₃N (100 mM) in MeCN:H₂O (0.8:1.2 mL) under N₂ atmosphere at 25 °C. Before continuing it is important to remark the experimental difficulty to obtain the photochemical formation of **PS**_{Ir}^{II} due to the following reasons, i) **PS**_{Ir}^{II} is extremely sensitive to O₂. All solvents and reagents should be free of O₂ (three freezing-pump-thaw at least are required). ii) Under reaction conditions **PS**_{Ir}^{II} precipitates at the critical concentration of about 0.1 mM and iii) compound **PS**_{Ir}^{II} is not stable under this conditions and decay during the reaction (Figure IV. 21). Despite these difficulties we considered interesting to qualitatively study the photochemical generation of the metastable **PS**_{Ir}^{II} and their reactivity against **1**^R.

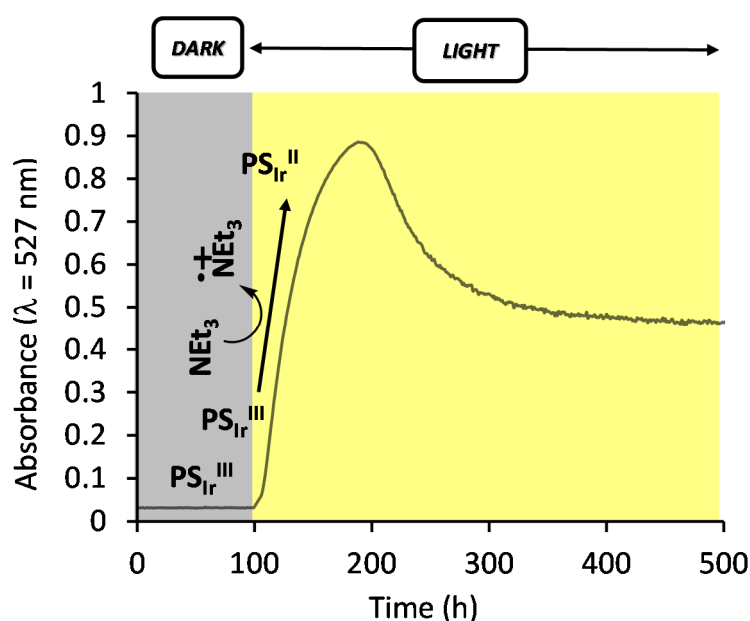


Figure IV. 21. UV/Vis monitoring at 527 nm of the self-decay of the photogenerated **PS**_{Ir}^{II} species by irradiating at $\lambda = 447$ nm. Conditions: [**PS**_{Ir}^{III}] = 0.1 mM, [Et₃N] = 100 mM, CH₃CN/H₂O (0.8:1.2 mL) at 25 °C.

Therefore, upon irradiation an oxygen free **PS**_{Ir} (0.25 mM) MeCN:H₂O (0.8:1.2 mL) solution containing Et₃N (100 mM) at 25 °C we observed the growing of three new bands centered at 385, 495 and 527 nm corresponding to the formation of the **PS**_{Ir}^{II} species (Figure IV. 20).³⁴⁴ The formation of **PS**_{Ir}^{II} was maximized after ca. 50 s of irradiation followed by a monotonic decay. In addition, neither in the dark, during the formation of **PS**_{Ir}^{II} or self-decay significant increase in pressure was observed, discarding the H₂ formation.

Next we study the reaction of the photogenerated **PS**_{Ir}^{II} with 0.1 eq of **1**^R under continuous light irradiation. We have selected the complexes **1**^{CO₂Et}, **1**^{Cl}, **1**^H, **1**^{DMM} and

1^{NMe2} to represent the differences in electronic requirements of the metal center. As stated photosensitizer **PS_{Ir}^{II}** was generated by *in-situ* irradiation ($\lambda = 447$ nm). While the amount of **PS_{Ir}^{II}** was maximized (ca. 50 s) **1^R** complexes (0.1 eq. vs **PS_{Ir}** dissolved in 50 μ L of CH₃CN) were added *via* syringe through the septa. The addition of the **1^R** promoted a fast vanishing of the spectral features belonging to the **PS_{Ir}^{II}** species (Figure IV. 20). We interpreted this phenomena based on the capacity of **PS_{Ir}^{II}** to promote the reduction events on **1^R** complexes which trigger the catalysis. Indeed the formation of H₂ was just observed after the addition of **1^R**. At this point it is important to highlight that no induction time was observed just after the addition of **1^R** complex (Figure IV. 20, *Bottom/Inset*). This is a strong evidence that **1^R** is the competent catalytic species, and the activity cannot be attributed to the formation of metal nanoparticles during the irradiation time

The first step occurring after the addition of the Co^{II} species implies a single electron reduction of Co^{II} to Co^I by **PS_{Ir}^{II}** which returns to **PS_{Ir}^{III}**. Since the redox potential for the Co^{I/0} redox couple ($E(\text{Co}^{I/0}) = -1.75$ to -1.55 V vs SCE) is more negative than the **PS_{Ir}^{III/II}** (-1.38 V vs SCE) we postulate that the next step is a protonation event that leads to the formation of a Co^{III}-H. Further reduction and protonation of Co-H species lead to the formation of H₂, recovering the Co^{II} starting compound and consuming the generated **PS_{Ir}^{II}** species in a catalytic manner. As expected, the H₂ production activities follow the order **1^{CO2Et}** > **1^{Cl}** > **1^H** > **1^{DMM}** > **1^{NMe2}**, consistent with the previous studies.

It is interesting to notice that a remaining **PS_{Ir}^{II}** concentration is present under irradiation conditions in presence of Co^{II}. The extension of the remaining **PS_{Ir}^{II}** is dependent on the electronic nature of the ligand: **1^{CO2Et}** < **1^{Cl}** < **1^H** < **1^{DMM}** < **1^{NMe2}** (Figure IV. 20, *Top*) with an inverse trend to the H₂ generation rate. The presence of **PS_{Ir}^{II}** is indicative that an equilibrium between the photocatalytic redox cycle and the catalytic cobalt cycle is established under these conditions.

IV.2.2.4. Labelling experiments with D₂O

Labelling experiments are a very powerful tool to get insights into the mechanism. Therefore, we have examined the kinetic isotopic effects (KIE) and isotopic

distribution by on-line pressure monitoring and on-line mass spectrometry. By on-line pressure monitoring we will extract the KIE related to the global rate (**KIE^g**) of the reaction, while in the on-line mass spectrometry we will obtain the KIE relative to the selectivity between H/D (**KIE^{sel}**). **KIE^g** values does not distinguish between isotopes and is only sensitive to the global reaction rate, while **KIE^{sel}** values measured is sensitive to H/D for all the selectivity steps of the water reduction reaction. Indeed, the scenario can be very complex as it is illustrated in Figure IV. 22.

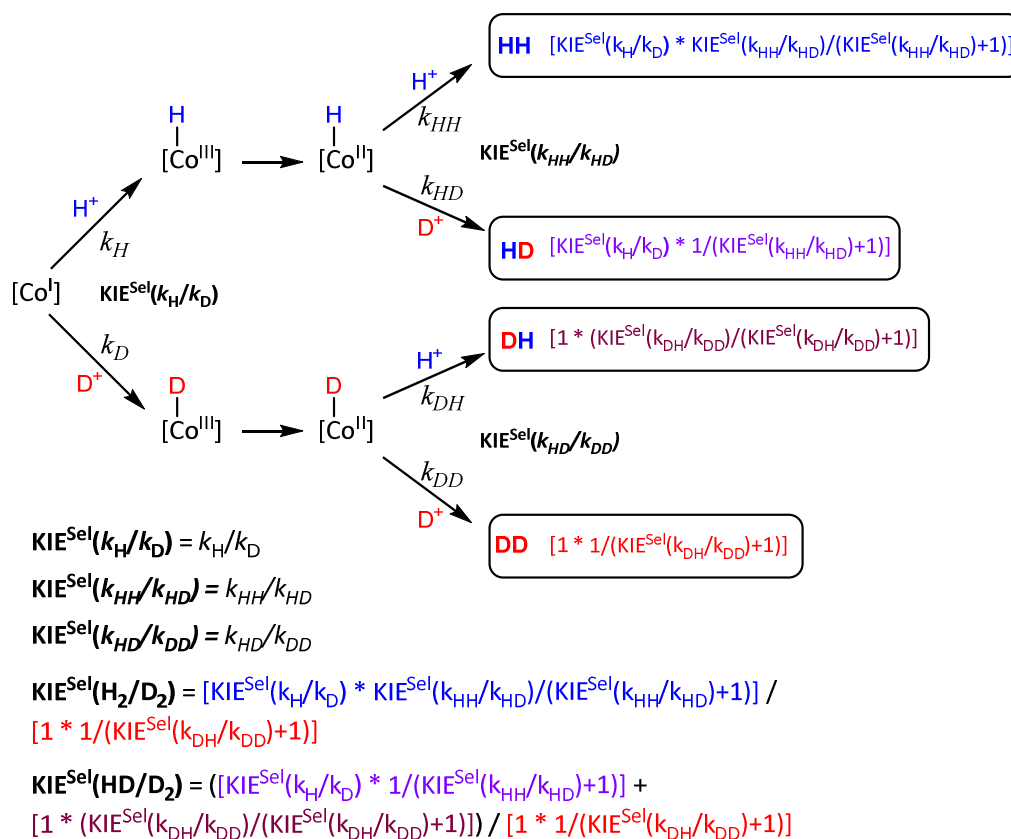


Figure IV. 22. Elementary steps where H/D selectivity can take place in the water reduction reaction and the equations to calculate the combined **KIE^{sel}**.

First, we monitored the rate of gas evolution from reaction with H₂O, D₂O (99%) and H₂O:D₂O (1:1) in the reaction mixture by using a pressure transducer. Water reduction conditions were set up as following: **1^R** (50 μM, R = CO₂Et, H and DMM), **PS_{Ir}** (150 μM), Et₃N (0.2 mL) in CH₃CN (4 mL) and H₂O and/or D₂O (6 mL). As shown in Figure IV. 23 (left) for catalyst **1^{CO₂Et}** the increase of D₂O in the reaction media promoted a significant decrease of the final catalytic activity, along with a slight alteration of the initial reaction rate (760-670 TON·h⁻¹, **KIE^g** (rate_{H₂O}/rate_(H₂O/D₂O)) = 1.03). In sharp contrast,

the reaction rates in complexes **1^H** and **1^{DMM}** were significantly reduced when using H₂O:D₂O (1:1) instead of pure H₂O, leading to a **KIE^g** of 1.38 and 2.61, respectively (Figure IV. 23, right). It seems that the **KIE^g** magnitude is influenced by the electronic nature of the ligand, being more important with less active catalytic systems. This may imply that the rate determining step (or rate modifying steps) in **1^{CO₂Et}** should not involve a cleavage or formation of a H-X bond.³⁴⁵ On the other hand, the **KIE^g** values **1^H** and **1^{DMM}** suggest a possible change of the rate-determining step among the series of **1^R** by the electronic nature of the ligand.

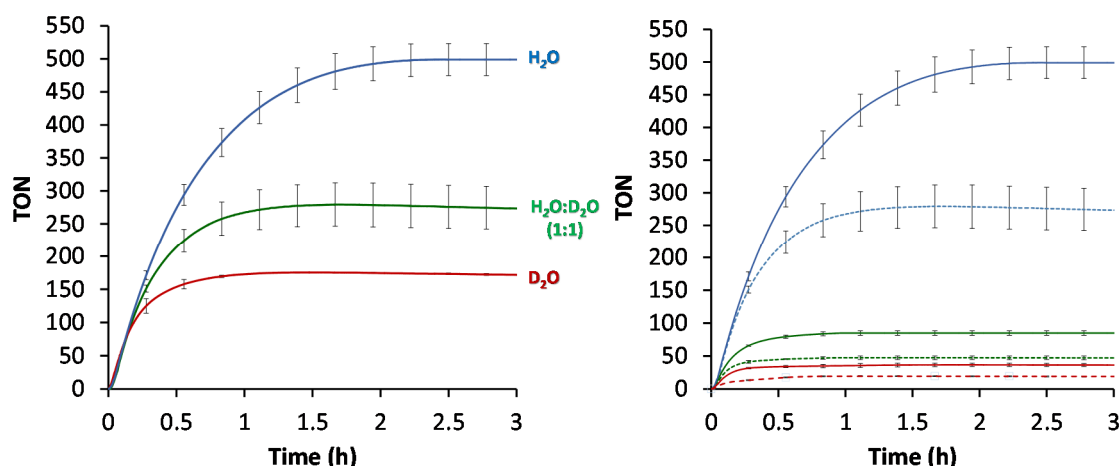


Figure IV. 23. *Left:* On-line hydrogen evolved versus time with **1^{CO₂Et}** (50 μM), **PS_{ir}** (150 μM) using CH₃CN:H₂O:Et₃N (4:6:0.2 mL) (blue), CH₃CN:H₂O:D₂O:Et₃N (4:3:3:0.2 mL) (green) or CH₃CN:D₂O:Et₃N (4:6:0.2 mL) (red) as solvent mixture and irradiated ($\lambda = 447$ nm) at 25 °C. Activities using a) H₂O: 500 ± 20 TON, initial rate = 760 ± 10 h⁻¹, b) H₂O/D₂O (1:1): 230 ± 30 TON, initial rate = 740 ± 20 h⁻¹ and c) D₂O: 145 ± 1 TON, initial rate = 670 ± 20 h⁻¹. *Right:* Hydrogen evolved by **1^{CO₂Et}** (blue), **1^H** (green) and **1^{DMM}** (red) using CH₃CN:H₂O:Et₃N (4:6:0.2 mL) (solid traces) or CH₃CN:H₂O:D₂O:Et₃N (4:3:3:0.2 mL) (dashed traces).

We have also monitored by on-line-MS the direct formation of H₂, HD and D₂ for the whole series of **1^R** complexes under the same catalytic conditions that the previous experiments (D₂O (99 %) and D₂O (49.5 %) solutions). It is important to notice that the ionization of H₂, HD and D₂ are different and therefore calibrations were done with H₂, HD and D₂ authentic samples (Figure IV. 38).

The MS-on-line gases evolved from light-driven water reduction reaction by **1^{CO₂Et}** in D₂O (99 % in deuterium) resulted in an isotopic distribution of 0.5% H₂, 9.1% HD and 90.4 % D₂ (Figure IV. 24). The H₂, HD and D₂ formation rates were different but with constant percentage during all irradiation time. All HD and H₂ measured can only be

attributed to 1 % of H₂O in the D₂O, suggesting a large kinetic isotopic selectivity. This result is very surprising since the KIE^E for **1**^{CO₂Et} was found to be around 1 and indicates again that that selective H/D step is not involve in the rate determining step. Moreover, this data also demonstrates that the hydrogen evolved is not a by-product derived from the Et₃N decomposition³⁴⁶ and the source of protons is indeed water.

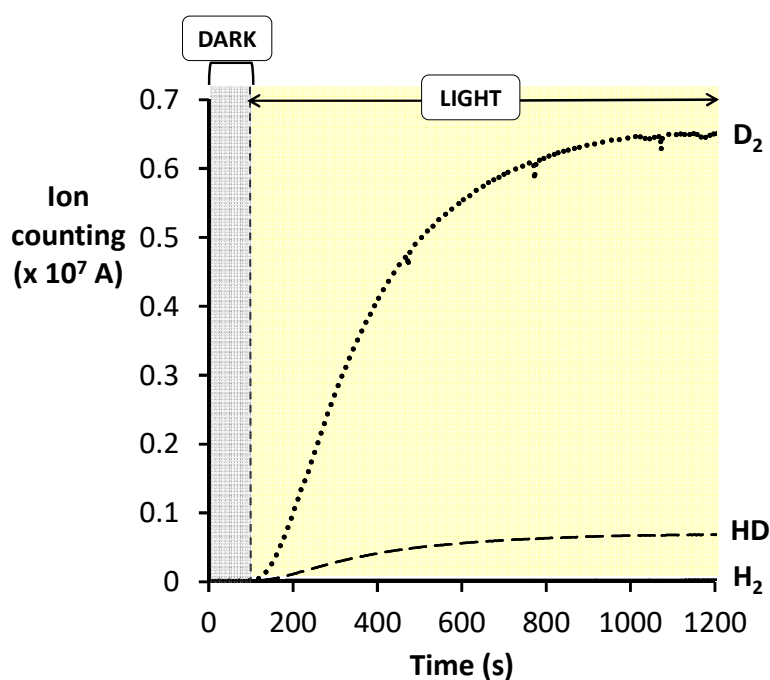


Figure IV. 24. On-line monitoring of the formation (Ion current) of H₂ (Solid trace), HD (dashed trace) and D₂ (dotted line) versus time using D₂O (99 % in deuterium). The current response was corrected relative to a previous calibration of HD and D₂. Conditions: **1**^{CO₂Et} (50 μM), **PS**_{Ir} (150 μM), MeCN:D₂O (0.8:1.2 mL), Et₃N (40 μL), reaction volume = 2 mL, irradiated at $\lambda = 447$ nm, under N₂ atmosphere.

As in the previous experiment, we monitored the gases formed by MS during the irradiation time but now replacing the D₂O by a H₂O:D₂O 1:1 mixture. As shown in the Figure IV. 25, for the case of **1**^{CO₂Et} the generation of gases follows the order H₂ > HD >> D₂. The same behavior is observed for the rest of the cobalt complexes. The isotopic distribution for **1**^R complexes is in the 61-69 % range for H₂, 29-35 range for HD and lower than 2.8 % for D₂. As shown in the Table IV. 4, H₂/D₂ (24-27.6), H₂/HD (1.7-2.3) and HD/D₂ (10.4-13.1) ratios represent the KIE^{Sel} under this conditions. Interestingly, these ratios are remained virtually constant during all irradiation time, suggesting that the mechanism is maintain unaffected during all the course of the reaction.

Table IV. 4. Summary of the **KIE^g** and **KIE^{sel}** measured.

1^R	KIE^g $V_{i(H_2O)}/V_{i(H_2O:D_2O)}$	KIE^{sel} (H₂/D₂)	KIE^{sel} (HD/D₂)	KIE^{sel} (H₂/HD)	H₂ (%)	HD (%)	D₂ (%)
1^{NMe2}	-	24.0 ±0.5	10.9 ±0.1	2.2 ±0.1	68 ±1	30 ±1	2.5 ±0.2
1^{DMM}	2.6	26.3 ±0.5	11.6 ±0.1	2.3 ±0.1	67.7 ±0.1	29.8 ±0.1	2.53 ±0.02
1^H	1.4	26.6 ±0.3	11.5 ±0.1	2.3 ±0.1	68.2 ±0.2	29.3 ±0.2	2.55 ±0.02
1^{Cl}	-	25.4 ±0.5	11.2 ±0.1	2.3 ±0.1	67.5 ±0.3	29.8 ±0.2	2.63 ±0.04
1^{CO2Et}	1.0	22.6 ±0.5	13.1 ±0.1	1.7 ±0.1	61.3 ±0.3	35.9 ±0.2	2.78 ±0.01
1^{CF3}	-	27.6 ±0.5	11.9 ±0.1	2.3 ±0.1	68.4 ±0.5	29.2 ±0.5	2.45 ±0.04
1^{NO2}	-	21.5 ±0.8	10.4 ±0.1	2.1 ±0.1	69 ±2	29 ±2	2.5 ±0.2

Conditions: **1^R** (50 μM), **PS** (150 μM), MeCN:H₂O:D₂O (0.8:0.6:0.6 mL), Et₃N (40 μL), reaction volume = 2 mL, irradiated at λ = 447 nm, under N₂ atmosphere.

The high values obtained for the **KIE^{sel}(H₂/D₂)** (21.5 - 27.6) and **KIE^{sel}(HD/D₂)** (10.4 - 13.1) are in agreement with two consecutive events where a H/D selective takes place, for instance i) the cobalt hydride bond formation and ii) the hydrogen-hydrogen bond formation events (Figure IV. 22). In both events the **KIE^{sel}** towards Co-H and H-H should be higher > 1 to meet the obtained KIE.

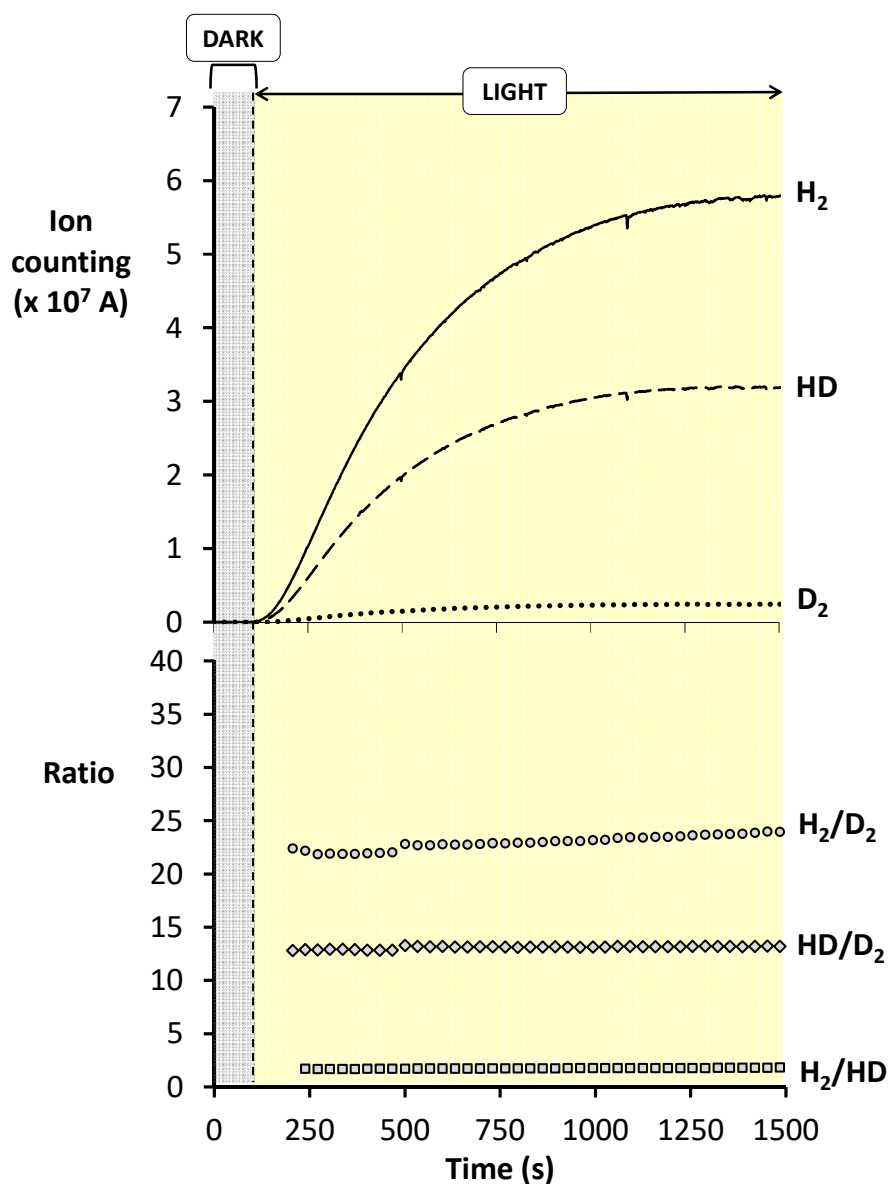


Figure IV. 25. Top: On-line monitoring of the formation (Ion current) of H₂ (Solid trace), HD (dashed trace) and D₂ (dotted line) versus time in a mixture of H₂O:D₂O (1:1). Bottom: Ratios of H₂/D₂ (dots), HD/D₂ (diamonds) and H₂/HD (squares) obtained from the ion current data. For the ratio determination, the ion current response was corrected relative to a previous calibration of HD and D₂. Conditions: **1**^{CO₂Et} (50 μM), **PS**_{ir} (150 μM), MeCN:H₂O:D₂O (0.8:0.6:0.6 mL), Et₃N (40 μL), reaction volume = 2 mL, irradiated at λ = 447 nm, under N₂ atmosphere.

IV.2.2.5. Eyring plot with **1**^{CO₂Et}

In order to evaluate the effect of the temperature in the reaction performance, we measured the photocatalytic activity of **1**^{CO₂Et} at different temperatures: 15, 25, 35 and 45 °C. The initial rate of the reaction increases linearly with the temperature. The increase of temperature has a positive impact in the catalytic activity linearly increasing the reaction rate. From the initial reaction rates an Eyring plot was conducted obtaining a ΔH^\ddagger value of 5.0 kcal·mol⁻¹. We note that this energy barrier is very low indicating that the catalytic system have a low dependence versus the temperature compared to other catalytic reactions. It is important to note, that the temperature could also affect the photoredox cycle and therefore it can modifies the Eyring analysis.

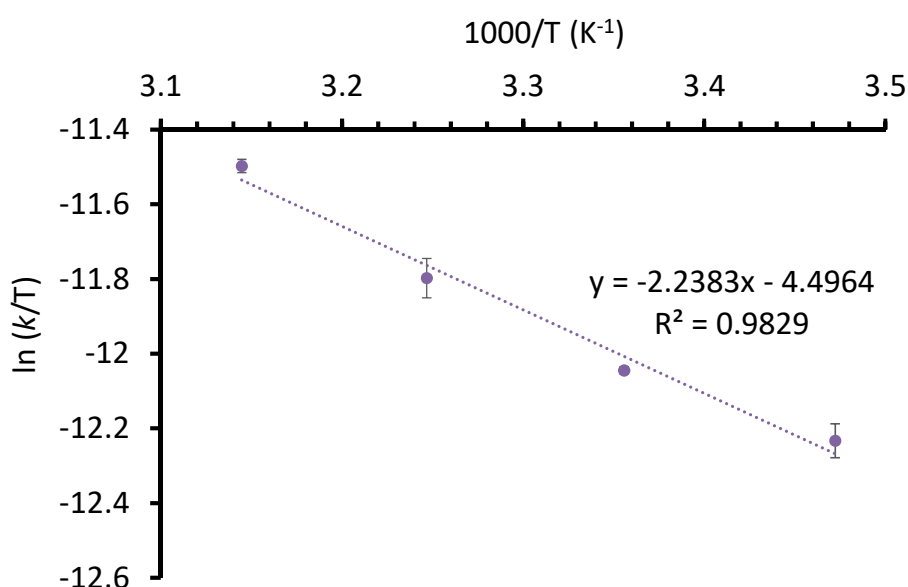


Figure IV. 26. Eyring plot with the catalyst **1**^{CO₂Et}.

On the other hand, we cannot discard that the increase of the temperature favors the degradation of the catalytic system. Indeed, Castellano and co-workers reported a tetrapyrrolyl cobalt catalyst that exhibited inverse dependence versus the temperature, observing a clear degradation of the activity at higher temperatures.⁹⁷

IV.2.2.6. Study of the effect of the presence of O₂ in the photochemical catalytic activity

One of the most important requirements for water spitting is that the catalyst for H₂ generation has to be operative under small concentration of O₂, which can facilitate the merging with the water oxidation process.³⁴⁷ However, while the design of WRC has been mainly focused in terms of good activity and robustness for its possible implementation in water splitting devices, there has been very little progress in the development of WRC able to operate in the presence of O₂. Molecular catalysts based

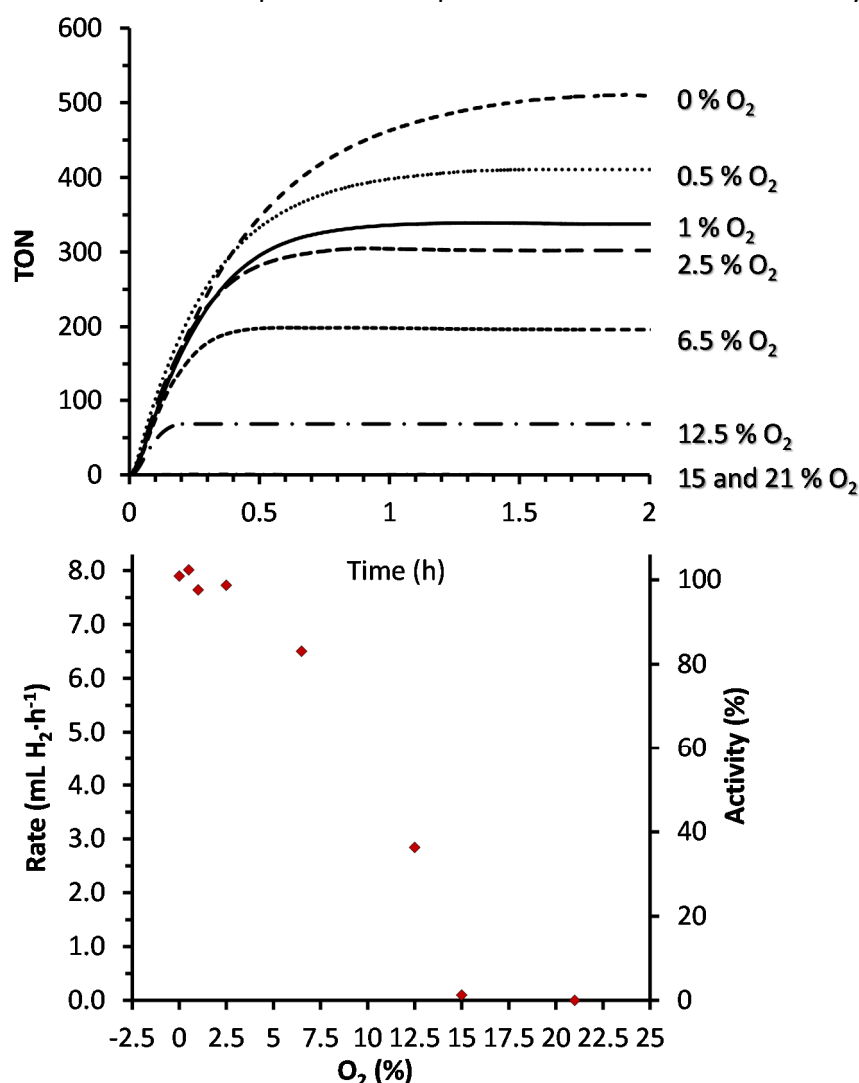


Figure IV. 27. Top: On-line hydrogen evolved versus time with **1**^{CO₂Et} (35 μM), **PSIr** (150 μM) using CH₃CN:H₂O:Et₃N (4:6:0.2 mL) as solvent and irradiated (λ = 447 nm) at 25 °C, in the presence of different concentrations of O₂. Bottom: Initial reaction rates for hydrogen evolution at different concentrations of O₂ in the headspace. Relative photocatalytic H₂ evolution activity compared to that under anaerobic conditions. TON: 512 ± 20 (0 % O₂), 410 ± 14 (0.5 % O₂), 340 ± 20 (1 % O₂), 305 ± 24 (2.5 % O₂), 200 ± 14 (6.5 % O₂), 69 ± 12 (12.5 % O₂), 4 ± 2 (15 % O₂).

on cobalt, including cobaloximes,³⁴⁸ cobalt-corrole³⁴⁹ and cobalt diamine-dioxime complexes³⁵⁰ have exhibited moderate tolerance to oxygen. We recently reported the complex [Co(OTf)(Py₂^Ttacn)](OTf) in which the 25 % of the H₂ production activity was still present under air compared to that anaerobic conditions.³¹⁴ Herein, we have also explored the capacity of the complexes based on ^{Y,X}Py^{Me}tacn ligands to reduce water to H₂ in the presence of varying concentrations of O₂ in the headspace. Due to the excellent catalytic performance of **1**^{CO₂Et} we have selected it as model catalyst for the study. The catalytic tests were carried out using 35 μM of **1**^{CO₂Et}, **PS**_{Ir} (150 μM) and using the standard solvent mixture of CH₃CN:H₂O:Et₃N (4:6:0.2 mL) and different concentration of O₂ in the headspace. In each case, the corresponding amount of O₂ was introduced into the headspace by a syringe through the septa. Before submitting the mixture to irradiation, it was strongly shaken and left it stirring for one hour to ensure that the O₂ in the gas phase is in equilibrium with liquid phase. Under anaerobic conditions, complex **1**^{CO₂Et} exhibited 512 ± 20 TON in 2 hours of irradiation. This corresponds to a total volume of 4.4 mL of hydrogen with an associated initial reaction rate of 7.9 mL H₂·h⁻¹. The photoactivity of the system is gradually inhibited by increasing the O₂ concentration in the headspace (Figure IV. 27, top). For instance, a reaction carried out under 1 % O₂ give a TON value of 340 ± 20 (2.9 ± 0.2 mL H₂, rate = 7.6 ± 0.2 mL H₂·h⁻¹), which corresponds to 66 % of the activity obtained in the absence of O₂. Remarkably, in the presence of 12.5 % of O₂, around 14 % of the photocatalytic activity under anaerobic conditions still remained (69 ± 12 TON, rate = 2.8 mL H₂·h⁻¹). However, the catalysis at higher O₂ concentrations promote at the complete inhibition of the photocatalytic activity. This total inhibition is not surprising since in most of the cases small traces of O₂ completely inhibits the catalytic activity in hydrogen production.³⁵¹

The analysis of the reaction rates reveal interesting information. At low concentrations of O₂ (up to 2.5 %) the catalytic system is able to maintain the initial reaction rate almost constant (between 7.9-7.7 mL H₂·h⁻¹) (Figure IV. 27, bottom). The O₂ concentration modifies the overall kinetic profile, having an impact on the lifetime of the catalytic system and total H₂ evolved. (Figure IV. 27, top). At oxygen concentrations higher than 2.5 % the reaction rates are also inhibited as it happens in the case of TON.

Upon increasing the O₂ concentration the total amount of e⁻ used for the oxygen reduction (4 electrons) increase while the e⁻ consume in the H₂ formation (2 electrons) decreased (Figure IV. 28). Therefore, one can envision the development of a photochemical process for O₂ reduction. Nevertheless, it is important to understand how O₂ is reduced if via a cobalt catalysis, previously observed under electrocatalytic conditions.^{114,352}, or via the formation of single O₂.

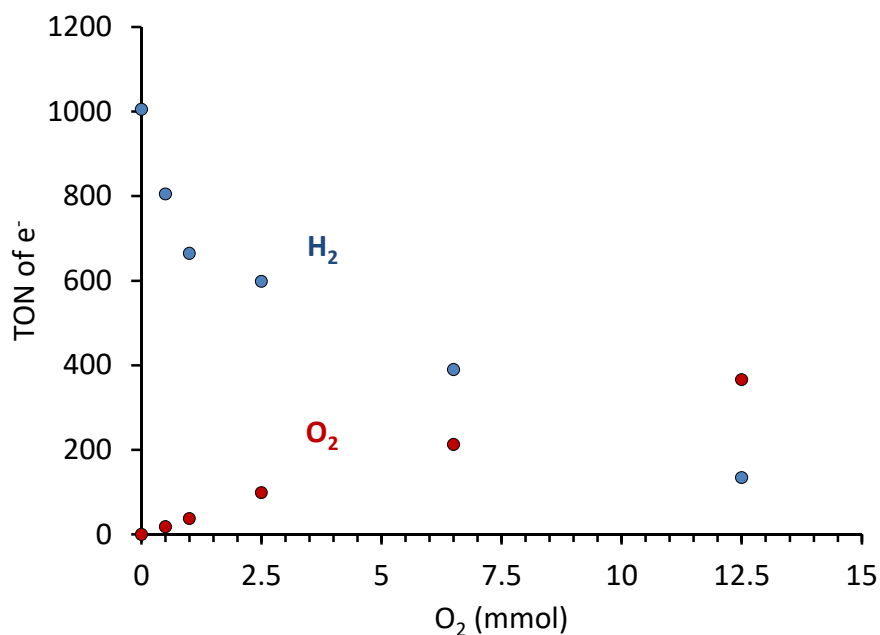
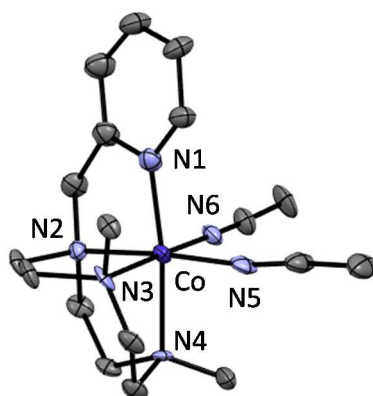


Figure IV. 28. TON of electrons (mmol e⁻ / mmol Cat) consumed for the formation of H₂ (blue dots) and O₂ reduction (red dots) versus the initial amount of O₂ (mmol) in the headspace.

IV.2.2.7. Mechanistic considerations and DFT calculations

In order progress in the understanding of the water reduction mechanism we computed the electrochemical redox potentials and pK_a values for the **1^R** series by DFT methods. The theoretical modelling was performed in collaboration with Dr. Josep Maria Lluís and Sergio Fernández from the University of Girona. We studied all possible spin states and coordination indexes for the Co^{III}, Co^{II}, Co^I, Co^{III}-H and Co^{II}-H species for all **1^R** complexes at B3LYP-D3/SMD(acetonitrile)/6-311+G**//B3LYP-D3/SMD(acetonitrile)/6-31+G* level of theory. To reduce the computational cost we have considered only acetonitrile as a solvent, therefore CH₃CN is the only additional ligand considered for saturation of the coordination sphere of the cobalt center. We were pleased to see that

the computational modelling reproduce for Co^{II} and Co^{III} complexes both the geometry (Figure IV. 29) and the spin state, being quadruplet and single, respectively, and consistent with the experimental magnetic susceptibility and NMR studies.



Bond	X-ray	DFT
	Average dist. (Å)	Average dist. (Å)
Co-N1	1.89(2)	1.964
Co-N2	1.942(4)	1.992
Co-N3	1.96(2)	1.948
Co-N4	2.06(2)	1.999
Co-N5	1.872(10)	1.923
Co-N6	1.90(2)	1.915

Figure IV. 29. *Left:* Thermal ellipsoid plots of Co^{III} (**1^H**) with (50 % probability). Solvent molecules and hydrogen atoms are omitted for clarity. Color code: cobalt (blue), nitrogen (light blue) and carbon (grey). *Right:* Comparison between the experimental and theoretical Co-N distances.

Modelled Co^I species in the triplet spin state are 10 kcal·mol⁻¹ lower than the singlet state. This electronic structure of the Co^I species results to be very interesting. Mulliken spin density shows a spin density strongly delocalized over the pyridines in **1^{CO₂Et}**, **1^{CF₃}** and **1^{NO₂}** complexes while for the others is mainly delocalized over the metal center (Figure IV. 30). This suggests that the electronic structure of the **1^{CO₂Et}** and **1^{NO₂}** Co^I complexes is best described as S = 1/2 Co^{II} center with a ferromagnetically couple electron delocalized over the pyridine ring resulting in a total S = 1 spin state. **1^{NO₂}** Co^I complex present an important electron density over the NO₂ group which is in agreement of its facility to be reduced. As judged by the Mulliken spin density found in **1^{CF₃}** Co^I some contribution of the electronic structure S = 3/2 Co^{II} antiferromagnetically with an electron over the pyridine S = -1/2 leading to a S = 1 total spin state is present. The important conclusion that arises from this preliminary study is that the incorporation of electron withdrawing substituents at the pyridine ring can transform a normal coordination ligand into a redox non-innocent ligand when combined with a low oxidation state metal center such as Co^I (Figure IV. 30).

In our case we were interested in to understand how the redox non-innocent character proposed by DFT calculations can affect (if any) the properties of this family of

complexes, such as their effect in cyclic voltammograms and electrocatalysts (Figure IV. 13).

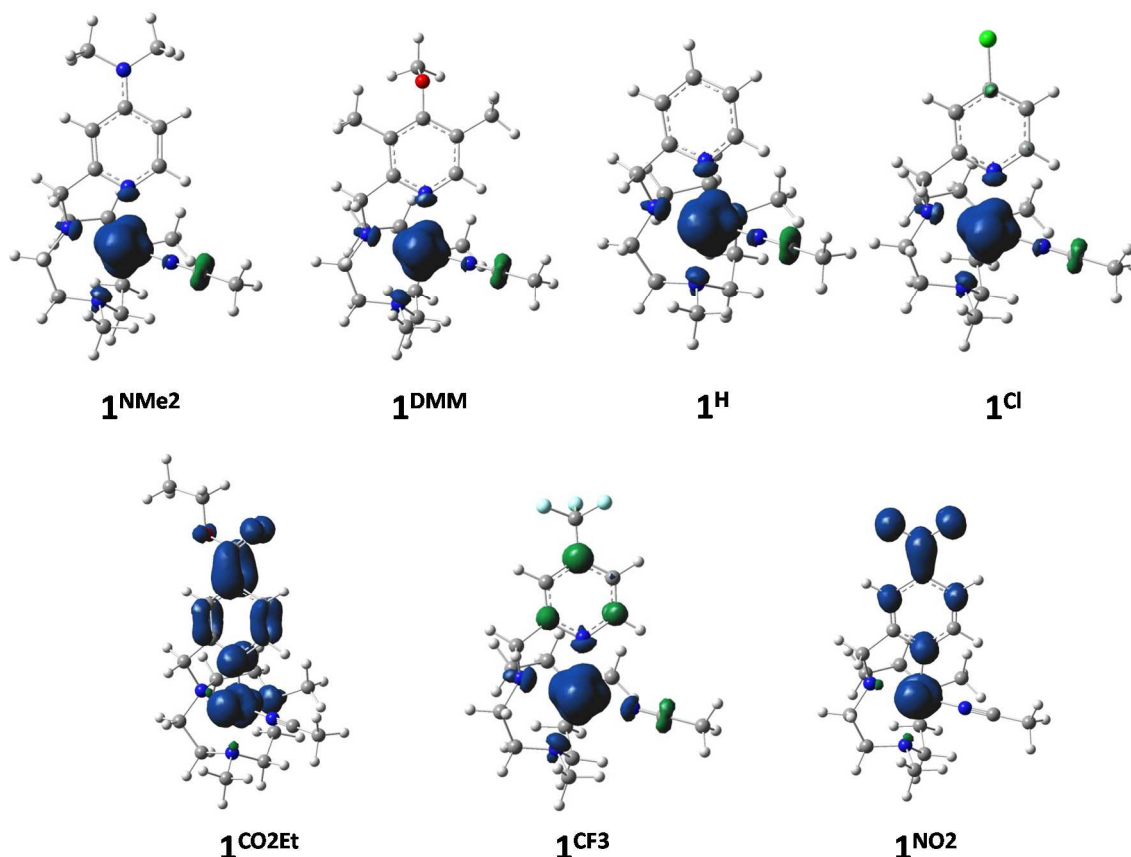


Figure IV. 30. Spin density isosurfaces of the seven formal Co^I intermediates in the triplet spin state computed at the B3LYP/6-31+G* level of theory. The spin density in the positive sign is coloured in blue and the spin density in the negative one is coloured in green.

First we evaluated if our theoretically modelled cobalt species were able to reproduce the experimental Co^{II/I} and Co^{III/II} redox values (Table IV. 5). The calculated redox values are in modest agreement with the experimental values. Theoretical values are 250-400 mV shifted to higher redox potentials respect to experimental ones. However, Hammett plot analysis of between the experimental and theoretical Co^{III/II} and Co^{II/I} redox potentials are in good agreement. Moreover, we have calculate the pK_a (Co^{III}-H) values (Table IV. 5) performed the Hammett plot, showing good a linear correlation and additionally we have compare the theoretical Co^{III/II} and Co^{II/I} redox potentials with the pK_a's (Figure IV. 31). Complexes **1^{NO2}** has only been considered for the Co^{III/II} analysis since for the rest of the values is out of range.

Table IV. 5. Summary of the experimental and theoretical E(Co^{II/I}) and E(Co^{III/II}) redox values vs. SCE and the theoretical pK_a (Co^{III}-H) values of **1^R** complexes.

1^R	σ	E (V)		E (V)		pK_a Co^{III}-H_{theo}
		Co^{II/I}_{exp}	Co^{II/I}_{theo}	Co^{III/II}_{exp}	Co^{III/II}_{theo}	
1^{NMe2}	-0.70	-1.40	-1.14	0.35	0.75	15.1
1^{DMM}	-0.41	-1.34	-1.11	0.37	0.81	14.4
1^H	0	-1.29	-1.06	0.45	0.88	12.8
1^{Cl}	0.23	-1.27	-1.07	0.5	1	12
1^{CO2Et}	0.45	-1.13	-0.95	0.49	0.93	11.6
1^{CF3}	0.54	-1.19	-0.92	0.51	1.03	10.8
1^{NO2}	0.78	-0.50	-0.41	0.57	0.96	1.6
PS_{Ir}^{II/III}		-1.38				

The analysis of the DFT Co^{III}-H pK_a values (Figure IV. 31, C) of **1^R** reveals that Co^{III}-H species are stabilized by electron donating groups (higher the pK_a lower the acidity). pK_a values range from 10.8 to 15.1. We exclude the **1^{NO2}** (pK_a 1.6), which again follows a completely different behavior to the rest. Under photochemical conditions the pH of the solution is c.a. 12. This imply that from **1^{NMe2}** to **1^{CF3}** the protonation of Co^I complexes shift from exergonic to endergonic. The additional energy input of the endergonic reaction may be reflected in the overall reaction rate. On the contrary, the reduction from Co^{II} to Co^I is more favorable when going from **1^{NMe2}** to **1^{CF3}**.

These results can help us to rationalize the reactivity in photocatalytic water reduction with **1^R** complexes. The increase in catalytic activity from **1^{NMe2}** to **1^{CO2Et}** could be argued due to a better facility to achieve the Co^I oxidation state. During this stage the Co^I protonation could still favored. Although, for the rest of the family from **1^{CO2Et}** to **1^{NO2}** the reduction from Co^{II} to Co^I is more favored, and the protonation of Co^I can be now exergonic and therefore inverting the overall trend of catalytic activity. This imply that the control of the rate of reaction is done by both the Co^{I/II} reduction event and Co^I protonation to Co^{III}-H, being the last one connected with the rate determining step. (Figure IV. 32). Our results are consistent with the theoretical studies initially proposed by Hammes-Schiffer with cobalt diglyoxime catalysts.²⁹¹

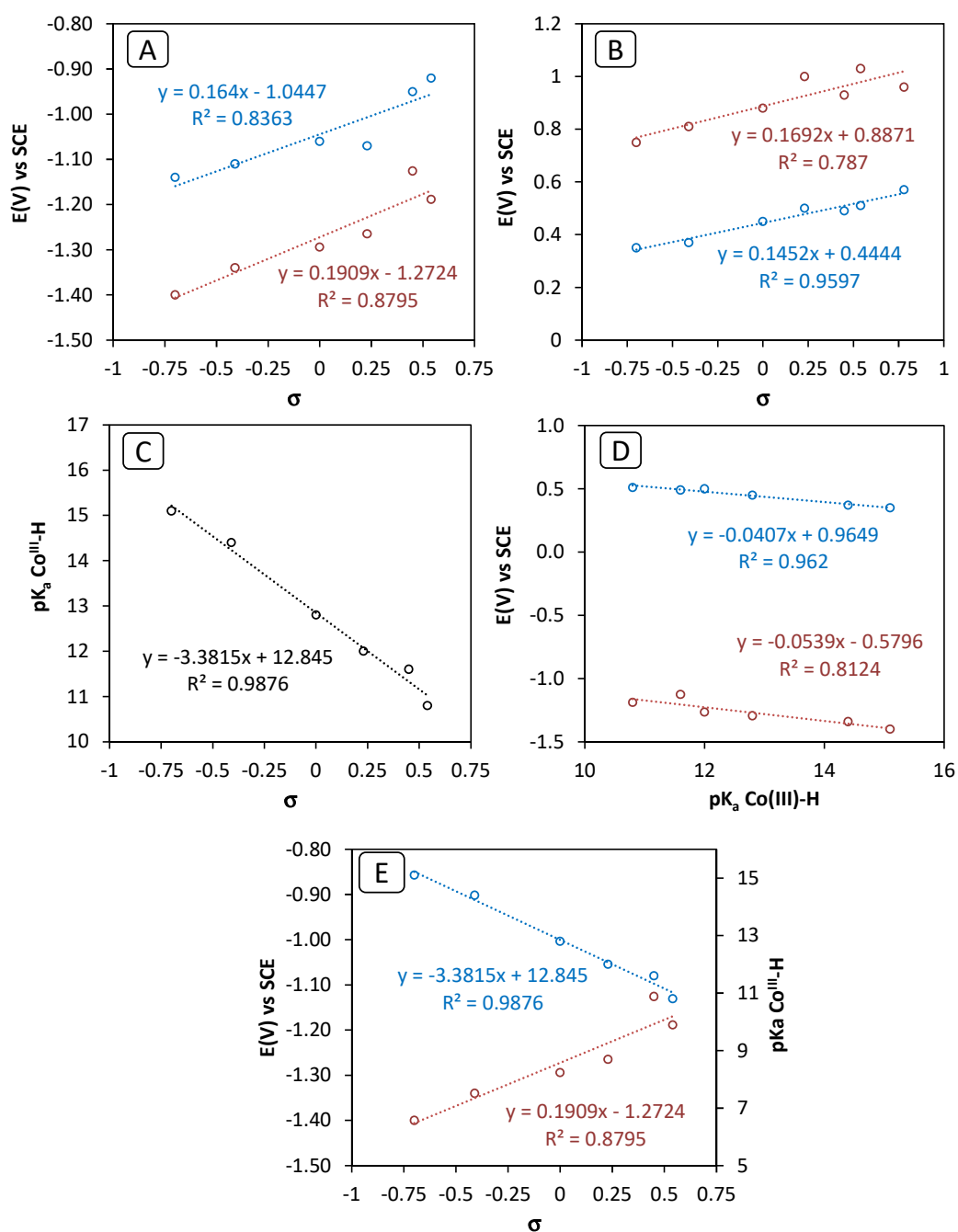


Figure IV. 31. Hammett plot of experimental (red) and theoretical (blue) A) $E(Co^{II})$ (V), B) $E(Co^{III})$ (V), C) Theoretical pK_a values and E) experimental $E(Co^{III})$ (V) and theoretical pK_a values and D) experimental $E(Co^{III})$ and $E(Co^{II})$ vs. theoretical pK_a values

On the other hand, we cannot discard the possibility that the low activity of the 1^{NO_2} could be attributed due to a decomposition process of the NO_2 group under photochemical conditions.^{353,354}

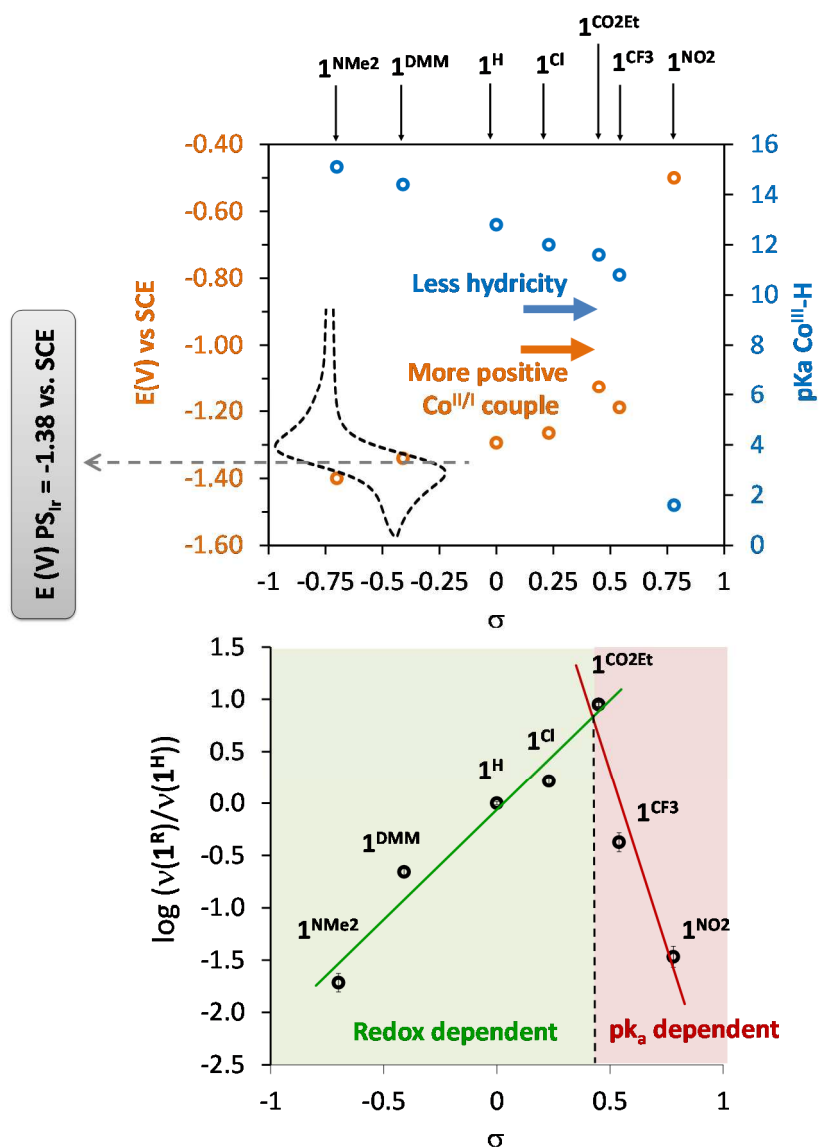


Figure IV. 32. Top: Experimental $E(V)$ ($\text{Co}^{III/II}$) and computed pK_a values vs. the Hammett constant. The dashed black trace corresponds to the cyclic voltammogram of the photosensitizer PS_{Ir} ($E(V) \text{ PS}_{\text{Ir}} (\text{III/II}) = -1.38 \text{ V vs. SCE}$). Bottom: Hammett plot of the relative reaction rates versus the Hammett substituent value (σ). v : Initial reaction rate determined at 10% conversion. The two main trends in reactivity are emphasized by green (redox dependent) and red (pK_a dependent).

IV.2.3. Electrocatalytic Proton Reduction to H₂

We investigated the electrocatalytic proton reduction to H₂ of the series of cobalt in CH₃CN as solvent using trifluoroacetic acid (TFA, pK_a=12.7 in acetonitrile)³⁰⁰ as a proton source to study the impact of the electron density of the ligand on the overpotential. The complex **1**^{NO₂} was not studied due to the unexpected electroactive behavior at -0.50 V. Electrocatalytic hydrogen evolution was evidenced in the CVs of **1**^R complexes by the appearance of a new irreversible wave that raise in current with increasing concentrations of TFA (Figure IV. 34). The linearity of the i_{cat}/i_p values versus [H⁺] is consistent with a second order process versus the concentration of protons. No saturation behavior is observed in the acid range studied (1-100 mM).

Interestingly, in all of the electrocatalytic proton reduction occurs at potentials positively shifted with respect to the Co^{II}/Co^I couple. The extent of the shift depends on the catalyst. Thus, the higher shifts are observed for complexes **1**^{NMe₂}, **1**^{DMM}, **1**^H and **1**^{Cl}, in which a new electrocatalytic wave is located around -0.9 V (at half wave intensity). This corresponds a shift ranging between 500 mV (**1**^{NMe₂}) to 370 mV (**1**^{Cl}). We note that the *onset* potential of the new electrocatalytic wave is observed at relatively positive potentials (about -0.6 V) which is very close to the thermodynamic potential of proton reduction (E°_{TFA} (V) = -0.51 V vs. SCE in MeCN). Interestingly, although complexes **1**^{CO₂Et} and **1**^{CF₃} also experiment an important shift of the catalytic wave showed higher overpotential than the rest (Figure IV. 33).

The reduction of the overpotential upon acid addition could be attributed to i) the formation of new speciation in solution, *via* ligand protonation or ii) to that the Co^{I/II} redox event is coupled with a proton transfer (PCET). By analogy with other systems reported in the literature, the shift in the electrocatalytic wave could be attributed to a proton transfer from the ligand to the metal complex. The anodic shift in the presence of acid has been also observed in cobalt diamine-dioxime systems,^{80,87,89} and supported by DFT calculations.^{128,355,356} The protonation event in cobalt aminopyridine systems has also been proposed.^{105,293}

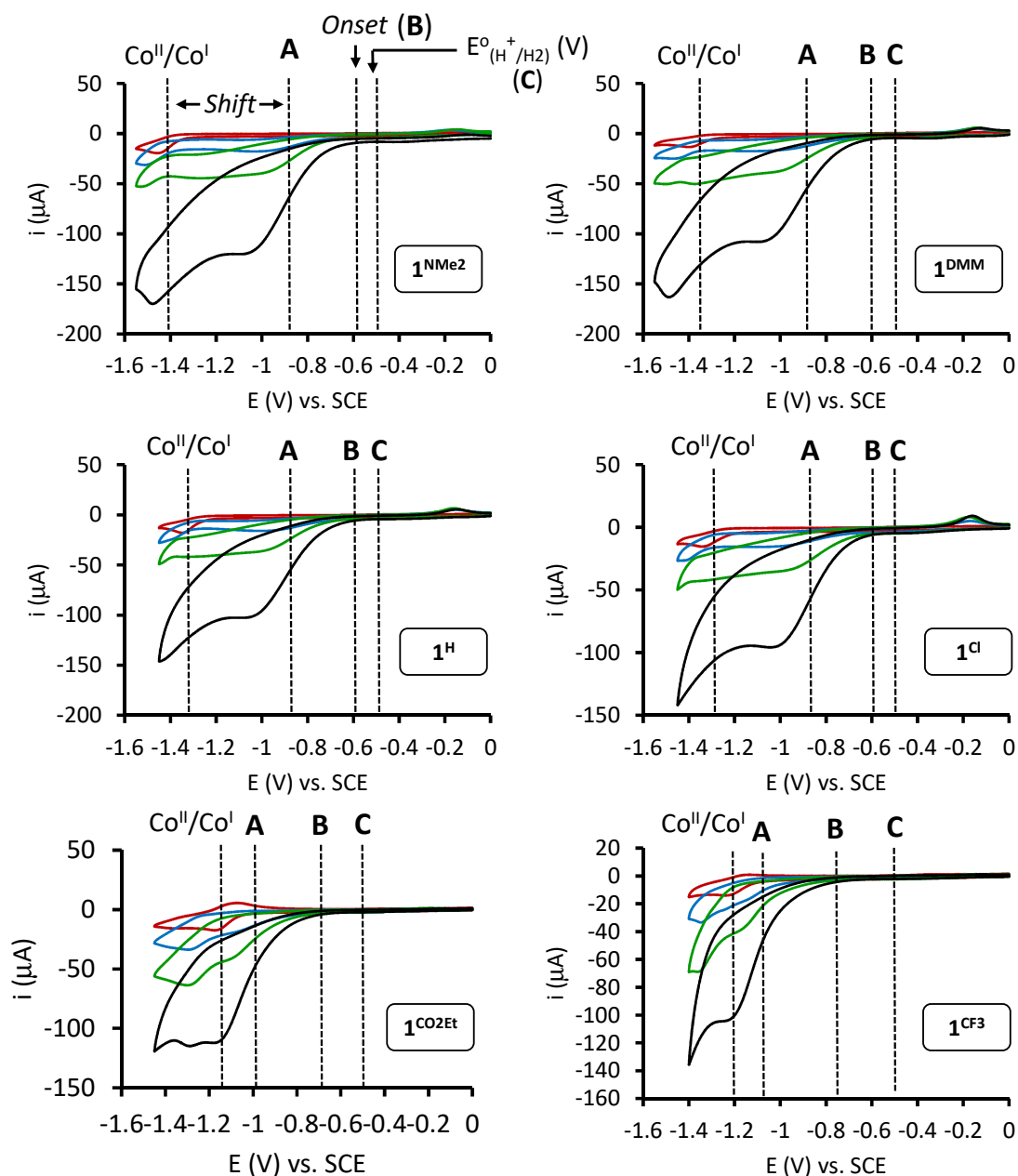


Figure IV. 33. Cyclic voltammograms of **1^R** complexes (1 mM) showing the growth of a new electrocatalytic wave due to the addition of TFA (red: 0 mM, light blue: 1 mM, green: 3 mM, black: 10 mM). A) Half wave potential of the electrocatalytic wave. B) Onset potential of the electrocatalytic wave C) Standard potential in proton reduction using TFA. Conditions: 0.1 M Bu₄NPF₆ (0.1 M) in MeCN, using a scan rate of 100 mV·s⁻¹. Glassy carbon electrode and SCE electrodes were used as working and reference electrodes, respectively.

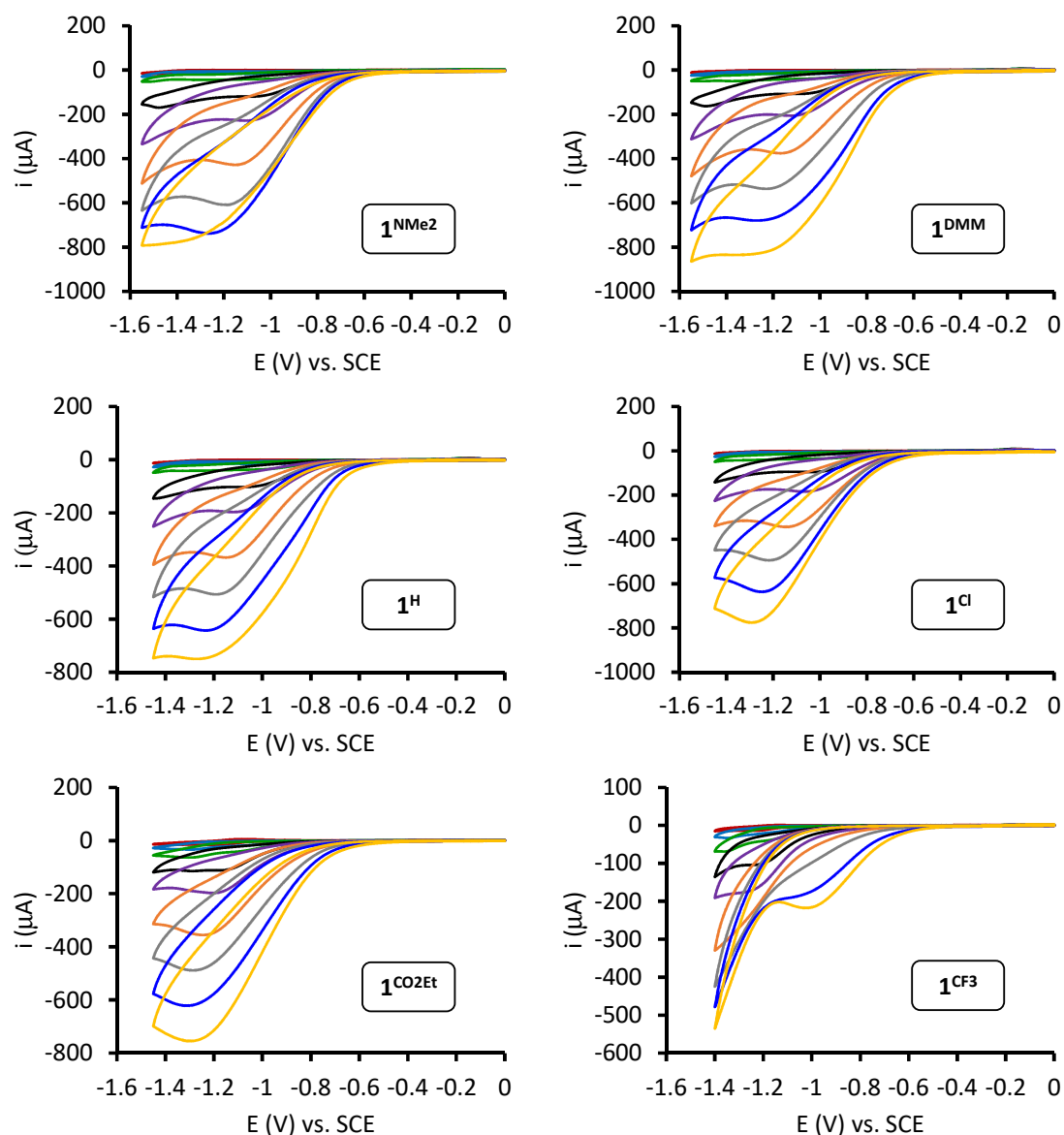


Figure IV. 34. Successive cyclic voltammograms of **1^R** complexes (1 mM) in acetonitrile containing Bu₄NPF₆ (0.1 M) in the presence of acid: TFA (red: 0 mM, light blue: 1 mM, green: 3 mM, black: 10 mM, purple: 20 mM, orange: 40 mM, grey: 60 mM, dark blue: 80 mM and yellow: 100 mM), measured at 100 mV·s⁻¹. Glassy carbon electrode and SCE electrodes were used as working and reference electrodes, respectively.

Based on previous studies reported in the literature,^{80,87,89} we can envision a general mechanism for H₂ production (Figure IV. 35, B). The catalytic cycle could start with a PCET promoting the formation of a Co^I specie with the ligand protonated. Afterwards, a second PCET step is then required to form a Co^{II}-hydride, having a protonated ligand. Then, H₂ is produced either through external protonation or through an intramolecular mechanism as suggested to occur at the active site of hydrogenases (Figure IV. 35, A).^{357,358} The role of proton relays have been demonstrated to be crucial

for promoting heterolytic H⁺/H₂ interconversion. A prototypical example is the nickel bisphosphine complexes developed by DuBois that contain amino sites in the second coordination sphere that release protons on the metal center.⁵¹

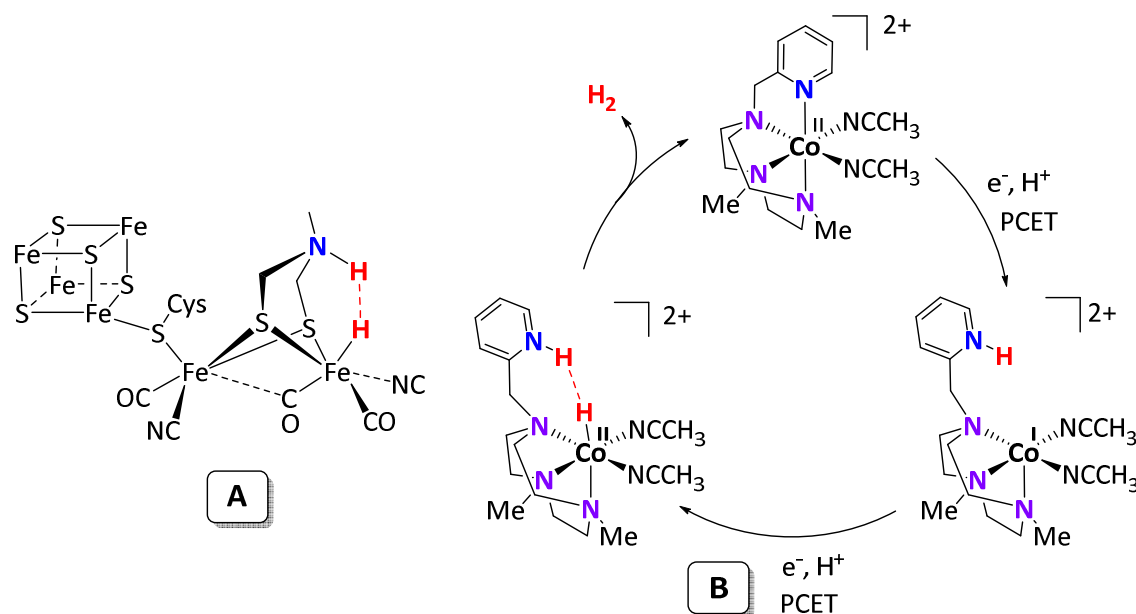


Figure IV. 35. A) Proposed structure of the [FeFe] hydrogenase active site based on crystallographic data.¹⁰ B) Possible pathway for hydrogen evolution involving PCET processes and protonated ligand.

It seems that higher electron density on the ligand higher H₂ evolution activities. This phenomena is evident in the range of 10-80 mM of TFA (Figure A. 2. 8). Indicating that the high shift observed in **1**^{NMe₂}- **1**^{Cl} systems could be attributed to the higher electron density on the pyridine moiety, favoring its protonation. Indeed, the strong electron withdrawing character of the CF₃ substituent could decrease the protonation of the pyridine. This is in agreement that **1**^{CF₃} requires higher concentrations of TFA (80 – 100 mM) compared with the **1**^{NMe₂}- **1**^{Cl} systems to observe the same shift of the electrocatalytic wave. Regarding to the efficiency, the improved catalytic activity when increasing the electron donating properties could be interpreted by an enhancement of the protonation event, favoring the proton relay process.

In the line with this argument is the performance of **1**^R with a much weaker acid, Et₃NH·TfO (pK_a = 18.82).³⁵⁹ The addition of Et₃NH·OTf to a 1 mM solution of **1**^H produce an increase in current at potentials more negative than the Co^{II}/ Co^I redox couple.³⁶⁰ The

absence of anodic shift suggests that in this case the ligand protonation (or a possible PCET event) do not take place (Figure IV. 36).

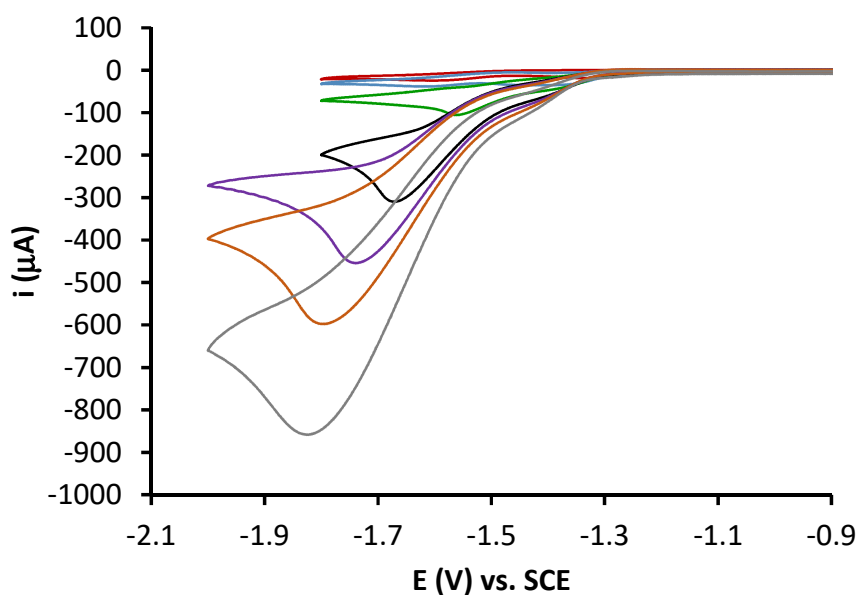


Figure IV. 36. Cyclic voltammograms of **1^H** (1 mM) in acetonitrile containing Bu₄NPF₆ (0.1 M) in the presence of different Et₃N TfOH concentrations (red: 0 mM, light blue: 1 mM, green: 3 mM, black: 10 mM, purple: 20 mM, orange: 40 mM and grey: 60 mM), measured at 100 mV·s⁻¹. Glassy carbon electrode and SCE electrodes were used as working and reference electrodes, respectively.

In summary, we have synthesized and fully characterized a new family of tetradentate aminopyridine Co^{II} complexes which share the same 1,3,5-triazacyclononane (tacn) as basic structure and electronically modified with pyridine arms. The electronic substituents on the pyridine not only influences the spectroscopic and structural features of the complex, but also has an important impact on the photocatalytic activity in H₂ evolution (TON = 26-500, TOF = 14-710). Under optimized conditions, up to 8500 TON (TOF_{max} = 52570) were achieved using the **1^{CO2Et}** complex. This electronic dependence of the ligand strongly supports that the catalytic activity is originated from the molecular complex operating in homogeneous phase.

By DFT calculations we concluded that the catalytic activity from **1^{NMe2}** to **1^{CO2Et}** could be argued due to a better facility to achieve the Co^I oxidation state, whereas for the systems **1^{CF3}** and **1^{NO2}** the protonation of the Co^I becomes an endergonic process and therefore it inverts the overall trend of catalytic activity. This results suggest that the

efficiency of the reaction is controlled by the Co^{II/I} reduction and by the protonation of Co^I to Co^{III}-H.

The same complexes were found active in the electrochemical reduction of protons. Using TFA we catalytic reaction occurs through a protonation of the ligand by a PCET step. In addition, the electrocatalytic activity can also be tuned with the electronic properties of the ligand. This work can help to the design of new homogeneous catalytic systems for H₂ production

IV.3. EXPERIMENTAL SECTION

IV.3.1. General Methods

All procedures were carried out under N₂ using standard vacuum line, Schlenk, and inert atmosphere glovebox techniques. Reagents and solvents were purchased from commercial sources as used as received unless otherwise stated. Triethylamine (Et₃N) ≥ 99 % purity and ascorbic acid (≥ 99 %) were purchased from Sigma-Aldrich® and used without further purification. Compounds 1-(*p*-toluensulfonyl)-1,4,7-triazacyclononane (T^stacn),³⁶¹ and [Ir(bpy)(ppy)₂]PF₆³⁰³ were synthesized according to the literature procedures. Anhydrous acetonitrile was purchased from Scharlab. Water (18.2 MΩ·cm) was purified with a Milli-Q Millipore Gradient AIS system. All the solvents were strictly degassed and stored in anaerobic conditions. All water reduction catalytic reactions were performed under N₂ otherwise notified.

IV.3.2. Physical Methods

Nuclear magnetic resonance (NMR) spectra were recorded on BrukerDPX300, DPX400 and DPX500 spectrometers using standard conditions (300 K). All ¹H chemical shifts are reported in ppm and have been internally calibrated to the residual protons of the deuterated solvent. The ¹³C chemical shifts have been internally calibrated to the carbon atoms of the deuterated solvent. The coupling constants were measured in Hz.

Elemental analyses were performed using a CHNS-O EA-1108 elemental analyzer from Fisons.

UV/Vis spectra were recorded on an Agilent 8453 diode array spectrophotometer (190-1100 nm range) in 1 cm quartz cells. A cryostat from Unisoku Scientific Instruments was used for the temperature control.

Mass Spectrometry. Electrospray ionization mass spectrometry (ESI-MS) experiments were performed on a Bruker Daltonics Esquire 3000 Spectrometer using a 1 mM solution of the analyzed compound, by introducing the sample directly into the ESI-source using a syringe. High resolution mass spectra (HRMS) were recorded on a Bruker MicroTOF-Q IITM instrument with an ESI source at Serveis Tècnics of the University of Girona. Samples were introduced into the mass spectrometer ion source by direct infusion through a syringe pump and were externally calibrated using sodium formate.

Electrochemistry. A standard three-electrode configuration was employed in conjunction with CHI Instruments potentiostat interfaced to a computer with CHI Instruments 600D software. Using one-compartment cell, all voltammetric scans were recorded using glassy carbon working electrode which was treated between experiments by means of a sequence of polishing with MicroPolish Powder (0.05

micron) before washing and sonification. Saturated calomel electrode (SCE) and Pt wire were used as reference and counter electrodes respectively.

On-line MS measurements have been performed using Omnistar GSD 301 C (Pfeiffer) quadrupole mass spectrometer apparatus.

Parallel Pressure Transducer Hardware. The parallel pressure transducer that we used for these studies is the same that previously was developed and described for water oxidation studies.³⁰⁴ This is composed by 8 differential pressure transducers (Honeywell-ASCX15DN, ± 15 psi) connected to a hardware data-acquisition system (base on Atmega microcontroller) controlled by a home-developed software program. The differential pressure transducer Honeywell-ASCX15DN is a 100 microseconds response, signal-conditioned (high level span, 4.5 V) output, calibrated and temperature compensated (0 °C to 70 °C) sensor. The differential sensor has two sensing ports that can be used for differential pressure measurements. The pressure calibrated devices to within ± 0.5 matm was offset and span calibrated *via* software with a high precision pressure transducer (PX409-030GUSB, 0.08% Accuracy). Each of the 8 differential pressure transducers (Honeywell-ASCX15DN, ± 15 psi) produce a voltage outputs that can directly transformed to a pressure difference between the two measuring ports. The voltage outputs were digitalized with a resolution of 0.25 matm from 0 to 175 matm and 1 matm from 176 to 1000 matm using an Atmega microcontroller with an independent voltage auto-calibration. Firmware Atmega microcontroller and control software were home-developed. The sensitivity of H₂ analytics allows quantifying the gas formed when low H₂ volumes are generated. Therefore, it could not be discarded that small amounts of H₂ were produced by inactive complexes.

Gas chromatography identification and quantification of gases. Gases at the headspace were analyzed with an Agilent 7820A GC System equipped with columns Washed Molecular Sieve 5A, 2m x 1/8" OD, Mesh 60/80 SS and Porapak Q, 4m x 1/8" OD, SS. Mesh: 80/100 SS and a Thermal Conductivity Detector. The quantification of the H₂ obtained was measured through the interpolation of a previous calibration using different H₂/N₂ mixtures.

X-Ray crystallography. Single crystals of 1R were mounted on a nylon loop for X-ray structure determination. The measurements were carried out on a BRUKER SMART APEX CCD diffractometer using graphite-monochromated MoK α radiation ($\lambda=0.71073$ Å). Programs used: data collection, Smart version 5.631 (Bruker AXS 1997-02); data reduction, Saint+ version 6.36A (Bruker AXS 2001); absorption correction, SADABS version 2.10 (Bruker AXS 2001). Structure solution and refinement was done using SHELXTL Version 6.14 (Bruker AXS 2000–2003). The structure was solved by direct methods and refined by full-matrix least-squares methods on F². The non-hydrogen atoms were refined anisotropically. The hydrogen atoms were placed in geometrically optimised position and forced to ride on the atom to which they are attached.

IV.3.3. Gas-Evolution-Monitoring Studies

All catalytic reactions were performed in a 15 mL vial capped with a septum. Each experiment was conducted in a volume-calibrated-vial equipped with stir-bars and containing the solvent mixture with the reagents, and then was connected to one port of a differential pressure transducer sensor (Honeywell-ASCX15DN, ± 15 psi). Each reaction had its own reference reaction, which was conducted at the other port of the differential pressure transducer sensor. The reaction and reference vials were kept under the same experimental conditions to minimise the system noise due to temperature– pressure fluctuations. In this sense, each vial was submitted and located just over a LED radiation source. Furthermore, in order to ensure a constant and stable irradiation, the LED sources were equipped with a water refrigeration system. Just before starting the reaction, the corresponding catalyst was added by syringe through the septum from a stock solution prepared in acetonitrile. The reaction began when the LEDs were turned on. At this point, the hydrogen evolved from the reactions was monitored by recording the increase in pressure of the headspace (1 s interval). The pressure increment was the result of the difference in pressure between the reaction and reference vials. After the hydrogen evolution reached a plateau the amount of the formed gas was captured and measured, equilibrating the pressure between reaction and reference vials. The hydrogen contained in each of the reactions was measured by analysing an aliquot of gas of the headspace (0.2 mL) by gas chromatography. GC measurements of H₂ corroborated the values obtained by pressure increments.

IV.3.4. Gas-Evolution Studies Performed in the Presence of Hg⁰

Catalytic reactions performed in the presence of Hg⁰ were carried out in a 15 mL vial capped with a septum. Each experiment was conducted in a volume-calibrated-vial equipped with stir-bars and containing the CH₃CN/H₂O (4:6) as the solvent mixture with all the reagents under N₂. The experiments were conducted in one port of a differential pressure transducer sensor, with a reference reaction at the other port. The reaction and reference vials were kept under the same experimental conditions to minimize the System noise due to temperature-pressure fluctuations. The experiments were carried out using the conditions (**1**^H (50 μ M), **PS**_{ir} (250 μ M), under the solvent mixture of CH₃CN:H₂O:Et₃N (4:6:0.2 mL)) and with and without Hg⁰ for comparison reasons. 30 min before starting the reaction Hg⁰ was added in large excess (1000 eq or 1.5 mL; 15% of the total reaction volume) by syringe through the septum. The solution was stirred for 30 min under and then the solution was submitted to LED irradiation at 447 nm. Hg⁰ was left in contact with the solution during the whole catalytic assay in order to poison the heterogeneous catalyst formed during the irradiation time. The hydrogen evolved from the reaction was monitored in real time by recording the increase in pressure of the headspace (1 s interval). The pressure increment was the result of the difference in pressure between the reaction and reference vials. After the hydrogen evolution

reached a plateau the amount of the formed gas was captured and measured, equilibrating the pressure between reaction and reference vials. The hydrogen contained in each of the reactions was measured by analyzing an aliquot of gas of the headspace (0.2 mL) by gas chromatography. GC measurements of H₂ corroborated the values obtained by pressure increments.

IV.3.5. UV/Vis Measurements with On-line Irradiation

The UV/Vis measurements with on-line irradiation were performed on a self-made apparatus using 1 cm quartz fluorescence cuvette in a fluorescence cuvette holder. LED (Royal blue, 447 nm) was placed perpendicular to the optical pathway of Agilent 8453 diode array spectrophotometer (190-1100 nm range). A cryostat from Unisoku Scientific Instruments was used for the temperature control.

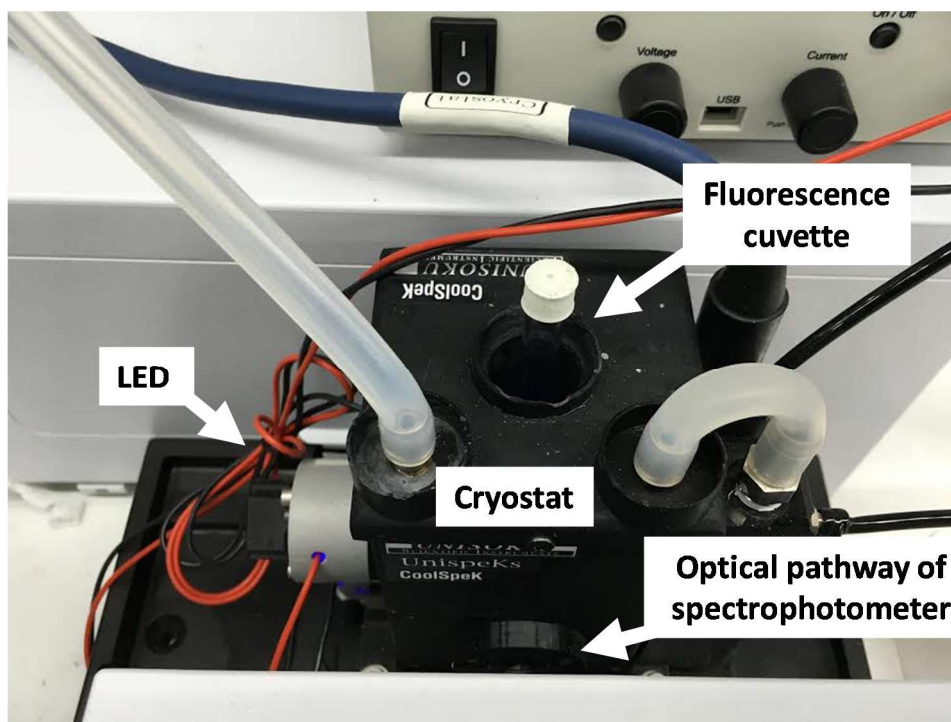


Figure IV. 37. Setup for UV/Vis measurement with on-line irradiation.

IV.3.6. Calibration of the on-line MS monitoring formation of H₂, HD and D₂.

We calibrated the response of H₂, HD and D₂ in the on-line mass spectrometer apparatus. The calibration was done by measuring known amounts of H₂, HD and D₂ in the headspace, and the response was plotted against the amount of gas (Figure IV. 38).

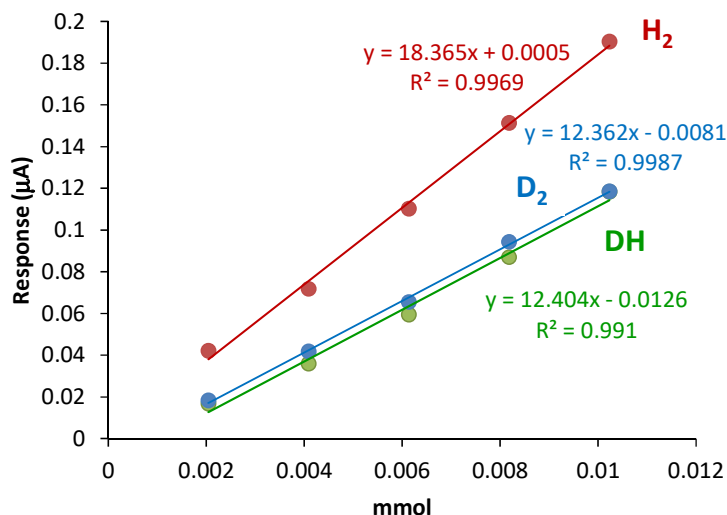


Figure IV. 38. Calibration of the response of H₂, DH and D₂ in the on-line mass spectrometer apparatus.

The HD and D₂ products for the injection were generated by reacting NaH with D₂O, and Li with D₂O, respectively.

IV.3.7. Acid Concentration Dependence Study

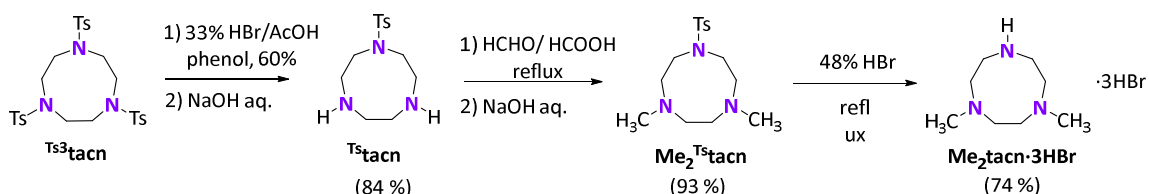
A 0.8 M stock solution of TFA was prepared in a CH₃CN solution of 0.1m Bu₄NPF₆. Aliquots of this solution were added to a degassed solution of 1 mM catalyst in CH₃CN. After the addition the solution was purged with N₂ before carrying out the cyclic voltammetry. The order with respect to [acid] was determined by plotting the current at the potential M^{II/I} versus the concentration of acid.

IV.3.8. Synthesis of Ligands

IV.3.8.1. Synthesis of 1,4-dimethyl-1,4,7-triazacyclononane trihydrobromide,

Me₂tacn·3HBr

The compound Me₂tacn·3HBr has been synthesized according to the procedure describe in the literature.³⁶¹



Scheme IV. 2. Synthesis of Me₂tacn·3HBr.

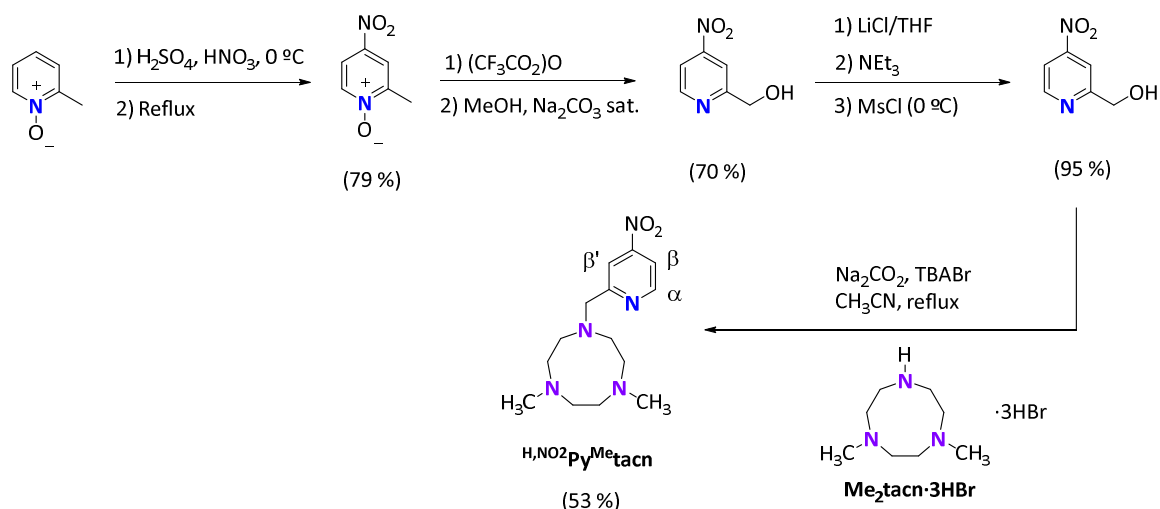
1-(p-toluensulfonyl)-1,4,7-triazacyclononane, Ts³tacn. Ts³tacn (24.6 g, 41.6 mmol) and phenol (35.2 g, 374 mmol) were mixed in 500 mL flask. A solution of HBr in acetic acid

(33%, 380 mL) was added with extreme care as an important evolution of HBr_(g) takes place. The mixture was gently heated with stirring to 90 °C which caused the complete dissolution of all the starting reagents giving rise to the formation of a dark solution. A colorless precipitate of 1-(*p*-toluenesulfonyl)-1,4,7-triazacyclononane·2HBr appeared within 2-4 h. After heating for 36 h, the mixture was cooled to room temperature and filtered. The solid was washed with diethyl ether (125 mL) and then dissolved in aqueous NaOH 1 M (320 mL). The resultant pink aqueous mixture was then extracted with CH₂Cl₂ (3 x 190 mL) the organic extracts dried with anhydrous MgSO₄, filtered and evaporated under reduced pressure. Drying the resultant oil under vacuum afforded 9.88 g the pure product (36.9 mmol, 84%). ¹H-NMR (CDCl₃, 400 MHz, 300 K) δ, ppm: 7.70 (d, *J* = 8.2 Hz, 2H, ArH), 7.34 (d, *J* = 8.2 Hz, 2H, ArH), 3.23-3.18 (m, 4H, TsN-CH₂-CH₂-NH), 3.12-3.09 (m, 4H, TsN-CH₂-CH₂-NH), 2.90 (s, 4H, HN-CH₂-CH₂-NH), 2.44 (s, 3H, Ar-CH₃), 1.85 (s, 2H, NH).

1,4-dimethyl-7-(*p*-toluenesulfonyl)-1,4,7-triazacyclononane, Me₂^{Ts}tacn. ^{Ts}tacn (7.75 g, 27.3 mmol) was dissolved in 37% formaldehyde (21.8 mL) and 98% formic acid (21.8 mL) and the resulting orange solution was refluxed for 24 hours. After cooling at room temperature, 9 mL HCl cc were added and the mixture was left stirring for 10 min. The solvent was removed under vacuum and a small amount of water (10 mL) was added to the resulting residue. The solution was brought to pH>14 by addition of NaOH 2 M. This caused the slow formation of a white precipitate corresponding to the desired product. After stirring for 20 h at room temperature, filtration of the mixture gave a white precipitate which was dissolved in 50 mL CH₂Cl₂ giving a pale yellow solution which was treated with 50 mL NaOH 4M. The aqueous layer was further extracted with 3 x 50 ml CH₂Cl₂. The combined organic layers were dried over anhydrous MgSO₄ and the solvent was removed under reduced pressure to yield 7.90 g of a crystalline white solid (25.4 mmol, 93%). ¹H-NMR (CDCl₃, 400 MHz, 300 K) δ, ppm: 7.67 (d, *J* = 8 MHz, 2H, ArH), 7.30 (d, *J* = 8 MHz, 2H, ArH), 3.25-3.23 (m, 4H, N-CH₂-CH₂), 2.89-2.91 (m, 4H, N-CH₂-CH₂), 2.69 (s, 4H, N-CH₂-CH₂), 2.42 (s, 3H, Ar-CH₃), 2.39 (s, 6H, N-CH₃).

1,4-dimethyl-1,4,7-triazacyclononane trihydrobromide, Me₂tacn·3HBr. Me₂tacn·3HBr (7.90 g, 25.4 mmol) was dissolved in 48% HBr (80 mL) and refluxed at 160 °C for 48 hours. After cooling at room temperature, the solvent of the black crude mixture was removed under reduced pressure. Addition of acetone (100 mL) and stirring for 3 hours afforded a fine pale precipitate which was filtered off and washed with acetone. The resulting pale grey solid was dissolved with boiling water (75 mL) and filtered. The solvent from the yellow filtrates was removed under reduced pressure and the resulting residue was treated with absolute ethanol (100 mL). A fine pale yellow precipitated appeared which was filtered off and dried under vacuum to yield 7.50 g of the desired product (18.7 mmol, 74%). ¹H-NMR (D₂O, 400 MHz, 300 K) δ, ppm: 3.50-3.44 (m, 4H, N-CH₂-CH₂), 3.34-3.32 (m, 4H, N-CH₂-CH₂), 3.23 (s, 4H, N-CH₂-CH₂), 2.80 (s, 6H, N-CH₃).

IV.3.8.2. Synthesis of the ligand 1,4-dimethyl-7-(4-nitro-2-pyridylmethyl)-1,4,7-triazacyclononane, ^{H,NO2}Py^{Me}tacn.



Scheme IV. 3. Synthesis of ^{H,NO2}Py^{Me}tacn ligand.

The ^{H,NO2}Py^{Me}tacn ligand was synthesized according to the procedure described in the literature.³¹⁹

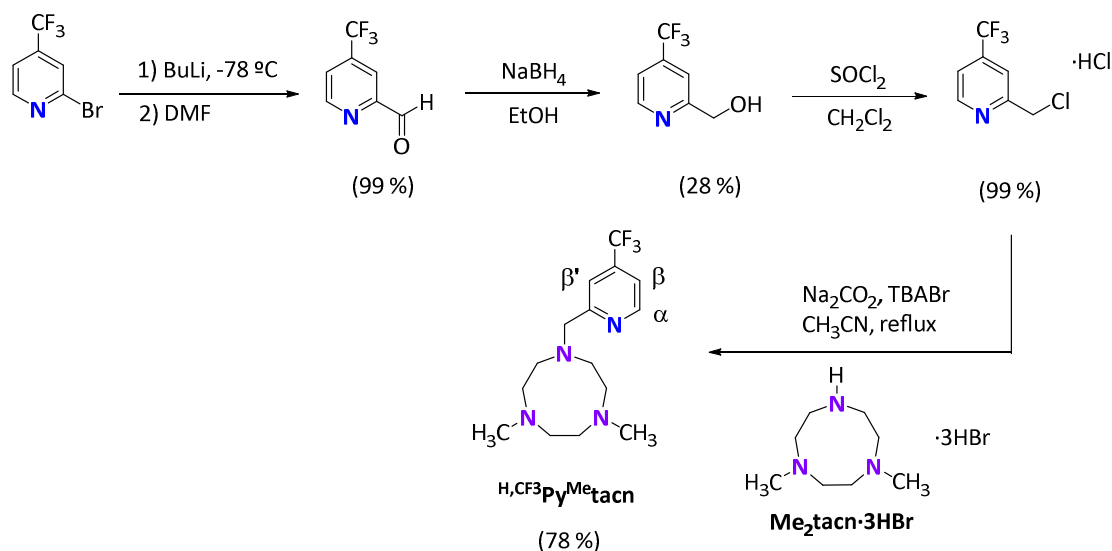
4-nitro-2-picoline N-oxide. To a mixture of 2-picoline N-oxide (13 g, 0.199 mols) and 18 M H₂SO₄ (45 mL) was added fuming HNO₃ (34.5 mL) dropwise at 0 °C. The resulting mixture was then heated to 105 °C and stirred for 2h. After cooling to room temperature, it was neutralized with Na₂CO₃ and extracted with CH₂Cl₂ several times. The combined organic extracts were dried over MgSO₄ and the volatile component was removed under vacuum to give 14.3 g (0.093 mol, 79%) of a pale yellow solid. ¹H-NMR (CDCl₃, 400 MHz, 300 K) δ, ppm: 8.32 (d, *J* = 7.6 Hz, H_α of py), 8.13 (d, *J* = 3.2 Hz, H_{β'} of py), 7.99 (dd, *J* = 7.6 Hz, *J*' = 3.2 Hz, H_β of py), 2.57 (s, 3H, CH₃). In agreement with that reported in the literature.³²⁶

4-nitro-pyridylmethanol. To a solution of 4-nitro-2-picoline N-oxide (8 g, 52 mmol) in CH₂Cl₂ (150 mL), a solution in trifluoroacetic anhydride (20 mL) in CH₂Cl₂ (40 mL) was added dropwise. After the red solution was stirred at room temperature for 3 days, the solvent was evaporated. MeOH (160 mL) and an aqueous saturated Na₂CO₃ solution (80 mL) were added and the mixture was stirred at room temperature 4 hours. Then, the mixture was concentrated under reduced pressure, and the organic compound was extracted with CH₂Cl₂ (4 x 50 mL). Combined organic layers were washed with brine solution (100 mL), dried over MgSO₄ and then the solvent removed under reduced pressure to lead the desired product as a yellow solid in 70% yield. (5.5 g, 34 mmol) was isolated. ¹H-NMR (CDCl₃, 400 MHz, 300 K) δ, ppm: 8.87 (d, *J* = 5.6 Hz, H_α of py), 8.08 (d, *J* = 1.6 Hz, H_{β'} of py), 7.95 (dd, *J* = 5.6 Hz, *J*' = 1.6 Hz, H_β of py), 4.94 (d, *J* = 5.2 Hz, 2H, CH₂), 3.17 (t, *J* = 5.2 Hz, OH). In agreement with that reported in the literature.³²⁶

4-nitro-2-chloromethylpyridine. A 100 mL flame dried round bottom flask was charged with 12 g of LiCl (0.28 mol) absolutely dried and 2 g of 4-nitro-pyridylmethanol (13 mmol). About 50 mL of THF was added under N₂ to obtain a pale yellow solution. Then, Et₃N (4.5 mL, 32.3 mmol) was added carefully and stirring always under N₂. Then, the mixture was cooled to 0 °C and MeSO₂Cl (3 mL, 39 mmol) was added dropwise at 0 °C. The reaction was stirred for 2 hours at 0 °C and then for 1 day at room temperature. The reaction was quenched by the addition of H₂O (15 mL) and neutralized using HCO₃⁻. The resulting solution was extracted 3 times with CH₂Cl₂. The combined organic layers were washed with a saturated NaCl solution, dried over MgSO₄, filtered and then the solvent removed under vacuum. The crude mixture was purified by column chromatography (CH₂Cl₂) to provide almost quantitative amount of the desired product (2.12 g, 12 mmol, 95%). ¹H-NMR (CDCl₃, 400 MHz, 300 K) δ, ppm: 8.88 (d, *J* = 5.6 Hz, H_α of py), 8.24 (d, *J* = 2 Hz, H_β of py), 7.98 (dd, *J* = 5.6 Hz, *J*' = 2 Hz, H_β of py), 4.80 (s, 2H, CH₂).

1,4-dimethyl-7-(4-nitro-2-pyridylmethyl)-1,4,7-triazacyclononane, ^{H,NO₂}Py^{Me}tacn. 4-nitro-2-chloromethylpyridine (0.431 g, 2.50 mmol), Me₂tacn-3HBr (1 g, 2.50 mmol) and anhydrous acetonitrile (40 mL) were mixed in a 100 mL flask. K₂CO₃ (1.90 g) and tetrabutylammonium bromide, TBABr (80 mg) were added directly as solids and the resulting mixture was heated at reflux under N₂ for 20 hours. After cooling to room temperature, the resulting red mixture was filtered and the filter cake was washed with CH₂Cl₂. The combined filtrates were evaporated under reduce pressure. To the resulting residue, 2 M NaOH (15 mL) was added and the mixture was extracted with CH₂Cl₂ (4 x 40 mL). The combined organic layers were dried over anhydrous MgSO₄ and the solvent was removed under reduced pressure. The resulting residue was treated with *n*-hexane (100 mL) and stirred for 12 hours. The mixture was filtered and the solvent from the red filtrates was removed under reduced pressure to yield 0.390 g of a red oil (1.33 mmol, 53 %). ¹H-NMR (CDCl₃, 400 MHz, 300 K) δ, ppm: 8.81 (d, *J* = 5.4 Hz, 1H, H_α of py), 8.41 (s, 1H, H_β of py), 7.87 (dd, *J* = 5.4 Hz, 1H, H_β of py), 4.00 (s, 2H, CH₂-py), 2.88-2.86 (m, 4H, N-CH₂-CH₂), 2.77 (s, 4H, N-CH₂-CH₂), 2.70-2.67 (m, 4H, N-CH₂-CH₂), 2.37 (s, 6H, N-CH₃).

IV.3.8.3. Synthesis of the ligand 1,4-dimethyl-7-(4-trifluoromethyl-2-pyridylmethyl)-1,4,7-triazacyclononane, ^{H,CF₃}Py^{Me}tacn.



Scheme IV. 4. Synthesis of ^{H,CF₃}Py^{Me}tacn ligand.

4-(trifluoromethyl)picolinaldehyde. To 2-bromo-4-(trifluoromethyl)pyridine (3.03 g, 13.42 mmol) in diethyl ether at -78 °C, BuLi (1.6 M in hexanes, 9.3 mL, 14.76 mmol) was added. After the addition a striking red colored solution was obtained. After 40 min, DMF (1.56 mL, 20.13 mmol) was added dropwise and the reaction mixture was stirred at -78 °C for a further 45 min. Then, the reaction mixture was allowed to come to RT over a period of 1 h. After that, the reaction was quenched with NH₄Cl and partitioned between water and ether. The organic layers were dried and evaporated to provide 4-(trifluoromethyl)picolinaldehyde (as a crude residue which was carried to the next step without further purification. ¹H-NMR (CDCl₃, 400 MHz, 300 °C) δ, ppm: 10.13 (s, 1H, CHO), 8.98 (d, *J* = 5.0 Hz, 1H, H_α of py), 8.16 (s, 1H, H_β of py), 7.75 (d, *J* = 5.0 Hz, 1H, H_β of py). In agreement with that reported in the literature.³⁶²

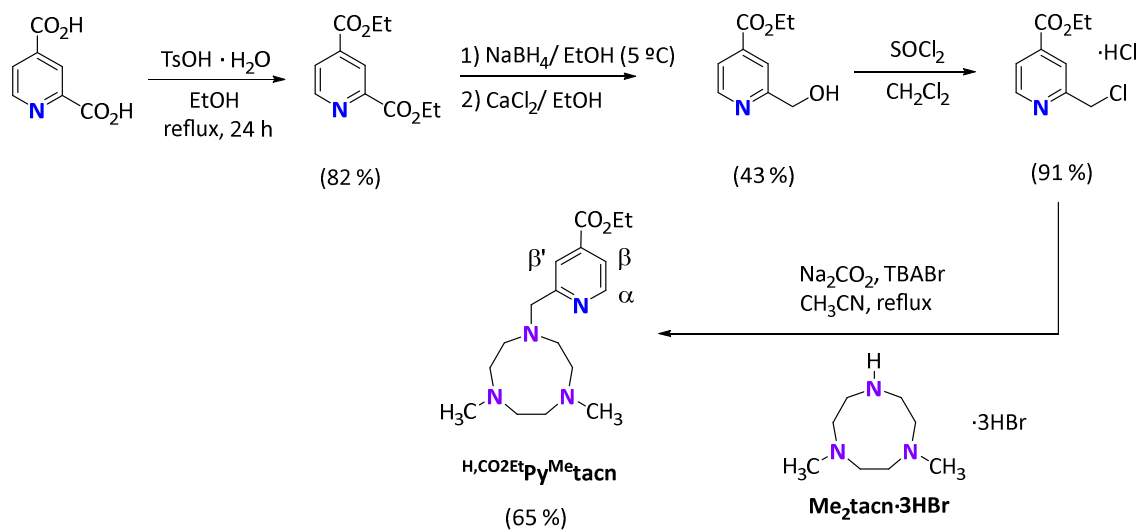
2-Hydroxymethyl-4-trifluoromethylpyridine. To a vigorously stirred solution of 4-(trifluoromethyl)picolinaldehyde (13.28 mmol) in EtOH (100 mL) at 0 °C was added dropwise NaBH₄ (0.553 g, 14.61 mmol, 1.1 eq.) dissolved in 20 mL of EtOH. After completing the addition of the reductant, the mixture was stirred for 2 hours at the same temperature and quenched with NH₄Cl. The organic solvent was removed by rotary evaporation giving a red oil. Then, saturated aqueous Na₂CO₃ solution (30 mL) was added and the product was extracted with CH₂Cl₂ (3 x 40 mL). The combined organic layers were dried over anhydrous MgSO₄ and the solvent was removed under reduced pressure. The resulting residue was purified by silica column chromatography with AcOEt/hexane (1:2) to give 0.660 g of 2-Hydroxymethyl-4-trifluoromethylpyridine as a

red oil (3.72 mmol, 28 %). ¹H-NMR (CDCl₃, 400 MHz, 300 K) δ, ppm: 8.70 (d, *J* = 5.0 Hz, 1H, H_α of py), 7.53 (s, 1H, H_β of py), 7.40 (d, *J* = 5.5 Hz, 1H, H_β of py), 4.83 (s, 2H, CH₂-py), 3.78 (s, br, 1H, OH). In agreement with that reported in the literature.³⁶²

2-chloromethyl-4-trifluoromethylpyridine hydrochloride. To a stirred solution of 2-Hydroxymethyl-4-trifluoromethylpyridine (0.660 g, 3.73 mmol) in CH₂Cl₂ (50 mL) was added SOCl₂ (1.4 mL, 18.63 mmol) slowly. After addition, the resulting mixture was stirred at RT overnight. The solvent was removed by bubbling N₂ into the crude mixture (gaseous HCl is formed during thus process and extreme cautions must be taken) and a pale brown solid was obtained. The crude product was suspended in 20 mL of diethyl ether and dried under vacuum. 0.856 g of a white solid was obtained (3.68 mmol, 99 %). ¹H-NMR (CDCl₃, 400 MHz, 300 K) δ, ppm: 8.84 (s, 1H, H_α of py), 8.00 (s, 1H, H_β of py), 7.76 (s, 1H, H_β of py), 5.00 (s, 2H, CH₂), 4.30 (s, 1H, OH). ESI-MS (*m/z*): 196.0 [M + H]⁺

1,4-dimethyl-7-(4-trifluoromethyl-2-pyridylmethyl)-1,4,7-triazacyclononane, H,CF₃Py^{Me}tacn. 2-chloromethyl-4-trifluoromethylpyridine hydrochloride (0.202 g, 0.871 mmol), Me₂tacn·3HBr (0.349 g, 0.871 mmol) and anhydrous acetonitrile (40 mL) were mixed in a 100 mL flask. Na₂CO₃ (0.6 g) and tetrabutylammonium bromide, TBABr (80 mg) were added directly as solids and the resulting mixture was heated at reflux under N₂ for 20 hours. After cooling to room temperature, the resulting red mixture was filtered and the filter cake was washed with CH₂Cl₂. The combined filtrates were evaporated under reduce pressure. To the resulting residue, 2 M NaOH (15 mL) was added and the mixture was extracted with CH₂Cl₂ (4 x 40 mL). The combined organic layers were dried over anhydrous MgSO₄ and the solvent was removed under reduced pressure. The resulting residue was treated with *n*-hexane (100 mL) and stirred for 12 hours. The mixture was filtered and the solvent from the red filtrates was removed under reduced pressure to yield 0.215 g of a yellow oil (0.68 mmol, 78 %). ¹H-NMR (CDCl₃, 400 MHz, 300 K) δ, ppm: 8.68 (d, *J* = 5.0 Hz, 1H, H_α of py), 7.86 (s, 1H, H_β of py), 7.34 (d, *J* = 5.0 Hz, 1H, H_β of py), 3.92 (s, 2H, CH₂-py), 2.83-2.81 (m, 8H, N-CH₂-CH₂), 2.74 (s, 6H, N-CH₃), 2.67-2.65 (m, 4H, N-CH₂-CH₂), 2.34 (s, 6H, N-CH₃). ESI-MS (*m/z*): 316.2 [M + H]⁺

IV.3.8.4. Synthesis of the ligand 1,4-dimethyl-7-(4-ethoxycarbonyl-2-pyridylmethyl)-1,4,7-triazacyclononane, ^{H,CO₂Et}Py^{Me}tacn.



Scheme IV. 5. Synthesis of ^{H,CO₂Et}Py^{Me}tacn. ligand.

The ^{H,CO₂Et}Py^{Me}tacnMe₂ ligand was synthesized according to the procedure described in the literature.³¹⁵

2,4-diethoxycarbonylpyridine. A solution of 2,4-pyridinedicarboxylic acid (5 g, 30 mmol) and *p*-toluenesulfonic acid monohydrate (14 g, 74 mmol) in ethanol (350 mL) was refluxed for 24 hours. After removing EtOH, CHCl₃ followed by saturated aqueous Na₂CO₃ (60 mL) were added and the mixture was extracted with CHCl₃ (4 times) and then dried over MgSO₄. By removing CHCl₃, 5.5 g of 2,4-diethoxycarbonylpyridine were obtained as a white solid (24.6 mmol, 82 %). ¹H-NMR (DMSO, 400 MHz, 300 K) δ, ppm: 8.92 (dd, *J* = 4.8 Hz, H_α of py), 8.33 (dd, *J* = 2.8 Hz, H_{β'} of py), 8.04 (dd, *J* = 4.8 Hz, H_β of py), 4.37 (q, *J* = 7.2 Hz, 4H, CO₂CH₂CH₃), 1.34 (t, *J* = 7.2 Hz, 6H, CO₂CH₂CH₃). In agreement with that reported in the literature.³⁶³

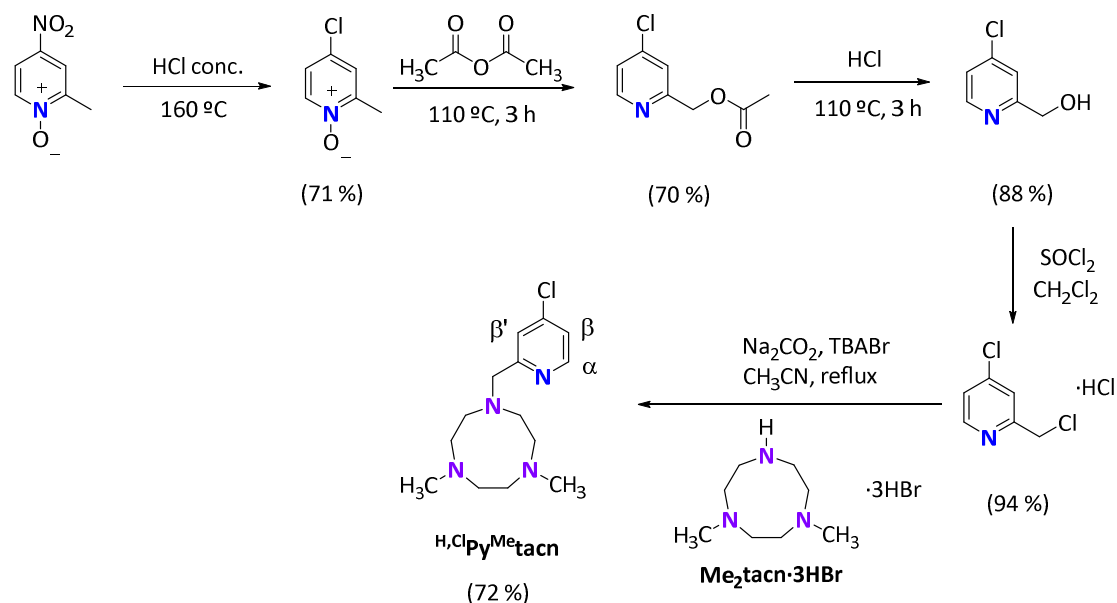
4-ethoxycarbonyl-2-hydroxymethylpyridine. A solution of CaCl₂ (2.8 g, 24.8 mmol) in EtOH at -5 to -10 °C was added dropwise with stirring to a degassed solution of 2,4-diethoxycarbonylpyridine (5.5 g, 24.5 mmol) and NaBH₄ (606 mg, 16 mmol) in EtOH (200 mL). After completing the addition of CaCl₂, the mixture was stirred for 2.5 hours at the same temperature and quenched with conc. H₂SO₄. Filtration to remove a white precipitate followed by removal of EtOH by rotary evaporator gave a white residue which was purified by silica column chromatography with AcOEt/hexane (8:1) to give 1.91 g of 4-ethoxycarbonyl-2-hydroxymethylpyridine as a white crystalline solid (10.5 mmol, 43 %). ¹H-NMR (CDCl₃, 400 MHz, 300 K) δ, ppm: 8.71 (d, *J* = 5.2 Hz, H_α of py), 7.83 (s, H_{β'} of py), 7.77 (dd, *J* = 5.2 Hz, H_β of py), 4.84 (d, *J* = 5.2 Hz, 2H, CH₂OH), 4.42 (q, *J* = 7.2 Hz, 2H, CO₂CH₂CH₃), 3.68 (t, *J* = 5.2 Hz, OH), 1.41 (t, *J* = 7.2 Hz, 3H, CO₂CH₂CH₃). In agreement with that reported in the literature.³⁶³

4-ethoxycarbonyl-2-chloromethylpyridine hydrochloride. SOCl₂ (4.08 g, 34.4 mmol) was added dropwise to an ice-cooled solution of 4-ethoxycarbonyl-2-hydroxymethylpyridine (1.90 g, 10.5 mmol) in CH₂Cl₂ anhydrous (35 mL) under N₂ with stirring. The mixture was stirred overnight at room temperature. After that, the CHCl₃ and the excess of SOCl₂ were removed by rotary evaporator to give a solid which was washed several times with Et₂O to yield 2.34 g of 4-ethoxycarbonyl-2-chloromethylpyridine hydrochloride as a white solid (9.91 mmol, 94 %). ¹H-NMR (CDCl₃, 400 MHz, 300 K) δ, ppm: 8.80 (d, *J* = 5.2 Hz, H_α of py), 8.45 (s, H_β of py), 8.24 (dd, *J* = 5.2 Hz, H_β of py), 5.14 (s, 2H, CH₂Cl), 4.52 (q, *J* = 7.2 Hz, 2H, CO₂CH₂CH₃), 1.46 (t, *J* = 7.2 Hz, 3H, CO₂CH₂CH₃). In agreement with that reported in the literature.³⁶³

1,4-dimethyl-7-(4-ethoxycarbonyl-2-pyridylmethyl)-1,4,7-triazacyclononane,

H₂CO₂EtPy^{Me}tacn. 4-ethoxycarbonyl-2-chloromethylpyridine hydrochloride (0.59 g, 2.50 mmol), Me₂tacn·3HBr (1 g, 2.50 mmol) and anhydrous acetonitrile (40 mL) were mixed in a 100 mL flask. Na₂CO₃ (1.90 g) and tetrabutylammonium bromide, TBABr (80 mg) were added directly as solids and the resulting mixture was heated at reflux under N₂ for 20 hours. After cooling to room temperature, the resulting yellow mixture was filtered and the filter cake was washed with CH₂Cl₂. The combined filtrates were evaporated under reduce pressure. To the resulting residue, 2 M NaOH (15 mL) was added and the mixture was extracted with CH₂Cl₂ (4 x 40 mL). The combined organic layers were dried over anhydrous MgSO₄ and the solvent was removed under reduced pressure. The resulting residue was treated with *n*-hexane (100 mL) and stirred for 12 hours. The mixture was filtered and the solvent from the yellow filtrates was removed under reduced pressure to yield 0.52 g of the pale yellow oil (1.62 mmol, 65 %). ¹H-NMR (CDCl₃, 400 MHz, 300 K) δ, ppm: 8.67 (d, *J* = 6.4 Hz, 1H, H_α of py), 8.06 (s, 1H, H_β of py), 7.70 (dd, *J* = 6.4 Hz, 1H, H_β of py), 4.41 (q, *J* = 9.6 Hz, 2H, CO₂CH₂CH₃), 3.91 (s, 2H, CH₂-py), 2.85-2.82 (m, 4H, N-CH₂-CH₂), 2.78 (s, 4H, N-CH₂-CH₂), 2.69-2.66 (m, 4H, N-CH₂-CH₂), 2.36 (s, 6H, N-CH₃), 1.41 (t, *J* = 9.6 Hz, 3H, CO₂CH₂CH₃).

IV.3.8.5. Synthesis of the ligand 1,4-dimethyl-7-(4-chloro-2-pyridylmethyl)-1,4,7-triazacyclononane, ^{H,Cl}Py^{Me}tacn.



Scheme IV. 6. Synthesis of ^{H,Cl}Py^{Me}tacn ligand.

The ^{H,Cl}Py^{Me}tacn ligand has been synthesized according to the procedure described in the literature.³¹⁹

4-chloro-2-picoline N-oxide. To 4-nitro-2-picolone N-oxide (10 g, 0.065 mol) in a pressure tube was added HCl conc. (50 mL). The solution was stirred at 160 °C for 24 h, the reaction mixture was cooled at RT and carefully neutralized with Na₂CO₃. The resulting aqueous solution was extracted with CH₂Cl₂ (3 x 30 mL). The combined organic layers were dried over MgSO₄ and the solvent was removed by rotary evaporation to obtain 6.59 g of a pale yellow solid (0.046 mol, 71%). ¹H-NMR (CDCl₃, 400 MHz, 300 K) δ, ppm: 8.17 (d, *J* = 6.0 Hz, H_α of py), 7.27 (d, *J* = 3.0 Hz, 1H, H_β of py), 7.15 (dd, *J* = 6.0 Hz, *J'* = 3.0 Hz, 1H, H_{β'} of py), 2.54 (s, 3H, CH₃). In agreement with that reported in the literature.³²⁶

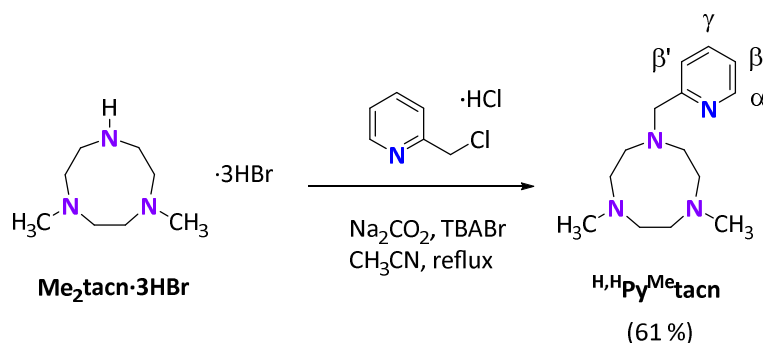
2-acetoxymethyl-4-chloropyridine. To 4-chloro-2-picoline N-oxide (6.5 g, 0.045 mmol) was added acetic anhydride (95 mL). The mixture was refluxed at 100 °C for 5 h. At this point a deep dark solution was observed. Then, the solution was cooled to RT and the volatile components were removed by using a high-vacuum rotary evaporator. Water (200 mL) was added to the remaining residue, and the resulting solution was neutralized with Na₂CO₃. After that, it was extracted with CH₂Cl₂ (3 x 30 mL). The combined organic layers were dried over MgSO₄ and the solvent was removed by rotary evaporation. The crude product was purified on silica gel using a mixture of CH₂Cl₂:MeOH (93:3), giving 5.84 g of a brown product (0.032 mol, 70%). ¹H-NMR (CDCl₃, 400 MHz, 300 K) δ, ppm: 8.49 (d, *J* = 6.0 Hz, 1H, H_α of py), 7.37 (d, *J* = 3.0 Hz, 1H, H_β of py), 7.26 (dd, *J* = 6.0 Hz, *J'* = 3.0 Hz, 1H, H_β of py), 5.21 (s, 2H, CH₂-O), 2.20 (s, 3H, CH₃). In agreement with that reported in the literature.³²⁶

2-hydroxymethyl-4-chloropyridine. To 2-acetoxymethyl-4-chloropyridine (3.5 g, 0.018 mmol) was added HCl 2 M (50 mL). After stirring at 80 °C for 3 h, the reaction mixture was cooled to RT and neutralized with Na₂CO₃. The resulting aqueous solution was extracted with CH₂Cl₂ (3 x 30 mL). The combined organic layers were dried over MgSO₄ and the solvent was removed by rotary evaporation to give a brown liquid. The crude product was purified on silica gel using a mixture of CH₂Cl₂:MeOH (95:5), giving 2.3 g of a white solid (0.015 mol, 85%). ¹H-NMR (CDCl₃, 400 MHz, 300 K) δ, ppm: 8.46 (d, *J* = 6.0 Hz, H_α of py), 7.32 (d, *J* = 3.0 Hz, 1H, H_{β'} of py), 7.23 (dd, *J* = 6.0 Hz, *J*' = 3.0 Hz, 1H, H_β of py), 4.76 (s, 2H, CH₂), 3.56 (s, br, 1H, OH). In agreement with that reported in the literature.³²⁶

2-chloromethyl-4-chloropyridine hydrochloride. To a stirred solution of 2-hydroxymethyl-2-chloropyridine (0.46 g, 3.16 mmol) in CH₂Cl₂ (50 mL) was added SOCl₂ (0.3 mL) slowly. After addition, the resulting mixture was stirred at RT overnight. The solvent was removed by bubbling N₂ into the crude mixture (gaseous HCl is formed during this process and extreme cautions must be taken) and a white solid was obtained. The crude product was suspended in 20 mL of diethyl ether and dried under vacuum. 0.48 g of a white solid was obtained (2.43 mmol, 77%). ¹H-NMR (CDCl₃, 400 MHz, 300 K) δ, ppm: 8.46 (d, *J* = 6.0 Hz, H_α of py), 7.52 (d, *J* = 3.0 Hz, 1H, H_{β'} of py), 7.27 (dd, *J* = 6.0 Hz, *J*' = 3.0 Hz, 1H, H_β of py), 4.66 (s, 2H, CH₂). In agreement with that reported in the literature.³²⁶

1,4-dimethyl-7-(4-chloro-2-pyridylmethyl)-1,4,7-triazacyclononane, H₂ClPy^{Me}tacn. 2-chloromethyl-4-chloropyridine hydrochloride (0.15 g, 0.75 mmol), Me₂tacn·3HBr (0.302 g, 0.75 mmol) and anhydrous acetonitrile (40 mL) were mixed in a 100 mL flask. K₂CO₃ (1.90 g) and tetrabutylammonium bromide, TBABr (80 mg) were added directly as solids and the resulting mixture was heated at reflux under N₂ for 20 hours. After cooling to room temperature, the resulting red mixture was filtered and the filter cake was washed with CH₂Cl₂. The combined filtrates were evaporated under reduced pressure. To the resulting residue, 2 M NaOH (15 mL) was added and the mixture was extracted with CH₂Cl₂ (4 x 40 mL). The combined organic layers were dried over anhydrous MgSO₄ and the solvent was removed under reduced pressure. The resulting residue was treated with *n*-hexane (100 mL) and stirred for 12 hours. The mixture was filtered and the solvent from the red filtrates was removed under reduced pressure to yield 0.152 g of a yellow oil (0.537 mmol, 72%). ¹H-NMR (CDCl₃, 400 MHz, 300 K) δ, ppm: 8.41 (dd, *J* = 5.4 Hz, *J*' = 0.5 Hz, 1H, H_α of py), 7.56 (d, *J* = 2.0 Hz, 1H, H_{β'} of py), 7.16 (dd, *J* = 5.5 Hz, *J*' = 2.1 Hz, 1H, H_β of py), 3.84 (s, 2H, CH₂-py), 2.84-2.82 (m, 4H, N-CH₂-CH₂), 2.75 (s, 4H, N-CH₂-CH₂), 2.68-2.65 (m, 4H, N-CH₂-CH₂), 2.36 (s, 6H, N-CH₃).

IV.3.8.6. Synthesis of the ligand 1,4-dimethyl-7-(2-pyridylmethyl)-1,4,7-triazacyclononane, ^{H,H}Py^{Me}tacn.

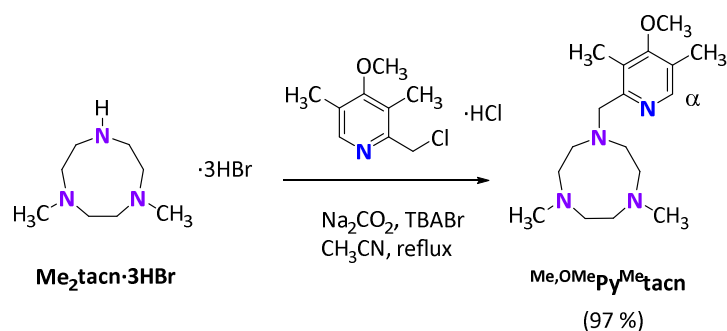


Scheme IV. 7. Synthesis of ^{H,H}Py^{Me}tacn ligand.

The ^{H,H}Py^{Me}tacn ligand has been synthesized according to the procedure described in the literature.³¹⁸

Commercially available 2-Picolyl chloride hydrochloride (0.43 g, 2.6 mmol), Me₂tacn·3HBr (1.02 g, 2.6 mmol) and anhydrous acetonitrile (40 mL) were mixed in a 100 mL flask. Na₂CO₃ (1.90 g) and tetrabutylammonium bromide, TBABr (80 mg) were added directly as solids and the resulting mixture was heated at reflux under N₂ for 20 hours. After cooling to room temperature, the resulting yellow mixture was filtered and the filter cake was washed with CH₂Cl₂. The combined filtrates were evaporated under reduce pressure. To the resulting residue, 2 M NaOH (15 mL) was added and the mixture was extracted with CH₂Cl₂ (4 x 40 mL). The combined organic layers were dried over anhydrous MgSO₄ and the solvent was removed under reduced pressure. The resulting residue was treated with *n*-hexane (100 mL) and stirred for 12 hours. The mixture was filtered and the solvent from the yellow filtrates was removed under reduced pressure to yield 0.39 g of a pale yellow oil (1.56 mmol, 61%). ¹H-NMR (CDCl₃, 400 MHz, 300 K) δ, ppm: 8.52 (d, *J* = 4.8 Hz, H_α of py), 7.66 (t, *J* = 7.8 Hz, 1H, H_{β'} of py), 7.48 (d, *J* = 7.8 Hz, 1H, H_β of py), 7.15 (m, 1H, H_γ of py), 3.85 (s, 2H, CH₂-py), 2.86-2.80 (m, 8H, N-CH₂-CH₂), 2.71-2.65 (m, 4H, N-CH₂-CH₂), 2.37 (s, 6H, N-CH₃).

IV.3.8.7. Synthesis of the ligand 1,4-dimethyl-7-(3,5-dimethyl-4-methoxy-2-pyridylmethyl)-1,4,7-triazacyclononane, *Me,OMePyMe*tacn.



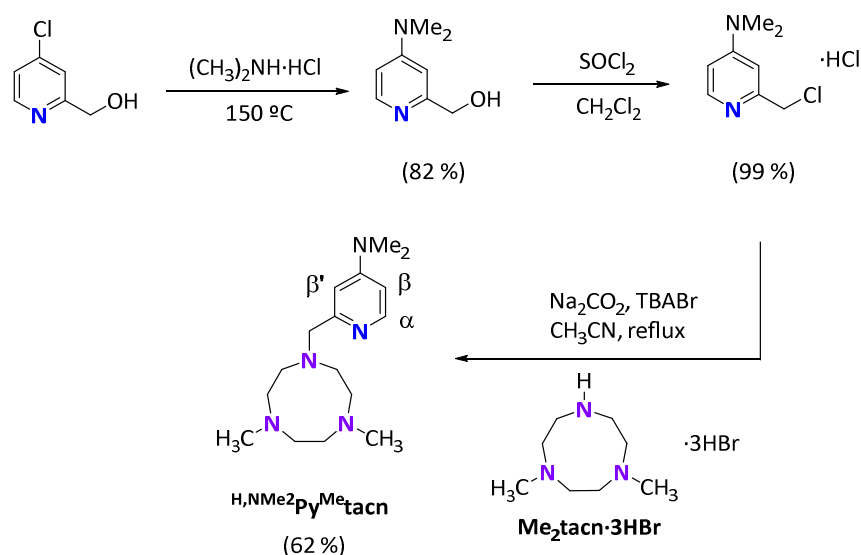
Scheme IV. 8. Synthesis of *Me,OMePyMe*tacn ligand.

The *Me,OMePyMe*tacn ligand has been synthesized according to the procedure described in the literature.³¹⁵

Commercially available (chloromethyl)-4-methoxy-3,5-dimethylpyridine (0.33 g, 1.5 mmol), *Me*₂tacn·3HBr (0.6 g, 1.5 mmol) and anhydrous acetonitrile (40 mL) were mixed in a 100 mL flask. Na₂CO₃ (1.3 g) and tetrabutylammonium bromide, TBABr (80 mg) were added directly as solids and the resulting mixture was heated at reflux under N₂ for 20 hours. After cooling to room temperature, the resulting yellow mixture was filtered and the filter cake was washed with CH₂Cl₂. The combined filtrates were evaporated under reduce pressure. To the resulting residue, 2 M NaOH (15 mL) was added and the mixture was extracted with CH₂Cl₂ (4 x 40 mL). The combined organic layers were dried over anhydrous MgSO₄ and the solvent was removed under reduced pressure. The resulting residue was treated with *n*-hexane (100 mL) and stirred for 12 hours. The mixture was filtered and the solvent from the yellow filtrates was removed under reduced pressure to yield 0.448 g of a pale yellow oil (0.146 mmol, 97%). ¹H-NMR (CDCl₃, 400 MHz, 300 K) δ, ppm: 8.15 (s, 1H, H_α of py), 3.77 (s, 3H, O-CH₃), 3.71 (s, 2H, CH₂-py), 2.82 -2.78 (m, 4H, N-CH₂-CH₂), 2.64 (s, 4H, N-CH₂-CH₂), 2.62 - 2.59 (m, 4H, N-CH₂-CH₂), 2.38 (s, 3H, py-CH₃), 2.31 (s, 6H, N-CH₃), 2.24 (s, 3H, py-CH₃).

IV.3.8.8. Synthesis of the ligand 1,4-dimethyl-7-(4-dimethylamino-2-pyridylmethyl)-1,4,7-triazacyclononane, *H,NMe2PyMe*tacn.

The *H,NMe2PyMe*tacn ligand has been synthesized according to the procedure described in the literature.³¹⁷



Scheme IV. 9. Synthesis of $\text{H,NMe}_2\text{PyMe tacn}$ ligand.

2-Hydroxymethyl-4-dimethylaminopyridine. To 2-hydroxymethyl-4-chloropyridine (2.3 g, 0.016 mol) in a pressure tube were added $(\text{CH}_3)_2\text{NH}\cdot\text{HCl}$ (6.5 g, 0.080 mmol), NaOH (3.0 g, 0.075 mmol), and water (10 mL). The resulting mixture was stirred and heated to 150 °C for 48 h and then cooled to RT, and water was removed by using a high-vacuum rotary evaporator. The remaining solid was extracted with CH_2Cl_2 (3 x 40 mL). The combined organic layers were dried over MgSO_4 , and the volatile components were removed by rotary evaporation to yield 2.0 g (82%) of a light brown solid. $^1\text{H-NMR}$ (CDCl_3 , 400 MHz, 300 K) δ , ppm: 8.12 (d, $J = 6.0$ Hz, 1H, H_α of py), 6.50 (s, 1H, $\text{H}_{\beta'}$ of py), 6.48 (m, 1H, H_β of py), 4.69 (s, 2H, CH_2), 4.44 (s, br, 1H, OH), 3.10 (s, 6H, $\text{N}(\text{CH}_3)_2$). In agreement with that reported in the literature.³²⁶

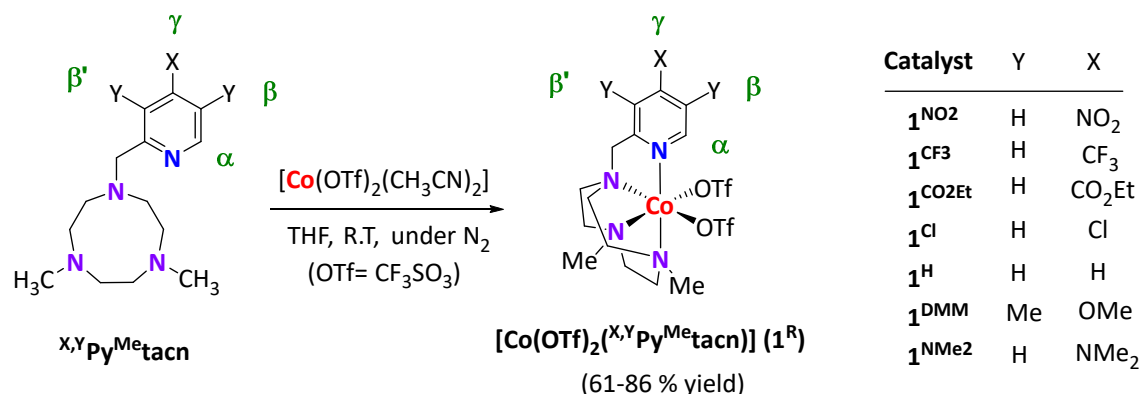
2-Chloromethyl-4-dimethylaminopyridine hydrochloride. To a stirred solution of 2-hydroxymethyl-4-dimethylamino-pyridine (2.7 g, 0.018 mmol) in CH_2Cl_2 (50 mL) was added SOCl_2 (2.8 g, 0.023 mmol) slowly. After addition, the resulting mixture was stirred at RT overnight. The solvent was removed by bubbling N_2 into the crude mixture (gaseous HCl is formed during this process and extreme cautions must be taken) and a pale brown solid was obtained. The crude product was suspended in 20 mL of diethyl ether and dried under vacuum. 3 g of a white solid was obtained (0.018 mmol, 99%). $^1\text{H-NMR}$ (CDCl_3 , 400 MHz, 300 K) δ , ppm: 8.19 (d, $J = 6.0$ Hz, H_α of py), 6.66 (d, $J = 3.0$ Hz, 1H, $\text{H}_{\beta'}$ of py), 6.44 (dd, $J = 6.0$ Hz, $J' = 3.0$ Hz, 1H, H_β of py), 4.56 (s, 2H, CH_2), 3.03 (s, 6H, $\text{N}(\text{CH}_3)_2$). In agreement with that reported in the literature.³²⁶

1,4-dimethyl-7-(4-dimethylamino-2-pyridylmethyl)-1,4,7-triazacyclononane, $\text{H,NMe}_2\text{PyMe tacn}$. 2-Chloromethyl-4-dimethylaminopyridine hydrochloride (0.26 g, 1.25 mmol), $\text{Me}_2\text{tacn}\cdot 3\text{HBr}$ (0.5 g, 1.25 mmol) and anhydrous acetonitrile (40 mL) were mixed in a 100 mL flask. K_2CO_3 (1 g) and tetrabutylammonium bromide, TBABr (80 mg) were

added directly as solids and the resulting mixture was heated at reflux under N₂ for 20 hours. After cooling to room temperature, the resulting red mixture was filtered and the filter cake was washed with CH₂Cl₂. The combined filtrates were evaporated under reduced pressure. To the resulting residue, 2 M NaOH (15 mL) was added and the mixture was extracted with CH₂Cl₂ (4 x 40 mL). The combined organic layers were dried over anhydrous MgSO₄ and the solvent was removed under reduced pressure. The resulting residue was treated with *n*-hexane (100 mL) and stirred for 12 hours. The mixture was filtered and the solvent from the red filtrates was removed under reduced pressure to yield 0.224 g of a red oil (0.77 mmol, 62%). ¹H-NMR (CDCl₃, 400 MHz, 300 K) δ, ppm: 8.13 (d, *J* = 6.0 Hz, 1H, H_α of py), 6.81 (d, *J* = 2.7 Hz, 1H, H_{β'} of py), 6.37 (dd, *J* = 6.0 Hz, *J*' = 2.7 Hz, 1H, H_β of py), 3.74 (s, 2H, CH₂-py), 3.00 (s, 6H, N(CH₃)₂), 2.82-2.79 (m, 8H, N-CH₂-CH₂), 2.70-2.68 (m, 4H, N-CH₂-CH₂), 2.36 (s, 6H, N-CH₃). In agreement with that reported in the literature.³¹⁷

IV.3.9. Synthesis of Complexes

1^R complexes were synthesized with the reaction of ^{X,Y}Py^{Me}tacn with one equivalent of [Co(OTf)₂(CH₃CN)₂]. We note the need to work under inert conditions (Glovebox, [O₂] < 1 ppm, [H₂O] < 1 ppm) due to their low stability in the presence of O₂.



Scheme IV. 10. General scheme of the synthesis of **1^R** complexes.

[Co(OTf)₂(^{H,H}Py^{Me}tacn)] (1^H**). In a glovebox, a suspension of [Co(OTf)₂(MeCN)₂] (442.05 mg, 1.00 mmol) in anhydrous THF (2 mL) was added dropwise to a vigorously stirred solution of ^{H,H}Py^{Me}tacn (250 mg, 1.00 mmol) in THF (2 mL). The cobalt triflate salt was quickly solubilized, and after few minutes, the solution became cloudy and a pale red precipitate appeared. After stirring for an additional 3h the solution was filtered off and the resulting solid was dried under vacuum. This solid was dissolved with CH₂Cl₂ and the slow diffusion of diethyl ether over the resultant solution afforded a red crystalline compound (518 mg, 0.85 mmol, 85% yield). ¹H-NMR (CD₃CN, 500 MHz, 298 K) δ, ppm: 222.94 (H_α), 186.37 (CH₂^{tacn}), 131.99 (CH₂^{tacn}), 103.24 (CH₂^{tacn}), 84.78 (H_β), 81.61 (N-CH₃), 60.87 (H_{β'}), 26.33 (H_γ), 21.67. ESI-MS (*m/z*): 456.0 [M - OTf]⁺,**

153.5 [M-2·OTf]²⁺. Anal. Calculated for C₁₆H₂₄CoF₆N₄O₆S₂: C, 31.74; N, 9.25; H, 4.00 %. Found: C, 31.75; N, 9.18; H, 4.08 %. UV/Vis (CH₃CN) λ_{max} (ε)= 256 (5500 M⁻¹·cm⁻¹).

[Co(OTf)₂(^{H,NMe2}Py^{Me}tacn) (1^{NMe2}). 1^{NMe2} was prepared in analogous manner to 1^H. A purple compound was obtained (150 mg, 83% yield). ¹H-NMR (CD₃CN, 500 MHz, 298 K) δ, ppm: 239.96 (H_α), 193.33 (CH₂^{tacn}), 127.14 (CH₂^{tacn}), 122.08 (CH₂^{tacn}), 94.04 (N-CH₃), 89.05 (H_β), 59.06 (H_β'), 28.19 (N(CH₃)₂), 18.34 (N(CH₃)₂), -13.95. ESI-MS (*m/z*): 499.1 [M - OTf]⁺, 175.0 [M-2·OTf]²⁺. Anal. Calculated for C₁₈H₂₉CoF₆N₅O₆S₂: C, 33.34; N, 10.80; H, 4.51 %. Found: C, 33.45; N, 10.95; H, 4.69 %. UV/Vis (CH₃CN) λ_{max} (ε)= 270 (17950 M⁻¹·cm⁻¹), 372 (1090 M⁻¹·cm⁻¹).

[Co(OTf)₂(^{Me,OMe}Py^{Me}tacn) (1^{DMM}). 1^{DMM} was prepared in analogous manner to 1^H. A red colored compound was obtained (310 mg, 86 % yield). ¹H-NMR (CD₃CN, 500 MHz, 298 K) δ, ppm: 230.57 (H_α), 183.60 (CH₂^{tacn}), 124.08 (CH₂^{tacn}), 109.97 (CH₂^{tacn}), 85.39 (N-CH₃), 25.63 (Me^{Py}), 20.14, 13.68 (Me^{Py}), 7.26 (OMe). ESI-MS (*m/z*): 514.1 [M - OTf]⁺, 182.5 [M-2·OTf]²⁺. Anal. Calculated for C₁₉H₃₀CoF₆N₄O₇S₂: C, 34.39; N, 8.44; H, 4.56 %. Found: C, 34.45; N, 8.40; H, 4.61 %. UV/Vis (CH₃CN) λ_{max} (ε)= 260 (5400 M⁻¹·cm⁻¹).

[Co(OTf)₂(^{H,Cl}Py^{Me}tacn) (1^{Cl}). 1^{Cl} was prepared in analogous manner to 1^H. A skin colored compound was obtained (120 mg, 70 % yield). ¹H-NMR (CD₃CN, 500 MHz, 298 K) δ, ppm: 221.87 (H_α), 190.03 (CH₂^{tacn}), 136.54 (CH₂^{tacn}), 102.29, 81.40 (N-CH₃), 80.10 (H_β), 56.51 (H_β'). ESI-MS (*m/z*): 490.0 [M - OTf]⁺, 170.5 [M-2·OTf]²⁺. Anal. Calculated for C₁₆H₂₃ClCoF₆N₄O₆S₂: C, 30.03; N, 8.76; H, 3.62 %. Found: C, 30.29; N, 8.54; H, 3.87 %. UV/Vis (CH₃CN) λ_{max} (ε)= 217 (13800 M⁻¹·cm⁻¹).

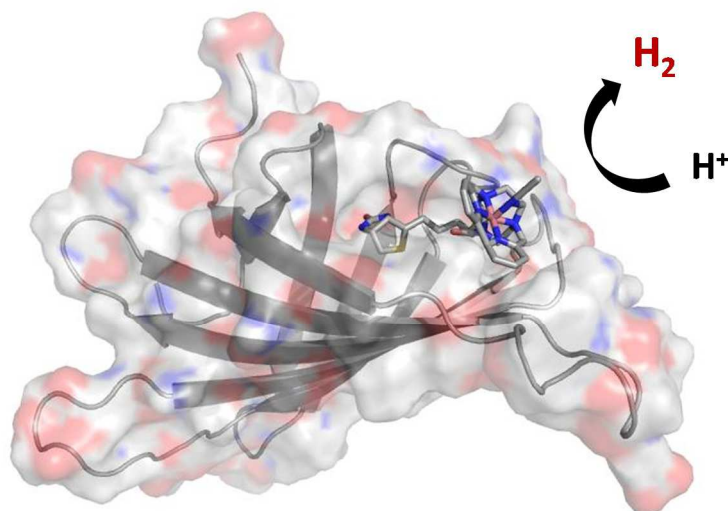
[Co(OTf)₂(^{H,CO2Et}Py^{Me}tacn) (1^{CO2Et}). 1^{CO2Et} was prepared in analogous manner to 1^H. An orange colored compound was obtained (213 mg, 82 % yield). ¹H-NMR (CD₃CN, 500 MHz, 298 K) δ, ppm: 215.30 (H_α), 184.89 (CH₂^{tacn}), 140.95 (CH₂^{tacn}), 135.63 (CH₂^{tacn}), 97.22, 80.16 (H_β + N-CH₃), 57.86 (H_β'), 20.82, 8.33 (CO₂CH₂CH₃), 4.54 (CO₂CH₂CH₃). ESI-MS (*m/z*): 528.1 [M - OTf]⁺, 189.5 [M-2·OTf]²⁺. Anal. Calculated for C₁₉H₂₈CoF₆N₄O₈S₂: C, 33.68; N, 8.27; H, 4.17 %. Found: C, 33.52; N, 8.15; H, 4.05 %. UV/Vis (CH₃CN) λ_{max} (ε)= 281 (6845 M⁻¹·cm⁻¹).

[Co(OTf)₂(^{H,CF3}Py^{Me}tacn) (1^{CF3}). 1^{CF3} was prepared in analogous manner to 1^H. A skin colored compound was obtained (105 mg, 61 % yield). ¹H-NMR (CD₃CN, 500 MHz, 298 K) δ, ppm: 213.42 (H_α), 186.17 (CH₂^{tacn}), 144.01 (CH₂^{tacn}), 139.20 (CH₂^{tacn}), 96.03, 78.82 (N-CH₃), 76.45 (H_β), 55.15 (H_β'), 20.80. ESI-MS (*m/z*): 524.1 [M - OTf]⁺, 187.5 [M-2·OTf]²⁺. Anal. Calculated for C₁₇H₂₃CoF₉N₄O₆S₂: C, 30.32; N, 8.32; H, 3.44 %. Found: C, 30.55; N, 8.08; H, 3.59%. UV/Vis (CH₃CN) λ_{max} (ε)= 268 (6250 M⁻¹·cm⁻¹).

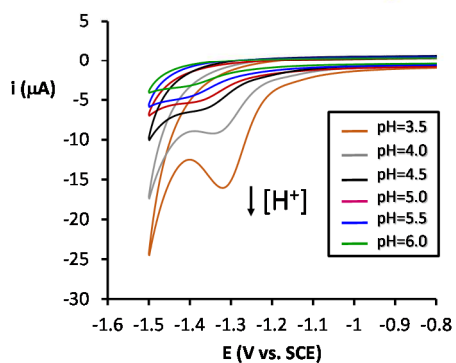
[Co(OTf)₂(^H,^{NO2}Py^{Me}tacn)] (1^{NO2}). 1^{NO2} was prepared in analogous manner to **1^H**. A skin colored compound was obtained (250 mg, 78 % yield). ¹H-NMR (CD₃CN, 500 MHz, 298 K) δ, ppm: 207.07 (**H_α**), 186.18 (CH₂^{tacn}), 147.39 (CH₂^{tacn}), 142.89 (CH₂^{tacn}), 93.60, 78.44 (N-CH₃), 73.74 (**H_β**), 53.56 (**H_{β'}**), 19.60. ESI-MS (*m/z*): 501.1 [M - OTf]⁺, 176.0 [M - 2·OTf]²⁺. Anal. Calculated for C₁₆H₂₃CoF₆N₅O₈S: C, 29.55; N, 10.77; H, 3.56 %. Found: C, 29.45; N, 10.98; H, 3.75 %. UV/Vis (CH₃CN) λ_{max} (ε) = 223 (16650 M⁻¹·cm⁻¹), 291 (5200 M⁻¹·cm⁻¹), 356 (2390 M⁻¹·cm⁻¹).

CHAPTER V

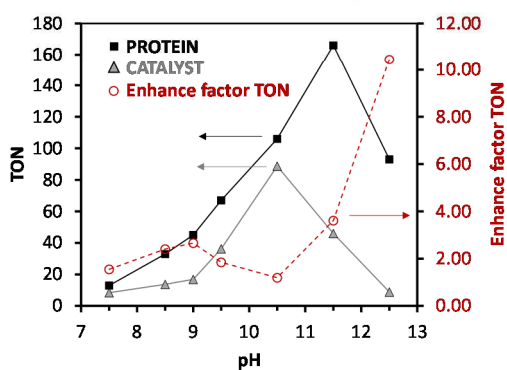
Improved Activity and Stability of a Cobalt Reduction Catalyst by Supramolecular Confinement in Streptavidin



Electrochemistry



Photochemistry



V. IMPROVED ACTIVITY AND STABILITY OF A COBALT REDUCTION CATALYST BY SUPRAMOLECULAR CONFINEMENT IN STREPTAVIDIN

V.1. STATE-OF-THE-ART

Streptavidin (SA) is a tetrameric protein (52.8 kDa) that has an extraordinary high affinity for biotin (also known as vitamin B7 or vitamin H). The binding of biotin to SA is one of the strongest non-covalent interactions known in nature (Dissociation constant (K_d) on the order of $\sim 10^{-14}$).³⁶⁴ The biotin-SA interaction has been exploited in biotechnological and biomaterial applications due to the unique strength of this noncovalent bonding. In addition, SA is extremely resistant to organic solvents, denaturants (e.g. guanidinium chloride or urea), and extreme values of temperature and pH.

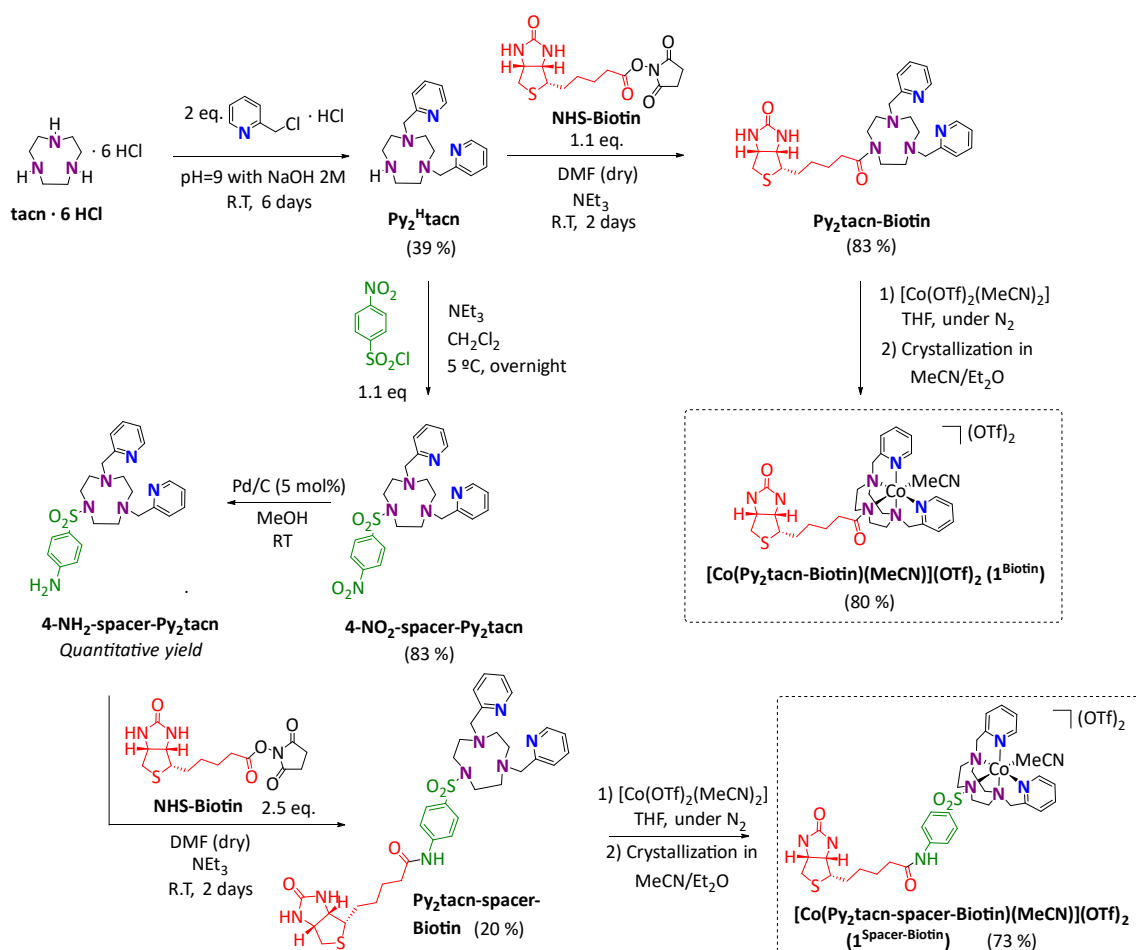
Taking advantage of these properties and based on the visionary initial report by Wilson and Whitesides in 1978,³⁶⁵ during the last years the potential of the biotin-SA technology has been exploited to create artificial metalloenzymes. Due to the high affinity of SA for biotin, a covalent link between biotin-catalyst ensures the quantitatively incorporation of the catalysts within the host protein. This straightforward methodology has been implemented in the development of enantioselective chemical transformations^{366,367} including hydrogenations,³⁶⁸⁻³⁷¹ alkylations,³⁷² sulfoxidations,³⁷³ olefin metathesis³⁷⁴ and cross-coupling reactions.³⁷⁵

Based on this promising methodology, the first aim of this Chapter is to proof the possibility of developing artificial metalloenzymes containing the cobalt catalysts developed in this Thesis. Our goal is to evaluate the effect in the catalytic outcome of the catalyst encapsulation in the enzyme cavity. To this end we focused our efforts in studying the activity of the complexes and the metalloenzymes in the electro and photochemical reduction of water to hydrogen.

V.2. RESULTS AND DISCUSSION

V.2.1. Synthesis of Ligands and Cobalt Complexes

First we designed two new cobalt complexes containing the biotin moiety linked to the aminopyridine ligand. The ligand framework is based on the pentadentate tacn ligand previously employed in the synthesis of complex **1_{Co}**. We developed two different strategies to introduce a biotin moiety covalently attached i) to one of the nitrogen atoms of the tacn backbone (ligand **Py₂tacn-Biotin**) or ii) to a moiety bonded to the free remaining amine mimicking the presence of a tosyl group, which also acts as a spacer between the biotin and the tacn backbone (ligand **Py₂tacn-spacer-Biotin**). Previous results reported by Thomas Ward stand out that the inclusion of a spacer provided an increase in the catalytic activity outcome.^{366,369}



Scheme V. 1. Synthesis of the biotinylated complexes **1^{Biotin}** and **1^{Spacer-Biotin}** employed in this work.

The synthesis of the biotin-functionalized ligand **Py₂tacn-Biotin** started with the preparation of the common precursor **Py₂Htacn**. This was prepared from a direct

dialkylation of the unprotected tacn structure (39 % yield). Following the general procedure described in the literature,³⁷⁶ biotinylation of the **Py₂^Htacn** structure using biotin *N*-hydroxysuccinimide active ester of D-biotin (NHS-biotin) gave rise to the Py₂tacn-Biotin ligand (**1^{Biotin}**) in good yield (80 % yield) (Scheme V. 1). On the other hand, the synthesis of the **Py₂tacn-spacer-Biotin** ligand starts with the incorporation of the phenylsulfonyl spacer moiety linked to the Py₂tacn skeleton. This was accomplished by the direct reaction of **Py₂^Htacn** with 4-nitrophenylsulfonyl chloride yielding the **4-NO₂-spacer-Py₂tacn** precursor (83 % yield). Hydrogenation of the NO₂ group to NH₂ was achieved using Pd/C in a quantitative yield (**4-NH₂-spacer-Py₂tacn**). Finally, direct biotinylation of this precursor with NHS-biotin generated the final desired **Py₂tacn-spacer-Biotin** ligand (73 % yield). Reaction of the ligands with one equivalent of [Co(OTf)₂(CH₃CN)₂] in THF at room temperature afforded the M^{II} five-coordinated complexes **[Co(Py₂tacn-Biotin)(MeCN)](OTf)₂** (**1^{Biotin}**) and **[Co(Py₂tacn-spacer-Biotin)(MeCN)](OTf)₂** (**1^{Spacer-Biotin}**) (Scheme V. 1).

In the case of the **Py₂tacn-Biotin** ligand the ¹H and ¹³C could be fully assigned using ¹H, ¹³C and bidimensional NMR techniques such as ¹H-¹H COSY and ¹H-¹³C HSQC. The full assignment of ¹H and ¹³C is depicted in the Figures V.1 -4.

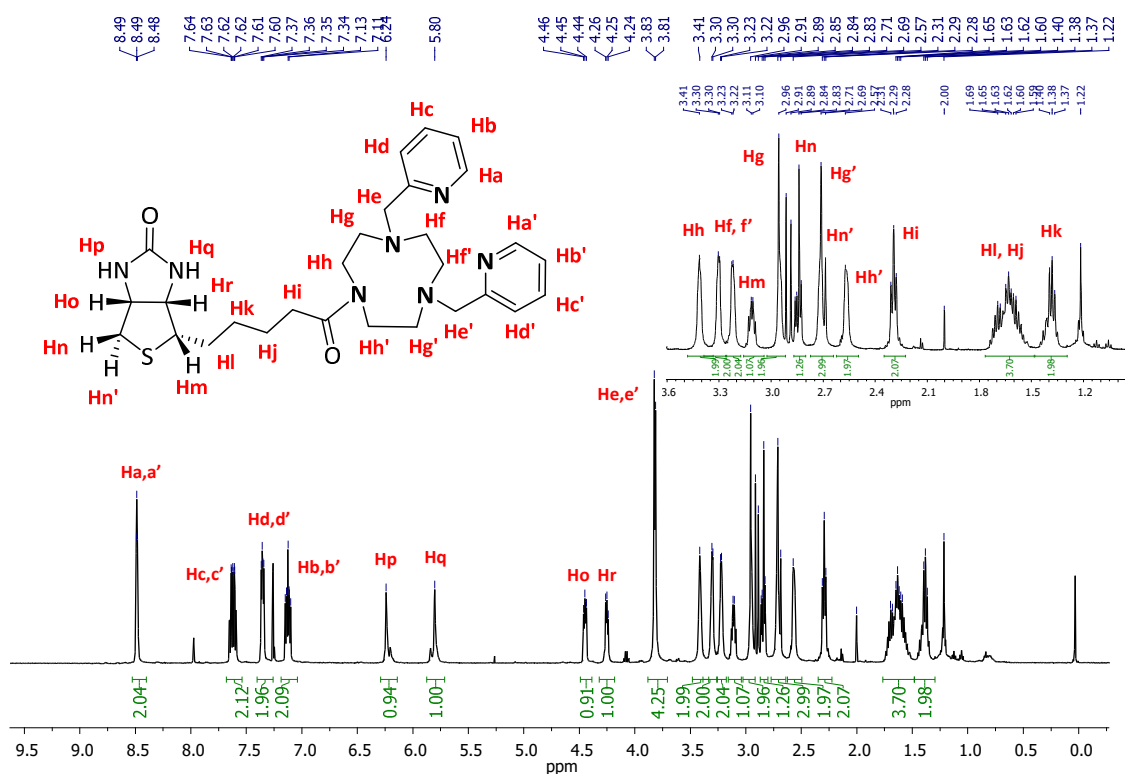


Figure V. 1. ¹H-NMR (CDCl₃, 500 MHz, 300 K) spectrum of **Py₂tacn-Biotin**.

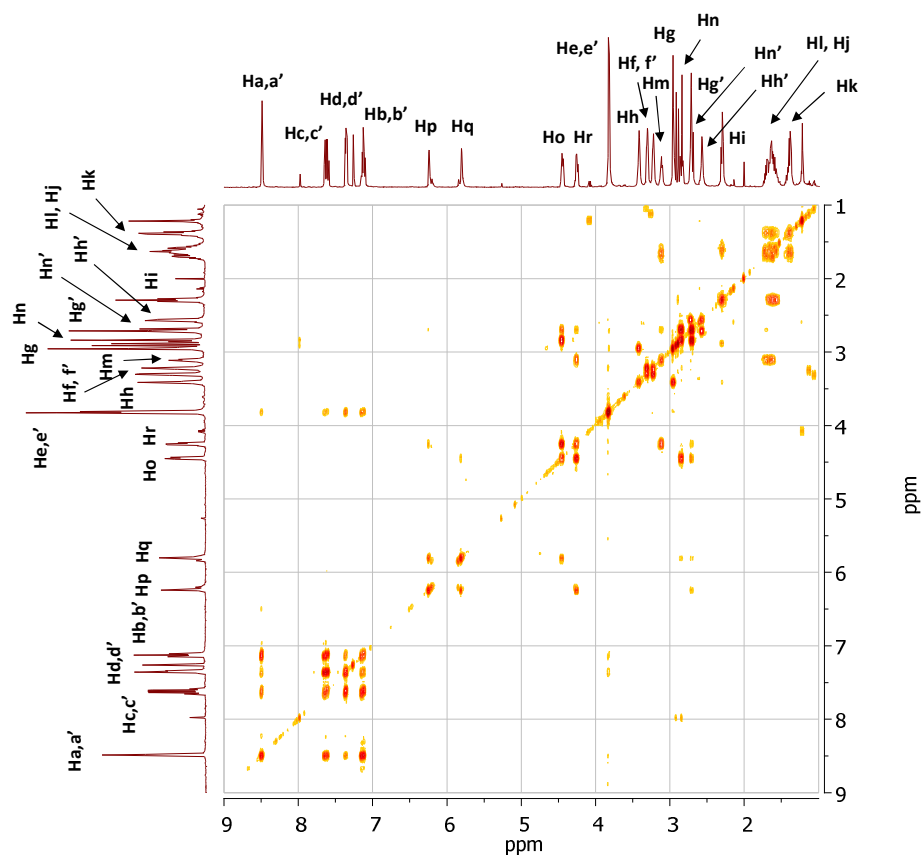


Figure V. 2. ^1H - ^1H COSY (CDCl_3 , 500 MHz, 300 K) spectrum of $\text{Py}_2\text{tacn-Biotin}$.

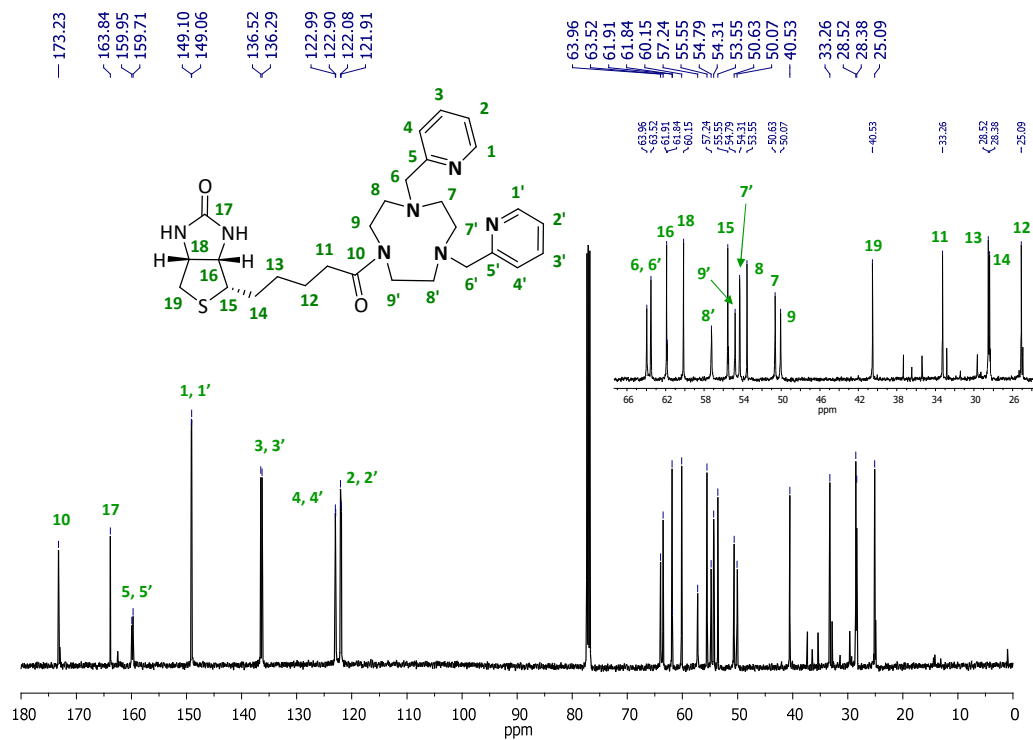


Figure V. 3. ^{13}C -NMR (CDCl_3 , 126 MHz, 300 K) spectrum of $\text{Py}_2\text{tacn-Biotin}$.

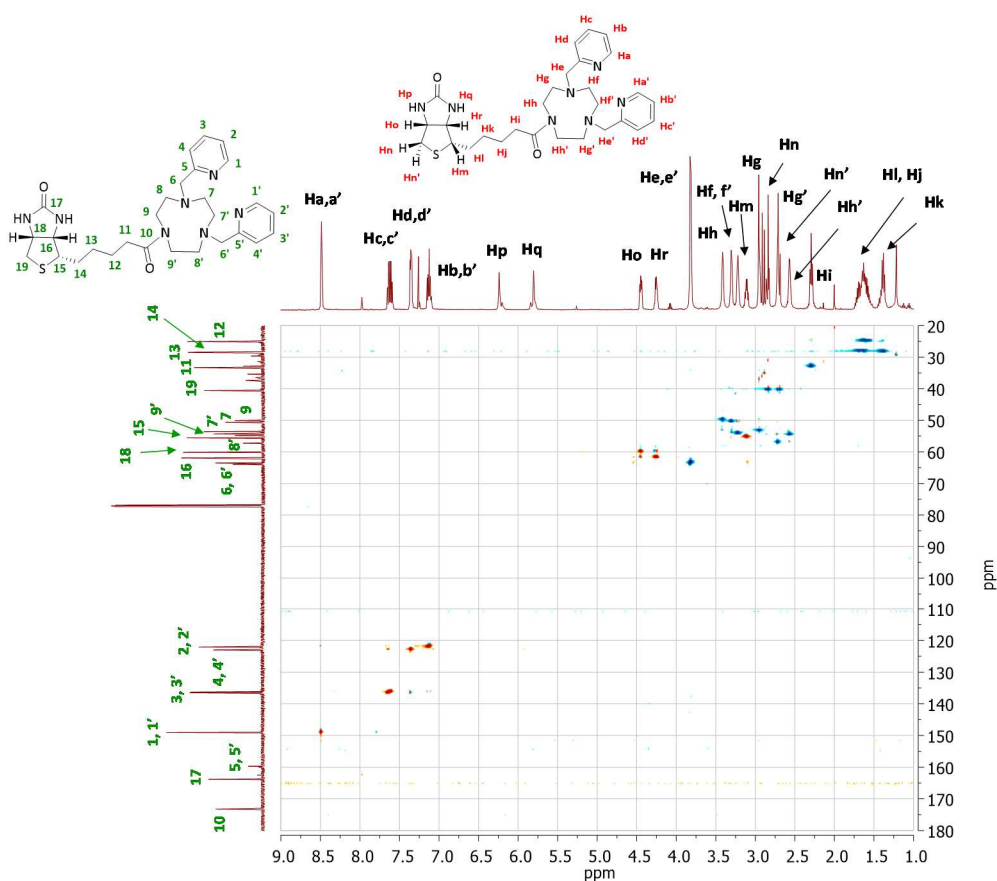


Figure V. 4. ^1H - ^{13}C HSQC (CDCl_3 , 126 MHz, 300 K) spectrum of **Py₂tacn-Biotin**.

V.2.2. Synthesis, Purification and Characterization of the **1^{Biotin}** C SA and **1^{Spacer-Biotin}** C SA metalloenzymes

V.2.2.1 Interaction of Streptavidin with **1^{Biotin}** and **1^{Spacer-Biotin}**

As previously proposed by Hofmann, the affinity of positively charged biotin derivatives for streptavidin and biotin is significantly lower than that of neutral biotin derivatives. This behavior is attributed to the repulsion between the positively charged protein host at neutral pH and the positively charged biotin-based guest compound.³⁷⁷ Taking into account the differences of the isoelectric points of streptavidin ($\text{pI} = 6.4$) and avidin ($\text{pI} = 10.4$), we rationalized that streptavidin as host protein could have a superior performance in the interaction with the cationic biotinylated cobalt catalysts **1^{Biotin}** and **1^{Spacer-Biotin}**. Therefore, we selected streptavidin as host protein for the incorporation of our designed cobalt complexes and determined the strength of the host-guest interaction of the **1^{Biotin}** C SA and **1^{Spacer-Biotin}** C SA pairs. As widely demonstrated in the literature there are four biotin-binding sites which are noncooperative.^{378,379} Therefore,

as shown below, assuming the noncooperative behavior, for the stability constant determination we have fit the data with a single binding constant.

The stability constant was determined using the well-established 2-(4'-hydroxyazobenzene)benzoic acid (HABA) displacement assay.³⁶⁹ This method has been widely used as a qualitative assay to evaluate biotinylated substrates. HABA binds to SA with lower affinity than Biotin, and consequently it can be stoichiometrically replaced by biotin in a titration experiment. The HABA \subset SA complex absorbs in the visible range, with a characteristic absorbance at 500 nm. The addition of the biotinylated compound causes the displacement of HABA inside the host protein, and thus it causes the loss of absorbance of the HABA \subset SA complex. The host protein was initially loaded with a large excess (50 molar excess) of in order to ensure the complete saturation of the binding sites of the biotin binding sites (eq. 1). The HABA displacement assay was carried out using 26 μ M of SA in 20 mM phosphate, 150 mM NaCl, pH 7.5 and saturated with 500 μ M HABA. After incubation at room temperature for 30 minutes, the resulting solution was used for spectrophotometric titration. From a stock solution of the biotinylated compound (0.40 mM) in DMSO, incremental amounts of compound were added to the HABA saturated SA, and the decrease of absorbance at 500 nm was monitored (DMSO was used to solubilize the biotinylated catalyst since it presents limited solubility in water). As depicted in Figure V. 5, the addition of the biotinylated complexes **1^{Biotin}** and **1^{Spacer-Biotin}** is followed by a concomitant decrease of the UV/Vis features of the HABA \subset SA complex, demonstrating the HABA displacement. From a qualitative point of view we can concluded that the association constant of the cobalt complexes is significantly higher than the HABA constant ($K_a = 3162 \text{ M}^{-1}$).

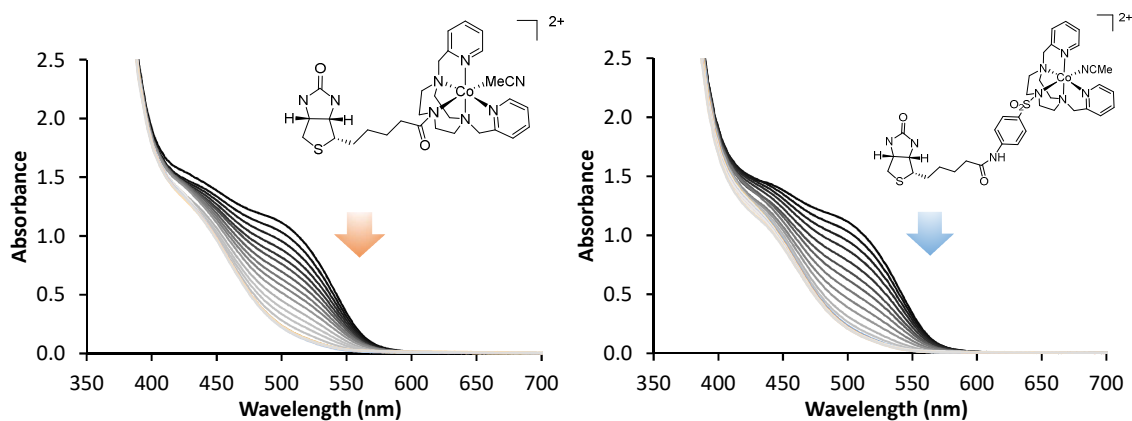


Figure V. 5. UV/Vis absorption decay of the HABA C SA complex upon the addition of different amounts of 1^{Biotin} (left) and $1^{\text{Spacer-Biotin}}$ (right). Conditions: 26 μM of SA in 20 mM phosphate, 150 mM NaCl, pH 7.5 and saturated with 500 μM HABA.

With a deeper analysis of the data we can estimate association constant for the displacement equilibrium depicted in Eq V. 2.



Considering the stability constant (K_{HABA}) of HABA C SA complex (Eq V. 3) reported in the literature ($\log K_{\text{HABA}} = 3.5$ ($R^2 = 0.997$))³⁸⁰ we have determined the stability constant of $[1^{\text{Biotin}}] \text{ C SA}$ ($K_{[1^{\text{Biotin}}] \text{ C SA}}$) according to Eq. V. 5.

$$K_{\text{HABA}} = \frac{[\text{HABA C SA}]}{[\text{HABA}] \times [\text{SA}]} \quad (\text{Eq. V. 3})$$

$$K_{\text{exch}} = \frac{[1^{\text{Biotin}} \text{ C SA}] \times [\text{HABA}]}{[\text{HABA C SA}] \times [1^{\text{Biotin}}]} \quad (\text{Eq. V. 4})$$

$$K_{[1^{\text{Biotin}}] \text{ C SA}} = \frac{[1^{\text{Biotin}} \text{ C SA}]}{[1^{\text{Biotin}}] \times [\text{SA}]} = K_{\text{HABA}} \times K_{\text{exch}} \quad (\text{Eq. V. 5})$$

The arrangement of Eq. V. 5 to the single quadratic Eq. V. 6 facilitates the calculation of the association constant, K_{exch} . All other variables $[\text{HABA}]_{\text{total}}$, $[\text{SA}]_{\text{total}}$ and $[1^{\text{Biotin}}]_{\text{total}}$ are known or can be calculated from the UV/VIS titration data $[\text{HABA C SA}]$.

$$(1 - K_{\text{exch}}) \times [\text{HABA C SA}]^2 \times (K_{\text{exch}} \times \{[\text{SA}]_{\text{total}} - [1^{\text{Biotin}}]\}) - ([\text{HABA}]_{\text{total}} - [\text{SA}]_{\text{total}}) \times [\text{HABA C SA}] + [\text{HABA}]_{\text{total}} - [\text{SA}]_{\text{total}} = 0 \quad (\text{Eq. V. 6})$$

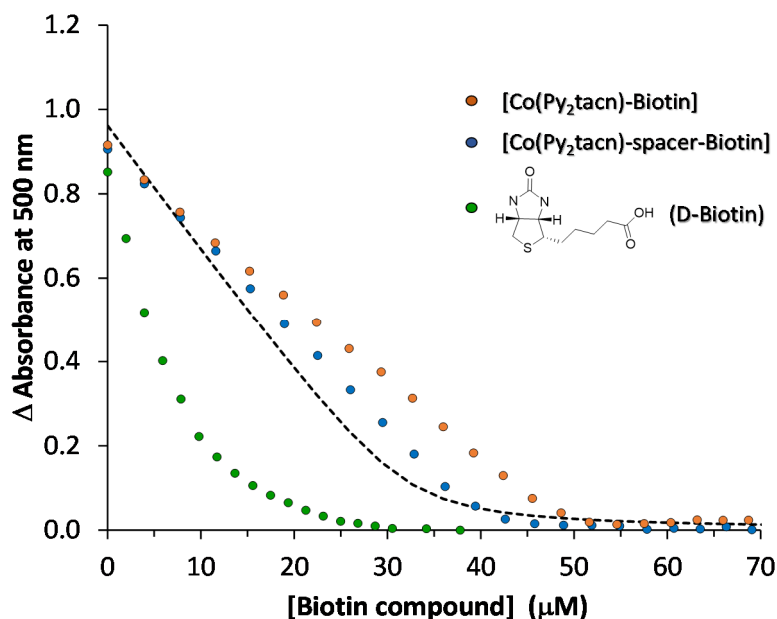


Figure V. 6. HABA displacement assay of streptavidin by **1^{Biotin}** (Orange dots) and **1^{Spacer-Biotin}** (Blue dots). Absorbance at 500 nm was monitored as a function of the biotinylated compound concentration. The titration with free D-Biotin has been included for comparative reasons. The dashed black trace is the theoretical fitted curve for the K_{exch} determination.

According to the quadratic equation to fit the K_{exch} parameter it can be used the minimum least-square of all of the data points $(\text{signal}_{\text{calculated}} - \text{signal}_{\text{measured}})^2$ and represent the theoretical titration curve. The calculated and the measured curves for HABA titrated with [**1^{Biotin}**] and [**1^{Spacer-Biotin}**] are depicted in Figure V. 6. Although the fitting is not perfect, the calculated K_{exch} can be used as an estimation. The obtained fitting of K_{exch} ($\log K_{\text{exch}} = 2.97$) lead to a stability constant $K_{[\text{1}^{\text{Biotin}}] \subset \text{SA}}$ of $2.95 \times 10^6 \text{ M}^{-1}$ ($\log K_{[\text{1}^{\text{Biotin}}] \subset \text{SA}} = 6.5$). Due to the fitting quality, very similar $K_{\text{catalyst} \subset \text{SA}}$ values were obtained for both cobalt-biotin catalysts and in the order of that reported in the literature for homogeneous biotinylated systems.³⁶⁹ However, from a qualitative point of view complex **1^{Spacer-Biotin}** is slightly less strongly attached to the pocket. These differences in affinity can be rationalized by the steric effects in the proximity of the biotin binding moiety.

Thus, the affinity for SA follows the order D-biotin > **1^{Spacer-Biotin}** > **1^{Biotin}**. The absence of a bulky group in the free D-biotin would explain its higher affinity for SA, compared to that obtained for **1^{Spacer-Biotin}** and **1^{Biotin}**. In contrast, **1^{Biotin}** catalyst presents

the lowest affinity for SA due to the steric effect imposed by the [Co(Py₂tacn)] unit near to the biotin moiety (Figure V. 7).

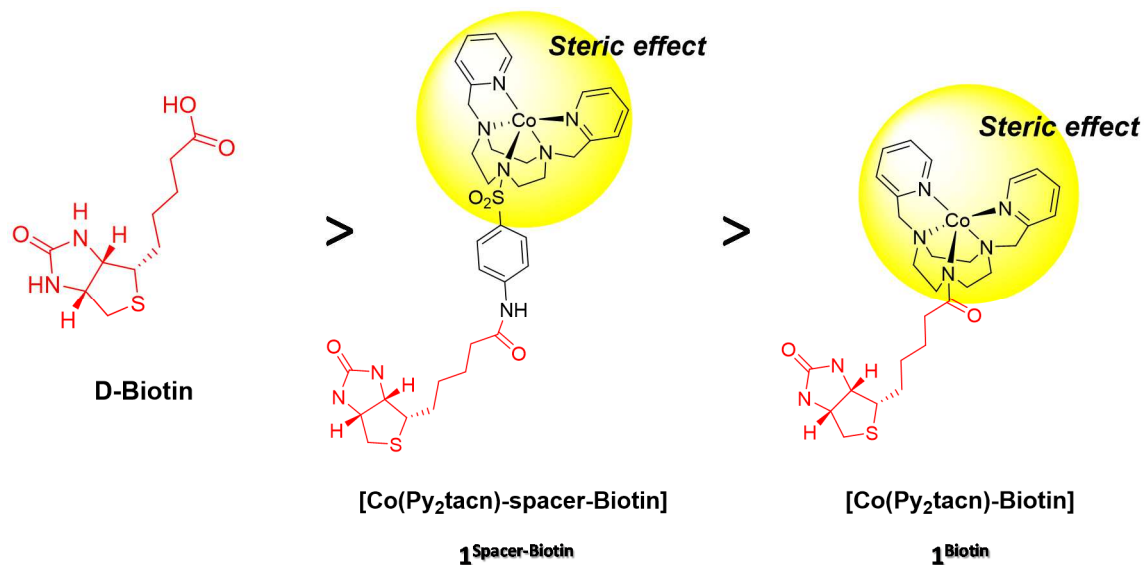


Figure V. 7. Differences in affinity with streptavidin measured by HABA titration.

According to the HABA titration experiments we can conclude that **1**^{Spacer-Biotin} and **1**^{Biotin} complexes are able to strongly and efficiently bind streptavidin as host protein. Owing to the remarkable affinity of biotin for streptavidin, the covalent linkage of the biotin anchored to the cobalt catalyst precursor ensures that the metal moiety is quantitatively incorporated within streptavidin. Therefore, we can develop cobalt-based artificial metalloenzymes by taking advantage of this biotin-streptavidin technology.³⁶⁶

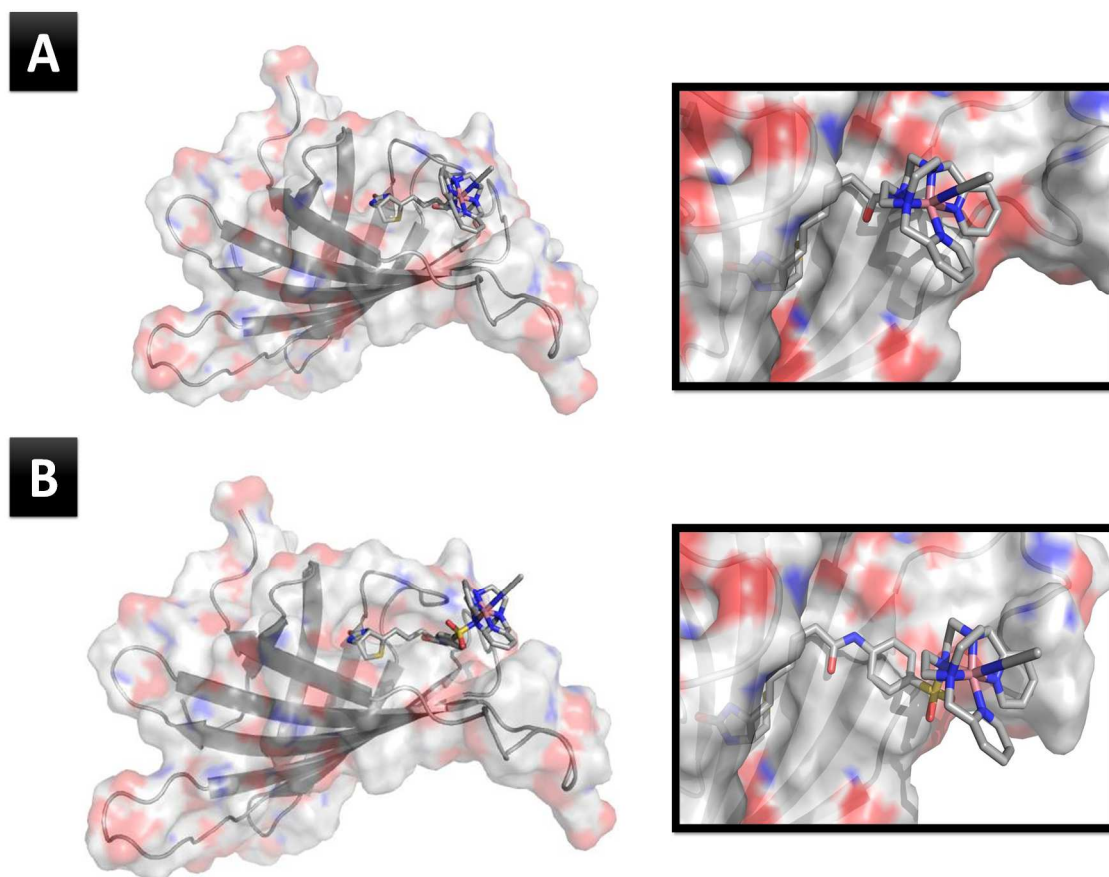


Figure V. 8. Computed models of the cobalt catalyst (1^{Biotin} (A), $1^{\text{Spacer-Biotin}}$ (B)) inside streptavidin (transparent surface).

V.2.2.2 Synthesis and Purification

Once we demonstrated that our biotinylated cobalt-based catalysts are able to strongly bind streptavidin, our next step was the synthesis of $1^{\text{Biotin}} \odot \text{SA}$ and $1^{\text{Spacer-Biotin}} \odot \text{SA}$ adducts by combining the corresponding cobalt catalyst with streptavidin. For the incorporation into streptavidin, a stock solution of 2 mg/mL of streptavidin in 100 mM Tris-HCl (pH 7.5) was incubated with 2- to 3-fold excess of biotin-cobalt catalyst. Because of the extremely high affinity of SA for biotin, SA-incorporated biotin-catalyst can be purified away from unbound Biotin-catalyst using a desalting P10-column. After 15 minutes of exposition, the resulting solution was passed through a PD10-desalting column (GE healthcare) previously equilibrated with the same buffer. The fractions from the column were collected as 1 mL fractions and analyzed by UV/Vis spectroscopy. The concentration of purified SA was determined spectrophotometrically using a molar

extinction coefficient of $41820 \text{ M}^{-1}\cdot\text{cm}^{-1}$ at 280 nm for SA.³⁸¹ The combined protein fractions gave rise to a stock solution of SA of around $20 \mu\text{M}$.

We determined the presence of cobalt in the purified solutions of **1^{Biotin}** ◯ SA and **1^{Spacer-Biotin}** ◯ SA by Inductively Coupled Plasma (ICP) spectrometry. We determined the concentration of cobalt from a well-known concentration of SA solution (0.0389 mg SA/mL , $7.33\cdot 10^{-4} \mu\text{mol SA/mL}$, determined by UV/Vis). From the cobalt concentration measured by ICP (0.0432 mg Co/L , $7.36\cdot 10^{-4} \mu\text{mol Co/mL}$) we could determine the stoichiometry SA:Co (1.005:1)

V.2.2.3 Characterization

In order to demonstrate the incorporation of the catalyst into the SA we also analyzed the purified solutions with different spectroscopic techniques.

Purified solutions **1^{Biotin}** ◯ SA and **1^{Spacer-Biotin}** ◯ SA show the same absorption features in the UV/Vis absorption spectrum, displaying the characteristic band of SA located at 280 nm ($\epsilon = 3.2 \text{ mg}\cdot\text{mL}^{-1}\cdot\text{cm}^{-1}$).³⁸² No additional absorption bands were observed attributed to the free cobalt catalyst, since free **1^{Biotin}** and **1^{Spacer-Biotin}** present minor absorbance in the same region (Figure V. 9, right).

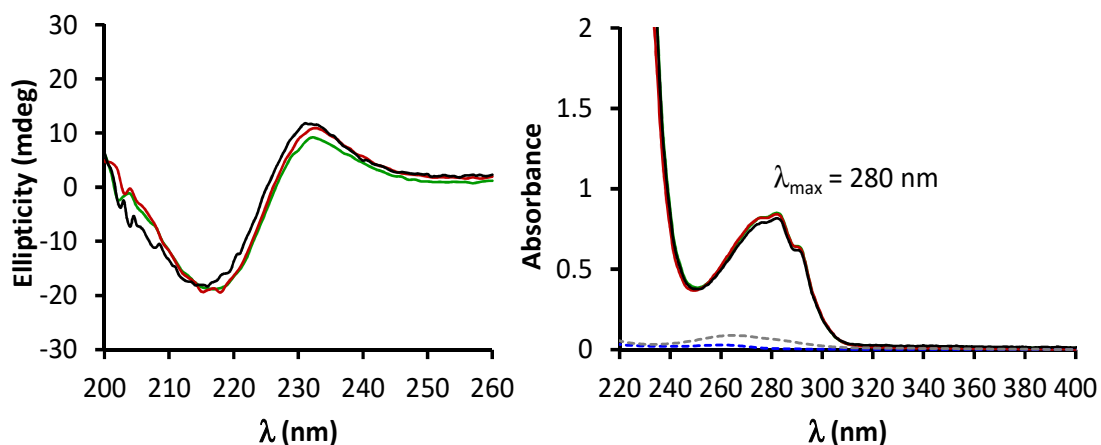


Figure V. 9. *Left:* CD spectra of SA (Black trace), **1^{Biotin}** (red trace) and **1^{Spacer-Biotin}** (green trace). Conditions: $5 \mu\text{M}$ protein, 100 mM Tris-HCl buffer, pH 7.5 at $20 \text{ }^\circ\text{C}$. *Right:* UV/Vis spectra of $5 \mu\text{M}$ solution of SA (solid black trace), **1^{Biotin}** (solid red trace) and **1^{Spacer-Biotin}** (solid green trace) measured in 100 mM Tris-HCl buffer, pH 7.5 at $20 \text{ }^\circ\text{C}$. The absorption of **1^{Biotin}** (dashed blue trace) and **1^{Spacer-Biotin}** (dashed grey trace) are included for comparative reasons

Circular dichroism (CD) spectroscopy helps us to evaluate the secondary structure of each protein.³⁸³ The spectra of **1**^{Biotin} C SA and **1**^{Spacer-Biotin} C SA recorded at 4°C are dominated by a minimum and maximum located at 217 and 233 nm, respectively. These values are slightly different from the ones obtained with streptavidin alone (215 and 232 nm) (Figure V. 9, left). These little change in the CD signal could be attributed to the binding event with the biotinylated catalyst. Indeed, it is well known that (according to the lock-and-key principle) streptavidin undergoes subtle structural changes upon biotin binding. In particular, the loop L-3,4 (between β -sheet 3 and β -sheet 4) becomes ordered upon binding and, thus, locking biotin in the binding site. This critical loop contains nine residues (36-44).³⁸⁴ The data provided by CD analysis does not clearly confirm the incorporation of the cobalt catalyst into SA, but assuming the binding, it seems that the secondary structure of the protein is not significantly modified by the presence of the catalyst.

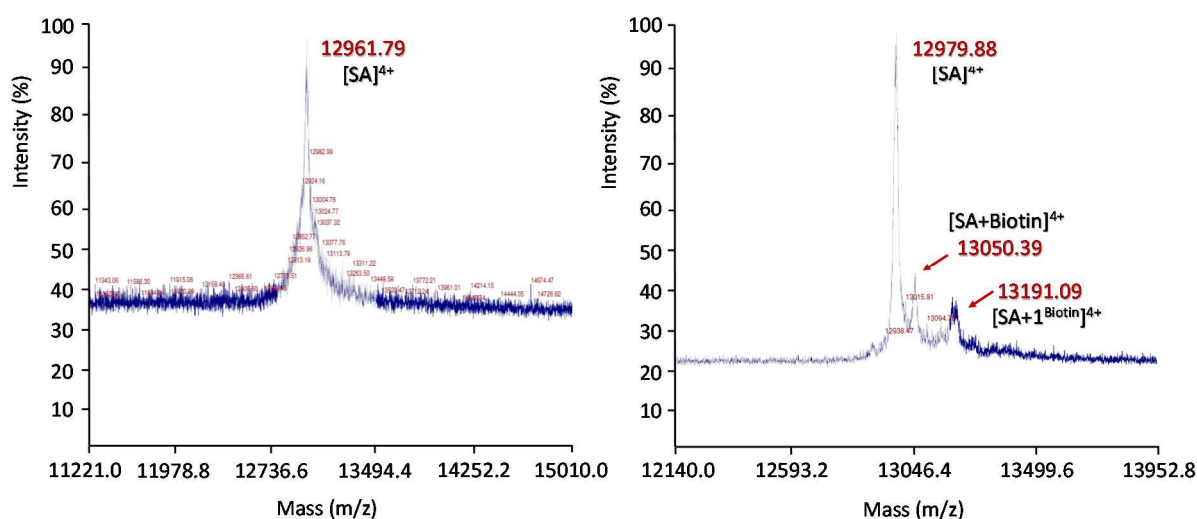


Figure V. 10. Positive MALDI-TOF spectra of SA (left) and **1**^{Biotin} C SA (right). Spectra were obtained by mixing directly on the target 1 μ L of the SA solution (from 20 μ M stock solution) with 1 μ L of the matrix (sinapinic acid, $5 \cdot 10^{-2}$ M in acetonitrile/H₂O, 4:1 v/v).

Using Matrix-assisted laser desorption ionization time-of-flight spectrometry (MALDI-TOFMS) we could verify the presence of the catalyst **1**^{Biotin} in the SA.³⁸⁵ As depicted in Figure V. 10 the MALDI-TOF of SA alone shows a mass distribution peak centered at 12961.79 Da corresponding to the monomer unit ($[SA]^{4+}$). However, the MALDI-TOF spectrum of **1**^{Biotin} C SA shows the most abundant ion peak of $[SA]^{4+}$ (12979.88 Da) together with the presence of two additional peaks at 13050.39 Da and 13191.09 Da corresponding to the four charged fragments of $[SA+Biotin]^{4+}$ and

$[\text{SA}+\mathbf{1}^{\text{Biotin}}]^{4+}$, respectively (Figure V. 10). The presence of the peak attributed to $[\text{SA}+\mathbf{1}^{\text{Biotin}}]^{4+}$ is a clear evidence that the biotinylated cobalt catalyst is attached to the host protein. The appearance of the $[\text{SA}+\text{Biotin}]^{4+}$ and $[\text{SA}]^{4+}$ peaks in the mass spectrum of a pure solution of $\mathbf{1}^{\text{Biotin}} \subset \text{SA}$ adduct is mainly attributed to the fragmentation process during the MALDI-TOF measurement.

Single crystals were obtained from a metalloenzyme stock solution of 26 mg/mL and using a *well solution* containing MgCl_2 (1M), polyethylene glycol (PEG, 60 %), and Tris-HCl (1 M, pH 8.5). The solution of protein (2 μL) was mixed with the *well solution* (2 μL) and it was crystallized by changing the concentration of the reagents contained in the *well solution*. Those single crystals have not been diffracted yet but they will be measured in a near future. Nevertheless, the single crystals proceeding from the purified from 20 μM stock solutions of $\mathbf{1}^{\text{Biotin}} \subset \text{SA}$ and $\mathbf{1}^{\text{Spacer-Biotin}} \subset \text{SA}$ suggest that they are protein crystals (Figure V. 11).

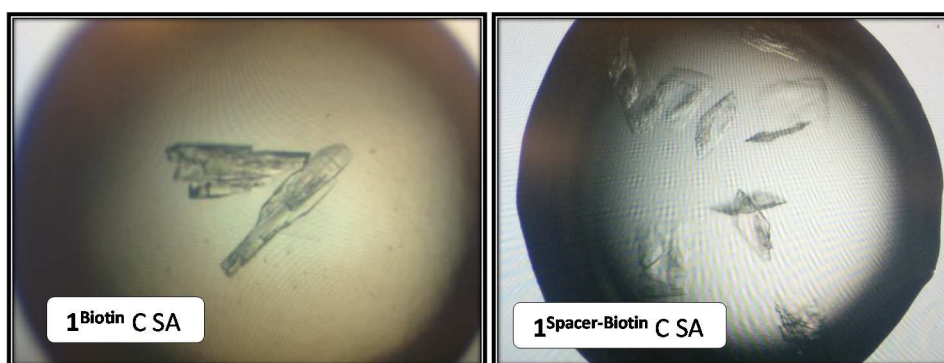


Figure V. 11.. Single crystals obtained of $\mathbf{1}^{\text{Biotin}} \subset \text{SA}$ and $\mathbf{1}^{\text{Spacer-Biotin}} \subset \text{SA}$.

V.2.3. Electrocatalytic Water Reduction to Hydrogen

In order to test the catalytic activity of the developed cobalt complex **1** SA metalloenzymes, we initially investigated the capacity of the biotinylated cobalt complexes **1**^{Biotin} and **1**^{Spacer-Biotin} in the electrochemical reduction of protons to hydrogen by cyclic voltammetry (CV). The pH range of study is from 3.5 to 6 with a 100 mM citrate buffer and 100 mM NaCl as electrolyte. Due to the low solubility of the biotinylated complexes in water, a stock solution of the catalyst in DMSO was added to the aqueous solution. We initially measured the CV of **1**^{Biotin} at pH 3.5 and we observed an irreversible peak at -1.36 V vs. SCE (Figure V. 12, A, orange trace) that is consistent with a catalytic process. Indeed, this rise of current is related with the evolution of bubbles over the electrode surface, presumably H₂.¹¹⁸ When the cathodic scan was performed in the absence of **1**^{Biotin}, the observed current was negligible at this redox potentials.

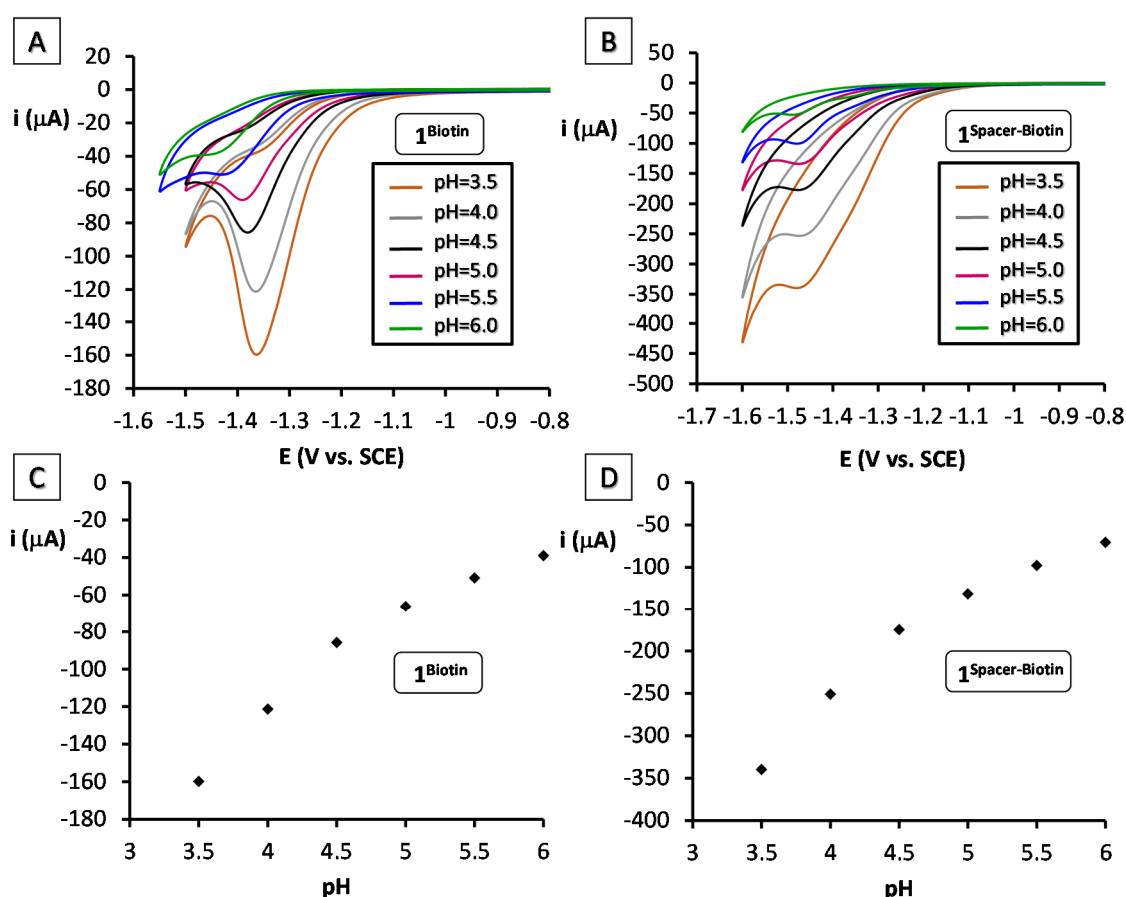


Figure V. 12. Successive cyclic voltammograms of 1 mM cobalt catalysts **1**^{Biotin} (A) and **1**^{Spacer-Biotin} (B) in 100 mM citrate buffer, 100 mM NaCl, at pH in the 3.5 to 6.0 range. Scan rate of 100 mV·s⁻¹ using a 0.28 cm² glassy carbon working electrode. Potentials are quoted versus SCE. C) Maximum peak intensity values versus the pH value in the case of **1**^{Biotin}. D) Maximum peak intensity values versus the pH value in the case of **1**^{Spacer-Biotin}.

Therefore, the electrocatalytic wave for proton reduction can be mainly attributed to the activity of $\mathbf{1}^{\text{Biotin}}$. Complex $\mathbf{1}^{\text{Biotin}}$ exhibits an onset of proton reduction at about -1 V at pH 3.5, which corresponds to an overpotential of 0.55 V,³⁸⁶ considering that -0.45 V vs. SCE is the thermodynamic potential for H₂ evolution at this pH.³⁸⁷ Complex $\mathbf{1}^{\text{Spacer-Biotin}}$ shows a higher onset potential (about -1.1 V at pH 3.5) with the maximum peak intensity shifted to a more negative potential (-1.47 V vs. SCE).

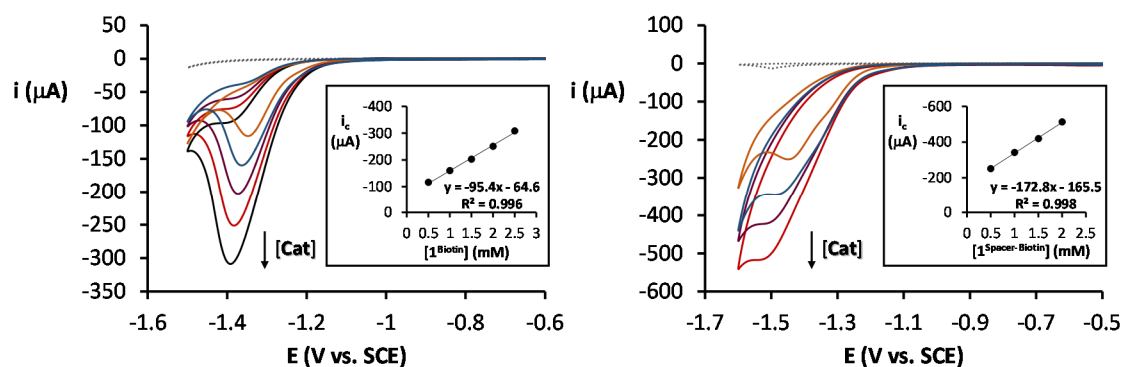


Figure V. 13. Successive CVs at increasing concentrations $\mathbf{1}^{\text{Biotin}}$ (left) and $\mathbf{1}^{\text{Spacer-Biotin}}$ (right). Conditions: 100 mM citrate buffer, 100 mM NaCl, at pH 3.5 using different catalyst concentrations: 0 mM (dashed grey) 0.5 mM (orange), 1 mM (blue), 1.5 mM (purple), 2 mM (red) and 2.5 mM (black). Scan rate of 100 mV·s⁻¹ using a 0.28 cm² glassy carbon working electrode. Potentials are quoted versus SCE. *Inset:* Electrocatalytic current (i_c) versus [Catalyst] showing a first order kinetics.

Analyzing with more detail the behavior of $\mathbf{1}^{\text{Biotin}}$ and $\mathbf{1}^{\text{Spacer-Biotin}}$ under electrocatalytic conditions, we observed that it displays a strong pH dependence. On the one hand, the electrocatalytic peak current (i_c) systematically increases as proton concentration increases (Figure V. 12, C and D). These results are consistent with an electrocatalytic proton reduction to H₂, which strongly depends on the proton concentration.^{86,99,115,388} On the other hand, both the onset and peak potential for proton reduction (E_p) were observed to shift to less negative potentials when increasing the proton concentration. The linear fit of the experimental pH dependence follows the standard form of the Nernst equation for PCET reactions.^{49,389,390} The catalytic peak potential of $\mathbf{1}^{\text{Biotin}}$ exhibited a Nernstian response in E_p of -0.036 V per pH unit. This is close to a -30 mV per pH dependence consistent with a 2 electron and 1 proton reduction process (Figure V. 15, right). This value is qualitatively similar to the -26 mV per pH unit reported for the Co(Py5) system⁹⁹ or to the -24 mV per pH unit observed in

cobalt diamine systems.⁸⁶ In the case of $\mathbf{1}^{\text{Spacer-Biotin}}$, there is a slight trend in E_p as a function of pH, along with an insignificant change of the onset magnitude. This suggests that there is no protonation event coupled to the reduction of Co^{II} to Co^{I} .

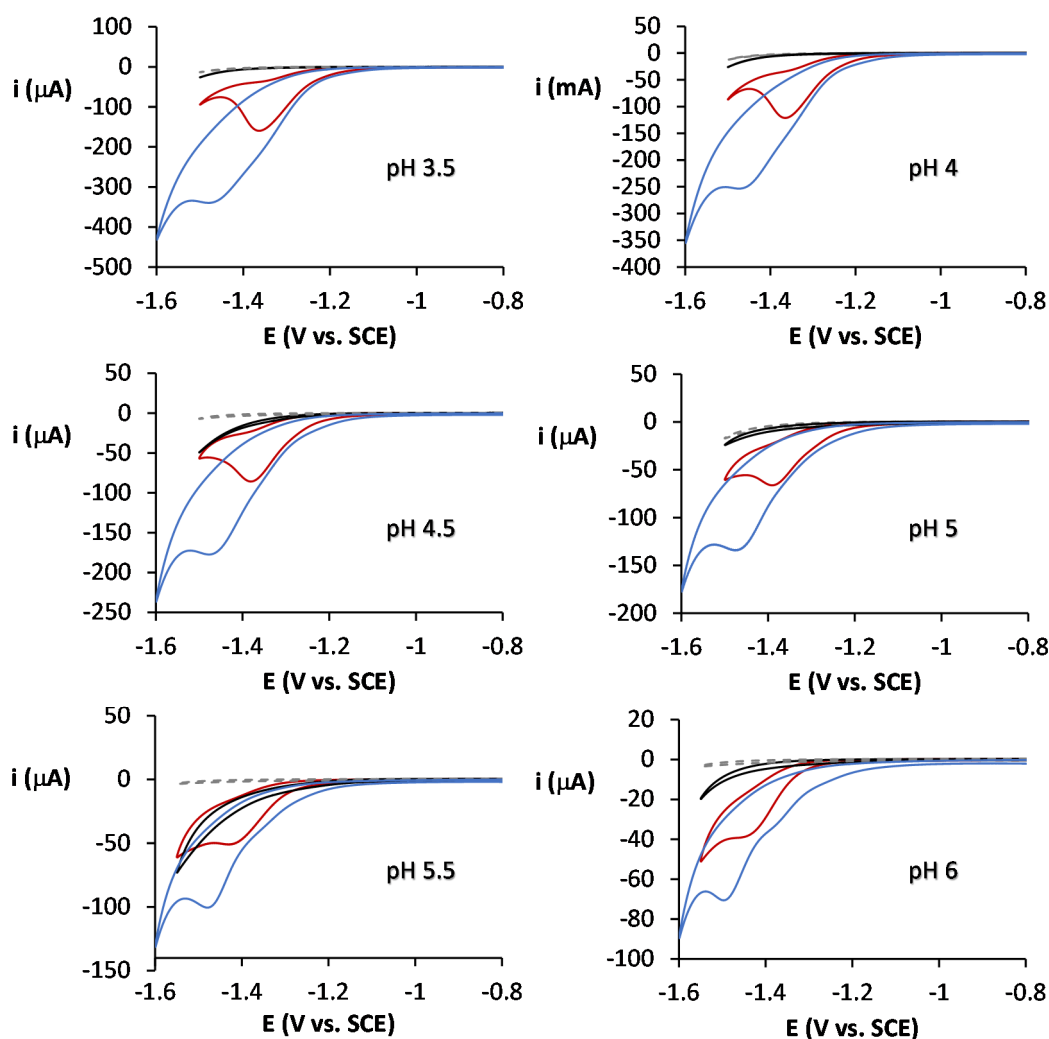


Figure V. 14. Cyclic voltammograms in 100 mM citrate buffer, 100 mM NaCl, at different pH values in the absence (dashed grey trace), and presence of 1 mM catalyst $\mathbf{1}^{\text{Biotin}}$ (red trace) and $\mathbf{1}^{\text{Spacer-Biotin}}$ (blue trace). The black CV correspond to the electrocatalytic current obtained after rinsing the electrode after the measurement of the cobalt solution. Scan rate of $100 \text{ mV}\cdot\text{s}^{-1}$ using a 0.28 cm^2 glassy carbon working electrode. Potentials are quoted versus SCE.

To confirm the molecular behavior of $\mathbf{1}^{\text{Biotin}}$ and $\mathbf{1}^{\text{Spacer-Biotin}}$, rinsing tests were performed. Consecutive scans on a 1 mM solution of catalyst at pH 3.5 showed negligible loss of catalytic current. Removal of the electrode from the cobalt solution, rinsing, and placing it into fresh buffer without cobalt catalyst showed no catalytic current. This result indicates the absence of active species attached to the electrode surface forming an electroactive film, for instance *via* decomposition and nanoparticle formation.⁹⁰ On

the other hand the catalytic current is dependent on the catalyst concentration, showing a first-order dependence (Figure V. 13).⁹⁶

Afterwards, we measured the electrocatalytic behavior of the purified catalyst C SA adducts. When the CV was measured in a protein solution of 10 μM , no electrocatalytic wave was observed (Figure V. 15, black CV). This phenomenon can be explained considering both the low concentration in solution and the insulation effect of the enzyme, reducing the rate of electron transfer from the surface of the active electrode to the catalyst in the pocket of the protein. To improve the signal and electronic contact we proceeded to make a thin film¹⁹¹ of $\mathbf{1}^{\text{Biotin}} \text{C SA}$ over the glassy carbon electrode by drop-casting and drying. The modified electrode gave a significant catalytic wave attributed to proton reduction (Figure V. 15, red CV). Unfortunately, we have noted that the catalytic wave was not stable and basically disappeared in the second CV scan, this is most likely due to a protein detachment during electrocatalysis.^{186,191} Importantly, no electrocatalytic behavior was observed when SA alone was deposited on the same conditions (Figure V. 15, green CV). Therefore, the electrocatalytic behavior observed with the catalyst C SA adduct can be attributed to the redox activity of the cobalt catalyst embedded within the protein pocket.

As observed with the free catalysts $\mathbf{1}^{\text{Biotin}}$ and $\mathbf{1}^{\text{Spacer-Biotin}}$, the catalyst adducts $\mathbf{1}^{\text{Biotin}} \text{C SA}$ and $\mathbf{1}^{\text{Spacer-Biotin}} \text{C SA}$ exhibited strong pH-dependence catalytic waves. First,

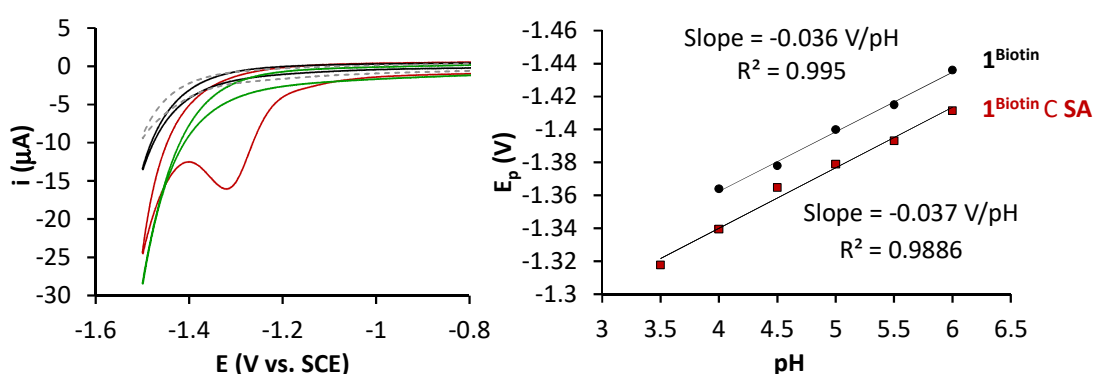


Figure V. 15. *Left:* Cyclic voltammogram of $\mathbf{1}^{\text{Biotin}} \text{C SA}$ adduct thin film on the surface (red trace) and in solution (black trace). The CV scan for bare electrode under the same conditions (dashed grey trace) and the CV of a thin film of SA alone (green trace) are included. Conditions: 100 mM citrate buffer, 100 mM NaCl, at pH 3.5. Scan rate of $100 \text{ mV}\cdot\text{s}^{-1}$ using a 0.28 cm^2 glassy carbon working electrode. Potentials are quoted vs SCE. *Right:* Plot of the peak potential (E_p) as a function of pH. The E_p value of $\mathbf{1}^{\text{Biotin}}$ at pH = 3.5 was removed from the plot E_p (V) vs. pH because it did not fit with the linear plot.

the electrocatalytic current (i_c) increases at decreased pH values, as expected for proton reduction activity (Figure V. 16). Secondly, the E_p values also follow the negative shift behavior when the pH value is decreased. This behavior is more significant in the case of $\mathbf{1}^{\text{Biotin}} \text{C SA}$, in which both E_p value (from -1.32 to -1.41 V) and onset potential values are significantly shifted (from -0.83 to -1.12 V). However, the $\mathbf{1}^{\text{Spacer-Biotin}} \text{C SA}$ adduct showed no significant modification on the potential values.

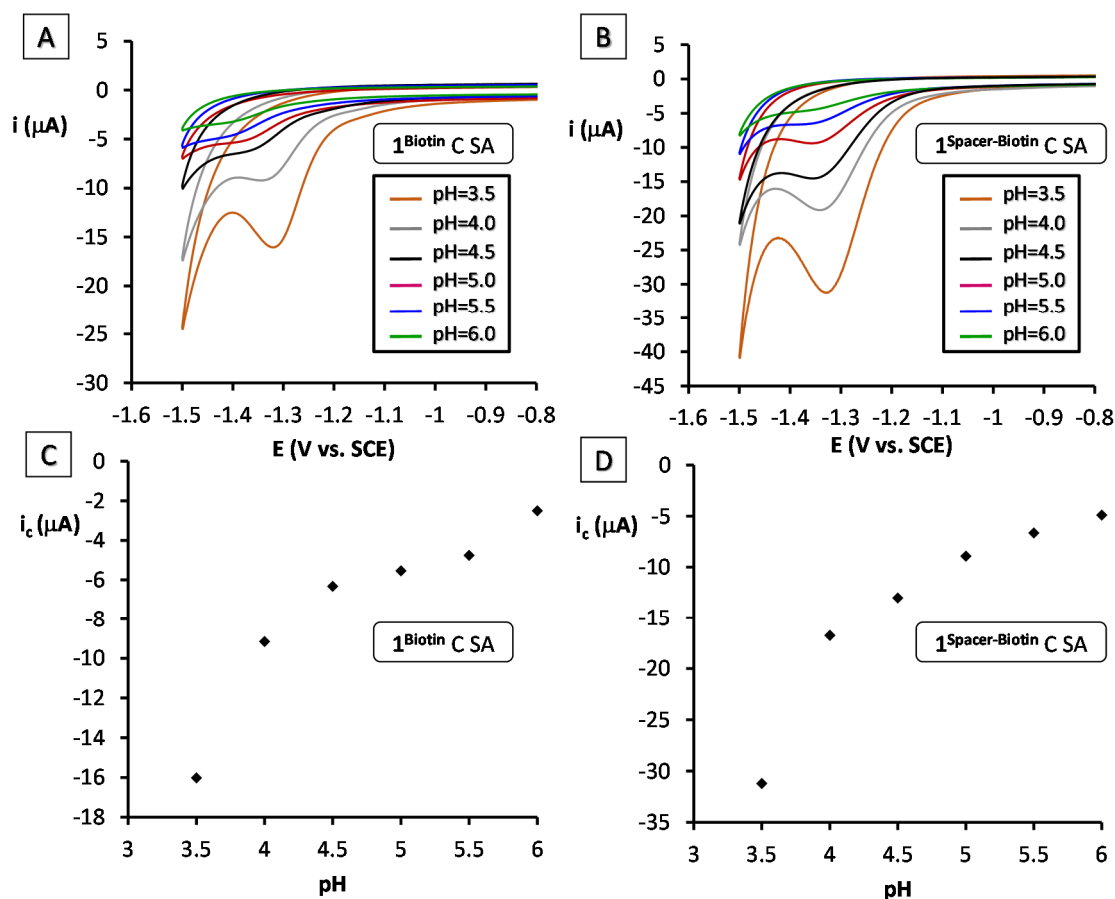


Figure V. 16. Successive cyclic voltammograms of $\mathbf{1}^{\text{Biotin}} \text{C SA}$ (A) and $\mathbf{1}^{\text{Spacer-Biotin}} \text{C SA}$ (B) adducts thin film on the surface in 100 mM citrate buffer, 100 mM NaCl, at pH in the 3.5 to 6.0 range. Scan rate of $100 \text{ mV}\cdot\text{s}^{-1}$ using a 0.28 cm^2 glassy carbon working electrode. Potentials are quoted versus SCE. C) Maximum peak intensity values versus the pH value in the case of $\mathbf{1}^{\text{Biotin}} \text{C SA}$. D) Maximum peak intensity values versus the pH value in the case of $\mathbf{1}^{\text{Spacer-Biotin}} \text{C SA}$.

The E_p values of $\mathbf{1}^{\text{Biotin}} \text{C SA}$ adduct follows a Nernstian response of 0.037 V per pH unit (Figure V. 15, right), as observed for $\mathbf{1}^{\text{Biotin}}$. Therefore, this is also consistent for a 2 electron and 1 proton reduction. On the other hand the $\mathbf{1}^{\text{Spacer-Biotin}} \text{C SA}$ adduct shows low dependence of the potential versus pH, consistent with no PCET in the $\text{Co}^{\text{II/I}}$ reduction event.⁸⁶

Table V. 1. Redox potentials (V) and overpotentials (η) of $\mathbf{1}^{\text{Biotin}}$ and $\mathbf{1}^{\text{Biotin}} \subset \text{SA}$ measured in aqueous solution at different pH values.

pH	$\mathbf{1}^{\text{Biotin}}$			$\mathbf{1}^{\text{Biotin}} \subset \text{SA}$			ΔE_p (mV) ^[d]	$\Delta \eta$ (mV) ^[e]
	E_p (V) ^[a]	Onset (V) ^[b]	η (mV) ^[c]	E_p (V) ^[a]	Onset (V) ^[b]	η (mV) ^[c]		
3.5	-1.36	~-0.98	534	-1.32	~-0.83	383	43	150
4.0	-1.37	~-1.06	583	-1.34	~-0.96	483	25	100
4.5	-1.38	~-1.08	574	-1.36	~-1.00	494	13	80
5.0	-1.40	~-1.11	574	-1.38	~-1.02	484	21	90
5.5	-1.42	~-1.16	595	-1.39	~-1.07	504	22	90
6.0	-1.44	~-1.23	635	-1.41	~-1.12	525	25	110

Glassy carbon and SCE were the working and reference electrodes, scan rate = 100 mV·s⁻¹ using a 0.28 cm² glassy carbon working electrode. Potentials determined in 100 mM citrate buffer, 100 mM NaCl, at different pH values. Potentials are quoted versus SCE. [a] E_p corresponds to the potential at the maximum peak intensity. [b] Potential at the onset catalytic wave. [c] Overpotential (η): Onset potential- standard potential at a given pH. [d] $\Delta E_p = E_p(\mathbf{1}^{\text{Biotin}}) - E_p(\mathbf{1}^{\text{Biotin}} \subset \text{SA})$ [e] $\Delta \eta = \eta(\mathbf{1}^{\text{Biotin}}) - \eta(\mathbf{1}^{\text{Biotin}} \subset \text{SA})$. Standard potentials have been calculated according to the formula $E^\circ(\text{pH}) = -0.241\text{V} - 0.059\text{V} \times \text{pH}$.

Table V. 2. Redox potentials (V) and overpotentials (η) of $\mathbf{1}^{\text{Spacer-Biotin}}$ and $\mathbf{1}^{\text{Spacer-Biotin}} \subset \text{SA}$ measured in aqueous solution at different pH values.

pH	$\mathbf{1}^{\text{Spacer-Biotin}}$			$\mathbf{1}^{\text{Spacer-Biotin}} \subset \text{SA}$			ΔE_p (mV) ^[d]	$\Delta \eta$ (mV) ^[e]
	E_p (V) ^[a]	Onset (V) ^[b]	η (mV) ^[c]	E_p (V) ^[a]	Onset (V) ^[b]	η (mV) ^[c]		
3.5	-1.47	~-1.10	653	-1.33	~-0.90	553	142	100
4.0	-1.47	~-1.10	623	-1.34	~-0.90	523	132	100
4.5	-1.47	~-1.10	594	-1.35	~-1.00	494	122	0
5.0	-1.47	~-1.10	564	-1.36	~-1.09	554	115	90
5.5	-1.48	~-1.10	535	-1.36	~-1.09	423	114	90
6.0	-1.49	~-1.10	505	-1.36	~-1.09	495	127	90

Glassy carbon and SCE were the working and reference electrodes, scan rate = 100 mV·s⁻¹ using a 0.28 cm² glassy carbon working electrode. Potentials determined in 100 mM citrate buffer, 100 mM NaCl, at different pH values. Potentials are quoted versus SCE. [a] E_p corresponds to the potential at the maximum peak intensity. [b] Potential at the onset catalytic wave. [c] Overpotential (η): Onset potential- standard potential at a given pH. [d] $\Delta E_p = E_p(\mathbf{1}^{\text{Spacer-Biotin}}) - E_p(\mathbf{1}^{\text{Spacer-Biotin}} \subset \text{SA})$ [e] $\Delta \eta = \eta(\mathbf{1}^{\text{Spacer-Biotin}}) - \eta(\mathbf{1}^{\text{Spacer-Biotin}} \subset \text{SA})$. Standard potentials have been calculated according to the formula $E^\circ(\text{pH}) = -0.241\text{V} - 0.059\text{V} \times \text{pH}$.

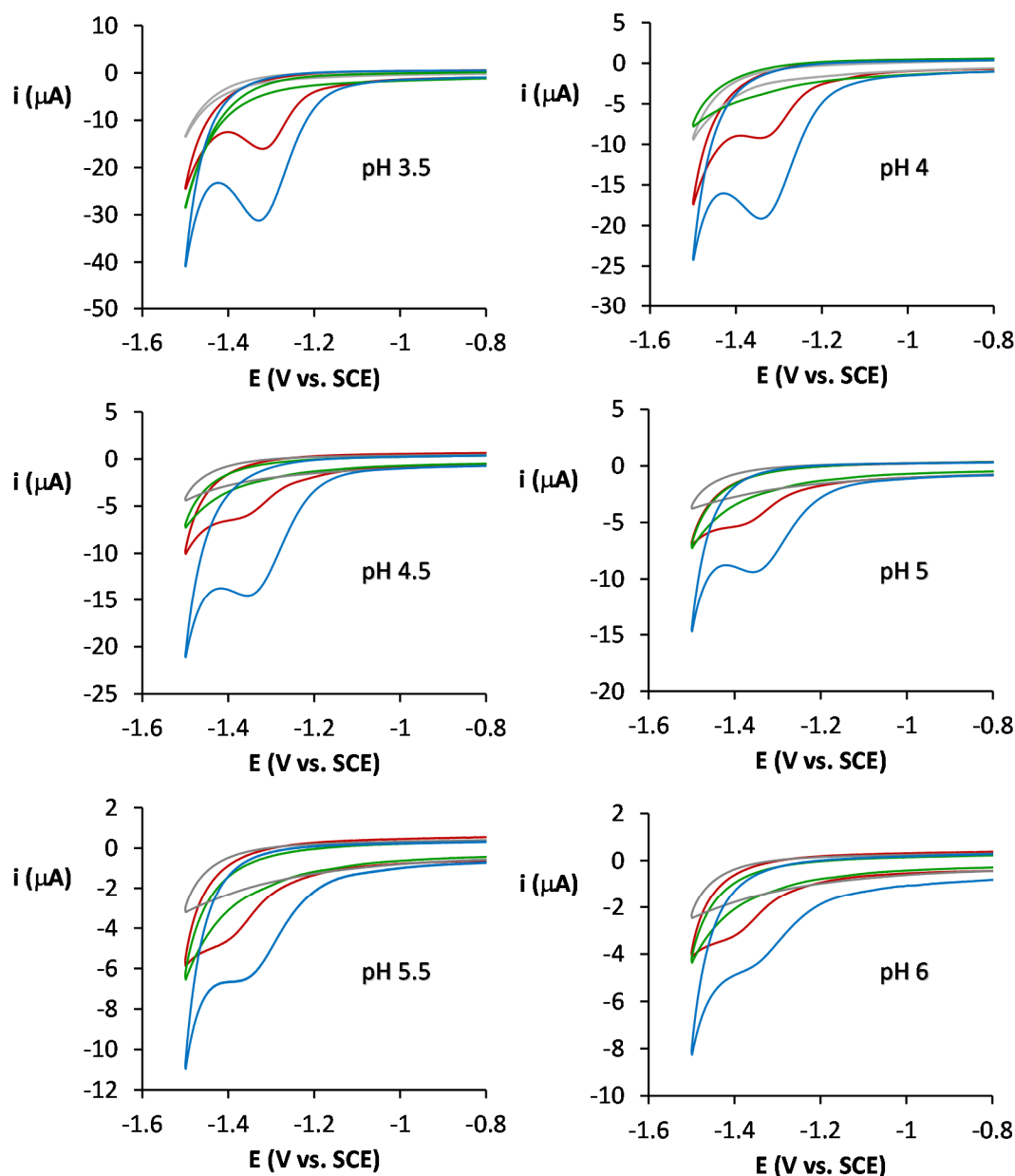


Figure V. 17. Cyclic voltammograms of $1^{\text{Biotin}} \text{C SA}$ (red trace) and $1^{\text{Spacer-Biotin}} \text{C SA}$ (blue trace) adducts thin film on the surface in 100 mM citrate buffer, 100 mM NaCl, at pH in the 3.5 to 6.0 range. The CV scan for bare electrode under the same conditions (grey trace) and the CV obtained from a thin of SA alone (green trace) are included. Scan rate of $100 \text{ mV}\cdot\text{s}^{-1}$ using a 0.28 cm^2 glassy carbon working electrode. Potentials are quoted versus SCE.

An important analysis is the comparison of the electrochemical behavior between complexes and the artificial metalloenzymes. The direct comparison is not straightforward since the protein concentration over the electrode is ill-defined. Therefore comparison between intensities is meaningless. On the other hand the potential of the redox events is very informative. CV depicted in Table V. 1 and Table V. 2 shows that the protein shell lets to reduce the electrocatalytic proton reduction potential. This is clearly observed in the E_p values and in the onset values (in the case of

$\mathbf{1}^{\text{Biotin}} \subset \text{SA}$ a shift in the onset value is not observed). The magnitude of shift (ΔE_p) is in the range of 13-43 mV for $\mathbf{1}^{\text{Biotin}} - \mathbf{1}^{\text{Biotin}} \subset \text{SA}$ systems (Table V. 1), and more evident in the case of $\mathbf{1}^{\text{Spacer-Biotin}} - \mathbf{1}^{\text{Spacer-Biotin}} \subset \text{SA}$ systems (114-142 mV) (Table V. 2) (Figure V. 18). Consequently, the shift in the redox potential leads to a decrease in the overpotential (η) for proton reduction ($\Delta\eta$: 90-150 mV (for $\mathbf{1}^{\text{Biotin}} - \mathbf{1}^{\text{Biotin}} \subset \text{SA}$) and 0-100 mV (for $\mathbf{1}^{\text{Spacer-Biotin}} \subset \text{SA}$), measured at the onset potential).

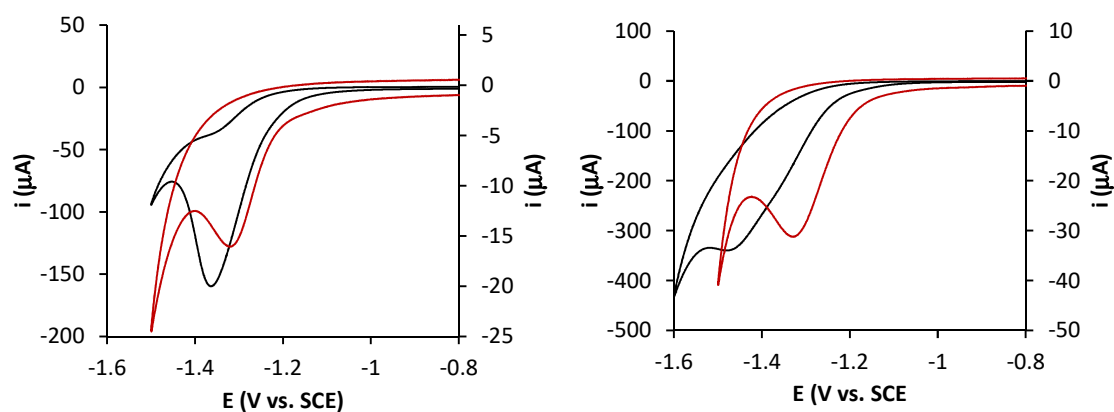


Figure V. 18. Cyclic voltammograms of *left*) $\mathbf{1}^{\text{Biotin}}$ (black trace) $\mathbf{1}^{\text{Biotin}} \subset \text{SA}$ (red trace) *Right*) $\mathbf{1}^{\text{Spacer-Biotin}}$ (black trace) $\mathbf{1}^{\text{Spacer-Biotin}} \subset \text{SA}$ (red trace). CVs measured in 100 mM citrate buffer, 100 mM NaCl, at pH 3.5. Scan rate of $100 \text{ mV}\cdot\text{s}^{-1}$ using a 0.28 cm^2 glassy carbon working electrode. Potentials are quoted versus SCE.

The appearance of a shift in the catalytic wave is consistent with previous results using $(\text{Co}(\text{dmgH})_2\text{pyCl})$, $\text{dmgH}_2 = \text{dimethylglyoxime}$) into the Photosystem I (PSI)¹⁷³ protein (negative shift of $\sim 140 \text{ mV}$), or cobaloxime derivatives into the heme pocket of apo *Sperm-whale* myoglobin (negative shift of $\sim 100 \text{ mV}$).¹⁷⁷ The interesting positive shifts obtained in our system proves that the catalyst is inside the protein and the secondary coordination sphere of the protein can change the electrocatalytic potential for water reduction. For this reason we rationalize that the appropriate protein pocket could provide a major positive shift in potential.

V.2.4. Photoinduced Water Reduction to Hydrogen

After studying the effect of the secondary protein structure in the electrochemical hydrogen generation, we next investigated whether the incorporation of the artificial metalloenzymes synthesized could also modulate and improve the intrinsic activity of the respective cobalt complexes in the light-driven hydrogen generation. To achieve this aim, the Co-catalytic systems were first tested with the partially water soluble $[\text{Ru}(\text{bpy})_3]\text{Cl}_2$ chromophore. All of the attempts to reduce water using this chromophore were unsuccessful, and low amounts of gas were obtained when using TEOA (0.4 M), Et_3N (0.4 M) or ascorbic acid (0.4 M) as sacrificial electron donors. This could be rationalized by the high negative potential provided by PS_{Ru} (-1.34 V vs. SCE) necessary to form the Co^{I} intermediate. Therefore, we decided to use $[\text{Ir}(\text{ppy})_2(\text{bpy})]\text{PF}_6$ (PS_{Ir}) photosensitizer,^{303,391-393} already studied in the previous chapters of this thesis. In a typical experiment, samples containing 5 μM of catalyst were irradiated with 1100 $\text{W}\cdot\text{m}^{-2}$ of visible light ($\lambda > 400 \text{ nm}$) in the presence of PS_{Ir} (250 μM), TEOA as sacrificial electron donor (0.4 M) in 100 mM aqueous phosphate buffer (containing 30% of MeCN to solubilize the photosensitizer) with 100 mM NaCl, over the course of 4 hours. The hydrogen evolved from the reaction vessel was quantified by analyzing aliquots of volume of the headspace of the anaerobic cuvette via gas chromatography as a function of time. We found that $\mathbf{1}^{\text{Biotin}}$ and $\mathbf{1}^{\text{Spacer-Biotin}}$ catalytic systems moderately produce H_2 under these conditions achieving TON ranging from 8-89, with associated initial TOF ranging from 2-49 h^{-1} . The photocatalytic activity is strongly dependent on the pH value of the solution (measured from pH 7.5 to 12.5). In the case of $\mathbf{1}^{\text{Spacer-Biotin}}$, a maximum activity was observed at pH 10.5 (TON: 89, TOF: 80 h^{-1}). The decrease in rate at higher pH values is likely due to the lower proton concentration in solution. On the contrary, lowering the pH value from 10.5 to 7.5 leads also to a lower initial rate of H_2 production, most probably due the decrease of the effective electron donor concentration (TEOA) by protonation.

Table V. 3. Light-driven water reduction to H₂ of **1^{Spacer-Biotin}** and **1^{Spacer-Biotin} C SA** at different pH.

pH	1^{Spacer-Biotin}		1^{Spacer-Biotin} C SA		Enhance factor	
	TON	Initial TOF (h ⁻¹)	TON	Initial TOF (h ⁻¹)	Enhance TON	Enhance Initial TOF
7.5	8	2	13	6	1.6	2.6
8.5	14	7	33	9	2.4	1.4
9.0	17	13	45	18	2.7	1.4
9.5	36	20	67	33	1.9	1.7
10.5	89	49	106	63	1.2	1.3
11.5	46	16	166	88	3.6	5.5
12.5	9	4	93	53	10.5	13.4

Conditions: 5 μM catalyst, 250 μM **PS_r**, 0.4 M TEOA in 0.4 mL MeCN:H₂O (3:7) mixture. The aqueous phase was a phosphate buffer containing 100 mM NaCl. pH: 7.5-12.5. Irradiation with 1100 W·m⁻² of visible light ($\lambda > 400$ nm).

Remarkably, the artificial metalloenzyme **1^{Spacer-Biotin} C SA** resulted to be a light-driven water reduction catalyst. But more importantly, it resulted to be a more active catalyst for the light-driven water reduction as judged by the TON (up to 166) and TOF values (up to 88 h⁻¹) (Table V. 3). This superior performance is observed in all of the pH range. Interestingly, the maximum in activity is shifted from 10.5 to pH 11.5 when the cobalt complex **1^{Spacer-Biotin}** is encapsulated into the SA, which lead to enhancements higher than one order of magnitude in the TON and TOF values at high pH values. Besides possible beneficial effect of protection or interaction with the residues of the pocket one can also argue that the effective proton concentration around the metal center is different at the bulk than in the pocket. We rationalize that the residues of the protein pocket create a local buffer effect, producing a higher effective proton concentration in the neighborhood of the cobalt center. This increase in the local concentration could explain the activity of the catalyst at very high pH values. It is important to highlight that the protonation of the Co^I is the proposed to be the rate determining step of the reaction (Chapter IX).

This result is very important because it could open the door to design water reduction catalysts that operate in basic media. This systems can have a large impact in the design of water splitting devices since water oxidation catalysts are much more effective and robust at basic pH values.⁶³

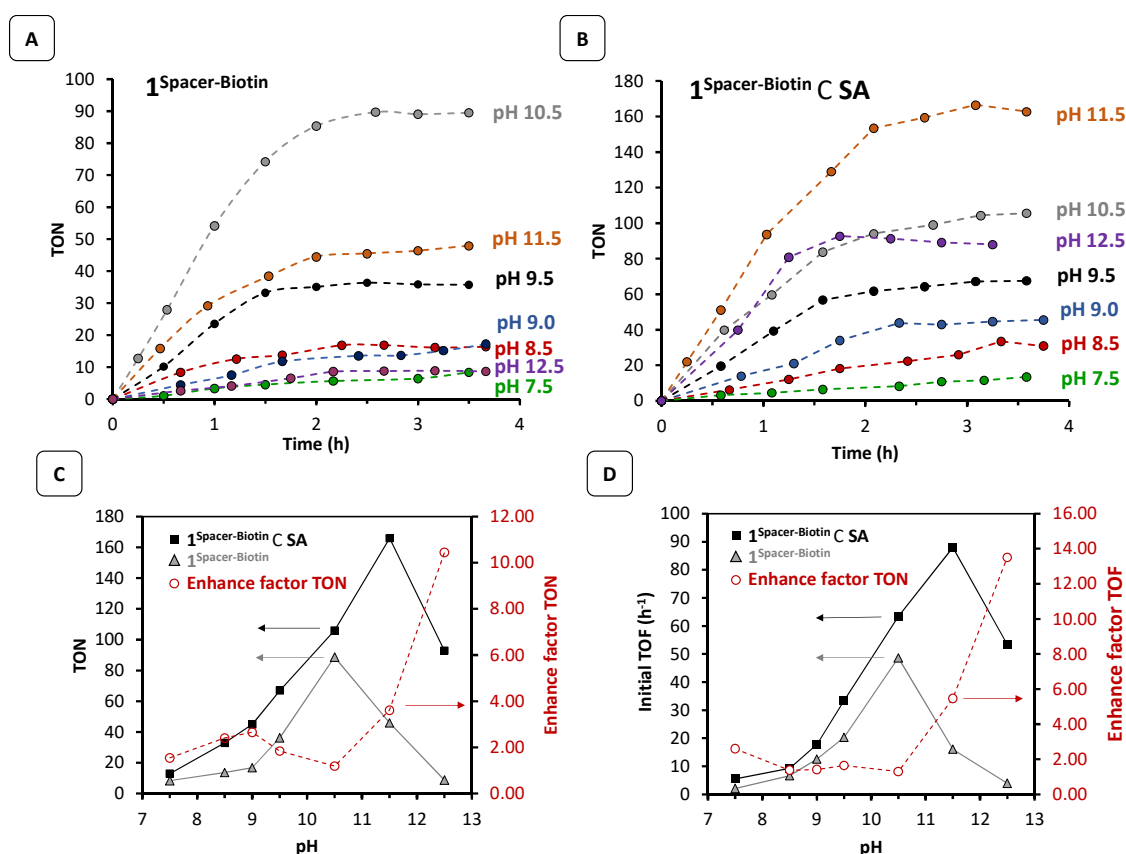


Figure V. 19. Photoinduced hydrogen production with 5 μM catalyst, 250 μM PS_{Ir} , 0.4 M TEOA in 0.4 mL aqueous phosphate buffer containing 100 mM NaCl, measured at different pH values. Irradiation with $1100 \text{ W}\cdot\text{m}^{-2}$ of visible light ($\lambda > 400 \text{ nm}$). A) Time traces of hydrogen evolved using $1^{\text{Spacer-Biotin}}$. B) Time traces of hydrogen evolved using $1^{\text{Spacer-Biotin C SA}}$. C) Activities represented as TON at different pH values in the case of $1^{\text{Spacer-Biotin}}$ (grey) and $1^{\text{Spacer-Biotin C SA}}$ (black). The red trace represents the TON enhance factor ($\text{TON}_{1^{\text{Spacer-Biotin C SA}}}/\text{TON}_{1^{\text{Spacer-Biotin}}}$) at different pH values. D) Activities represented as initial TOF (h^{-1}) at different pH values in the case of $1^{\text{Spacer-Biotin}}$ (grey) and $1^{\text{Spacer-Biotin C SA}}$ (black). The red trace represents the enhance factor in TOF ($\text{TOF}_{1^{\text{Spacer-Biotin C SA}}}/\text{TOF}_{1^{\text{Spacer-Biotin}}}$) at different pH values.

We also investigated photoredox catalyst based on Earth abundant elements - ($[\text{Cu}(\text{bathocuproine})(\text{Xantphos})](\text{PF}_6)$ (PS_{Cu})),³⁹⁴ also employed in Chapter V for the reduction of ketones. The activity of the artificial metalloenzymes and peptides tested in the literature mainly relies on the use of the aqueous-soluble $[\text{Ru}(\text{bpy})_3]^{2+}$.^{169,172,177,184,191} Therefore the use of an Earth abundant element photoredox catalyst is an important improvement. However, PS_{Cu} presents low solubility in water and therefore it requires the use of an organic solvent for its solubilization. Although SA is a strong protein capable to maintain the secondary structure at extreme pH values and at high concentrations of organic solvent, the application of these metalloenzymes for H_2 evolution in a mixture containing organic solvent is challenging. In order to check

its stability, we titrated by circular dichroism a solution of 5 μM **1^{Spacer-Biotin} C SA** with MeCN with the aim to study the stability of the protein at increasing amount of organic solvent. We found that the **1^{Spacer-Biotin} C SA** is able to maintain the secondary protein structure up to 50% volume of MeCN in solution, as demonstrated by the conservation of the CD signal. Nevertheless, a loss of ellipticity was observed when 55% volume of MeCN was present in the solution (Figure V. 20). Based on these results we decided to investigate the capacity of our catalytic systems combined with **PS_{Cu}** in the photoinduced hydrogen production using a solvent mixture of MeCN:H₂O (4:6), in which the chromophore was completely soluble.

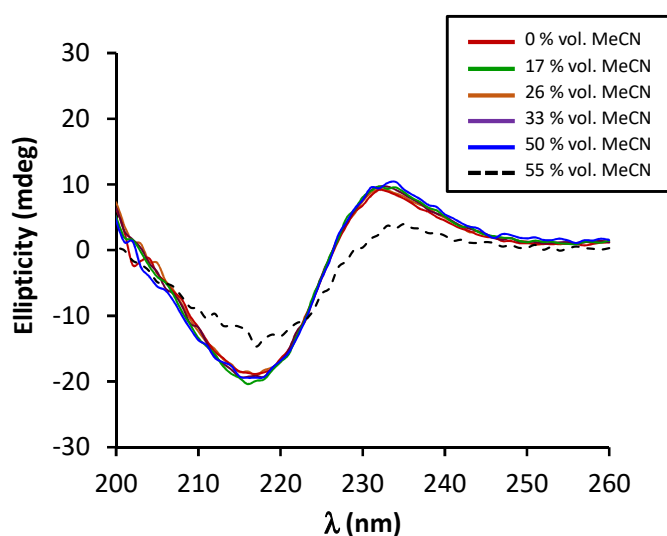


Figure V. 20. CD spectra of **1^{Spacer-Biotin} C SA** at different percentages of MeCN in the solvent mixture. Conditions: 5 μM protein, 100 mM Tris·HCl buffer, pH 7.5 at 20 °C. The CD signals were corrected according to the dilution of the addition.

We found that the use of **PS_{Cu}** provided improved activities as long as higher reaction times compared to that obtained with **PS_{Ir}**. Thus, **1^{Biotin}** and **1^{Spacer-Biotin}** depicted excellent activities providing 174 and 200 TON, respectively, with an initial TOF of 26 and 32 h^{-1} (Figure V. 4). Direct comparison of the photoinduced catalysis with the adduct systems **1^{Biotin} C SA** and **1^{Spacer-Biotin} C SA** showed a clear enhancement of the catalytic activity, compared with the free catalytic systems **1^{Biotin}** and **1^{Spacer-Biotin}**, as previously observed in the case of **PS_{Ir}**. **1^{Biotin} C SA** and **1^{Spacer-Biotin} C SA** afforded TON values of 315 (TOF = 43 h^{-1}) and 394 (TOF = 55 h^{-1}), respectively (Figure V. 4), together with an enhancement of the overall lifetime of the catalytic system (around 1 hour) (Figure V.

21). These results confirm that the protein environment plays an important role in the overall increase of performance of the cobalt center, affecting not only the stability (protecting the catalytic center towards side-reactions) but also improving its catalytic activity. These results are consistent with the previously results reported by Ghirlanda and co-workers with the cobalt protoporphyrin IX (CoP) protected by myoglobin (CoMyo).¹⁸⁴

Table V. 4. Photocatalytic activities in H₂ evolution using **PS_{Cu}** as photoredox catalyst.

TON	TON	Initial TOF (h ⁻¹)	Enhance TON	Enhance Initial TOF
1^{Biotin}	174	26	1.8	1.7
1^{Biotin} C SA	315	43		
1^{Spacer-Biotin}	200	32	2	1.7
1^{Spacer-Biotin} C SA	394	55		

Conditions: 5 μM catalyst, 250 μM **PS_{Cu}**, 0.4 M Et₃N in 0.4 mL of MeCN:H₂O (4:6). Irradiation with 1100 W·m⁻² of visible light (λ > 400 nm).

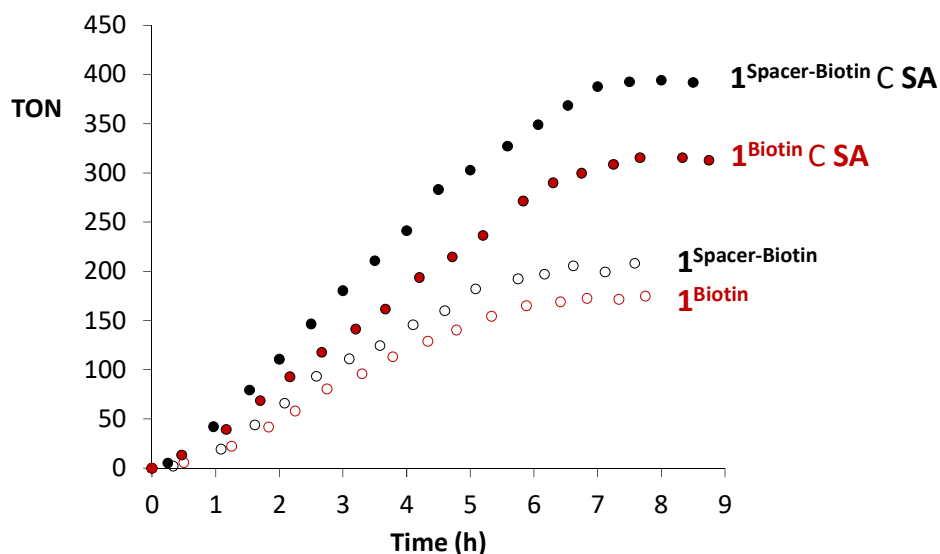


Figure V. 21. Time-traces in H₂ evolution catalyzed by **1^{Biotin}** (empty red dots), **1^{Spacer-Biotin}** (empty black dots), **1^{Biotin} C SA** (full red dots) and **1^{Spacer-Biotin} C SA** (full black dots). Conditions: 5 μM catalyst, 250 μM **PS_{Cu}**, 0.4 M Et₃N in 0.4 mL of MeCN:H₂O (4:6). Irradiation with 1100 W·m⁻² of visible light (λ > 400 nm).

The role of the protein matrix has been extensively demonstrated in [FeFe] hydrogenases, in which the intrinsic activity of the diiron core is clearly modulated and enhanced thanks to the interactions of the secondary shell.¹⁸² Furthermore, this idea has been extended and exploited by introducing metal complexes into hydrophobic

environments, such as chitosan,¹⁵³ cyclodextrine,¹⁵⁴ micelles,¹⁵⁵ metal-organic frameworks¹⁵⁶ and dendrimers.¹⁵⁷ These alternatives based on no-protein environment also let to the increase of the stability as well as the activity of the inorganic catalytic system in photoinduced H₂ production. One of the advantages of using metalloenzymes is that the second coordination sphere could be modulate by mutation.

In summary, we have synthesized biotinylated cobalt complexes that are able to bind efficiently with streptavidin. This led to the synthesis of new cobalt artificial metalloenzymes based on the biotin-streptavidin technology. These new metalloenzymes are able to reduce water to hydrogen under electro- and photochemical conditions. The approach is alternative to the classic organic chemical transformations using streptavidin as platform for biohybrid catalysts. We found that the incorporation of the cobalt catalysts into the protein scaffold have many beneficial effects: decrease the overpotential for electrocatalytic hydrogen production, significantly improves the light-driven hydrogen production and enhances the overall stability under photocatalytic conditions. Moreover, we discover that the maximum in activity of the catalyst is displaced to higher pH values that could be a consequence of a local buffered effect of the pocket environment.

We have demonstrated that the modular nature of tacn ligands tacn ligands let to modify the activity through the modification of the second-sphere of the catalyst. This works opens up the opportunity to further improve the cobalt catalyst for hydrogen reduction by controlling the second coordination sphere by introducing specific mutations in the protein scaffold. Future studies will be focused on the extension of the applicability of this systems in photocatalytic chemical transformations.

V.3. EXPERIMENTAL SECTION

V.3.1. Materials

Reagents and solvents were purchased from commercial sources as used as received unless otherwise stated. Triethylamine (Et_3N) $\geq 99\%$ purity) and triethanolamine (TEOA $\geq 99\%$ purity) were purchased from Sigma-Aldrich® and used without further purification. Compounds $[\text{Ir}(\text{bpy})(\text{ppy})_2]\text{PF}_6$ (PS_{Ir}),³⁰³ and $[\text{Cu}(\text{bathocuproine})(\text{Xantphos})]\text{PF}_6$ (PS_{Cu}),³⁹⁵ were synthesized according to the literature procedures. Anhydrous acetonitrile was purchased from Scharlab. Water (18.2 $\text{M}\Omega\cdot\text{cm}$) was purified with a Milli-Q Millipore Gradient AIS system. All solvents were strictly degassed and stored under anaerobic conditions.

V.3.2. Instrumentation and Experimental Procedures

UV/Vis spectra were acquired on a Varian Cary 50 Bio Spectrophotometer. Gas chromatography was carried out on a SRI instruments, Model no. 310C GC using a 5Å molecular sieve column with a thermal conductivity detector and argon carrier gas.

All NMR spectra are recorded in CDCl_3 in a Varian 400 or 500 MHz instrument, as noted

CD spectra were recorded in a JASCO J-815 spectropolarimeter. All the CD spectra were recorded in 10mM Tris buffer (pH=7.5) using 5 μM of protein.

Electrochemical experiments were carried out using a CH-instruments 1242B potentiostat. For all electrochemical measurements, a three-electrode system was used. The electrodes used were a 3-mm diameter glassy carbon working electrode with a surface area of 0.28 cm^2 , platinum mesh counter electrode, and a saturate calomel reference electrode. 100 mM citrate and 25 mM NaCl buffer of desired pH (3.5, 4.0, 4.5, 5.0, 5.5 and 6.0) was utilized to record the cyclic voltammogram. All potentials quoted versus SCE. All scan were performed at 100 $\text{mV}\cdot\text{s}^{-1}$ scan rate. All electrolyte solutions were degassed with freeze and pump techniques. Working electrodes were polished with 1 μM alumina for 5 minutes, followed by 10 minutes of sonication, prior to use. The electrochemical measurements of the catalysts were performed adding the catalyst dissolved in an aqueous solution (10 mM catalyst) containing 5% DMSO to solubilize the catalyst. The final percentage of DMSO in the electrochemical cell was 0.5%.

For the protein thin film measurements a drop of 20 μM stock solution of protein was added and dried over the glassy carbon working surface. After drying, the electrochemical measurement was performed by directly submerging the glassy carbon into the solution.

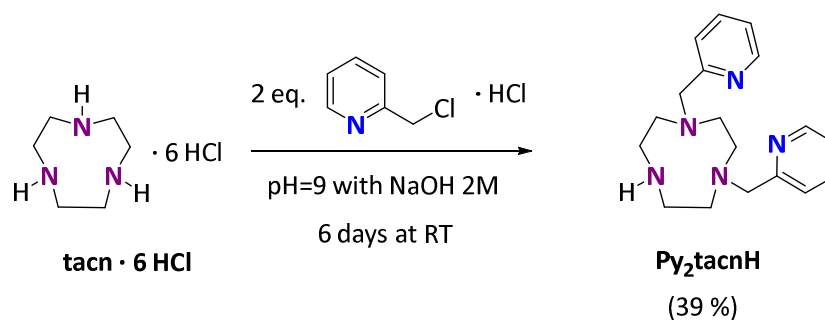
Photoinduced H_2 production Irradiation was performed using a 450W xenon lamp with a 400 nm cutoff filter, irradiating at a constant 1100 W/m^2 throughout the experiment.

For each experiment, 400 μL of reaction mixture containing all of the reagents, were added to an airtight 1 mm cuvette and degassed extensively with argon prior to illumination. During irradiation time course 100 μL samples of the headspace were removed with a gas-tight syringe and injected directly for analysis by GC. Calibration was achieved by injection of various volumes of a 1% H_2 , 99% N_2 gas mixture onto the GC.

The synthesis of the of $\mathbf{1}^{\text{Biotin}} \subset \text{SA}$ and $\mathbf{1}^{\text{Spacer-Biotin}} \subset \text{SA}$ adducts was carried out by combining the corresponding cobalt catalyst with streptavidin. For the incorporation into streptavidin, a stock solution of 2 mg/mL of streptavidin in 100 mM Tris-HCl (pH 7.5) was incubated with 2- to 3-fold excess of biotin-cobalt catalyst. Because of the extremely high affinity of SA for biotin, SA-incorporated biotin-catalyst can be purified away from unbound Biotin-catalyst using a desalting P10-column. After 15 minutes of exposition, the resulting solution was passed through a PD10-desalting column (GE healthcare) previously equilibrated with the same buffer. The fractions from the column were collected as 1 mL fractions and analyzed by UV/Vis spectroscopy. The concentration of purified SA was determined spectrophotometrically using a molar extinction coefficient of $41820 \text{ M}^{-1}\cdot\text{cm}^{-1}$ at 280 nm for SA.³⁸¹ The combined protein fractions gave rise to a stock solution of SA of around 20 μM .

V.3.3. Synthesis of Ligands

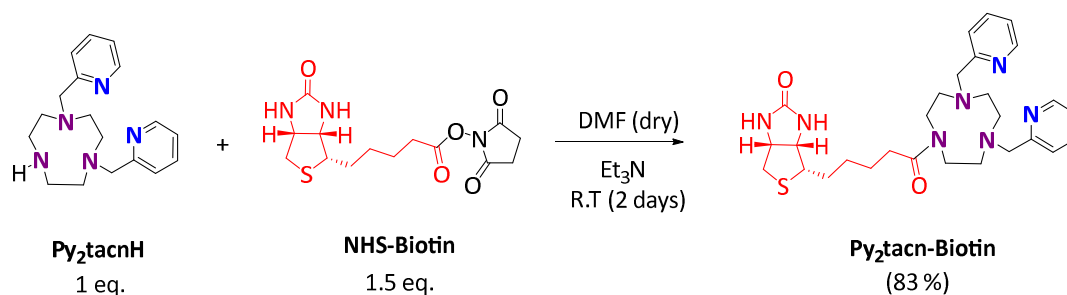
1,4-bis(2-pyridylmethyl)-1,4,7-triazacyclononane, Py_2tacnH . In a 100mL flask $\text{tacn}\cdot 6\text{HCl}$ (1 g, 2.87 mmol), 2-Picolyl chloride hydrochloride (0.94 g, 5.74 mmol), and water (30 mL) were mixed and stirred to achieve a complete dissolution. Then NaOH 2 M was added to basify up to pH 9. The resulting red solution was stirred for 3 days at room temperature and then, NaOH 2 M was added again to readjust the pH to 9. The mixture was stirred another 3 days. After that the reaction was quenched by the addition of NaOH 2 M to pH 13. The solution was evaporated under reduced pressure and the resulting red oil was redissolved with NaOH 2 M and extracted with CH_2Cl_2 (3 x 60mL). The combined organic layers were then dried over anhydrous MgSO_4 , filtered and the solvent was removed with rotary evaporator. The resulting crude red mixture was purified by basic alumina column chromatography (AcOEt : MeOH : drops of ammonia) to provide 0.344 g (1.105 mmol, 39 %) of the desired product. $^1\text{H-NMR}$ (CDCl_3 , 300 MHz, 300K) δ , ppm: 8.53 (d, $J= 4.5 \text{ Hz}$, 2H, H_2 of py), 7.61 (dt, $J= 7.8 \text{ Hz}$, 2H, H_4 of py), 7.44 (d, $J= 7.8 \text{ Hz}$, 2H, H_5 of py), 7.15 (m, 2H, H_3 of py), 3.88 (s, 4H, CH_2), 2.81-2.73 (m, 8H, N- CH_2 - CH_2), 2.66 (s, 4H, N- CH_2 - CH_2).



Scheme V. 2. Synthesis of the basic structure Py_2tacnH .

Py_2tacn -Biotin. The synthesis of Py_2tacn -Biotin was synthesized by biotinylicating the endocyclic secondary free amine from the tacn backbone by using biotin *N*-hydroxysuccinimide (NHS-biotin) in the presence of Et_3N in DMF (Scheme V. 2). We have followed the general procedure described in the literature.³⁷⁶

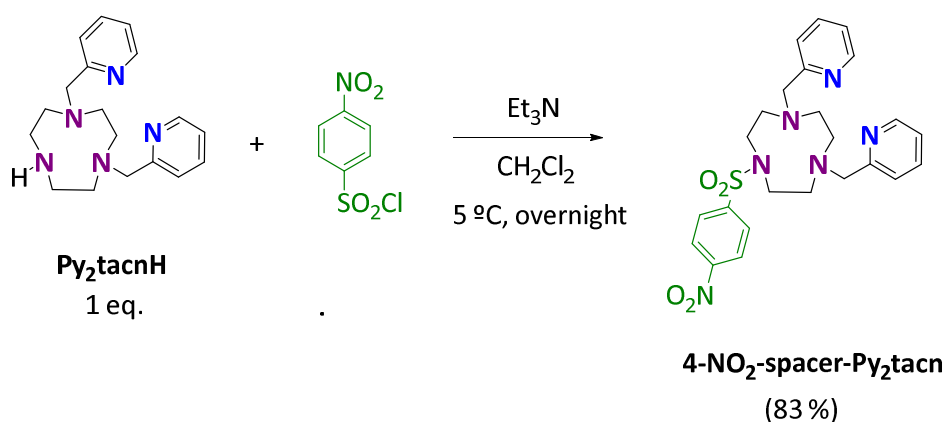
Biotin *N*-hydroxysuccinimide active ester of D-biotin (NHS-biotin) (180 mg, 0.500 mmol), Py_2tacn (104 mg, 0.333 mmol, 1 eq.), and triethylamine (0.17 mL, 1.2 mmol) were mixed in 4.5 mL of dry DMF. The reaction mixture was stirred at room temperature for 2 days under argon atmosphere. After that, it was slowly diluted with water (10 mL) and acidified with HCl (2 M) up to pH 1. The solution was extracted with CH_2Cl_2 (3x10 mL) in order to remove the unreacted NHS-biotin. Then, the aqueous solution was further basified up to pH 10 by the addition of NaOH (2M), and extracted with CH_2Cl_2 (3x10 mL). The combined organic layers were then dried over anhydrous MgSO_4 , filtered and the solvent was removed with rotary evaporator. After drying under vacuum a pale yellow solid was obtained (0.148g, 0.275 mmol, 83 % yield) and used without further purification. $^1\text{H-NMR}$ (CDCl_3 , 500 MHz, 300K) δ , ppm: 8.49 (m, 2H, **Ha** and **Ha'**), 7.62 (m, 2H, **Hc** and **Hc'**), 7.35 (m, 2H, **Hd** and **Hd'**), 7.13 (m, 2H, **Hb** and **Hb'**), 6.24 (s, 1H, **Hp**), 5.80 (s, 1H, **Hq**), 4.45 (m, 1H, **Ho**), 4.25 (m, 1H, **Hr**), 3.83 (s, 2H, **He**), 3.81 (m, 1H, **He**), 3.41 (m, 2H, **Hh**), 3.30 (m, 2H, **Hf**), 3.23 (m, 2H, **Hf'**), 3.11 (m, 1H, **Hm**), 2.96 (s, 2H, **Hg**), 2.84 (m, 2H, **hn**), 2.71 (s, 2H, **Hg'**), 2.69 (s, 2H, **hn'**), 2.57 (br, 2H, **hh'**), 2.29 (t, $J = 8.05$ Hz, 2H, **hi**), 1.70-1.59 (m, 4H, **hi** and **hj**), 1.38 (m, 2H, **hk**). $^{13}\text{C-NMR}$ (CDCl_3 , 126 MHz, 300K) δ , ppm: 173.2 (C_{10}), 163.8 (C_{17}), 159.9 (C_5), 159.7 ($\text{C}_{5'}$), 149.1 (C_1), 149.0 ($\text{C}_{1'}$), 136.5 (C_3), 136.3 ($\text{C}_{3'}$), 123.0 (C_4), 122.9 ($\text{C}_{4'}$), 122.1 (C_2), 121.9 ($\text{C}_{2'}$), 63.9 (C_6), 63.5 ($\text{C}_{6'}$), 61.9 (C_{16}), 60.2 (C_{18}), 57.2 ($\text{C}_{8'}$), 55.6 (C_{15}), 54.8 ($\text{C}_{9'}$), 54.3 ($\text{C}_{7'}$), 53.6 (C_8), 50.6 (C_7), 50.1 (C_9), 40.5 (C_{19}), 33.3 (C_{11}), 28.5 (C_{13}), 28.4 (C_{14}), 25.1 (C_{12}). MALDI-TOFMS (m/z): 538.7327 $[\text{M}+\text{H}]^+$.



Scheme V. 3. Synthesis of $\text{Py}_2\text{tacn-Biotin}$.

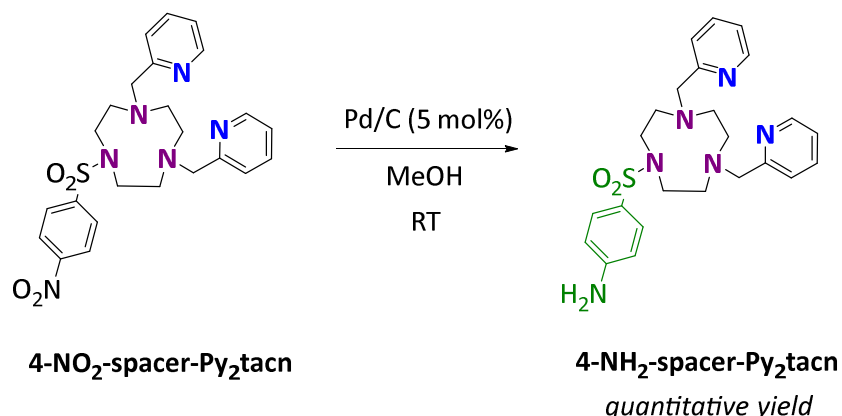
4-NO₂-spacer- Py_2tacn . The introduction of the 4-nitrobenzenesulfonyl moiety into the Py_2tacn backbone was performed following the general procedure described in the literature.³⁷⁰

A CH_2Cl_2 solution (10 mL) containing 4-nitrophenylsulfonyl chloride (224 mg, 0.981 mmol, 1.1 eq.) was added dropwise at 5 °C to a solution of Py_2tacn (278 mg, 0.892 mmol, 1 eq.) and Et_3N (0.3 mL) in CH_2Cl_2 (25 mL). The yellowish solution was left stirred overnight at room temperature. Then, the solvent was removed under reduced pressure and 10 mL of water at pH 1 were added. The aqueous solution was then washed with CH_2Cl_2 (3x10 mL) in order to remove the unreacted 4-nitrophenylsulfonyl chloride. After that, the resulting aqueous solution was further basified up to pH 10 by the addition of NaOH (2M), and extracted with CH_2Cl_2 (3 x 10 mL). The combined organic layers were then dried over MgSO_4 , filtered and the solvent was removed with rotary evaporator. After drying under vacuum an orange oil was obtained (367 mg, 0.740 mmol, 83 % yield). ¹H-NMR (CDCl_3 , 400 MHz, 300K) δ , ppm: 8.53-8.52 (m, 2H), 8.36-8.33 (m, 2H), 7.97-7.95 (m, 2H), 7.68-7.64 (m, 2H), 7.46-7.44 (m, 2H), 7.19-7.15 (m, 2H), 3.89 (s, 4H), 3.31 (m, 4H), 3.19 (m, 4H), 2.79 (s, 4H). ¹³C-NMR (CDCl_3 , 101 MHz, 300K) δ , ppm: 159.65, 149.87, 149.08, 144.74, 136.42, 128.21, 124.30, 123.20, 122.04, 63.75, 55.94, 50.78. MALDI-TOFMS (m/z): 497.1945 [M+H]⁺.



Scheme V. 4. Synthesis of 4-NO₂-spacer- Py_2tacn .

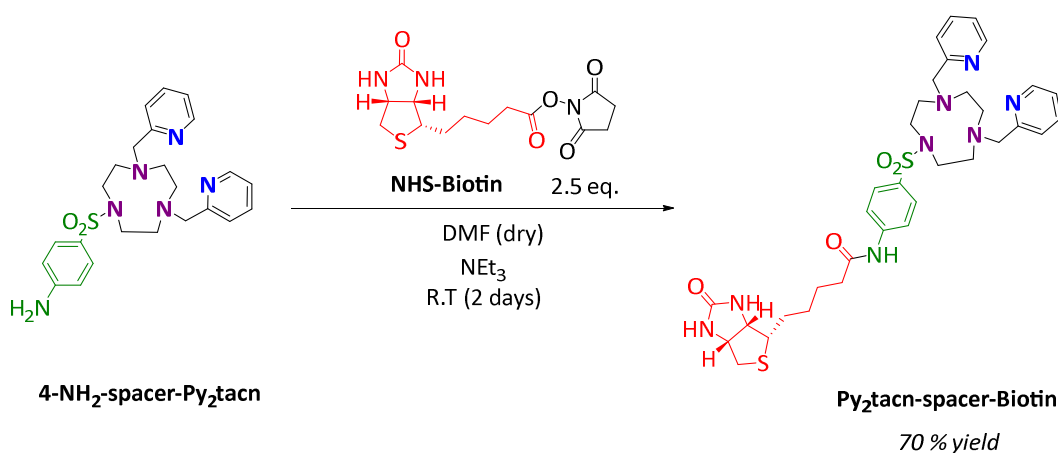
4-NH₂-spacer-Py₂tacn. The reduction of NO₂ group from the spacer moiety into NH₂ was performed following the general procedure described in the literature.³⁷⁰



Scheme V. 5. Synthesis of 4-NH₂-spacer-Py₂tacn.

A flame dried round bottom flask containing a suspension of Pd/C (19.59 mg, 5 mol%) in MeOH (20 mL) was charged with 4-NO₂-spacer-Py₂tacn (177 mg, 0.356 mmol). The schlenk was purged three times with argon and filled with hydrogen (1 atm). The reaction was vigorously stirred for 4 hours at RT. Afterwards, the hydrogen was carefully released and the suspension was removed by filtration through a celite plug. The organic solvent was evaporated and the resulting product dried under vacuum, offering a pale yellow solid (165 mg, 0.356 mmol, quantitative yield). This compound is very unstable and it was used in the next step without any purification. ¹H-NMR (CDCl₃, 400 MHz, 300K) δ , ppm: 8.52-8.51 (m, 2H), 7.67-7.61 (m, 4H), 7.50-7.48 (m, 2H), 7.18-7.16 (m, 2H), 7.02-7.00 (m, 2H), 7.19-7.15 (m, 2H), 3.89 (s, 4H), 3.21 (m, 4H), 3.14 (m, 4H), 2.83 (s, 4H). MALDI-TOFMS (m/z): 467.5017 [M+H]⁺.

Py₂tacn-spacer-Biotin. The biotinylated ligand Py₂tacn-spacer-Biotin was synthesized according to the general procedure described in the literature.³⁷⁶

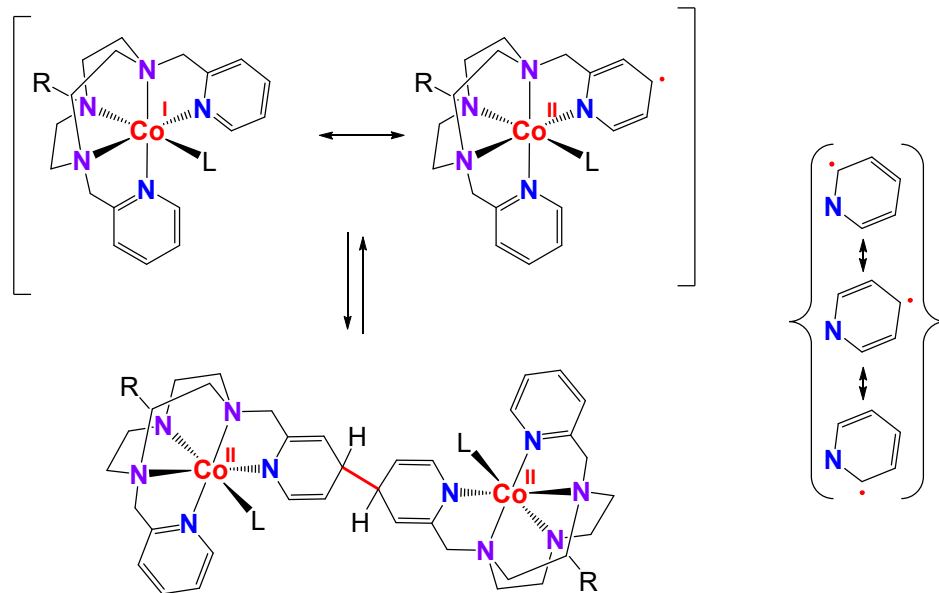


Scheme V. 6. Synthesis of Py₂tacn-spacer-Biotin.

Biotin *N*-hydroxysuccinimide active ester of D-biotin (NHS-biotin) (91.5 mg, 0.268 mmol, 2.5 eq.), 4-NH₂-spacer-Py₂tacn (50 mg, 0.107 mmol, 1 eq.), and triethylamine (0.1 mL, 0.8 mmol) were mixed in 2.5 mL of dry DMF. The reaction mixture was stirred at room temperature for 2 days under argon atmosphere. After that, it was slowly diluted with water (10 mL) and acidified with HCl (2 M) up to pH 1. The solution was extracted with CH₂Cl₂ (3x10 mL) in order to remove the unreacted NHS-biotin. Then, the aqueous solution was further basified up to pH 10 by the addition of NaOH (2M), and extracted with CH₂Cl₂ (3x10 mL). The combined organic layers were then dried over anhydrous MgSO₄, filtered and the solvent was removed with rotary evaporator. After drying under vacuum a pale yellow solid was obtained (0.049 g, 0.071 mmol, 66 % yield) and used without further purification. ¹H-NMR (CDCl₃, 500 MHz, 300K) δ, ppm: 8.51-8.50 (m, 2H), 7.66-7.46 (m, 8H), 7.17-7.15 (m, 2H), 4.49 (m, 1H), 4.30 (m, 1H), 3.88 (s, 4H), 3.27-3.13 (m, 8H), 2.79 (s, 4H), 1.80-1.27 (m, 6H). MALDI-TOFMS (m/z): 693.53 [M+H]⁺.

CHAPTER VI

Synthesis, Characterization and Reactivity of Cobalt Intermediates in Low-Oxidation State



VI. SYNTHESIS, CHARACTERIZATION AND REACTIVITY OF COBALT INTERMEDIATES IN LOW-OXIDATION STATE

VI.1. STATE-OF-THE-ART

The development of effective catalysts requires a fundamental understanding of reaction mechanisms.^{83,87,396,397} State of the art characterization experiments based on ESI-MS,^{97,105} electrochemistry,^{86,136} spectroelectrochemistry^{97,105,133,398} and steady-state UV/Vis spectroscopy,^{113,399} and EPR^{113,400} coupled with time-resolved IR spectroscopy,^{401,402} transient absorption spectroscopy^{97,105,133,398} and pulse radiolysis¹⁰⁵ techniques have been performed. Besides all the studies carried out until now, the formation of a Co^I intermediate in the water reduction catalytic cycle has been indirectly proposed based on dynamics with the photosensitizer and theoretically described due to the intrinsic difficulty.^{126,141}

Another approach has been the *in-situ* generation in organic solvents of the low oxidation state intermediates starting from Co^{III} or Co^{II} species by strong reducing agents (such as Co(Cp)₂ or Co(Cp*)₂),^{113,141,313,345} Na/Hg¹⁰⁵ or by bulk electrochemistry.^{112,142} However, even in these cases the characterization is still rough and only few reactivity studies have been performed. Putative *in-situ* generated Co^I intermediates react with protons to yield H₂ and cobalt species in higher oxidation state (Co^{II} and/or Co^{III}).^{113,136,141,313,349,398}

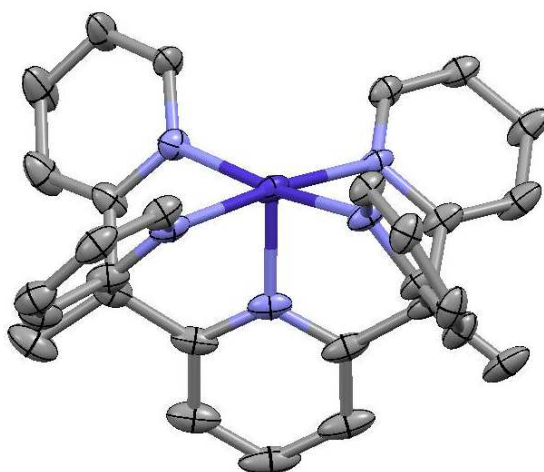


Figure VI. 1. Crystal structure (Ellipsoids 50 % probability level) of [Co^I(PY5Me₂)](BPh₄) complex reported by J. Long and C. Chang groups.¹⁰¹ In purple, blue and grey there are the Co, N and C atoms, respectively; H atoms are omitted for clarity.

An important progress in the characterization of Co^I complexes has recently achieved by J. Long and C. Chang groups.¹⁰¹ They reported the synthesis of $[\text{Co}^I(\text{PY5Me}_2)](\text{BPh}_4)$ by reaction of PY5Me_2 with $\text{Co}^I(\text{PPh}_3)_3\text{Cl}$ followed by chloride abstraction with NaBPh_4 . The X-ray structure of $[\text{Co}^I(\text{PY5Me}_2)](\text{BPh}_4)$ shows a pentacoordinate square planar pyramidal cobalt complex (Figure VI. 1). Unfortunately, only UV/Vis spectroscopy data was reported. The isolated $[\text{Co}^I(\text{PY5Me}_2)](\text{BPh}_4)$ complex reacts in CH_3CN with a large excess of tosic acid to form the $[\text{Co}^{II}(\text{PY5Me}_2)\text{NCCH}_3]$ complex and 0.6 equivalents of H_2 for every two equivalents of Co^I .

One of the difficulties of the characterization of Co^I intermediates in photocatalytic reactions is their optically silent nature. In this regard, X-ray absorption spectroscopy (XAS) is a well-known spectroscopic technique used to determine the local geometry and/or electronic structure of matter, which is very sensitive and therefore is a unique tool for monitoring. XAS experiments require an intense and tuneable X-ray beam of a synchrotron radiation. Recently, seminal pump-probe Laser – X-ray Transient Absorption Spectroscopy (L-XTA)¹ (Co K-edge) studies on photosensitizer-cobaloxime systems^{139,403} have revealed a change in the oxidation state and modifications in the bonding. However, these studies were carried out in dry organic solvents.

Reaching a specific low oxidation state at the metal center is not always possible due to an inherent instability of metal complexes towards environment or energetically limitations. In the later case, the introduction of a redox active ligand could beneficially facilitate the generation of the active formal oxidation state of the complex.⁴⁰⁴⁻⁴¹¹ Such redox non-innocent ligands (RNILs) are molecular scaffolds that are able to delocalize part of the electronic density of the complexes into a place in their structure where redox processes can also take place. These ligands can be simply carbene, imido or oxo groups or elaborated ligands such as imines, pyridine-imines, catechol, o-aminophenol and o-phenylenediamine moieties.

¹ In L-XTA experiments a pump Laser is synchronized with an X-ray beam of given energy (Co K-edge in the case of this experiments) to directly probe the transient electronic and geometric changes at the element of study.

In extreme cases even ligands such as a pyridine can also act as redox non-innocent ligand.^{408,409} This unusual reactivity was reported by P. Holland's group in the $L'Fe(pyridine)_2$ ($L' = 2,4$ -bis(2,6-diisopropylimino)pentyl) complex. Reactivity, spectroscopy and theoretical studies support that an electron is delocalized over the pyridine ring. Diagnosis of this electron delocalization is the establishment of an equilibrium between the monomeric and dimeric forms by a C-C bond formation at the para position of the pyridine (Figure VI. 2).

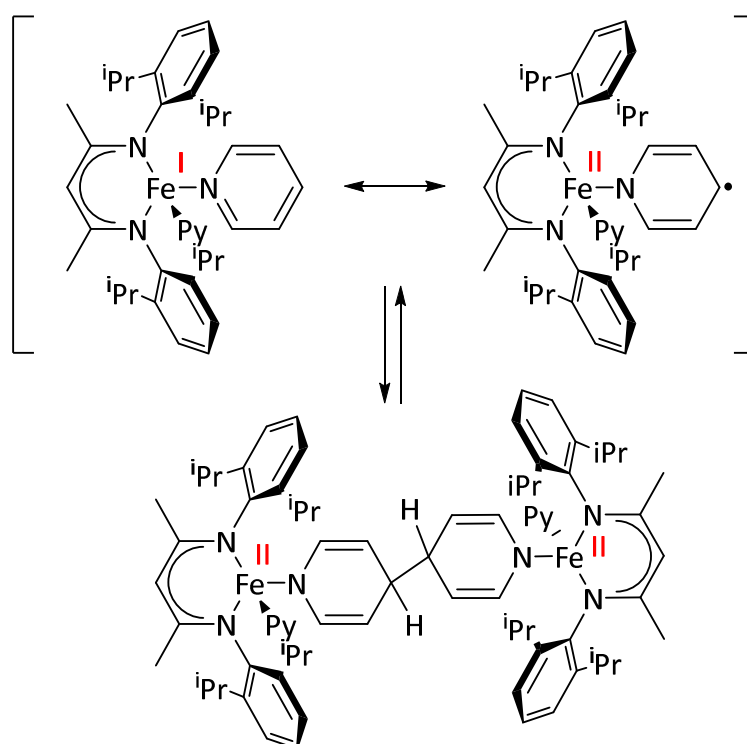


Figure VI. 2. Redox non-innocent nature of the $L'Fe(pyridine)_2$ ($L' = 2,4$ -bis(2,6-diisopropylimino)pentyl) complex and the reversible C-C bond formation at the para-position of the pyridine reduction.

In the context of water reduction it has been proposed that pyridine-imine⁴¹² bi-pyridine^{100,342} and pyrazine⁴¹³ based ligands could act as RNILs. However, for pyridine-imine based complexes no spectroscopic evidences have been reported so far. The RNIL nature of the remaining ligands is only supported by theoretical and electrochemical studies. The limited amount of information in the literature about the Co^I oxidation state in relation with water reduction catalysis manifests the intrinsic difficulty to study those systems.

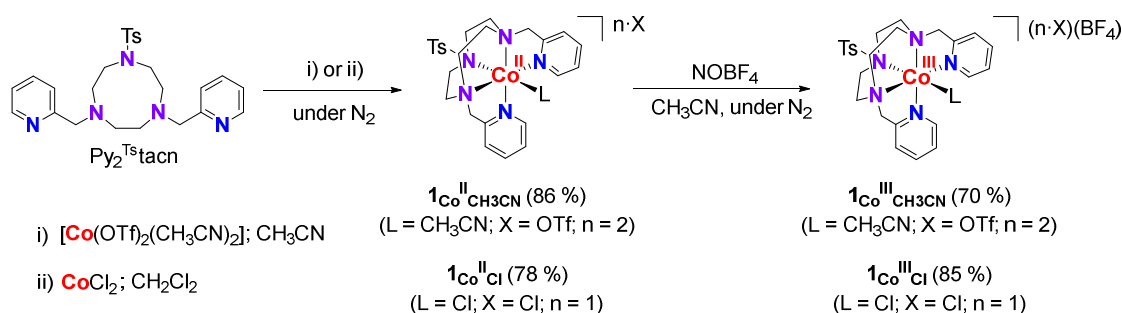
Taking into consideration the state-of-the-art of the field we become interested into further explore the Co^I oxidation state derived from complex $\mathbf{1}_{\text{Co}}$. In this thesis, it is described the *in-situ* formation of $\mathbf{PS}_{\text{Ir}}^{\text{II}}$ and its reaction with $\mathbf{1}_{\text{Co}}^{\text{II}}$ to form the putative $\mathbf{1}_{\text{Co}}^I$ intermediate in the way to form cobalt hydrides and finally H_2 *via* protonation. Therefore, access to the $\mathbf{1}_{\text{Co}}^I$ intermediate will allow the study of its reactivity against H_2O and acids. These studies will provide further understanding of the operative mechanism in the reduction of water, ketones and aldehydes catalyzed by pentadentate aminopyridine cobalt complexes.

VI.2. RESULTS AND DISCUSSION

We performed a study to fully characterize the $\text{Py}_2^{\text{Ts}}\text{tacn}$ cobalt complex in oxidation state (I). We have studied the structure in solution by EPR and NMR and in solid state by EXAFS and SQUID magnetometry. Different synthetic strategies were followed to obtain the cobalt complex in low oxidation state: i) by direct reaction of $\text{Co}(\text{PPh}_3)_3\text{Cl}$ with $\text{Py}_2^{\text{Ts}}\text{tacn}$, ii) by reduction of $\mathbf{1}_{\text{Co}^{\text{II}}}$ with strong reducing agents and iii) by *in-situ* photochemical reduction with the $\text{PS}_{\text{Ir}}/\text{Et}_3\text{N}$ system. To complete the study we have synthesized and characterized complexes $\mathbf{1}_{\text{Co}^{\text{II}}}\text{L}$ and $\mathbf{1}_{\text{Co}^{\text{III}}}\text{L}$ ($\text{L} = \text{CH}_3\text{CN}$, OTf and Cl).

VI.2.1. Synthesis and Characterization of Cobalt Complexes $\mathbf{1}_{\text{Co}^{\text{I}}}\text{Cl}$, $\mathbf{1}_{\text{Co}^{\text{II}}}\text{L}$ and $\mathbf{1}_{\text{Co}^{\text{III}}}\text{L}$

Compounds $\mathbf{1}_{\text{Co}^{\text{II}}}\text{CH}_3\text{CN}$ and $\mathbf{1}_{\text{Co}^{\text{II}}}\text{Cl}$ were obtained straightforward by direct reaction of $\text{Py}_2^{\text{Ts}}\text{tacn}$ with $[\text{Co}(\text{OTf})_2(\text{CH}_3\text{CN})_2]$ in CH_3CN and CoCl_2 in CH_2Cl_2 , respectively (Scheme VI. 1). These Co^{II} compounds were purified by slow diffusion of diethylether in a CH_2Cl_2 solution affording crystalline products suitable for X-ray diffraction analysis. Good yields in the synthesis of $\mathbf{1}_{\text{Co}^{\text{III}}}\text{CH}_3\text{CN}$ and $\mathbf{1}_{\text{Co}^{\text{III}}}\text{Cl}$ complexes were obtained by one electron oxidation of the $\mathbf{1}_{\text{Co}^{\text{II}}}\text{CH}_3\text{CN}$ and $\mathbf{1}_{\text{Co}^{\text{II}}}\text{Cl}$ precursors with 1 equivalent of NOBF_4 .



Scheme VI. 1. Synthesis of compounds $\mathbf{1}_{\text{Co}^{\text{n}}}\text{L}$ (n = II or III and L = NCCH_3 or Cl).

The structure of the complexes was first studied in solution by ^1H -NMR spectroscopy in CD_3CN . As expected $\mathbf{1}_{\text{Co}^{\text{II}}}\text{CH}_3\text{CN}$ and $\mathbf{1}_{\text{Co}^{\text{II}}}\text{Cl}$ are paramagnetic compounds exhibiting spectral windows expanding from -120 to 310 ppm, which is in agreement with a $t_{2g}^5 e_g^2$ or a $t_{2g}^6 e_g^1$ Co^{II} configuration. The ^1H -NMR spectra of $\mathbf{1}_{\text{Co}^{\text{II}}}\text{Cl}$ and $\mathbf{1}_{\text{Co}^{\text{II}}}\text{CH}_3\text{CN}$ at 235 K are clearly different (Figure VI. 3) indicating that Cl is not replaced by CD_3CN in $\mathbf{1}_{\text{Co}^{\text{II}}}\text{Cl}$. The paramagnetic spectra of both complexes are temperature dependent, observing a significant signal broadening at temperatures above 280 K ($\mathbf{1}_{\text{Co}^{\text{II}}}\text{Cl}$) and 260 K ($\mathbf{1}_{\text{Co}^{\text{II}}}\text{MeCN}$) (Figure A. 3. 1 and Figure A. 3. 2). This behaviour may indicate a fluxional

process at room and higher temperatures since the expected behavior for paramagnetic complexes is a signal broadening when decreasing the temperature. On the other hand, the Co^{III} complexes are diamagnetic compounds, as expected for a low-spin d^6 configuration (Figure VI. 3).

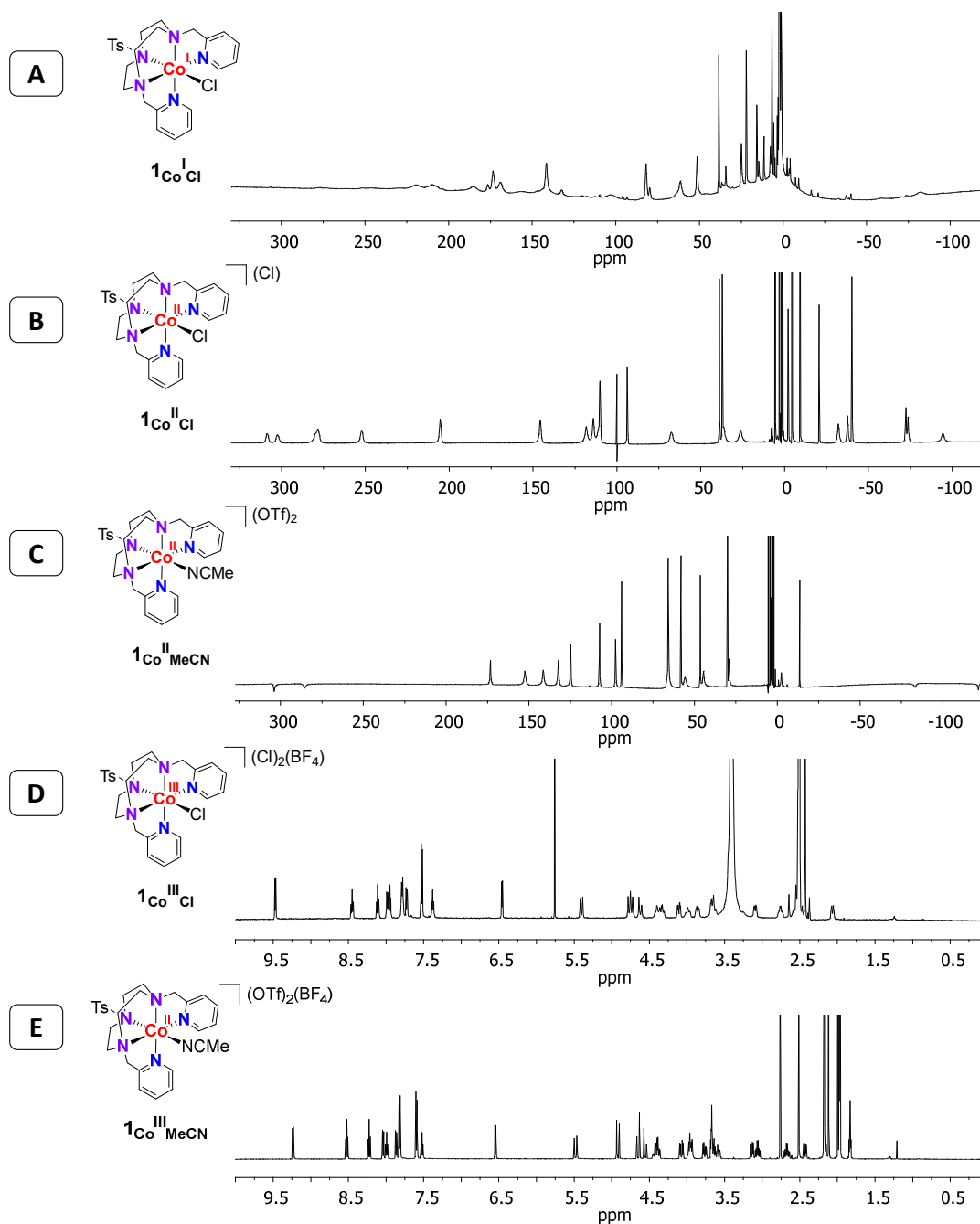


Figure VI. 3. A, B and C) Paramagnetic $^1\text{H-NMR}$ spectra measured at 235 K (500 MHz, CD_3CN) of the chemically synthesized compounds $1_{\text{Co}^{\text{I}}\text{Cl}}$, $1_{\text{Co}^{\text{II}}\text{Cl}}$ and $1_{\text{Co}^{\text{II}}\text{CH}_3\text{CN}}$, respectively. D) $^1\text{H-NMR}$ spectrum of $1_{\text{Co}^{\text{III}}\text{Cl}}$ in d_6 -DSMO at 298 K. E) $^1\text{H-NMR}$ spectrum of $1_{\text{Co}^{\text{III}}\text{CH}_3\text{CN}}$ in CD_3CN at 298 K.

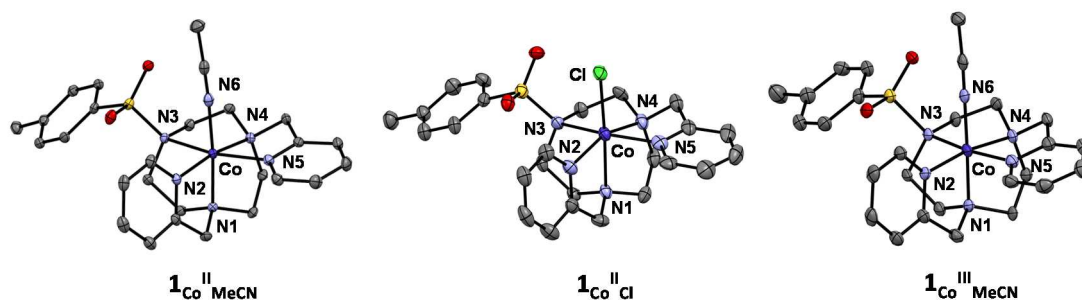


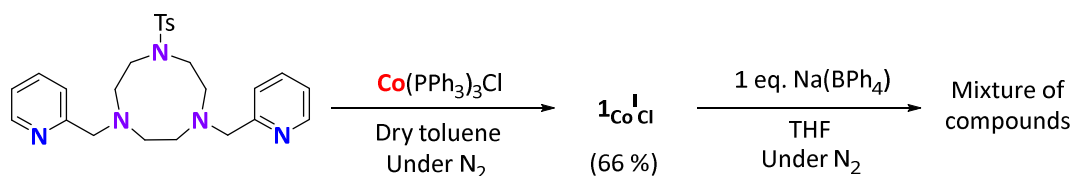
Figure VI. 4. Crystal structures of the cobalt complexes $\mathbf{1Co}^{\text{II}}_{\text{CH}_3\text{CN}}$, $\mathbf{1Co}^{\text{II}}_{\text{Cl}}$ and $\mathbf{1Co}^{\text{III}}_{\text{CH}_3\text{CN}}$. Ellipsoids are drawn at the 50 % probability level. Solvent molecules and hydrogen atoms are omitted for clarity. Color code: cobalt (blue), nitrogen (light blue), oxygen (red), fluor (yellow), carbon (grey) and sulfur (orange).

The solid state molecular structure of complexes $\mathbf{1Co}^{\text{II}}_{\text{CH}_3\text{CN}}$, $\mathbf{1Co}^{\text{II}}_{\text{Cl}}$ and $\mathbf{1Co}^{\text{III}}_{\text{CH}_3\text{CN}}$ was determined by X-ray diffraction analysis (Figure VI. 4). The coordination geometry around the metal ion is slightly distorted from idealized octahedral geometries. The five coordination sites of the Co^{II} center are occupied by three N atoms from the triazacyclononane (tacn) backbone and two from the pyridines leading to a chiral environment. Both enantiomers are present in the crystallographic unit cell. The additional coordination site of the octahedral geometry is occupied by the exogenous CH_3CN ligand ($\mathbf{1Co}^{\text{II}}_{\text{CH}_3\text{CN}}$ and $\mathbf{1Co}^{\text{III}}_{\text{CH}_3\text{CN}}$) or Cl^- anion ($\mathbf{1Co}^{\text{II}}_{\text{Cl}}$).

The complexes crystallize in a monoclinic ($\mathbf{1Co}^{\text{II}}_{\text{CH}_3\text{CN}}$) or triclinic ($\mathbf{1Co}^{\text{III}}_{\text{CH}_3\text{CN}}$ and $\mathbf{1Co}^{\text{II}}_{\text{Cl}}$) crystal system (Table A. 3. 1). The averaged Co-N bond lengths for the Co^{II} complexes are 1.9-2.4 Å, characteristic for $S = 3/2$ Co^{II} complexes.^{97,292} All Co-N bond distances of $\mathbf{1Co}^{\text{II}}_{\text{CH}_3\text{CN}}$ are contracted upon one electron oxidation⁴¹⁴ ($\mathbf{1Co}^{\text{III}}_{\text{CH}_3\text{CN}}$), showing the largest decrease from 2.3856(17) Å to 2.373 (4) Å (for the Co-N_{3tosyl} bond). The Co-N_{3tosyl} bond distances are observed larger than the Co-N_{py} distances, this is attributed to the electron withdrawing character of the tosyl moiety (See Table 3. 2 for selected bond lengths and angles).

We attempted the synthesis of a cobalt complex in oxidation state (I) with the $\text{Py}_2^{\text{T}}\text{stacn}$ ligand by one electron reduction of $\mathbf{1Co}^{\text{II}}_{\text{Cl}}$ using $\text{Co}(\text{Cp}^*)_2$ or $\text{Na}(\text{Hg})$, however the reactions were not clean and the Co^{I} compound was accompanied by important amounts of side-products. More successful was the equimolar reaction of $\text{Co}(\text{PPh}_3)_3\text{Cl}$ with $\text{Py}_2^{\text{T}}\text{stacn}$ in toluene solution. After purification we isolated a deep blue solid highly unstable towards H_2O and O_2 . In contrast with the synthetic method previously reported

by Long, Chang and co-workers¹⁰¹ for the synthesis of $[\text{Co}^{\text{I}}(\text{PY5Me}_2)](\text{BPh}_4)$ all attempts to remove the Cl anion by $\text{Na}(\text{BPh}_4)$ failed in obtaining a clean product. Indeed the product formed after the reaction was proven to be highly unstable. The first isolated deep blue solid ($\mathbf{1}_{\text{Co}^{\text{I}}\text{Cl}}$) was indefinitely stable as solid, so we carried out the characterization and study the reactivity.



Scheme VI. 2. Synthesis of $\mathbf{1}_{\text{Co}^{\text{I}}\text{Cl}}$ and their reactivity with $\text{Na}(\text{BPh}_4)$.

The isolated $\mathbf{1}_{\text{Co}^{\text{I}}\text{Cl}}$ shows a main set of paramagnetic signals in the $^1\text{H-NMR}$ spectrum ranged from -100 °C to 250 ppm. In addition, it can be observed a small quantity of a second compound with much lower intensity (Figure VI. 5). $^1\text{H-NMR}$ spectra at varied temperatures (VT- $^1\text{H-NMR}$) indicate a possible dynamic behaviour. The broad signals in the $^1\text{H-NMR}$ spectrum at room temperature become well-defined at 270 K and at lower temperature the signals become broader again (Figure A. 3. 3).

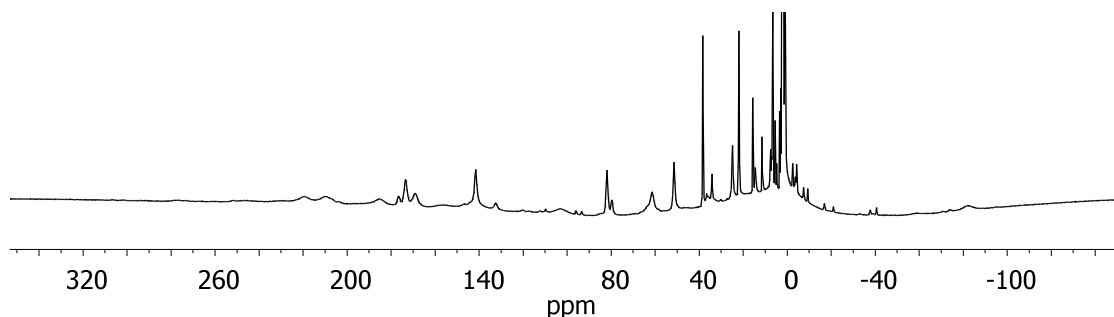


Figure VI. 5. $^1\text{H-NMR}$ (CD_3CN , 500 MHz, 235 K) paramagnetic spectrum of $\mathbf{1}_{\text{Co}^{\text{I}}\text{Cl}}$.

In order to gain some insight into the light-driven reactivity we explored the *in-situ* photogeneration of Co^{I} species by irradiation with a LED at 447 nm. The irradiation of a CD_3CN solution of $\mathbf{1}_{\text{Co}^{\text{II}}\text{Cl}}$ (20 mM) containing PS_{Ir} (20 mM) and Et_3N (240 mM) in a NMR tube at 250 K during 15 min lead to the complete disappearance of signals belonging to $\mathbf{1}_{\text{Co}^{\text{II}}\text{Cl}}$ and the appearance of a new set of paramagnetic signals. The resulting $^1\text{H-NMR}$ spectrum was almost identical to the one of the chemically synthesized $\mathbf{1}_{\text{Co}^{\text{I}}\text{Cl}}$ (Figure VI. 6), matching not only the main set of signals but also the

very low intensity set of $^1\text{H-NMR}$ signals. This result suggests that two species could be in equilibrium.

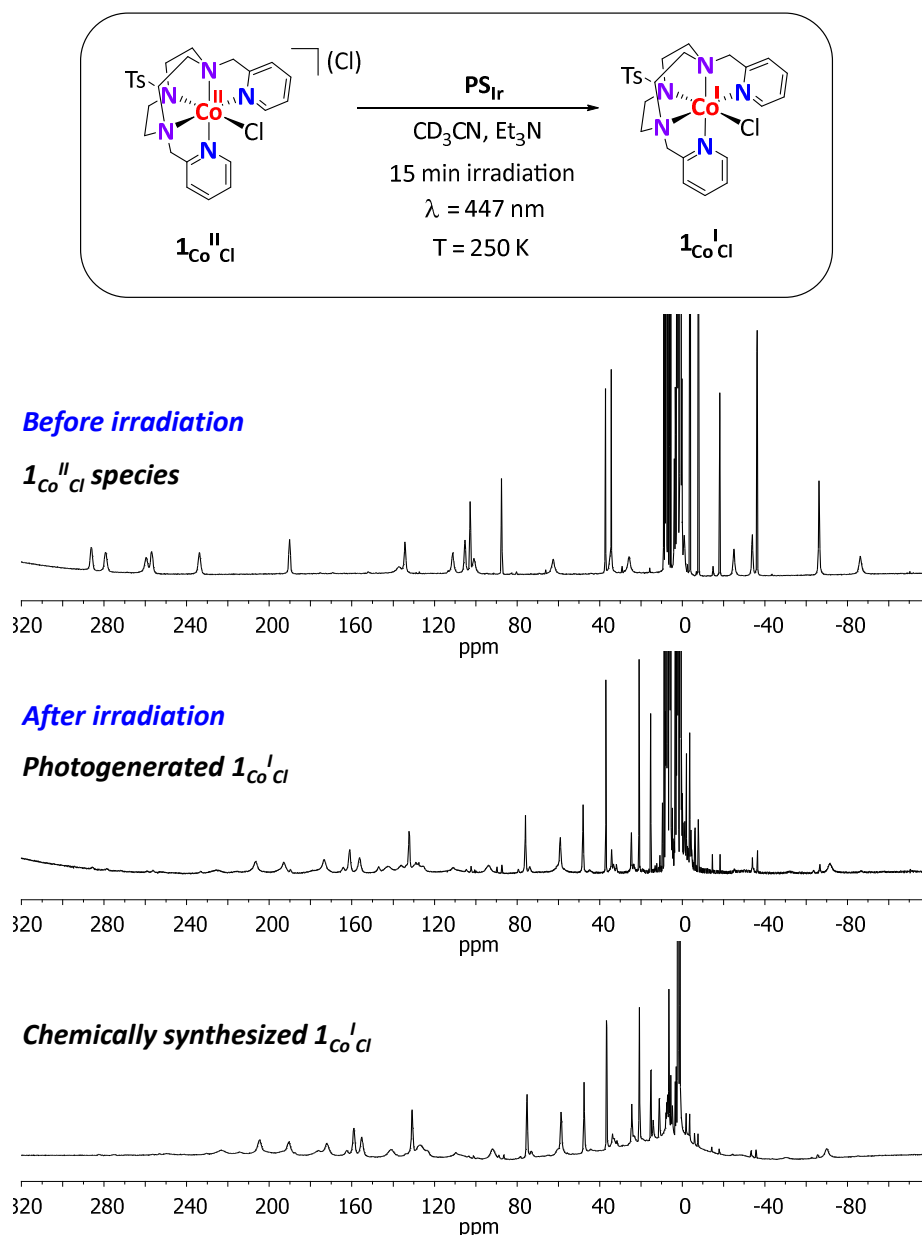


Figure VI. 6. Photoreduction of $\mathbf{1}_{\text{Co}^{\text{II}}\text{Cl}}$ to $\mathbf{1}_{\text{Co}^{\text{I}}\text{Cl}}$. *Top:* $^1\text{H-NMR}$ paramagnetic spectrum before irradiation. *Middle:* $^1\text{H-NMR}$ paramagnetic spectrum after 15 min of irradiation. *Bottom:* $^1\text{H-NMR}$ paramagnetic spectrum of the chemically synthesized $\mathbf{1}_{\text{Co}^{\text{I}}\text{Cl}}$ compound. Conditions: $\mathbf{1}_{\text{Co}^{\text{II}}\text{Cl}}$ (20 mM), PS_{Ir} (20 mM), Et_3N (240 mM) in CD_3CN irradiating at 250 K ($\lambda = 447 \text{ nm}$).

The same NMR-tube photoredox study was carried out using $\mathbf{1}_{\text{Co}^{\text{II}}\text{CH}_3\text{CN}}$. Again after 15 min of irradiation at 250 K the signals belonging to $\mathbf{1}_{\text{Co}^{\text{II}}\text{Cl}}$ completely disappear and a new set of paramagnetic signals appear, but clearly different to the ones corresponding to $\mathbf{1}_{\text{Co}^{\text{I}}\text{Cl}}$ (Figure VI. 7). This difference in $^1\text{H-NMR}$ spectrum indicates that the chloride anion should be bonded to the Co^{I} center.

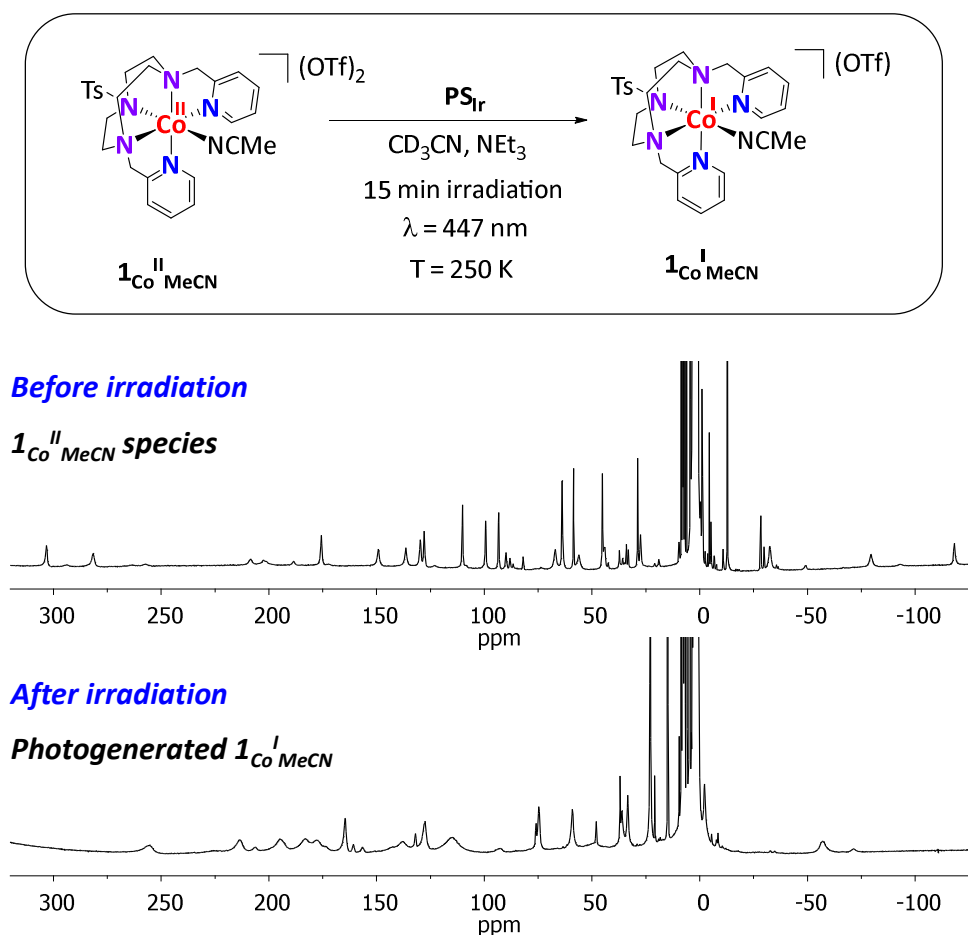


Figure VI. 7. Photoreduction of $\mathbf{1}_{\text{Co}^{\text{II}} \text{CH}_3\text{CN}}$ to $\mathbf{1}_{\text{Co}^{\text{I}} \text{CH}_3\text{CN}}$. *Top:* $^1\text{H-NMR}$ paramagnetic spectrum before irradiation. *Middle:* $^1\text{H-NMR}$ paramagnetic spectrum after 15 min of irradiation. *Bottom:* $^1\text{H-NMR}$ paramagnetic spectrum of the chemically synthesized $\mathbf{1}_{\text{Co}^{\text{I}} \text{Cl}}$ compound. Conditions: $\mathbf{1}_{\text{Co}^{\text{II}} \text{CH}_3\text{CN}}$ (20 mM), PS_{Ir} (20 mM), Et_3N (240 mM) in CD_3CN irradiating at 250 K ($\lambda = 447 \text{ nm}$).

We measured the EPR spectra of complexes $\mathbf{1}_{\text{Co}^{\text{II}} \text{Cl}}$, $\mathbf{1}_{\text{Co}^{\text{II}} \text{CH}_3\text{CN}}$ and $\mathbf{1}_{\text{Co}^{\text{I}} \text{Cl}}$ at 10 K using butyronitrile as solvent. The EPR features are observed in the region close to $g = 2$, consistent with Co^{II} and Co^{I} complexes reported in the literature.^{112,400} The significant different EPR features between $\mathbf{1}_{\text{Co}^{\text{II}} \text{Cl}}$ and $\mathbf{1}_{\text{Co}^{\text{II}} \text{CH}_3\text{CN}}$ confirm that the Cl anion remains coordinated to the Co centre (Figure VI. 8).

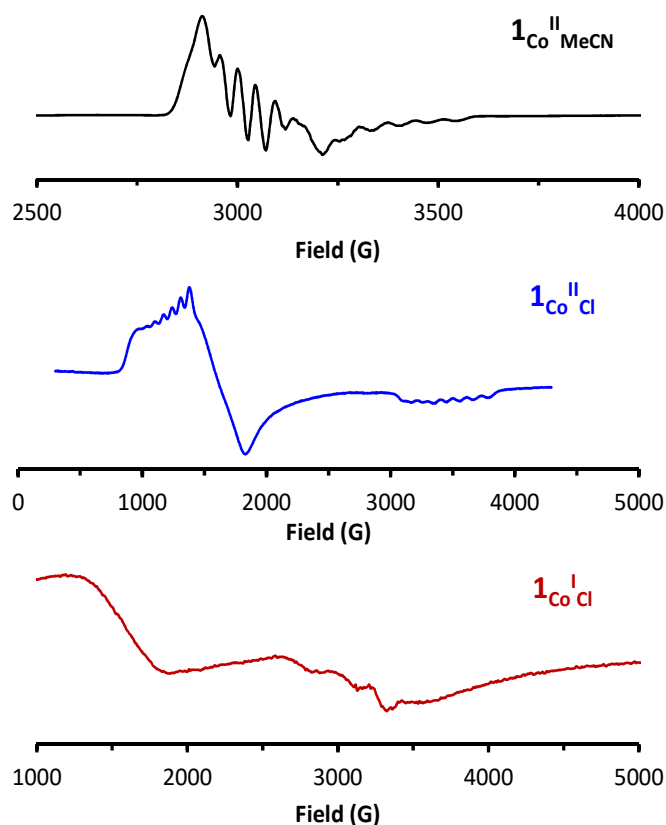


Figure VI. 8. X-band EPR spectra (10 K) of butyronitrile solutions of 1 mM $1_{\text{Co}}^{\text{II}}_{\text{CH}_3\text{CN}}$ (black), $1_{\text{Co}}^{\text{II}}_{\text{Cl}}$ (blue) and $1_{\text{Co}}^{\text{I}}_{\text{Cl}}$ (red). Microwave frequency, 9.63 GHz; modulation frequency, 100 KHz.

VI.2.1.1. X-ray Absorption Fine Structure Characterization (XAS and EXAFS) of $1_{\text{Co}}^{\text{I}}_{\text{L}}$, $1_{\text{Co}}^{\text{II}}_{\text{L}}$ and $1_{\text{Co}}^{\text{III}}_{\text{L}}$ ($\text{L} = \text{Cl}$ or CH_3CN)

To further understand the coordination structure of the cobalt complex in the lower oxidation state ($1_{\text{Co}}^{\text{I}}_{\text{Cl}}$ and $1_{\text{Co}}^{\text{I}}_{\text{CH}_3\text{CN}}$) we have performed an X-ray Absorption Fine Structure Characterization in collaboration with Dr. V. Martin-Diaconescu. We have also studied the homologous complexes $1_{\text{Co}}^{\text{II}}_{\text{L}}$ and $1_{\text{Co}}^{\text{III}}_{\text{L}}$ ($\text{L} = \text{Cl}$ or CH_3CN) to have a proper reference for the evaluation of both the energies and the fitting model.

XAS data for $1_{\text{Co}}^{\text{I}}_{\text{Cl}}$, $1_{\text{Co}}^{\text{II}}_{\text{Cl}}$ and $1_{\text{Co}}^{\text{III}}_{\text{Cl}}$ is collected in Figure VI. 9. The resulting $1_{\text{Co}}^{\text{I}}_{\text{Cl}}$ species gave a Co K-edge spectrum with a pre-edge feature centered at 7709.4 eV and a rising edge at ~ 7718.3 eV (using the half-high method). Interestingly, the $1_{\text{Co}}^{\text{II}}_{\text{Cl}}$ analogue exhibits a slightly lower rising edge feature at ~ 7717.8 eV. The comparable rising edge energies for $1_{\text{Co}}^{\text{II}}_{\text{Cl}}$ than $1_{\text{Co}}^{\text{I}}_{\text{Cl}}$ suggests similar effective charges for the two metal centers. The apparent equivalent oxidation state at the cobalt center in $1_{\text{Co}}^{\text{I}}_{\text{Cl}}$ and

$1_{\text{Co}}^{\text{II}}\text{Cl}$ cannot be rationalized at this stage and will be done in the discussion section. Nevertheless, the pre-edge is more intense and at a slightly higher energy (~ 7709.6 eV) for the Co^{II} than the Co^{I} center, consistent with a stronger metal-ligand interaction. It is also important to consider that the rising edge can often be obscured by $1s \rightarrow 4p$ transitions which can shift to lower energy with increased covalency.^{415,416} In the current case the $1s \rightarrow 3d$ transitions for $1_{\text{Co}}^{\text{II}}\text{Cl}$ which are antibonding with respect to the ligand-metal bond are destabilized with respect to $1_{\text{Co}}^{\text{I}}\text{Cl}$ suggesting a slightly stronger metal-ligand bond in the $1_{\text{Co}}^{\text{II}}\text{Cl}$ analogue, which can also contribute to a lower $1s \rightarrow 4p$ transition and an apparent lower rising edge for $1_{\text{Co}}^{\text{II}}\text{Cl}$ than $1_{\text{Co}}^{\text{I}}\text{Cl}$. Data acquired for complex $1_{\text{Co}}^{\text{III}}\text{Cl}$ has an XAS profile consistent with a Co^{III} center, having a most intense pre-edge in the series at 7710.0 eV with a rising edge at 7719.6 eV.

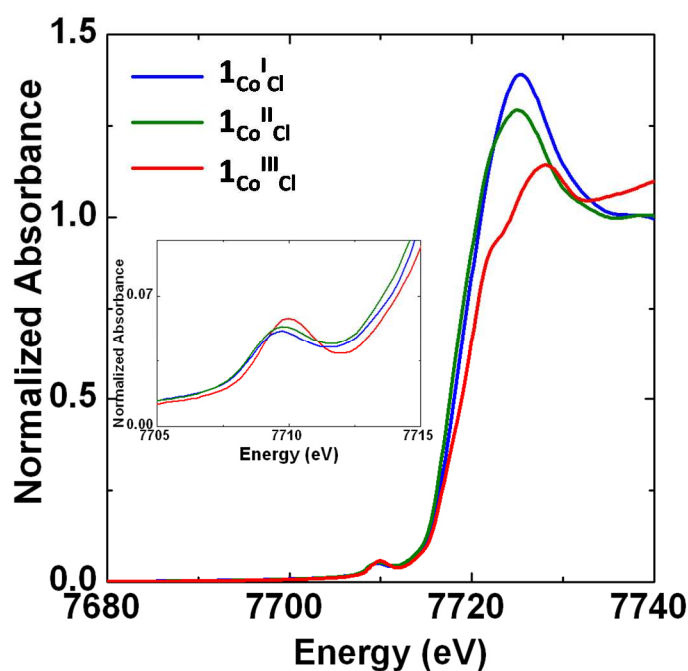


Figure VI. 9. XANES spectra of chemically generated 1_{Co}^nCl series ($n = 1, 2, 3$)

Bond distances for the cobalt coordination sphere of $1_{\text{Co}}^{\text{II}}\text{Cl}$ obtained by analysis of the Extended X-ray Absorption Fine Structure (EXAFS) Co K-edge spectrum are in good agreement with the X-ray diffraction data and DFT calculations (by Dr. F. Acuña-Parés), which validates our fitting model used in the EXAFS analysis. The same fitting model was also applied for $1_{\text{Co}}^{\text{III}}\text{Cl}$ EXAFS Co K-edge spectrum also resulting in a good agreement with the DFT calculations (Table VI. 1). As expected, a general contraction of the coordination shell around the cobalt center is observed.

Table VI. 1. Selected theoretical and experimental distances (Å) obtained by EXAFS and X-ray.

	PATH*	EXAFS			X-ray	DFT
		r(Å)	$\sigma^2(\times 10^3 \text{ \AA}^2)$	%R	Average dist. (Å)	Average dist. (Å)
$\mathbf{1}_{\text{Co}}^{\text{I}}\text{Cl}$	4 N/O	2.12(1)	6(2)	4.8	2.130(5)	2.12
	1 N/O	2.41(1)	6(5)			2.46
	1 Cl	2.33(2)	4(2)			2.58
$\mathbf{1}_{\text{Co}}^{\text{II}}\text{Cl}$	4 N/O	2.13(1)	4(1)	1.4	2.300(2)	2.15
	1 N/O	2.36(2)	12(3)			2.36
	1 Cl	2.31(1)	2(1)			2.37
$\mathbf{1}_{\text{Co}}^{\text{III}}\text{Cl}$	4 N/O	2.00(1)	7(1)	2.5		2.03
	1 N/O	2.20(1)	7(1)			2.32
	1 Cl	2.28	1(1)			2.25

More complex is the analysis of the $\mathbf{1}_{\text{Co}}^{\text{I}}\text{Cl}$ EXAFS Co K-edge spectrum. The best fitting model tested includes six coordination positions, being one of those a Cl atom. EXAFS analysis shows a general small bond distance increase in the first coordination shell. The EXAFS fitting shows four Co-N/O bonds paths with an average distance of 2.12 Å and additional N/O scatter at 2.41 Å of the cobalt center. Based in EXAFS analysis we modelled by DFT the structure of $\mathbf{1}_{\text{Co}}^{\text{I}}\text{Cl}$ with the $\text{Py}_2^{\text{T}}\text{stacn}$ ligand and a chloride atom coordinate to the cobalt center. The resulting model matches good the EXAFS models of the Co-N/O bonds paths and satisfactory in the Co-N(Ts) coordinate ($\Delta d = 0.05$ Å, considering the expected flat energy surface for the Co-N(Ts) bond). However, there is a important 0.25 Å discrepancy between the DFT and EXAFS Co-Cl bond distances. Nevertheless, the EXAFS distances are still closer to the molecular structure of $\mathbf{1}_{\text{Co}}^{\text{II}}\text{Cl}$ determined by X-ray diffraction analysis than to the DFT-modelled $\mathbf{1}_{\text{Co}}^{\text{I}}\text{Cl}$ geometry. At this point it is important to remark that all samples were analyzed by $^1\text{H-NMR}$ after the EXAFS experiments ensuring the integrity of the samples during the measurements.

We have also studied the XAS data for $\mathbf{1}_{\text{Co}}^{\text{II}}\text{CH}_3\text{CN}$, $\mathbf{1}_{\text{Co}}^{\text{III}}\text{CH}_3\text{CN}$ and the *in-situ* formed $\mathbf{1}_{\text{Co}}^{\text{I}}\text{CH}_3\text{CN}$ *via* irradiation of a solution containing $\mathbf{1}_{\text{Co}}^{\text{II}}\text{CH}_3\text{CN}$, $\text{PS}_{\text{Ir}}^{\text{II}}$ and Et_3N (Figure VI. 10). The $\mathbf{1}_{\text{Co}}^{\text{II}}\text{CH}_3\text{CN}$ spectrum shows a pre-edge at 7709.9 eV and a rising edge at 7718.7 eV, both higher in energy than the reported for the $\mathbf{1}_{\text{Co}}^{\text{II}}\text{Cl}$ analogue consistent with the

absence of Cl^- and a less electron donating coordination sphere. One electron oxidation results in $\mathbf{1}_{\text{Co}^{\text{III}}}\text{CH}_3\text{CN}$ with a rising edge energy of 7720.7 eV and a pre-edge at 7710.3 eV representative of a Co^{III} metal center.

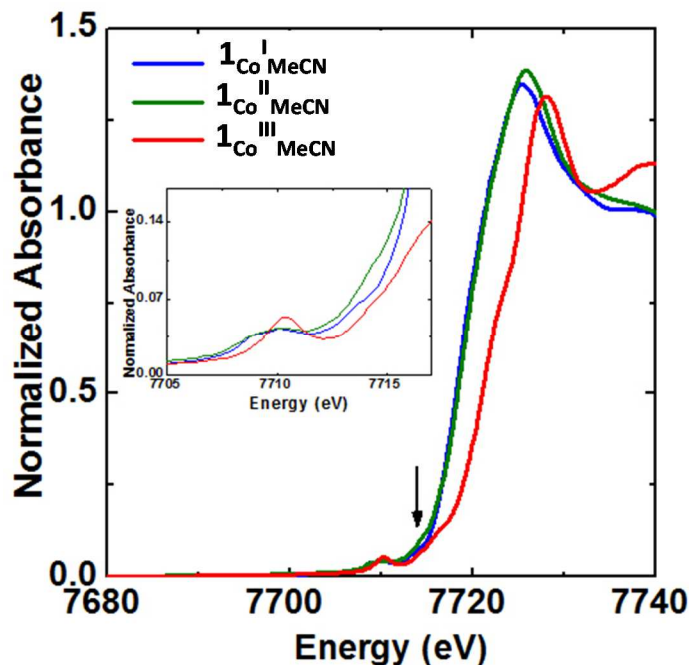
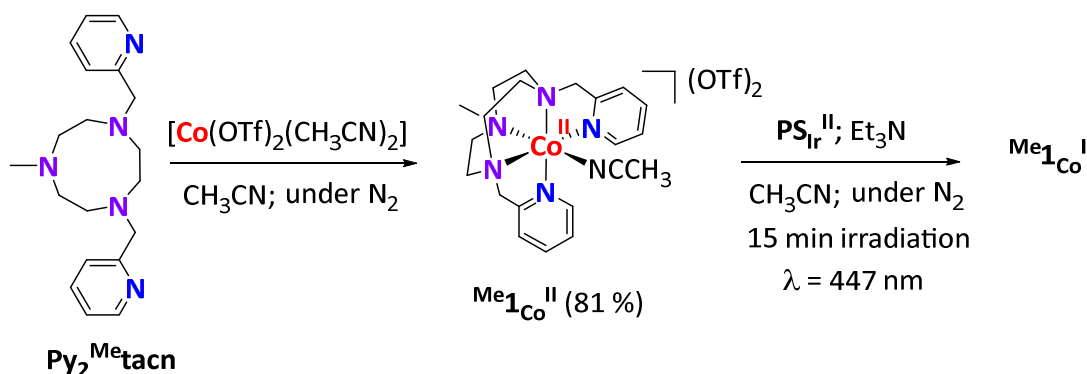


Figure VI. 10. XANES spectra of the photochemically generated $\mathbf{1}_{\text{Co}^{\text{I}}}\text{MeCN}$ compound with the chemically synthesized $\mathbf{1}_{\text{Co}^{\text{n}}}\text{MeCN}$ ($n = 2, 3$).

The $\mathbf{1}_{\text{Co}^{\text{I}}}\text{CH}_3\text{CN}$ sample for the XAS study was obtained in experimental conditions equivalent to the ones used for the $^1\text{H-NMR}$ studies, in which full formation of a new compound is observed (Figure VI. 7). Therefore, we prepared a solution of sample $\mathbf{1}_{\text{Co}^{\text{I}}}\text{CH}_3\text{CN}$ by irradiating a solution containing $\mathbf{1}_{\text{Co}^{\text{II}}}\text{CH}_3\text{CN}$ (15 mM), PS_{Ir} (7.5 mM) and Et_3N (140 mM) (See section VI.3.2) at 447 nm during 15 min. The resulting sample has a XAS spectrum profile (Figure VI. 10, $\mathbf{1}_{\text{Co}^{\text{I}}}\text{CH}_3\text{CN}$) with a similar rising edge (~ 7718.7 eV) and a split pre-edge slightly lower in energy (7709.5 eV) than the starting $\mathbf{1}_{\text{Co}^{\text{II}}}\text{CH}_3\text{CN}$. However, a change is observed where metal to ligand charge transfer features are expected to occur, at 7714.2 eV, just above in energy to the pre-edge.⁴¹⁶ Again, an apparent equivalent oxidation state (II) at the cobalt center in the formal Co^{I} species $\mathbf{1}_{\text{Co}^{\text{I}}}\text{CH}_3\text{CN}$ is intriguing.



Scheme VI. 3. Synthesis of compounds Me_1Co^n ($n = \text{I or II}$).

In order to discard that a reduction is taking place over the tosyl group of the ligand, preventing the formation of cobalt (I), we have prepared the analogous Co^{II} and Co^{I} complexes with the $\text{Py}_2^{\text{Me}}\text{tacn}$ ligand (Scheme VI. 3). Similar XANES profiles are also observed for this pair of complex $\text{Me}_1\text{Co}^{\text{I}}$ and $\text{Me}_1\text{Co}^{\text{II}}$. (Figure VI. 11, *left*). Apparently both have the same oxidation state. Furthermore the analogues $\mathbf{1}_{\text{Co}^{\text{I}}\text{CH}_3\text{CN}}$ and $\text{Me}_1\text{Co}^{\text{I}}$ are quite similar, however the rising edge for the methyl analogue is slightly higher in energy at 7719.2 eV with a slightly more intense pre-edge suggesting a higher effective charge at the metal center (Figure VI. 11, *right*). The fact that the same phenomena was also observed for $\text{Me}_1\text{Co}^{\text{I}}$ suggests that the tosyl group is not the reason behind this apparent oxidation state (II) at the cobalt center in formal Co^{I} species. The integrity of the samples was ensured by $^1\text{H-NMR}$ analysis after the EXAFS analysis.

An explanation for this apparent oxidation state (II) at the formal Co^{I} complexes could be a possible non-innocent behaviour of the ligand. This argument will be further elaborated in the following sections.

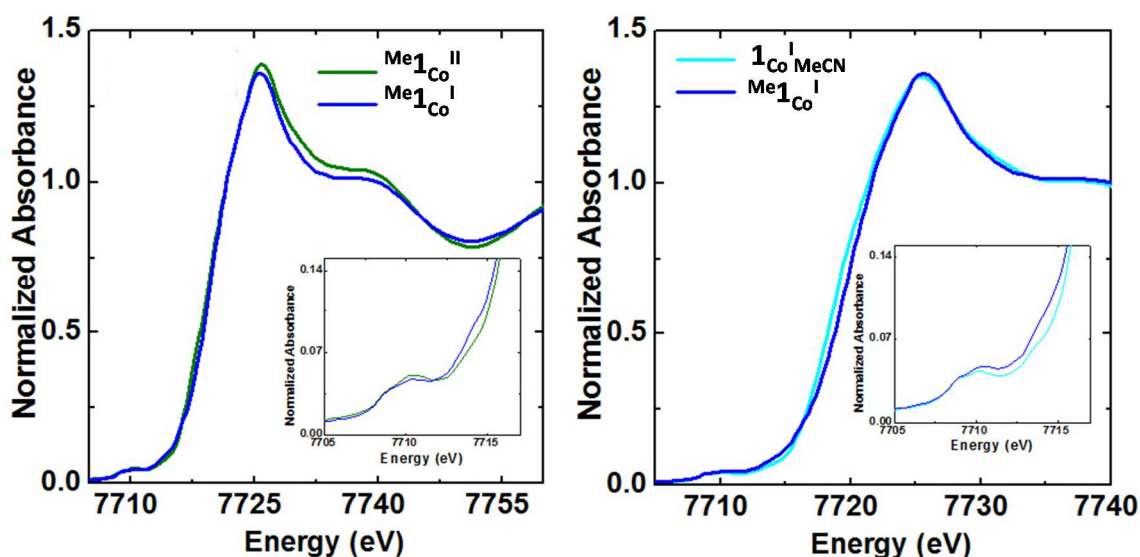


Figure VI. 11. *Left:* XANES spectra of $\text{Me}^1\text{Co}^{\text{II}}$ and the photochemically generated $\text{Me}^1\text{Co}^{\text{I}}$ compound. *Right:* XANES spectra of $1\text{Co}^{\text{II}}\text{MeCN}$ and $\text{Me}^1\text{Co}^{\text{I}}$.

VI.2.1.3. Magnetic measurements by SQUID magnetometry

To gain more information about the nature of $1\text{Co}^{\text{I}}\text{Cl}$ and $1\text{Co}^{\text{II}}\text{Cl}$ we have measured the magnetic properties using Superconducting Quantum Interference Device magnetometry (SQUID) from 300 K to 2 K. At room temperature, the product of the magnetic susceptibility and temperature ($\chi \cdot T$) is $2.5 \text{ emu} \cdot \text{mol}^{-1} \cdot \text{K}$ and $4 \text{ emu} \cdot \text{mol}^{-1} \cdot \text{K}$ for $1\text{Co}^{\text{I}}\text{Cl}$ and $1\text{Co}^{\text{II}}\text{Cl}$, respectively (Figure VI. 12). These values correspond to a typical $\text{Co}^{\text{II}} S = 3/2$ and a Landé factor g equal to 2.4 and 2.9 respectively.⁴¹⁷ We rationalize these results by considering that i) $1\text{Co}^{\text{I}}\text{Cl}$ is indeed Co^{II} or ii) the additional electron on the $1\text{Co}^{\text{I}}\text{Cl}$ system is not localized in a Co ion orbital, and could be delocalized in the pyridine ring. In this case, due to the delocalization, the contribution of this electron cannot be spotted because of the low value of Pauli paramagnetism. The difference in the g values could be due to a different distorted environment of Co as it can be seen by the EXAFS analysis. As expected, the $\chi \cdot T$ product decreases below 100 K due to the depopulation of the higher energy Kramer's doublets.¹¹²

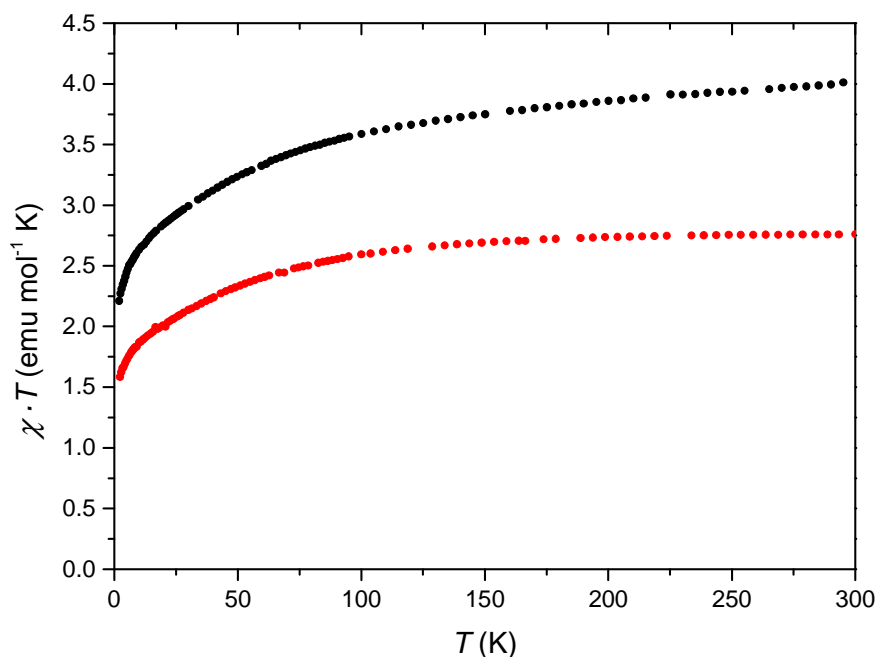


Figure VI. 12. $\chi \cdot T$ as a function of temperature from 300 to 2 K. The red dots correspond to $1\text{Co}^{\text{I}}\text{Cl}$ and the black ones to $1\text{Co}^{\text{II}}\text{Cl}$

VI.2.2. Reactivity of Co^{I} Species

The chemical and photochemical synthesis of $1\text{Co}^{\text{I}}\text{Cl}$ produces the same compound, clearly different to the homologous $1\text{Co}^{\text{II}}\text{Cl}$. Presumably $1\text{Co}^{\text{I}}\text{Cl}$ possesses an extra electron respect to $1\text{Co}^{\text{II}}\text{Cl}$. However, EXAFS and SQUID measurements are not conclusive and could be interpreted as a Co^{II} $S = 3/2$. Therefore, we decided to investigate the reactivity of $1\text{Co}^{\text{I}}\text{Cl}$ with trifluoroacetic acid and H_2O as proton sources and O_2 by ^1H -NMR spectroscopy and XAS.

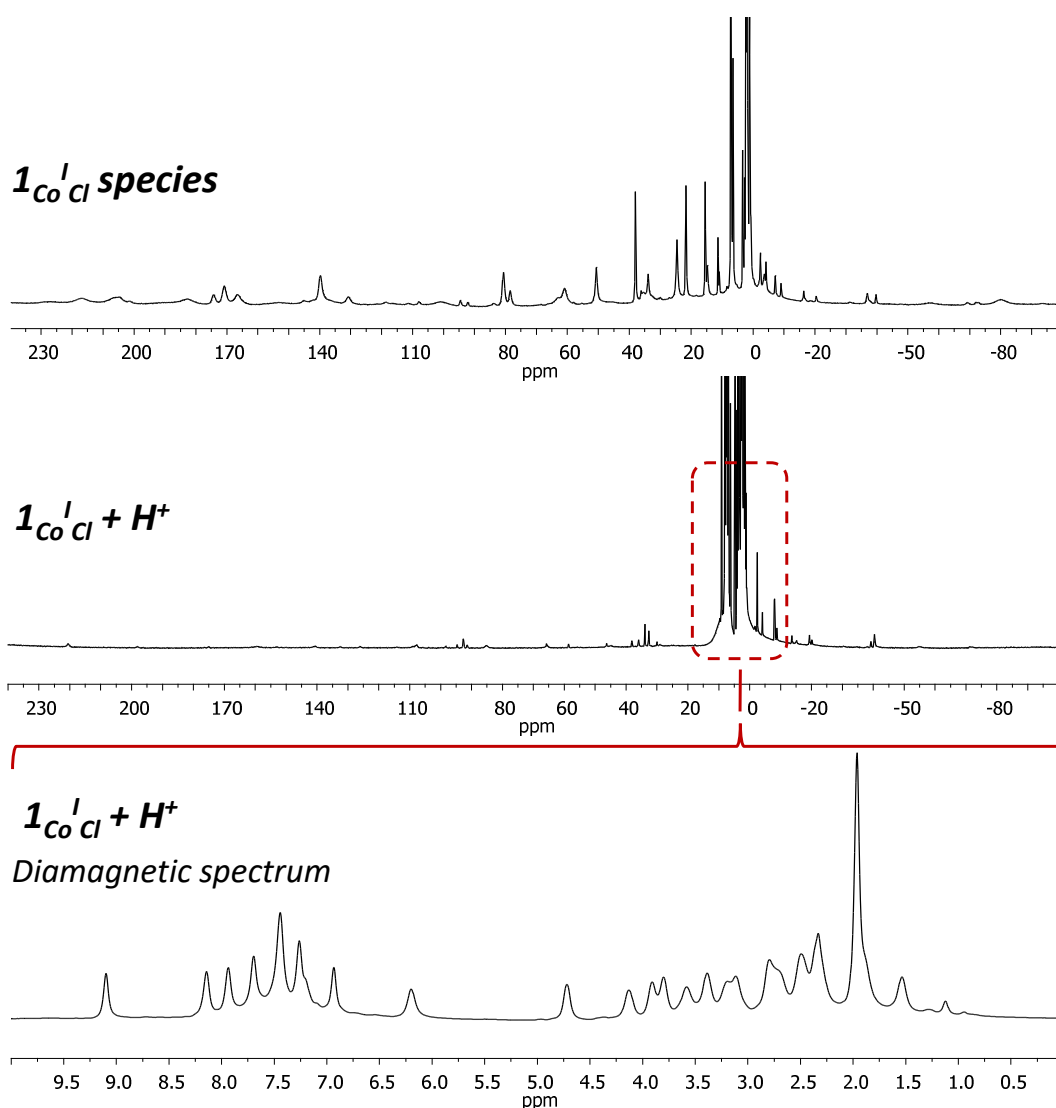


Figure VI. 13. Protonation of $1_{\text{Co}}^{\text{I}}\text{Cl}$ analyzed by $^1\text{H-NMR}$ (CD_3CN , 500 MHz, 238 K). *Top*: $^1\text{H-NMR}$ paramagnetic spectrum of $1_{\text{Co}}^{\text{I}}\text{Cl}$ before the addition of TFA. *Middle*: $^1\text{H-NMR}$ paramagnetic spectrum of $1_{\text{Co}}^{\text{I}}\text{Cl}$ after the addition of 3 eq. TFA. *Bottom*: $^1\text{H-NMR}$ spectrum of $1_{\text{Co}}^{\text{I}}\text{Cl}$ after the addition of 3 eq. TFA.

Reaction of $1_{\text{Co}}^{\text{I}}\text{Cl}$ with 3 eq of trifluoroacetic acid (TFA) was performed in a NMR tube at low temperature (238 K). The addition of TFA produces a vanishing of the $1_{\text{Co}}^{\text{I}}\text{Cl}$ paramagnetic NMR signals and the appearance of a diamagnetic NMR signals (Figure VI. 13). The formation of a diamagnetic compound could be attributed to generation of Co^{III} species. To confirm this hypothesis we performed the study of the reaction product of $1_{\text{Co}}^{\text{I}}\text{Cl}$ with 3 eq of TFA by XAS.

The new compound exhibits a rising edge energy and a pre-edge at 7710.2 eV consistent with Co^{III} , ~ 0.1 eV higher in energy than the chemically synthesized $1_{\text{Co}}^{\text{III}}\text{Cl}$

indicating a stronger metal-ligand interaction in the complex that destabilizes the Co 3d manifold (Figure VI. 14).

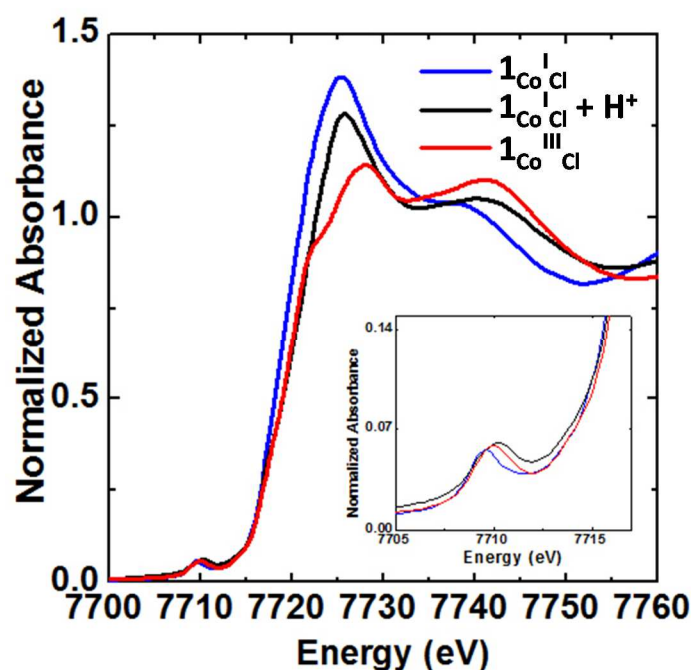


Figure VI. 14. XANES spectra of the $1\text{Co}^{\text{I}}\text{Cl}$ precursor, the product derived from the reaction of $1\text{Co}^{\text{I}}\text{Cl}$ with TFA ($1\text{Co}^{\text{I}}\text{Cl} + \text{H}^+$), and the $1\text{Co}^{\text{III}}\text{Cl}$ synthesized by one electron oxidation of $1\text{Co}^{\text{II}}\text{Cl}$.

An analogous experiment was performed with the photogenerated $1\text{Co}^{\text{I}}\text{CH}_3\text{CN}$ species. As expected, the addition of an excess of TFA also produces the formation of a diamagnetic compound. In this case, the ^1H -NMR spectrum of new formed compound resembles to $1\text{Co}^{\text{III}}\text{CH}_3\text{CN}$. XAS analysis is again consistent with the formation of Co^{III} species having a pre-edge at 7710.3 eV. Furthermore increased intensity is observed for the shoulder, at ~ 7722 eV in $1\text{Co}^{\text{I}}\text{CH}_3\text{CN} + \text{H}^+$ versus the chemically synthesized $1\text{Co}^{\text{III}}\text{CH}_3\text{CN}$ compound (Figure VI. 15). Such shoulders are often correlated with $1s \rightarrow 4p$ transitions and shake down contributions, and can offer insight into both covalency and geometry at the metal center.^{415,418} As the pre-edge intensities for the two complexes are similar, the overall coordination environment is expected to also be similar however the pre-edge of $1\text{Co}^{\text{I}}\text{CH}_3\text{CN} + \text{H}^+$ is slightly higher in energy than for $1\text{Co}^{\text{III}}\text{CH}_3\text{CN}$ which together with the $1s \rightarrow 4p$ shoulder might suggest a slight increase in the metal-ligand bond strengths. This difference might also be consistent with the variation in sample environment $1\text{Co}^{\text{I}}\text{CH}_3\text{CN} + \text{H}^+$ being a solution sample and $1\text{Co}^{\text{III}}\text{CH}_3\text{CN}$ a solid.

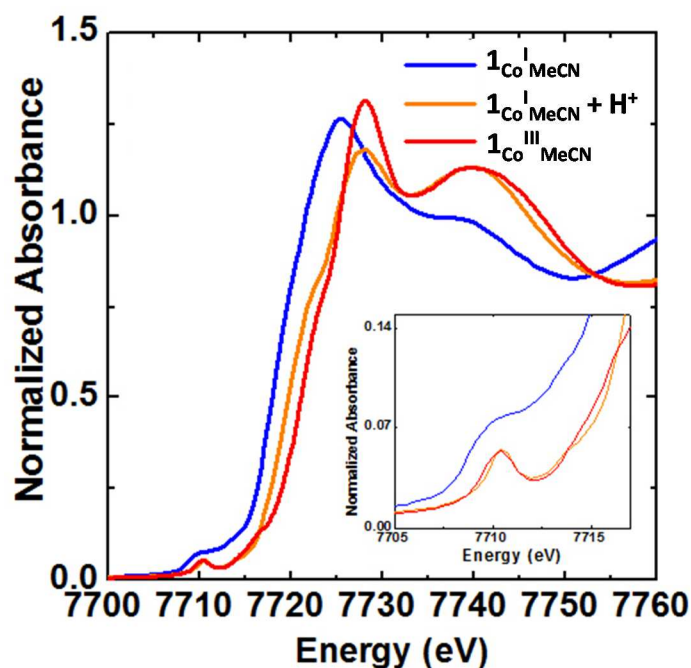


Figure VI. 15. XANES spectra of the photochemically generated $1\text{Co}^{\text{I}}\text{Cl}$ precursor, the product derived from the reaction of $1\text{Co}^{\text{I}}\text{Cl}$ with TFA ($1\text{Co}^{\text{I}}\text{Cl} + \text{H}^+$), and the $1\text{Co}^{\text{III}}\text{Cl}$ synthesized from $1\text{Co}^{\text{I}}\text{Cl}$ by one electron oxidation.

Reaction of $1\text{Co}^{\text{I}}\text{Cl}$ with an excess of H_2O (20 μL in 0.6 mL CD_3CN at 300 K) under anaerobic conditions has also been evaluated, which produces the disappearance of the paramagnetic NMR signals of the blue $1\text{Co}^{\text{I}}\text{Cl}$ compound yielding a red soluble compound ($1\text{Co}^{\text{I}}\text{Cl} + \text{H}_2\text{O}$) (Figure VI. 16) and an insoluble white solid ($1\text{Co}^{\text{I}}\text{Cl} + \text{H}_2\text{O}$ (S)). The new red soluble compound presents a well-defined diamagnetic ^1H -NMR, which is a qualitative indication that Co^{III} species are formed.

We studied by XANES and EXAFS the product formed from the reaction of $1\text{Co}^{\text{I}}\text{Cl}$ with water. To prepare the samples we reacted a pellet composed by $1\text{Co}^{\text{I}}\text{Cl}$ (20 mg) and cellulose (20 mg), previously XANES measured, with water (100 μL) under argon atmosphere at room temperature. We observed the formation of a red solution and a green solid. After decantation the green solid was washed with CH_3CN and both compounds were exposed to vacuum until dryness. Interestingly, XANES profile (Figure VI. 17) as well as EXAFS analysis (Figure VI. 18) of the red soluble compound ($1\text{Co}^{\text{I}}\text{Cl} + \text{H}_2\text{O}$) have a similar profile to that of $1\text{Co}^{\text{III}}\text{CH}_3\text{CN}$ but in which EXAFS analysis indicates Cl is still bound to the metal centre.

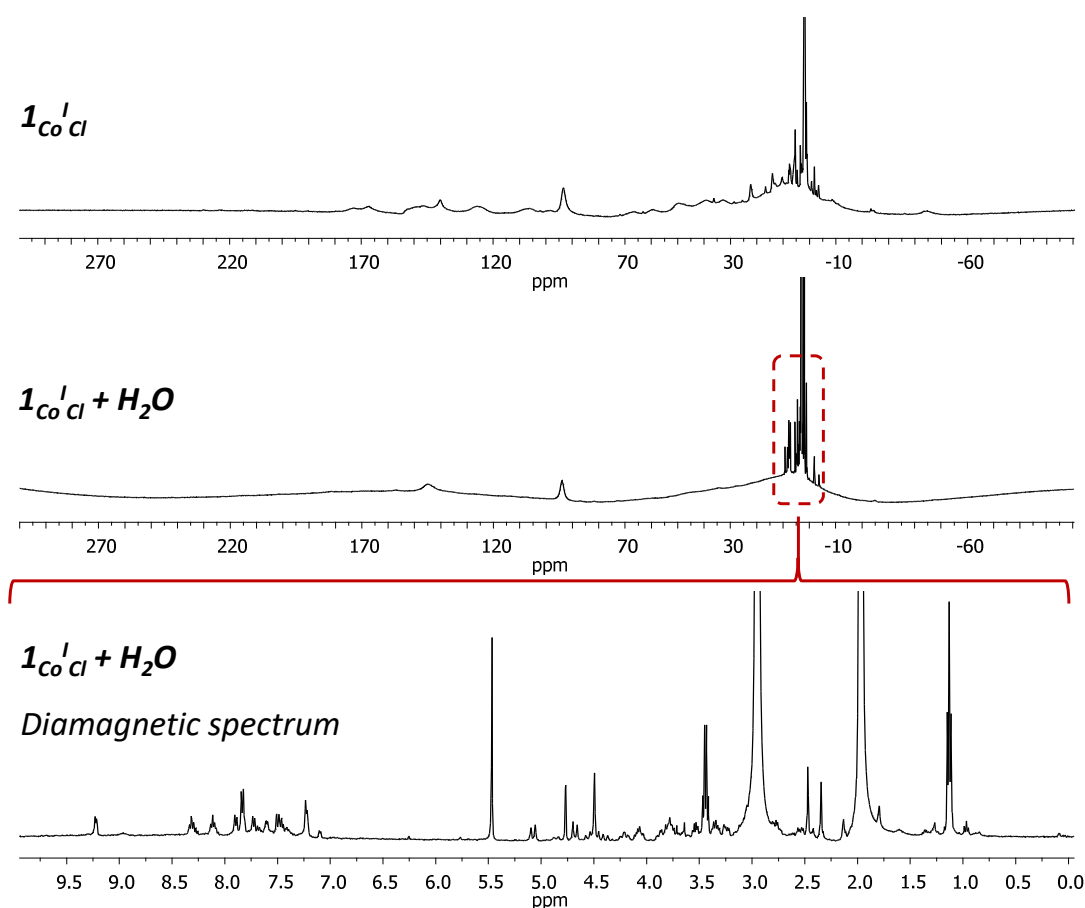


Figure VI. 16. Protonation of $1_{\text{Co}}^{\text{I}}\text{Cl}$ with H_2O analyzed by ^1H -NMR (CD_3CN , 500 MHz, 300 K). *Top*: ^1H -NMR paramagnetic spectrum of $1_{\text{Co}}^{\text{I}}\text{Cl}$ before the addition of H_2O . *Middle*: ^1H -NMR paramagnetic spectrum of $1_{\text{Co}}^{\text{I}}\text{Cl}$ after the addition of H_2O . *Bottom*: ^1H -NMR spectrum of $1_{\text{Co}}^{\text{I}}\text{Cl}$ after the addition of H_2O .

In addition, the green solid ($1_{\text{Co}}^{\text{I}}\text{Cl} + \text{H}_2\text{O}$ (S)) can be assigned to cobalt oxide nanoparticles. We rationalized this result by means of the similar reactivity of $1_{\text{Co}}^{\text{I}}\text{Cl}$ species with water. We could presume that reaction of $1_{\text{Co}}^{\text{I}}\text{Cl}$ with water produces Co^{III} hydride species and an equivalent hydroxide anion. Co^{III} hydride species reacts also with a water molecule to produce H_2 and an additional hydroxide equivalent. Therefore, reaction media become highly basic, facilitating the decoordination of the Co^{III} ion forming cobalt oxide. Reaction of $1_{\text{Co}}^{\text{I}}\text{Cl}$ under aerobic conditions with an excess of H_2O ($0.1 \mu\text{L}$) ($1_{\text{Co}}^{\text{I}}\text{Cl} + \text{O}_2 + \text{H}_2\text{O}$) or only the exposition to O_2 ($1_{\text{Co}}^{\text{I}}\text{Cl} + \text{O}_2$) produces similar final Co^{III} species (Figure VI. 19). EXAFS analysis indicates 6 coordinated metal centers with N/O ligands replacing Cl, while the decrease in the pre-edge intensity is consistent with less p-d mixing into the d manifold consistent with the presence of water as ligand (Figure VI. 20).

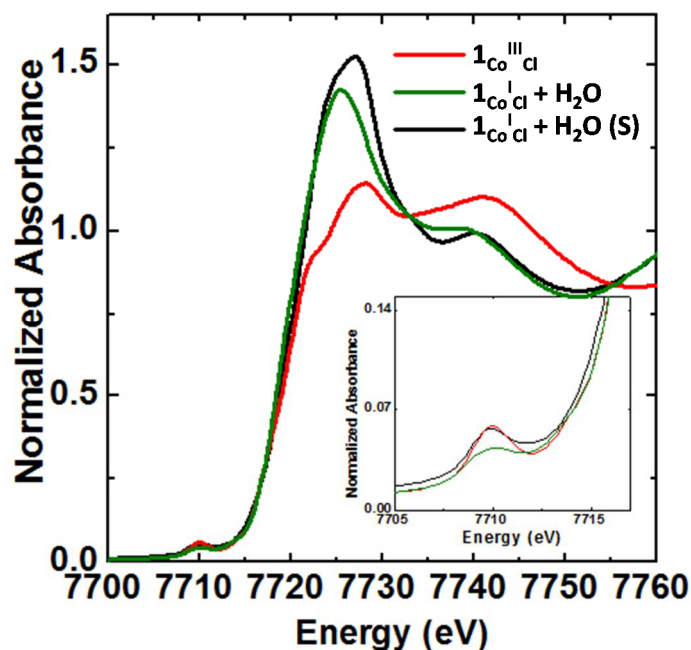


Figure VI. 17. XAS analysis of $1_{\text{Co}}^{\text{I}}\text{Cl}$ reactivity against water under anaerobic conditions.

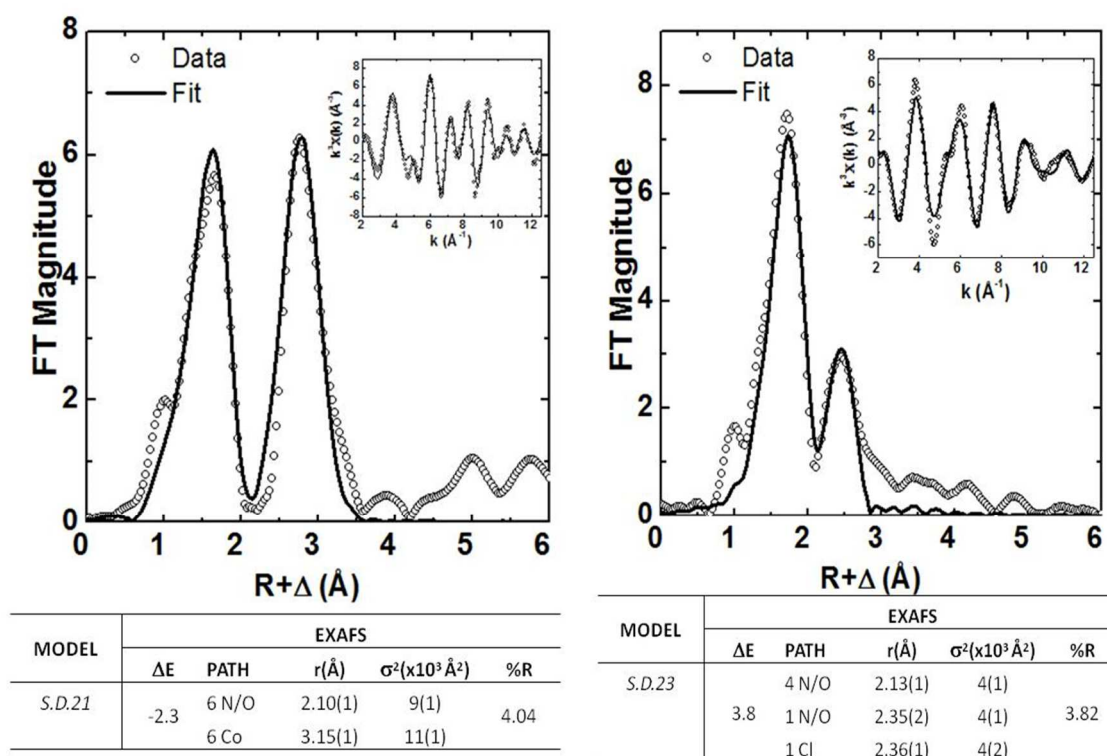


Figure VI. 18. *Left*: Fourier transformed spectra of $1_{\text{Co}}^{\text{I}}\text{Cl} + \text{H}_2\text{O}$ (S) (no phase correction, FT, window = $2-12.5 \text{\AA}^{-1}$). *Right*: Fourier transformed spectra of $1_{\text{Co}}^{\text{I}}\text{Cl} + \text{H}_2\text{O}$ (no phase correction, FT, window = $2-12.5 \text{\AA}^{-1}$) *Insets*: k^3 -weighted unfiltered EXAFS spectra. *Bottom tables*: selected path distances parameters for the various models from EXAFS analysis.

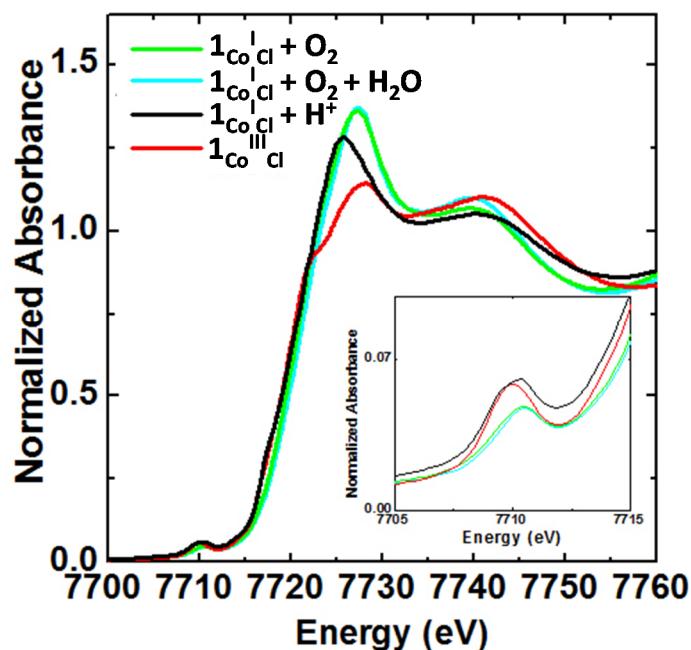


Figure VI. 19. Comparison between the XAS data obtained from the $1_{\text{Co}}^{\text{I}}\text{Cl}$ reactivity against oxygen, oxygen and water, protons and the $1_{\text{Co}}^{\text{III}}\text{Cl}$.

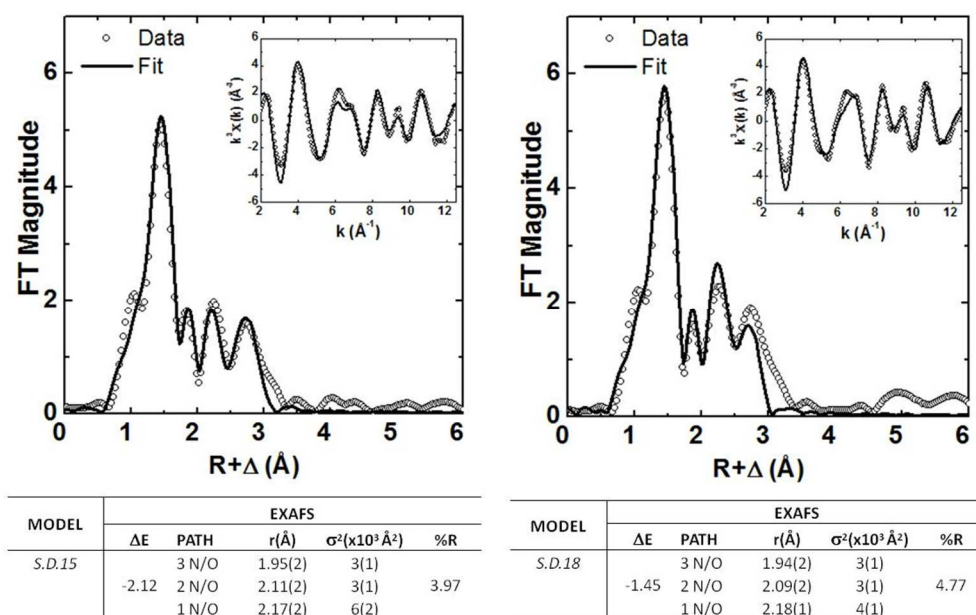


Figure VI. 20. Left: Fourier transformed spectra of $1_{\text{Co}}^{\text{I}}\text{Cl} + \text{O}_2$ (no phase correction, FT, window= 2–12.5 Å⁻¹). Right: Fourier transformed spectra of $1_{\text{Co}}^{\text{I}}\text{Cl} + \text{O}_2 + \text{H}_2\text{O}$ (no phase correction, FT, window= 2–12.5 Å⁻¹). Insets: k^3 -weighted unfiltered EXAFS spectra. Bottom tables: selected path distances parameters for the various models from EXAFS analysis.

As a summary, the reactivity observed for $1_{\text{Co}^{\text{I}}}$ complexes against O_2 , protons, and H_2O is characteristic of other cobalt (I) metal centers based on aminopyridine ligands. Indeed, we also examined the reaction of $1_{\text{Co}^{\text{II}}}$ with H_2O (excess) and O_2 (12 h) resulting in not apparent reaction. Therefore, we can conclude that although $1_{\text{Co}^{\text{I}}}$ complexes are electronically more similar to cobalt (II) metal centers, their reactivity suggests that these complexes are reduced in one electron respect to $1_{\text{Co}^{\text{II}}}$ complexes.

Study of the electronic structure of 1_{Co^n} ($n = \text{I}$ and II) by DFT calculations. Finally, with the aim to give some light into this intriguing discrepancy between the XAS, SQUID and observed reactivity, we have examined the electronic structure of the DFT modelled structures (Figure VI. 21). Interestingly, $1_{\text{Co}^{\text{I}}}$ ($S = 1$) presents an important spin density located over one of the pyridines. In the limit case, we can consider that one electron has been fully transferred to the pyridine ring leading to a Co^{II} metal center, explaining the XAS and SQUID measurements and the observed reactivity.

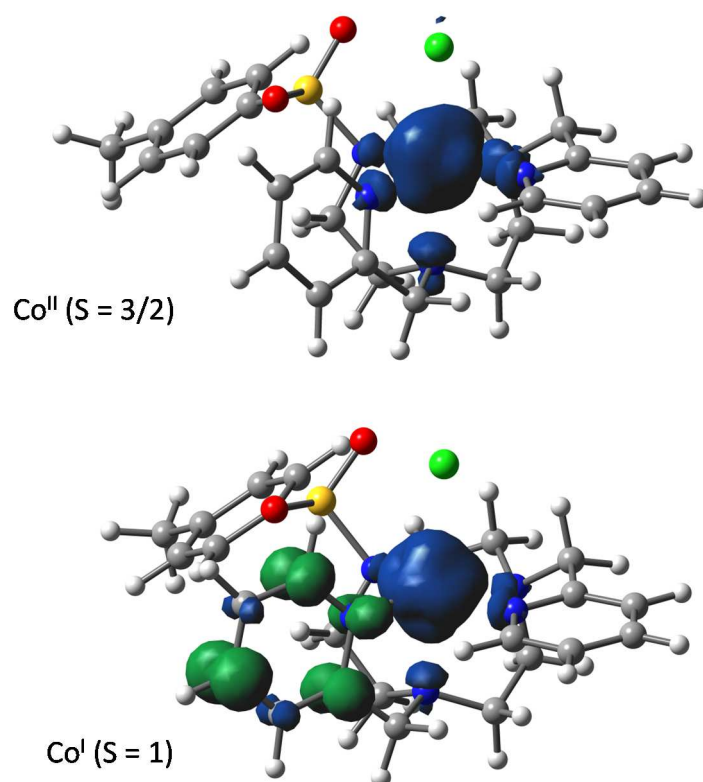


Figure VI. 21. Spin density obtained for the DFT modelled $1_{\text{Co}^{\text{I}}}$ and $1_{\text{Co}^{\text{II}}}$ complexes.

Based on all the studies presented in this Chapter we propose that the electron density at the $1_{\text{Co}^{\text{I}}}\text{L}$ center can be delocalized over the pyridine moiety leading to a formal Co^{II} metal center. Two reduced pyridines by one electron can react through the para position of the pyridine to yield a Co^{I} dimer,⁴⁰⁸ which if it is in equilibrium with the monomer it can also explain the XAS and SQUID experiments and the observed reactivity (Figure VI. 22).

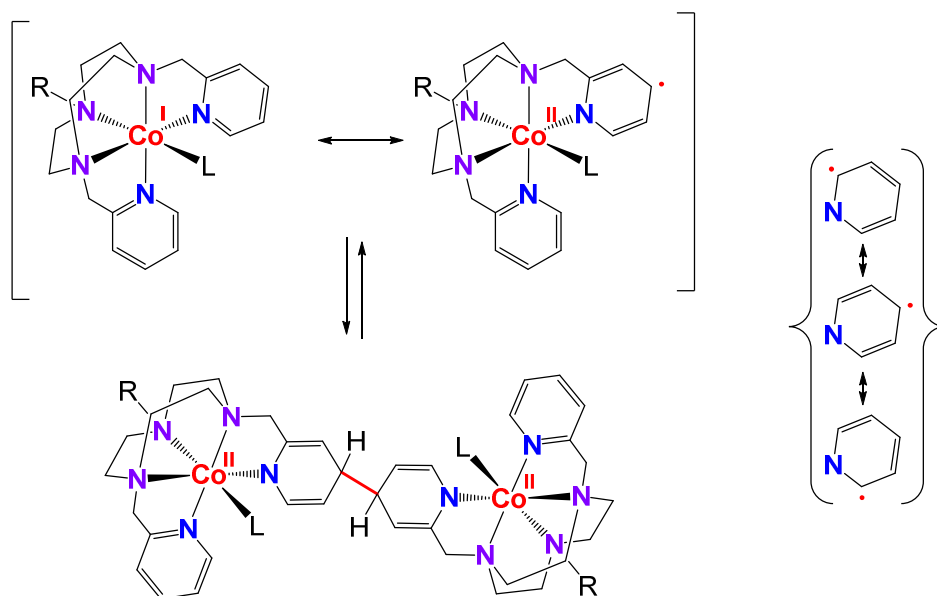


Figure VI. 22. Hypothetic redox non-innocent nature of the pyridine moiety in the $1_{\text{Co}^{\text{I}}}\text{L}$ complex and the reversible C-C bond formation at the para-position of the pyridine reduction.

VI.2.3. Photocatalytic Activity in H_2 Evolution

In order to test if $1_{\text{Co}^{\text{I}}}\text{L}$, $1_{\text{Co}^{\text{II}}}\text{L}$ and $1_{\text{Co}^{\text{III}}}\text{L}$ can be involved in the H_2 evolution catalytic cycle we have tested their catalytic activity in the light-driven H_2 evolution under standard conditions (Figure VI. 23). We used $([\text{Cu}(\text{bathocuproine})(\text{Xantphos})](\text{PF}_6))$ (PS_{Cu}) as photocatalyst, which is very appealing since it is formed by earth abundant elements. Interestingly, $1_{\text{Co}^{\text{I}}}\text{L}$ and $1_{\text{Co}^{\text{II}}}\text{L}$ complexes exhibited significant H_2 catalytic activity except for $1_{\text{Co}^{\text{III}}}\text{L}$. This could be due to the slower halide replacement in the Co^{III} oxidation state than for Co^{II} or Co^{I} . Very interestingly, the in-situ reaction of $\text{Co}(\text{PPh}_3)_3\text{Cl}$ with the $\text{Py}_2^{\text{T}}\text{tacn}$ ligand forms a very active catalyst, while $\text{Co}(\text{PPh}_3)_3\text{Cl}$ alone is not active. In summary, the observed similar photocatalytic activity in H_2 evolution for the $1_{\text{Co}^{\text{n}}}\text{L}$ family suggests that all oxidation states under catalytic conditions reach the active species or can participate in the catalytic cycle.

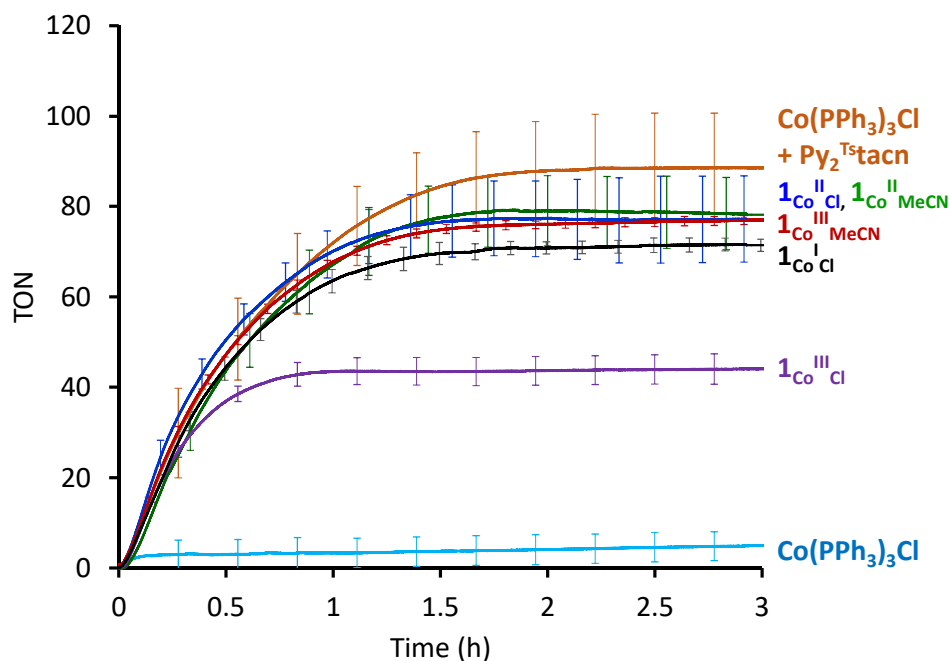


Figure VI. 23. On-line H₂ evolved versus time for **1_{Co}ⁿL** ($n = 1, 2, 3$) complexes (50 μ M), **PS_{Co}** (250 μ M) in CH₃CN:H₂O:NEt₃ (4:6:0.2 mL) as solvent mixture and irradiated ($\lambda = 447$ nm) at 25 °C. The catalytic activity of the starting Co(PPh₃)₃Cl salt with and without the presence of the Py₂^Ttacn ligand is also included.

VI.3. EXPERIMENTAL SECTION

VI.3.1. Physical Methods

Nuclear magnetic resonance (NMR) spectra were recorded on Bruker AV400 and AV500 spectrometers using standard conditions. All ^1H chemical shifts are reported in ppm and have been internally calibrated to the residual protons of the deuterated solvent.

SQUID measurements. The magnetic properties were measured using a MPMS-XL magnetometer (Quantum Design). Grained powder of the compounds were placed in a polycarbonate capsule inside a glove box and then quickly inserted into the magnetometer using a straw. Magnetic susceptibility measurements were carried out in the 2-300 K range at different fields. Diamagnetic corrections were applied.

XAS measurements. Samples were either prepared as solids diluted in boron nitride or as ~15 mM solutions in acetonitrile. Samples were loaded into holders having Kapton tape windows and stored under anaerobic conditions at liquid nitrogen temperatures until run. Data on samples at the Diamond synchrotron (3.0 GeV, 300mA storage ring) were collected at 77 K in transmission mode at beamline B18 equipped with a liquid nitrogen cryostat and a Si(111) double crystal monochromator. Data on samples at the SOLEIL synchrotron (2.75 GeV, 400mA storage ring) were collected at 25 K in fluorescence mode SAMBA beamline equipped with a liquid helium cryostat, a Si(220) double crystal monochromator and a Canberra 35-element Ge pixel array detector.

Data was calibrated to the first inflection point of Co foil taken as 7709.5 eV and normalized using the Athena software package⁴¹⁹. A linear pre-edge function together with a quadratic polynomial for the post-edge, were used for background subtraction and normalization of the edge jump to 1. The AUTOBK algorithm was used for EXAFS data extraction with a spline between a k of 1 and 14.5 \AA^{-1} with a R_{bkg} value of 1 \AA . EXAFS analysis was carried out using the Artemis program equipped with the IFEFFIT engine and the FEFF6 code.⁴²⁰⁻⁴²² Unless otherwise specified, the k^3 -weighted data was fit in r -space over a k -range of $2 - 13 \text{ \AA}^{-1}$ having an r -range of $1 - 3.2 \text{ \AA}$ and a Kaiser-Bessel window with a window sill of 2. Scattering paths were fit with a global S_0^2 value and ΔE_0 parameter with the initial E_0 value set to the inflection point of the rising edge. Furthermore paths were fit in terms of Δr_{eff} and σ^2 as previously described.^{422,423} The goodness of fit was assessed by minimizing the R_{factor} (%R) and over-fitting was controlled by minimizing the number of adjustable parameters and ensuring an appropriate decrease in the reduced χ^2 (χ^2_{v}) with an increasing number of variables.

To further understand the reactivity at the metal center X-ray absorption spectroscopy (XAS) at the Co K-edge was applied as a direct probe of electronic structure and coordination environment. Metal K-edge absorption spectroscopy consists of core 1s electron excitations either to unoccupied or partially unoccupied molecular orbitals (bound transitions) resulting in the XANES (X-ray absorption near edge structure) region of the spectra, or excitations to the continuum (ionization) which together with

backscattering of the ionized electron by nearby nuclei is sensitive to the effective nuclear charge, ligand speciation and bond metrics at the metal center (EXAFS = Extended X-ray Absorption Fine Structure).⁴²⁴ For cobalt, XAS has had wide ranging applications from investigating ions in solutions,⁴²⁵ to mixed-valence lattice frameworks,⁴²⁶ to synthetic model complexes mimicking protein chemistry⁴²⁷ and even Co speciation in cancer cells⁴²⁸. Spectra for Co^{II} centers show a pre-edge feature resulting from $1s \rightarrow 3d$ bound transitions centered around ~ 7709 eV with a rising edge spanning the $\sim 7720 - 7721$ eV region. Upon a one electron oxidation up to a 1.9 eV shift can be expected in the rising edge concomitant with a ~ 0.5 to 1.0 eV shift in the pre-edge.⁴²⁵⁻⁴²⁹ Molecular Co^I intermediates have also been reported in hydrogen evolving photocatalytic systems but clean spectra remain elusive.¹³⁹ On the other hand Co^I centers coordinated by phosphorous based ligands show pre-edge features at ~ 7708.9 eV (when corrected for 0.5 eV difference in calibration method).⁴¹⁸ With this in mind the speciation and reactivity of several Co complexes involved in the hydrogen generation cycle were investigated.

X-Ray crystallography. Single crystals were mounted on a nylon loop for X-ray structure determination. The measurements were carried out on a BRUKER SMART APEX CCD diffractometer using graphite-monochromated $\text{MoK}\alpha$ radiation ($\lambda = 0.71073 \text{ \AA}$). Programs used: data collection, Smart version 5.631 (Bruker AXS 1997-02); data reduction, Saint+ version 6.36A (Bruker AXS 2001); absorption correction, SADABS version 2.10 (Bruker AXS 2001). Structure solution and refinement was done using SHELXTL Version 6.14 (Bruker AXS 2000–2003). The structure was solved by direct methods and refined by full-matrix least-squares methods on F^2 . The non-hydrogen atoms were refined anisotropically. The hydrogen atoms were placed in geometrically optimized position and forced to ride on the atom to which they are attached.

VI.3.2. General Procedure for the Photogeneration of $\mathbf{1_{Co^I}Cl}$ and $\mathbf{1_{Co^I}MeCN}$ Species

The photochemical generation of $\mathbf{1_{Co^I}Cl}$ and $\mathbf{1_{Co^I}MeCN}$ species was carried out by irradiating ($\lambda = 447 \text{ nm}$) a CD_3CN (1 mL) solution containing $\mathbf{1_{Co^{II}Cl}}$ or $\mathbf{1_{Co^{II}MeCN}}$ (20 mM), $\mathbf{PS_{Ir}}$ (20 mM) and Et_3N (240 mM) in a NMR tube at 250 K during 15 min.

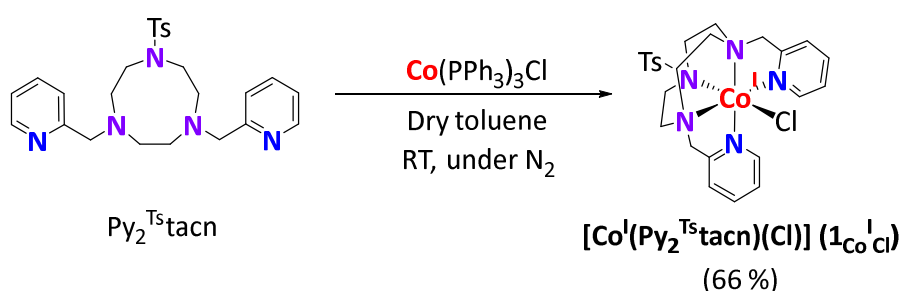
The same procedure was followed for the samples measured in the synchrotron but using the conditions: $\mathbf{1_{Co^{II}CH_3CN}}$ (15 mM), $\mathbf{PS_{Ir}}$ (7.5 mM) and Et_3N (140 mM) in CH_3CN for 15 min. After the irradiation time, the samples were dropped on liquid N_2 and measured.

VI.3.3. Synthesis of the Complexes and Characterization

VI.3.3.1. Synthesis of $\text{Co}(\text{PPh}_3)_3\text{Cl}$

We followed the procedure available in the literature with slightly modifications.⁴³⁰ $\text{CoCl}_2 \cdot 6\text{H}_2\text{O}$ (2 g, 8.47 mmol) and PPh_3 (6.67 g, 25.47 mmol) were mixed in 75 mL of degassed CH_3CN . After few minutes a deep blue suspension was obtained attributed to the formation of $\text{Co}(\text{PPh}_3)_2\text{Cl}_2$. After stirring this solution under N_2 at reflux temperature for 30 min, Zn (0.553 g, 8.46 mmol) was added directly as solid and a bright green slurry was obtained after few minutes. After stirring for an additional 2 hours, the green product was precipitated with 50 mL $\text{EtOH}:\text{H}_2\text{O}$ (1:1). This product was collected by filtration under N_2 using Schlenk apparatus. The resulting solid was washed with 50 mL of absolute EtOH and then slurried under N_2 with 2M HCl (50 mL) for 1 h. The solid was filtered under N_2 and washed with H_2O (25 mL) and EtOH (25 mL), and then dried at room temperature under vacuum to yield $\text{Co}(\text{PPh}_3)_3\text{Cl}$ (6.95 g, 93 % yield). The product, a bright green solid, was moderately air stable and was best stored under N_2 .

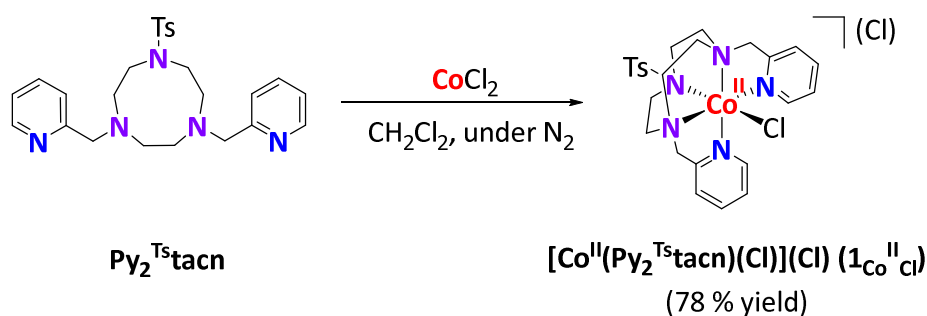
VI.3.3.2. Synthesis of $[\text{Co}^{\text{I}}(\text{Cl})(\text{Py}_2^{\text{Ts}}\text{tacn})]$ ($1_{\text{Co}^{\text{I}}\text{Cl}}$)



Scheme VI. 4. Synthesis of $[\text{Co}^{\text{I}}(\text{Cl})(\text{Py}_2^{\text{Ts}}\text{tacn})]$ ($1_{\text{Co}^{\text{I}}\text{Cl}}$).

In a glovebox, a solution of $\text{Py}_2^{\text{Ts}}\text{tacn}$ (0.150 g, 0.322 mmol) in anhydrous toluene (2 mL) was added dropwise to a vigorously stirred suspension of $\text{Co}(\text{PPh}_3)_3\text{Cl}$ (0.283 g, 0.321 mmol) in toluene (10 mL). After stirring overnight at room temperature a dark solution with a blue solid appeared. The reaction was filtered with cannula, and the remaining blue solid was washed with 20 mL toluene and 20 mL diethyl ether to remove the residual PPh_3 and dried under vacuum. This solid was dissolved with anhydrous CH_3CN , filtered through Celite and the solvent was removed in the vacuum line affording a deep blue compound (0.119 g, 0.214 mmol, 66 % yield). $^1\text{H-NMR}$ (CD_3CN , 500 MHz, 235 K) δ , ppm: 219.46, 210.37, 185.77, 176.59, 173.76, 168.74, 156.87, 141.56, 132.34, 102.95, 81.89, 79.78, 60.89, 51.41, 38.37, 34.21, 24.87, 21.92, 15.59, 11.38.

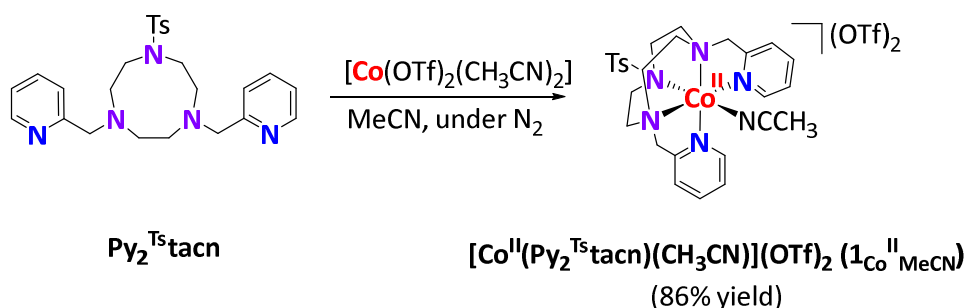
VI.3.3.3. Synthesis of $[\text{Co}^{\text{II}}(\text{Cl})(\text{Py}_2^{\text{Ts}}\text{tacn})]\text{Cl}$ ($\mathbf{1}_{\text{Co}^{\text{II}}\text{Cl}}$)



Scheme VI. 5. Synthesis of $[\text{Co}^{\text{II}}(\text{Cl})(\text{Py}_2^{\text{Ts}}\text{tacn})](\text{Cl})$ ($\mathbf{1}_{\text{Co}^{\text{II}}\text{Cl}}$).

In a glovebox, a suspension of CoCl_2 (0.028 g, 0.215 mmol) in anhydrous CH_2Cl_2 (2 mL) was added dropwise to a vigorously stirred solution of $\text{Py}_2^{\text{Ts}}\text{tacn}$ (0.100 g, 0.215 mmol) in CH_2Cl_2 (5 mL). The cobalt chloride salt was quickly solubilized, and after few minutes, the solution became deep purple. After stirring for an additional 3 h the solution was passed through Celite and the slow diffusion of diethyl ether over the resultant solution afforded a blue crystalline compound (0.105 g, 0.176 mmol, 78 % yield). $^1\text{H-NMR}$ (CD_3CN , 500 MHz, 235 K) δ , ppm: 308.68, 302.36, 278.50, 252.31, 205.39, 145.72, 118.31, 114.08, 110.15, 93.84, 67.51, 38.87, 37.11, 36.30, 26.23, -2.16, -4.41, -9.62, -20.55, -32.11, -37.64, -40.18, -72.41, -73.66, -94.47. HR-ESI-MS (m/z): 559.1213 $[\text{M} - \text{Cl}]^+$, 262.0760 $[\text{M} - 2\text{Cl}]^{2+}$.

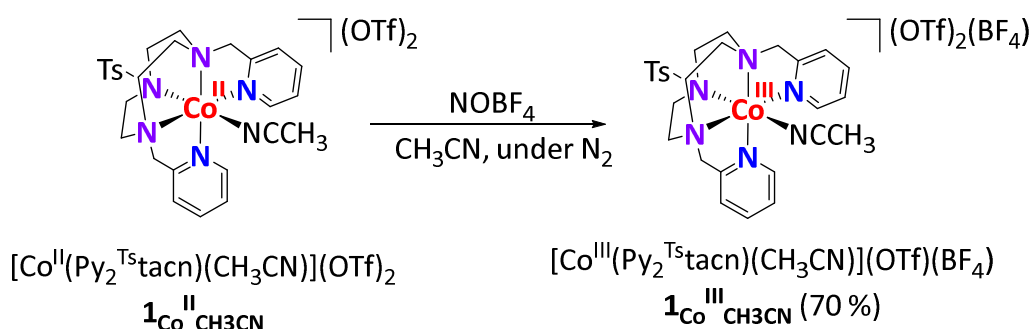
VI.3.3.4. Synthesis of $[\text{Co}(\text{Py}_2^{\text{Ts}}\text{tacn})(\text{CH}_3\text{CN})](\text{OTf})_2$ ($\mathbf{1}_{\text{Co}^{\text{II}}\text{CH}_3\text{CN}}$)



Scheme VI. 6. Synthesis of $[\text{Co}^{\text{II}}(\text{Py}_2^{\text{Ts}}\text{tacn})(\text{CH}_3\text{CN})](\text{OTf})_2$ ($\mathbf{1}_{\text{Co}^{\text{II}}\text{CH}_3\text{CN}}$).

This compound was synthesized in a similar manner to the compound $\mathbf{1}_{\text{Co}}$ (Chapter III). In a glovebox, a suspension of $[\text{Co}(\text{OTf})_2(\text{CH}_3\text{CN})_2]$ (113 mg, 0.257 mmol) in anhydrous CH_3CN (2 mL) was added dropwise to a vigorously stirred solution of $\text{Py}_2^{\text{Ts}}\text{tacn}$ (120 mg, 0.257 mmol) in CH_3CN (2 mL). The cobalt triflate salt was quickly solubilized, and after few minutes, the solution became deep red. After stirring for an additional 3 h the solution was passed through Celite and the slow diffusion of diethyl ether over the resultant solution afforded a red crystalline compound (191 mg, 0.221 mmol, 86 % yield). $^1\text{H-NMR}$ (CD_3CN , 500 MHz, 298 K) δ , ppm: $^1\text{H-NMR}$ (CD_3CN , 300 MHz, 300 K) δ , ppm: 118.28, 55.72, 3.92, 3.76, 2.22, 9.42 HR-ESI-MS (m/z): 673.1054 $[\text{M} - \text{OTf}]^+$, 262.0766 $[\text{M} - 2\text{OTf}]^{2+}$.

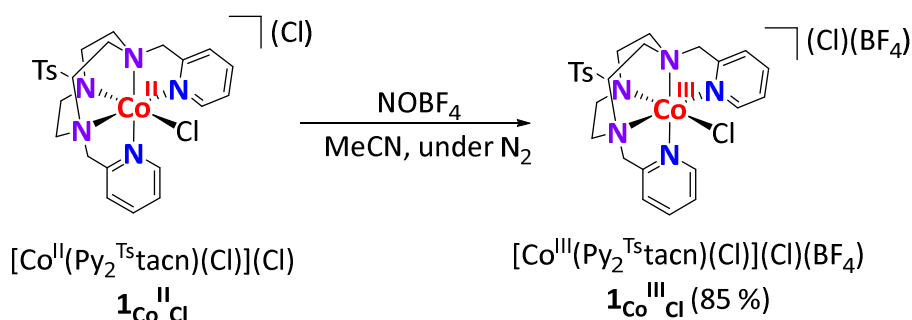
VI.3.3.5. Synthesis of $[\text{Co}^{\text{II}}(\text{Py}_2^{\text{Ts}}\text{tacn})(\text{CH}_3\text{CN})](\text{OTf})_2(\text{BF}_4)$ ($\mathbf{1}_{\text{Co}^{\text{II}}\text{CH}_3\text{CN}}$)



Scheme VI. 7. Synthesis of $[\text{Co}^{\text{III}}(\text{Py}_2^{\text{Ts}}\text{tacn})(\text{CH}_3\text{CN})](\text{OTf})(\text{BF}_4)$ ($\mathbf{1}_{\text{Co}^{\text{III}}\text{CH}_3\text{CN}}$).

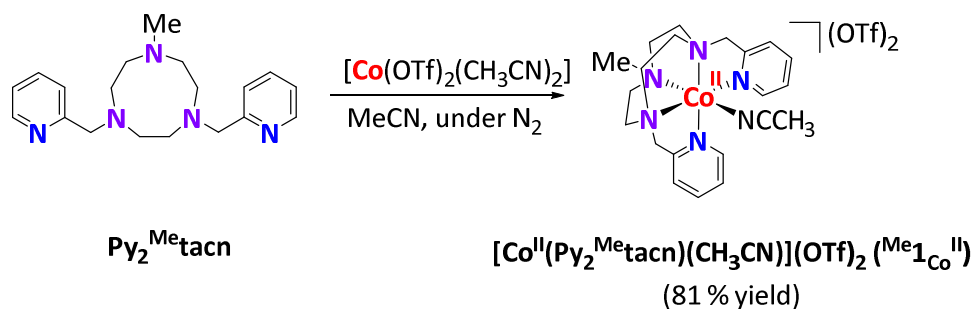
1 equivalent of NOBF_4 (0.030 g, 0.231 mmol) was added dropwise to 1 equivalent of $\mathbf{1}_{\text{Co}^{\text{II}}\text{CH}_3\text{CN}}$ (0.200 g, 0.231 mmol) in 5 mL CH_3CN . The red solution of $\mathbf{1}_{\text{Co}^{\text{II}}\text{CH}_3\text{CN}}$ intensified in color. The reaction was allowed to stir an additional 2 hours before being filtered and concentrated to 1 mL. The slow diffusion of diethyl ether over this solution afforded a red crystalline compound (0.149 g, 0.156 mmol, 70 % yield). $^1\text{H-NMR}$ (CD_3CN , 400 MHz, 298 K) δ , ppm: 9.24, 8.52, 8.22, 8.04, 7.99, 7.87, 7.82, 7.60, 7.51, 6.55, 5.48, 4.92, 4.65, 4.40, 4.08, 3.94, 3.79, 3.68, 3.08, 2.66, 2.42.

VI.3.3.6. Synthesis of $[\text{Co}^{\text{III}}(\text{Py}_2^{\text{Ts}}\text{tacn})(\text{Cl})](\text{Cl})(\text{BF}_4)$ ($\mathbf{1}_{\text{Co}^{\text{III}}\text{Cl}}$)



Scheme VI. 8. Synthesis of $[\text{Co}^{\text{III}}(\text{Cl})(\text{Py}_2^{\text{Ts}}\text{tacn})](\text{Cl})(\text{BF}_4)$ ($\mathbf{1}_{\text{Co}^{\text{III}}\text{Cl}}$).

1 equivalent of NOBF_4 (0.039 g, 0.334 mmol) was added dropwise to a vigorously stirred solution of $\mathbf{1}_{\text{Co}^{\text{II}}\text{Cl}}$ (0.200 g, 0.336 mmol) in 5 mL CH_3CN . After few minutes a purple precipitate appeared. After stirring for an additional 2 hours the solution was filtered off and the resulting solid was washed with diethyl ether and dried under vacuum to yield a purple compound (0.164 g, 0.240 mmol, 85 % yield). $^1\text{H-NMR}$ (CD_3CN , 500 MHz, 298 K) δ , ppm: 9.45, 8.38, 8.06, 7.90, 7.77, 7.66, 7.50, 7.36, 6.42, 5.74, 5.36, 4.64, 4.33, 4.08, 3.98, 3.82, 3.60, 3.36, 3.01, 2.78.

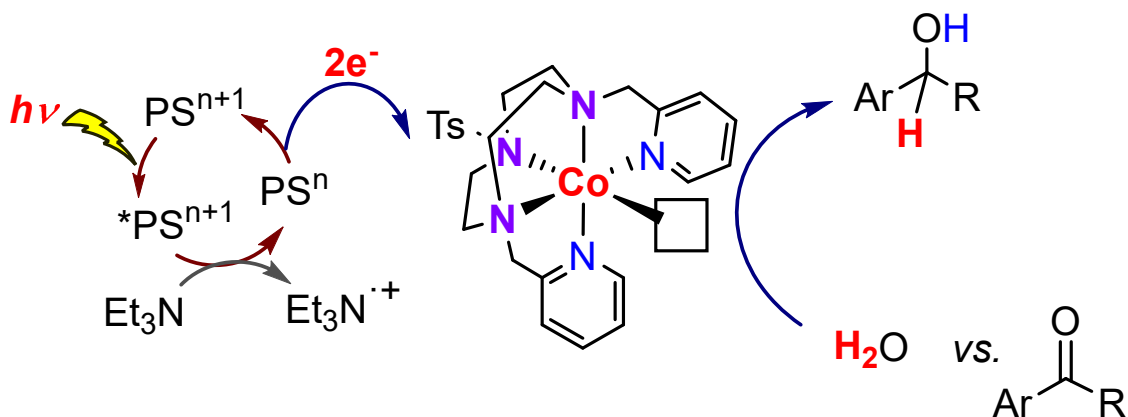
VI.3.3.7. Synthesis of $[\text{Co}^{\text{II}}(\text{Py}_2^{\text{Me}}\text{tacn})(\text{CH}_3\text{CN})](\text{OTf})_2$ ($^{\text{Me}}\mathbf{1}_{\text{Co}^{\text{II}}}$)


Scheme VI. 9. Synthesis of $[\text{Co}^{\text{II}}(\text{Py}_2^{\text{Me}}\text{tacn})(\text{CH}_3\text{CN})](\text{OTf})_2$ ($^{\text{Me}}\mathbf{1}_{\text{Co}^{\text{II}}}$).

Was synthesized in analogous manner as the $\mathbf{1}_{\text{Co}^{\text{II}}}\text{CH}_3\text{CN}$ complex, obtaining 251 mg of red crystals (0.368 mmol, 81 %). $^1\text{H-NMR}$ (CD_2Cl_2 , 400 MHz, 400 K) δ , ppm: 202.50, 168.03, 162.17, 155.19, 127.58, 119.74, 104.57, 70.05, 53.78, 50.21, 42.49, 41.21, 35.03, 16.12. Anal. Calcd for $\text{C}_{21}\text{H}_{27}\text{CoF}_6\text{N}_5\text{O}_6\text{S}_2$: C, 36.95; N, 10.26; H, 3.99 %. Found: C, 36.91; N, 10.14; H, 3.99 %. ESI-MS (m/z): 533.2 $[\text{M-OTf}]^+$, 192.0 $[\text{M-2OTf}]^{2+}$.

CHAPTER VII

Cobalt Complexes Catalyzed Light-Driven Reduction of Ketones and Aldehydes Using Water and Et₃N as Source of Hydride



VII. COBALT COMPLEXES CATALYZED LIGHT-DRIVEN REDUCTION OF KETONES AND ALDEHYDES USING WATER AND Et₃N AS SOURCE OF HYDRIDE

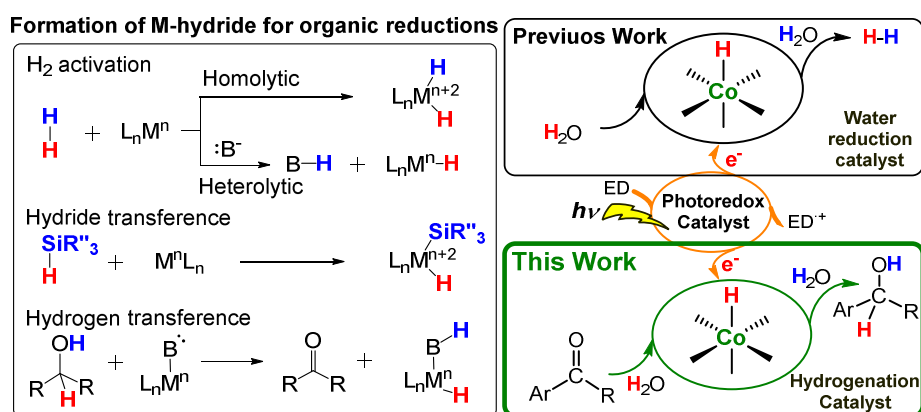
VII.1. STATE-OF-THE-ART

The mimicking of natural photosynthesis have the potential to provide greener and light-driven methodologies for sustainable fuel production but also synthetic methods.² It is important to highlight that added value chemicals have less scaling and economic restrictions than the production of energy carriers. Therefore, the use of concepts derived from natural and artificial photosynthesis to perform selective transformations is highly appealing.⁴³¹ Indeed, very interesting examples related on the reduction of organic molecules using light as energy source appeared during the progress of this work. The asymmetric reduction of acetophenones and α -ketoglutarate has achieved by coupling i) a sacrificial electron donor, ii) a photosensitizer, iii) a novel-metal catalyst, iv) an electron carrier and v) an enzyme that finally carried out the enantioselective transformation.^{251,261,262,432} Holland, Corma and co-workers achieved the stereoselective hydrogenation of conjugated C=C bonds of ketoisophorone by combining the photocatalytic activity of Au nanoparticles (NPs) supported on TiO₂ with the enzymatic activity of oxidoreductases by means of FAD⁺ as mediator and cofactor.²⁷⁸ These excellent results obtained with enzymes show the viability of selective light-driven reductions of organic substrates using water as the hydrogen source.⁴³² However, the complexity of these catalytic systems difficult their optimization and study of the mechanisms that are involved.

An appealing approach to accomplish this aim is to exploit the powerful combination of photoredox catalysts with well-defined molecular complexes.²⁵⁰ In this regard, molecular systems based on Rh,²⁸⁶ Ru,²⁸⁵ Ir²⁸⁴ and Co²⁸⁹ has been explored. For instance, König and co-workers selectively photoreduced ($\lambda = 455$ nm) aldehydes into alcohols in the presence of ketones by coupling proflavine (PF) as photocatalyst with [Cp*Rh^{III}(bpy)Cl]Cl in the presence of TEOA as sacrificial electron donor.²⁸⁶ Moreover, the cobalt B₁₂ complex (cyanoaquacobyrinic acid) embedded on the surface of TiO₂ (B₁₂-TiO₂ hybrid) was also found to be an active heterogeneous catalyst for the light-driven ($\lambda =$

365 nm) reduction of alkenes to alkenes, although the formation of dimeric products was important.²⁴⁵

Since transition metal hydride complexes (M-H) are intermediates in hydrogen evolution catalysis,⁸⁸ and target transformations of organic molecules are those related to the M-H heterolytic (H⁻ transfer) or homolytic (H[•] transfer), we envisioned that photogenerated M-H from well-defined water reduction complexes could engage this challenging transformations. Our hypothesis is that our readily available cobalt catalysts for H₂O reduction could also be applied for the transformation of organic compounds. This approach is very appealing since it could bring important advantages such as i) these systems are water resistant ii) they have low sensitivity to oxygen and iii) new or alternative selectivities can be obtained, respect to the traditional methods. To test our hypothesis, we will use as model reaction the reduction of organic functionalities such as ketones and aldehydes due to their simplicity and relevance.



Scheme VII. 1. General scheme for the synthesis of M–H and the reduction of carbonyl compounds.

The reduction of carbonyl compounds to alcohols has been conducted through the use of stoichiometric chemical reductants such as LiAlH₄,⁴³³ nickel-aluminium alloy,⁴³⁴ tri-*n*-butyltin hydride,⁴³⁵ sodium formate,⁴³⁶ alkyl phosphines,⁴³⁷ poly(methylhydrosiloxane),⁴³⁸ or borane reagents such as zinc borohydride,⁴³⁹ NaBH₄,⁴⁴⁰ NaBH₃CN,⁴⁴¹ BH₃-THF⁴⁴² and amine boranes.^{443,444} In this line, remarkable efforts have been focused on replacing strong stoichiometric chemical reductants by milder reaction conditions and hydrogenation catalysts based on cost-effective first-row transition metals due to their abundance, low cost and harmlessness.⁴⁴⁵⁻⁴⁵⁰ Nonetheless,

developed organometallic cobalt and iron catalysts employ rather strong reduction agents (metal hydrides or silanes) and/or usually suffer of highly sensitivity towards O₂ and H₂O (Scheme VII. 1). Truly, molecular catalytic systems based on earth abundant elements resilient to O₂, operating in H₂O that can reduce organic substrates using light as energy source, and water and electron donor as hydride source, could made a breakthrough in the synthesis of drugs, pesticides and organic chemicals in general.

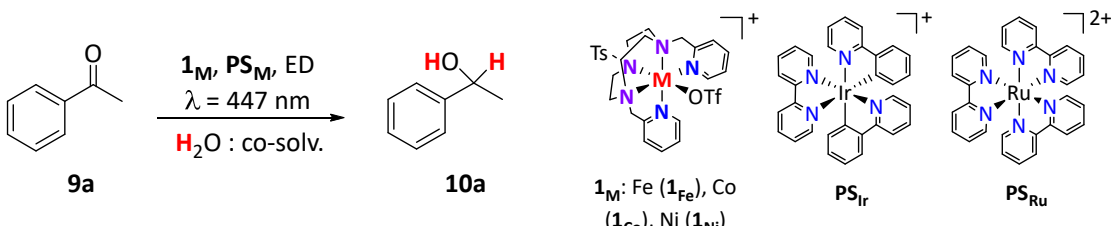
In Chapter III, we described a robust cobalt coordination complex [Co(OTf)(Py₂^{Ts}tacn)](OTf) (**1_{Co}**) that is a highly active homogeneous catalyst for light-driven and electrochemical H₂O reduction to H₂. Mechanistic investigations suggested that molecular cobalt-hydride intermediates are involved in the H₂ formation when using aminopyridine-based cobalt complexes. Based on these findings, we envisioned that the photochemically-obtained Co-H species could be potential catalytic intermediates for the reduction of organic functionalities using the combination of light, H₂O and Et₃N as the hydrogen source (Scheme VII. 1).

VII.2. RESULTS AND DISCUSSION

VII.2.1. Screening of the Conditions

To test our hypothesis, we started evaluating the capacity of the cobalt complex **1_{Co}** to reduce acetophenone (**9a**, selected as model substrate for our studies) into 1-phenylethanol (**10a**) under equivalent conditions to those employed in light-driven H₂ evolution (standard catalytic conditions used in Chapter III were [M(OTf)(Py₂^{Ts}tacn)](OTf) (M = Co (**1_{Co}**), Fe (**1_{Fe}**), Ni (**1_{Ni}**)) (1 mol%), [Ir(bpy)(ppy)₂](PF₆) (**PS_{Ir}**, ppy = 2-phenylpyridine) (0.5 mol%), Et₃N (2.1 eq.) in H₂O:CH₃CN (3.5:1.5 mL) and 5 h of irradiation at 447±20 nm). Under this conditions, only the cobalt complex **1_{Co}** yielded significant alcohol formation (23 %), with quantitative recovery of the ketone. The inactivity of the relative iron (**1_{Fe}**) and nickel (**1_{Ni}**) complexes can be explained by the no generation of stable M-H intermediates under the photochemical conditions.³¹⁴ Encouraged with this result, we next screened catalyst/photosensitizer/electron-donor ratios and solvent mixtures, maximizing the alcohol yield up to 65 % (Table VII. 1). The use of TEOA and ascorbic acid as sacrificial electron donors did not give rise significant alcohol yield, 17 and 11 % respectively, even when ascorbic acid was combined with [Ru(bpy)₃](PF₆)₂ (**PS_{Ru}**) (11 % yield).

Control experiments demonstrated that all of the components are necessary for the light-driven reduction of **9a** (Table VII. 1). In the absence of **PS_{Ir}**, **1_{Co}** or and Et₃N, no **10a** was detected (Table VII. 1, entries 12-14). In absence of **1_{Co}** traces amounts of 2,3-diphenyl-2,3-butanediol (**9a-pinacol**) (14 % yield) were observed.²⁴⁹ This has important mechanism implications and will be discussed in the appropriate section. When CH₃CN was missing in the reaction mixture, no desired product was observed because of the insolubility of **PS_{Ir}** in aqueous solution (Table VII. 1, entry 15). Whereas the lack of H₂O in the reaction vessel, all of the components were solubilized but no **10a** was formed due to the absence of H⁺ necessary for the formation of the M-H active specie (Table VII. 1, entry 16). Control experiments in the absence of light did not yield any trace of alcohol. Indeed, we monitored the **10a** formation under light-dark cycling conditions. The reduction was suppressed in the absence of irradiation and the activity could be restored with similar kinetics when the light was present again (Figure VII. 1). This result clearly demonstrates that the reaction is light-promoted.

Table VII. 1. Screening conditions for the light-driven acetophenone reduction.


Entry	Cat (3 mol%)	PS	H ₂ O:CH ₃ CN (mL:mL)	ED (eq.)	Yield 10a (%)
1 ^[a]	[Co(OTf)(Py ₂ ^{Ts} tacn)](OTf) (1 _{Co})	PS _{Ir}	3.5:1.5	Et ₃ N (2.1)	23
2	[Fe(OTf)(Py ₂ ^{Ts} tacn)](OTf) (1 _{Fe})	PS _{Ir}	3.5:1.5	Et ₃ N (2.1)	n.d.
3	[Ni(OTf)(Py ₂ ^{Ts} tacn)](OTf) (1 _{Ni})	PS _{Ir}	3.5:1.5	Et ₃ N (2.1)	n.d.
4	1 _{Co}	PS _{Ir}	3.5:1.5	Et ₃ N (8.5)	30
5	1 _{Co}	PS _{Ir}	8:2	Et ₃ N (8.5)	65
6	1 _{Co}	PS _{Ir}	8:2	TEOA (8.5)	17
7	1 _{Co}	PS _{Ir}	8:2	AscH (6)	< 4
8	1 _{Co}	PS _{Ru}	8:2	AscH (6)	11
9	1 _{Co}	PS _{Ru}	8:2	Et ₃ N (8.5)	<3
10 ^[b]	1 _{Co}	PS _{Ir}	8:2	Et ₃ N (8.5)	n.d.
11 ^[c]	1 _{Co}	PS _{Ir}	8:2	Et ₃ N (8.5)	n.d.
12	1 _{Co}	PS _{Ir}	8:2	-	n.d.
13	1 _{Co}	-	8:2	Et ₃ N (8.5)	n.d.
14	-	PS _{Ir}	8:2	Et ₃ N (8.5)	< 1 ^d
15	1 _{Co}	PS _{Ir}	10:0	Et ₃ N (8.5)	n.d.
16	1 _{Co}	PS _{Ir}	0:10	Et ₃ N (8.5)	< 1
17	[Co(OTf) ₂ (MeCN) ₂]	PS _{Ir}	8:2	Et ₃ N (8.5)	< 4
18	Py ₂ ^{Ts} tacn	PS _{Ir}	8:2	Et ₃ N (8.5)	n.d.
19	[Co(OTf) ₂ (MeCN) ₂] + bpy	PS _{Ir}	8:2	Et ₃ N (8.5)	<1
20	[Co(OTf) ₂ (MeCN) ₂] + 2·bpy	PS _{Ir}	8:2	Et ₃ N (8.5)	6
21	[Co(bpy) ₃](OTf) ₂	PS _{Ir}	8:2	Et ₃ N (8.5)	<5

Reaction conditions: [**9a**] = 16.5 mM, [PS] = 1.5 mol% in CH₃CN:H₂O:Et₃N (2:8:0.2 mL), irradiation 5 h at $\lambda = 447 \pm 20$ nm and 30 °C.^[a] [**9a**] = 66 mM, Cat = 1 mol%, [PS] = 1 mol%. **PS**_{Ir} = [Ir(bpy)(ppy)₂](PF₆), **PS**_{Ru} = [Ru(bpy)₃](PF₆)₂, **1**_{Co} = [Co(OTf)(Py₂^{Ts}tacn)](OTf), ^[b] In the dark. ^[c] In the dark under H₂ atmosphere. ^[d] 14 % yield of 2,3-diphenyl-2,3-butanediol (**9a-pinacol**). ED = Electron donor, TEOA: triethanolamine. AscH: Ascorbic acid. n.d.= not detected. Yields determined by GC analysis after workup relative to a calibrated internal standard.

We notice that the reduction of ketones to alcohols in aqueous media is a very remarkable achievement since under those conditions the cobalt hydride species are

highly reactive against protons producing H₂. This is more remarkable even if it is considered that the effective concentration of the water is 3 order of magnitude higher than the concentration of the ketone.

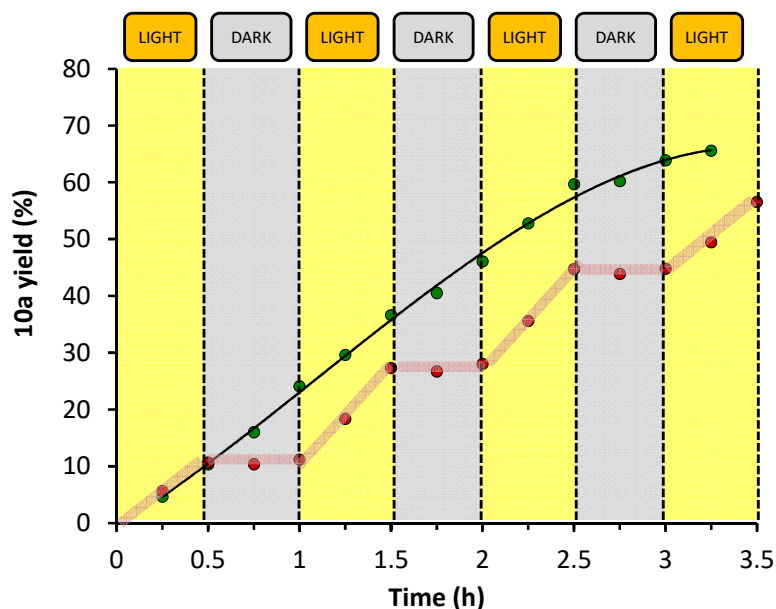


Figure VII. 1. Photoinduced **10a** formation under varied light conditions. Green dots: formation of **9a** under constant light irradiation. Red dots: formation of **10a** under light-dark cycles: yellow area corresponds to irradiation at $\lambda = 447$ nm, and grey corresponds to no irradiation of the sample. Conditions: **1**_{co} (3.8 μ mol, 3 mol%), **PS**_{ir} (2.5 μ mol, 2 mol%), substrate **9a** (0.126 mmol, 12.4 mM) in MeCN:H₂O:Et₃N (2:8:0.2 mL) irradiated at $\lambda = 447$ nm and 30 °C. The yield of **10a** was determined by GC analysis after the workup using a calibrated internal standard.

Next, we monitored by ¹H-NMR the conversion of **9a** into **10a** under the optimized reaction conditions. Reactions were performed directly into the NMR tube irradiating during different periods of time (Figure VII. 2). The starting ketone is cleanly converted into the alcohol without the formation of detectable by-products such as pinacols (Figure VII. 3). The reaction took longer reaction time to be complete in the NMR monitoring experiments, most probably due to the different irradiation conditions respect to the catalysis.

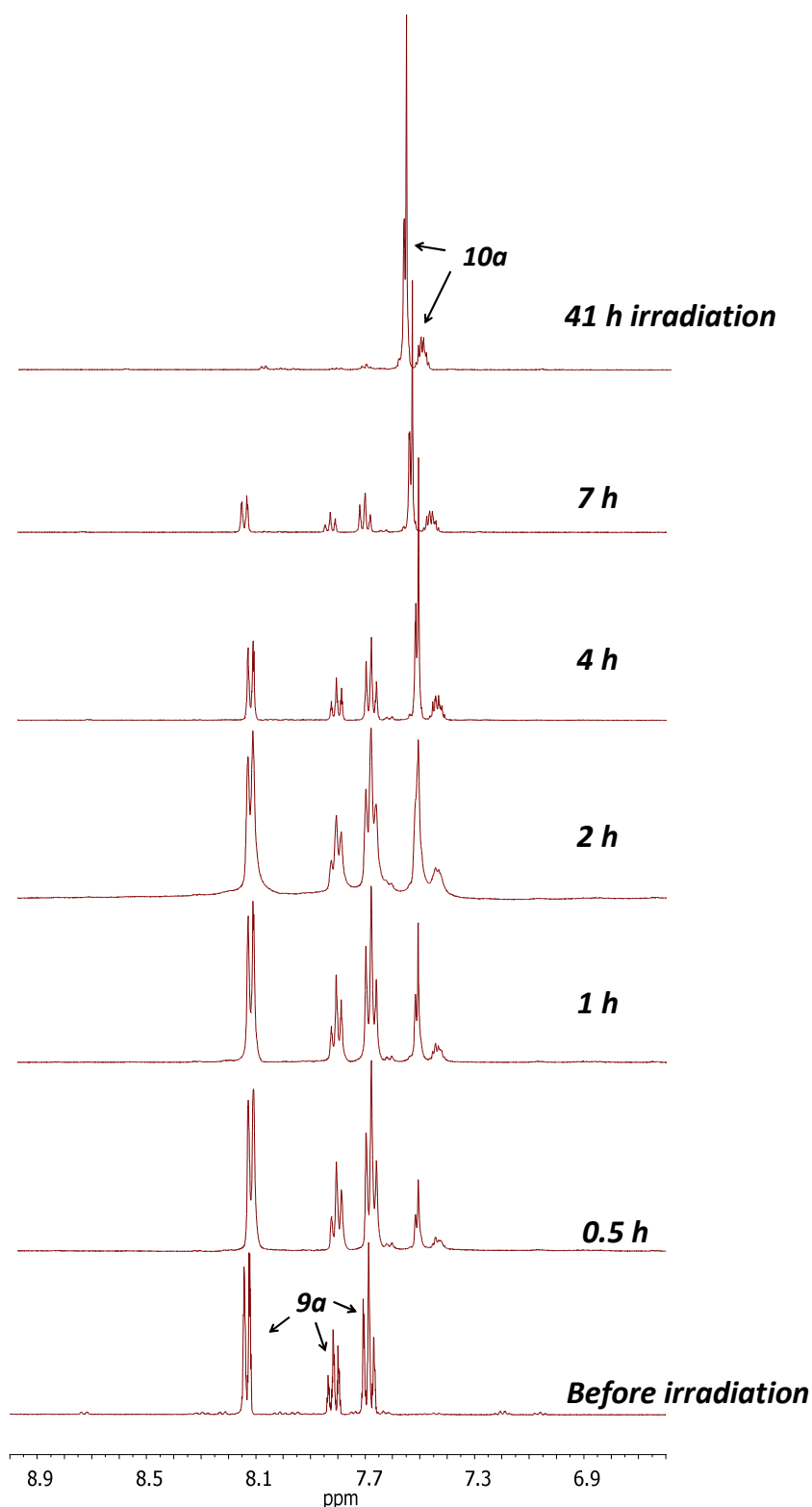


Figure VII. 2. ¹H-NMR (400 MHz, 300 K) spectra recorded at different irradiation times. Conditions: **1_{co}** (0.32 μmol, 3 mol%), **PS_{ir}** (1.2 μmol, 1.14 mol%), **9a** (10.5 μmol, 20.6 mM) in CD₃CN:D₂O:Et₃N (0.15:0.35:0.01 mL) irradiated (λ = 447 nm) at 30 °C, under N₂. The amount of **PS_{ir}** was reduced to 1.14 mol% in order to guarantee its solubilization in deuterated solvents. Each ¹H-NMR spectrum corresponds to a different reaction in order to have continued irradiation.

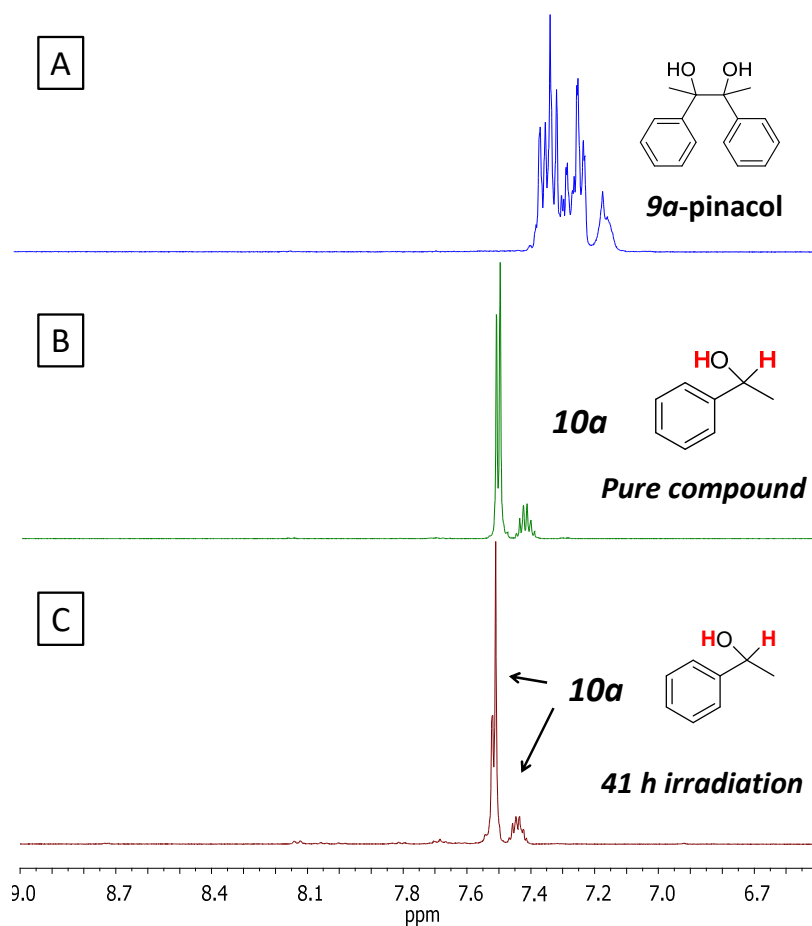
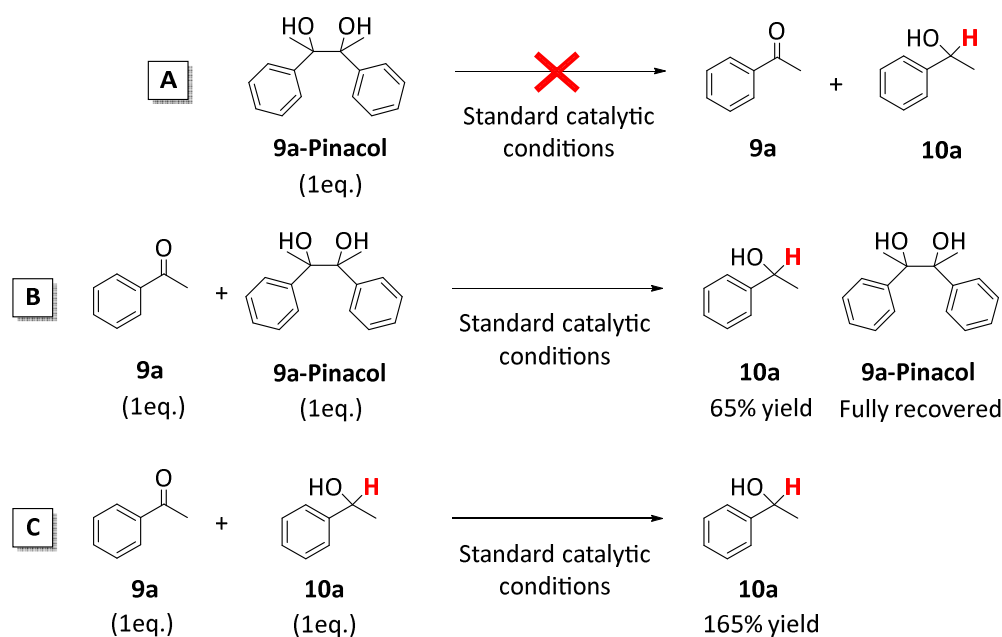


Figure VII. 3. ¹H-NMR spectra (400 MHz, 300 K) in CD₃CN:D₂O:Et₃N (0.15:0.35:0.01 mL) of A) ¹H-NMR spectrum of a mixture of the meso forms of 2,3-diphenyl-2,3-butanediol (**9a-pinacol**). B) ¹H-NMR of the pure 1-phenylethanol (**10a**). C) crude mixture after 41 h of irradiation ($\lambda = 447$ nm) using **1**_{co} (0.32 μ mol, 3 mol%), **PS**_r (1.2 μ mol, 1.14 mol%), substrate (10.5 μ mol, 20.6 mM) at 30 °C, under N₂.

In order to guarantee that pinacols are not formed under catalytic conditions we have also checked the stability of the 2,3-diphenyl-2,3-butanediol (**9a-pinacol**). When **9a-pinacol** was exposed to catalytic conditions, it was fully recovered without appreciable formation of **9a** and **10a**. Moreover, when it was exposed in the presence of 1 eq. of **9a**, the reaction proceeded in the same yield as in the absence of **9a-pinacol**. This suggests that the formation of **10a** is not related to a chemical transformation of the **9a-pinacol** product (Scheme VII. 2). In addition, experiments in the presence of **10a** shows that **9a** and **10a** are not in equilibrium at the end of the reaction.



Scheme VII. 2. A) Stability of **9a-Pinacol** under standard catalytic conditions. **9a-Pinacol** was fully recovered without formation of traces of other products. B) Reduction of **9a** to **10a** in the presence of 1 eq. of **9a-Pinacol**. C) Reduction of **9a** in the presence of 1 eq. of **10a**.

VII.2.2. Influence of the Structure of the Cobalt Catalyst

We have compared the catalytic capacity of **1_{Co}** with cobalt complexes based on multipyridine ligand architecture such as the pentadentate complexes **2-4** and the tetradentate **5-7** (Figure VII.4). We have also studied the cobaloxime complex **8**, which is well known to be an efficient catalyst for light-driven hydrogen.^{174,451,452} Photocatalytic ketone reduction of cobalt complexes **1_{Co}-8** series was performed with the aim to evaluate the ligand influence on the catalytic activity. In all the cases, we observed photocatalytic activity, but it depends on the used catalyst (Figure VII. 5, Top). Initial reaction rate and yield of **10a** formation follows the same order (**1_{Co}** > **2** > **7** > **5** > **6** > **4** > **8** > **3**) being **1_{Co}** clearly the most efficient (65 % yield, initial rate = 0.065 mmol **10a**·h⁻¹) of the series. In addition, the combination of [Co(OTf)₂(MeCN)₂] with different amounts of bpy (2,2'-bipyridine) lead to low **10a** yield (6 %, Table VII. 1, entries 19-21).

The conversion of **9a** into **10a** was accompanied by the formation of H₂. The hydrogen evolved during the reaction was monitored online and quantified as previously described (See Chapter III). The hydrogen evolution time traces for **1_{Co}-8** complexes are depicted in the Figure VII. 6. As anticipated, the activity of water reduction to H₂ is

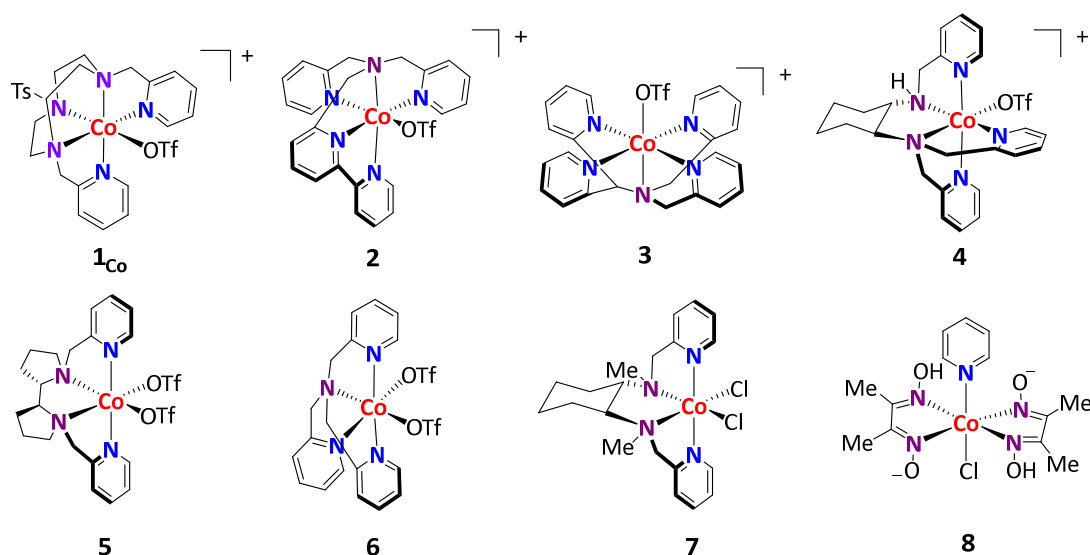


Figure VII. 4. Selected cobalt complexes for the study. **1_{co}**: [Co^{II}(OTf)(Py₂^{Ts}tacn)](OTf), **2**: [Co^{II}(OTf)(DPA-Bpy)](OTf), **3**: [Co^{II}(OTf)(N4Py)](OTf), **4**: [Co^{II}(OTf)(H-CDPy₃)](OTf), **5**: [Co^{II}(OTf)₂(PDP)], **6**: [Co^{II}(OTf)₂(TPA)], **7**: [Co^{II}(Cl)₂(BpcMe)], and **8**: [Co^{III}(Cl)(Py)(Gloxim)].

strongly dependent on the structure of the ligand coordinated to the cobalt center. Thus, the amount of H₂ formed follows the order **2** < **3** < **4** < **8** < **1_{co}** < **7** < **5** < **6**, being [Co(OTf)₂(TPA)] (**6**) complex the most effective of the series (0.264 mmol H₂, initial rate = 0.022 mmol H₂·h⁻¹) and the faster one the [Co(Cl)₂(BpcMe)] (**7**) (Initial rate = 0.257 mmol H₂·h⁻¹). Unfortunately the activity of **7** had a limited lifetime of about 1 h (Figure VII. 5, *Middle*). Notably, in the absence of substrate **9a**, the H₂ evolved increase accordantly to the capacity of the metal complex to reduce the ketone to alcohol (Figure VII. 5, *Bottom*). For instance, the initial rate and H₂ evolved yield of complex **1_{co}** is reduced in about 60 % and in 85 %, respectively when **9a** is present in the reaction mixture. In sharp contrast, the initial rate and H₂ evolved yield of complex **6** is only reduce in an 8 % and 20 % in the presence of **9a**. However, the modification of the water reduction activity can be directly related to the amount of alcohol produced (0.11 mmol **10a** with **1_{co}**, 0.019 mmol **10a** with **6**). In general, the amount of the alcohol produced together with the H₂ produced in the presence of ketone are comparable with the total amount of H₂ produced is absence of ketone in the reaction vessel.

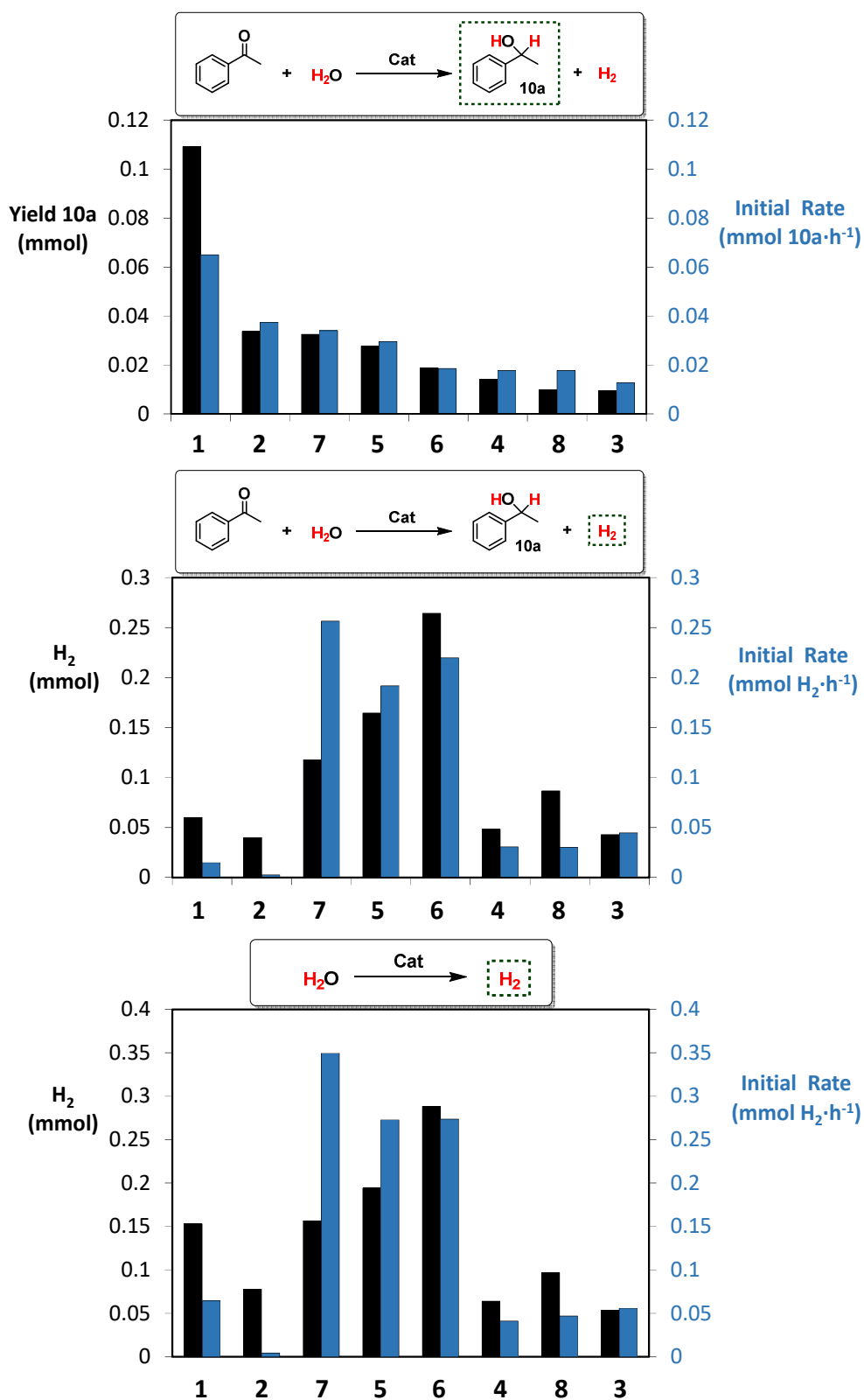


Figure VII. 5. Photocatalytic activities of different cobalt-based complexes in H₂ and **10a** formation. *Top:* **10a** formation activities. *Middle:* H₂ formation activities in the presence of **9a**. *Bottom:* H₂ formation activities in the absence of **9a**. Reaction conditions: **9a** (0.168 mmol, 16.5 mM), **PS_{Ir}** (2.5 μmol, 1.5 mol%), **cobalt catalyst** (5 μmol, 3 mol%), MeCN:H₂O:Et₃N (2:8:0.2 mL), irradiating (λ = 447 nm) for 5 h at 30 °C under N₂. The initial reaction rates in **10a** formation have been determined at the first 15 min of irradiation.

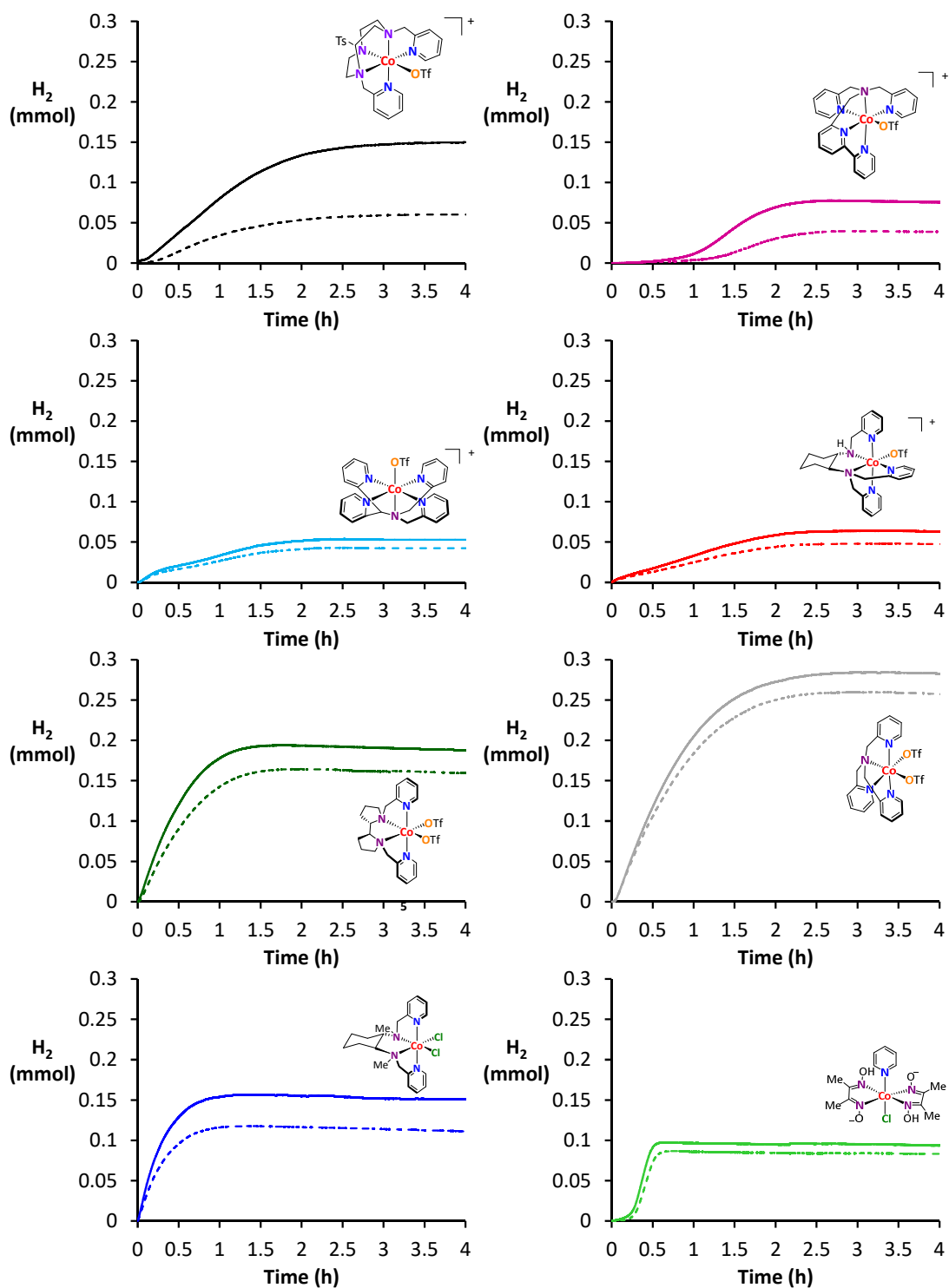


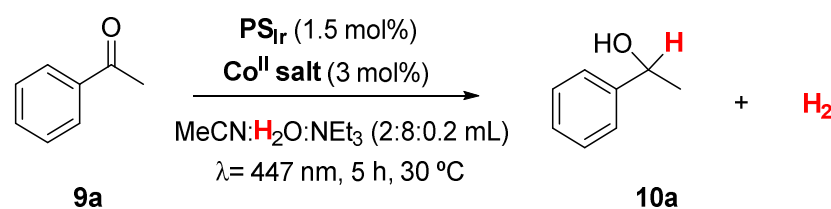
Figure VII. 6. On-line monitoring of the photochemical H_2 production in the absence (solid line) and presence of acetophenone (dashed line) for complexes **1_{Co}**-**8**. Reaction conditions in the absence of substrate: **PS_{Ir}** (2.5 μmol), **cobalt catalyst** (5 μmol). Reaction conditions in the presence of substrate: **[9a]** (0.168 mmol, 16.5 mM), **PS_{Ir}** (2.5 μmol , 1.5 mol%), **cobalt catalyst** (5.04 μmol , 3 mol%). In all cases a solvent mixture of MeCN:H₂O:Et₃N (2:8:0.2 mL) was used, irradiating ($\lambda = 447 \text{ nm}$) at 30 °C under N₂. The amount of H₂ was quantified by GC analysis when the hydrogen evolved reached a plateau.

In general the ketone reduction activity is strongly dependent on the electronic and structural nature of the ligand coordinated to the cobalt center. Looking in more detail, it appears to be some degree of a trend in the ketone reduction reaction. For the set of complexes with pentadentate aminopyridine ligands, the activity is related to the basicity of the ligand. The same type of trend is observed within the cobalt complexes with tetradentate aminopyridine ligands. The complexes with aminopyridine pentadentate ligands **1_{Co}** and **2** displays excellence selectivity towards the reduction of ketone (Ratio H₂/**10a**: 0.6 (**1_{Co}**), 1.2 (**2**)). This evidences that the photocatalytic ketone reduction activities can be modulated and improved by the rational design of the ligand architecture. On the other hand, under catalytic conditions employed the studied tetradentate complexes resulted to be more active than the pentadentate ones in H₂ evolution. Arguably, the use of tetradentate ligands seems to offer higher selectivity towards the formation of H₂ (Ratio H₂/**10a**: 3.6 (**7**), 5.9 (**5**) and 13.9 (**6**)). Due to the high performance of **1_{Co}**, we have selected it for further studies.

VII.2.3. *In-situ* formation of the cobalt catalyst. Anion effect.

One of the important issues is to determine the effect and key points of possible ligand hydrolysis and the effect of the additional ligands over the coordination sphere of the cobalt center. With this aim we have tested the catalytic activity of mixtures 1:1 Py₂^{Ts}tacn ligand : cobalt salt. Our hypothesis is that the ligand is strongly coordinated to the cobalt complexes even in aqueous solution and therefore could be formed *in-situ* prior catalysis. This also allow us to quickly study the effect of different anions on the catalysis outcome.

First we tested the simple cobalt salts without the presence of the Py₂^{Ts}tacn ligand such as [Co^{II}(OTf)₂(MeCN)₂], Co^{II}SO₄, Co^{II}(OAc)₂, Co^{II}(acac)₂, Co^{II}Cl₂ and Co^{II}(NO₃)₂. In all cases negligible amounts of **10a** (< 4 % yield) and H₂ (< 3 % respect to the obtained in the presence of the ligand) were observed (Table VII. 2). Likewise, ligand Py₂^{Ts}tacn alone was not found catalytically active (Table VII. 1, entry 18). Remarkably, when one equivalent of Py₂^{Ts}tacn ligand was directly added to the reaction mixture containing the cobalt metal source just before irradiation, the formation of **10a** was observed with similar yields to the preformed **1_{Co}** (53-66 % vs. 65 %) (Table VII. 2 and Figure VII. 7).

Table VII. 2. Cobalt salts screened in presence and absence of $\text{Py}_2^{\text{Tstacn}}$ ligand and substrate **9a**.

Cobalt salt precursor	[9a] (μmol)	$\text{Py}_2^{\text{Tstacn}}$ (n eq.)	H_2 (mL)	H_2 (μmol)	9a (μmol)	10a yield (%)	$\text{H}_2 + 10\text{a}$ (μmol)
$\text{Co}^{\text{II}}\text{SO}_4$	165	-	<0.001	0.03	4.5	3	4.5
	165	1	1.5	59	95	57	155
	-	1	4.1	169	-	-	-
$\text{Co}^{\text{II}}(\text{OAc})_2$	165	-	<0.001	0.02	4.2	2	4.2
	165	1	1.3	54	104	62	158
	-	1	3.5	142	-	-	-
$\text{Co}^{\text{II}}(\text{acac})_2$	165	-	0	0	7.5	5	7.5
	165	1	1.5	59	98	58	157
	-	1	3.9	162	-	-	-
$\text{Co}^{\text{II}}\text{Cl}_2$	165	-	0.1	1.7	1.9	1	3.6
	165	1	1.4	57	92	55	150
	-	1	3.7	150	-	-	-
$\text{Co}^{\text{II}}(\text{NO}_3)_2$	165	-	0.03	1.1	5.5	3	6.6
	165	1	1.3	51	90	53	141
	-	1	3.4	140	-	-	-
$\text{Co}^{\text{II}}(\text{OTf})_2$	165	-	0.01	0.2	6.7	4	7.2
	165	1	1.5	62	109	66	171
	165	2	1.0	42	94	56	136
	165	3	0.7	30	74	44	104
	165	4	0.5	22	59	35	81
	-	1	4.2	172	-	-	-

Reaction conditions: **9a** (0.168 mmol, 16.5 mM), PSIr (2.5 μmol , 1.5 mol%), Co^{II} salts (5 μmol , 3 mol%), MeCN:H₂O: Et₃N (2:8:0.2 mL), irradiating at $\lambda = 447 \text{ nm}$ for 5 h at 30 °C under N₂.

These suggest that in all cases the anionic ligand plays a minor role although slightly detrimental.¹⁰⁴ Large excess of $\text{Py}_2^{\text{Tstacn}}$ ligand plays a detrimental role. The combination of $[\text{Co}(\text{OTf})_2(\text{MeCN})_2]$ with two or higher stoichiometric amounts of $\text{Py}_2^{\text{Tstacn}}$ reduce the reaction yield. This fact can be rationalized by the saturation of the cobalt coordination sphere. These results provide strong evidence towards $\text{Py}_2^{\text{Tstacn}}$ cobalt complexes with free sites as the main responsible for the catalytic behaviour, and it cannot be attributed to free metal in solution. Arguably, the cobalt complex **1_{Co}** is directly responsible for the ketone reduction.

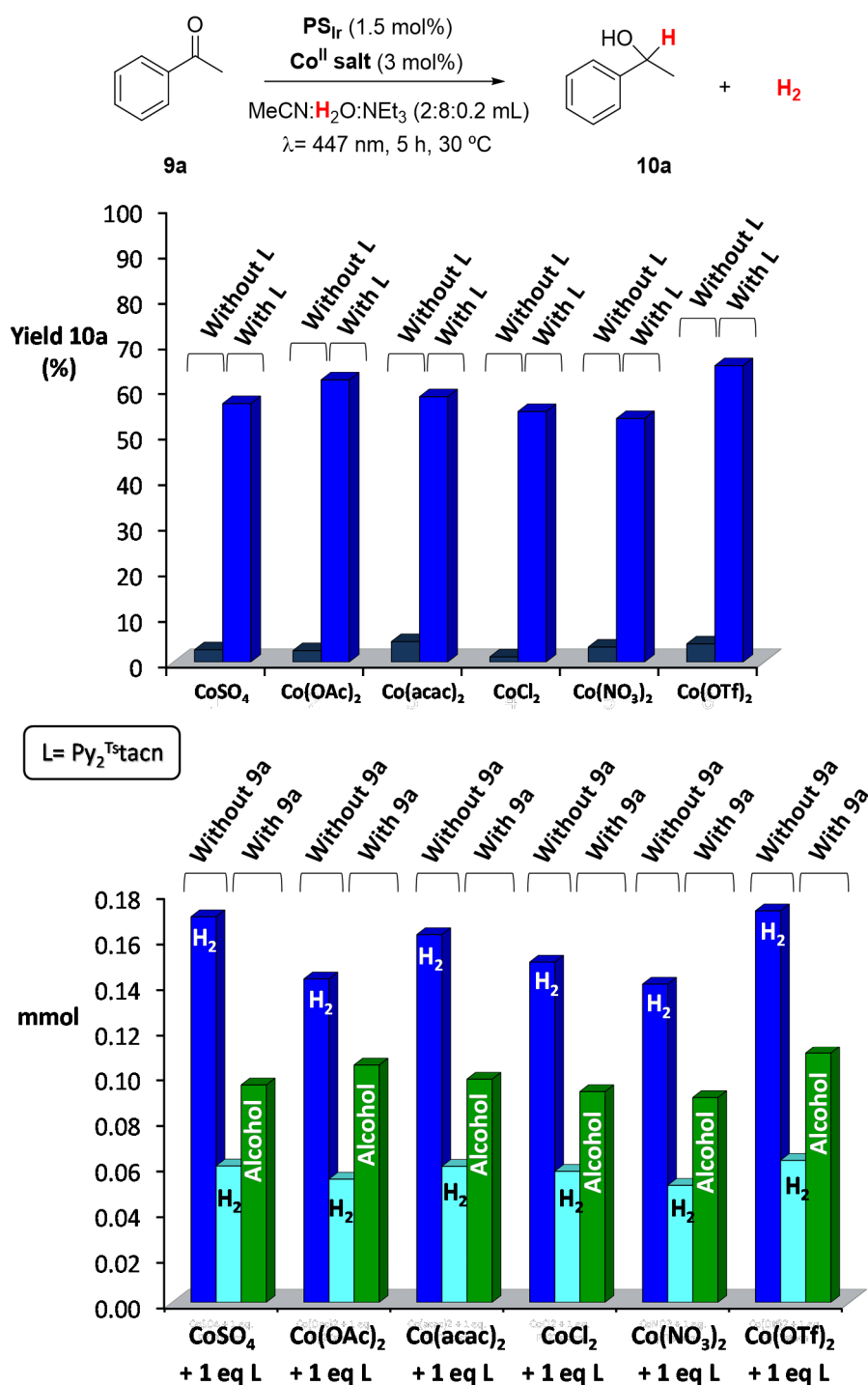


Figure VII. 7. *Top:* Effect of the presence of the ligand Py₂^{Tstacn}. Photocatalytic acetophenone reduction to **10a** using different cobalt salts in the absence (dark blue columns) and in the presence of 1 eq. of ligand (L=Py₂^{Tstacn}) (blue columns). The addition of ligand give rise to a substantial improvement of yield. *Bottom:* Mmol of H₂ and **10a** produced with different cobalt salts in the presence of Py₂^{Tstacn}. *Dark blue:* mmol of H₂ produced in the absence of **9a**. *Light blue:* mmol of H₂ produced in the presence of **9a**. *Green:* mmol of **10a** produced. Reaction conditions: [**9a**] (0.168 mmol, 16.5 mM), PS_{Ir} (2.5 μmol, 1.5 mol%), **cobalt salt** (5 μmol, 3 mol%), MeCN:H₂O: Et₃N (2:8:0.2 mL), irradiating at λ = 447 nm for 5 h at 30 °C under N₂. It should be noted that the total amount of mmol of products is similar in the presence and absence of substrate for each catalytic system.

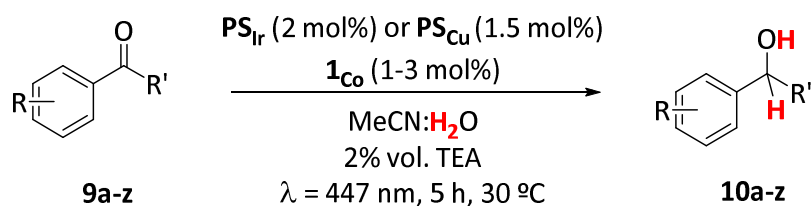
VII.2.4. Substrate screening

Encouraged by the high activity of **1c_o**, we explored the substrate scope of the catalytic system using the optimized conditions. The scope presented in Table VII. 3 shows the ability of the catalytic system to reduce a variety of aromatic ketones and aldehydes. The alcohol yields were influenced by the size of the alkyl group (R') of the ketone **9b** – **9e** (Table VII. 3, entries 2-5). Indeed, the catalytic test of 3-methyl-1-phenylbutan-1-one (**9aa**) and 2,2-dimethyl-1-phenyl-1-propan-1-one (**9ab**) yielded low quantities of the reduced product (8 and 3 % respectively) most probably due to the high steric hindrance imposed by the α -carbonyl substituents.

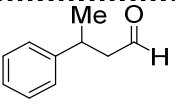
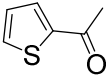
The substrates 1,2-diphenylethan-1-one (**9f**) and α -tetralone (**9g**) were reduced with similar yields: 54 and 50 respectively (Table VII. 3, entries 6 and 7). In the case of methyl-acetophenones, the substitution in *para*- (**9i**), *meta*- (**9j**) or *ortho*- (**9k**) position of the aromatic ring influences the outcome of the reaction (33 %, 69 % and 4 %, respectively). We attribute the low yield obtained with **9k** because of the proximity of the *ortho* methyl group to the carbonyl group.

On the other hand, the conversion of methoxy-substituted acetophenones (**9m**-**9o**) took place, in agreement with the reactivity derived from the electronic effects (Table VII. 3, entries 13-15). The substrate **9m** which contains an electron-donating MeO substituent at the *para* position of the aromatic ring, was observed to react slowly (Initial rate = 0.010 mmol · h⁻¹), consistent with the less electrophilic nature of the carbonyl group.

The selective photochemical transformation of organic molecules containing halogen atoms is always challenging, since dehalogenation process can be a competitive pathway.^{200,202} In this regard, the catalytic system shows good tolerance in the reduction of acetophenones containing fluorine and chloride atoms in the aromatic ring. According to GC-analysis, substrates **9p**-**9u** were reduced with good yields to the corresponding halogenated alcohols **10p**-**10u** (81-92 % yield) without dehalogenated products (Table VII. 3, Entries 16-21). However, brominated products such as 4-bromoacetophenone and 2-bromo-4-methylacetophenone produced a large quantity of non-brominated products (**10a** and **10i**). The heteroaromatic acyl substrate **9z** was also reduced in moderate yield (23 % yield) (Table VII. 3, entry 26)

Table VII. 3. Light-driven reduction of selected carbonyl compounds.

Ent.	Subs.	Sub [%] ^[c]	Yield [%] ^[c]		
			$\text{PS}_{\text{Ir}}^{\text{[a]}}$	$\text{PS}_{\text{Cu}}^{\text{[b]}}$	
1		R': -Me (9a)	25	65	92 (90)
2		R': -Et (9b)	40	55	92 (89)
3		R': - ⁱ Pr (9c)	71	21	80 (77)
4 ^[e]		R': -Bu (9d)	72	24	92 (90)
5		R': -CycloPr (9e)	70	22	82 (78)
6		R': -CH ₂ Ph (9f)	44	54 ^[e]	99 (90)
7		9g	43	50	94 (91)
8		9h	0	(91) ^[e]	93 (90)
9		R: 4-Me (9i)	57	33	94 (89)
10		R: 3-Me(9j)	22	69	94 (88)
11		R: 2-Me(9k)	95	4	32 ^[f] (31)
12		R: 4- ^t Bu (9l)	64	25	90 (92)
13		R: 4-MeO (9m)	61	10	43 (42)
14		R: 3-MeO (9n)	40	56	96 (93)
15		R: 3,4,5-tri-MeO (9o)	14	75	95 (90)
16		R: 2-F (9p)	0	88	93
17		R: 4-F (9q)	10	89	99 (94)
18		R: 2,4-F (9r)	17	82	98 (96)
19		R: 4-Cl (9s)	3	88	92 ^[g]
20	R: 3-Cl (9t)	5	81 ^[h]	72 ^[h]	
21	R: 4-Cl-3-Me (9u)	0	95	92 (94)	
22 ^[i]		R: MeO- (9v)	0	90	94 (90)
23 ^[i]		R: Me (9w)	0	93	93 (91)
24 ^[i]		R: 3,5-di- ^t Bu (9x)	0	91 ^[j]	98 (93)

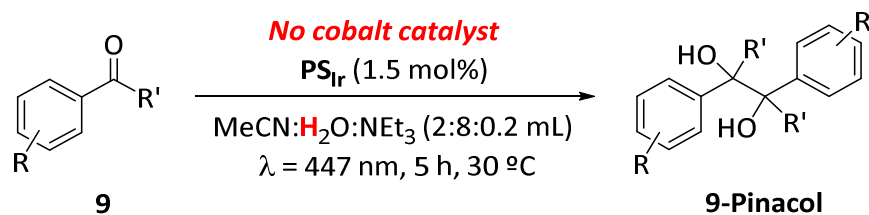
25		9y	80	11	40 ^[k]
26		9z	49	23	50 (45)

[a] Standard catalytic conditions (scc): **1_{Co}** (3 mol%), **PS_{Ir}** (2 mol%), Substrate (0.126 mmol) in MeCN:H₂O:Et₃N (2:8:0.2 mL) irradiated (447 nm) for 5 h at 30 °C under N₂. [b] **1_{Co}** (1 mol%), **PS_{Cu}** (1.5 mol%), Substrate (0.168 mmol) in MeCN:H₂O:Et₃N (4:6:0.2 mL) irradiated (447 nm) for 5 h at 30 °C under N₂. [c] Yields and unreacted substrate were determined by GC analysis relative to calibrated internal standard after workup. Averages by triplicates. Sub = unreacted substrate. [d] Isolated yields between parentheses. [e] MeCN:H₂O:Et₃N (3:7:0.2 mL). [f] **1_{Co}** (2 mol%). [g] Formation of 1-phenylethanol was detected (5 % yield). [h] The formation of the dimeric product 2,3-bis(4-chlorophenyl)butane-2,3-diol was observed (7 % using **PS_{Ir}** and 19 % using **PS_{Cu}**). [i] 1.5 h of irradiation. [j] Due to the low solubility of the compound, the solvent mixture employed was MeCN:H₂O:Et₃N (4:6:0.2 mL). [k] 3-phenylbut-2-en-1-ol (**9ak**) (45 % yield) was obtained as byproduct.

Remarkably, more electron poor substrates such as aldehydes **9v-9x** were fully converted into alcohols with excellent yields (Table VII. 3, Entries 22-24). Moreover, the catalytic system is also able to reduce the aliphatic aldehyde **9y** (11 % yield) although in low yield. It is important to remark that the reduction of all of the substrates tested is not observed in the absence of the cobalt catalyst.

VII.2.5. Formation of pinacols

As previously noted, in the presence of a cobalt catalyst no dimeric products have been detected except for the case of the electron deficient ketone **9t**, in which 2,3-bis(4-chlorophenyl)butane-2,3-diol (**9t-pinacol**) was formed in 7 % yield (Table VII. 3, entry 20). On the other hand, control experiments in absence of cobalt catalyst reveal negligible amounts of alcohol (< 1 % yield) for all tested substrates. Interestingly, in the absence of cobalt catalyst is observed the formation of pinacols for the most electro-deficient substrates (Table VII. 3). The yields of pinacol range from 4 to 37 % yield, and depend on the structure of the substrate. Our results partially agree with the previous results reported by Rueping and co-workers.²⁴⁹ In Chapter IX we will analyze in detail the formation of these dimeric products and their implications in the mechanism.

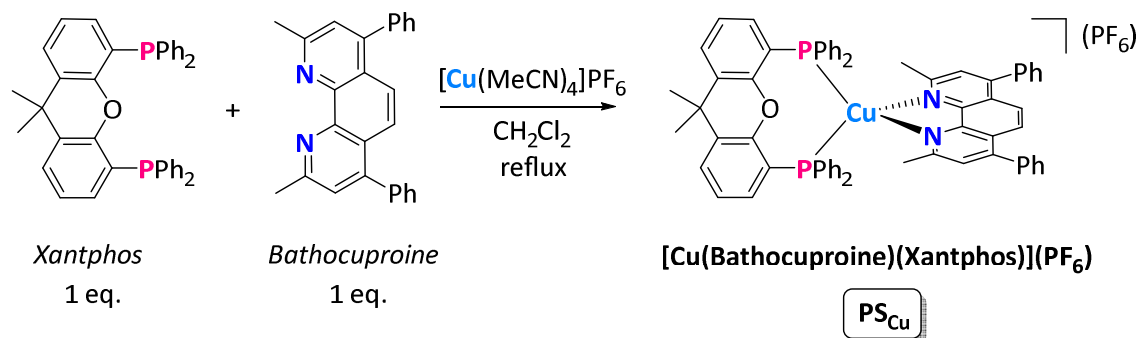
Table VII. 4. Yields of **9-pinacols** obtained in the control experiments in the absence of cobalt catalyst.

Nº	Compound	Yield pinacol (%)	Nº	Compound	Yield pinacol (%)
1		14	7		31
2		20	8		28
3		5	9		22 ^[a]
4		4	10		24 ^[b]
5		10	11		37
6		15			

Conditions: [9] (0.168 mmol, 16.5 mM), **PSIr** (2.55 μ mol, 1.5 mol%), MeCN:H₂O: Et₃N (2:8:0.2 mL), irradiating at $\lambda = 447$ nm for 5 h at 30 °C under N₂. **9-Pinacol** yields are isolated yields. [a] Formation of acetophenone was detected (24 % yield). [b] Formation of 3-methylacetophenone was detected (25 % yield) (determined by GC analysis).

VII.2.6. Catalytic Reactions Using PS_{Cu}

In order to replace the PS_{Ir} by an earth abundant element-based photoredox catalyst, we investigated the previously studied $([\text{Cu}(\text{bathocuproine})(\text{Xantphos})](\text{PF}_6))$ (PS_{Cu}) photocatalyst in the reduction of H_2O to H_2 by Beller *et. al.*³⁹⁴ The PS_{Cu} complex was straightforwardly synthesized with good yield (85 %) by mixing a stoichiometric amount of Xantphos, bathocuproine and the Cu^{I} metal salt source $[\text{Cu}(\text{MeCN})_4]\text{PF}_6$ (Scheme VII. 3). The use of bathocuproine as dinitrogen ligand scaffold is interesting since it provides higher long-lived metal-to-ligand charge-transfer (MLCT) excited states, compared with the other bipyridine analogues, because of the improvement of the steric and electronic factors. Moreover, the methyl groups located at the 2- and 9-positions difficult expansion of the coordination sphere of the metal center, and therefore preventing the exciplex quenching.⁴⁵³ Additionally, the steric effects imposed by these methyl groups favor the tetrahedral geometry instead to the preferred square-planar geometry in the formal Cu^{II} excited state, and thus slowing the nonradiative decay.⁴⁵⁴ This effect can be explained by the increase in the energy gap between the Cu d orbitals and the ligand π^* orbitals in the destabilized emissive state, as pointed out by Riesgo *et al.*⁴⁵⁴ On the other hand, the presence of the electronegative phenyl substituents on the bathocuproine moiety extend the aromaticity of the phenanthroline backbone and thus providing a lower energy π^* state and hence this facilitates the metal-to-ligand charge transfer (MLCT) transition, $d^{10}\pi^*0 \rightarrow d^9\pi^*1$, allowing the chromophore to harvest visible light (bathochromic shift).⁴⁵⁵



Scheme VII. 3. Synthesis of the Cu^{I} -based photoredox catalyst PS_{Cu} .

In addition, the presence of the Xantphos ligand not only enhances the lifetime of the excited species⁴⁵⁶ but also confers a higher stability to the photoredox system.³⁹⁴ The absorption and fluorescence spectra of PS_{Cu} are similar to the PS_{Ir} (Figure VII. 8). PS_{Cu}

also shows strong absorption bands in the UV region and a moderate band in the near UV region at about 400 nm, attributed to a MLCT transition. According these mentioned properties, **PS_{Cu}** could be a suitable noble-metal-free light-harvesting system ($\lambda = 447$ nm) for our catalytic studies.

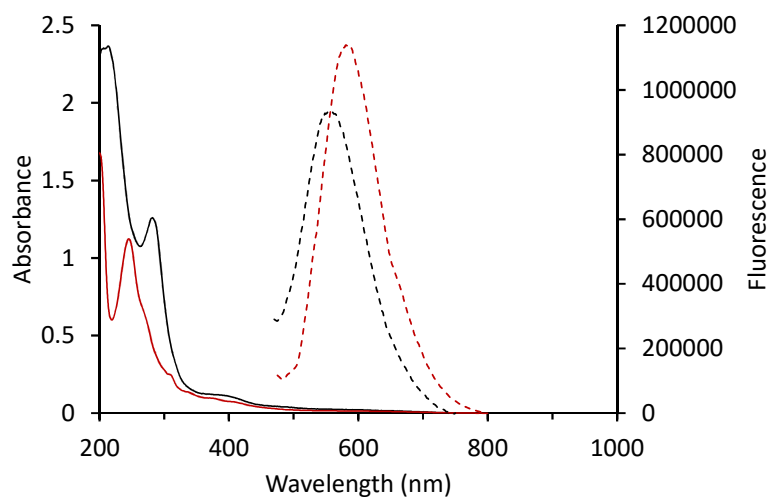


Figure VII. 8. Absorption (solid traces) and fluorescence (dashed traces) spectra of **PS_{ir}** (red) and **PS_{Cu}** (black) in MeCN, 25 °C.

We initially tested the **PS_{Cu}** chromophore by using the equivalent conditions employed with **PS_{ir}**. We observed that using MeCN:H₂O (2:8) as solvent mixture less than 1 % of **10a** was obtained at the end of the irradiation time. We attributed the absence of activity due to the precipitation of the chromophore in the reaction mixture. In order to solubilize the **PS_{Cu}** we increased the amount of the organic solvent up to 70 %. This modification produce almost a fully reduction of **9a** into **10a** (93 %) and only 5 % of the starting material was recovered. Interested with this promising result, we further increased the amount of the organic solvent, up to 50 %, observing full conversion of the reduction of **9a**. Further increase of the amount of MeCN lead to a dropped of the activity (38 % yield of **10a** in H₂O:MeCN (3:7)) (See section A.4.2.1). This lost in the photocatalytic activity could be attributed to different effects i) the change of the properties of the solvent, such as polarity, dielectric constant and diffusion coefficient, which ultimately induce an aggregation process⁴⁵⁷ or ii) the reduction of the effective proton concentration, which affect to the viability of forming the putative Co-H intermediate. Based on these results, we decided to use MeCN:H₂O (4:6) in order to guarantee all of the components completely dissolved in solution for the further experiments conducted **PS_{Cu}**.

Next, we tested the influence of PS_{Cu} loading in the outcome of the reaction from 0.3 to 2.4 mol%, with the optimized solvent mixture of MeCN:H₂O (4:6) (See section A.4.2.2). The catalytic activity systematically increase by increasing the PS_{Cu} amount up quantitative yields of ketone reduction with amounts of $\text{PS}_{\text{Cu}} > 1.2$ mol%.

The next step was to optimize the $\mathbf{1}_{\text{Co}}$ loading. We varied the % molar of $\mathbf{1}_{\text{Co}}$ from 0.005 to 5 mol%, at a fixed concentration of PS_{Cu} . We observed quantitative reduction of $\mathbf{9a}$ using only 0.25 mol% of cobalt catalyst. However, at lower catalyst loadings the yield gradually decrease, but together with an increase of $\text{TON}_{\mathbf{1}_{\text{Co}}}$ (TON: mol $\mathbf{10a}$ /mol $\mathbf{1}_{\text{Co}}$), reaching up to 1400 TON when using just 0.005 mol% of $\mathbf{1}_{\text{Co}}$ (Figure VII. 9 and section A.4.2.3 for detailed information).

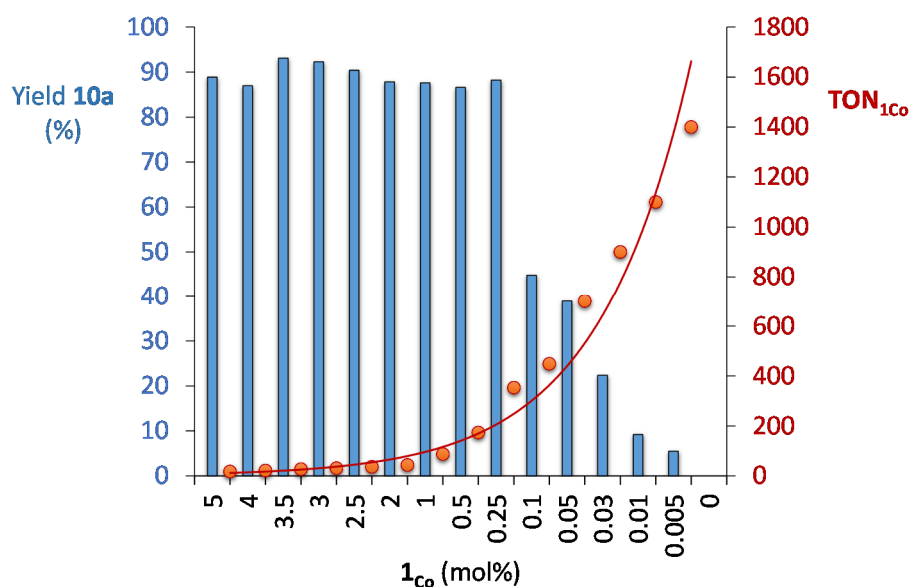


Figure VII. 9. Optimization of the $\mathbf{1}_{\text{Co}}$ loading in the photocatalytic reduction of $\mathbf{9a}$ using PS_{Cu} as chromophore.

Clearly the use of PS_{Cu} provide much higher activities than with PS_{Ir} . We attributed this difference in performance to a substantial increase of the lifetime of the catalytic system, since the initial reaction rates in $\mathbf{9a}$ reduction were found to be equivalent for both systems under the same conditions (0.065 and 0.064 mmol $\mathbf{10a}\cdot\text{h}^{-1}$ with PS_{Ir} and PS_{Cu} , respectively) (Figure VII. 10). When using PS_{Cu} as chromophore, the catalytic system is sensitive on the amount of Et₃N. Quantitative conversion of $\mathbf{9a}$ into $\mathbf{10a}$ was observed with just 4 equivalents of Et₃N (Figure VII. 11, left). We notice that the ketone reduction is competing with the H₂ formation as showed in Figure VII. 13. Both processes imply the consumption of 2 electrons. Approximately every Et₃N equivalent

contribute with half electron in the ketone reduction, and most probably the difference is consumed to produce H₂ (Figure VII. 11, left).

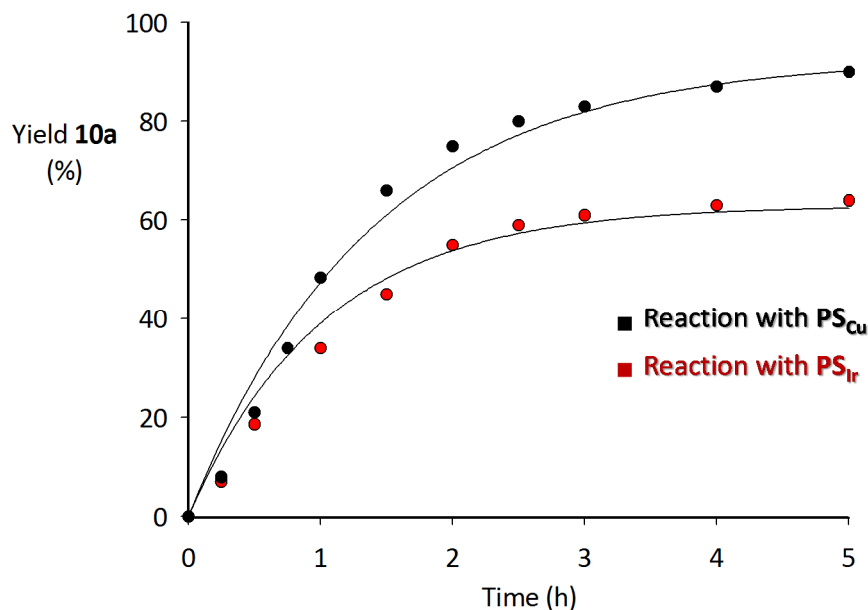


Figure VII. 10. Photocatalytic conversion of **9a** into **10a** catalyzed by **1co** using **PS_{Cu}** (black dots) compared with the reaction performed with **PS_{Ir}** (red dots) versus the reaction time (h). Conditions: **9a** (0.168 mmol, 16.5 mM), **PS** (2.5 μmol, 1.5 mol%), **1co** (5 μmol, 3 mol%) in MeCN:H₂O:Et₃N (4:6:0.2 mL) irradiated at $\lambda = 447$ nm at 30 °C under N₂. Each data point corresponds to a different reaction experiment.

Under these conditions the photocatalytic ketone reduction is compatible with low concentrations of O₂ in the headspace. Although the activity is clearly inhibited by the presence of O₂, 25 % of activity was still maintained with 10 % volume of O₂ in the headspace (Figure VII. 11, right).

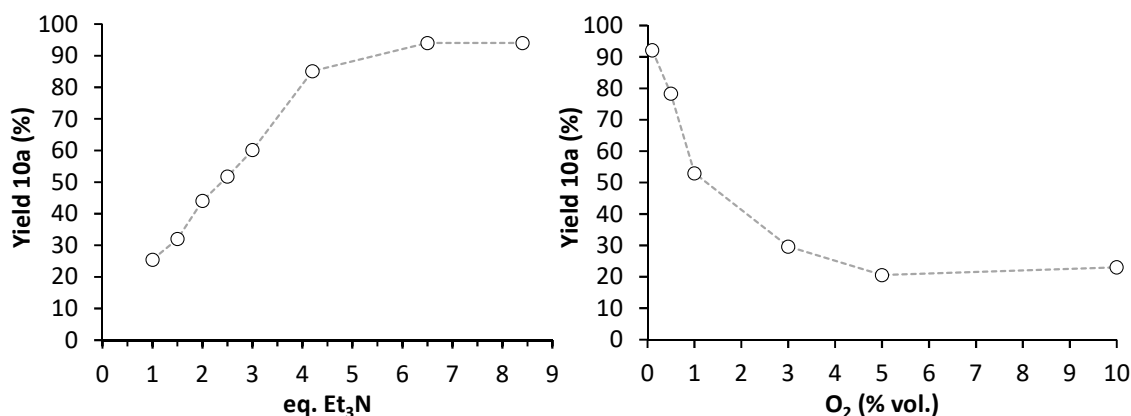


Figure VII. 11. *Left:* Photocatalytic activities in **9a** reduction at different Et₃N loadings (equivalents versus **9a**). *Right:* Effect of the presence of O₂ in the photocatalytic **9a** reduction.

Using the optimized conditions with **PS_{Cu}** we studied the whole family of aromatic ketones and aldehydes using only 1 mol% of **1_{Co}** (See Table VII. 5). To our delight, the use of **PS_{Cu}** substantially improved alcohol yields (80-99 %), and only substrates **9k**, **9m**, **9y** and **9z** gave lower yields. Analytics reveal the absence of by-products or pinacols in all of the substrates screened, except in the case of **9t** which the alcohol was accompanied by 2,3-bis(4-chlorophenyl)butane-2,3-diol in 19 % yield. All of the products have been isolated and identified by ¹H and ¹³C NMR spectroscopy, and the retention times obtained by GC techniques have been compared with those obtained with authentic samples.

Table VII. 5. Control experiments when using **PS_{Cu}** as chromophore.

Entry	Cat (3 mol%)	PS _{Cu} (mol %)	H ₂ O:CH ₃ CN (mL:mL)	Et ₃ N (eq.)	Yield (%) ^[a]
1	1_{Co}	-	6:4	8.5	n.d.
2	1_{Co}	1.5	10:0	8.5	<1
3	1_{Co}	1.5	0:10	8.5	n.d.
4	1_{Co}	1.5	6:4	-	n.d.
5^[b]	1_{Co}	1.5	6:4	8.5	n.d.
6^[c]	1_{Co}	1.5	6:4	8.5	n.d.
7	[Co(OTf) ₂ (MeCN) ₂]	1.5	6:4	8.5	n.d.
8^[d]	[Co(OTf) ₂ (MeCN) ₂]: Bathocuproine	1.5	6:4	8.5	n.d.
9^[e]	[Co(OTf) ₂ (MeCN) ₂]: Xantphos	1.5	6:4	8.5	n.d.

Reaction conditions: [**9a**] (0.168 mmol, 16.5 mM), irradiating at $\lambda = 447$ nm for 5 h at 30 °C under N₂. [a] Yields determined by GC analysis after workup relative to a calibrated internal standard. [b] In the dark. [c] In the dark under H₂ atmosphere [d] Reaction performed using Co(OTf)₂(MeCN)₂:Bathocuproine (1:1). [e] Reaction performed using [Co(OTf)₂(MeCN)₂]:Xantphos (1:1).

Control experiments showed that all the components were needed for the light-driven reduction to proceed (Table VII. 5). Additionally, no alcohol was detected when [Co(OTf)₂(MeCN)₂] was combined with an stoichiometric amount of bathocuproine⁴⁵⁸ or Xantphos⁴⁵⁸. Consequently, the activity cannot be attributed to the formation of a coordination compound formed with **PS_{Cu}** free ligands with free cobalt in solution. Therefore, the catalytic activity is exclusively belonging to the complex **1_{Co}** as well.

VII.2.7. Preliminary Mechanistic Studies

As previously mentioned in this chapter, the formation of alcohol is accompanied by the production of H₂. The observation that H₂ is also formed during the light-driven reduction of **9a-z** lead us to compare the yield and formation rate of H₂ with the ketone. Interestingly, as more alcohol formed lower is the total amount of H₂ obtained together with an inhibition of its reaction rate formation (**9a** < **9b** < **9c**, Figure VII. 12). Therefore it appears to be some trend in the H₂ production activity with the feasibility of the substrate to be reduced.

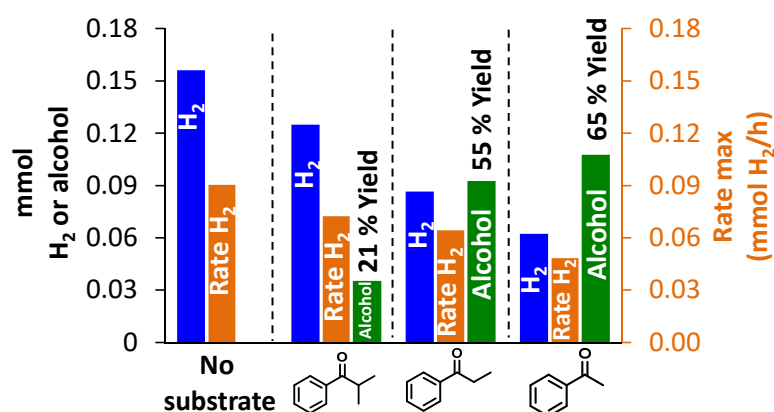


Figure VII. 12. Mmol of **10a**, **10b** and **10c** formed, H₂ generated and H₂ initial rates. Standard catalytic conditions (Table VII. 1) were used modifying the solvent mixture to MeCN:H₂O:Et₃N (3:7:0.2 mL) to guarantee the solubility of all of the components.

In the same line, the increase of substrate concentration inhibited the H₂ formation while increased the total amount of **10a** obtained. The H₂ formation dependence on the ketone reactivity points towards a common Co-H intermediate. Indeed, the sum of both (H₂ + **10a**) remains virtually constant (Figure VII. 13, A and C). It is important to note that under our catalytic conditions (15 mM **9a**) the observed rates for both **10a** and H₂ formation are similar. However, taking into consideration the relative concentrations of **9a** (2-54 mM) and H₂O (55 M), the putative Co-H catalytic intermediate must be highly selective towards **9a** versus H₂O. In addition, a 1st order dependence in **9a** concentration is obtained at low concentrations of substrate (0-20 mM, Figure VII. 13, D), which become substrate independent at higher **9a** concentrations (>20 mM). As expected, H₂ formation is inhibited following the same trend (Figure VII. 13, A and D). All these results are indicative that both H₂O reduction to H₂ and ketone reduction to alcohols share a common intermediate, most likely a Co-H species.

In the fact that the sum of both ($\text{H}_2 + \mathbf{10a}$) are maintained constant it may suggests that the rate-determining step has to be before the consumption of the common Co-H species, and therefore in the formation of Co-H.

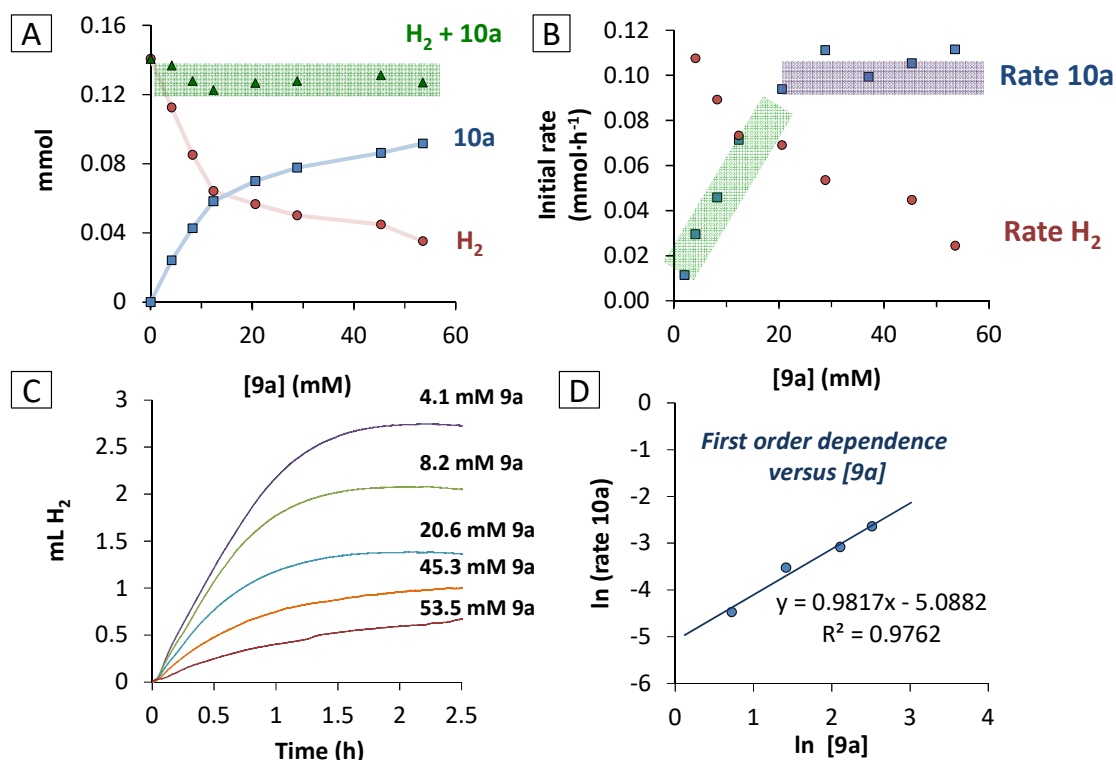


Figure VII. 13. A) Mmol of **10a** (blue dots) and H_2 (red dots) obtained and the sum of both (green dots) and B) initial rates of **10a** and H_2 formation versus **[9a]**. C) On-line monitoring of the photochemical H_2 production in the presence of increasing concentrations of **9a**. D) In-In plot of the initial rates for the **10a** formation versus **[9a]** showing the first-order dependence. Standard catalytic conditions (Table VII. 1) were used for the experiments A-B modifying the solvent mixture to MeCN:H₂O:Et₃N (3:7:0.2 mL) to guarantee the substrate solubility at 54 mM of **9a**.

VII.2.8. Molecularity of the Catalytic System: Hg^0 Poisoning Experiments

To investigate the effect on the catalytic activity of possible nanoparticles formed during the irradiation time, a poisoning experiment with large excess of Hg^0 (1.5 g, > 2000 eq.) was performed. The Hg^0 was added 15 min before starting the irradiation. The catalytic assay was conducted under standard catalytic conditions and in the presence and absence of Hg^0 for comparison reasons. The results evidenced that the presence of Hg^0 provided not only the same alcohol (61 % yield **10a**) and H_2 yield but also similar kinetics (Figure VII. 14). Therefore, nanoparticles are unlikely to be responsible for the

observed ketone reduction activity, suggesting that the activity belongs exclusively to the homogeneous cobalt catalyst.²⁹⁹ However, these results does not rule out the possible formation of nanoparticles derived from a decomposition process of the catalytic system, as previously demonstrated in the Chapter III by using DLS and NTA experiments.⁴⁵⁹

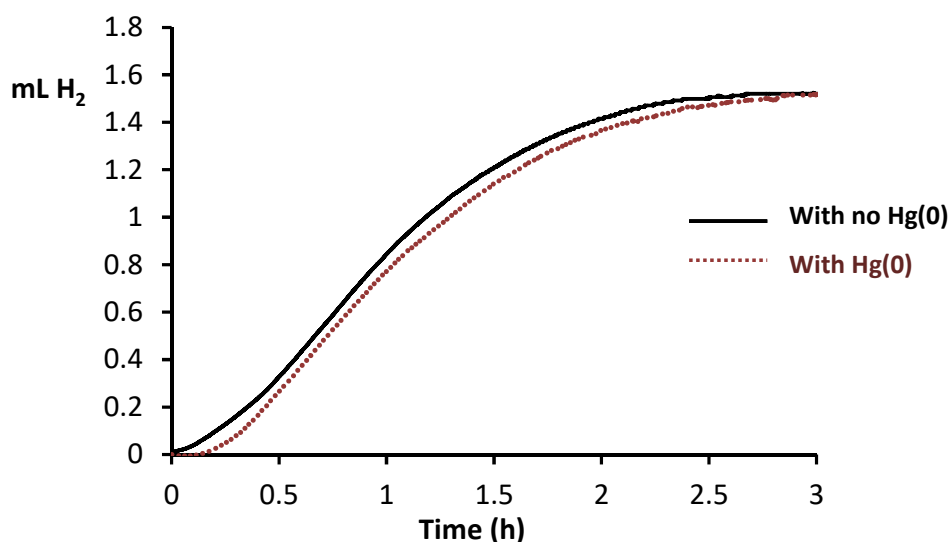


Figure VII. 14. Photocatalytic H₂ production in the absence (black line) and presence (red-dotted line) of Hg(0) (>2000 eq.). Conditions: **1** (3.8 μmol, 3 mol%), **PS_{ir}** (2.5 μmol, 2 mol%), substrate (0.126 mmol, 12.4 mM) in MeCN:H₂O:Et₃N (2:8:0.2 mL) irradiated at λ = 447 nm and 30 °C. The yield of **10a** was determined after the hydrogen evolved reached a plateau. Yield of **10a**: 65 % in absence of Hg(0) and 61 % in the presence of Hg(0).

VII.2.9. Evaluation of the Hydrogen Source: Deuterium Incorporation Studies

In an effort to gain insight into the source of hydrogen atoms, a series of deuterium-labelling experiments were conducted. The final products were recovered from the reaction mixture and characterized by ¹H NMR spectroscopy and MS. Using the solvent mixture MeCN:D₂O:Et₃N (2:8:0.2 mL), and in the absence of a metal catalyst, the substrate **9a** was fully transformed into the corresponding labelled product [**D**]-**9a**, containing deuterium atoms in the alfa-position (Figure VII. 15, left, B). The deuteration of the methyl group of the substrate can be explained by H/D scrambling process that takes place in the basic conditions imposed by the presence of triethylamine as sacrificial electron donor, being D₂O the source of deuterides. These results are in agreement with the deuteration of ketones reported in the literature using D₂O under basic conditions.⁴⁶⁰⁻⁴⁶² Furthermore, the incorporation of deuterides on the final product **10a**

was also evaluated. The final product **[D]-10a**, fully labelled with deuterium atoms on the aliphatic chain was obtained at the end of the reaction when the catalytic assay was conducted in D₂O under N₂ and H₂ atmosphere (Figure VII. 15, left, C and D). These results suggests that the source of hydrides cannot be attributed to a molecular hydrogen activation process,^{450,463-466} and H₂O is the source of hydrogen atoms. Replacing the organic solvent CH₃CN by CD₃CN, no deuterium incorporation was observed in **10a**. Figure VII. 16 shows the molecular peak ion of the alcohol obtained at different catalytic conditions. The incorporation position of deuterides into the final product were identified by NMR. By ¹H NMR the signals attributed to the C-H and CH₃ hydrogens were significantly suppressed in the deuterated product, indicating the deuteration of these position when using D₂O (Figure VII. 17). Additionally, in the ¹³C NMR the carbons attached to D atoms appeared as multiplet (Figure VII. 18).

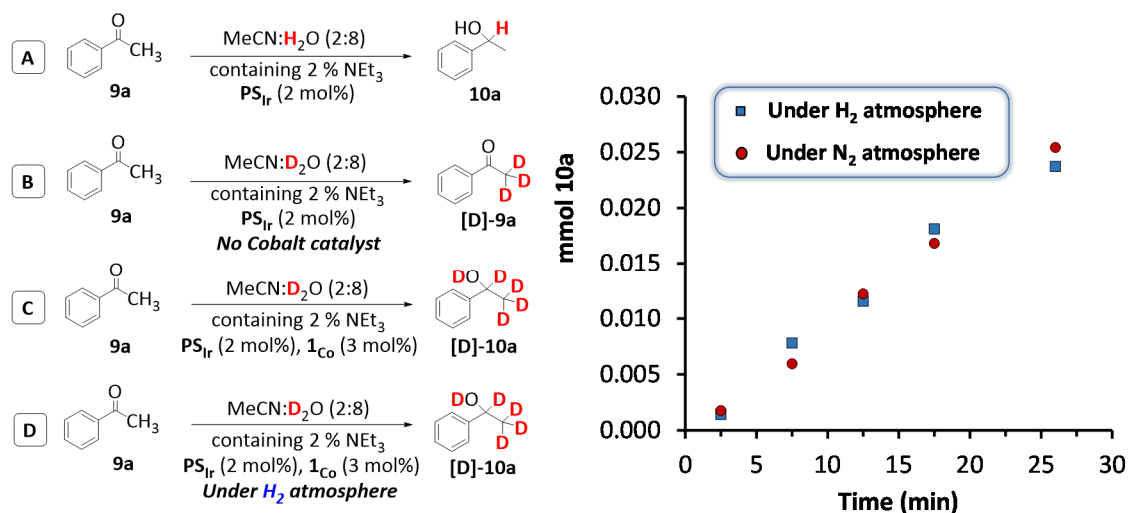


Figure VII. 15. Left: Isolated products using H₂O or D₂O (99.9 % in deuterium) in the solvent mixture: A) Reaction using H₂O, B) Blank experiment using D₂O, C) Reaction using D₂O and C) Reaction using D₂O under an atmosphere of hydrogen gas. Conditions: substrate (0.126 mmol, 12.4 mM), in MeCN:D₂O:Et₃N (2:8:0.2 mL) during 5h under irradiation at 447 nm. Right: Formation of **10a** catalyzed by cobalt complex **1**_{Co} under H₂ (blue squares) or N₂ (red cycles) atmosphere. Conditions: **1**_{Co} (3.8 μmol, 3 mol%), PS_{Ir} (2.5 μmol, 2 mol%), **9a** (0.126 mmol, 12.4 mM) in MeCN:H₂O:Et₃N (2:8:0.2 mL) irradiated at λ = 447 nm and 30 °C. Each value of **10a** yield is the result of an individual experiment. The yield of **10a** was determined by GC analysis after the workup using a calibrated internal standard. Reaction rate for **9a**→**10a** under N₂ atmosphere 0.061 mmol·h⁻¹ and under H₂ atmosphere 0.060 mmol·h⁻¹.

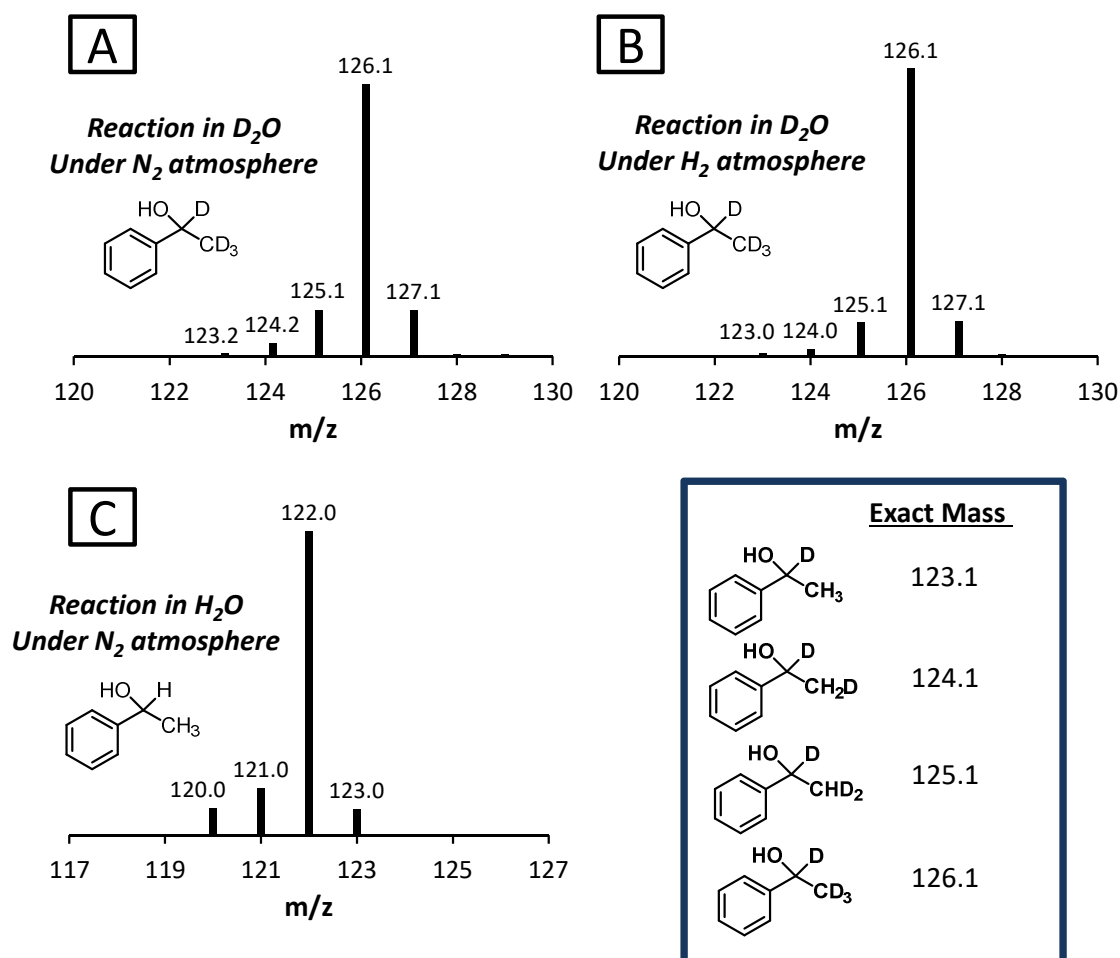


Figure VII. 16. Molecular ion measured by EI GC-MS from the reduction of **9a** when replacing the H₂O (C) by D₂O (A and B). Conditions: **1**_{Co} (3.8 μmol, 3 mol%), **PS**_r (2.5 μmol, 2 mol%), substrate (0.126 mmol, 12.4 mM) in MeCN:H₂O(or D₂O):Et₃N (3:7:0.2 mL) irradiated at λ= 447 nm and 30 °C under N₂ (A and C) or H₂ (B) atmosphere.

Another evidence comes from the same kinetics and **10a** yield measured in the presence (64 % yield, 0.060 mmol·h⁻¹) and absence (65 % yield, 0.061 mmol·h⁻¹) of H₂ in the atmosphere (Figure VII. 15, right). Indeed, when the reaction was conducted in the dark but under H₂ atmosphere, any trace of alcohol was detected (Table VII. 1, entries 10 and 11). Therefore, the H₂ evolved during the reaction does not participate in the reduction of the organic substrate, and the postulated active Co-H specie is formed directly from water.

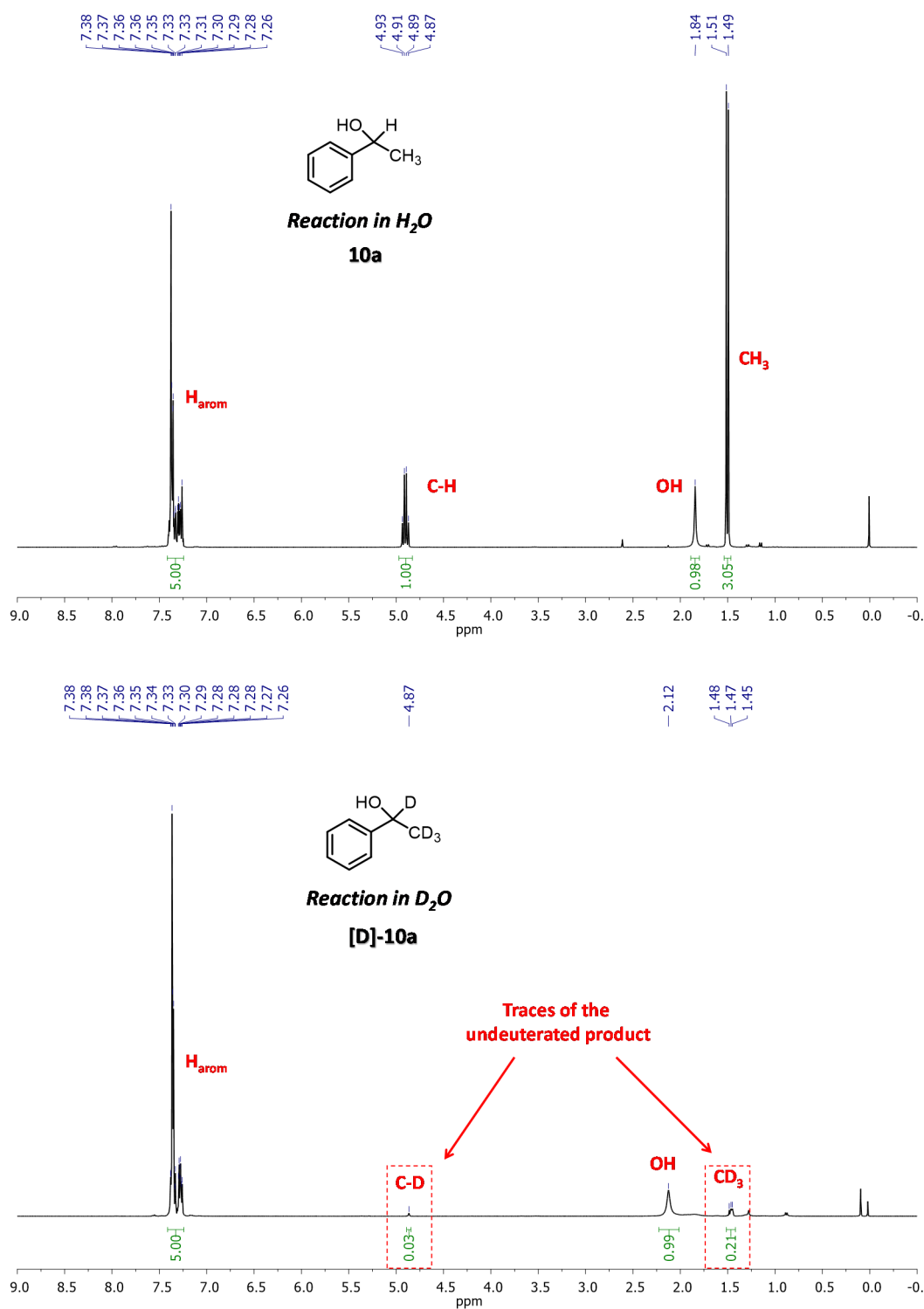
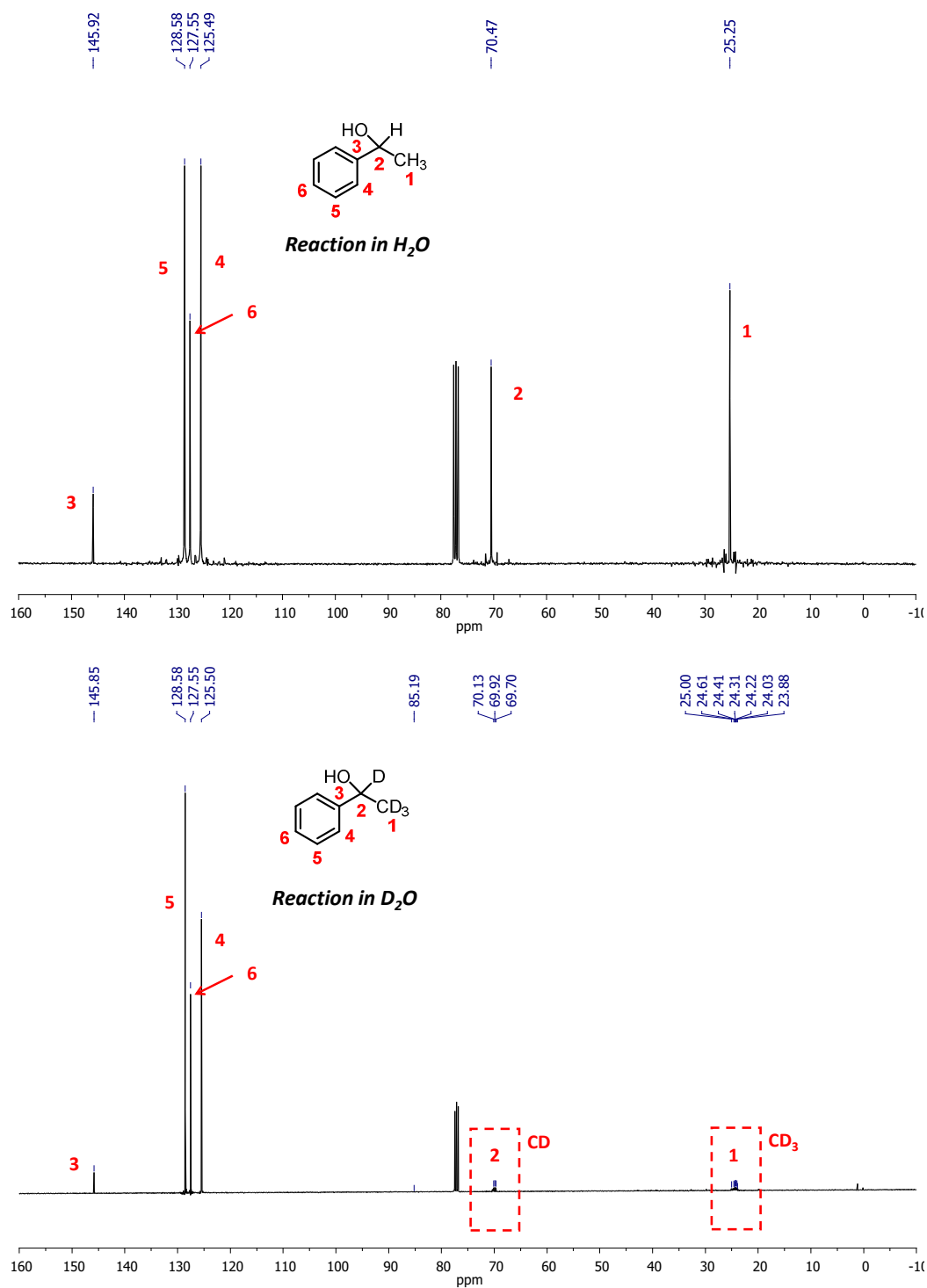
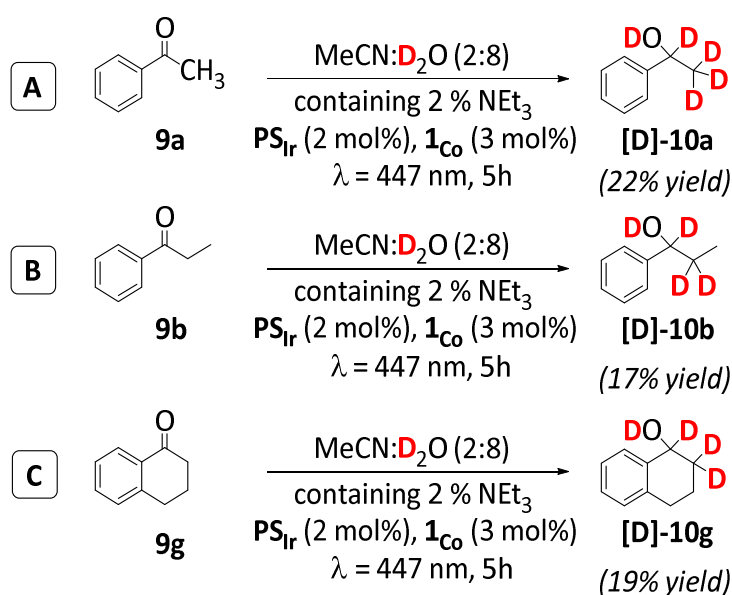


Figure VII. 17. ¹H-NMR spectrum (CDCl₃, 400 MHz, 300 K) of the isolated product **10a** using H₂O (Top) or D₂O (99.9 % in deuterium) (Bottom) in the solvent mixture. Conditions: **1**_{co} (3.8 μmol, 3 mol%), **PS**_{ir} (2.5 μmol, 2 mol%), substrate (0.126 mmols, 12.4 mM) in MeCN:H₂O(or D₂O):Et₃N (3:7:0.2 mL) irradiated at λ= 447 nm and 30 °C, under N₂.



VII.2.10. A new straightforward Way for the Synthesis of Deuterium-Labelled Alcohols

The synthesis of high deuterated alcohols is very challenging in organic synthesis.⁴⁶⁷ The common methods to selective deuterate alcohols are based on the selective reduction of ketones and aldehydes using stoichiometric reductants such as NaBD₄, LiAlD₄ and SiDMe₂Ph/F⁻. This procedures involve the generation of enormous amounts of hazardous waste together with a high cost process.⁴⁶⁸ Thus, the use of D₂O as deuterium source is highly attractive considering the low cost of D₂O. Therefore, the selective deuteration of alcohols using D₂O has been studied by using catalytic systems based on iridium, molybdenum, ruthenium, osmium and ruthenium.^{469,470} Although these systems can selectively label alcohols on the α and β -positions, in most cases a high temperature is required together with high loading of bases (20 % relative to the substrate). The catalytic system that herein is presented lead to the synthesis of α -deuterated alcohols directly obtained from the respective ketone. The straightforward procedure let in a single step the conversion of the aromatic carbonyl compounds into alcohols, since D₂O is the source of both deuterides and deuteriums. The Scheme VII. 4 exhibits the application of this catalytic system for the synthesis of the selectively deuterated alcohols [D]-10a, [D]-10b and [D]-10g (with moderate yields: 17-22 %). The deuteration of the final products were analyzed by MS and ¹H and ¹³C NMR.



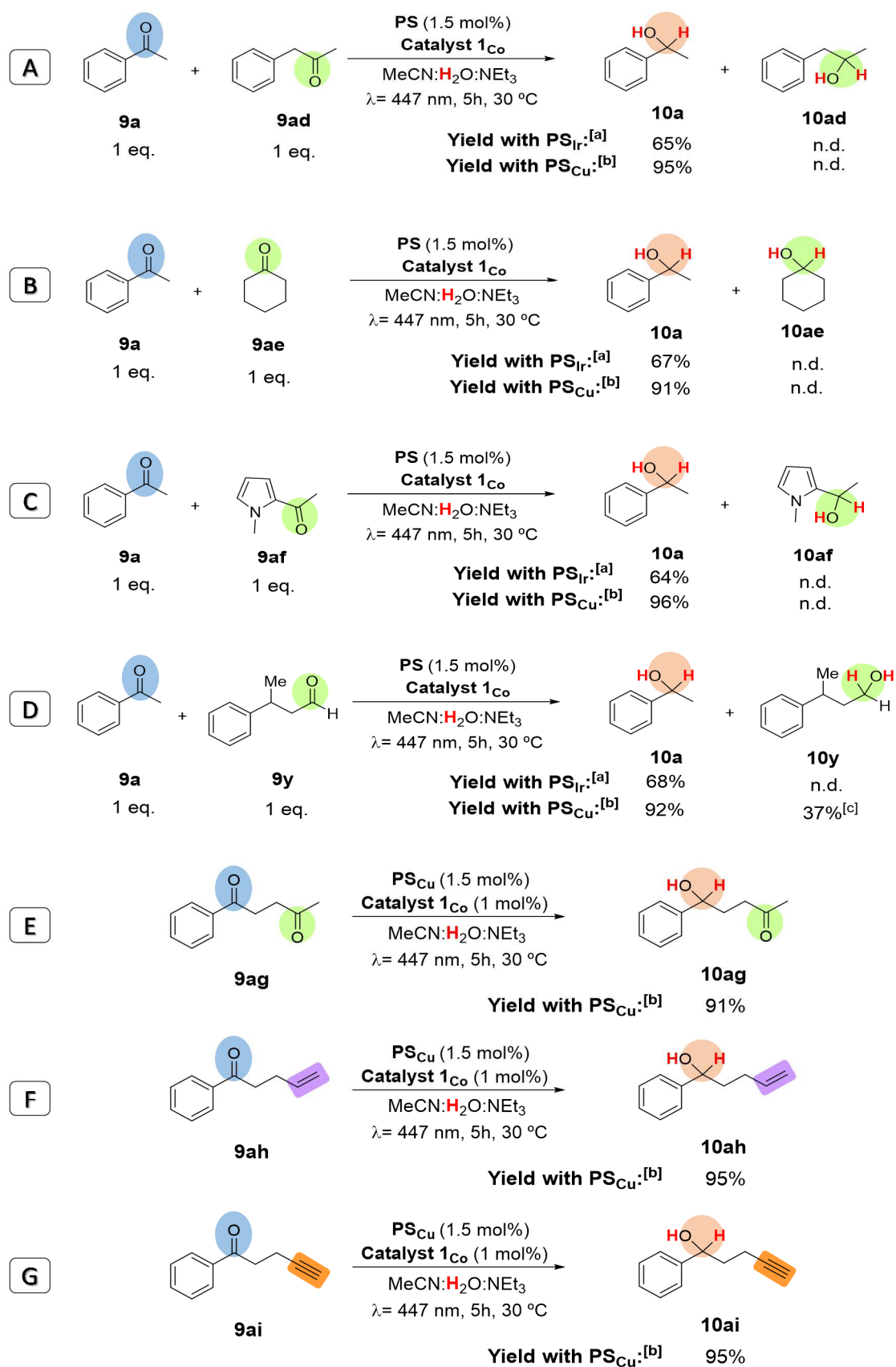
Scheme VII. 4. Synthesis of the deuterium-labeled alcohols [D]-10a, [D]-10b, [D]-10g.

The molecular peaks obtained for **[D]-10b** ($m/z= 139.1$) and **[D]-10g** ($m/z= 151.1$) were consistent with the incorporation of 3 deuterides on the organic molecule. On the other hand, the signals corresponding to the C-H and CH₂ (*alfa*) were not observed in ¹H NMR, and appeared as multiplet in ¹³C NMR, when D₂O was used as deuteride source, indicating the deuteration of this positions. Remarkably, no deuteration was observed in any other position of the alcohol product (See section A.4.3).

To the best of our knowledge this is the first catalytic system able to generate at room temperature α -deuterated alcohols from the unlabeled unsaturated relative material.

VII.2.11. Selectivities

As we hypothesized in the introduction, this alternative methodology could potentially bring new patterns of selectivity. With this aim, competing experiments were performed (Scheme VII. 5). Remarkably, the photocatalytic system was able to reduce in an exquisite manner **9a** in the presence of 1-phenylpropan-2-one (**9ad**), cyclohexanone (**9ae**) or 2-acetyl-1-methylpyrrole (**9af**) (Scheme VII. 5, entries A-C). Moreover, the product **10a** was the only reduced product observed, even when **9a** was fully consumed and the irradiation time was prolonged to 24 h. These preference for the aromatic ketones is extended to an aliphatic ketone, alkene and alkyne. We selected 1-Phenyl-1,4-pentanedione (**9ag**), 1-Phenyl-1,4-penten-1-one (**9ah**) and 1-Phenyl-4-pentyn-1-one (**9ai**) as model substrates for the study. As shown in Scheme VII. 5 (entries E-G), the reduction of **9ag**, **9ah** and **9ai** selectively gave the products corresponding the reduction of the aromatic ketone: 5-Hydroxy-5-phenylpentan-2-one (**10ag**), 1-Phenyl-4-penten-1-ol (**10ah**) and 1-Phenyl-4-pentyn-1-ol (**10ai**) (See section A.4.4). Importantly, any product derived from the reduction of an aliphatic functional group was detected even in the absence of **9a**. More challenging is the selective reduction of aromatic ketones in presence of the highly reactive aliphatic aldehydes. This selectivity is not trivial and the current methods rely on protection-deprotection steps.



Scheme VII. 5. Selective reduction of aromatic ketones in the presence of aliphatic ketones, aldehyde, alkene and alkyne. The conditions employed using PS_{Ir} and PS_{Cu} are described in Table VII. 3.

The competition between stoichiometric amounts of acetophenone (**9a**) in the presence of the aliphatic aldehyde 3-phenylbutanal (**9y**) proved that using PS_{Ir} only **9a** was reduced (68 % yield), and the reduced product **10y** derived from **9y** reduction was not detected at the end of the reaction. We note that this substrate is reduced under catalytic conditions, (Table VII. 3, entry 25). In the case of using PS_{Cu} , under optimized conditions to maximize the reactivity, the ketone was fully reduced together with the presence of the reduced aldehyde **10y** in 37 % yield (Scheme VII. 5, entry D). Monitoring the competitive reaction by GC (Figure 19) it can be observed that only the aldehyde started to be reduced after **9a** was almost converted into **10a**. Once the acetophenone was fully reduced, the aliphatic compound started being reduced in a more substantial fashion. This experiments provide the bases to develop highly selective reductions of aromatic ketones in the presence of aliphatic ketones, aldehydes, olefins and alkynes.

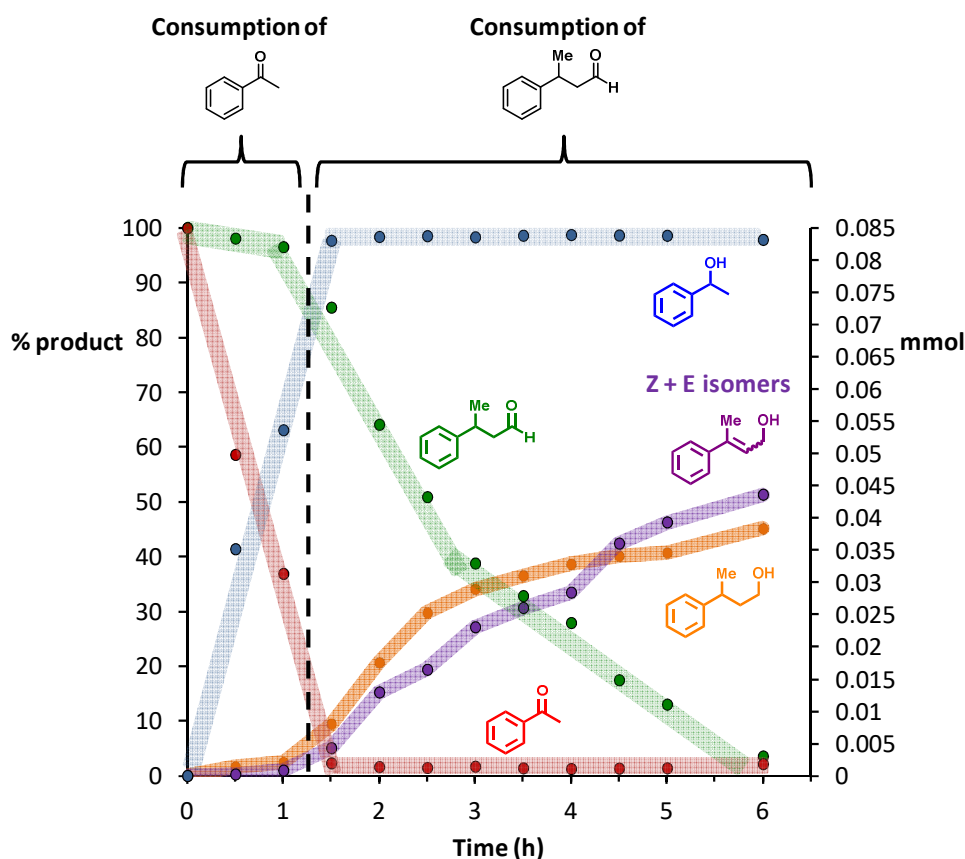


Figure VII. 19. Photocatalytic conversion during the irradiation time of acetophenone and 3-phenylbutanal in a (1:1) competition experiment. Red: acetophenone, green: 3-phenylbutanal, blue: 1-phenylethanol, orange: 3-phenylbutan-1-ol and purple: 3-phenylbut-2-en-1-ol isomers. The wide colored lines does not fit de data points but represent a general trend of the activity.

This striking selectivity towards the reduction acetophenone in the presence of 3-phenylbutanal, are in agreement with their initial reduction reaction rates measured in non-competitive reactions: 0.065 mmol·h⁻¹ (for **10a**) and 0.014 mmol·h⁻¹ (for **10y**).

We note that the formation of the reduced product 3-phenylbutan-1-ol was accompanied with the formation of (*E*)-3-phenylbut-2-en-1-ol and (*Z*)-3-phenylbut-2-en-1-ol as byproducts. The formation of these secondary products were not observed in the first minutes of the reaction, when 3-phenylbutan-1-ol was the only reduced product observed. Moreover, compounds (*E*)-3-phenylbut-2-en-1-ol and (*Z*)-3-phenylbut-2-en-1-ol are intact under photocatalytic conditions, proving not to be intermediates.

In order to get an explanation of these sharp selectivities towards the reduction of the aromatic compound, we computed the energetic barriers associated for the reduction of cyclohexanone, water and acetophenone. These theoretical calculations were performed by Dr. Ferran Acuña, from the University of Girona. Based on previous results reported in the literature in which a common reduction to Co^I is then followed by protonation yielding a Co^{III}-H specie.^{137,145,471} It has been suggested that the Co^{III}-H can be further photochemically reduced to Co^{II}-H specie that can be subsequently protonated to generate H₂. The heterolytic H₂ production pathway is proposed as favor especially for cobalt complexes with aminopyridine ligands.^{88,136,145}

On the other hand, the homogeneous hydrogenation of ketones mediated by organometallic cobalt complexes is proposed *via* Co^{II}-H intermediates.^{450,463,464,466} Therefore, is reasonable to propose a heterolytic pathway involving a common Co^{II}-H intermediate for both H₂ and alcohol formation. As shown in the Figure VII. 20, the photochemical formation of the Co^{II}-H intermediate is thermodynamically feasible. We should notice that the B3LYP Valence triple-zeta energies include solvent effects, spin contamination correction, dispersion effect and are corrected by pH and concentration. The energetic barrier observed for the reduction of cyclohexanone is also feasible ($\Delta G^\ddagger = 11.7 \text{ kcal}\cdot\text{mol}^{-1}$), however it is higher in energy compared to the H₂ ($\Delta G^\ddagger = 10.5 \text{ kcal}\cdot\text{mol}^{-1}$) and aromatic alcohol ($\Delta G^\ddagger = 8.4 \text{ kcal}\cdot\text{mol}^{-1}$) formation processes, which are close in energy. This energy barriers are in excellent agreement with the selectivities observed.

The low energy difference between the H₂ and the ketones reduction could explain the observed competition. In the fact that water is used as solvent and it is in large amount (55 M) compared to the organic substrates (16.5 mM). The large excess of water as substrate implies that H₂ is produced by the protonation of Co^{II}-H specie during the reaction time. This would explain the intrinsic formation of H₂ even at high concentrations of acetophenone. More interestingly, the H₂ formation would prevent the reaction of the Co^{II}-H with the aliphatic substrate, which have a slight larger barrier but still could produce the sharp selectivity, even if the acetophenone is fully consumed or is not at all in the reaction media. Indeed, under the later conditions, H₂ is produced under similar rate and amount that in the absence of the aliphatic ketone. This model shows that H₂O can serve also as a sacrificial substrate providing outstanding selectivities, which are not trivial with homogeneous catalytic systems.⁴⁷²

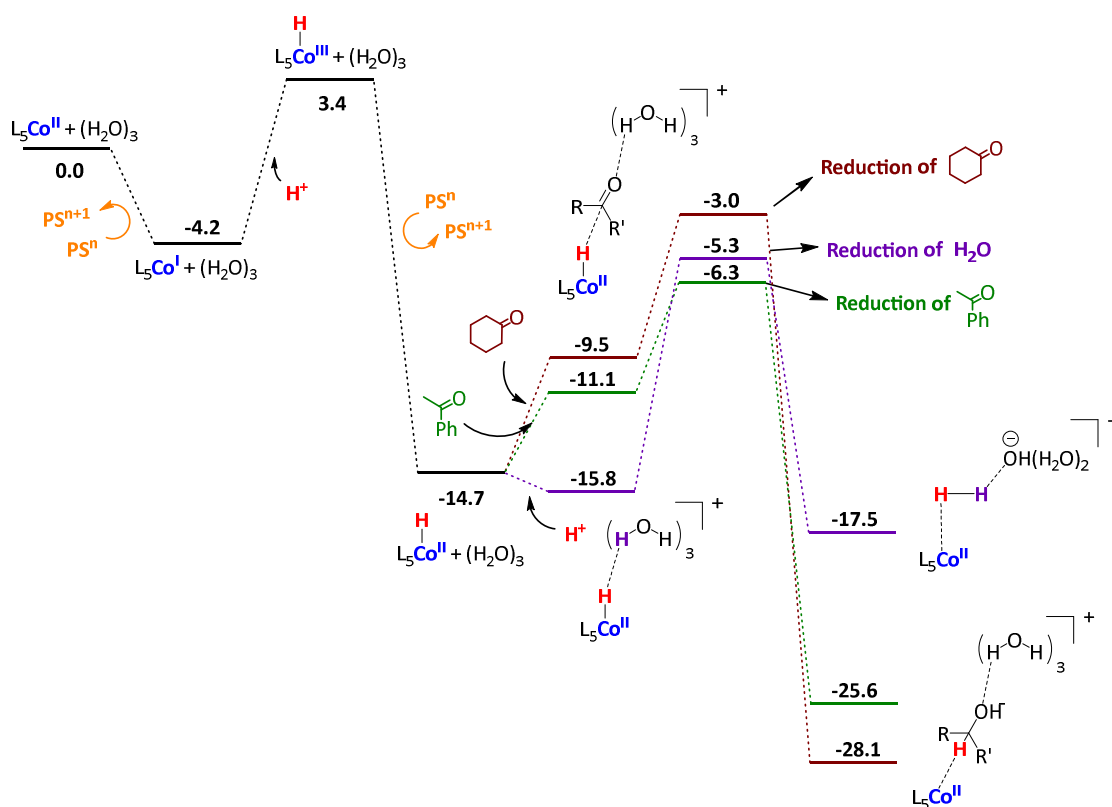
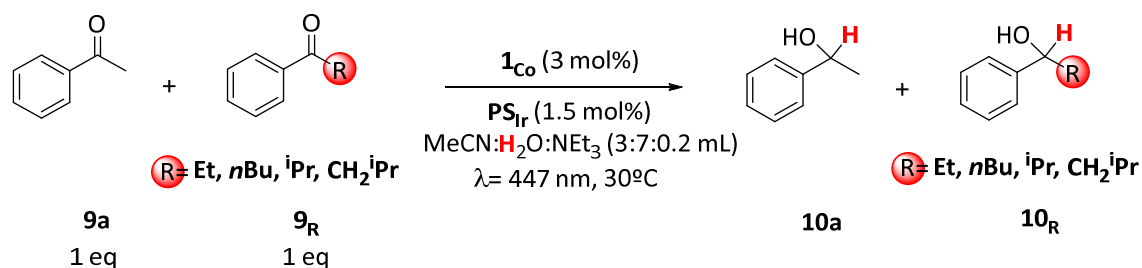


Figure VII. 20. DFT-modelled free-energy profiles for the reduction of cyclohexanone, water and acetophenone with the complex **1**_{Co}. The L₅ level refers to the pentadentate Py₂^{Ts}tacn ligand. Gibbs energies are in kcal·mol⁻¹.

VII.2.12. Analysis of the Steric Effects

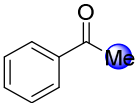
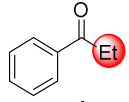
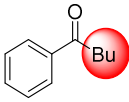
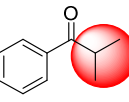
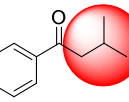
As previously described, the catalytic system is very sensitive to the electronic and structural nature of carbonyl compound, and substrates with steric hindrance present less feasibility towards the reduction process. Although this could limit the applicability of the catalytic system, this can be an advantage for selective reductions between substrates with different steric properties. Based on this idea, we decided to study the reduction of **9a** in the presence of an equimolar amount of a substrate containing a bulky group in the α -carbonyl position. The bulky substrates **9_R** (R (bulky substituent) selected for this study were: propiophenone (**9b**, R= Et), isobutyrophenone (**9c**, R= *i*Pr), valerophenone (**9d**, R= *n*Bu) and isovalerophenone (**9aj**, R= CH₂*i*Pr).



Scheme VII. 6. Analysis of the steric effects by competition experiments.

Through competition experiments containing equimolar amounts of **9a:9_R** (1:1) (Table VII. 6) we measured the initial rates formation of **10a** and **10_R** products. The Log-plot of the relative reaction rates of **10_R** relative to **10a** as a function of the Charton values (ν) gave a linear plot. From the linear correlation in the Charton plot the slope value of $\Psi = -5.32$ could be extracted (Figure VII. 21). The large magnitude Ψ value evidenced that the reaction outcome is highly sensitive to the nature of the substituent size, providing better selectivities.⁴⁷³ Accordingly, as the bulky-substituted acetophenones differently interact with the catalyst, it provides different selectivities: 1:1.5 (**10b:10a**), 1:4.1 (**10d:10a**), 1:14.9 (**10c:10a**) and 1:273 (**10aj:10a**).

Table VII. 6. Log-Plot of the mmol produced of **10_R** (R (bulky substituent)= Me, Et, *n*Bu, ^{*i*}Pr or CH₂^{*i*}Pr) relative to **10a** as a function of the Charton values (*v*) using standard catalytic conditions. Reaction time: 30 min. Charton values: *v* (Me)= 0.52, *v* (Et)= 0.56, *v* (*n*Bu)= 0.68, *v* (^{*i*}Pr)= 0.76, *v* (CH₂^{*i*}Pr)= 0.98.

9a	9_R	Charton value (<i>v</i>)	Rate 10a (mmol·h ⁻¹)	Rate 10_R (mmol·h ⁻¹)	Ratio rate 10a /rate 10_R	Log (Ratio rate 10a /rate 10_R)
		0.56	0.047	0.031	1.5	-0.18
		0.68	0.052	0.013	4.1	-0.61
		0.76	0.061	0.004	14.9	-1.17
		0.98	0.064	2.3·10 ⁻⁴	273	-2.44

Conditions: **9a** (0.084 mmol, 8.2 mM), **10_R** (0.084 mmol, 8.2 mM), **PS_{Ir}** (2.5 μmol, 1.5 mol%), **1_{Co}** (5 μmol, 3 mol%), MeCN:H₂O: Et₃N (2:8:0.2 mL), irradiating (λ= 447 nm) at 30 °C under N₂.

Correlating the size of the substrate with the outcome of the catalysis has widely been performed in enantioselective reactions. Thus, it is possible to correlate the product enantiomeric ratio with the Charton values of the substrate or of the ligand employed.^{474,475} From these plots the Ψ values obtained differs depending on the substrate employed, chiral ligand and the nature of the reaction. For instance, the enantioselective aziridination of styrenes with Mn-salen complexes reported by Komatsu⁴⁷⁶ a Ψ value of 1.42 was obtained, indicating that a larger substituent on the β-position of the styrene leads to a better outcome.

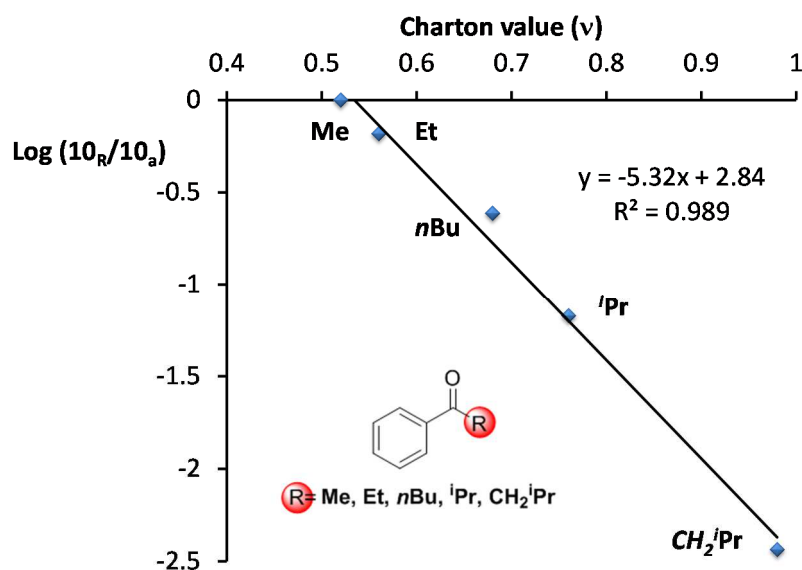
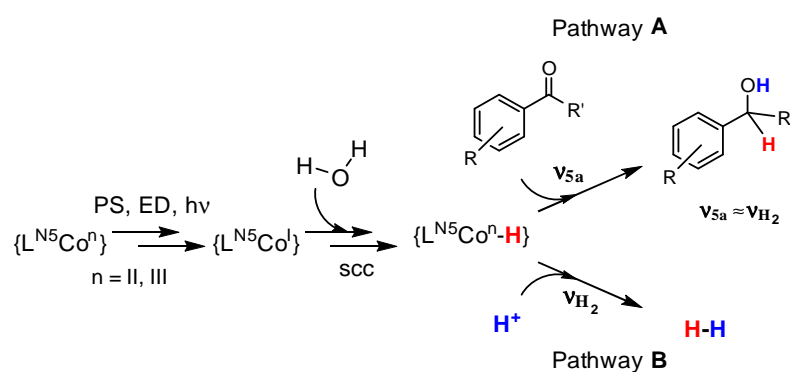


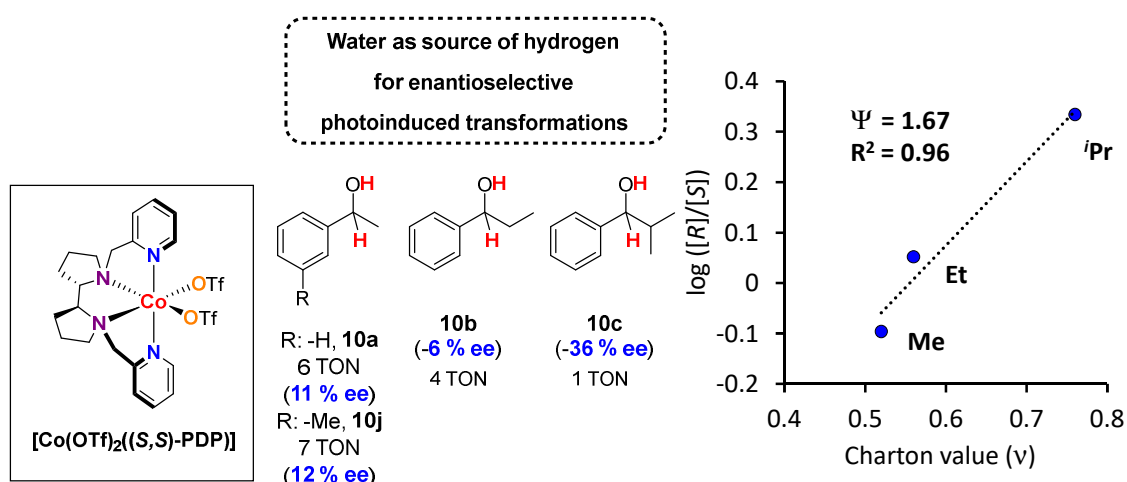
Figure VII. 21. Log-Plot of the relative r of 10_R (R (bulky substituent) = Me, Et, n Bu, i Pr, CH_2i Pr) relative to 10_a as a function of the Charton values (v) using standard catalytic conditions. Charton values: v (Me) = 0.52, v (Et) = 0.56, v (n Bu) = 0.68, v (i Pr) = 0.76, v (CH_2i Pr) = 0.98. Reaction time: 15 min. For the substrate $R = i$ Bu, no alcohol formation could be detected, and only the alcohol 10_a was produced.

VII.2.13. Chiral Induction

Our preliminary results points towards a general mechanism for the reduction of ketones, aldehydes and H_2O (Scheme VII. 7). It is well-known that used photoredox catalysts under the light-driven conditions are reducing enough to form $\{L^{N5}Co\}$ species,³¹⁴ which after protonation may form an $\{L^{N5}Co^{III}-H\}$ intermediate and its subsequent reduction may lead to an $\{L^{N5}Co^{II}-H\}$ species.^{88,105,136} Both, the $\{L^{N5}Co^{III}-H\}$ and $\{L^{N5}Co^{II}-H\}$ species could be responsible for the reduction of the carbonyl groups^{450,464} (Scheme VII. 7, pathway A), although the reduction of protons to hydrogen most probably occurs towards the $\{L^{N5}Co^{II}-H\}$ species.⁹⁷

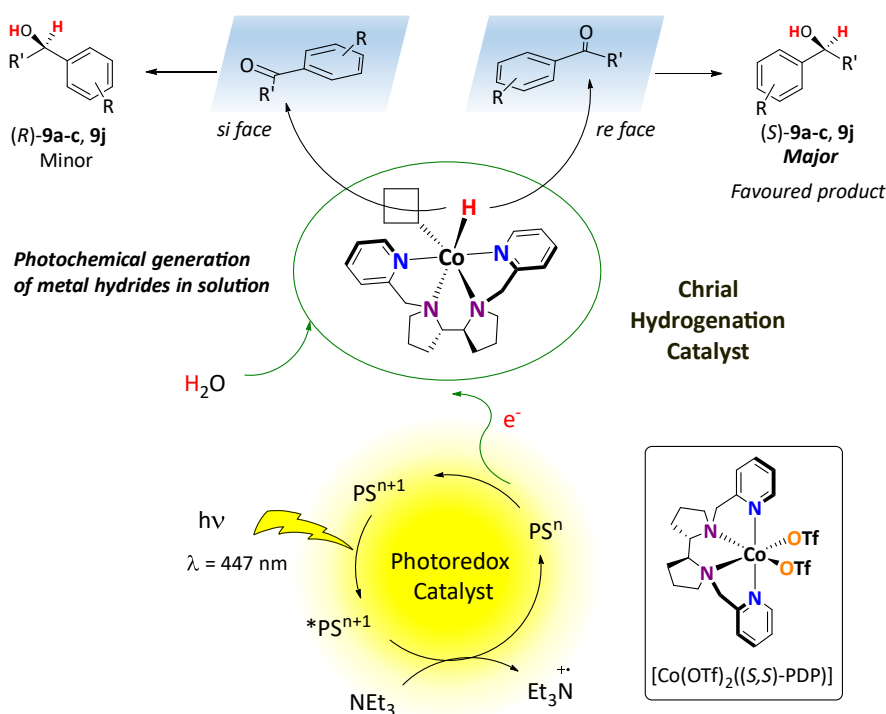


Scheme VII. 7. General proposed mechanism for the reduction of ketones, aldehydes and H_2 involving a common cobalt intermediate.



Scheme VII. 8. Asymmetric reduction of **9c**, **9b**, **9a** and **9j** catalyzed by [Co(OTf)₂((S,S)-PDP)].

Therefore, the existence of a well-defined cobalt-hydride species responsible for the carbonyl reduction should enable chiral induction, although it is highly challenging in an aqueous reaction.^{261,477-482} Indeed, our preliminary studies showed a chiral induction influenced by the substrate size (ee of 36 %, 6 %, 11 % and 12 % for **9c**, **9b**, **9a** and **9j**, respectively), when using [Co(OTf)₂((S,S)-PDP)] ((S,S)-PDP = (-)-2-(((S)-2-((S)-1-(pyridin-2-ylmethyl)pyrrolidin-2-yl)pyrrolidin-1-yl)methyl) pyridine) as a chiral cobalt catalyst under our optimized catalytic conditions (Scheme VII. 8).



Scheme VII. 9. General scheme for the chiral reduction of ketones using H₂O and light catalyzed by a homogeneous chiral cobalt catalyst.

Although the ee shown herein are low compared to that obtained in hydrogenation using homogeneous systems,⁴⁸³ they demonstrate the existence of a direct interaction between the catalyst and the substrate, and opens up the way to develop enantioselective reduction of organic substrates using H₂O as a source of hydrogen (Scheme VII. 9).

In summary, in this chapter we describe a new pathway for reducing ketones and aldehydes to alcohols using a Co-based catalyst, with H₂O and Et₃N as the source of hydrides and visible light as the driving force to regenerate the Co-based active species. The catalytic activity of the cobalt complex is strongly dependent on the structural and coordination properties of the ligand. Kinetic studies have shown that both reduction reactions, H₂O to H₂ and ketones to alcohols are competing reactions, strongly supporting that both share a common well-defined intermediate. For this reason, we envision that readily available H₂O reduction catalysts will also be found active in the reduction of these and other organic substrates. This new pathway provides remarkable selectivities towards the reduction of the aromatic carbonyl group. Moreover, the use of **PS_{Co}** as photoredox catalyst gave rise to a significant improvement of the outcome of the reaction, together with a decreased cobalt catalyst loadings. Remarkably, the reduction takes place in aqueous media where cobalt-hydrides species are formed and subsequently reduces the carbonyl groups. These results pave the way for (enantio)selective organic reductions by artificial catalytic systems that operates entirely with earth-abundant elements, using visible light as the driving force and H₂O as a source of hydrides.

However, more experiments are required in order to get insights into the mechanistic nature of the photocatalytic ketone reduction to alcohol. Chapter IX collects mechanistic probes and displays more detailed proposed mechanism for the reduction of ketones and aldehydes.

VII.3. EXPERIMENTAL SECTION

VII.3.1. Material and Reagents

Reagents and solvents were purchased from commercial sources as used as received unless otherwise stated. Triethylamine (Et_3N) $\geq 99\%$ purity and ascorbic acid (AsCH) ($\geq 99\%$) were purchased from Sigma-Aldrich® and used without further purification. The photosensitizers $[\text{Ir}(\text{bpy})(\text{ppy})_2]\text{PF}_6$ (**PS_{Ir}**),³⁰³ and $[\text{Cu}(\text{bathocuproine})(\text{Xantphos})]\text{PF}_6$ (**PS_{Ir}**)³⁹⁵ were synthesized according to the literature procedures. Anhydrous acetonitrile was purchased from Scharlab. Water (18.2 M Ω ·cm) was purified with a Milli-Q Millipore Gradient AIS system. All solvents were strictly degassed and stored under anaerobic conditions.

VII.3.2. Instrumentation

Nuclear magnetic resonance (NMR) spectra were recorded on Bruker Fourier300, AV400, AV500 and AVIII500 spectrometers using standard conditions (300 K). All ^1H chemical shifts are reported in ppm and have been internally calibrated to the residual protons of the deuterated solvent. The ^{13}C chemical shifts have been internally calibrated to the carbon atoms of the deuterated solvent. The coupling constants were measured in Hz.

Elemental analyses were performed using a CHNS-O EA-1108 elemental analyzer from Fisons.

UV/Vis spectra were recorded on an Agilent 8453 diode array spectrophotometer (190-1100 nm range) in 1 cm quartz cells. A cryostat from Unisoku Scientific Instruments was used for the temperature control.

Mass Spectrometry. Electrospray ionization mass spectrometry (ESI-MS) experiments were performed on a Bruker Daltonics Esquire 3000 Spectrometer using a 1 mM solution of the analyzed compound, by introducing the sample directly into the ESI-source using a syringe. High resolution mass spectra (HRMS) were recorded on a Bruker MicroTOF-Q IITM instrument with an ESI source at Serveis Tècnics of the University of Girona. Samples were introduced into the mass spectrometer ion source by direct infusion through a syringe pump and were externally calibrated using sodium formate.

Electrochemistry. A standard three-electrode configuration was employed in conjunction with CHI Instruments potentiostat interfaced to a computer with CHI Instruments 600D software. Using one-compartment cell, all voltammetric scans were recorded using glassy carbon working electrode which was treated between experiments by means of a sequence of polishing with MicroPolish Powder (0.05 micron) before washing and sonification. Saturated calomel electrode (SCE) and Pt wire were used as reference and counter electrodes respectively.

Gas chromatography analysis. The analysis and quantification of the starting materials and products were carried out on an Agilent 7820A gas chromatograph (HP5 column, 30m or Cyclosil-B column, 30m) and a flame ionization detector. The enantioselectivity was determined by comparison with the pure samples synthesized by the reported procedures.⁴⁸⁴

GC-MS spectral analyses were performed on an Agilent 7890A gas chromatograph interfaced with an Agilent 5975c MS mass spectrometer.

Photochemical analysis. Fluorescence measurements were carried out on a Fluorolog Horiba Jobin Yvon spectrofluorimeter equipped with photomultiplier detector, double monochromator and Xenon light source. All **PS_{Ir}** solutions were excited at 450 nm and the emission intensity was collected from 520 to 800 nm. In a typical experiment, to a 10 μ M solution of **PS_{Ir}** in MeCN:H₂O (0.6:1.4) was added the appropriate amount of quencher in a screw-top quartz cuvette. All of the quencher stock solutions were prepared under strict anaerobic conditions. After degassing the sample with a stream of argon for 10 minutes, the emission of the sample was collected.

Online MS measurements have been performed using Omnistar GSD 301 C (Pfeiffer) quadrupole mass spectrometer apparatus.

Parallel Pressure Transducer Hardware. The parallel pressure transducer that we used for these studies is the same that previously was developed and described for water oxidation studies.³⁰⁴ This is composed by 8 differential pressure transducers (Honeywell-ASCX15DN, ± 15 psi) connected to a hardware data-acquisition system (base on Atmega microcontroller) controlled by a home-developed software program. The differential pressure transducer Honeywell-ASCX15DN is a 100 microseconds response, signal-conditioned (high level span, 4.5 V) output, calibrated and temperature compensated (0 $^{\circ}$ C to 70 $^{\circ}$ C) sensor. The differential sensor has two sensing ports that can be used for differential pressure measurements. The pressure calibrated devices to within ± 0.5 matm was offset and span calibrated *via* software with a high precision pressure transducer (PX409-030GUSB, 0.08 % Accuracy). Each of the 8 differential pressure transducers (Honeywell-ASCX15DN, ± 15 psi) produce a voltage outputs that can directly transformed to a pressure difference between the two measuring ports. The voltage outputs were digitalized with a resolution of 0.25 matm from 0 to 175 matm and 1 matm from 176 to 1000 matm using an Atmega microcontroller with an independent voltage auto-calibration. Firmware Atmega microcontroller and control software were home-developed. The sensitivity of H₂ analytics allows quantifying the gas formed when low H₂ volumes are generated. Therefore, it could not be discarded that small amounts of H₂ were produced by inactive complexes.

Gas chromatography identification and quantification of gases. Gases at the headspace were analyzed with an Agilent 7820A GC System equipped with columns Washed Molecular Sieve 5A, 2m x 1/8" OD, Mesh 60/80 SS and Porapak Q, 4m x 1/8" OD, SS. Mesh: 80/100 SS and a Thermal Conductivity Detector. The quantification of the H₂ obtained was measured through the interpolation of a previous calibration using different H₂/N₂ mixtures.

Light source. The reactions were performed using Royal-Blue ($\lambda = 447 \pm 20$ nm) LUXEON Rebel ES LED, Mounted on a 10mm Square Saber - 1030 mW @ 700mA (Datasheet: <https://www.luxeonstar.com/assets/downloads/ds68.pdf>) as a light source.

VII.3.3. Experimental Procedures

VII.3.3.1. General procedure employed in reaction screening conditions for the light-driven reduction of compounds. All catalytic reactions were conducted in a vigorous stirring under irradiation for 5 hours in 15 mL capped vials with a septum under nitrogen atmosphere at 30 °C, unless otherwise indicated. Catalytic assays using **PS_{Ir}** as chromophore were performed in MeCN:H₂O: Et₃N (2:8:0.2 mL) or (3:7:0.2 mL) reaction mixture, substrate (12.4 mM), **PS_{Ir}** (2.5 μ mol, 2 mol%), **1_{Co}** (3.8 μ mol, 3 mol%). Catalytic reactions carried out using **PS_{Cu}** as chromophore were performed in MeCN:H₂O:Et₃N (4:6:0.2 mL) reaction mixture, substrate (16.5 mM), **PS_{Cu}** (2.5 μ mol, 1.5 mol%), **1_{Co}** (1.7 μ mol, 1 mol%). A 447 nm LED was employed as a light source. 1,3,5-trimethoxybenzene was added as internal standard after the reaction and the reaction was quenched by adding 2 mL of CH₂Cl₂. The crude reaction mixtures were purified by extraction with CH₂Cl₂ (3 x 3 mL), the combined organic layers were dried over MgSO₄ and passed through a silica plug which was eluted with AcOEt. The resulting organic solution was subjected to GC analysis to determine the conversion of **9** and the yield of the desired products **10**.

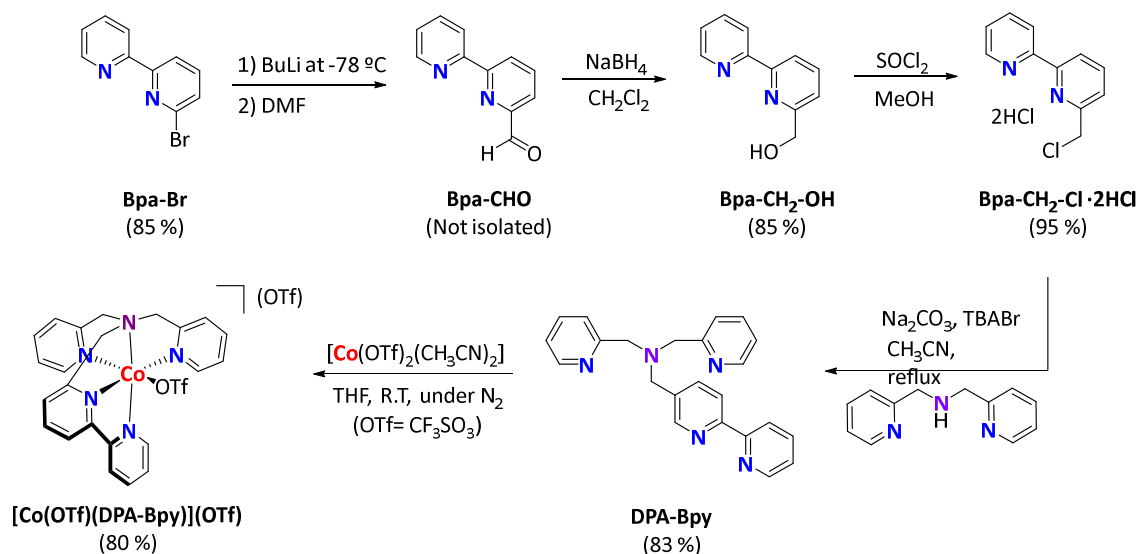
VII.3.3.2. General procedure for the alcohol isolation. Ketones **9** (0.168 mmol, 16.5 mM), **1_{Co}** (1.7 μ mol, 1 mol%), **PS_{Cu}** (2.5 μ mol, 1.5 mol%) in a MeCN:H₂O:Et₃N (4:6:0.2 mL) solution were irradiated ($\lambda = 447$ nm for 5 h) at 30 °C under N₂. The crude mixtures of 8 different reactions for each compound were combined and purified by extraction with CH₂Cl₂ (3 x 40 mL). Organic fractions were combined, dried over MgSO₄ and the solvent removed under pressure. The resulting residue was purified by silica gel column chromatography with Hexane/AcOEt (9:1) to obtain the desired pure alcohol **10**.

VII.3.3.3. Gas-evolution monitoring studies. Each experiment was conducted in a 20 mL volume-calibrated-vial capped with a septa equipped with stir-bars and containing the solvent mixture and reagents. Each reaction vial was connected to one of the ports of a differential pressure transducer sensor (Honeywell-ASCX15DN) and the other port to a reference reaction. Reference reactions, have all components of the reaction except the catalyst. The reaction and reference vials are kept under the same experimental conditions to compensate the noise due to temperature-pressure fluctuations. In order

to ensure a constant and stable irradiation, the LED sources were equipped with a water refrigeration system. This is composed for a refrigerated aluminium block by a Huber cryothermostat (refrigeration system, Minichiller -40°C-20°C). This block is shaken by an Orbital Shaker (IKA KS 260 Basic Package) which provides the agitation of the reaction vessels during the irradiation time. The aluminium block accommodates 16 vials (20 mL) capped with septum in which the reaction takes place. Each vial is submitted and located over a LED irradiation source (Royal-Blue Rebel LEDs ($\lambda = 447 \pm 20$ nm)). The reaction began when the LEDs were turned on. At this point, the hydrogen evolved from the reactions was monitored by recording the increase in pressure of the headspace (1 second interval). The pressure increment is the result of the difference in pressure between the reaction and reference vials. After the hydrogen evolution reached a plateau the amount of the gas formed was measured equilibrating the pressure between reaction and reference vials. The gasses at the headspace of reaction vials and references in each of the reactions were quantified by the analysis of an aliquot of gas at the headspace (0.2 mL) by gas chromatography.

VII.3.3.4. Poisoning studies with Hg^0 . Catalytic reactions performed in the presence of $Hg(0)$ were carried out in a 15 mL vial capped with septa. Each experiment was conducted following the general procedure employed in reaction conditions for the light-driven reduction of compounds **9**, with the additional monitorization of the H_2 produced from the reaction. $Hg(0)$ was added in large excess (>2000 eq. with respect to catalyst) before starting the reaction by a syringe through the septum. The solution was stirred for 5 minutes under a vigorous magnetic stirring and then the solution was irradiated with a LED at 447 nm.

VII.3.4. Synthesis of cobalt complexes

VII.3.4.1. Synthesis of $[\text{Co}(\text{OTf})(\text{DPA-Bpy})](\text{OTf})$ (2)Scheme VII. 10. Synthesis of $[\text{Co}(\text{OTf})(\text{DPA-Bpy})](\text{OTf})$.

(6-(2-Pyridyl)-2-pyridyl)methan-1-ol (Bpy-CH₂-OH). The synthesis of this compound has been performed following the procedure described in the literature with slightly modifications.^{485,486}

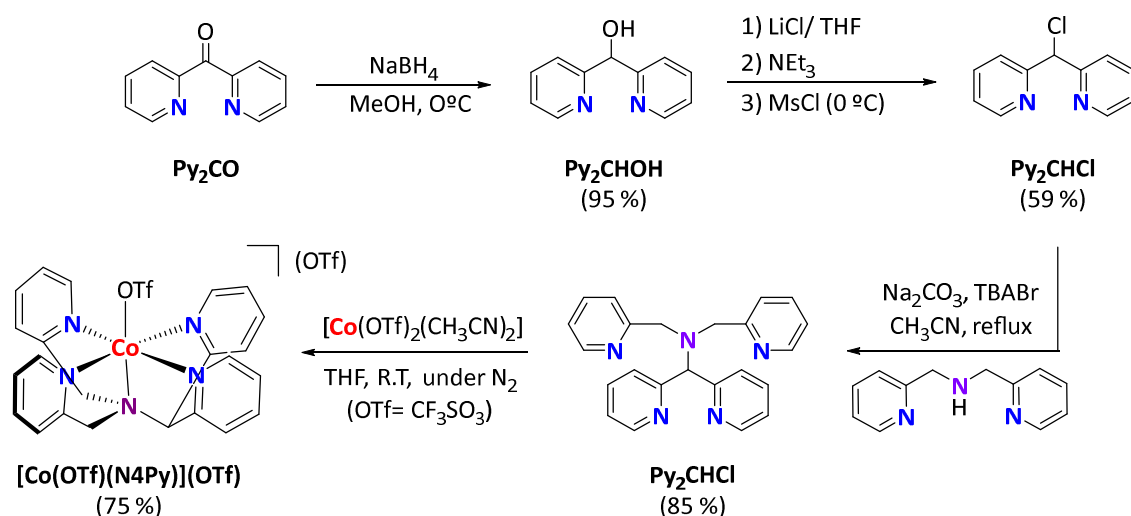
To an anhydrous solution of 6-bromo-2,2'-bipyridine (1 g, 4.3 mmol) in 10 mL of Et₂O:hexane:THF (6:2:2) was added dropwise *n*BuLi (2.75 mL, 4.4 mmol, 1.6 M in hexane), at -78 °C under argon atmosphere. After the addition was completed, the red mixture was stirred 2 hours at the same temperature. Then, a solution of DMF (0.67 mL, 9.7 mmol) in 5 mL of diethylether was added slowly and it was left stirred one hour at -78 °C and an additional 1 hour at room temperature. The reaction mixture was quenched by the addition of HCl 1M at 0 °C. NaOH (2M, 30 mL) was added to the resulting residue, and the mixture was extracted with CH₂Cl₂ (4x40 mL). The combined organic layers were dried over MgSO₄ and the solvent was removed under reduced pressure. After drying under vacuum the resulting red oil obtained, it was dissolved with MeOH (50 mL) and NaBH₄ (179 mg, 4.7 mmol) was added slowly directly as solid at 0 °C. After all the NaBH₄ was added, the ice bath was removed and the solution was left stirred overnight. The reaction was quenched by the addition of NH₄Cl (1M solution in water, 30 mL), and stirred for 10 min. After that, the solution was made alkaline with NaOH and extracted with CH₂Cl₂ (3 x 50 mL). The combined CH₂Cl₂ layers were dried over MgSO₄ and the solvent evaporated under reduced pressure. The resulting oil product was purified by silica column chromatography (Hexane:AcOEt 1:1) to afford the desired product (85 % yield) as a white solid. ¹H-NMR (CDCl₃, 400 MHz, 300 K) δ, ppm: 8.65 (ddd, 1H, *J* = 1.0, 1.8, 4.8 Hz), 8.39 (dt, 1H, *J* = 4.8, 7.8 Hz), 8.30 (dd, 1H, *J* = 0.7, 7.8 Hz), 7.80 (dt, 1 H, *J* = 1.8, 7.8 Hz), 7.79 (t, 1H, *J* = 7.8 Hz), 7.30 (ddd, 1 H, *J* = 1.0, 4.8, 7.8 Hz), 7.23 (dd, 1H, *J* = 0.7, 7.8 Hz), 4.81 (s, 2 H), 4.06 (br, 1 H).

N,N-Bis(2-pyridinylmethyl)-2,20-bipyridine-6-methanamine (DPA-Bpy). The synthesis of this compound has been performed following the procedure described in the literature with slightly modifications.⁴⁸⁷

5-(chloromethyl)-2,2'-bipyridine hydrochloride (101 mg, 0.363 mmol), di-(2-picolyl)amine (75 mg, 0.363 mmol) and anhydrous acetonitrile (40 mL) were mixed in a 100 mL flask. Na₂CO₃ (0.5 g) and tetrabutylammonium bromide (TBABr) (40 mg) were added directly as solids and the resulting mixture was heated at reflux temperature for 24 hours. After cooling to room temperature, the resulting orange solution was filtered and the filter cake was washed with CH₂Cl₂. The combined filtrates were evaporate under reduced pressure. NaOH (2 M, 30 mL) was added to the resulting residue, and the mixture was extracted with CH₂Cl₂ (4x40 mL). The combined organic layers were dried over MgSO₄ and the solvent was removed under reduced pressure. The resulting oil product was purified by silica column chromatography (Hexane:AcOEt 1:1) to afford the desired product (110 mg, 0.300 mmol, 83 % yield) as a yellow oil. ¹H-NMR (CDCl₃, 500 MHz, 300 K) δ, ppm: 3.88 (s, 4H, 2 x CH₂), 3.90 (s, 2H, CH₂), 7.07 (dt, *J* = 5.76 Hz, 2H), 7.21 (dt, *J* = 8.4 Hz, 1H), 7.46 (d, *J* = 8.0 Hz, 1H), 7.59 (d, *J* = 6.5 Hz, 2H), 7.60 (d, *J* = 6.5 Hz, 2H), 7.71 (dt, *J* = 7.5 Hz, 1H), 7.73 (dt, *J* = 7.5 Hz, 1H), 8.17 (d, *J* = 7.5 Hz, 1H), 8.36 (d, *J* = 8.0 Hz, 1H), 8.46 (d, *J* = 5Hz, 2H), 8.58 (d, *J* = 5.0Hz, 1H).

[Co(DPA-Bpy)(OTf)](OTf) (2). In a glovebox, a suspension of Co(OTf)₂(MeCN)₂ (131 mg, 0.300 mmol) in anhydrous THF (2 mL) was added dropwise to a vigorously stirred solution of DPA-Bpy ligand (110 mg, 0.300 mmol) in THF (2 mL). After few minutes, a brown solution appeared. After stirring for an additional 5 hours, Et₂O (3 mL) was added, and the resulting solid was filtered off and dried under vacuum. The solid was dissolved in CH₂Cl₂, filtered through Celite, and the slow diffusion of diethyl ether into the solution produced a pale brown solid (174 mg, 0.240 mmol, 80 %). ¹H-NMR (CD₃CN, 400 MHz, 260K) δ, ppm: 224.52, 208.60, 166.72, 121.28, 83.00, 80.43, 70.16. HR-ESI-MS (*m/z*): 575.0649 [M - OTf]⁺, 213.0561 [M-2·OTf]²⁺.

VII.3.4.2. Synthesis of [Co(OTf)(N4Py)](OTf) (3).



Scheme VII. 11. Synthesis of [Co(OTf)(N4Py)](OTf).

Di(2-pyridyl)methanol (Py₂CHOH). Compound di(2-pyridyl)methanol has been synthesized according to the procedure described in the literature with slightly modifications.⁴⁸⁸

To a mixture of di-2-pyridyl ketone (5.07 g, 27.5 mmol) in MeOH (50 mL) was slowly added 1.11 g of NaBH₄ (29.3 mmol) directly as solid at 0°C. After all the NaBH₄ was added, the ice bath was removed and stirring continued overnight. Removal of the solvent under reduced pressure was followed by addition of water (20 mL) and the mixture was acidified with 2 M HCl and stirred for 10 min. The clear solution was made alkaline with dilute ammonia and extracted with CH₂Cl₂ (3 x 50 mL). The combined CH₂Cl₂ layers were dried (MgSO₄) and the solvent evaporated to give di(2-pyridyl)methanol (4.85 g, 26 mmol, 95 %) as a yellow oil, which was used without further purification. ¹H-NMR (CDCl₃, 400 MHz, 300K) δ, ppm: 5.88 (s, 2H, CH and OH), 7.13 - 7.17 (m, 2H), 7.49 - 7.52 (m, 2H), 7.60 - 7.64 (m, 2H), 8.52 (m, 2H).

Di(2-pyridyl)methyl chloride (Py₂CHCl). A 100 mL flame dried round bottom flask was charged with 7.8 g of LiCl (185 mmol) absolutely dried and 2 g of di(2-pyridyl)methanol (10.7 mmol). Around 50 mL of THF was added under N₂ to obtain a pale yellow solution. Then, Et₃N (3.7 mL, 25.6 mmol) was added carefully and stirring always under N₂. After that, the mixture was cooled to 0 °C. Finally, MeSO₂Cl (2 mL, 26 mmol) was added dropwise at 0 °C. The stirring continued for 2 hours at the same temperature and then for 1 day at room temperature. The reaction was quenched by the addition of H₂O (15 mL) and neutralized using HCO₃⁻. The resulting solution was extracted 3 times with CH₂Cl₂. The combined organic layers were then washed with a saturated NaCl solution. The red organic phase was then dried over MgSO₄, filtered and the solvent removed under vacuum. The crude mixture was purified by column chromatography (AcOEt) to

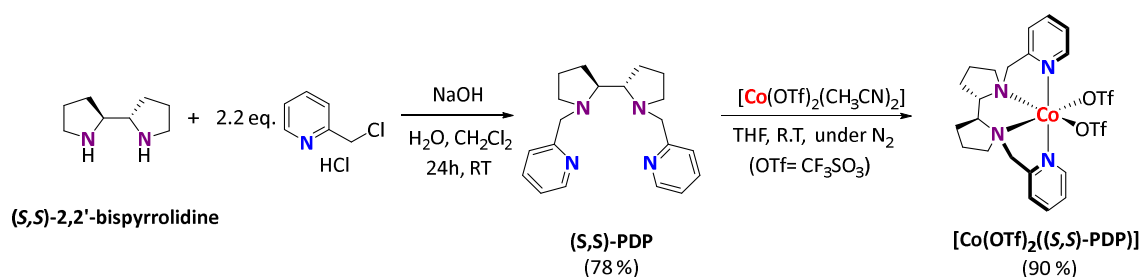
provide 1.3 g (6.35 mmol, 59 %) of the desired product. $^1\text{H-NMR}$ (CDCl_3 , 400 MHz, 300K) δ , ppm: 6.20 (s, 1H), 7.14 - 7.20 (m, 2H), 7.60 - 7.73 (m, 4H), 8.51 - 8.54 (m, 2H).

***N,N'*-bis(2-pyridylmethyl)-*N*-(bis-2-pyridylmethyl)amine (N4Py).** Compound N4Py has been synthesized according to the procedure described in the literature with slightly modifications.⁴⁸⁹

Di-(2-picolyl)amine (147 mg, 0.738 mmol), di(2-pyridyl)methyl chloride (152 mg, 0.738 mmol) and anhydrous acetonitrile (40 mL) were mixed in a 100 mL flask. Na_2CO_3 (1.5 g) and tetrabutylammonium bromide (TBABr) (80 mg) were added directly as solids and the resulting mixture was heated at reflux temperature for 4 days. After cooling to room temperature, the resulting orange solution was filtered and the filter cake was washed with CH_2Cl_2 . The combined filtrate were evaporate under reduced pressure. NaOH (2M, 30 mL) was added to the resulting residue, and the mixture was extracted with CH_2Cl_2 (4x40 mL). The combined organic layers were dried over MgSO_4 and the solvent was removed under reduced pressure. The resulting oil product was purified by silica column chromatography (CH_2Cl_2 :MeOH 30:1) to afford the desired product (85 % yield) as a yellow oil. $^1\text{H-NMR}$ (CDCl_3 , 400 MHz, 300K) δ , ppm: 3.69 (s, 4H, CH_2), 5.34 (s, 1H, CH), 7.13 (m, 4H, Py), 7.62 (m, 8H, Py), 8.48 (d, $J = 7$ Hz, 2H, Py), 8.57 (d, $J = 7$ Hz, 2H, Py).

[Co(OTf)(N4Py)](OTf) (3). In a glovebox, a suspension of $\text{Co}(\text{OTf})_2(\text{MeCN})_2$ (191 mg, 0.434 mmol) in anhydrous THF (2 mL) was added dropwise to a vigorously stirred solution of N4Py ligand (160 mg, 0.434 mmol) in THF (2 mL). After few minutes, a brown solution appeared. After stirring for an additional 5 hours, Et_2O (3 mL) was added, and the resulting solid was filtered off and dried under vacuum. This solid was dissolved in CH_2Cl_2 , filtered through Celite, and the slow diffusion of diethyl ether into the solution produced a pale brown solid (0.325 mmol, 75 %). $^1\text{H-NMR}$ (CD_3CN , 400 MHz, 400K) δ , ppm: 171.33, 131.77, 86.12, 69.18, 67.92, 57.95, 48.33, 15.47, 9.62, -23.86. Anal. Calcd for $\text{C}_{25}\text{H}_{21}\text{CoF}_6\text{N}_5\text{O}_6\text{S}_2$: C, 41.44; N, 9.67; H, 2.92 %. Found: C, 41.52; N, 9.74; H, 2.99 %. HR-ESI-MS (m/z): 575.0645 [$\text{M} - \text{OTf}$] $^+$, 213.0560 [$\text{M} - 2 \cdot \text{OTf}$] $^{2+}$.

VII.3.4.3. Synthesis of [Co(OTf) $_2$ ((*S,S*)-PDP)] (5)



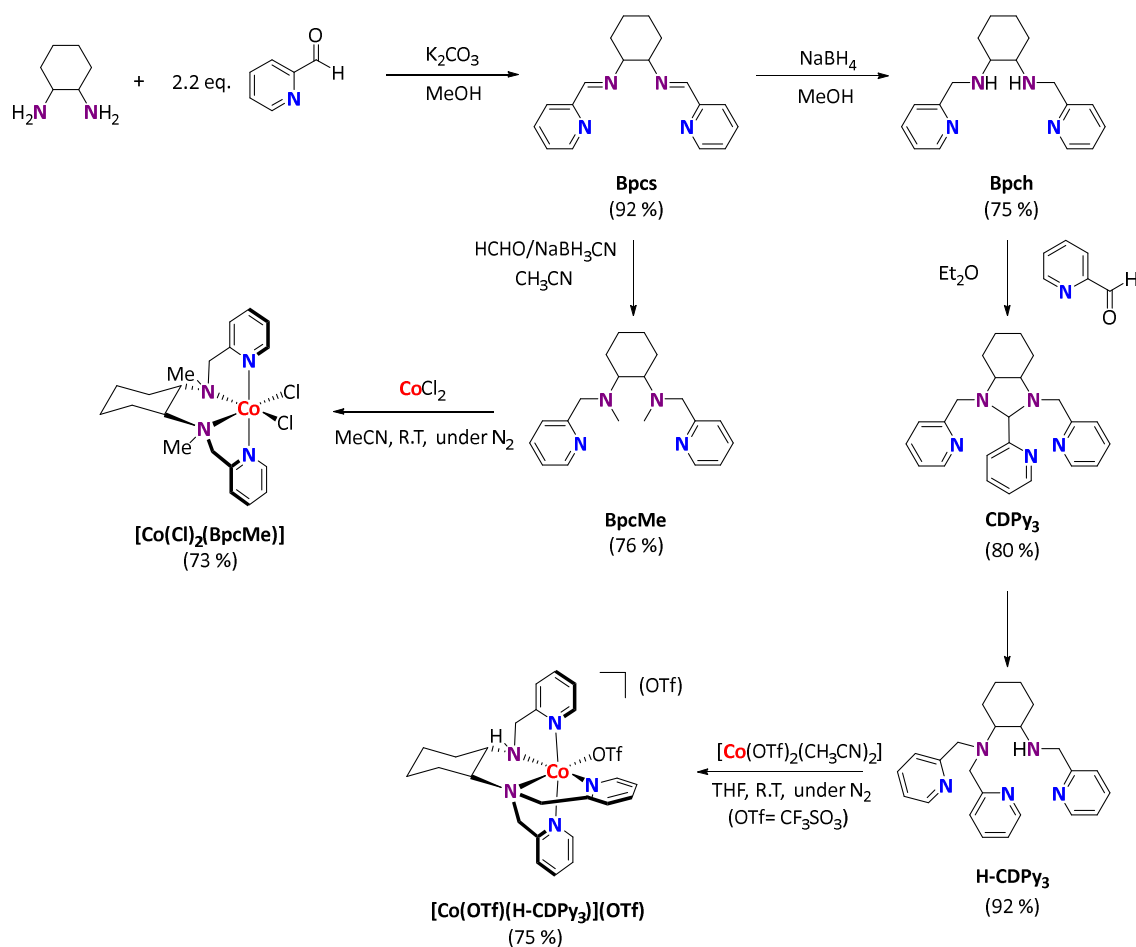
Scheme VII. 12. Synthesis of [Co(OTf) $_2$ ((*S,S*)-PDP)].

Compound (*S,S*)-PDP has been synthesized following the procedure described in the literature.⁴⁹⁰

(-)-2-(((S)-2-((S)-1-(pyridin-2-ylmethyl)pyrrolidin-2-yl)pyrrolidin-1-yl)methyl)pyridine ((S,S)-PDP). A 200 mL round bottom flask was charged with a stir bar, (S,S)-2,2'-bispyrrolidine (200 mg, 1.41 mmol, 1.0 eq.), H₂O (5 mL), and CH₂Cl₂ (5 mL).

Solid NaOH pellets (4.5 eq., 0.253 g, 6.33 mmol) were added, followed by 2-picoyl chloride·HCl (2.2 eq., 0.519 g, 3.10 mmol). After 24 h stirring at room temperature, the reaction mixture was diluted with 1M NaOH. The aqueous layer was extracted with CH₂Cl₂ (3 x 50 mL), and the organic extracts were combined, dried over MgSO₄, and concentrated in vacuo. The crude ligand was purified by silica gel chromatography using a mixture of CH₂Cl₂: MeOH: NH₃ (100:5:2) to obtain 0.355 g of the desired product (1.10 mmol, 78 % yield) as yellow oil. ¹H-NMR (CDCl₃, 400 MHz, 300 K) δ, ppm: 8.49 (dd, *J* = 0.8, 4.8 Hz, 2H), 7.60 (dt, *J* = 2.0, 7.8 Hz, 2H), 7.39 (d, *J* = 7.6 Hz, 2H), 7.11 (dd, *J* = 5.2, 6.0 Hz, 2H), 4.19 (d, *J* = 14.0 Hz, 2H), 3.49 (d, *J* = 14.4 Hz, 2H), 2.99 (p, *J* = 4.4 Hz, 2H), 2.79 (m, 2H), 2.22 (appq, *J* = 8.4 Hz, 2H), 1.77-1.64 (m, 8H).

[Co(OTf)₂((S,S)-PDP)] (5). In a glovebox, a suspension of Co(OTf)₂(MeCN)₂ (0.483 g, 1.10 mmol) in anhydrous THF (2 mL) was added dropwise to a vigorously stirred solution of (S,S)-PDP ligand (0.355 g, 1.10 mmol) in THF (2 mL). After few minutes, a pink-red solution was obtained. After stirring for an additional 2 hours, Et₂O was added and the pink solid was filtered off and dried under vacuum. This solid was dissolved in CH₂Cl₂, filtered through Celite, and the slow diffusion of diethyl ether into the solution produced a pink solid (0.669 g, 0.984mmol, 90 %). ¹H-NMR (CD₃CN, 500 MHz, 260K) δ, ppm: 283.60, 107.68, 102.66, 73.13, 52.52, 34.40, 23.80, 20.16, -6.18, -21.19, -98.76. HR-ESI-MS (*m/z*): [M - OTf]⁺, [M-2·OTf]²⁺.

VII.3.4.4. Synthesis of $[\text{Co}(\text{Cl})_2(\text{BpcMe})]$ (7) and $[\text{Co}(\text{OTf})(\text{H-CDPy}_3)](\text{OTf})$ (4).Scheme VII. 13. Synthesis of $[\text{Co}(\text{BpcMe})\text{Cl}_2]$ and $[\text{Co}(\text{OTf})(\text{H-CDPy}_3)](\text{OTf})$.Synthesis of $[\text{Co}(\text{Cl})_2(\text{BpcMe})]$ (7)

The ligand BpcMe has been synthesized according to the literature procedures.⁴⁹¹

(±)-(N,N'-bis(pyridin-2-ylmethylene)cyclohexane-1,2-diamine) (Bpcs). 2-Pyridinecarboxaldehyde (2.44 g, 22.75 mmol) in MeOH (20 mL) was added to a solution of (±)-*trans*-diaminocyclohexane (1.30 g, 11.37 mmol) in MeOH (50 mL) and at 0 °C. Then, K_2CO_3 (3.14 g) was added directly as solid. The reaction mixture was stirred overnight, allowing the bath and reaction mixture to warm to room temperature over this time. The solvent was removed under reduced pressure and the residue was extracted with CH_2Cl_2 (3 x 30 mL). The combined organic layers were dried over MgSO_4 , and the solvent was removed under reduced pressure to give the desired product in 92 % yield (3.06 g, 10.46 mmol). $^1\text{H-NMR}$ (CDCl_3 , 300 MHz, 300K) δ , ppm: 8.55 (2H, ddd, $J = 5.0$ Hz, 1.7 Hz, 0.9 Hz), 8.32 (2H, s), 7.89 (2H, dt, $J = 7.9$ Hz, 1.0 Hz), 7.65 (2H, dt, $J = 7.6$ Hz, 1.7 Hz), 7.23 (2H, ddd, $J = 7.5$ Hz, 4.8 Hz, 1.3 Hz), 3.50-3.59 (2H, m), 1.80-1.92 (6H, m), 1.47-1.57 (2H, m).

(±)-(N,N'-bis(2-pyridinylmethyl)cyclohexane-1,2-diamine (Bpch). To a stirred solution of Bpcs (3.06 g, 10.46 mmol) in MeOH (70 mL) was slowly added NaBH₄ (1.74 g, 0.044 mmol). After stirring for 4 hours, the solvent was removed under reduced pressure. To the resulting residue, distilled water (30 mL) and CH₂Cl₂ (30 mL) were added, and it was extracted (3 x 30 mL). The combined organic layers were dried over MgSO₄, and the solvent was removed under reduced pressure to give the desired product in 75 % yield (2.306 g, 7.84 mmol). ¹H-NMR (CDCl₃, 300 MHz, 300K) δ, ppm: 8.52 (dd, 2H), 8.12 (td, 2H), 7.39 (d, 2H), 7.10-7.37 (m, 2H), 3.94 (dd, 4H), 2.27-2.35 (m, 2H), 2.16-2.10 (m, 2H), 1.06-1.86 (m, 8H).

(±)-N,N'-dimethyl-(N,N'-bis(2-pyridinylmethyl)cyclohexane-1,2-diamine (BpcMe). To a solution of Bpch (0.625 g, 2.11 mmol) in CH₃CN (30 mL) was added formaldehyde (1.78 mL, 37 % w/w). The resulting solution was stirred for 30 minutes. NaBH₃CN (0.427 g, 6.78 mmol) dissolved in the minimum amount of CH₃CN was added dropwise. The pH was adjusted to 7 using a solution of acetic acid in CH₃CN. The resulting solution was left stirred for 4 hours. After that, the solvent was removed under reduced pressure and the resulting residue was dissolved with NaOH 2M (15 mL) and CH₂Cl₂ (30 mL). The organic phase was separated and the aqueous phase was extracted with CH₂Cl₂ (2 x 30 mL). The combined organic layers were dried over MgSO₄, and the solvent was removed under reduced pressure. The resulting oil product was purified by silica column chromatography (CH₂Cl₂:MeOH 1:1) to afford the desired product (0.519 g, 1.602 mmol, 76 % yield) as yellow oil. ¹H-NMR (CDCl₃, 400 MHz, 300K) δ, ppm: 8.52 (d, 2H), 7.58-7.60 (m, 4H), 7.09-7.16 (m, 2H), 3.88 (dd, 4H), 2.70-2.66 (m, 2H), 2.30 (s, 6H), 1.76-2.05 (m, 4H), 1.17-1.33 (m, 4H).

[Co(Cl)₂(BpcMe)] (7).⁴⁹² In a glovebox, a solution of CoCl₂ (115 mg, 0.886 mmol) in anhydrous CH₃CN (2 mL) was added dropwise to a vigorously stirred solution of BpcMe ligand (287 mg, 0.886 mmol) in CH₃CN (2 mL). After few minutes, a purple solid precipitated. After stirring for an additional 2 hours, this solid was filtered off, washed with CH₃CN (3x 2 mL) and dried under vacuum. This solid was dissolved in CH₂Cl₂, filtered through Celite, and the slow diffusion of diethyl ether into the solution produced a purple solid (293 mg, 0.645 mmol, 73 %). ¹H-NMR (CD₃CN, 500 MHz, 260K) δ, ppm: 83.55, 74.16, 68.23, 51.15, 45.68, 43.85, 39.94, 22.63, 20.21, 18.74, 15.74, 39.94, 22.63, 20.21, 18.74, 15.74, 12.40, 8.22, -9.12, -33.38, -69.69. HR-ESI-MS (m/z): 418.3121 [M - Cl]⁺.

Synthesis of [Co(OTf)(H-CDPy₃)](OTf)

Compound H-CDPy₃ has been synthesized following the procedure described in the literature.^{493,494}

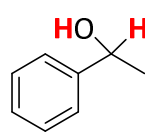
(2-(pyridin-2-yl)-1,3-bis(pyridin-2-ylmethyl)octahydro-1H-benzo[d]imidazole (CDPy₃). (±)-(N,N'-bis(2-pyridinylmethyl)cyclohexane-1,2-diamine (Bpch) (2.36 g, 7.96 mmol) was dissolved in dry ether (65 mL), under N₂ atmosphere. Picolinaldehyde (0.861, 7.96

mmol) was added dropwise to the mixture. The resultant mixture was maintained overnight at room temperature resulting in the formation of a small amount of pale yellow precipitate. The reaction mixture was filtered and the filtrate was concentrated in vacuo to give the resultant aminal as a yellow oil. The crude product was purified by alumina chromatography using CH₂Cl₂:MeOH (99:1) to obtain a pure light yellow oil (2.45 g, 6.37 mmol, 80 % yield). ¹H-NMR (CDCl₃, 400 MHz, 300 K) δ, ppm: 8.28 (m, 3H), 7.45 (m, 2H), 7.31 (m, 3H), 7.13 (d, J = 7.94 Hz, 1H), 6.93 (m, 3H), 4.84 (s, 1H), 3.96 (d, J = 14.3 Hz, 1H), 3.86 (d, J = 14.3 Hz, 1H), 3.61 (d, J = 15.6 Hz, 1H), 3.54 (d, J = 15.6 Hz, 1H), 2.90 (m, 1H), 2.56 (m, 1H), 1.62 (m, 4H), 1.16 (m, 4H).

***N,N',N''*-tris(pyridine-2-ylmethyl)cyclohexane-1,2-diamine (H-CDPy₃)**. The aminal intermediate CDPy₃ (0.247 g, 0.639 mmol) was dissolved in dry MeOH (11 mL) and placed under N₂ atmosphere. To this solution, a suspension of NaBH₃CN (48.2 mg in 2 mL MeOH) was added dropwise, followed by trifluoroacetic acid (0.1 mL). The reaction mixture was maintained overnight at room temperature and the progress of the reaction was monitored by TLC. Once the reaction completed, as judged by the TLC analysis, 20 mL of NaOH 2M was added and the mixture was stirred for 6 hours at room temperature. The solution was extracted with CH₂Cl₂ (3 x 30 mL), and the combined organic layers were dried over MgSO₄, filtered and concentrated to give the final H-CDPy₃ ligand (0.229 g, 0.591 mmol, 92 % yield) as light yellow oil. The product was found to be pure by ¹H-NMR, and it was used to the next step without further purification. ¹H-NMR (CDCl₃, 400 MHz, 300K) δ, ppm: 8.41 (bm, J = 4.9 Hz, 3H), 7.59 (m, 3H), 7.54 (m, 3H), 7.27 (s, 1H), 7.06 (m, 3H), 3.85 (m, 6H), 2.49 (bm, 2H), 2.09 (bm, 2H), 1.72 (bm, 3H), 1.21 (bm, 3H).

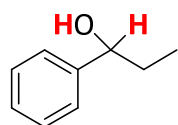
[Co(OTf)(H-CDPy₃)](OTf) (4). In a glovebox, a suspension of Co(OTf)₂(MeCN)₂ (0.259 g, 0.590 mmol) in anhydrous THF (2 mL) was added dropwise to a vigorously stirred solution of H-CDPy₃ ligand (0.229 g, 0.590 mmol) in THF (2 mL). After few minutes, a brown solid appeared. After stirring for an additional 2 hours, Et₂O was added and the brown solid was filtered off and dried under vacuum. This solid was dissolved in CH₂Cl₂, filtered through Celite, and the slow diffusion of diethyl ether into the solution produced a brown solid (0.329 g, 0.442 mmol, 75 %). ¹H-NMR (CD₃CN, 500 MHz, 260K) δ, ppm: 99.84, 88.77, 83.14, 78.36, 69.73, 66.33, 59.08, 43.04, 40.23, 34.19, 33.29, 29.70, 26.35, 24.85, 16.65, 12.94, 11.45, -1.63. HR-ESI-MS (m/z): 595.1266 [M - OTf]⁺, 223.0895 [M - 2·OTf]²⁺.

VII.3.5. Characterization of the Isolated Alcohols

**10a**

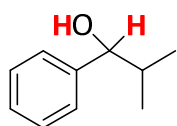
1-Phenylethanol (10a). $^1\text{H-NMR}$ (CDCl_3 , 300 MHz, 300 K) δ , ppm: 7.38-7.28 (m, 5H, H_{arom}), 4.90 (q, 1H, CH, $J = 6.6$ Hz), 1.84 (br, 1H, OH). 1.50 (d, 3H, CH_3 , $J = 6.6$ Hz).

$^{13}\text{C}\{^1\text{H}\}$ -NMR (CDCl_3 , 75 MHz, 300 K) δ , ppm: 145.9, 128.6, 127.5, 125.5, 70.5, 25.3.

**10b**

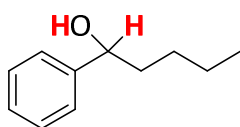
1-Phenyl-1-propanol (10b). $^1\text{H-NMR}$ (CDCl_3 , 300 MHz, 300 K) δ , ppm: 7.35-7.28 (m, 5H, H_{arom}), 4.60 (t, 1H, CH, $J = 6.6$ Hz), 1.80 (m, 2H, $\text{CH}_2\text{-CH}_3$). 0.92 (t, 3H, CH_3 , $J = 7.2$ Hz).

$^{13}\text{C}\{^1\text{H}\}$ -NMR (CDCl_3 , 75 MHz, 300 K) δ , ppm: 144.9, 128.7, 127.8, 126.3, 76.3, 32.2, 10.5.

**10c**

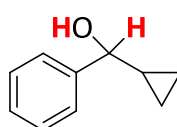
2-Methyl-1-phenylpropan-1-ol (10c). $^1\text{H-NMR}$ (CDCl_3 , 300 MHz, 300 K) δ , ppm: 7.35-7.26 (m, 5H, H_{arom}), 4.36 (d, 1H, CH-CH-(CH_3) $_2$, $J = 6.6$ Hz), 1.95 (m, 1H, CH-CH-(CH_3) $_2$). 1.85 (br, 1H, OH), 1.00 (d, 3H, CH-CH-(CH_3) $_2$, $J = 6.9$ Hz), 0.80 (d, 3H, CH-CH-(CH_3) $_2$, $J = 6.9$ Hz).

$^{13}\text{C}\{^1\text{H}\}$ -NMR (CDCl_3 , 75 MHz, 300 K) δ , ppm: 143.9, 128.4, 127.6, 126.8, 80.3, 35.5, 19.2, 18.5.

**10d**

1-Phenyl-pentanol (10d). $^1\text{H-NMR}$ (CDCl_3 , 300 MHz, 300 K) δ , ppm: 7.36-7.26 (m, 5H, H_{arom}), 4.66 (t, 1H, CH-(CH_2) $_3$ - CH_3 , $J = 6.0$ Hz), 1.89 (br, 1H, OH). 1.79-1.71 (m, 2H, CH- CH_2 -(CH_2) $_2$ - CH_3), 1.39-1.28 (m, 4H, CH- CH_2 -(CH_2) $_2$ - CH_3), 0.89 (t, 3H, CH- CH_2 -(CH_2) $_2$ - CH_3 , $J = 6.9$ Hz).

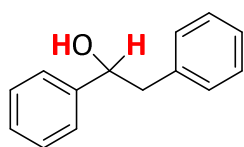
$^{13}\text{C}\{^1\text{H}\}$ -NMR (CDCl_3 , 75 MHz, 300 K) δ , ppm: 145.2, 128.6, 127.7, 126.2, 74.9, 39.0, 28.2, 22.9, 14.3.

**10e**

Cyclopropyl phenylmethanol (10e). $^1\text{H-NMR}$ (CDCl_3 , 400 MHz, 300 K) δ , ppm: 7.42-7.40 (m, 2H, H_{arom}), 7.36-7.32 (m, 2H, H_{arom}), 7.29-7.24 (m, 1H, H_{arom}), 3.99 (d, 1H, CH-CH-(CH_2) $_2$, $J = 8.28$ MHz), 2.12 (br, 1H, OH), 1.20 (m, 1H, CH-CH-(CH_2) $_2$), 0.63-0.59 (m, 1H, CH-CH-(CH_2) $_2$), 0.57-0.50 (m, 1H, CH-CH-(CH_2) $_2$), 0.49-0.43 (m, 1H, CH-CH-(CH_2) $_2$), 0.39-0.34

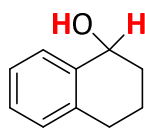
(m, 1H, CH-CH-(CH_2) $_2$).

$^{13}\text{C}\{^1\text{H}\}$ -NMR (CDCl_3 , 101 MHz, 300 K) δ , ppm: 144.0, 128.5, 127.6, 126.1, 78.6, 19.3, 3.7, 2.9.

**10f**

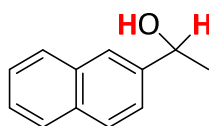
1,2-diphenylethan-1-ol (10f). $^1\text{H-NMR}$ (CDCl_3 , 300 MHz, 300 K) δ , ppm: 7.39-7.22 (m, 10H, H_{arom}), 3.92 (dd, 1H, CH, $J = 8.13$ MHz, $J = 5.16$ MHz), 3.05 (m, 2H, CH_2), 1.99 (br, 1H, OH).

$^{13}\text{C}\{^1\text{H}\}$ -NMR (CDCl_3 , 75 MHz, 300 K) δ , ppm: 143.8, 138.1, 129.6, 128.5, 128.4, 127.6, 126.6, 125.9, 75.4, 46.1.

**10g**

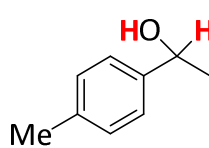
1,2,3,4-tetrahydro-1-naphthol (10g). $^1\text{H-NMR}$ (CDCl_3 , 300 MHz, 300 K) δ , ppm: 7.45-7.42 (m, 1H, H_{arom}), 7.22-7.19 (m, 2H, H_{arom}), 7.12-7.09 (m, 1H, H_{arom}), 4.78 (t, 1H, CH, $J = 5.07$ MHz), 2.89-2.68 (m, 2H, CH_2), 2.05-1.88 (m, 2H, CH_2), 1.84-1.73 (m, 2H, CH_2).

$^{13}\text{C}\{^1\text{H}\}$ -NMR (CDCl_3 , 75 MHz, 300 K) δ , ppm: 139.1, 137.4, 129.2, 128.9, 127.8, 126.4, 68.3, 32.5, 29.5, 19.1.

**10h**

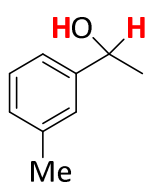
1-(2-naphthyl)ethanol (10h). $^1\text{H-NMR}$ (CDCl_3 , 300 MHz, 300 K) δ , ppm: 7.86-7.82 (m, 4H, H_{arom}), 7.53-7.44 (m, 4H, H_{arom}), 5.08 (q, 1H, CH, $J = 6.0$ MHz), 1.58 (d, 3H, CH_3 , $J = 6.0$ MHz).

$^{13}\text{C}\{^1\text{H}\}$ -NMR (CDCl_3 , 75 MHz, 300 K) δ , ppm: 134.5, 138.8, 133.6, 133.2, 128.6, 128.3, 128.0, 126.5, 126.1, 124.1, 124.0, 70.8, 25.5.

**10i**

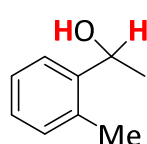
1-(4-methylphenyl)ethanol (10i). $^1\text{H-NMR}$ (CDCl_3 , 300 MHz, 300 K) δ , ppm: 7.26 (m, 2H, H_{arom}), 7.16 (m, 2H, H_{arom}), 4.87 (q, 1H, CH, $J = 6.4$ MHz), 2.34 (s, 3H, CH_3), 1.82 (br, 1H, OH), 1.48 (d, 3H, CH_3 , $J = 6.4$ MHz).

$^{13}\text{C}\{^1\text{H}\}$ -NMR (CDCl_3 , 75 MHz, 300 K) δ , ppm: 143.1, 137.3, 129.4, 125.6, 70.4, 25.3, 21.3.

**10j**

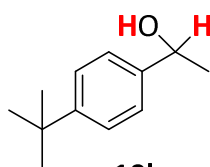
1-(3-methylphenyl)ethanol (10j). $^1\text{H-NMR}$ (CDCl_3 , 300 MHz, 300 K) δ , ppm: 7.27-7.07 (m, 4H, H_{arom}), 4.86 (q, 1H, CH, $J = 6.4$ MHz), 2.36 (s, 3H, CH_3), 1.85 (br, 1H, OH), 1.48 (d, 3H, CH_3 , $J = 6.4$ MHz).

$^{13}\text{C}\{^1\text{H}\}$ -NMR (CDCl_3 , 75 MHz, 300 K) δ , ppm: 145.8, 138.2, 128.4, 128.2, 126.1, 122.5, 70.4, 25.1, 21.5.

**10k**

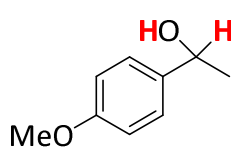
1-(2-methylphenyl)ethanol (10k). $^1\text{H-NMR}$ (CDCl_3 , 300 MHz, 300 K) δ , ppm: 7.52 (m, 1H, H_{arom}), 7.25-7.12 (m, 3H, H_{arom}), 5.13 (q, 1H, CH, $J = 6.4$ MHz), 2.35 (s, 3H, CH_3), 1.74 (br, 1H, OH), 1.46 (d, 3H, CH_3 , $J = 6.4$ MHz).

$^{13}\text{C}\{^1\text{H}\}$ -NMR (CDCl_3 , 75 MHz, 300 K) δ , ppm: 143.8, 134.2, 130.4, 127.2, 126.4, 124.5, 66.8, 23.9, 18.9.

**10l**

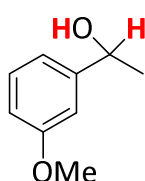
1-(4-(tert-butyl)phenyl)ethanol (10l). $^1\text{H-NMR}$ (CDCl_3 , 400 MHz, 300 K) δ , ppm: 7.43-7.33 (m, 4H, H_{arom}), 5.89 (q, 1H, CH, $J = 6.4$ MHz), 2.01 (br, 1H, OH), 1.52 (d, 3H, CH_3 , $J = 6.4$ MHz), 1.36 (s, 9H, $(\text{CH}_3)_3$).

$^{13}\text{C}\{^1\text{H}\}$ -NMR (CDCl_3 , 101 MHz, 300 K) δ , ppm: 150.4, 142.8, 125.4, 125.2, 70.2, 34.5, 31.4, 24.9.

**10m**

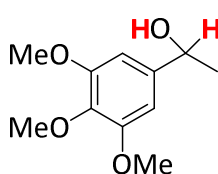
1-(4-methoxyphenyl)ethanol (10m). $^1\text{H-NMR}$ (CDCl_3 , 300 MHz, 300 K) δ , ppm: 7.31 (m, 2H, H_{arom}), 6.88 (m, 2H, H_{arom}), 4.86 (q, 1H, CH, $J = 6.6$ MHz), 3.81 (s, 3H, OCH_3), 2.74 (br, 1H, OH), 1.48 (d, 3H, CH_3 , $J = 6.4$ MHz).

$^{13}\text{C}\{^1\text{H}\}$ -NMR (CDCl_3 , 75 MHz, 300 K) δ , ppm: 158.9, 138.0, 126.7, 113.8, 69.9, 55.3, 25.0.

**10n**

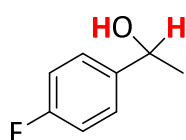
1-(3-methoxyphenyl)ethanol (10n). $^1\text{H-NMR}$ (CDCl_3 , 300 MHz, 300 K) δ , ppm: 7.28 (m, 1H, H_{arom}), 6.97 (m, 2H, H_{arom}), 6.82 (m, 1H, H_{arom}), 4.89 (q, 1H, CH, $J = 6.4$ MHz), 3.84 (s, 3H, OCH_3), 1.92 (br, 1H, OH), 1.51 (d, 3H, CH_3 , $J = 6.4$ MHz).

$^{13}\text{C}\{^1\text{H}\}$ -NMR (CDCl_3 , 75 MHz, 300 K) δ , ppm: 159.7, 147.6, 129.5, 117.7, 112.9, 110.9, 70.3, 55.2, 25.2.

**10o**

1-(3,4,5-trimethoxyphenyl)ethanol (10o). $^1\text{H-NMR}$ (CDCl_3 , 400 MHz, 300 K) δ , ppm: 6.58 (s, 2H, H_{arom}), 4.81 (q, 1H, CH, $J = 6.4$ MHz), 3.85 (s, 6H, 3- OCH_3), 3.82 (s, 3H, 4- OCH_3), 2.31 (br, 1H, OH), 1.47 (d, 3H, CH_3 , $J = 6.4$ MHz).

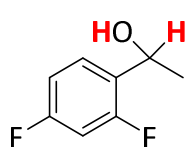
$^{13}\text{C}\{^1\text{H}\}$ -NMR (CDCl_3 , 101 MHz, 300 K) δ , ppm: 153.2, 141.8, 137.0, 102.2, 70.4, 60.8, 56.0, 25.2.

**10q**

1-(4-fluorophenyl)ethanol (10q). $^1\text{H-NMR}$ (CDCl_3 , 400 MHz, 300 K) δ , ppm: 7.35-7.31 (m, 2H, H_{arom}), 7.05-7.00 (m, 2H, H_{arom}), 4.86 (q, 1H, CH, $J = 6.4$ MHz), 2.44 (br, 1H, OH), 1.46 (d, 3H, CH_3 , $J = 6.4$ MHz).

$^{19}\text{F}\{^1\text{H}\}$ -NMR (CDCl_3 , 376 MHz, 300 K) δ , ppm: -115.5 (s, 1F, 4-F),

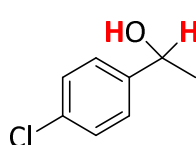
$^{13}\text{C}\{^1\text{H}\}$ -NMR (CDCl_3 , 101 MHz, 300 K) δ , ppm: 162.1 (d, $J_{\text{C,F}} = 245.9$ MHz), 141.5 (d, $J_{\text{C,F}} = 3.1$ MHz), 127.03 (d, $J_{\text{C,F}} = 8.1$ MHz), 115.18 (d, $J_{\text{C,F}} = 21.4$ MHz), 69.7, 25.2.

**10r**

1-(2,4-difluorophenyl)ethan-1-ol (10o). $^1\text{H-NMR}$ (CDCl_3 , 400 MHz, 300 K) δ , ppm: 7.49-7.43 (m, 1H, H_{arom}), 6.91-6.86 (m, 1H, H_{arom}), 6.80-6.75 (m, 1H, H_{arom}), 5.16 (q, 1H, CH, $J = 6.4$ MHz), 2.33 (br, 1H, OH), 1.49 (d, 3H, CH_3 , $J = 6.4$ MHz).

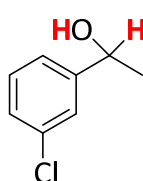
$^{19}\text{F}\{^1\text{H}\}$ -NMR (CDCl_3 , 376 MHz, 300 K) δ , ppm: -112.2 (d, 1F, 4-F, $J_{\text{F,F}} = 7.1$ MHz), -116.2 (d, 1F, 2-F, $J_{\text{F,F}} = 7.1$ MHz).

$^{13}\text{C}\{^1\text{H}\}$ -NMR (CDCl_3 , 101 MHz, 300 K) δ , ppm: 162.1 (dd, $J_{\text{C,F}} = 248.6$ MHz, $J_{\text{C,F}'} = 12.2$ MHz), 159.5 (dd, $J_{\text{C,F}} = 248.6$ MHz, $J_{\text{C,F}'} = 12.2$ MHz), 128.6 (dd, $J_{\text{C,F}} = 13.7$ MHz, $J_{\text{C,F}'} = 3.7$ MHz), 127.5 (dd, $J_{\text{C,F}} = 9.6$ MHz, $J_{\text{C,F}'} = 6.2$ MHz), 111.2 (dd, $J_{\text{C,F}} = 21.0$ MHz, $J_{\text{C,F}'} = 3.7$ MHz), 103.6 (t, $J_{\text{C,F}} = 25.7$ MHz), 63.9 (d, $J_{\text{C,F}} = 2.6$ MHz), 24.1.

**10s**

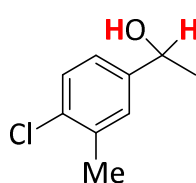
1-(4-chlorophenyl)ethanol (10s). $^1\text{H-NMR}$ (CDCl_3 , 400 MHz, 300 K) δ , ppm: 7.37-7.28 (m, 4H, H_{arom}), 4.85 (q, 1H, CH, $J = 6.4$ MHz), 2.36 (br, 1H, OH), 1.46 (d, 3H, CH_3 , $J = 6.4$ MHz).

$^{13}\text{C}\{^1\text{H}\}$ -NMR (CDCl_3 , 101 MHz, 300 K) δ , ppm: 144.3, 133.0, 128.6, 126.8, 69.7, 25.2.

**10t**

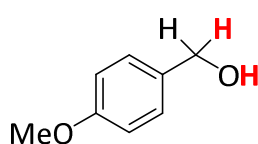
1-(3-chlorophenyl)ethanol (10t). $^1\text{H-NMR}$ (CDCl_3 , 500 MHz, 300 K) δ , ppm: 7.39-7.18 (m, 4H, H_{arom}), 4.89 (q, 1H, CH, $J = 6.4$ MHz), 2.66 (br, 1H, OH), 1.50 (d, 3H, CH_3 , $J = 6.4$ MHz).

$^{13}\text{C}\{^1\text{H}\}$ -NMR (CDCl_3 , 126 MHz, 300 K) δ , ppm: 147.8, 134.3, 129.8, 127.5, 125.6, 123.5, 69.8, 25.2.

**10u**

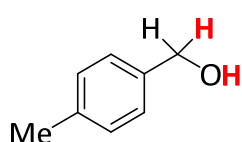
1-(3-chloro-4-methylphenyl)ethanol (10u). $^1\text{H-NMR}$ (CDCl_3 , 500 MHz, 300 K) δ , ppm: 7.32-7.13 (m, 3H, H_{arom}), 4.86 (q, 1H, CH, $J = 6.4$ MHz), 2.40 (s, 3H, CH_3), 1.95 (br, 1H, OH), 1.49 (d, 3H, CH_3 , $J = 6.4$ MHz).

$^{13}\text{C}\{^1\text{H}\}$ -NMR (CDCl_3 , 126 MHz, 300 K) δ , ppm: 144.3, 136.1, 133.2, 129.1, 128.0, 124.1, 69.8, 25.2, 20.1.

**10v**

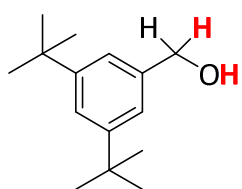
1-(4-methoxyphenyl)methanol (10v). $^1\text{H-NMR}$ (CDCl_3 , 300 MHz, 300 K) δ , ppm: 7.30 (m, 2H, H_{arom}), 6.90 (m, 2H, H_{arom}), 4.62 (d, 2H, CH_2 , $J = 4.9$ MHz), 3.81 (s, 3H, OCH_3), 1.59 (br, 1H, OH).

$^{13}\text{C}\{^1\text{H}\}$ -NMR (CDCl_3 , 75 MHz, 300 K) δ , ppm: 159.2, 133.2, 128.7, 113.9, 65.0, 55.4.

**10w**

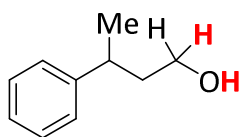
1-(4-methylphenyl)methanol (10w). $^1\text{H-NMR}$ (CDCl_3 , 300 MHz, 300 K) δ , ppm: 7.28-7.16 (m, 2H, H_{arom}), 4.65 (s, 2H, CH_2), 2.35 (s, 3H, CH_3), 1.62 (br, 1H, OH).

$^{13}\text{C}\{^1\text{H}\}$ -NMR (CDCl_3 , 75 MHz, 300 K) δ , ppm: 138.2, 137.6, 129.5, 127.4, 65.4, 21.4.

**10x**

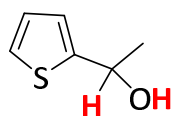
(3,5-di-tert-butylphenyl)methanol (10x). $^1\text{H-NMR}$ (CDCl_3 , 400 MHz, 300 K) δ , ppm: 7.41 (s, 1H, H_{arom}), 7.25 (s, 2H, H_{arom}), 4.71 (s, 2H, CH_2), 1.76 (br, 1H, OH), 1.37 (s, 9H, $(\text{CH}_3)_3$).

$^{13}\text{C}\{^1\text{H}\}$ -NMR (CDCl_3 , 101 MHz, 300 K) δ , ppm: 151.1, 140.0, 121.8, 121.4, 66.2, 31.5.

**10y**

3-phenylbutan-1-ol (10y). $^1\text{H-NMR}$ (CDCl_3 , 400 MHz, 300 K) δ , ppm: 7.33-7.14 (m, 5H, H_{arom}), 3.55-3.48 (m, 2H, CH_2), 2.88-2.83 (m, 1H, CH), 1.83 (m, 2H, CH_2), 1.65 (br, 1H, OH), 1.26 (d, $J = 7.0$ Hz, 3H, CH_3).

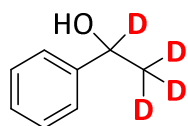
$^{13}\text{C}\{^1\text{H}\}$ -NMR (CDCl_3 , 101 MHz, 300 K) δ , ppm: 146.8, 128.5, 127.0, 126.1, 61.2, 41.0, 36.5, 22.4.

**10z**

1-(thiophen-2-yl)ethan-1-ol (10z). $^1\text{H-NMR}$ (CDCl_3 , 400 MHz, 300 K) δ , ppm: 7.28-7.25 (m, 1H, H_{arom}), 7.01-6.97 (m, 2H, H_{arom}), 5.15 (q, 1H, CH, $J = 6.4$ MHz), 2.16 (br, 1H, OH), 1.62 (d, $J = 6.4$ Hz, 3H, CH_3).

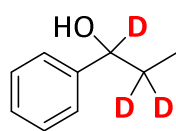
$^{13}\text{C}\{^1\text{H}\}$ -NMR (CDCl_3 , 101 MHz, 300 K) δ , ppm: 149.9, 126.7, 124.4, 123.2, 66.3, 25.3.

VII.3.6. Characterization of the Deuterated Alcohols

**[D]-10a**

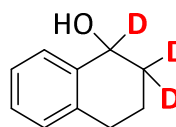
1-phenylethan-1,2,2,2- d_4 -1-ol ([D]-10a). $^1\text{H-NMR}$ (CDCl_3 , 300 MHz, 300 K) δ , ppm: 7.26-7.38 (m, 5H, H_{arom}), 2.12 (s, 1H, OH).

$^{13}\text{C}\{^1\text{H}\}$ -NMR (CDCl_3 , 101 MHz, 300 K) δ , ppm: 145.9 (C_3), 128.6 (C_5), 127.5 (C_4), 125.5 (C_6), 69.9 (t, $J = 21.2$ Hz, C_2), 24.3 (m, C_1).

**[D]-10b**

1-phenylpropan-1,2,2-*d*₃-1-ol ([D]-10b). ¹H-NMR (CDCl₃, 500 MHz, 300 K) δ, ppm: 7.38-7.30 (m, 5H, **H_{arom}**), 1.99 (s, 1H, **OH**), 0.93 (s, 3H, **CH₃**).

¹³C{¹H}-NMR (CDCl₃, 126 MHz, 300 K) δ, ppm: 144.5 (C₄), 128.4 (C₆), 127.5 (C₇), 125.9 (C₅), 75.5 (t, *J* = 22.7 Hz, C₂), 31.1 (m, C₂), 9.9 (C₁).

**[D]-10g**

1,2,3,4-tetrahydronaphthalen-1,2,2-*d*₃-1-ol ([D]-10g). ¹H-NMR (CDCl₃, 500 MHz, 300 K) δ, ppm: 7.45 (m, 1H, **H_{arom}**), 7.23 (m, 2H, **H_{arom}**), 7.13 (m, 1H, **H_{arom}**), 2.88-2.75 (m, 2H, **H_c**), 2.02-1.76 (m, 2H, **H_b**).

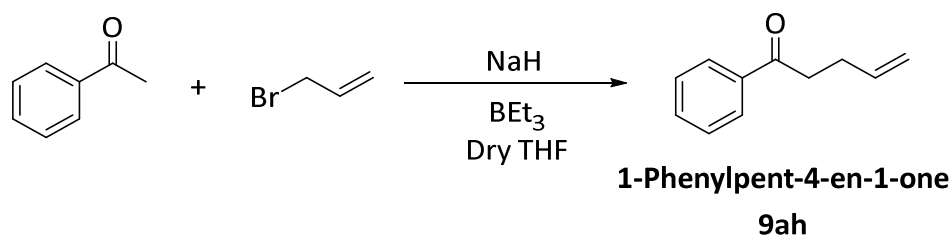
¹³C{¹H}-NMR (CDCl₃, 126 MHz, 300 K) δ, ppm: 138.7 (C₁₀), 137.2 (C₅), 129.0, 128.7, 127.56, 126.1, 67.6 (m, C₁), 31.6 (m, C₂), 29.2 (C₄), 18.6

(C₃).

VII.3.7. Selectivities

VII.3.7.1. Synthesis of the substrates

Synthesis of 1-Phenylpent-4-en-1-one (**9h**)

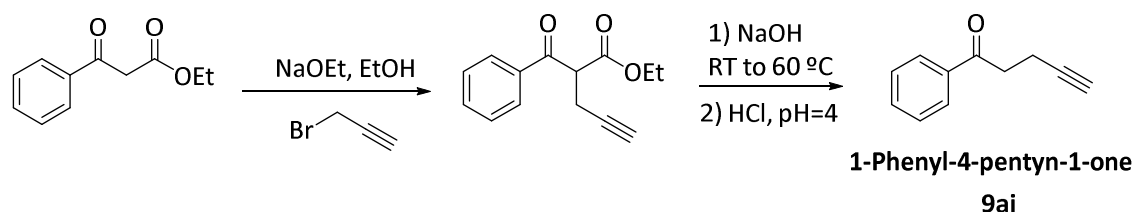


Scheme VII. 14. Synthesis of 1-phenyl-4-en-1-one (**9ah**).

A solution of acetophenone (5.2 mL, 44 mmol, 1.0 eq.) in 20 mL of dry THF was added dropwise over 20 min to a suspension of sodium hydride (2.11 g, 52.8 mmol, 1.2 eq.) in dry THF (100 mL) at 0°C under nitrogen atmosphere. The yellow suspension was stirred at room temperature for 30 min and BEt₃ (56 mL 1M in THF, 56 mmol, 1.2 eq.) was added dropwise over 20 min. The resulting yellow solution was further stirred for 30 min and allyl bromide (5.8 mL, 68 mmol, 1.5 eq.) was added dropwise over 15 min and the resulting solution was left stirring overnight at room temperature. The reaction was quenched by the addition of 50 mL of 1:1 mixture of 30 % NaOH and 30 % H₂O₂ at 0 °C over 30 min. The reaction mixture was then diluted with H₂O (100 mL), the layers were separated and the organic layer diluted with Et₂O (100 mL) and washed with H₂O (2 x 50 mL). The combined water layers were extracted with CH₂Cl₂ (3 x 50 mL) and the combined organic layers were dried over MgSO₄ and the solvent were removed under reduced pressure. The resulting oil product was purified by silica column chromatography (Hexane:AcOEt 30:1) to afford the desired product (65 % yield) as colorless oil. ¹H-NMR (CDCl₃, 300 MHz, 300 K) δ, ppm: 8.00-7.97 (m, 2H, **H_{arom}**), 7.61-7.55

(m, 1H, H_{arom}), 7.51-7.46 (m, 2H, H_{arom}), 5.97-5.86 (m, 1H, $\text{CH}=\text{CH}_2$), 5.13-5.02 (m, 2H, $\text{CH}=\text{CH}_2$), 3.10 (t, 2H, $J = 7.2$ Hz), 2.51 (q, 2H, $J = 6.6$ Hz).

Synthesis of 1-Phenyl-4-pentyn-1-one (**9ai**)

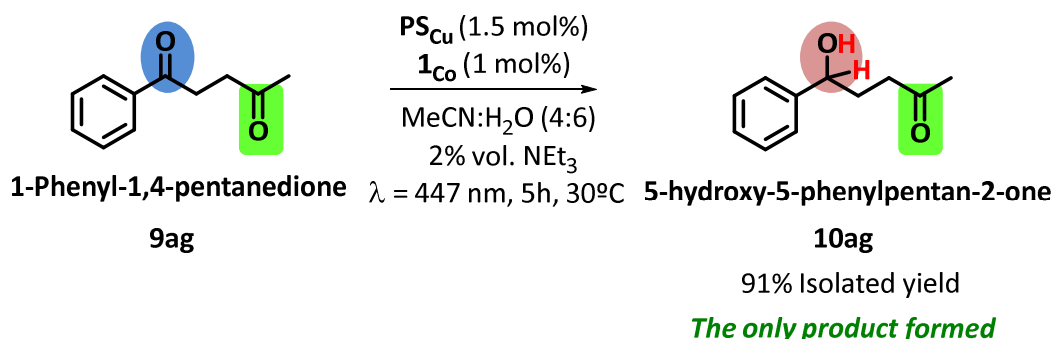


Scheme VII. 15. Synthesis of 1-Phenyl-4-pentyn-1-one (**9ai**).

In a mixture of ethyl benzoylacetate (5.76 g, 30 mmol, 1.0 eq.) in a 50 mL of anhydrous ethanol were added 2.25 g of NaOEt (33 mmol, 1.1 eq.). After stirring the mixture for 15 min, propargyl bromide (3.76 mL, 80 % wt solution in toluene, 33 mmol, 1.1 eq.) was added dropwise at 0 °C within 30 minutes. The resulting orange solution was stirred at room temperature for 1 day. After that, the sodium bromide was filtered off, and the solvent removed under vacuum in a rotary evaporator. To the residue was added 24 mL (60 mmol) of 10 % aq. NaOH, and the mixture was stirred 3 hour at room temperature and at 60 °C for another 3 hours. Then, the crude mixture was cooled to ambient temperature, acidified with conc. HCl to a pH of 4 and extracted with CH_2Cl_2 (3x 50 mL). The combined organic layers were dried over MgSO_4 and the solvent were removed under reduced pressure. The resulting oil product was purified by silica column chromatography (Hexane:AcOEt 30:1) to afford the desired alkyne product (75 % yield) as a pale yellow solid. $^1\text{H-NMR}$ (CDCl_3 , 300 MHz, 300 K) δ , ppm: 8.01-7.98 (m, 2H, H_{arom}), 7.62-7.57 (m, 1H, H_{arom}), 7.52-7.46 (m, 2H, H_{arom}), 3.27 (t, 2H, $J = 7.1$ Hz, $\text{CH}_2\text{CH}_2\text{C}\equiv\text{CH}$), 2.68 (td, 2H, $J = 7.1$ Hz, $J' = 2.7$ Hz, $\text{CH}_2\text{CH}_2\text{C}\equiv\text{CH}$), 2.00 (t, 1H, $J = 2.7$ Hz, $\text{C}\equiv\text{CH}$).

VII.3.7.2. NMR characterization of the reduced products **10ag**, **10ah** and **10ai**

VII.3.7.2.1. Reduction of 1-Phenyl-1,4-pentanedione



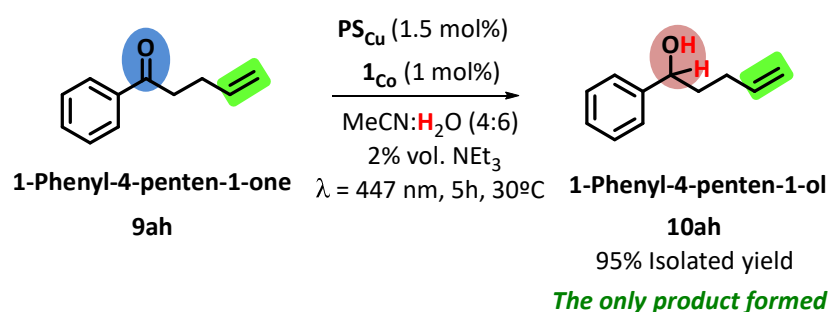
1-Phenyl-1,4-pentanedione (0.168 mmol, 16.5 mM), **1_{Co}** (1.7 μmol , 1 mol%), **PS_{Cu}** (2.5 μmol , 1.5 mol%) in a MeCN:H₂O:Et₃N (4:6:0.2 mL) solution were irradiated at $\lambda = 447$ nm for 5 h at 30 °C under N₂. The crude mixtures of 5 different reactions were combined

and purified by extraction with CH_2Cl_2 (3 x 40 mL). Organic fractions were combined, dried over MgSO_4 and the solvent removed under pressure. The resulting residue was purified by silica gel column chromatography with Hexane/AcOEt (8:2) to obtain 161 mg (95 % yield) of alcohol product which was identified as **5-Hydroxy-5-phenylpentan-2-one**.

$^1\text{H-NMR}$ (CDCl_3 , 400 MHz, 300 K) δ , ppm: 7.39-7.28 (m, 5H, H_{arom}), 4.71 (t, 1H, $\text{CH-CH}_2\text{-CH}_2$, $J = 6.5$ Hz), 2.74 (br, 1H, OH), 2.55 (t, 2H, $\text{CH-CH}_2\text{-CH}_2$, $J = 6.5$ Hz), 2.14 (s, 3H, CH_3), 2.00 (m, 2H, $\text{CH-CH}_2\text{-CH}_2$).

$^{13}\text{C}\{^1\text{H}\}\text{-NMR}$ (CDCl_3 , 101 MHz, 300 K) δ , ppm: 209.5, 144.3, 128.4, 127.5, 125.7, 73.4, 39.8, 32.6, 29.9.

VII.3.7.2.2. Reduction of 1-Phenyl-4-penten-1-one.

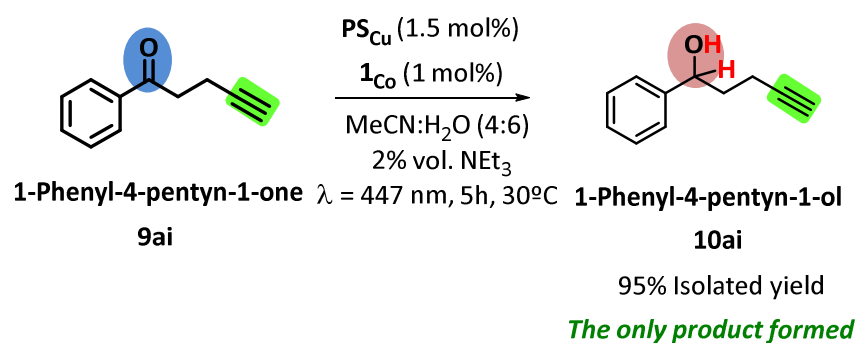


1-Phenyl-4-penten-1-one (0.168 mmol, 16.5 mM), **1_{Co}** (1.7 μmol , 1 mol%), **PS_{Cu}** (2.5 μmol , 1.5 mol%) in a MeCN:H₂O:Et₃N (4:6:0.2 mL) solution were irradiated at $\lambda = 447$ nm for 5 h at 30 °C under N₂. The crude mixtures of 5 different reactions were combined and purified by extraction with CH_2Cl_2 (3 x 40 mL). Organic fractions were combined, dried over MgSO_4 and the solvent removed under pressure. The resulting residue was purified by silica gel column chromatography with Hexane/AcOEt (9:1) to obtain 150 mg (95 % yield) of alcohol product which was identified as **1-Phenyl-4-penten-1-ol**.

$^1\text{H-NMR}$ (CDCl_3 , 400 MHz, 300 K) δ , ppm: 7.39-7.30 (m, 5H, H_{arom}), 5.87 (ddt, 1H, $\text{CH}_2\text{-CH}_2\text{-CH=CH}_2$, $J = 17.0$ Hz, $J' = 10.0$ Hz and $J'' = 6.5$ Hz), 5.09-5.05 (m, 1H, $\text{CH=CH}^{\text{e}}\text{H}^{\text{f}}$), 5.03-5.00 (m, 1H, $\text{CH=CH}^{\text{e}}\text{H}^{\text{f}}$), 4.73-4.69 (m, 1H, $\text{CH-CH}_2\text{-CH}_2$), 2.19-2.11 (m, 2H, $\text{CH-CH}_2\text{-CH}_2$), 1.94-1.81 (m, 2H, $\text{CH-CH}_2\text{-CH}_2$).

$^{13}\text{C}\{^1\text{H}\}\text{-NMR}$ (CDCl_3 , 101 MHz, 300 K) δ , ppm: 144.6, 138.2, 128.5, 127.6, 125.9, 114.9, 74.0, 38.1, 30.1.

VII.3.7.2.3. Reduction of 1-Phenyl-4-pentyn-1-one



1-Phenyl-4-pentyn-1-one (0.168 mmol, 16.5 mM), $\mathbf{1}_{\text{Co}}$ (1.7 μmol , 1 mol%), PS_{Cu} (2.5 μmol , 1.5 mol%) in a MeCN:H₂O:Et₃N (4:6:0.2 mL) solution were irradiated at $\lambda = 447 \text{ nm}$ for 5 h at 30 °C under N₂. The crude mixtures of 5 different reactions were combined and purified by extraction with CH₂Cl₂ (3 x 40 mL). Organic fractions were combined, dried over MgSO₄ and the solvent removed under pressure. The resulting residue was purified by silica gel column chromatography with Hexane/AcOEt (9:1) to obtain 145 mg (92 % yield) of alcohol product which was identified as **1-Phenyl-4-pentyn-1-ol**.

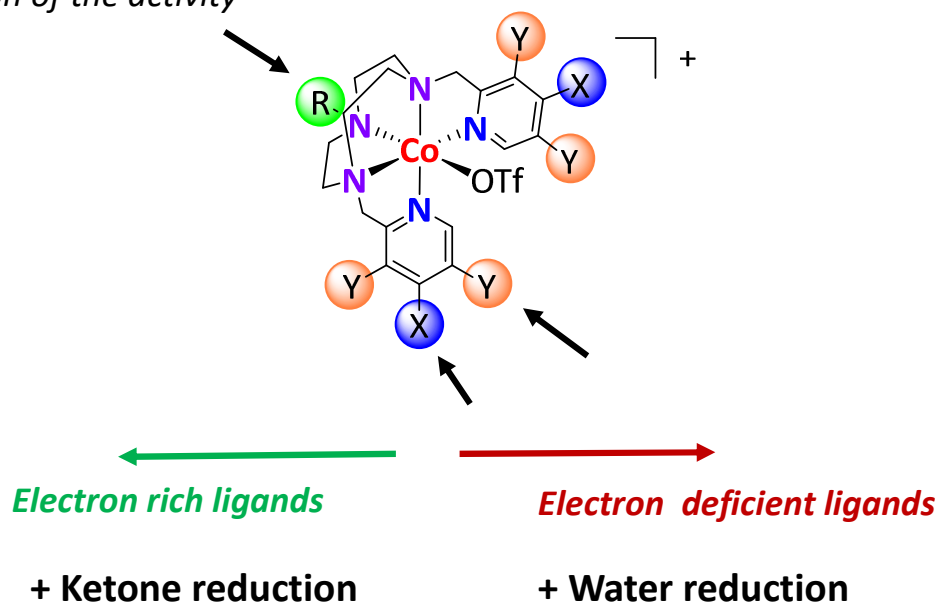
¹H-NMR (CDCl₃, 400 MHz, 300 K) δ , ppm: 7.39-7.28 (m, 5H, H_{arom}), 4.86 (dd, 1H, CH-CH₂-CH₂, $J = 8.2 \text{ Hz}$, $J' = 5.5 \text{ Hz}$), 2.41-2.22 (m, 2H, CH-CH₂-CH₂), 2.06-1.88 (m, 3H, CH-CH₂-CH₂≡-H).

¹³C{¹H}-NMR (CDCl₃, 101 MHz, 300 K) δ , ppm: 144.0, 128.5, 127.7, 125.8, 83.9, 73.1, 68.9, 37.3, 15.1.

CHAPTER VIII

Influence of the Electronic Effects in Cobalt Catalysts on Photocatalytic Ketone Reduction

Modulation of the activity



VIII. INFLUENCE OF THE ELECTRONIC EFFECTS IN COBALT CATALYSTS ON PHOTOCATALYTIC KETONE REDUCTION

VIII.1. STATE-OF-THE-ART

The effect of the electronic nature of the ligand in the catalytic outcome can be a very powerful strategy to get information about the mechanism. However, the inherent complexity of the mechanism and the lack of a broad library of cobalt complexes limits the information that can be extracted about the reduction mechanism. In this regard, in Chapter VII we have shown that the photocatalytic activity in ketone reduction depends on the structural properties of the ligand. We have also noticed that, in general, pentadentate aminopyridine cobalt complexes are more active than tetradentate ones in alcohol production.

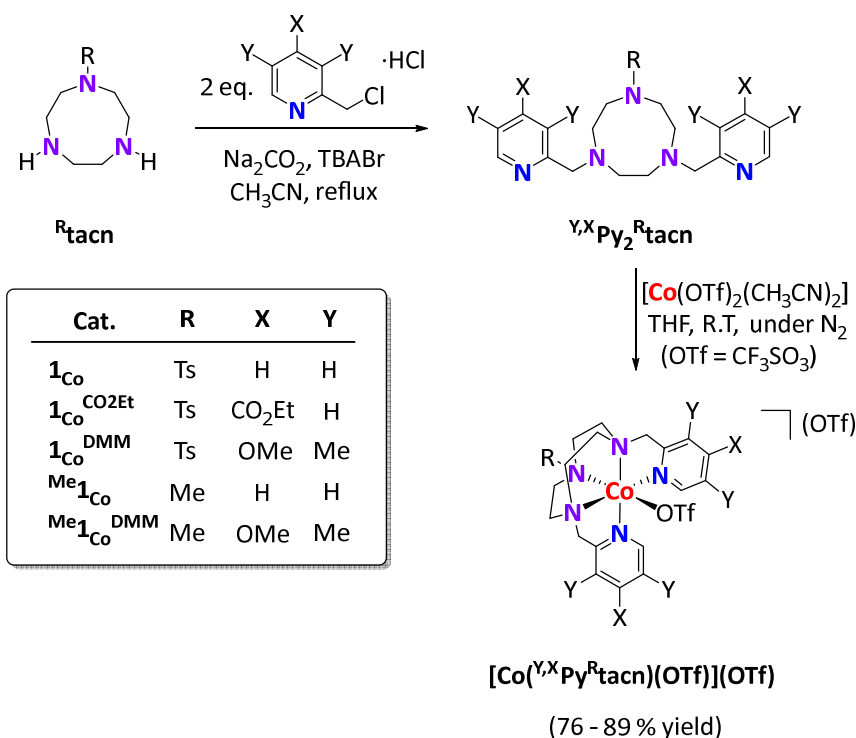
Furthermore, in Chapter IV we have developed a new family of cobalt complexes based on tetradentate ligands with the general structure $[\text{Co}(\text{OTf})_2(\text{Me},\text{Y},\text{XPytacn})]$ that can efficiently catalyze the photo- and electrochemical H_2 production. More importantly, the catalytic activity can be systematically tuned by modification of the groups located at the pyridine ring. We concluded that the proton reduction activity was controlled by either the potential of the $\text{Co}^{\text{II/I}}$ redox event and the $\text{pK}_a(\text{Co}^{\text{II}}-\text{H})$ value, which are strongly dependent on the electronic nature of the ligand.

Inspired by these results we became interested in studying the effect of the electronic nature of the ligand in the photocatalytic ketone reduction efficiency. In particular, we aim to test the series of tetradentate cobalt complexes previously studied in H_2 evolution. We also propose new pentadentate cobalt complexes with the general structure $[\text{Co}(\text{OTf})(\text{X},\text{YPy}^{\text{R}}\text{tacn})](\text{OTf})$. This information will be of value for the design of more active ketone reduction catalysts.

VIII.2. RESULTS AND DISCUSSION

VIII.2.1. Synthesis and Characterization of Cobalt Complexes

We decided to modify the catalyst $[\text{Co}^{\text{II}}(\text{OTf})(\text{Py}_2^{\text{Ts}}\text{tacn})](\text{OTf})$ (**1_{Co}**) based on the pentadentate ligand due to its high catalytic efficiency in the ketone reduction and its modularity. We have introduced modifications on the basic Py_2tacn structure in two different places of the ligand to produce a family with the general formula $^{\text{Y,X}}\text{Py}_2^{\text{R}}\text{tacn}$ (4,7-bis(4-Y-3,5-X-pyridine-2-ylmethyl)-7-R-1,4,7-triazacyclononane). Substituents at the pyridine provide fine control over the electronic nature of the metal center without introducing steric effects. In this regard, two derivatives were obtained, $^{\text{H,CO}_2\text{Et}}\text{Py}_2^{\text{Ts}}\text{tacn}$ by modifying the γ position with an ester group and $^{\text{Me,OMe}}\text{Py}_2^{\text{Ts}}\text{tacn}$ by introducing a methoxide at γ position and methyl groups at the β position of the pyridine.^{323,324} Both, were obtained in excellent yields (> 90 %) from a direct alkylation of the monotosylated 1,4,7-triazacyclononane (Tstacn) moiety with the appropriate functionalized picolyl chloride in acetonitrile (Scheme VIII. 1).



Scheme VIII. 1. General scheme for the preparation of the ligands and complexes employed in this study.

We also replaced the tosyl group at the nitrogen of the triazacyclononane ring by a methyl group, obtaining the $\text{Py}_2^{\text{Me}}\text{tacn}$ and $^{\text{Me,OMe}}\text{Py}_2^{\text{Me}}\text{tacn}$ ligands (Scheme VIII.

1). Those ligands were prepared from the dialkylation of the tacn moiety followed by a methylation step (29 and 33 % yield, respectively).

Complexes $\mathbf{1}_{\text{Co}}^{\text{CO}_2\text{Et}}$, $\mathbf{1}_{\text{Co}}^{\text{DMM}}$, $\text{Me}\mathbf{1}_{\text{Co}}$ and $\text{Me}\mathbf{1}_{\text{Co}}^{\text{DMM}}$ with the general formula $[\text{Co}(\text{OTf})(^{\text{Y,X}}\text{Py}_2^{\text{R}}\text{tacn})](\text{OTf})$ (X and Y refer to the groups at the γ and β positions of the pyridine and R refers to the substitution at the N-7 of the triazacyclononane ring) were prepared (Scheme VIII. 1) by reaction of $^{\text{Y,X}}\text{Py}_2^{\text{R}}\text{tacn}$ ligands with an equimolar amount of $[\text{Co}^{\text{II}}(\text{OTf})_2(\text{MeCN})_2]$ in THF at room temperature in good yields (76 - 89 % yield). All complexes were characterized by $^1\text{H-NMR}$, ESI-MS and elemental analysis. Additionally, complexes $\mathbf{1}_{\text{Co}}^{\text{CO}_2\text{Et}}$ and $\mathbf{1}_{\text{Co}}^{\text{DMM}}$ were also characterized by UV/Vis absorption spectroscopy and their spin state has also been determined. The molecular structure of complexes $\mathbf{1}_{\text{Co}}^{\text{DMM}}$ and $\text{Me}\mathbf{1}_{\text{Co}}^{\text{DMM}}$ was also determined by X-ray diffraction. Complex $\mathbf{1}_{\text{Co}}$ has already been described in Chapter III, however the photocatalytic reduction activity of this complex will be included for comparative reasons.

All complexes showed characteristic broad signals in their $^1\text{H-NMR}$ spectra from -100 to 300 ppm, which is in agreement with a $t_{2g}^5 e_g^2$ or $t_{2g}^6 e_g^1$ configuration for the Co^{II} paramagnetic species. The paramagnetic spectra of $\mathbf{1}_{\text{Co}}^{\text{CO}_2\text{Et}}$, $\mathbf{1}_{\text{Co}}$ and $\mathbf{1}_{\text{Co}}^{\text{DMM}}$ are temperature dependent with a significant signal sharpening at lower temperature (Figure A. 5. 5 and Figure A. 5. 6). This could be an indication that these cobalt complexes present a dynamic behavior at room temperature. The magnetic moment (μ_{eff} 3.8-3.9 BM, range 235-330 K) measured for $\mathbf{1}_{\text{Co}}^{\text{CO}_2\text{Et}}$, $\mathbf{1}_{\text{Co}}$ and $\mathbf{1}_{\text{Co}}^{\text{DMM}}$ complexes using the Evans' NMR method³³¹⁻³³³ are in good agreement with d^7 high-spin Co^{II} complexes ($S = 3/2$).^{96,334,335} On the other hand, UV/Vis spectra of $\mathbf{1}_{\text{Co}}^{\text{CO}_2\text{Et}}$, $\mathbf{1}_{\text{Co}}$ and $\mathbf{1}_{\text{Co}}^{\text{DMM}}$ present intense transitions from 200 to 300 nm attributed to LLCT and MLCT.^{293,294}

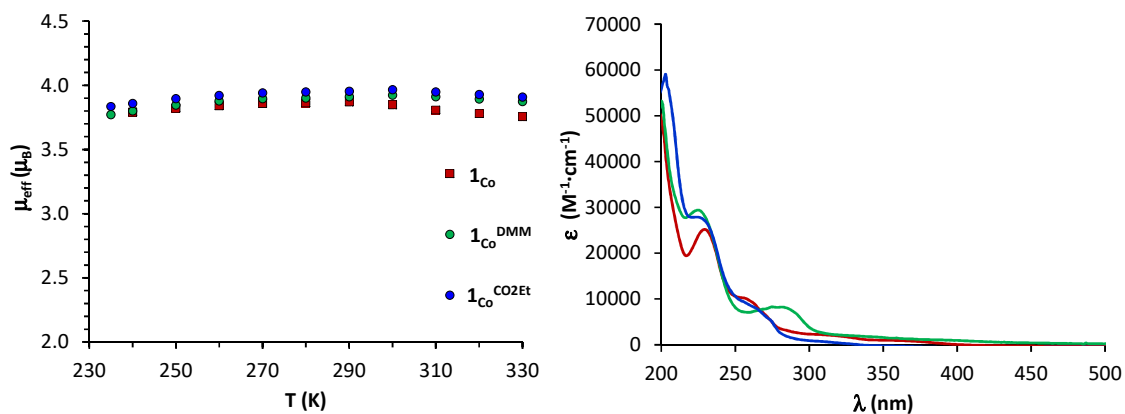


Figure VIII. 1. *Left:* Representation of the effective magnetic moment of $1_{\text{Co}}^{\text{CO}_2\text{Et}}$, 1_{Co} and $1_{\text{Co}}^{\text{DMM}}$ as a function of temperature. μ_{eff} values were obtained in CD_3CN using the Evans' method. *Right:* UV/Vis absorption spectra of a 50 μM solution of $1_{\text{Co}}^{\text{CO}_2\text{Et}}$ (blue), 1_{Co} (red) and $1_{\text{Co}}^{\text{DMM}}$ (green) in MeCN at 298 K.

The solid state structure of $1_{\text{Co}}^{\text{DMM}}$ and $\text{Me}1_{\text{Co}}^{\text{DMM}}$ could be determined by X-ray diffraction analysis (Figure VIII. 2). The coordination geometry around the metal ion is distorted from the idealized octahedral geometries. Five of the coordination sites of the Co^{II} center are occupied by the three N atoms of triazacyclononane (tacn) and two N atoms of the pyridines. The pentadentate coordination provides one ligand-exchangeable coordination site that is occupied by a triflate anion. The averaged Co-N bond lengths are 2.0-2.3 Å (Table A. 5. 2), characteristic of high-spin Co^{II} complexes with $S = 3/2$.^{97,292} Interestingly, the Co-N₃ bond distance is observed higher in $1_{\text{Co}}^{\text{DMM}}$ (2.326(4) Å) than in $\text{Me}1_{\text{Co}}^{\text{DMM}}$ (2.174(3) Å) due to the lower coordination character of the tosyl-nitrogen.

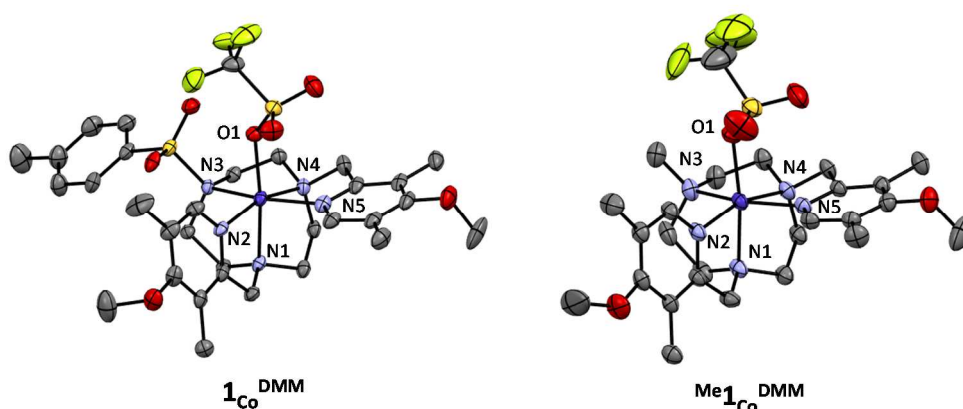


Figure VIII. 2. Crystal structures of the cobalt complexes $1_{\text{Co}}^{\text{DMM}}$ (50 % probability) and $\text{Me}1_{\text{Co}}^{\text{DMM}}$ (30 % probability). Solvent molecules and hydrogen atoms are omitted for clarity. Color code: cobalt (blue), nitrogen (light blue), oxygen (red), fluor (yellow), carbon (grey) and sulfur (orange).

VIII.2.2. Activities of the Complexes Based on Pentadentate Aminopyridine Ligands

The photocatalytic activity of the cobalt complexes in H₂ formation was evaluated employing photosensitizers **PS**_{Ir} and **PS**_{Cu}. Initially, we used the standard catalytic conditions of 50 μM of **catalyst**, 250 μM of **PS**_{Ir} in a MeCN:H₂O (2:8) solvent mixture and Et₃N as sacrificial electron donor. As depicted in Figure VIII. 3 all complexes were found active in water reduction ranging from 96 to 212 TON. Interestingly, as described in Chapter IV for tetradentate systems, the increase of the electron withdrawing character of the substituents at the pyridine led to an activity enhancement: **1**_{Co}^{CO₂Et} (212 TON) > **1**_{Co} (180 TON) > **1**_{Co}^{DMM} (112 TON). On the other hand, the N3-substitution also influenced the activity. Replacement of the tosyl group by a methyl promoted a decrease in the activities compared to the respective tosyl complexes (^{Me}**1**_{Co} (148 TON), ^{Me}**1**_{Co}^{DMM} (96 TON)). These results evidence that the activity in H₂ production can be also modulated through the electronic modification of the pentadentate tacn ligands.

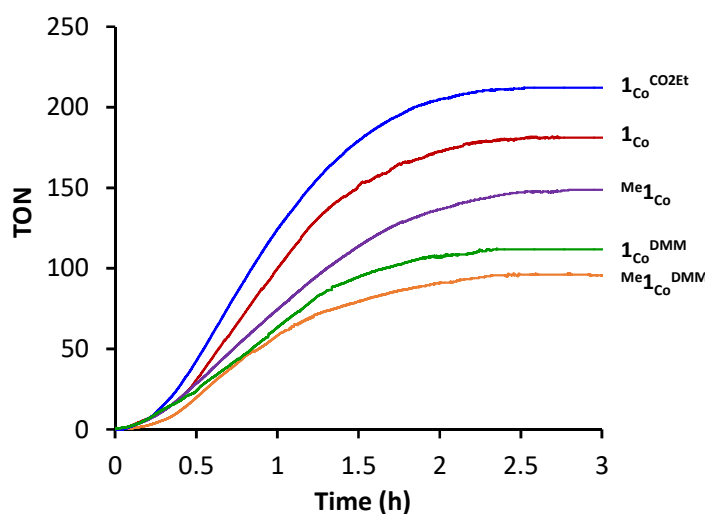


Figure VIII. 3. On-line hydrogen evolved versus time with the cobalt complexes (50 μM), **PS**_{Ir} (250 μM) using CH₃CN:H₂O: Et₃N (2:8:0.2 mL) as solvent and irradiated (λ = 447 nm) at 25 °C. **1**_{Co}^{CO₂Et} (blue), **1**_{Co} (red), ^{Me}**1**_{Co} (purple), **1**_{Co}^{CO₂Et} (green) and ^{Me}**1**_{Co}^{CO₂Et} (orange). TON= n(H₂)/n(**Cat**).

To study the ketone reduction activity, we employed the standard catalytic conditions optimized in Chapter VII. First all complexes resulted to be active in the photocatalytic reduction of **9a**, but more importantly, the activity strongly depends on the ligand employed. Very interestingly, the **10a** formation follows the inverse trend that the H₂ evolution, being now catalyst **1**_{Co}^{CO₂Et} the less active of the series (18 % yield in

10a). Tosyl complexes $\mathbf{1}_{\text{Co}}^{\text{DMM}}$ and $\mathbf{1}_{\text{Co}}$ are clearly the most efficient catalysts for the ketone reduction (67 and 65 % yield, respectively). Methylated $\text{Me}\mathbf{1}_{\text{Co}}^{\text{DMM}}$ (30 % yield) and $\text{Me}\mathbf{1}_{\text{Co}}$ (24 % yield) catalysts were found less active than the relative tosylated ones.

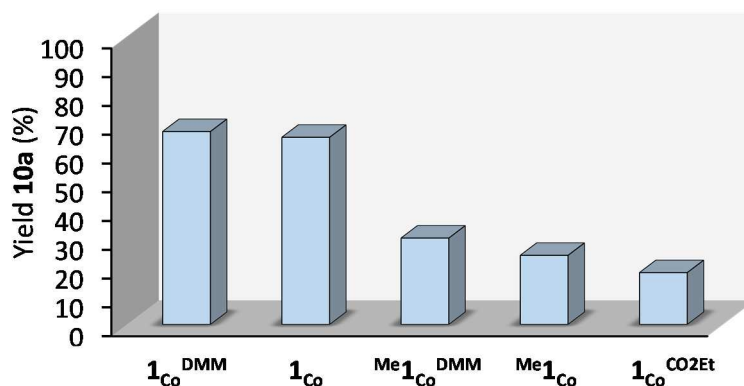


Figure VIII. 4. Photocatalytic activities of the studied catalysts in **10a** formation under standard catalytic conditions.

As expected, the conversion of **9a** into **10a** was accompanied with the formation of H_2 . We monitored online the H_2 evolved in the reaction for complexes $\mathbf{1}_{\text{Co}}^{\text{CO}_2\text{Et}}$, $\mathbf{1}_{\text{Co}}$ and $\mathbf{1}_{\text{Co}}^{\text{DMM}}$. In the absence of substrate, the H_2 evolved follows the same trend previously observed: $\mathbf{1}_{\text{Co}}^{\text{CO}_2\text{Et}}$ (0.19 mmol, $0.09 \text{ mmol}\cdot\text{h}^{-1}$) > $\mathbf{1}_{\text{Co}}$ (0.15 mmol, $0.08 \text{ mmol}\cdot\text{h}^{-1}$) > $\mathbf{1}_{\text{Co}}^{\text{DMM}}$ (0.10 mmol, $0.07 \text{ mmol}\cdot\text{h}^{-1}$). Notably, in the presence of **9a**, the H_2 evolved decreases according to the capacity of the metal complex to reduce the ketone to alcohol. A dramatic decrease in the H_2 production activity was observed with catalysts $\mathbf{1}_{\text{Co}}$ (0.06 mmol, $0.03 \text{ mmol}\cdot\text{h}^{-1}$) and $\mathbf{1}_{\text{Co}}^{\text{DMM}}$ (0.03 mmol, $0.02 \text{ mmol}\cdot\text{h}^{-1}$), very active for ketone reduction, whereas in the case of $\mathbf{1}_{\text{Co}}^{\text{CO}_2\text{Et}}$ the presence of substrate slightly decreased the activity in H_2 formation (0.018 mmol, $0.08 \text{ mmol}\cdot\text{h}^{-1}$). Such modification of the water reduction activity is directly related to the amount of **10a** produced (0.03 mmol **10a** with $\mathbf{1}_{\text{Co}}^{\text{CO}_2\text{Et}}$, 0.11 mmol **10a** with $\mathbf{1}_{\text{Co}}$ and $\mathbf{1}_{\text{Co}}^{\text{DMM}}$) (Figure VIII. 5).

Complexes $\mathbf{1}_{\text{Co}}$ and $\mathbf{1}_{\text{Co}}^{\text{DMM}}$ display excellent selectivity towards the reduction of ketones (Ratio **10a**/ H_2 : 1.7 ($\mathbf{1}_{\text{Co}}$), 3.3 ($\mathbf{1}_{\text{Co}}^{\text{DMM}}$)), whereas complex $\mathbf{1}_{\text{Co}}^{\text{CO}_2\text{Et}}$ with electron withdrawing groups presents low selectivity towards ketone reduction (Ratio **10a**/ H_2 : 0.2).

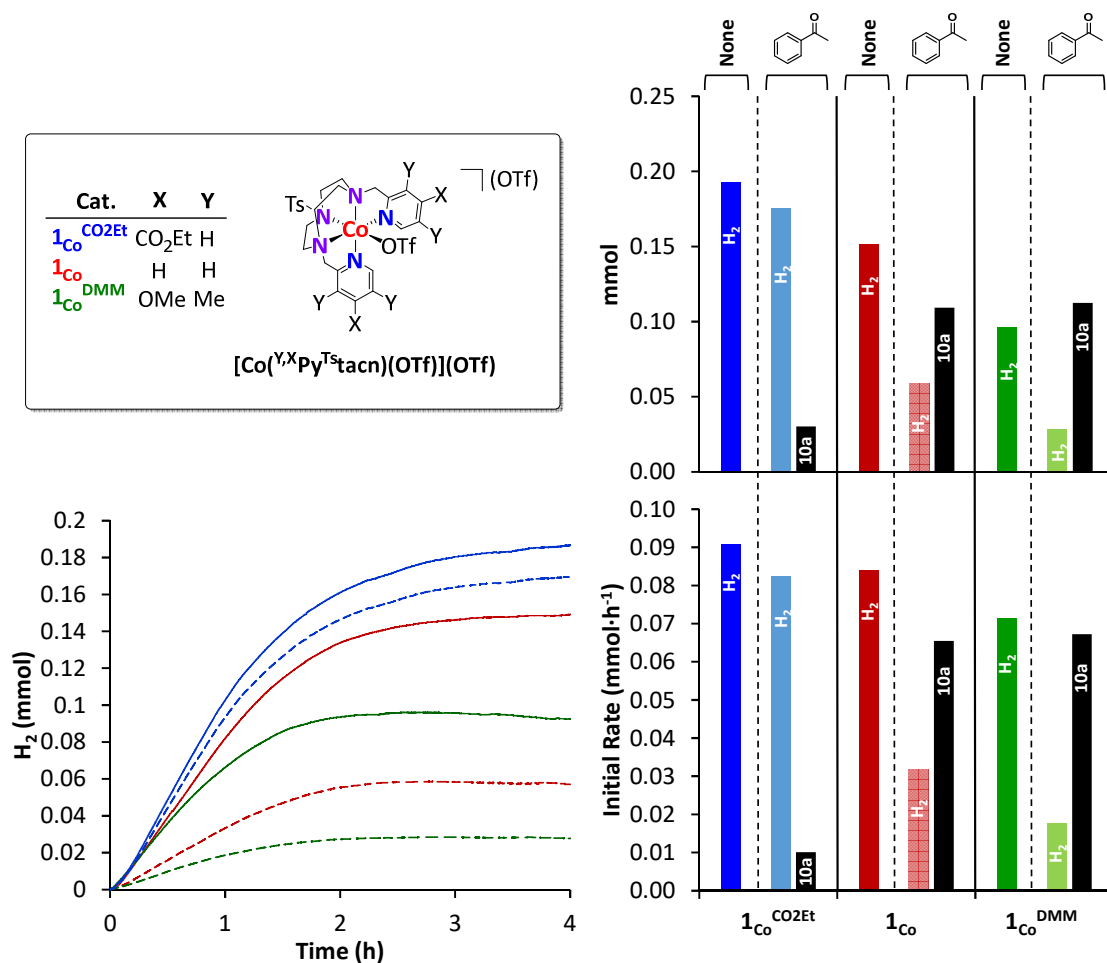


Figure VIII. 5. *Left:* Online monitoring of the photochemical H₂ production in the absence (solid line) and presence of **9a** (dashed line) for $1_{\text{Co}}^{\text{CO}_2\text{Et}}$ (blue), 1_{Co} (red) and $1_{\text{Co}}^{\text{DMM}}$ (green). Conditions in absence of **9a**: **PS**_{Ir} (2.5 μmol), **1**^R (5 μmol). Conditions in presence of **9a**: [**9a**] (0.168 mmol, 16.5 mM), **PS**_{Ir} (2.5 μmol, 1.5 mol%), **1**^R (5.04 μmol, 3 mol%). Solvent mixture: MeCN:H₂O:Et₃N (2:8:0.2 mL), Irradiation λ = 447 nm at 30 °C under N₂. *Right:* Photocatalytic activities of $1_{\text{Co}}^{\text{CO}_2\text{Et}}$ (blue), 1_{Co} (red) and $1_{\text{Co}}^{\text{DMM}}$ (green) in H₂ and **10a** formation in the presence (pale-colored columns) and absence (dark-colored columns) of substrate. The black columns are the photocatalytic activities in **9a** reduction.

We performed the same experiments replacing **PS**_{Ir} by **PS**_{Cu}, in order to evaluate the influence of the photoredox catalyst on the electronic effects. In addition, the replacement of **PS**_{Ir} by **PS**_{Cu} was highly beneficial, obtaining quantitative yields for the **9a** reduction. Therefore, we could study in detail the H₂ evolution during the substrate consumption and after it was fully consumed. We employed the optimized conditions of Chapter VII (**1**^R (170 μM), **PS**_{Cu} (250 μM), in MeCN:H₂O:Et₃N (4:6:0.2 mL)) and measured the online H₂ evolved catalyzed by $1_{\text{Co}}^{\text{CO}_2\text{Et}}$, 1_{Co} and $1_{\text{Co}}^{\text{DMM}}$ at different concentrations of **9a** (2.0 – 49.4 mM **9a**). In addition, the quantity of reduced **9a** when no more H₂ was produced was also analyzed. As previously depicted, the presence of **9a**

in the $\text{PS}_{\text{Ir}} - \mathbf{1}_{\text{Co}}^{\text{CO}_2\text{Et}}$ combination inhibits the H_2 formation depending on the concentration of **9a**, although with very similar kinetic profile than in its absence (Figure VIII. 6).

Likewise, the presence of **9a** in the $\text{PS}_{\text{Cu}} - \mathbf{1}_{\text{Co}}^{\text{CO}_2\text{Et}}$ catalytic system also inhibits the H_2 evolution upon increasing the **9a** concentration up to saturation (about 20-25 mM). At 24.7 mM of **9a** there is a 37 % inhibition of the H_2 formation (120 μmol of H_2 produced). At the same time the amount of the reduced product is also saturated at about 20-25 mM of **9a**, yielding 50 μmol of **10a**. Interestingly, these particular behavior suggests that two mechanisms for the H_2 formation operate at the same time and that one is inhibited by the presence of **9a**.

In contrast, the H_2 production activity of $\mathbf{1}_{\text{Co}}$ and $\mathbf{1}_{\text{Co}}^{\text{DMM}}$ was strongly inhibited by increasing the substrate concentration. Interestingly, since the later catalysts can completely reduce **9a** to **10a** under the reaction conditions, the inhibition of the H_2 evolution finishes once the substrate is fully consumed. This is clearly illustrated by the change in the kinetic profile of the H_2 evolution. Once the substrate is fully consumed, the kinetic profile of the H_2 evolution follows the measured in absence of substrate. This is agreement with the fact that the time needed for the H_2 profile to change increases with the concentration of **9a** (Figure VIII. 6).

The total amount of **10a** formed during the catalysis with catalyst $\mathbf{1}_{\text{Co}}$ and $\mathbf{1}_{\text{Co}}^{\text{DMM}}$ linearly increases together with a decrease of the formed H_2 . A saturation in the **10a** production can be observed at concentrations higher than 20 mM of **9a** (as previously observed in Chapter VII using PS_{Ir}). Quantitative **9a** reduction is obtained with $\mathbf{1}_{\text{Co}}$ and $\mathbf{1}_{\text{Co}}^{\text{DMM}}$ from 2.0 to 16.5 mM **9a**. In this two cases, we propose that a common cobalt hydride intermediate is the main responsible for the **9a** or water reduction, without the existence of significant parallel mechanisms responsible for the H_2 formation, as in the case of $\mathbf{1}_{\text{Co}}^{\text{CO}_2\text{Et}}$. In summary, the selectivity towards the reduction of the ketone (Ratio **10a**/ H_2 at 24.7 mM **9a**) follows the order 4.6 ($\mathbf{1}_{\text{Co}}^{\text{DMM}}$) > 3.5 ($\mathbf{1}_{\text{Co}}$) > 0.4 ($\mathbf{1}_{\text{Co}}^{\text{CO}_2\text{Et}}$), which agrees with the electronic donating character of the ligand.

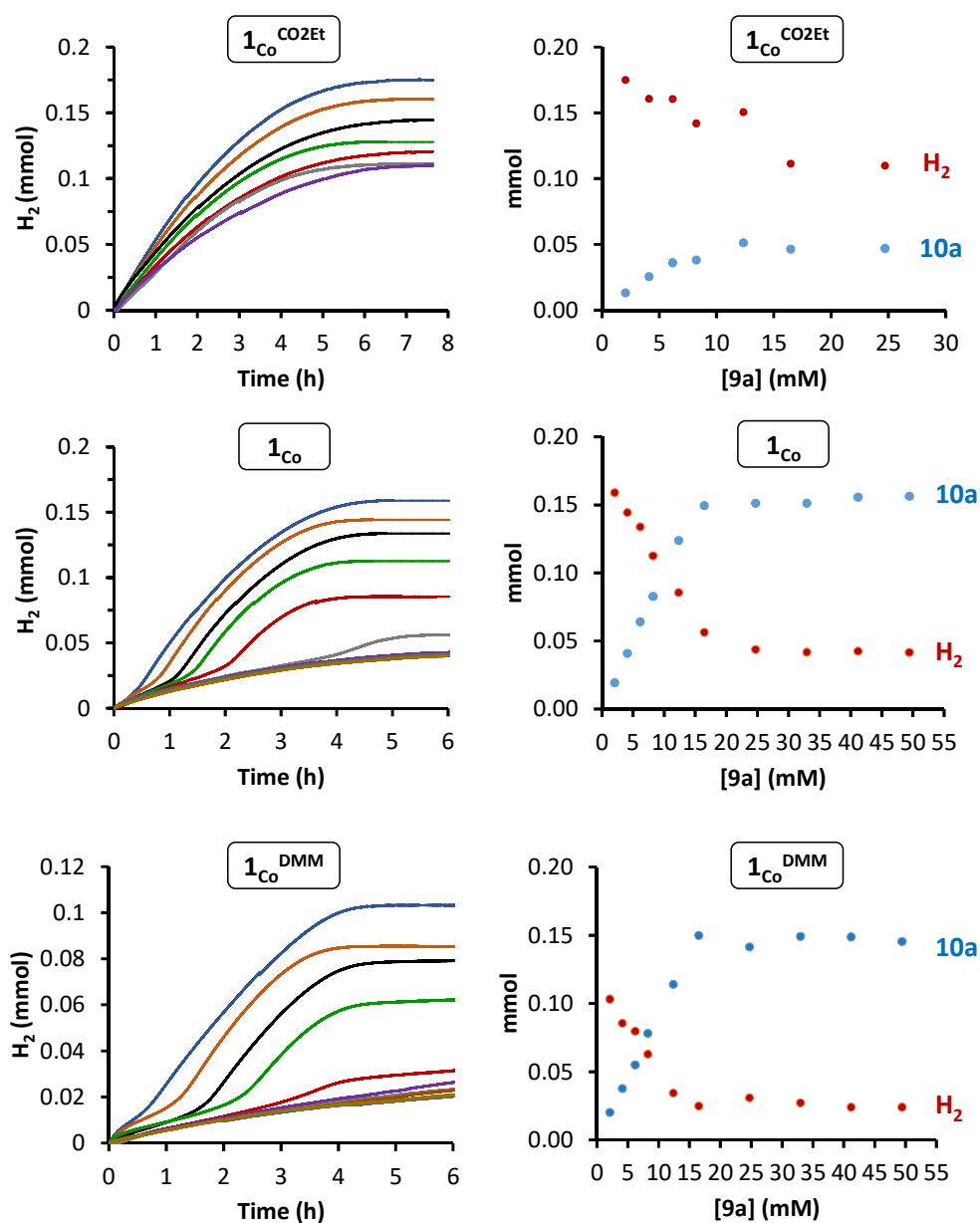


Figure VIII. 6. *Left:* Online monitoring of the photochemical H_2 production at different concentrations of **9a**: 2.0 (blue), 4.1 (orange), 6.2 (black), 8.3 (green), 12.4 (red), 16.5 (grey), 24.7 (purple), 32.9-49.4 (brown colors). *Right:* mmol of **10a** (blue dots) and H_2 (red dots) obtained at the end of the catalytic assay. Conditions: **Cobalt catalyst** (1.7 μmol), **PS_{Cu}** (250 μM , 2.5 μmol), in MeCN:H₂O:Et₃N (4:6:0.2 mL), irradiating at $\lambda = 447 \text{ nm}$, 30 °C.

VIII.2.3. Activities of Complexes Based on Tetradentate Aminopyridine Ligands

Fascinated by the behavior of the pentadentate systems, then we decided to study the tetradentate cobalt complexes presented in Chapter IV. As depicted in Figure VIII. 7 the catalytic activity is also controlled by the electronic nature of the ligand. The increase of the electron donating character of the ligand lead to an enhancement of the catalytic outcome in the alcohol production. For instance, complex **1^{NMe2}** provided 48 %

yield in **10a** formation whereas for the electron deficient **1^{CO2Et}** catalyst only 10 % of **9a** was reduced at the end of the catalytic assay. Again we note that the ketone reduction trend is inverse to the observed for the H₂ production, as mentioned in Chapter IV.

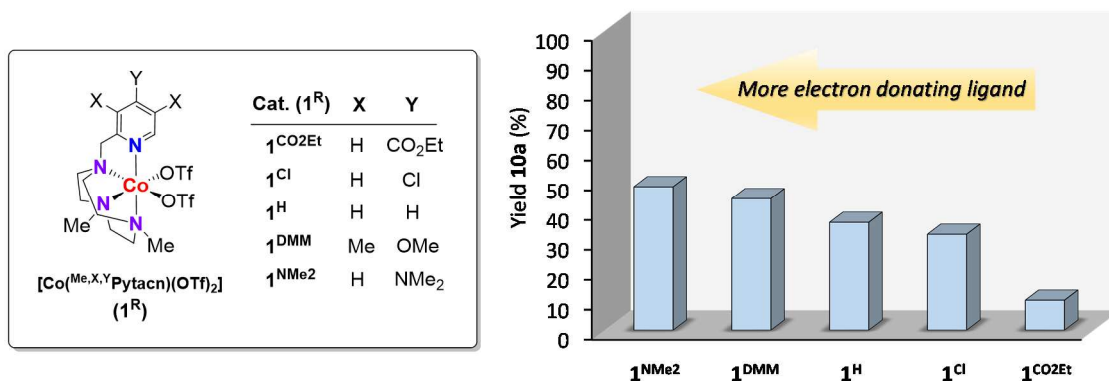


Figure VIII. 7. Photocatalytic activities of the tetradentate [Co(OTf)₂(^{Me,X,Y}PyTacn)] systems in **10a** formation using standard catalytic conditions.

VIII.2.4. General Discussion

As a general overview, it seems that there is an electronic trend in the reduction of ketones catalyzed by the presented cobalt complexes. For the set of complexes with pentadentate and tetradentate aminopyridine ligands, the activity is enhanced by increasing the electron donating character of the ligand. Complexes **1_{Co}** and **1_{Co}^{DMM}** display excellent selectivity towards the reduction of ketones, compared to the analogous **1_{Co}^{CO2Et}**. This evidences that the photocatalytic ketone reduction can be modulated and improved by a rational design of the ligand architecture.

The computed pK_a (Co^{III}-H) values in aqueous media of the series follows the order **1_{Co}^{DMM}** (10.2) > **1_{Co}** (7.0) > **1_{Co}^{CO2Et}** (-1.5), indicating a more hydride basicity when increasing the electron donating character of the ligand. This is consistent with a hydride reduction mechanism

VIII.3. EXPERIMENTAL SECTION

VIII.3.1. Material and Reagents

Reagents and solvents were purchased from commercial sources as used as received unless otherwise stated. Triethylamine (Et_3N) $\geq 99\%$ purity and ascorbic acid (AsCh) ($\geq 99\%$) were purchased from Sigma-Aldrich® and used without further purification. The photosensitizers $[\text{Ir}(\text{bpy})(\text{ppy})_2]\text{PF}_6$ (**PS_{Ir}**),³⁰³ and $[\text{Cu}(\text{bathocuproine})(\text{Xantphos})]\text{PF}_6$ (**PS_{Ir}**)³⁹⁵ were synthesized according to the literature procedures. Anhydrous acetonitrile was purchased from Scharlab. Water (18.2 M Ω ·cm) was purified with a Milli-Q Millipore Gradient AIS system. All solvents were strictly degassed and stored under anaerobic conditions.

VIII.3.2. Instrumentation

Nuclear magnetic resonance (NMR) spectra were recorded on Bruker Fourier300, AV400, AV500 and AVIII500 spectrometers using standard conditions (300 K). All ^1H chemical shifts are reported in ppm and have been internally calibrated to the residual protons of the deuterated solvent. The ^{13}C chemical shifts have been internally calibrated to the carbon atoms of the deuterated solvent. The coupling constants were measured in Hz.

Elemental analyses were performed using a CHNS-O EA-1108 elemental analyzer from Fisons.

UV/Vis spectra were recorded on an Agilent 8453 diode array spectrophotometer (190-1100 nm range) in 1 cm quartz cells. A cryostat from Unisoku Scientific Instruments was used for the temperature control.

Mass Spectrometry. Electrospray ionization mass spectrometry (ESI-MS) experiments were performed on a Bruker Daltonics Esquire 3000 Spectrometer using a 1 mM solution of the analyzed compound, by introducing the sample directly into the ESI-source using a syringe. High resolution mass spectra (HRMS) were recorded on a Bruker MicroTOF-Q IITM instrument with an ESI source at Serveis Tècnics of the University of Girona. Samples were introduced into the mass spectrometer ion source by direct infusion through a syringe pump and were externally calibrated using sodium formate.

Gas chromatography analysis. The analysis and quantification of the starting materials and products were carried out on an Agilent 7820A gas chromatograph (HP5 column, 30m or Cyclosil-B column, 30m) and a flame ionization detector. The enantioselectivity was determined by comparison with the pure samples synthesized by the reported procedures.⁴⁸⁴

Parallel Pressure Transducer Hardware. The parallel pressure transducer that we used for these studies is the same that previously was developed and described for water oxidation studies.³⁰⁴ This is composed by 8 differential pressure transducers (Honeywell-ASCX15DN, ± 15 psi) connected to a hardware data-acquisition system (base on Atmega microcontroller) controlled by a home-developed software program. The differential pressure transducer Honeywell-ASCX15DN is a 100 microseconds response, signal-conditioned (high level span, 4.5 V) output, calibrated and temperature compensated (0 °C to 70 °C) sensor. The differential sensor has two sensing ports that can be used for differential pressure measurements. The pressure calibrated devices to within ± 0.5 matm was offset and span calibrated *via* software with a high precision pressure transducer (PX409-030GUSB, 0.08 % Accuracy). Each of the 8 differential pressure transducers (Honeywell-ASCX15DN, ± 15 psi) produce a voltage outputs that can directly transformed to a pressure difference between the two measuring ports. The voltage outputs were digitalized with a resolution of 0.25 matm from 0 to 175 matm and 1 matm from 176 to 1000 matm using an Atmega microcontroller with an independent voltage auto-calibration. Firmware Atmega microcontroller and control software were home-developed. The sensitivity of H₂ analytics allows quantifying the gas formed when low H₂ volumes are generated. Therefore, it could not be discarded that small amounts of H₂ were produced by inactive complexes.

Gas chromatography identification and quantification of gases. Gases at the headspace were analyzed with an Agilent 7820A GC System equipped with columns Washed Molecular Sieve 5A, 2m x 1/8" OD, Mesh 60/80 SS and Porapak Q, 4m x 1/8" OD, SS. Mesh: 80/100 SS and a Thermal Conductivity Detector. The quantification of the H₂ obtained was measured through the interpolation of a previous calibration using different H₂/N₂ mixtures.

Light source. The reactions were performed using Royal-Blue ($\lambda = 447 \pm 20$ nm) LUXEON Rebel ES LED, Mounted on a 10mm Square Saber - 1030 mW @ 700mA (Datasheet: <https://www.luxeonstar.com/assets/downloads/ds68.pdf>) as a light source.

VIII.3.3. Experimental Procedures

VIII.3.3.1. General procedure employed in reaction screening conditions for the light-driven reduction of compounds. All catalytic reactions were conducted in a vigorous stirring under irradiation for 5 hours in 15 mL capped vials with a septum under nitrogen atmosphere at 30 °C, unless otherwise indicated. Catalytic assays using **PS_{Ir}** as chromophore were performed in MeCN:H₂O:Et₃N (2:8:0.2 mL) reaction mixture, substrate (16.4 mM), **PS_{Ir}** (2.5 μ mol, 2 mol%), **1_{Co}** (3.8 μ mol, 3 mol%). Catalytic reactions carried out using **PS_{Cu}** as chromophore were performed in MeCN:H₂O:Et₃N (4:6:0.2 mL) reaction mixture, **9a** (2.0-49.5 mM), **PS_{Cu}** (2.5 μ mol), **1_{Co}** (1.7 μ mol). A 447 nm LED was

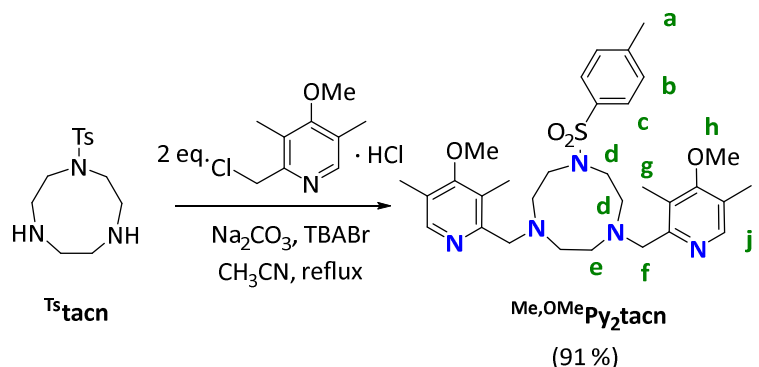
employed as a light source. 1,3,5-trimethoxybenzene was added as internal standard after the reaction and the reaction was quenched by adding 2 mL of CH₂Cl₂. The crude reaction mixtures were purified by extraction with CH₂Cl₂ (3 x 3 mL), the combined organic layers were dried over MgSO₄ and passed through a silica plug which was eluted with AcOEt. The resulting organic solution was subjected to GC analysis to determine the conversion of **9** and the yield of the desired products **10**.

VII.3.3.2. Gas-evolution monitoring studies. Each experiment was conducted in a 20 mL volume-calibrated-vial capped with a septa equipped with stir-bars and containing the solvent mixture and reagents. Each reaction vial was connected to one of the ports of a differential pressure transducer sensor (Honeywell-ASCX15DN) and the other port to a reference reaction. Reference reactions, have all components of the reaction except the catalyst. The reaction and reference vials are kept under the same experimental conditions to compensate the noise due to temperature-pressure fluctuations. In order to ensure a constant and stable irradiation, the LED sources were equipped with a water refrigeration system. This is composed for a refrigerated aluminium block by a Huber cryothermostat (refrigeration system, Minichiller -40°C-20°C). This block is shaken by an Orbital Shaker (IKA KS 260 Basic Package) which provides the agitation of the reaction vessels during the irradiation time. The aluminium block accommodates 16 vials (20 mL) capped with septum in which the reaction takes place. Each vial is submitted and located over a LED irradiation source (Royal-Blue Rebel LEDs ($\lambda = 447 \pm 20$ nm)). The reaction began when the LEDs were turned on. At this point, the hydrogen evolved from the reactions was monitored by recording the increase in pressure of the headspace (1 second interval). The pressure increment is the result of the difference in pressure between the reaction and reference vials. After the hydrogen evolution reached a plateau the amount of the gas formed was measured equilibrating the pressure between reaction and reference vials. The gasses at the headspace of reaction vials and references in each of the reactions were quantified by the analysis of an aliquot of gas at the headspace (0.2 mL) by gas chromatography.

VIII.3.4. Synthesis of the Ligands and Complexes

The synthesis of the complex Me_1Co is described in Chapter VI.

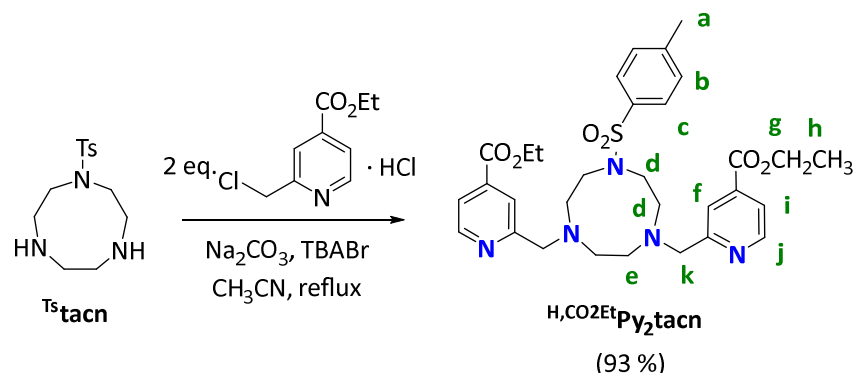
VIII.3.4.1. Synthesis of 4,7-bis(4-methoxy-3,5-dimethyl-pyridine-2-ylmethyl)-7-(p-toluenesulfonyl)-1,4,7-triazacyclononane, ($Me,OMePy_2^{Ts}tacn$)



Scheme VIII. 2. Synthesis of $Me,OMePy_2^{Ts}tacn$.

2-Chloromethyl-4-methoxy-3,5-dimethylpyridine hydrochloride (0.94 g, 4.24 mmol), Ts^{tacn} (0.60 g, 2.12 mmol) and anhydrous acetonitrile (40 mL) were mixed in a 100 mL flask. Na_2CO_3 (1.20 g) and tetrabutylammonium bromide (TBABr, 80 mg) were added directly as solids and the resulting mixture was heated at reflux for 22 hours under N_2 . After cooling at room temperature, the resulting orange mixture was filtered and the filter cake was washed with CH_2Cl_2 . The combined filtrates were evaporated under reduce pressure. To the resulting residue, 2 M NaOH (15 mL) was added and the mixture was extracted with CH_2Cl_2 (4 x 40 mL). The combined organic layers were dried over $MgSO_4$ and the solvent was removed under reduced pressure. The resulting residue was treated with *n*-hexane (100 mL) and stirred for 12 hours. The mixture was filtered and the solvent from the yellow filtrates was removed under reduced pressure to yield 1.12 g of a pale yellow solid (1.93 mmol, 91 %). 1H -NMR ($CDCl_3$, 300 MHz, 300 K) δ , ppm: 8.11 (s, 2H, H_j), 7.56 (d, 2H, $^3J(H,H) = 8.2$ Hz, H_c), 7.23 (d, 2H, $^3J(H,H) = 8.2$ Hz, H_b), 3.72 (s, 10H, $H_f + H_h$), 3.00-3.03 (m, 8H, H_d), 2.64 (s, 4H, H_e), 2.40 (s, 3H, H_a), 2.30 (s, 6H, H_g), 2.22 (s, 6H, H_i). ^{13}C -NMR ($CDCl_3$, 75 MHz, 300 K) δ , ppm: 164.10, 157.27, 148.34, 142.82, 135.80, 129.46, 127.08, 126.10, 125.06, 62.95, 59.78, 56.18, 56.01, 50.23, 21.44, 13.22, 11.15. ESI-MS: m/z : 582.4 $[M+H]^+$, 291.7 $[M+2H]^{2+}$. Anal. Calcd for $C_{31}H_{43}N_5O_4S$: C, 64.00; N, 12.04; H, 7.45 %. Found: C, 64.36; N, 11.82; H, 7.62 %.

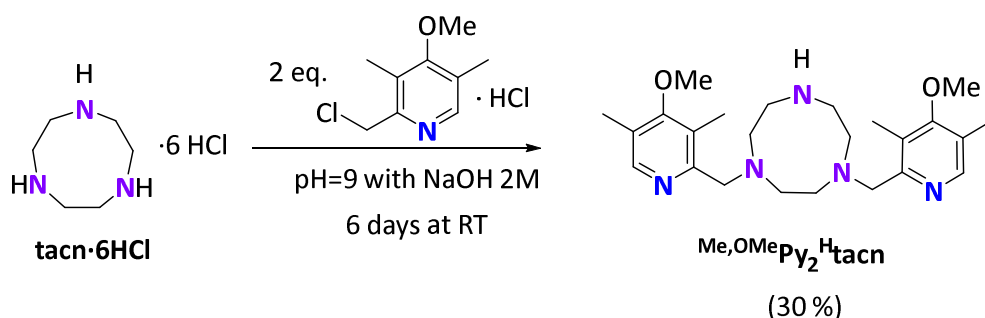
VIII.3.4.2. Synthesis of 4,7-bis(4-ethoxycarbonyl-2-pyridylmethyl)-7-(p-toluenesulfonyl)-1,4,7-triazacyclononane, ($^{\text{H,CO}_2\text{Et}}\text{Py}_2\text{Tstacn}$)



Scheme VIII. 3. Synthesis of $^{\text{H,CO}_2\text{Et}}\text{Py}_2\text{Tstacn}$.

Ligand $^{\text{H,CO}_2\text{Et}}\text{Py}_2\text{Tstacn}$ was synthesized following the same synthetic procedure that in $^{\text{Me,OMe}}\text{Py}_2\text{Tstacn}$ (93 %). $^1\text{H-NMR}$ (CDCl_3 , 300 MHz, 300 K) δ , ppm: 8.66 (dd, $^3J(\text{H,H})= 5.1$ Hz, $^3J'(\text{H,H})= 0.8$ Hz, 2H, **H_j**), 8.00 (dd, $^3J(\text{H,H})= 1.5$ Hz, $^3J'(\text{H,H})= 0.8$ Hz, 2H, **H_f**), 7.70 (dd, $^3J(\text{H,H})= 5.1$ Hz, $^3J'(\text{H,H})= 1.6$ Hz, 2H, **H_i**), 7.65 (d, $^3J(\text{H,H})= 8.3$ Hz, 2H, **H_c**), 7.27 (d, $^3J(\text{H,H})= 8.3$ Hz, 2H, **H_b**), 4.40 (q, $^3J(\text{H,H})= 7.1$ Hz, 4H, **H_e**), 3.95 (s, 4H, **H_k**), 3.27-3.17 (m, 8H, **H_d**), 2.84 (s, 4H, **H_e**), 2.40 (s, 3H, **H_a**), 1.39 (t, $^3J(\text{H,H})= 7.1$ Hz, 6H, **H_h**). $^{13}\text{C-NMR}$ (CDCl_3 , 75 MHz, 300K) δ , ppm: 165.64, 161.54, 150.11, 143.31, 138.45, 136.27, 129.91, 127.39, 122.71, 121.42, 63.67, 62.04, 56.00, 55.81, 51.03, 21.75, 14.49. ESI-MS: m/z : 610.3 $[\text{M}+\text{H}]^+$. Anal. Calcd for $\text{C}_{31}\text{H}_{39}\text{N}_5\text{O}_6\text{S}$: C, 61.07; N, 11.49; H, 6.45 %. Found: C, 60.95; N, 11.39 ; H, 6.36 %.

VIII.3.4.3. Synthesis 4-bis(4-methoxy-3,5-dimethyl-pyridine-2-ylmethyl)-1,4,7-triazacyclononane ($^{\text{Me,OMe}}\text{Py}_2\text{Htacn}$)

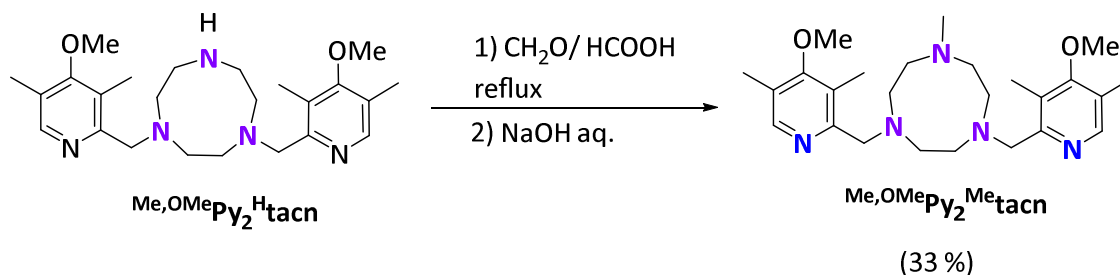


Scheme VIII. 4. Synthesis of $^{\text{Me,OMe}}\text{Py}_2\text{Htacn}$.

In a 100mL flask tacn·6HCl (1.0 g, 2.87 mmol), 4-methoxy-3,5-dimethyl-2-chloromethylpyridine hydrochloride (1.27 g, 5.74 mmol), water (30mL) and acetonitrile (25 mL) were mixed and stirred to achieve a complete dissolution. Then NaOH 2 M was

added to basificate to pH 9. The resulting red solution was stirred for 3 days at room temperature and then, NaOH 2 M was added again to readjust the pH to 9. The mixture was stirred another 3 days. After that the reaction was quenched by the addition of NaOH 2 M to pH 13. The solution was evaporated under reduced pressure and the resulting red oil was redissolved with NaOH 2 M and extracted with CH₂Cl₂ (3 x 60mL). The combined organic layers were then dried over anhydrous MgSO₄, filtered and the solvent was removed with rotary evaporator. The resulting crude red mixture was purified by basic alumina column chromatography (AcOEt : MeOH : drops of ammonia) to provide 0.365 g (0.85 mmol, 29.7 %) of the desired product. ¹H-NMR (CDCl₃, 400 MHz, 300K) δ, ppm: 10.82 (br, 1H, NH), 8.23 (s, 2H, H₂ of Py), 3.83 (s, 4H, N-CH₂-Py), 3.75 (s, 6H, 2xOCH₃), 3.05-2.97 (m, 8H, N-CH₂-CH₂), 2.76 (s, 4H, N-CH₂-CH₂), 2.24 (s, 6H, 2xCH₃), 2.17 (s, 6H, 2xCH₃). ¹³C-NMR (CDCl₃, 101 MHz, 300K) δ, ppm: 164.33, 155.85, 148.65, 125.56, 124.84, 60.02, 55.89, 51.86, 46.95, 13.31, 10.52. ESI-MS (m/z): 428.3 [M+H]⁺, 214.6 [M+2H]²⁺. Anal. Calcd for C₂₄H₃₇N₅O₂·CH₂Cl₂: C, 58.59; H, 7.67; N, 13.66 %. Found: C, 57.90; H, 8.33; N, 13.60 %.

VIII.3.4.4. Synthesis of 1-methyl-4,7-bis(4-methoxy-3,5-dimethyl-pyridine-2-ylmethyl)-1,4,7-triazacyclononane (Me,OMePy₂^Htacn)

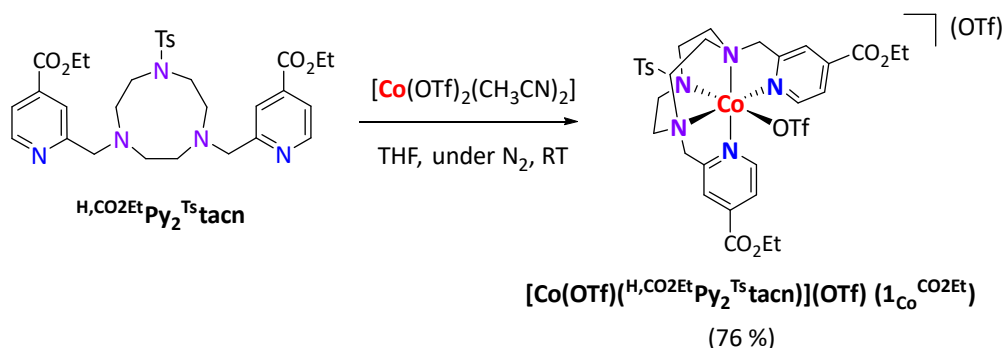


Scheme VIII. 5. Synthesis of Me,OMePy₂^{Me}tacn.

Me,OMePy₂^Htacn (0.35 g, 0.82 mmol) was dissolved in 37 % formaldehyde (3mL), 98 % formic acid (3mL) and water (2.5 mL) and the resulting yellow solution was refluxed for 30 hours. After cooling to room temperature, 3 mL HCl cc were added and the mixture was left stirring for 10 minutes. The solvent was removed under vacuum and a small amount of water (10 mL) was added to the resulting residue. The solution was brought to pH>14 by the addition of NaOH 4 M. After stirring 20 min at room temperature the aqueous layer was further extracted with 3x50mL CH₂Cl₂. The combined organic layers were dried over anhydrous MgSO₄ and the solvent was removed under reduced pressure. The resulting residue was treated with *n*-hexane (75 mL) and stirred for 12 hours. The mixture was filtered and the solvent from de yellow filtrates was removed under reduced pressure to yield 0.12 g of a colorless oil (0.27 mmol, 33 %). ¹H-NMR (CDCl₃, 400 MHz, 300 K) δ, ppm: 8.10 (s, 2H, H₂ of Py), 3.73 (s, 6H, 2xOCH₃), 3.63 (s, 4H, N-CH₂-Py), 2.83 (m, 4H, N-CH₂-CH₂), 2.70 (m, 4H, N-CH₂-CH₂), 2.54 (s, 4H, N-CH₂-CH₂), 2.34 (s, 6H, 2xCH₃), 2.21 (s, 6H, 2xCH₃), 2.19 (s, 3H, N-CH₃). ¹³C-NMR (CDCl₃, 101 MHz,

300K) δ , ppm: 164.10, 157.64, 148.22, 126.13, 124.97, 63.92, 59.79, 56.05, 55.71, 55, 44.90, 13.24, 11.27. ESI-MS (m/z): 442.3 $[M+H]^+$. Anal. Calcd for $C_{25}H_{39}N_5O_2 \cdot 1/3CH_2Cl_2$: C, 64.75; H, 8.51; N, 14.90 %. Found: C, 65.39; H, 8.77; N, 14.32 %.

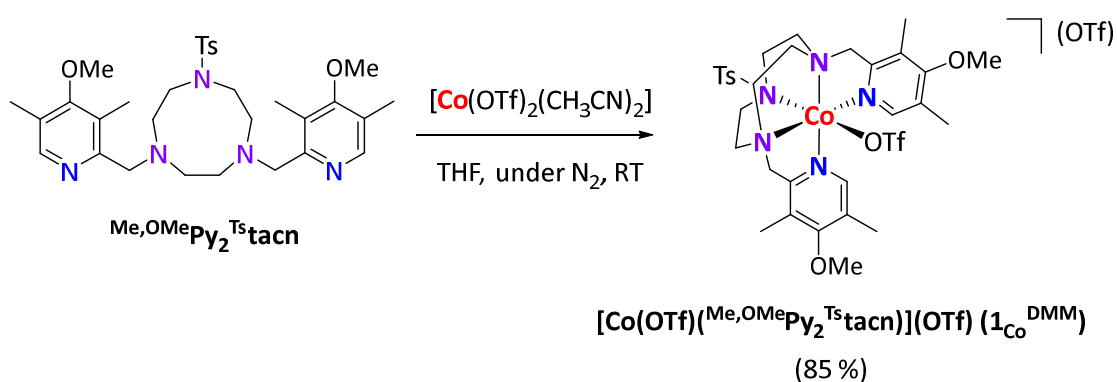
VIII.3.4.5. Synthesis of $[Co(OTf)(^{H,CO_2Et}Py_2^{Ts}tacn)](OTf)$



Scheme VIII. 6. Synthesis of $1_{Co}^{CO_2Et}$.

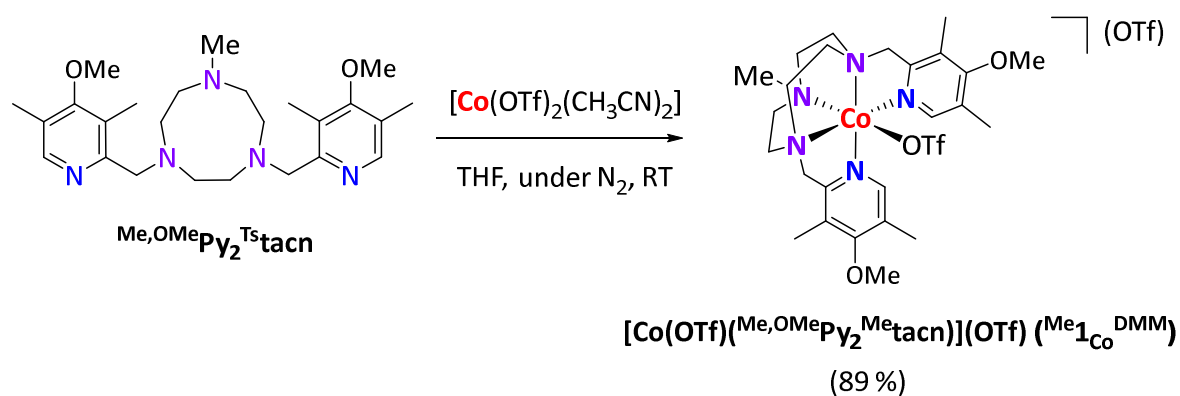
In a glovebox, a solution of $[Co(OTf)_2(MeCN)_2]$ (216 mg, 0.492 mmol) in anhydrous THF (1 mL) was added dropwise to a vigorously stirred solution of $^{H,CO_2Et}Py_2^{Ts}tacn$ (300 mg, 0.492 mmol) in THF (1 mL). After few minutes, the solution become cloudy and a brown precipitate appeared. After stirring for an additional 2 hours the solution was filtered off and the resulting solid dried under vacuum. The obtained solid was dissolved in CH_2Cl_2 (3 mL), filtered through Celite[®] and crystallized by slow diffusion of diethyl ether into CH_2Cl_2 yielding a 362 mg of a brown crystalline solid (0.373 mmol, 76 %). Anal. Calcd for $C_{33}H_{39}CoF_6N_5O_{12}S_3$: C, 41.00; N, 7.24; H, 4.07 %. Found: C, 40.89; N, 7.20; H, 4.14 %. HR-ESI-MS (m/z): 817.1469 $[M - OTf]^+$, 334.0976 $[M-2 \cdot OTf]^{2+}$.

VIII.3.4.6. Synthesis of $[Co(OTf)(^{Me,OMe}Py_2^{Ts}tacn)](OTf)$



Scheme VIII. 7. Synthesis of 1_{Co}^{DMM} .

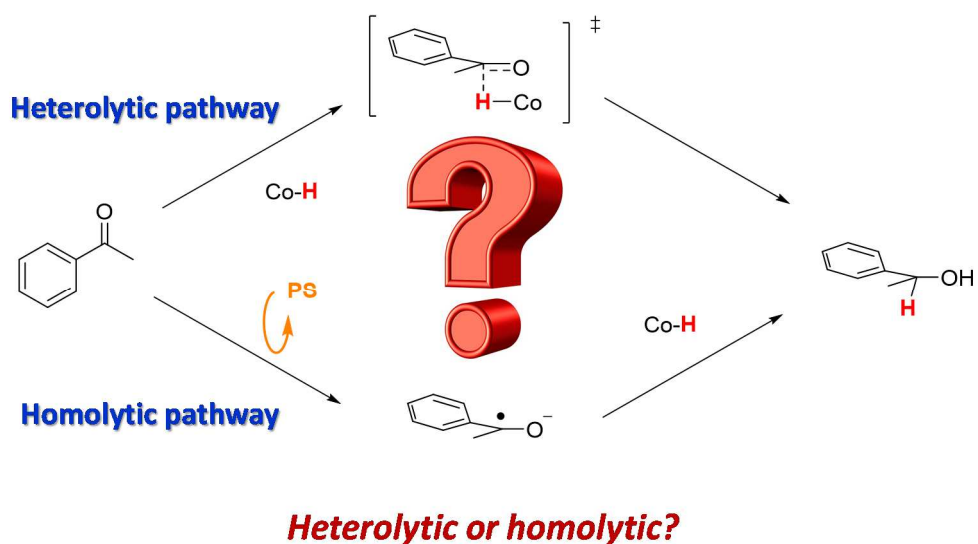
1_{Co}^{DMM} as a crystalline pink solid was synthesized following the same synthetic procedure as described for complex $1_{Co}^{CO_2Et}$ (85 %). Anal. Calcd for $C_{33}H_{43}CoF_6N_5O_{10}S_3$: C, 42.22; N, 7.46; H, 4.62 %. Found: C, 42.53; N, 7.64 ; H, 4.59 %. HR-ESI-MS (m/z): 789.1889 $[M - OTf]^+$, 320.1190 $[M-2 \cdot OTf]^{2+}$.

VIII.3.4.7. Synthesis of $[\text{Co}(\text{OTf})(^{\text{Me,OMe}}\text{Py}_2^{\text{H}}\text{tacn})](\text{OTf})$ Scheme VIII. 8. Synthesis of $\text{Me}_1\text{Co}^{\text{DMM}}$.

$\text{Me}_1\text{Co}^{\text{DMM}}$ was synthesized in analogous manner as the $\text{Me}_1\text{Co}^{\text{DMM}}$ complex, obtaining 145 mg of red crystals (0.181 mmol, 89 %). $^1\text{H-NMR}$ (CD_2Cl_2 , 400 MHz, 400 K) δ , ppm: 42.09, 15.95, 4.17, 3.98, 2.84, 2.70, 2.55, 2.46, 2.24, -1.239. Anal. Calcd for $\text{C}_{27}\text{H}_{39}\text{CoF}_6\text{N}_5\text{O}_8\text{S}_2$: C, 40.6; N, 8.77; H, 4.92 %. Found: C, 40.27; N, 8.66; H, 4.74 %. ESI-MS (m/z): 649.13 $[\text{M-OTf}]^+$, 250.01 $[\text{M-2OTf}]^{2+}$.

CHAPTER IX

Mechanistic Studies on Photochemical Reduction of Ketones Catalyzed by Cobalt Complexes



IX. MECHANISTIC STUDIES ON PHOTOCHEMICAL REDUCTION OF KETONES CATALYZED BY COBALT COMPLEXES

IX.1. STATE-OF-THE ART

Photochemical and electrochemical hydrogen evolution catalyzed by molecular cobalt complexes is proposed to occur through the formation of a Co-H species by the protonation of a Co^I intermediate.^{101,113,136,142,349} In Chapter VII we have described the chemical synthesis, characterization and basic reactivity of the formal Co^I intermediate [Co(Cl)(Py₂T^stacn)]. Despite extensive mechanistic studies,^{130,136} the difficulty to characterize some key intermediates, such as the cobalt hydride species,^{131,132,134} still keeps the mechanistic proposals under debate.^{88,105,130,135-137} In general, for the aminopyridine cobalt complexes two different catalytic mechanism may operate, the so call heterolytic and homolytic one. In the heterolytic mechanism, the metal hydride intermediate, either Co^{II}-H or Co^{III}-H, undergoes a protonation to form hydrogen.⁸³ Several theoretical calculations by DFT calculations support the heterolytic mechanism involving a Co^{II}-H derived from the reduction of Co^{III}-H of as the intermediate species from which H₂ is evolved.^{126-128,355} On the other hand, in the proposed homolytic mechanism, a bimolecular hydrogen atom transfer reaction between two Co^{III}-H species forms a H₂ molecule and two Co^{II} species.^{130,402,495} It is important to note that both pathways can coexist,¹³⁶ and that switching from an heterolytic to an homolytic pathway can simply be a matter of experimental conditions, such as the relative concentration of the species involved in the reaction.^{137,150}

On the other hand, the hydrogenation of ketones, aldehydes and olefins catalyzed by organometallic cobalt complexes it is proposed to proceed through cobalt hydride intermediates.^{450,463,464,466} These cobalt hydrides have such a higher reactivity that can even hydrogenate CO₂.⁴⁹⁶

Hydrogen atom (H·) transfer (HAT) from transition-metal hydrides to organic molecules is an important step for a large number of transformations.⁴⁹⁷ For instance, HAT pathways have been proposed in alkene reduction with chromium,⁴⁹⁸ tungsten,⁴⁹⁹ vanadium,⁵⁰⁰ manganese⁵⁰¹ and cobalt⁵⁰² hydrides. In the case of cobalt complexes, in 1975 Halpern discovered the capacity of the *in situ* generated (CO)₄CoH to reduce

anthracene *via* a HAT mechanism.^{502,503} Since then, cobalt complexes have been used as HAT catalysts in organic transformations such as acrylate polymerization,⁵⁰⁴ reduction of olefins^{505,506} or cyclizations.^{497,507,508} Recently, it has been applied the use of cobaloximes⁵⁰⁷ for radical cyclizations of olefins triggered by H₂ gas as source hydrogen atoms. The authors proposed a Co^{III}-H as key intermediate responsible for the HAT event.⁵⁰⁷

In Chapter VII we showed that our set of cobalt complexes are efficient catalysts for the reduction of aromatic ketones and aldehydes under typical photocatalytic conditions for hydrogen evolution. Moreover, our preliminary mechanistic studies suggested that the activity belongs to a well-defined molecular cobalt species. Additionally, competition experiments between water and acetophenone reduction suggested that a common Co-H species are involved in both catalytic cycles.

However the reaction mechanism can be more complex for the reduction of organic substrates. Under our standard catalytic conditions, we observed the formation of small quantities of pinacol dimer only in the case of the electron poor substrate 3'-chloroacetophenone (**9t**) (Yield **9t-pinacol**: 7% using **PS_{Ir}** and 19% using **PS_{Cu}**). In the blank experiments, without the presence of the cobalt complex, we observed the formation of significant amounts of pinacols for the most electron poor ketones such as **9a-b**, **9h-j**, **9n-p** and **9s-u**. Pinacols are formed in the absence of cobalt and mainly inhibited in its presence. These results indicate that the ketyl radical anion⁵⁰⁹ could be formed under catalytic conditions and therefore needs to be considered in the mechanistic proposal.² Moreover, these data is consistent with the formation of pinacols using photoredox catalysts reported by Rueping and co-workers.²⁴⁹

With this considerations in mind, we postulate two different mechanistic scenarios for the reduction of ketones, which are illustrated in Figure IX. 1.^{83,88,136,145,148}

² The pK_a of the ketyl radical anion is 9.9 ± 0.2, therefore under catalytic conditions, pH around 12 we expect the ketyl radical anion to be present in solution instead of the ketyl radical. (ref 509)

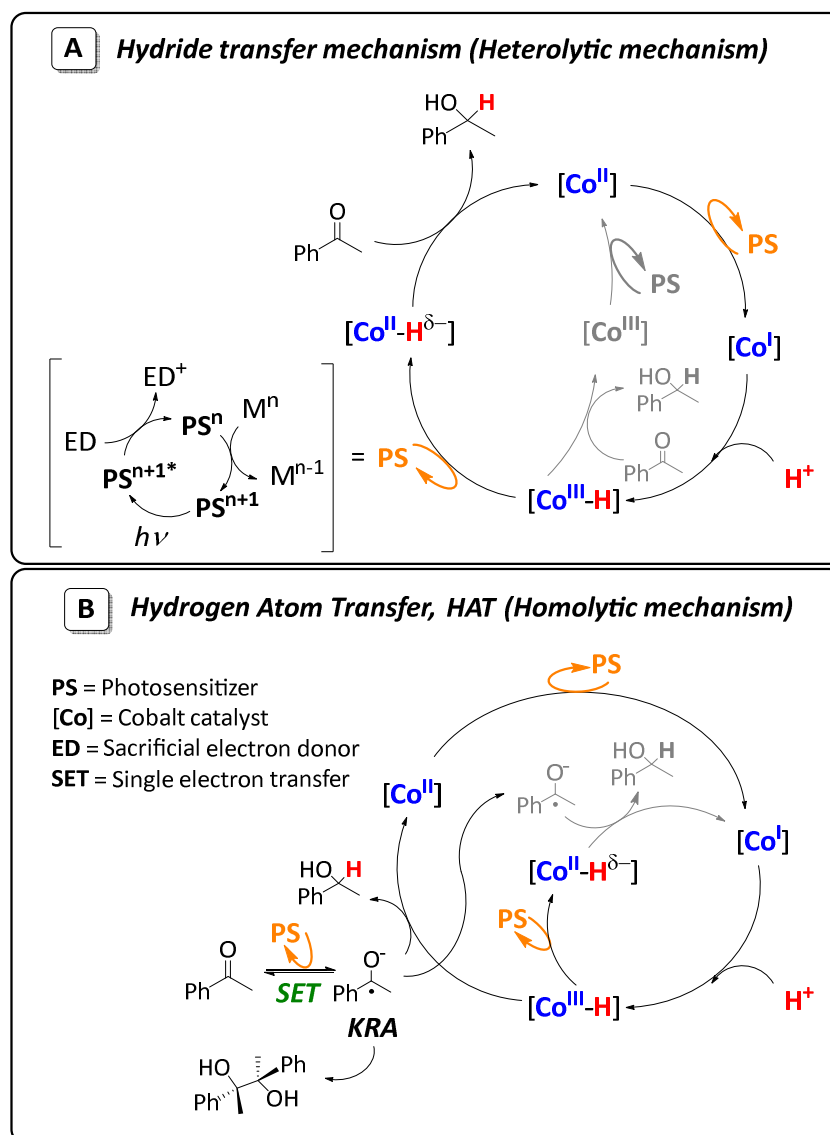


Figure IX. 1. Homolytic and heterolytic mechanisms for ketone reduction catalyzed by a molecular cobalt complex.

- A heterolytic pathway where the putative Co-H species formed in solution acts as hydride donor to the ketone. The photoredox catalyst in combination with the electron donor (Et_3N) reduces the cobalt complex but not the ketone. The formation of alcohol only depends on the regeneration of the active cobalt hydride species (Figure IX. 1, A). $\text{Co}^{\text{II}}\text{-H}^{140-142}$ species are postulated to directly transfer the hydride to the ketone to form the alcoholate/alcohol.^{2,43,44}
- A homolytic pathway where the formation of alcohol takes place through the prior formation of a ketyl radical anion (KRA) intermediate. The KRA is formed in very low concentration by the action of the photoredox catalyst, as suggested by the pinacol formation in the blank experiments. Then, the formed KRAs are

rapidly trapped by the Co-H species *via* a hydrogen atom transfer (HAT) mechanism. This pathway is also supported by the HAT mechanisms operative in the reduction of unsaturated substrates by Co^{III}-H cobaloximes.^{507,510}

IX.2. RESULTS AND DISCUSSION

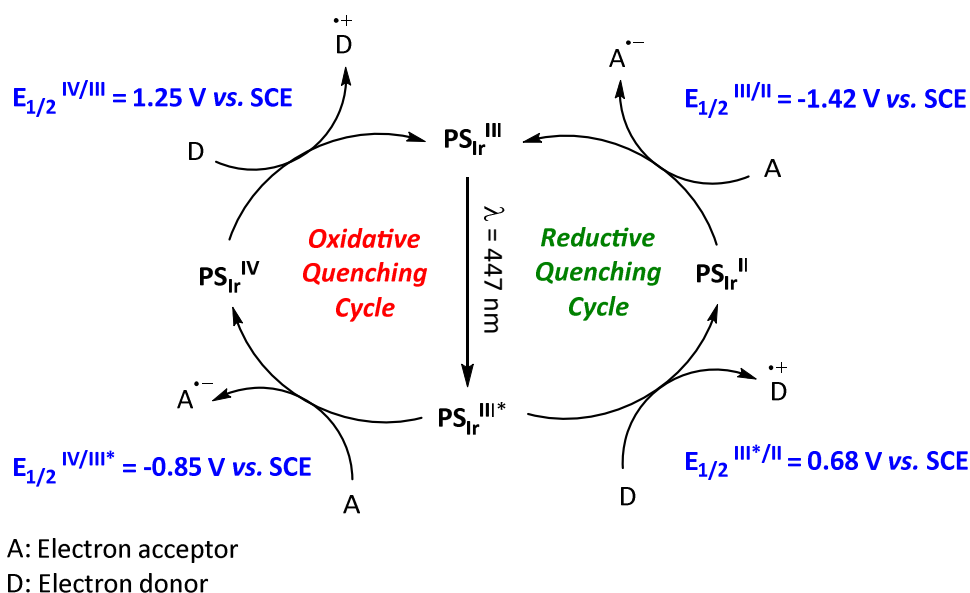
The main aim of this chapter is to shed some light on the operative mechanism of the light-driven ketone and aldehyde reduction presented in Chapter VII. With this purpose we have studied: **2.1)** the **PS_{Ir}** photoredox cycle; **2.2)** the catalytic reactivity of substrates including radical clocks and the relationship between reactivity and redox potentials and **2.3)** the characteristics of the transition state (free energy relationships, labelling studies and kinetics) by experimental studies. In addition, and in collaboration with Dr. F. Acuña, we have extracted information about the mechanism by theoretical modelling (section 2.4). All the studies have been performed with **1_{Co}** due its good performance and mainly with **PS_{Ir}** in order to facilitate the study. We have rationalized how the electronic effects at the substrates and at the metal center influence the reactivity, according to the proposed mechanism.

IX.2.1. Studies on the [Ir(ppy)₂(bpy)](PF₆) Photoredox Cycle

Before analyzing the mechanism, it is informative to consider the photochemistry of the prototypical photoredox catalyst [Ir(ppy)₂(bpy)](PF₆) (**PS_{Ir}**). The overall system for the photoinduced electron transfer can be described as represented in Scheme IX. 1. Basically, the photoredox catalyst undergoes three stages: photoexcitation, electron transfer and regeneration of the ground state. The process starts with the absorption of the photon promoting the excitation of one electron from the metal to a ligand-centered π^* orbital (**PS_{Ir}^{III*}**). This generates a long-lived triplet state [***Ir(ppy)₂(bpy)**]⁺ (**PS_{Ir}^{III*}**) species ($\tau_0 = 390$ ns)²⁹⁵ that can trigger single electron transfer (SET) process. (Scheme IX. 1). The photoexcited species are both more oxidizing and more reducing than the ground-state species. For instance, the redox couple **PS_{Ir}^{IV/III*}** ($E_{1/2}^{IV/III*} = -0.85$ vs. SCE) shows that **PS_{Ir}^{III*}** is more reductive than the ground state **PS_{Ir}^{III}** ($E_{1/2}^{IV/III} = 1.25$ vs. SCE). At the same time, the redox couple **PS_{Ir}^{III*/II}** ($E_{1/2}^{III*/II} = 0.68$ vs. SCE) is significantly more oxidizing than the ground state **PS_{Ir}^{III}** ($E_{1/2}^{III/II} = -1.42$ vs. SCE).^{295,511}

Accordingly, **PS_{Ir}^{III*}** species act as oxidant or as reductant depending on the reactants in the reaction media, by the so called reductive or oxidative quenching cycles, respectively.¹⁹⁷ In the oxidative quenching **PS_{Ir}^{III*}** reduces the electron acceptor (A) generating the strong oxidant **PS_{Ir}^{IV}** ($E_{1/2}^{IV/III} = 1.25$ vs. SCE) that is able to carry out

further chemical transformations. Alternatively, $\text{PS}_{\text{Ir}}^{\text{III}*}$ operates as an oxidant against electron donors to give the reduced species $\text{PS}_{\text{Ir}}^{\text{II}}$, forming a strong reductant ($E_{1/2}^{\text{III}/\text{II}} = -1.42$ vs. SCE) (Scheme IX. 1). The most common reductive quenchers are tertiary amines like Et_3N .²⁰¹



Scheme IX. 1. Oxidative and reductive quenching cycle of PS_{Ir} .

Therefore, we initially studied the quenching properties of PS_{Ir} with **9a**, **1c_o** and Et_3N under our experimental conditions by fluorescence quenching experiments. In addition, we have further studied the reaction of the *in-situ* formed $\text{PS}_{\text{Ir}}^{\text{II}}$ under continuous light irradiation against **1c_o** and with **9a**.

IX.2.1.1. Fluorescence quenching studies. We have examined the excited state fluorescence quenching of PS_{Ir} in the presence of the different molecular species involved in the catalytic reaction. It is known that upon excitation, the PS_{Ir} ($\lambda_{\text{exc}} = 450$ nm) generates an excited species in the single state that fully evolves to the triplet excited state ($\text{PS}_{\text{Ir}}^{\text{III}*}$). These species undergoes a characteristic emission with a λ_{max} at 584 nm (Figure VII. 8). The decrease in the fluorescence intensity of $\text{PS}_{\text{Ir}}^{\text{III}*}$ upon concomitant addition of different concentrations of the quencher refers the presence of non-radiative deactivation mechanism of $\text{PS}_{\text{Ir}}^{\text{III}*}$ *via* aggregation, electron transfer, and energy transfer processes between $\text{PS}_{\text{Ir}}^{\text{III}*}$ and the quencher (Et_3N , cobalt catalyst or acetophenone).

The relationship between the concentration of quencher and the emission intensity can be studied by the Stern-Volmer equation and it allows us to obtain the quenching constant (k_q) between $\text{PS}_{\text{Ir}}^{\text{III}*}$ and the quencher:

$$\frac{I_0}{I} = 1 + k_q \tau_0 [Q] \quad (\text{Eq. IX. 1})$$

Where I_0 : emission of $\text{PS}_{\text{Ir}}^{\text{III}*}$ in the absence of quencher, I : emission of $\text{PS}_{\text{Ir}}^{\text{III}*}$ in the presence of quencher, k_q : quenching rate constant, λ_0 : excited-state lifetime in the absence of quencher, $[Q]$: concentration of quencher.

The fluorescence quenching studies have been performed with Et_3N (0 - 0.93 M), **9a** (0 - 35 mM) and **1c_o** (0 - 2.4 mM) as quenchers in the concentration range of the catalytic studies. As depicted in the Figure IX. 2, the addition of Et_3N promotes a significant fluorescence quenching of the excited species $\text{PS}_{\text{Ir}}^{\text{III}*}$. The plot of the ratio I_0/I against $[\text{Et}_3\text{N}]$ gave rise to a straight line having a y -intercept equal to 1 and a slope proportional to the quenching rate constant. Using the λ_0 value measured by Single-Photon Counting under our catalytic conditions ($\tau_0 = 153$ ns), the quenching rate constant was determined to be $k_q = 1.52 \cdot 10^7 \text{ M}^{-1} \cdot \text{s}^{-1}$. This value is in agreement with the studies reported in the literature for a single-electron transfer reductive quenching of $\text{PS}_{\text{Ir}}^{\text{III}*}$ with Et_3N ($k_q = 1.9 \cdot 10^7 \text{ M}^{-1} \cdot \text{s}^{-1}$ MeCN:H₂O (4:1)).³⁹¹ No fluorescence oxidative quenching of $\text{PS}_{\text{Ir}}^{\text{III}*}$ was observed for **9a** and **1c_o** under catalytic concentration. Therefore, we can conclude that Et_3N is the only fluorescence quencher under catalytic conditions.^{303,391,512,513} The fluorescence quenching experiments along with the formation of new Ir species when the cuvette is irradiated (shown in Chapters III and IV) suggest that the reductive quenching is the operative mechanism, through the formation of $\text{PS}_{\text{Ir}}^{\text{II}}$.³⁴⁴ Flash photolysis experiments also support this hypothesis.³⁰³

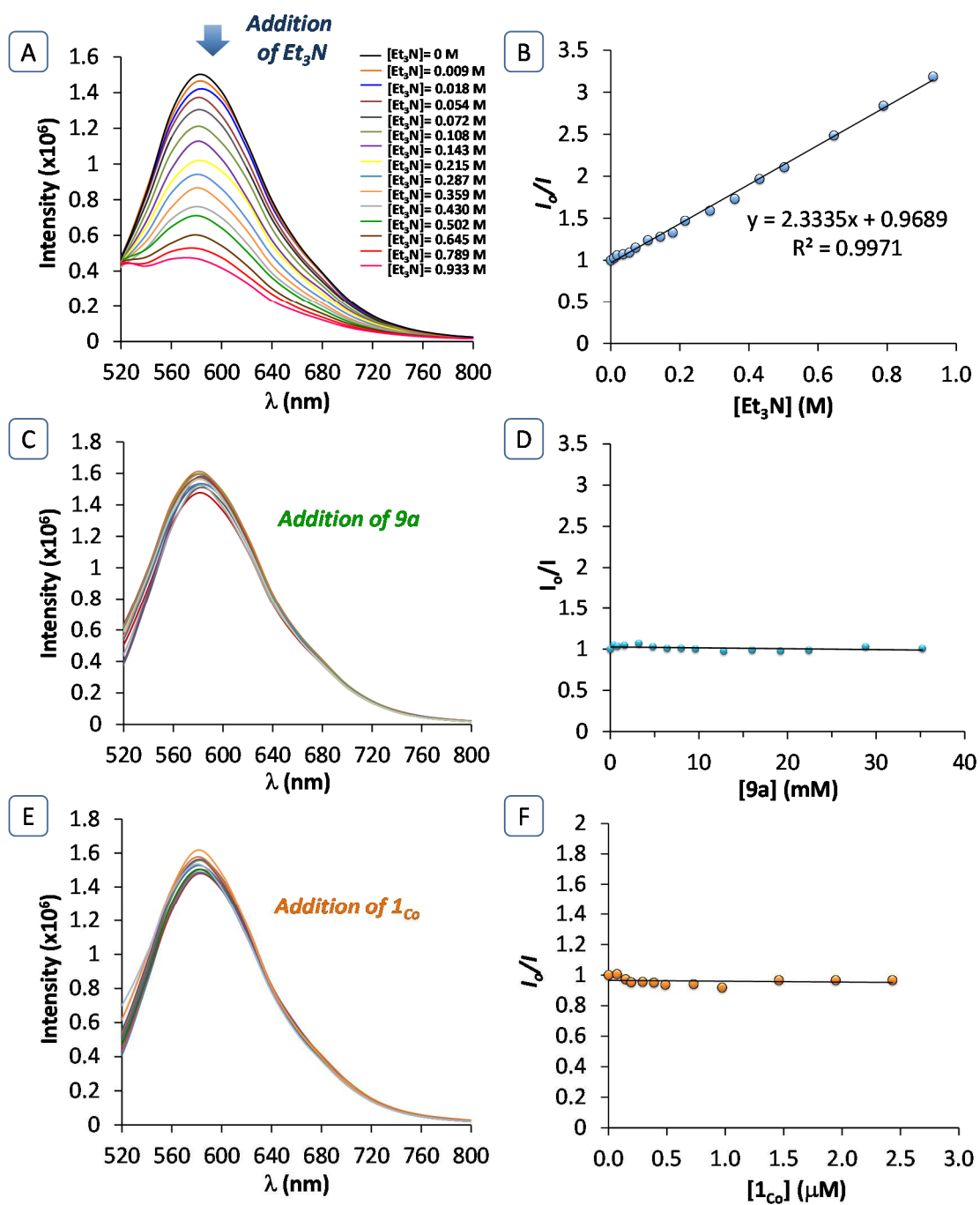
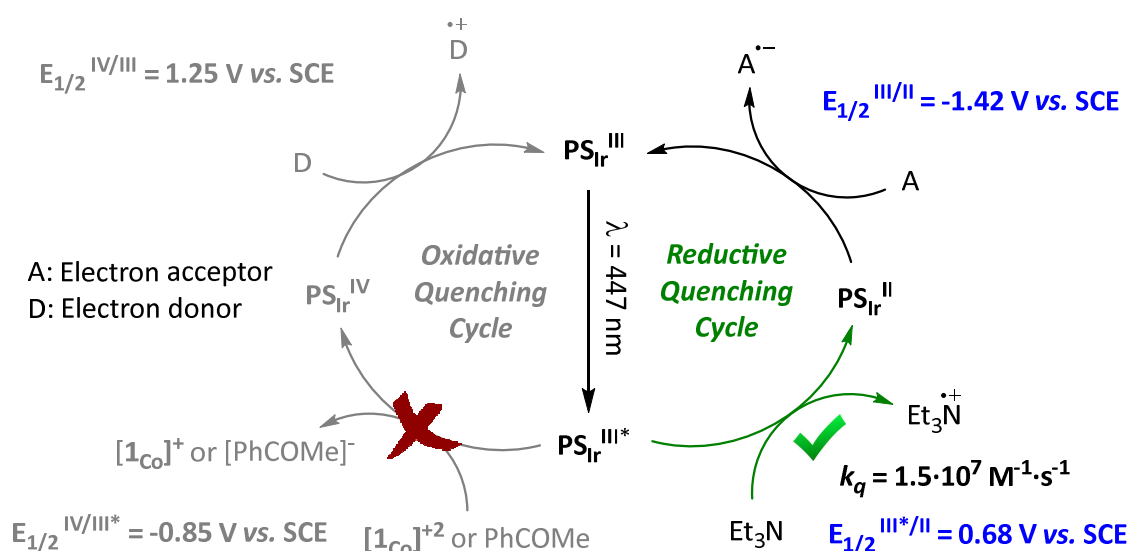


Figure IX. 2. Emission spectra of PSIr upon excitation at 450 nm in the presence of different concentrations Et_3N (A), **9a** (C) and **1_{co}** (E). Stern-Volmer plot for photoluminescence quenching of PSIr by Et_3N (B), **9a** (D) and **1_{co}** (F).



Scheme IX. 2. Plausible oxidative quenching pathway of $\text{PS}_{\text{Ir}}^{\text{III}*}$ through Et_3N as electron donor.

IX.2.1.2. In-Situ Synthesis and Reactivity of $\text{PS}_{\text{Ir}}^{\text{II}}$ with 1_{Co} and $9a$. If a reductive quenching pathway is operative in the photocatalytic cycle, this should provide the generation of the photoreduced photosensitizer ($\text{PS}_{\text{Ir}}^{\text{II}} = [\text{Ir}^{\text{II}}(\text{ppy})_2(\text{bpy})]\text{PF}_6$).³⁴⁴ Then, this $\text{PS}_{\text{Ir}}^{\text{II}}$ could perform a single electron transfer to a one electron acceptor, and thus recovering the initial $\text{PS}_{\text{Ir}}^{\text{III}}$ species. Therefore, we have studied the reaction of $\text{PS}_{\text{Ir}}^{\text{II}}$ with the cobalt catalyst 1_{Co} and $9a$ (as plausible electron acceptors) by UV/Vis spectroscopy in a similar manner as described in Chapter IV. Prior to this study, we have optimized the reaction conditions in order to extend the stability of $\text{PS}_{\text{Ir}}^{\text{II}}$ and ensure the complete solubility. The reduced photosensitizer $\text{PS}_{\text{Ir}}^{\text{II}}$ was generated *in-situ* by irradiating ($\lambda = 447 \text{ nm}$, about $5 \pm 5 \cdot 10^{17} \text{ photons} \cdot \text{s}^{-1}$) a MeCN:H₂O (0.8:1.2) solution containing PS_{Ir} (50 μM) and Et_3N (100 mM) as electron donor under strict anaerobic conditions. The irradiation was conducted at 5°C in order to minimize the decomposition of $\text{PS}_{\text{Ir}}^{\text{II}}$.⁵¹⁴ Decomposition of $\text{PS}_{\text{Ir}}^{\text{II}}$ can be most likely attributed to a ligand dissociation as previously observed by Bernhard *et al.*⁵¹⁵⁻⁵¹⁷ The reaction was followed by UV/Vis. Figure IX. 3 shows the monitored absorbance at 527 nm and U/Vis spectra on key stages of the light-driven reduction of $\text{PS}_{\text{Ir}}^{\text{III}}$ to $\text{PS}_{\text{Ir}}^{\text{II}}$ and the reaction with 1_{Co} . During the dark regime, complex PS_{Ir} remains unchanged (Figure IX. 3, Spectrum A). The irradiation of the cuvette triggers the formation of new signals corresponding to $\text{PS}_{\text{Ir}}^{\text{II}}$ (Figure IX. 3, Spectrum B), which after around 100 s arrives to a static concentration. This static concentration lasts for about 20 s (Figure IX. 3, Spectrum C). $\text{PS}_{\text{Ir}}^{\text{II}}$ presents new UV/Vis bands at λ_{max} values of 385, 495 and 527 nm (Figure IX. 3). While the $\text{PS}_{\text{Ir}}^{\text{II}}$ static concentration regime was

achieved (ca. 100 s) $\mathbf{1}_{\text{Co}}$ was added to the UV/Vis cuvette through a syringe under N_2 . The addition of $\mathbf{1}_{\text{Co}}$ promoted the fast vanishing of the absorption bands belonging to PSIr^{II} (< 2 s, mixing time) (Figure IX. 3, Spectrum D). Then, PSIr^{II} species was partly regenerated upon irradiation (Figure IX. 3, Spectrum E, F). Based on these results, along with the fluorescence quenching experiments, we propose that the excited state $\text{PSIr}^{\text{III}*}$ is reductively quenched by Et_3N to give strong reducing PSIr^{II} species ($E(\text{PSIr}^{\text{III}/\text{II}}) = -1.42 \text{ V vs SCE}$).²⁹⁵ The fast decay of the PSIr^{II} UV/Vis features with a concomitant formation of PSIr^{III} by the addition of $\mathbf{1}_{\text{Co}}$ implies a fast electron transfer from PSIr^{II} to $\mathbf{1}_{\text{Co}}$ to give PSIr^{III} and a formal $\mathbf{1}_{\text{Co}}^{\text{I}}$. This is in agreement with the redox potential of the $\text{Co}^{\text{II/I}}$ redox couple of $\mathbf{1}_{\text{Co}}$ ($E_{1/2} = -1.1 \text{ V vs SCE in MeCN}$). Since we work in aqueous media, the putative $\{\text{Co}^{\text{I}}\}$ generated can be protonated to form $\{\text{Co}^{\text{III}}\text{-H}\}$. Under this conditions it should be quickly reduced to $\{\text{Co}^{\text{II}}\text{-H}\}$ forming H_2 by protonation and recover the starting $\{\text{Co}^{\text{I}}\}$. This cobalt catalytic cycle establishes an equilibrium with the photoredox mechanism leading to a recovery of certain amount of PSIr^{II} . Therefore, the $\mathbf{1}_{\text{Co}}$ catalytic cycle cannot efficiently consume all the PSIr^{II} photogenerated under this conditions.

Then, we titrated the *in-situ* obtained PSIr^{II} by analyzing the PSIr^{II} consumption versus the amount of $\mathbf{1}_{\text{Co}}$ added to the solution (Figure IX. 5). As expected, the PSIr^{II} consumption increases upon increasing the amount of $\mathbf{1}_{\text{Co}}$ added (Figure IX. 4 and Figure IX. 5). From the titration experiment it can be estimated that the concentration of PSIr^{II} generated under this conditions was around $7.5 \mu\text{M}$ (Figure IX. 4). This value is 15% of the initial concentration of PSIr^{III} ($50 \mu\text{M}$), suggesting an equilibrium between PSIr^{III} and PSIr^{II} species. On the basis of the titration results we estimated an extinction coefficient of $13800 \text{ M}^{-1}\cdot\text{cm}^{-1}$ at a λ value of 527 nm for PSIr^{II} . We noticed that in this region, PSIr^{II} is the only compound in solution that has a strong absorption. PSIr^{III} , $\mathbf{1}_{\text{Co}}$ and $\mathbf{1}_{\text{Co}}^{\text{I}}$ do not present any absorption in this spectral window.

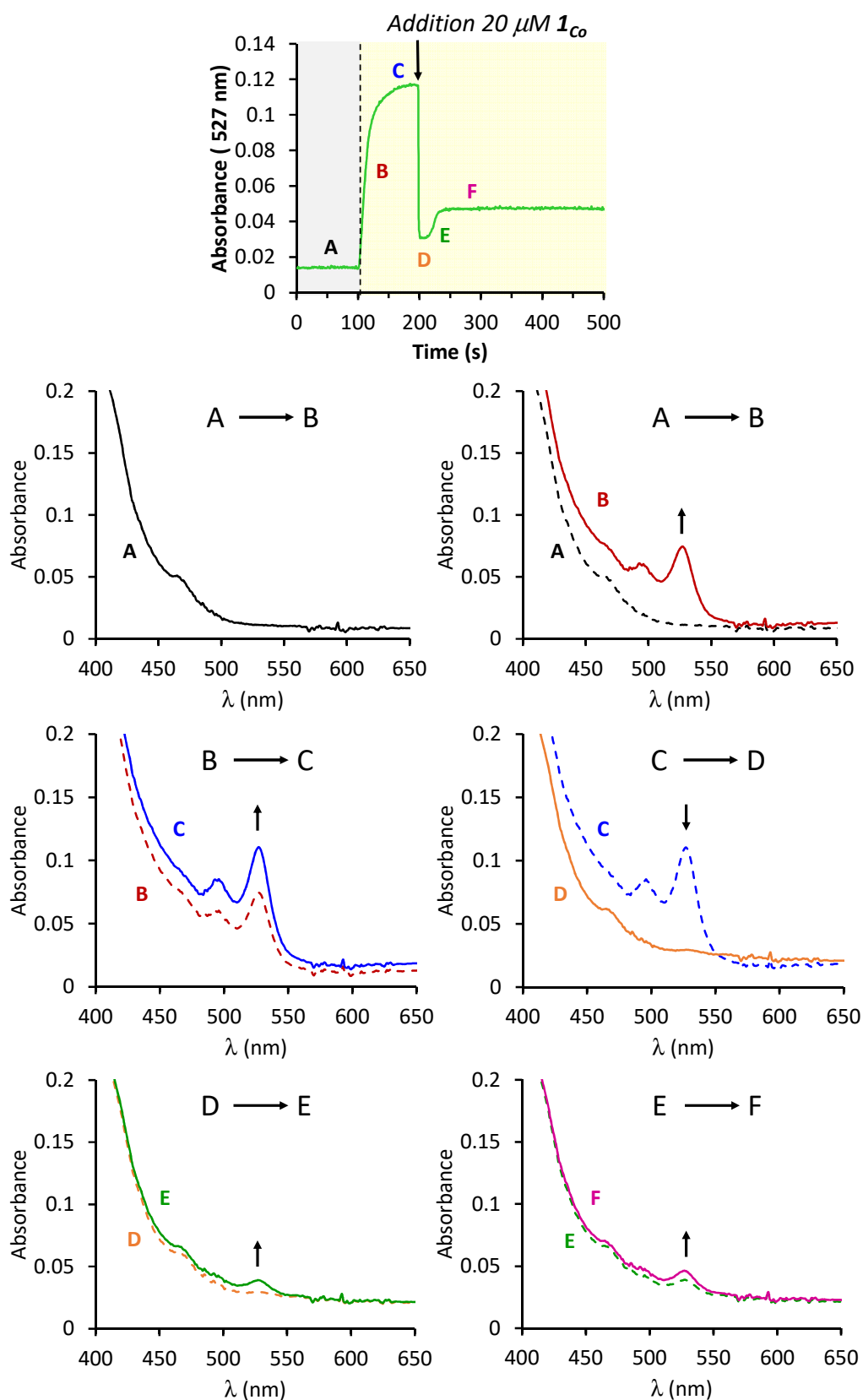


Figure IX. 3. UV/Vis spectra at different irradiation times (447 nm). A) In dark. After B) 10 s of irradiation, C) after 100 s irradiation. D) After the addition of 1_{Co} . E) At half regeneration of PS_{Ir}^{II} after the addition of 1_{Co} . F) At fully regeneration of PS_{Ir}^{II} after the addition of 1_{Co} .

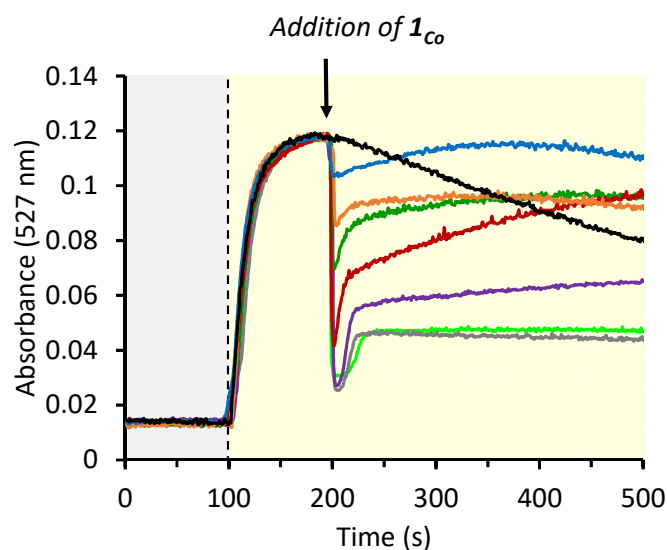


Figure IX. 4. UV/Vis monitoring ($\lambda = 527$ nm) of PSIr^{III} photoreduction with Et_3N to form PSIr^{II} at $\lambda = 447$ nm and subsequent addition of different amounts of $\mathbf{1}_{\text{Co}}^{\text{II}}$ catalyst: 0 μM “self-decay” (black), 1.25 μM (blue), 2.5 μM (orange), 5 μM (green), 7.5 μM (red), 10 μM (purple), 12.5 μM (grey) and 20 μM (light green). Conditions: $[\text{PSIr}^{\text{III}}] = 50$ μM , $\text{Et}_3\text{N} = 2000$ eq., $V_{\text{total}} = 2$ mL, $\text{CH}_3\text{CN} : \text{H}_2\text{O} (0.8 : 1.2)$ at 5°C , under N_2 .

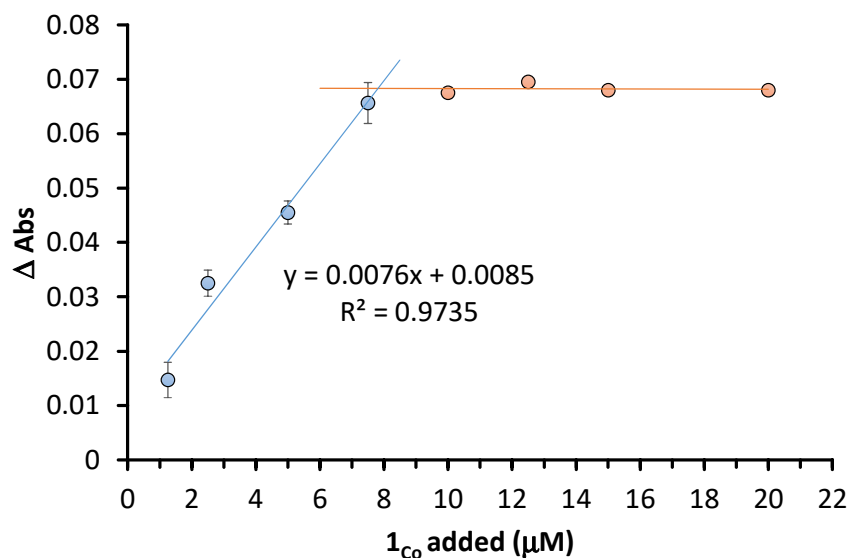


Figure IX. 5. Titration of the photogenerated PSIr^{II} species with $\mathbf{1}_{\text{Co}}$. Consumption extent (Δ Abs (at $\lambda = 527$ nm)) of the PSIr^{II} species at different additions of $\mathbf{1}_{\text{Co}}$. Values are duplicate average.

The addition of acetophenone (**9a**, 10 μM) instead of $\mathbf{1}_{\text{Co}}$ also promoted the vanishing of the spectral feature of PSIr^{II} , but with a kinetic profile equivalent to the blank (Figure IX. 6) that could be attributed to a reaction with O_2 . The pinacol formation

contribution, if it exists, is very small and in agreement with the catalytic blank experiments in the absence of cobalt, where small quantities of pinacols are formed.

These experiments show that the reduction of $\mathbf{1}_{\text{Co}}$ ($E(\text{Co}^{\text{II/I}}) = -1.1 \text{ V vs. SCE}$ in MeCN) by the $\text{PS}_{\text{Ir}}^{\text{II}}$ species is much feasible than the ketone reduction and in line with the redox potential values of $\text{PS}_{\text{Ir}}^{\text{III/II}}$, $\mathbf{9a}^{0/-1}$ and $\mathbf{1}_{\text{Co}}^{\text{II/I}}$. Nevertheless, the feasibility of an electron transfer to the ketone, lead us to consider the possible formation of small amounts of KRA in solution that could be involved in the mechanism.

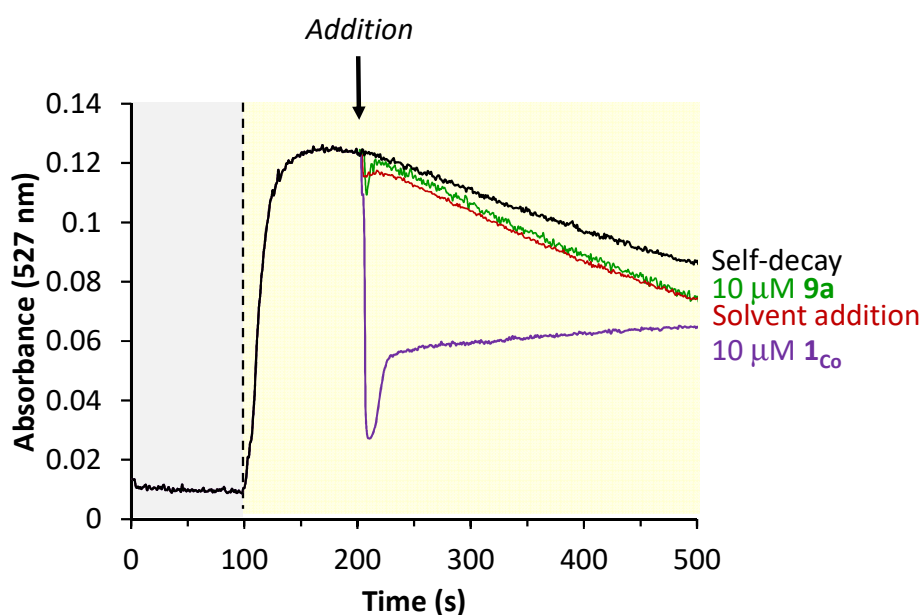
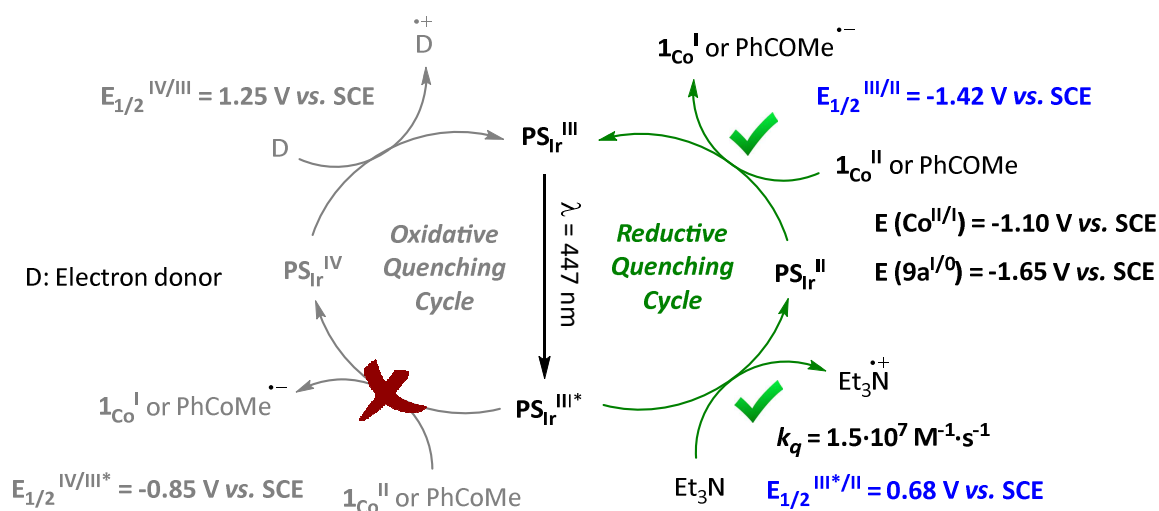


Figure IX. 6. UV/Vis monitoring ($\lambda = 527 \text{ nm}$) of $\text{PS}_{\text{Ir}}^{\text{III}}$ photoreduction with Et_3N to form $\text{PS}_{\text{Ir}}^{\text{II}}$ at $\lambda = 447 \text{ nm}$ and subsequent addition of solvent alone (red trace), $10 \mu\text{M}$ of $\mathbf{9a}$ (green trace) and $10 \mu\text{M}$ $\mathbf{1}_{\text{Co}}$ (purple trace). Conditions: $[\text{PS}_{\text{Ir}}^{\text{III}}] = 50 \mu\text{M}$, $\text{Et}_3\text{N} = 2000 \text{ eq.}$, reaction volume = 2 mL , $\text{CH}_3\text{CN}:\text{H}_2\text{O}$ ($0.6 : 1.4$) at 5°C , under N_2 .

In summary, the photoredox catalyst is reductively quenched by Et_3N forming the strong reductant $\text{PS}_{\text{Ir}}^{\text{II}}$, which is able to reduce $\mathbf{1}_{\text{Co}}^{\text{II}}$ to $\mathbf{1}_{\text{Co}}^{\text{I}}$ or the substrate to, most probably, KRA. The redox potential and the reactivity of $\text{PS}_{\text{Ir}}^{\text{II}}$ with $\mathbf{1}_{\text{Co}}$ and $\mathbf{9a}$ shows that the electron transfer to the ketone is thermodynamically less favorable than to the cobalt complex. Finally, the last electron transfer recovers the initial $\text{PS}_{\text{Ir}}^{\text{III}}$ species restarting the photocatalytic cycle (Scheme IX. 3).



Scheme IX. 3. Plausible reductive quenching pathway operating under photocatalytic conditions for PSIr through Et_3N as electron donor and the subsequent oxidation of the PSIr^{II} .

IX.2.2. Reactivity Studies

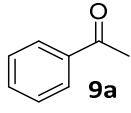
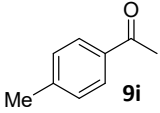
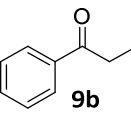
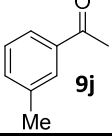
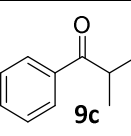
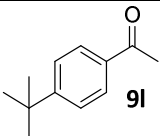
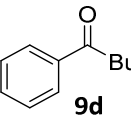
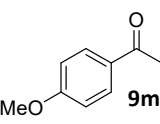
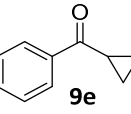
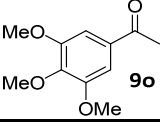
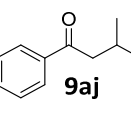
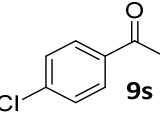
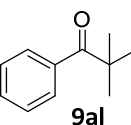
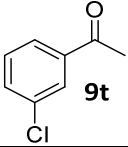
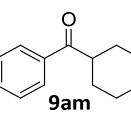
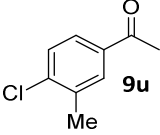
In order to get further insight into the postulated presence of KRAs under photocatalytic conditions and the implications in the photocatalytic mechanism we have analyzed with further details: i) the formation of pinacols, ii) the reduction of substrates that cannot form KRAs and iii) the reactivity of radical clocks.

IX.2.2.1. Formation of pinacols

As shown in Chapter VII, photocatalytic studies in absence of $\mathbf{1Co}$ show the formation of pinacols. This is attributed to the dimerization of KRAs²⁴⁹ generated by the photoredox catalyst.^{205,209,249,518}

Interestingly, the formation of pinacol was dependent on the ketone employed and the conditions. For instance, pinacols were absent with substrates **9c-e** and **9aj-9am**, which bear bulky groups at the α position to the carbonyl (Table IX. 1, entries 3-8). On the other hand, the reductive coupling was significantly higher for substrates containing electron withdrawing substituents (**9s-u**). Additionally, the formation of dimers increases at higher ketone concentrations. For instance, at concentrations of 16.5 mM and 200 mM of **9a** (and 250 μM PSIr), 0.011 mmol (14 % yield) and 0.151 mmol (16 % yield) of **9a-pinacol** were obtained, respectively. The yield increased up to 28% at $[\mathbf{9a}] = 200 \text{ mM}$ and $[\text{PSIr}] = 500 \mu\text{M}$, but up to 61% at $[\mathbf{9a}] = 50 \text{ mM}$ and $[\text{PSIr}] = 500 \mu\text{M}$. The large impact in the yield by changing both $[\text{PSIr}]$ and $[\mathbf{9a}]$ suggests a bimolecular process.

Table IX. 1. Formation of **9-pinacol** for selected substrates in the absence of cobalt catalyst.

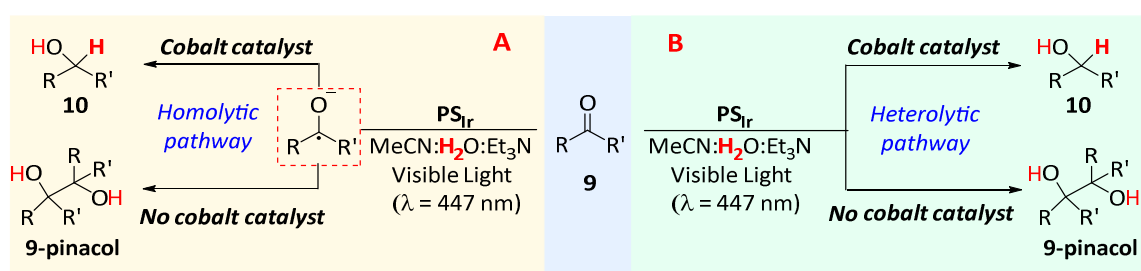
Entry	Compound	E (V) ^[a]	Yield pinacol (%) ^[b]	Entry	Compound	E (V) ^[a]	Yield pinacol (%) ^[b]
1		-1.65	14	9		-1.69	4
2		-1.66	5	10		-1.64	10
3		-1.70	<i>n.d.</i>	11		-1.67	<i>n.d.</i>
4		-1.66	<i>n.d.</i>	12		-1.75	<i>n.d.</i>
5		-1.70	<i>n.d.</i>	13		-1.63	31
6		-1.65	<i>n.d.</i>	14		-1.56	22
7		-1.75	<i>n.d.</i>	15		-1.54	37
8		-1.69	<i>n.d.</i>	16		-1.58	24

[a] Redox potentials measured in MeCN:H₂O:Et₃N (4:6:0.2) and determined at the half-wave potential. [b] Isolated yield.

It is important to remark that **9-pinacol** formation is fully suppressed in the presence of cobalt catalyst, even at very low concentrations of **1_{Co}** (**1_{Co}** (2 μM) for this experiment **PS_{Cu}** (250 μM) was used). The exception was the most easily reducible ketone (**9t**), yielding a 7% of **9t-pinacol**.

We can explain the presence and absence of pinacols in function of the conditions and of the ketone employed by two different scenarios (Scheme IX. 4). In

scenario **A**, the ketone is reduced to a ketyl radical and trapped by the cobalt hydride (*via* HAT, homolytic pathway) avoiding the formation of pinacol. This mechanism implies a very low concentration of KRA and that $10 \cdot k_d [\text{KRA}]^2 < k_{\text{HAT}} [\text{KRA}'] [\text{Co-H}]$ (where $[\text{KRA}]$ and $[\text{KRA}']$ are the concentrations of KRA in the absence and presence of cobalt and $[\text{Co-H}]$ is the steady state concentration of cobalt hydride in solution). In scenario **B**, the ketyl radical anion is virtually not formed due to reaction of $[\text{PS}_{\text{Ir}}^{\text{II}}]$ with the catalytic Co^{II} or Co^{III} intermediates. Therefore, the ketone is reduced *via* hydride transfer from the Co-H species (heterolytic pathway). The formation of 7% yield of **9t-pinacol** in the presence of **1c_o** suggests that for **9t** both scenarios are operative at the same time.



Scheme IX. 4. Reactivity of ketones in the presence and absence of cobalt catalyst under photocatalytic conditions.

Since the ketyl radical anion is presumably formed by a single electron transfer from $\text{PS}_{\text{Ir}}^{\text{II}}$ to the substrate we measured the redox potential of **9a**. In MeCN, the difference between KRA ($E(\mathbf{9a}^{0/-}) = -2.14 \text{ V vs. SCE}$)⁵¹⁹ and $\text{PS}_{\text{Ir}}^{\text{II}}$ ($E(\text{PS}_{\text{Ir}}^{\text{III/II}}) = -1.38 \text{ V vs. SCE}$ in MeCN) redox potentials (0.76 V) clearly prevents the KRA formation in such conditions ($\Delta G^0 = -nF\Delta E = 17.5 \text{ kcal}\cdot\text{mol}^{-1}$) (Figure IX. 7). However, in MeCN:H₂O (4:6) a significant anodic shift^{520,521} in the **9a** reduction was observed ($E(\mathbf{9a}^{0/-}) = -1.65 \text{ V vs. SCE}$),³ closer to the PS_{Ir} reduction potential.⁴ The redox potentials did not change in the presence of Et₃N (2% vol.) (Figure IX. 8).

³ The observed shift in MeCN:H₂O (4:6) can be attributed to the C=O activation by H-bonding.(ref 520 and 521)

⁴ Under these conditions it was difficult to measure, but it was maintained almost constant ($E(\text{PS}_{\text{Ir}}^{\text{III/II}}) = -1.38 \text{ V vs. SCE}$).

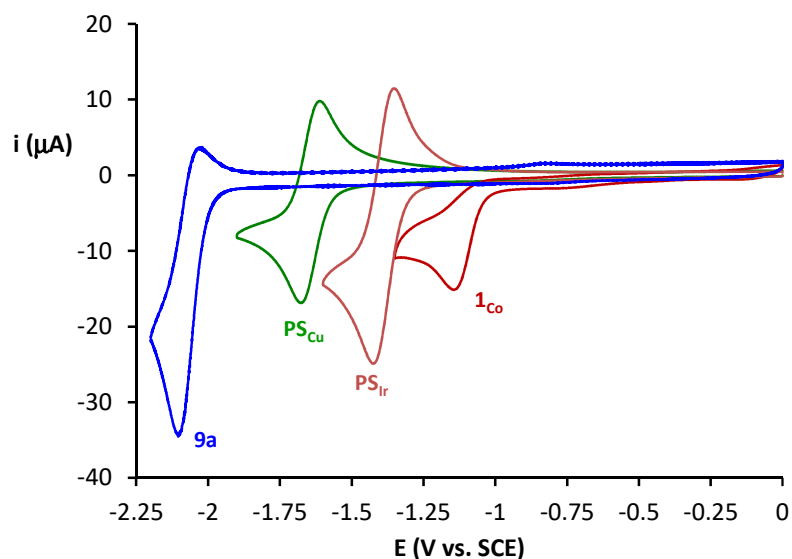


Figure IX. 7. Cyclic voltammograms of 1_{Co} (1 mM, red), PS_{Ir} (1 mM, orange), PS_{Cu} (1 mM, green) and acetophenone ($9a$) (1 mM, blue) were recorded using Bu_4NPF_6 (0.1 M) as a supporting electrolyte and glassy carbon as working electrode in dry acetonitrile. Scan rate= 100 mV/s. For the irreversible waves, the E values have been determined at the half intensity of the wave.⁵²² $E(1_{Co}^{II/I}) = -1.10$ V ; $E(PS_{Ir}^{III/II}) = -1.38$ V; $E(PS_{Cu}^{I/0}) = -1.64$ V, $E(9a^{0/-1}) = -2.14$ V.

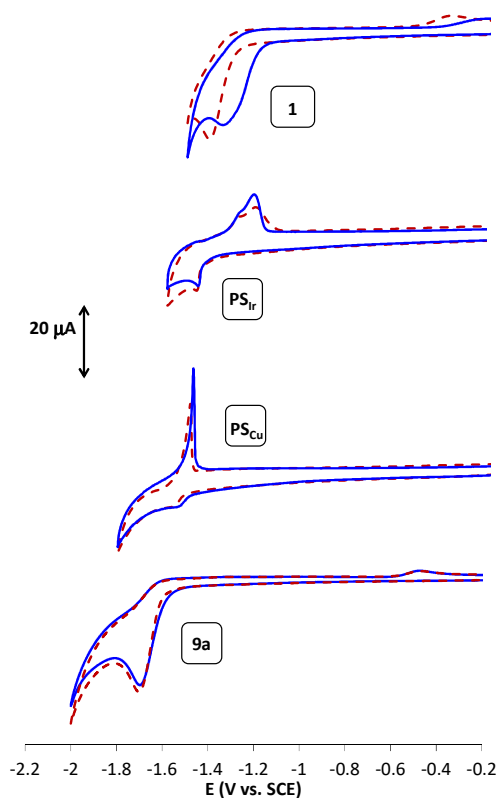


Figure IX. 8. Cyclic voltammograms of 1_{Co} (1 mM), PS_{Ir} (250 μM), PS_{Cu} (250 μM) and acetophenone ($9a$) (1 mM) in the solvent mixture MeCN:H₂O (4:6) (blue) and MeCN:H₂O:Et₃N (4:6:0.2) (red dashed) using KNO_3 (0.1 M) as a supporting electrolyte and glassy carbon as working electrode. Scan rate= 100 mV/s. For the irreversible waves, the E values have been determined at the half intensity of the wave.⁵²² $E(1_{Co}^{III/II}) = -1.34$ V, $E(PS_{Ir}^{III/II}) = -1.47$ V, $E(9^{0/-1}) = -1.65$ V.

Although the redox potential for the reduction of **9a** to the KRA under catalytic conditions is higher than the redox potential provided by $\text{PS}_{\text{Ir}}^{\text{II}}$, the formation of small quantities of reduced ketone is thermodynamically feasible in the absence of $\mathbf{1}_{\text{Co}}$ ($\Delta G^{\circ} = +6.2 \text{ kcal}\cdot\text{mol}^{-1}$). Using our data, it is possible to do a rough estimation of the [KRA] and yields. For instance, under catalytic conditions, the concentration of $\text{PS}_{\text{Ir}}^{\text{II}}$ can be expected in the 1 – 10 % range, as judged by the UV/Vis $\text{PS}_{\text{Ir}}^{\text{II}}$ titration experiments with $\mathbf{1}_{\text{Co}}$. Considering the Nernst Equation, the **9a** ketyl radical concentration in absence of $\mathbf{1}_{\text{Co}}$ can be estimated in the 4.5 – 50 nM range. Then, we can also estimate a range for the KRA dimerization rate ($8.3\cdot 10^{-9} - 1.0\cdot 10^{-6} \text{ M}\cdot\text{s}^{-1}$)^{509 5} and estimate a **9a-pinacol** theoretical yield versus the $\text{PS}_{\text{Ir}}^{\text{II}}$ percentage in the steady state regime at different reaction times (Figure IX. 9). Although our model does not consider the $\text{PS}_{\text{Ir}}^{\text{II}}$ formation of the $\text{PS}_{\text{Ir}}^{\text{II}}\text{-9a}$ electron transfer rates, the estimated $\text{PS}_{\text{Ir}}^{\text{II}}$ percentage (5-15 %) to explain the pinacol formation (13 %) is in good agreement with the UV/Vis titration experiments under different under different conditions.

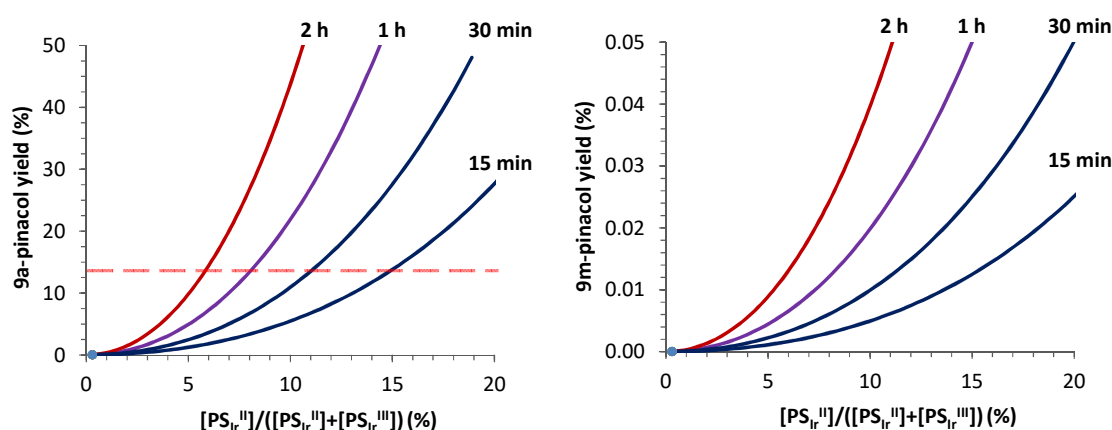


Figure IX. 9. Theoretical estimation of the pinacol yield (%) versus the percentage of $\text{PS}_{\text{Ir}}^{\text{II}}$ in solution for **9a** ($E = -1.65 \text{ V}$, left) and **9m** ($E = -1.74 \text{ V}$, right).

Likewise, we can calculate the theoretical yield for other substrates. In Table IX. 1 and Figure A. 6. 6 there are the measured reduction potentials of the selected substrates under catalytic conditions. **9m** is the ketone with the highest redox potential that does not form pinacols and its steric properties are similar to **9a**.

⁵ $d[\text{KRA}]/dt = k_d[\text{KRA}]^2$, the dimerization rate constant for **9a** is known to be $> 4\cdot 10^8 \text{ M}^{-1}\cdot\text{s}^{-1}$. (ref 509).

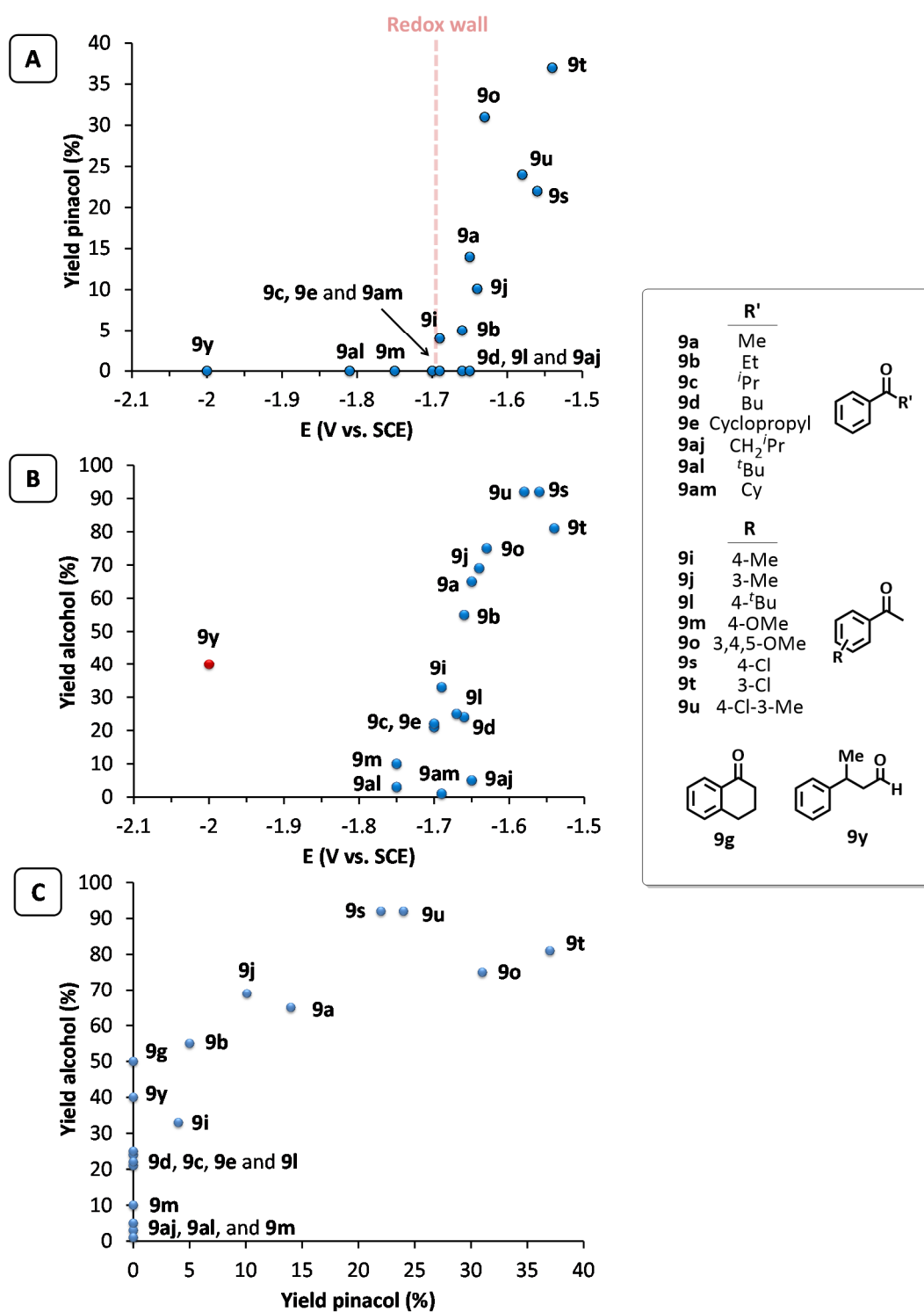


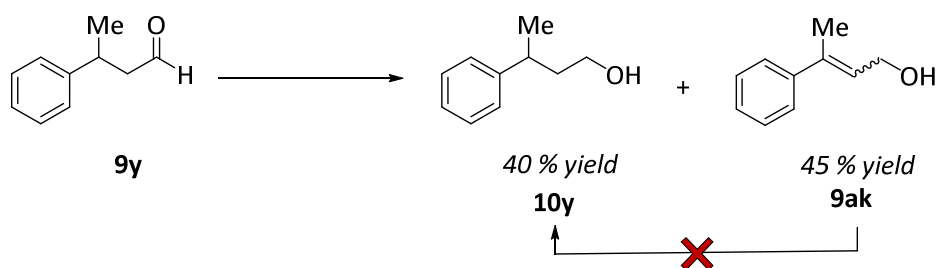
Figure IX. 10. Correlation between A) Yield pinacol-redox potential substrate B) Yield alcohol-redox potential substrate C) Yield alcohol – yield pinacol.

Gratifyingly, our rough model estimates less than 0.1 % yield for **9m**, which is in agreement with the experimental results. Moreover, there is a correlation between the redox potential of the ketones and the amount of pinacol formed (Figure IX. 10, A). No

pinacols were formed at redox potentials less negative than -1.70 V vs. SCE. On the other hand, it is not surprising that steric effects in the α -position of the ketone inhibit the radical dimerization process (Table IX. 1). For instance, although substrates **9d** ($E(\mathbf{9d}^{0/-}) = -1.66$ V vs SCE) and **9aj** ($E(\mathbf{9aj}^{0/-}) = -1.65$ V vs. SCE) have a similar redox potential than **9a**, they do not form the corresponding pinacols.

In a similar manner, the alcohol yield becomes more important by the increase of the redox potential (or electrophilicity) of the substrate, with the exception of the sterically hindered substrates (Figure IX. 10, B). Both mechanisms, the alcohol formation through HAT (homolytic pathway) and the hydride transfer (heterolytic pathway) are consistent with the correlation.

An important exception is the reduction of 3-Phenylbutanal (**9y**) into 3-Phenylbutan-1-ol (**10y**). This aliphatic aldehyde has the lowest redox potential of the series ($E = -2.52$ V vs. SCE in MeCN and < -2 V in MeCN:H₂O (4:6), Figure IX. 11), but it also has the lowest steric effect. The redox potential of **9y** is significantly lower than the PS_{Ir} ($\Delta G^{\circ} = +14.3$ kcal·mol⁻¹) and, as expected, the derived pinacol was not detected in absence of the cobalt catalyst. However, alcohol **10y** is formed in only 40% yield in the presence of **1co**. The large redox $\mathbf{9y-PS}_{\text{Ir}}$ difference and the still formation of **10y** points towards to a hydride attack mechanism to the carbonyl group (heterolytic pathway). It is important to note that under catalytic conditions 3-phenyl-2-en-1-ol (**9ak**) was observed as by-product. However, this was discarded as precursor of **10y** since when it was subjected to the catalytic conditions no **10y** was formed.



Scheme IX. 5. Conversion of **9y** into 3-phenylbutan-1-ol (**10y**) and 3-phenyl-2-en-1-ol (**9ak**).

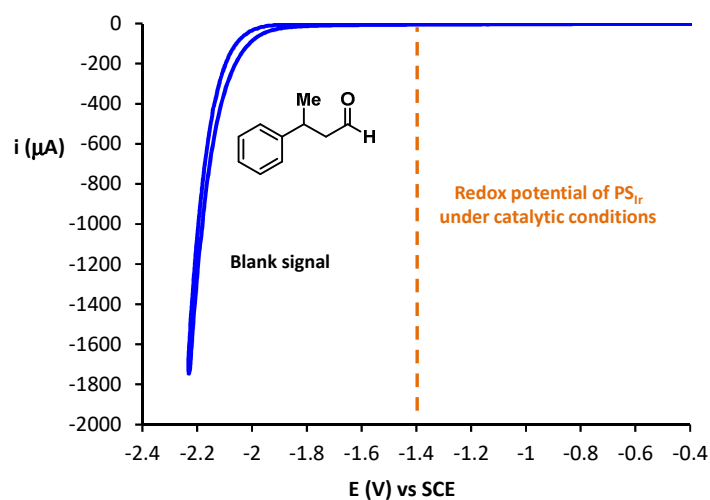


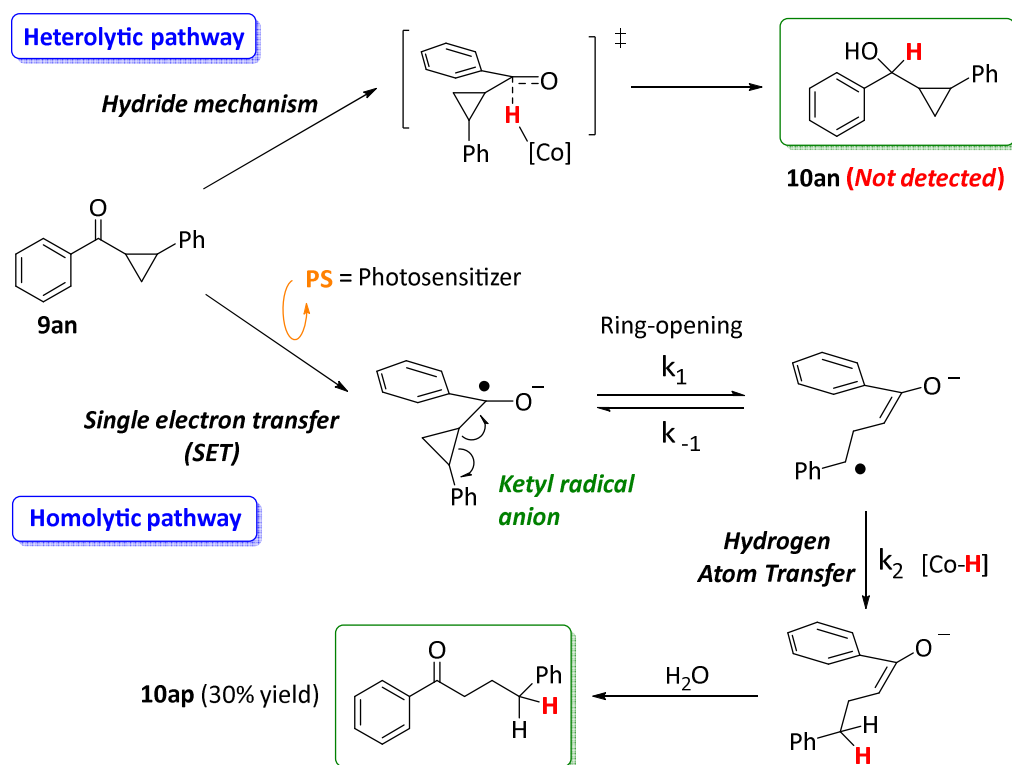
Figure IX. 11. Cyclic voltammetry of 3-phenylbutanal (5 mM) in the solvent mixture MeCN:H₂O (4:6) with KNO₃ (0.1 M) as a supporting electrolyte, using glassy carbon working electrode and at scan rate of 100 mV/s.

Finally, the comparison between the yield of pinacols (%) (in the absence of cobalt) versus the yield of alcohol (%) (in the presence of cobalt) shows also a correlation between both processes (Figure IX. 10, C). Substrates with steric hindrance in the *alpha* position (e.g. **9c-9e**), afford relevant amounts of the corresponding alcohols, with no detection of the pinacol formation. A clear example is the case of α -tetralone (**9g**), in which no dimeric products were detected, despite being reduced in 50 % yield in the presence of cobalt. These results indicate that the pinacol formation process is more influenced by the steric effects than the ketone reduction.

IX.2.2.2. Radical clocks and probes

In order to identify the ketyl radical anion under catalytic conditions we have performed experiments with cyclopropyl ketones as radical clocks and tempo as a radical probe.

IX.2.2.2.1. Radical clocks. Aryl cyclopropyl ketones have been used as diagnostic probes to identify SET reactions in several organic transformations.²⁰⁹ The reason is that the formation of a ketyl radical very rapidly rearranges by the opening of the cyclopropyl ring.⁵²³⁻⁵²⁷



Scheme IX. 6. Heterolytic and homolytic pathway for the reduction of aryl cyclopropyl ketones.

We selected **9an** since the ring opening of the ketyl radical anion ($E(9an^{0/-}) = -1.60$ V vs. SCE, under catalytic conditions) is exothermic by -2.3 kcal \cdot mol $^{-1}$ and occurs with a rate constant of $\sim 10^7$ s $^{-1}$.^{528,527} When **9an** was reduced under photocatalytic conditions (using MeCN:H₂O (5:5) in order to guarantee the solubilization of **9an**), it gave the ring-opened 1,4-diphenylbutan-1-one (**10ap**) product in 30% yield. Alcohols phenyl(2-phenylcyclopropyl)methanol (**10an**) and 1,4-diphenylbutan-1-ol (reduced product of **10ap**) were not detected (Scheme IX. 6). This experiment clearly demonstrates that the ketyl radical anion can be generated by SET from the PS_{ir} in the presence of cobalt catalyst in substrates that have a redox potential below -1.6 V vs SCE.

IX.2.2.2.2. Reaction in the presence of TEMPO. If the ketyl radical is formed under catalytic conditions, we wondered whether the presence of a radical scavenger could affect the catalytic activity. Therefore, we performed a catalytic assay in the presence of TEMPO (2,2,6,6-tetramethyl-1-piperidinyloxy free radical) (1 equiv. versus **9a**). We also monitored the proton reduction to H₂ in the presence of TEMPO in order to have more information about the activity of the catalytic system over the time.

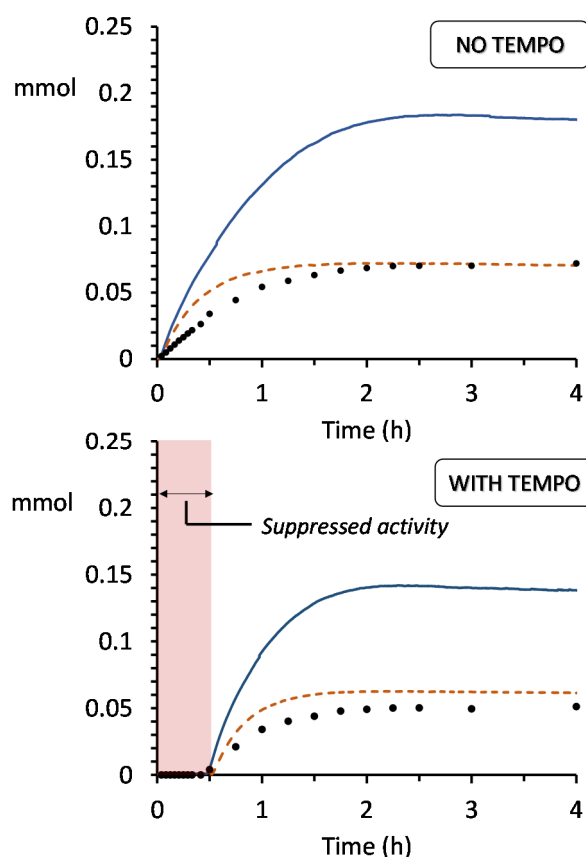


Figure IX. 12. Effect of TEMPO in the formation of H₂ and ketone reduction. *Top:* No TEMPO. *Bottom:* Presence of TEMPO (1 eq. versus **9a**). Solid blue traces: H₂ evolved versus time in the absence of **9a**. Dashed orange traces: H₂ evolved versus time in the presence of **9a**. Dark dots: Formation of alcohol **10a** versus time. Reaction conditions: **9a** (0.126 mmol, 12.4 mM), **PS_{ir}** (2.5 μmol, 2 mol%), **1_{Co}** (3.8 μmol, 3 mol%), MeCN:H₂O: Et₃N (3:7:0.2 mL), irradiating (λ = 447 nm) for 5 h at 30 °C under N₂. The red region corresponds to the time (0.5 h) that the activity was completely suppressed.

We found that in the presence of TEMPO the catalytic activity of both H₂ and ketone reduction was fully suppressed during the first 30 min of irradiation. After this induction time, H₂ and **10a** are formed with similar kinetics that a reaction without TEMPO (Figure IX. 12). Moreover, the final yield of alcohol was similar (62% yield) to a reaction in absence of TEMPO (65% yield). Since H₂ generation was also inhibited in the

presence of the radical scavenger, we cannot conclude anything about the presence or absence of organic radicals. Consequently, TEMPO should be used with caution in photochemical studies and in our case it is not suitable as mechanical probe. Indeed, the inhibition during the first reaction minutes could be attributed to a direct TEMPO ($E = -0.026 \text{ V vs. Ag/Ag}^+$)⁵²⁹ reduction by the PS_{Ir} or *via* a very fast HAT mechanism involving Co-H species, as observed with cobaloximes.⁵⁰⁷

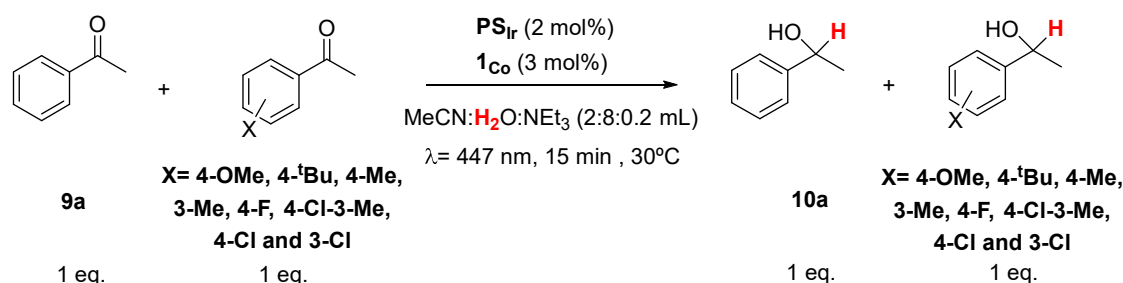
IX.2.3. Studies to Characterize the Transition State in Ketone Reduction

In order to get information about the transition state in ketone reduction we have performed i) a Hammett plot analysis and ii) kinetic isotopic experiments.

IX.2.3.1. Hammett plot analysis

We performed a Hammett plot analysis by equimolar competition experiments of *para*- and *meta*-substituted acetophenone derivatives (4-OMe, 4-^tBu, 4-Me, 3-Me, H, 4-F, 4-Cl-3-Me, 4-Cl and 3-Cl) against **9a** under our standard catalytic conditions (Table IX. 2). The product ratios were determined at 10% conversion by GC-FID analysis using 3,4,5-trimethoxybenzene as internal standard.

Table IX. 2. Effects of the ring-substitution on rates of acetophenone reduction by **1_{Co}** under photochemical conditions.



Substituent (X)	σ	$k_{\text{X}}/k_{\text{H}}$	$\log(k_{\text{X}}/k_{\text{H}})$
4-OMe	-0.27	0.094	-1.029
4- ^t Bu	-0.2	0.332	-0.479
4-Me	-0.17	0.230	-0.639
3-Me	-0.07	0.834	-0.079
H	0	1.000	0.000
4-F	0.06	2.746	0.439
4-Cl-3-Me	0.16	7.182	0.856
4-Cl	0.23	12.088	1.082
3-Cl	0.37	44.281	1.646

$k_{\text{X}}/k_{\text{H}}$: Ratio between the reduction of substituted acetophenone and acetophenone. σ values were obtained from the literature.⁵³⁰

Using the relative ratios obtained by each competition experiment, a Hammett plot was constructed by plotting $\log(k_X/k_H)$ vs σ ,^{324,530} obtaining a ρ value of +4.08 (Figure IX. 13). The large positive value of ρ indicates that there is a substantial buildup of negative charge in the activated complex as proceeds through to the transition state. While there is a clear dependence of the reaction rate on the electron density of the acetophenone, the magnitude of the dependence is higher than in any other hydride addition reactions, such as the reduction of substituted acetophenones using NaBH_4 ($\rho = +3.06$)⁵³¹ and the reduction of substituted benzophenones with LiAlH_4 ($\rho = +1.95$).⁵³² In contrast, the ρ values for the hydrogenation of acetophenones using homogeneous catalysts is usually much lower ($\rho = +0.99$).⁵³³ However, the ρ value for the reduction of benzaldehydes is even higher using NaBH_4 .⁵³⁴

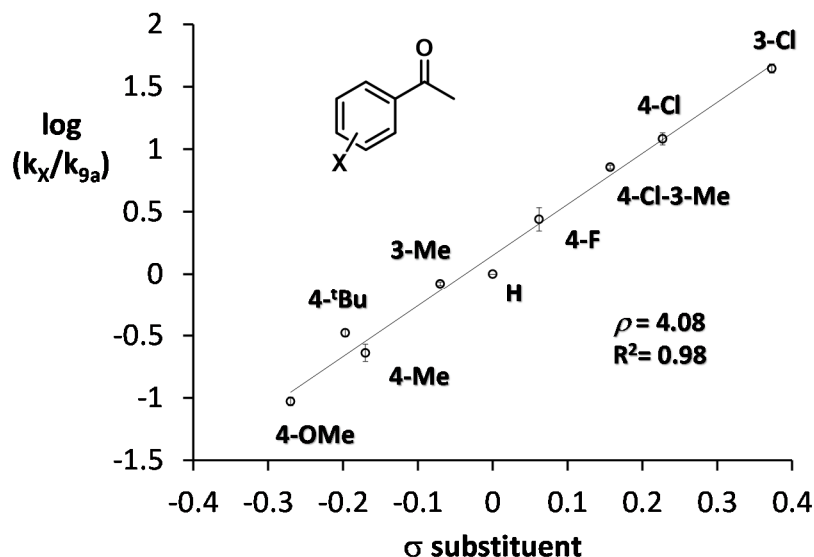


Figure IX. 13. Hammett plot analysis of the light-driven ketone reduction.

Finally, by plotting the relative reaction rates versus the redox potential of **9**, a linear correlation was also observed ($R^2 = 0.89$) (Figure IX. 14). In general terms, the more negative the potential of the substrate the less feasible is the reaction. This is in parallel with the more electrophilicity of the carbonyl group. We note that a better fitting is obtained when using the σ Hammett parameter ($R^2 = 0.98$).

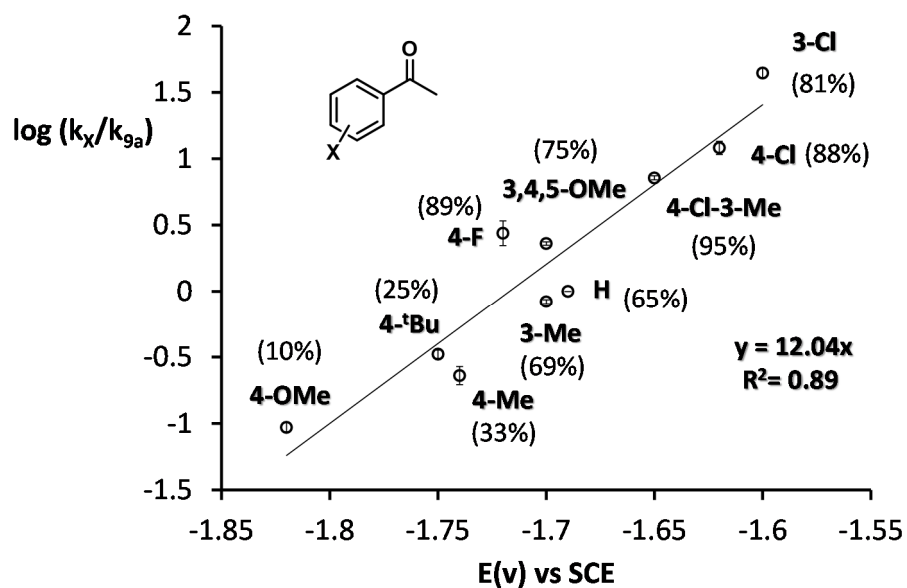


Figure IX. 14. Correlation between the relative reaction rates in the reduction of ring-substituted acetophenones and the redox potential of the substrate.

IX.2.3.2. Kinetic isotopic studies

IX.2.3.2.1. Kinetic Isotopic Effect of D₂O as Solvent

Additional evidence of the nature of intermediates are obtained from Kinetic Isotopic Effect (KIE) experiments in the reduction of **9a** when H₂O was replaced by D₂O. The KIE has been determined by two different forms. On one hand, we monitored by ¹H-NMR spectroscopy the conversion of **9a** into **10a** in a NMR tube irradiated at different times (2.5-18 min). As depicted in the Figure A. 6. 1, acetophenone was cleanly converted into 1-phenylethanol linearly versus the reaction time. By replacing H₂O by D₂O, **9a** was also linearly converted into **10a** but at lower reaction rate (Figure A. 6. 2). The KIE value obtained was 2.9 (Figure A. 6. 3). This value was also corroborated by monitoring the reaction by GC. In this case, a KIE value of 2.8 was obtained (Figure A. 6. 4).

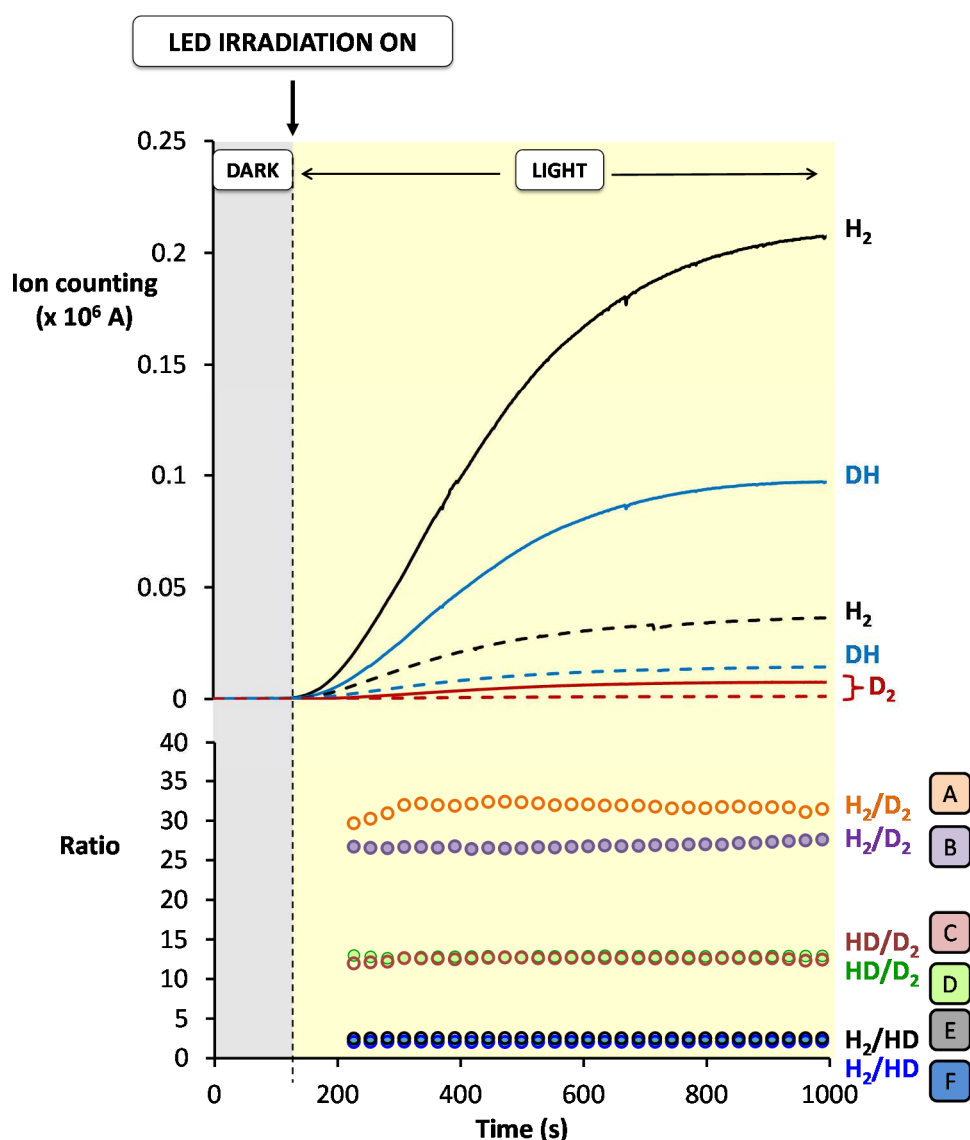


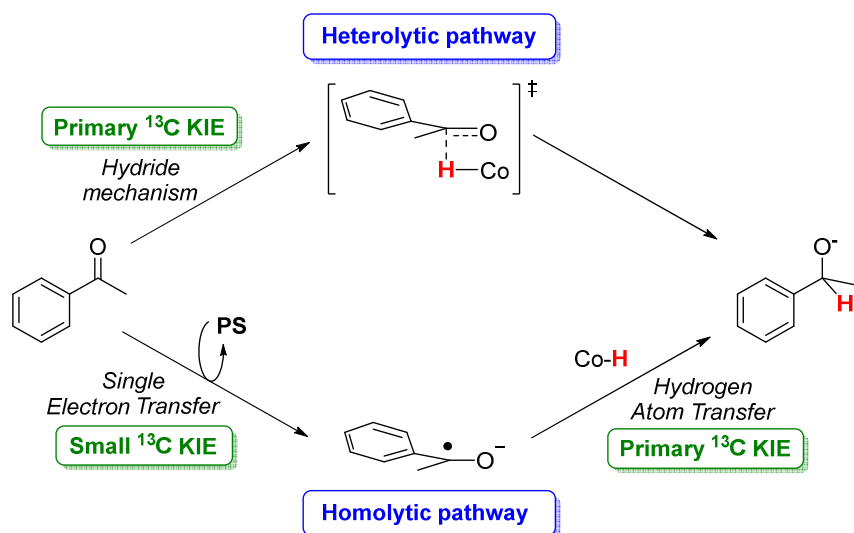
Figure IX. 15. *Top:* online MS-monitoring of the formation of H₂, HD and D₂ (Ion current) versus time. Black traces: H₂ evolved in the absence (black line) and presence of **9a** (dashed black line). Blue traces: HD evolved in the absence (blue line) and presence of **9a** (dashed blue line). Red traces: D₂ evolved in the absence (red line) and presence of **9a** (dashed red line). *Bottom:* H₂/D₂, HD/D₂ and H₂/HD ratios determined by the online MS-measurements versus the reaction time. Only ratios after the first 100 seconds are represented since measure errors in the beginning are larger. Ratios in presence (traces A, C, E) and absence of **9a** (traces B, D, F). Conditions: **PS**_{ir} (250 μM), **1**_{Co} (1 μmol), MeCN:H₂O:D₂O: Et₃N (0.6:0.7:0.7:0.04), reaction volume= 2 mL, irradiated at λ = 447 nm at room temperature.

The KIE value for H₂/D₂ evolution measured under catalytic conditions in presence (**9a**, 12.4 mM) and absence of substrate are 3.75±0.75 and 5.5±0.5, respectively, when replacing H₂O by D₂O in a MeCN:H₂O(D₂O):Et₃N (3:7:0.2) mixture, and using **PS**_{ir} (250 μM) and **1**_{Co} (370 μM). This indicates that the formation or cleavage of the Co-H bond and O-H bond of H₂O is involved in the rate-determining step of the reaction.³⁴⁵ On the other hand, the online-MS measured H₂/D₂, HD/D₂ and H₂/HD

isotopic ratios remains almost constant in the presence ($H_2/D_2= 31.7$, $HD/D_2= 12.5$, $H_2/HD= 2.5$) and absence ($H_2/D_2= 26.8$, $HD/D_2= 12.9$, $H_2/HD= 2.1$) **9a**, when using a mixture of $H_2O:D_2O$ (1:1) (See footnote Figure IX. 15 for conditions). Taking into consideration both facts, the existence of competitive mechanisms (H_2 vs alcohol formation) and that the sum of the reaction rate of H_2 evolution and **9a** reduction is independent on the substrate concentration suggests that the rate determining step could not be on the H-H or the C-H bond formation step. This is also in agreement with the observed saturation of the reaction rate of upon increasing the ketone concentration (shown in Chapter VII). Therefore, the rate determining step should be located in the Co-H bond formation step. KIE agrees with two H/D selective steps being one of those the rate determining step.

IX.2.3.2.2. Determination of natural abundance multiple ^{13}C Kinetic Isotope Effects in the reduction of acetophenone under photocatalytic conditions

The ^{13}C -carbonyl KIE value can aid us to discern between two possible rate-determining steps: 1) electron transfer (SET) and 2) hydride nucleophilic addition (HM) or hydrogen atom transfer (HAT) (Scheme IX. 7).^{535,536,537} The carbonyl carbon KIE is expected to be large for a rate-determining step localized at the C-H formation in the Hydride or HAT mechanism since the carbon of the carbonyl is strongly involved in the C-H bond formation step. On the contrary, the carbon KIE should be smaller for a rate-determining step located at the electron transfer step, since the carbon does not contribute in the reaction coordination motion.^{538,539}



Scheme IX. 7. Two possible mechanistic pathways with their corresponding kinetic isotopic effect.

A pre-requisite for the natural abundance ^{13}C kinetic isotope effect determination is that the reaction has to approach the completion to enrich enough the sample in ^{13}C . Fortunately, the photocatalytic acetophenone reduction to 1-phenylethanol is quantitative when using PS_{Cu} as photosensitizer. Therefore, we have used PS_{Cu} to carry out the measurements. The multiple ^{13}C natural abundance KIEs have been measured following the NMR methodology described in the literature by Singleton *et al.*⁵⁴⁰

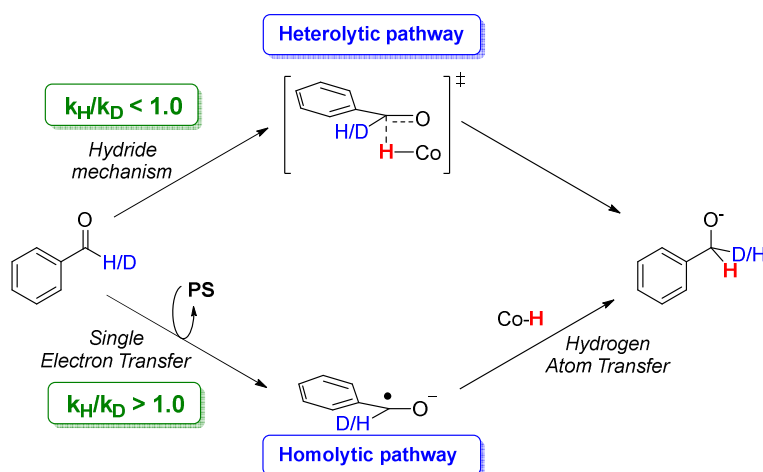
The experiment was performed using $\mathbf{1}_{\text{Co}}$ (1 mol%), PS_{Cu} (1.5 mol%), acetophenone (16.5 mM) at 25 °C and stopping the reaction at 89.5 % conversion (remaining starting material was determined by GC analysis and ^1H -NMR). The remaining acetophenone was isolated by column chromatography on silica gel and analyzed with ^{13}C -NMR. The changes in the isotopic composition were internally calibrated relative to the para carbon of the acetophenone, assuming that the KIE for this position is negligible (Figure IX. 23). The analysis was compared with a sample of the starting acetophenone.

The resulting KIEs summarized in Figure IX. 16 shows a small positive ^{13}C -KIE ($k_{12\text{C}}/k_{13\text{C}} = 1.025$) at the carbonyl carbon. The value is comparable to carbonyl- ^{14}C KIEs observed for the polar nucleophilic additions to benzophenone with LiAlH_4 ($k_{12\text{C}}/k_{14\text{C}} = 1.024$), NaBH_4 ($k_{12\text{C}}/k_{14\text{C}} = 1.066$), AlH_3 ($k_{12\text{C}}/k_{14\text{C}} = 1.021$), BH_3 ($k_{12\text{C}}/k_{14\text{C}} = 1.035$), LiBH_4 ($k_{12\text{C}}/k_{14\text{C}} = 1.043$), Me_2CuLi ($k_{12\text{C}}/k_{14\text{C}} = 1.029$), and MeMgI ($k_{12\text{C}}/k_{14\text{C}} = 1.056$).⁵⁴¹⁻⁵⁴³ In all of these reactions the C-nucleophile bond formation was concluded to be rate-

IX.2.3.2.3. Secondary Deuterium Kinetic Isotopic Effects

Secondary Kinetic Isotopic Effects (SDKIE) have been also typically used to provide information about the nature of the rate-determining step and therefore helping to discern between SET and polar mechanisms in aldehydes (Scheme IX. 8).^{545,546,547}

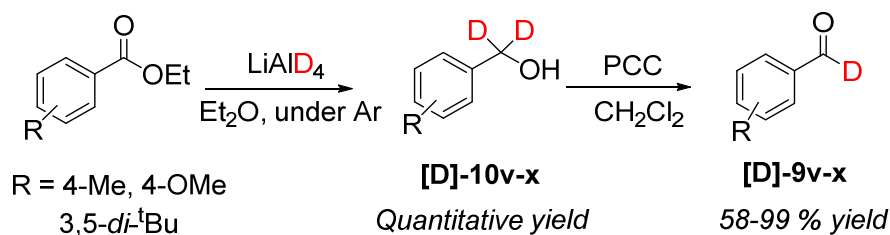
For a heterolytic mechanism, where the rate-determining step is the nucleophilic addition, an inverse kinetic effect ($k_H/k_D < 1.0$) is expected. The inverse SDKIE is due to an increase in the bending frequencies at the reacting carbon at the transition state, which results in a greater lowering of the zero point energy upon deuterium substitution than in the starting material.^{544,548} On the other hand, for the rate-determining single-electron transfer (SET) or HAT, the SDKIE should be normal ($k_H/k_D > 1.0$).^{547,548} SDKIEs greater than unity have also been observed for the reaction of nucleophiles with benzaldehydes,⁵⁴⁴ involving a SET electron transfer mechanism.^{547,548}



Scheme IX. 8. Two possible mechanistic pathways with their corresponding expected SDKIE.

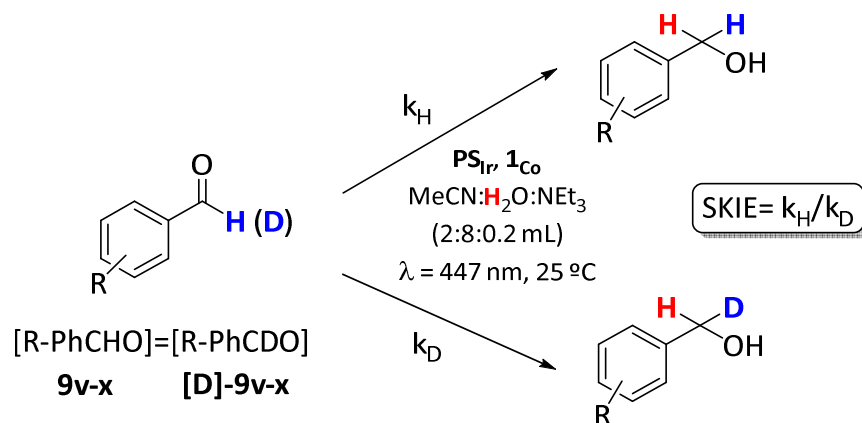
Substrates 4-methylbenzaldehyde (**9w**) 4-methoxybenzaldehyde (**9v**) and 3,5-di-*tert*-butylbenzaldehyde (**9x**) were selected for the study. The determination of the k_H/k_D values has been carried out by measuring the difference in the proportion of alcohols derived from the reduction of non-labelled (**9v-x**) : labelled (**[D]-9v-x**) (1:1) aldehydes in competition experiments. The synthesis of deuterium-labelled aldehydes (**[D]-9v-x**) was accomplished after two different steps. First, the corresponding substituted ester (R = Me, OMe, 3,5-*di-t*Bu) was quantitatively reduced to the corresponding deuterium-labelled alcohol **[10]-10v-x** using LiAlD₄ in ethereal solution. After that, pyridinium chlorochromate (PCC) was used to oxidize the labelled alcohols **[10]-10v-x** to the

corresponding deuterium-labelled aldehydes **[D]-9v-x** in yields between 58-99 %. (Scheme IX. 9).



Scheme IX. 9. General scheme of the reduction of labelled aldehydes **[D]-9v-x**.

The unreported labelled alcohols **[D]-10v-x** were synthesized using the described procedures for the synthesis of deuterated benzylic alcohol.⁵⁴⁹⁻⁵⁵¹ The deuteration in the benzylic position was confirmed by ¹H-NMR and ¹³C-NMR (Figure A. 6. 9 and Figure A. 6. 10), for the case of **[D]-10v**). The ¹³C-NMR the appearance of the benzylic carbon as quintuplet at ~64-65 ppm was consistent with CD₂ moiety (Figure A. 6. 10) for the case of **[D]-9v**). Finally, the molecular peaks analyzed by GC-MS of 124.1 (**[D]-10v**), 140.0 (**[D]-10w**) and 221.1 (**[D]-10x**) were consistent with the general molecular formula containing 2 deuterium atoms in the molecule. Finally, the D atom in the labelled aldehydes **[D]-9v-x** was confirmed by ¹H-NMR and ¹³C-NMR (Figure A. 6. 11 and Figure A. 6. 12). Carbonyl and *ipso* carbon appeared as triplet in the ¹³C-NMR due to the coupling with the deuterium atom. Moreover, the molecular peaks analyzed by GC-MS of 121.1 (**[D]-9v**), 137.1 (**[D]-9w**) and 219.1 (**[D]-9x**) were consistent with 1 deuterium atom incorporation per molecule (See section A.6.5 for details)



Scheme IX. 10. Strategy followed for the SDKIE determination.

The determined isotope ratios of the formed alcohol at 10% of conversion were quantified by $^1\text{H-NMR}$ spectroscopy after workup. Benzylic CH_2 and CHD signals of the alcohol are separated only by 0.02 ppm at 500 MHz. Thus, the ratio between half of the signal was used to avoid the overlapping and determine the Kinetic Isotopic Effects (Figure IX. 17).

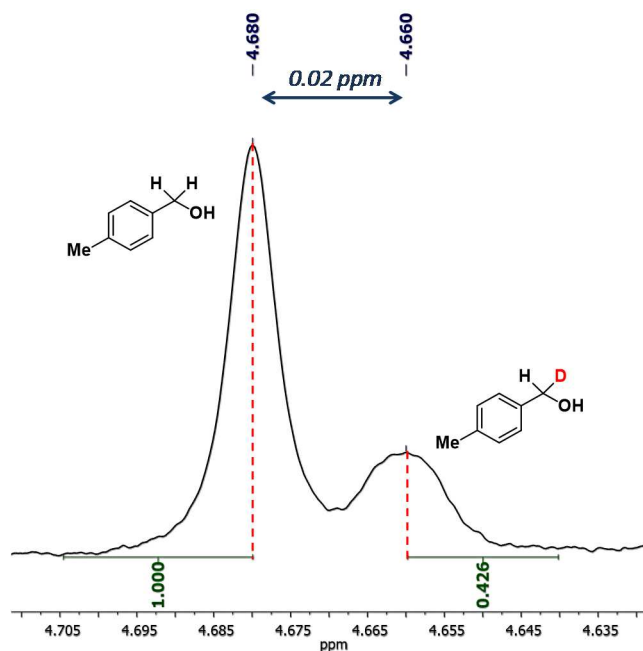


Figure IX. 17. $^1\text{H-NMR}$ spectrum (CDCl_3 , 500 MHz) of the benzylic CH_2 : CHD signals. The ratio of the labelled:unlabelled products for the 4-Me-PhCHO:4-Me-PhCDO (1:1) reduction products was found to be 1.17. $\text{SDKIE} = \frac{k_{\text{H}}}{k_{\text{D}}} = 1.17$.

The experimental SDKIEs higher than one ($k_{\text{H}}/k_{\text{D}} > 1.0$) for benzaldehydes (Table IX. 3) indicates that reaction proceeds through a rate-selective SET step followed by a concomitant HAT by a Co-H species.

Table IX. 3. SDKIEs for the reduction of substituted aldehydes.

Entry	9 : [D]-9 (1:1)	Conv [%] ^[a]	SDKIE: $k_{\text{H}}/k_{\text{D}}$ ^[b]
1		22	1.17
2		17	1.07
3		21	1.19

[a] Conversions determined by GC analysis. [b] SDKIE values determined using standard catalytic conditions.

IX.2.3.3. Kinetics: reaction orders

The initial reactions rates showed linear dependence with the concentration of **1**_{Co} and **PS**_{Ir} and the log-log plot is consistent with a half-order and a first order dependence, respectively (Figure IX. 18). More interesting it is the dependence observed versus the substrate concentration. As previously depicted in Chapter VII, the reaction shows first order dependence versus **9a** when using low concentrations of **9a** (0–20 mM), also observed using 4-methylacetophenone (**9i**) and 4-methoxyacetophenone (**9m**). However, in the case of the electron poor substrate 4-chloroacetophenone (**9s**), the reaction was independent (zero order) on the substrate concentration. ($k_0(\mathbf{9s}) = 18.2 \text{ mM}\cdot\text{h}^{-1}$). As it is shown in Figure IX. 18 the reduction of **9s** is much faster than **9a**.

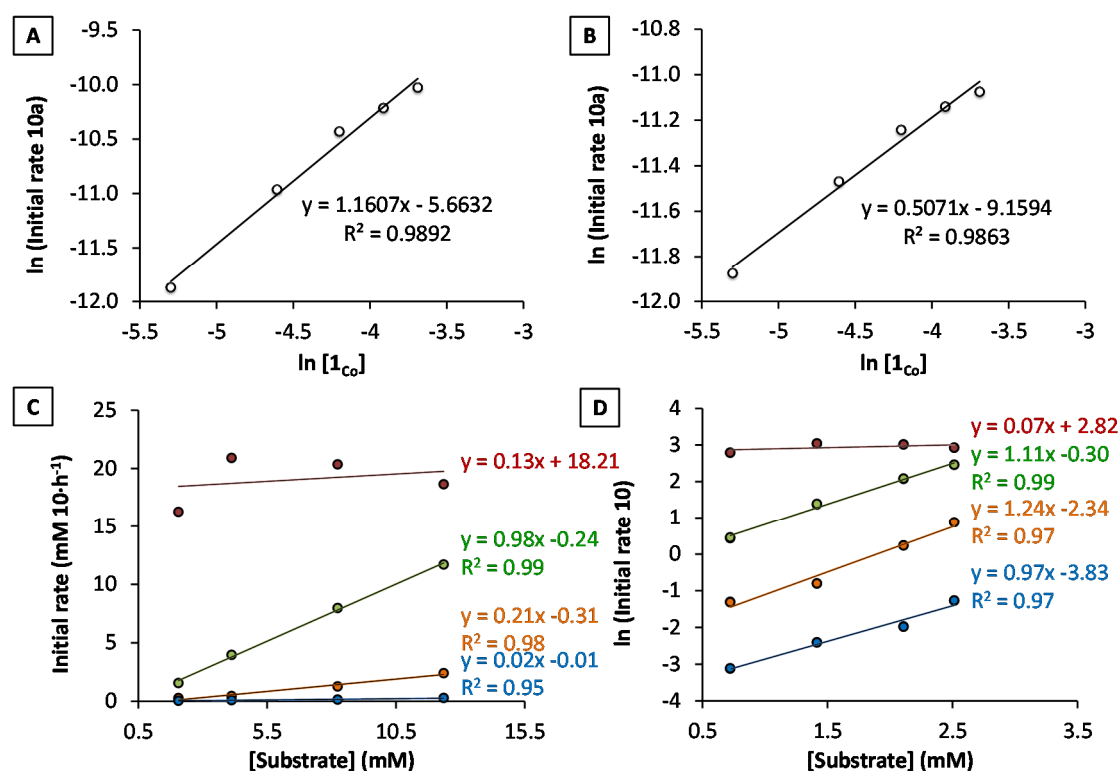


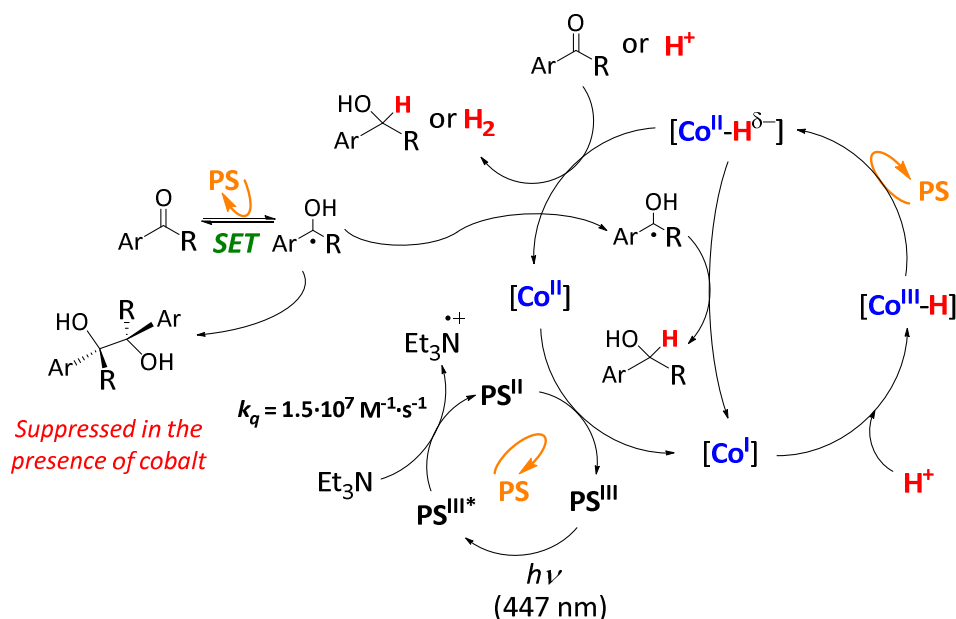
Figure IX. 18. Reaction order versus **1**_{Co} (A), **PS**_{Ir} (B) and substrate (D). C) Initial rates in the reduction of **9s** (red), **9a** (green), **9i** (orange) and **9m** (blue).

The change of behavior is very informative about the mechanism. With the KIE obtained replacing H₂O by D₂O and the water – ketone reduction competition experiments (Figure A. 6. 3), we can propose that the rate determining step of the reaction is in the Co^I protonation step. Therefore, since the water reduction to hydrogen is competing with the ketone reduction, in a heterolytic mechanism the reaction order is not zero but 1st order regarding the substrate. On the other hand, since the

concentration of ketyl radical anion is directly dependent on the concentration of the ketone, a SET-HAT reaction should be also order one respect the ketone. Alternatively, if the ketone reduction becomes faster than the water reduction, these two processes are not competitive anymore. In this case, the reaction order respect the ketone should be zero since the rds is in the Co-H formation step. We can have this behavior with highly reactive ketones (Figure IX. 18, substrate **9s**) or alternatively under high concentration of ketones (Figure VII. 8). The last scenario could explain all the results and suggest that the main mechanism operating is the HM.

IX.2.4. General Mechanistic Discussion

On the basis of the results discussed in this Chapter the exact mechanism is not completely clear but it seems that the heterolytic pathway may be the main responsible for the ketone reduction, although the contribution of the homolytic pathway can not be discarded. The reaction starts with the absorption of light by $\text{PS}_{\text{Ir}}^{\text{III}}$ species generating the long-lived excited $\text{PS}_{\text{Ir}}^{\text{III}*}$ species. This excited state of the iridium photosensitizer ($E(\text{PS}_{\text{Ir}}^{\text{III}*}/\text{II}) = 0.68 \text{ V vs. SCE}$) can be reductively quenched by Et_3N ($k_q = 1.5 \cdot 10^7 \text{ M}^{-1} \cdot \text{s}^{-1}$) to give the reduced iridium $\text{PS}_{\text{Ir}}^{\text{II}}$ species. The latter is a strong reductant ($E(\text{PS}_{\text{Ir}}^{\text{III}}/\text{II}) = -1.42 \text{ V vs. SCE}$) capable of reducing the Co^{II} ($E(\mathbf{1}_{\text{Co}}^{\text{II}/\text{I}}) = -1.34 \text{ V vs. SCE}$) complex to the formal Co^{I} intermediate (Co^{I} characterized in Chapter VI). Alternatively, $\text{PS}_{\text{Ir}}^{\text{II}}$ could also be responsible of the generation of ketyl radical species in solution through a SET to the substrate. According to the UV/Vis experiments the reduction of $\mathbf{1}_{\text{Co}}$ is thermodynamically more favorable ($E(\mathbf{1}_{\text{Co}}^{\text{II}/\text{I}}) = -1.35 \text{ V vs. SCE}$) than the formation of ketyl radical species ($E(\mathbf{9a}^{\text{I}/0}) = -1.65 \text{ V vs. SCE}$), although this last process cannot be discarded under catalytic conditions. In the absence of cobalt, these ketyl radical species can undergo the formation of dimeric products.



Scheme IX. 11. Proposed mechanism for the photocatalytic ketone reduction catalyzed by cobalt complexes.

Then, Co^{I} species catches a proton from water forming $\text{Co}^{\text{III}}\text{-H}$ that is then further reduced to $\text{Co}^{\text{II}}\text{-H}$ facilitated by $\text{PS}_{\text{Ir}}^{\text{II}}$. Afterwards, $\text{Co}^{\text{II}}\text{-H}$ can form the alcohol by the direct transfer of the hydride to the substrate (heterolytic pathway) or by a HAT mechanism involving a ketyl radical species (homolytic pathway) (Scheme IX. 11).

In order to corroborate this proposed mechanism and that $\text{Co}^{\text{II}}\text{-H}$ is the responsible for the ketone reduction, theoretical modelling studies were performed by Dr. F. Acuña.

We studied all possible spin states and speciation for the Co^{II} complex $\mathbf{1}_{\text{Co}}$ under catalytic conditions and we found that one electron reduction of $\text{Co}^{\text{II}}\text{-NCCH}_3$ to $\text{Co}^{\text{I}}\text{-NCCH}_3$ ($S = 1$) by the reduced $\text{PS}_{\text{Ir}}^{\text{II}}$ is favoured with a ΔG value of $-4.2 \text{ kcal}\cdot\text{mol}^{-1}$. Then, $\text{Co}^{\text{I}}\text{-NCCH}_3$ can be protonated to generate a $\text{Co}^{\text{III}}\text{-H}$ ($S = 0$) intermediate ($\Delta G = 7.6 \text{ kcal}\cdot\text{mol}^{-1}$), but its reduction to $\text{Co}^{\text{II}}\text{-H}$ is extremely favourable ($\Delta G = -18.1 \text{ kcal}\cdot\text{mol}^{-1}$). Therefore it points towards a $\text{Co}^{\text{II}}\text{-H}$ intermediate as a main candidate for active species. The preference in reactivity over HAT or hydride mechanism will be marked by the hydride/hydrogen character of the terminal H, *i.e.* by the polarization of the Co-H bond.

Analysis of the Hirshfeld's charge on the H moiety ($q(\text{H}) = -0.24$) and the Mayer bond order index for the Co-H bond ($\text{B.O} = 0.88$) show that the terminal H of $\text{Co}^{\text{II}}\text{-H}$

presents an important hydride character, with the Co-H bond being slightly polarized to the H⁻ moiety. The dissociation energy of the hydride ($\Delta G_{H^-}^0 = 36.9 \text{ kcal}\cdot\text{mol}^{-1}$) suggests that the hydride donor ability of Co^{II}-H is higher than in most of the commonly used main group hydrides, such as [BH₄]⁻ ($\Delta G_{H^-}^0 = 50.0 \text{ kcal}\cdot\text{mol}^{-1}$) and [AlH₄]⁻ ($\Delta G_{H^-}^0 = 43.0 \text{ kcal}\cdot\text{mol}^{-1}$),⁵⁵² making this intermediate a highly powerful hydride transfer agent (Figure IX. 19). On the contrary the less hydride character observed in Co^{III}-H species ($q(\text{H}) = -0.08$, B.O = 0.93, $\Delta G_{H^-}^0 = 51.9 \text{ kcal}\cdot\text{mol}^{-1}$) may correlates with a less catalytic activity in hydride transfer.

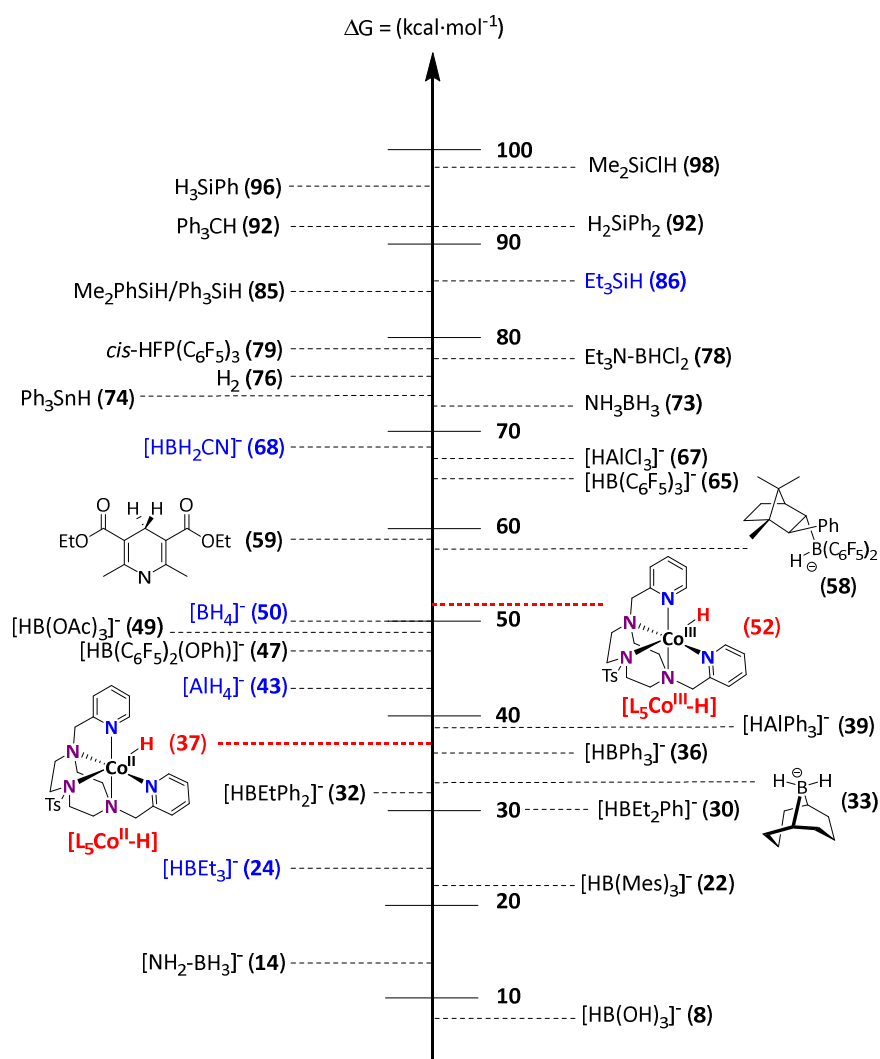


Figure IX. 19. Calculated hydride donor abilities for selected main group hydrides in acetonitrile reported in the literature.⁵⁵² Our calculated Co^{III}-H and Co^{II}-H intermediates are included in the diagram for comparison reasons. Figure adapted with permission from reference⁵⁵². Copyright (2015) American Chemical Society.

In the case of the homolytic mechanism, the formation of the ketyl radical is feasible in energy ($\Delta G = 3.2 \text{ kcal}\cdot\text{mol}^{-1}$), and the subsequent HAT step by a $\text{Co}^{\text{II}}\text{-H}$ intermediate can conduct directly to the formation of the final alcohol recovering a formal Co^{I} intermediate. However, the free energy shows that **TS_homo_t** is $5.4 \text{ kcal}\cdot\text{mol}^{-1}$ higher than **TS_heter_q**, clearly indicating that the preferred reaction pathway is the heterolytic one. The energetic feasibility of the hydride transfer event to a ketone $\text{C}=\text{O}$ group was previously reported for several transition metal catalyst based on Rh,^{553,554} Ru,^{555,556} Fe^{557,558} and also for main group hydrides such NaBH_4 .⁵⁵⁹

Finally, the calculated free energy barriers for the heterolytic formation of the C-H bond in different substituted acetophenones follows the order $\Delta G^{\ddagger}_{\text{H}} < \Delta G^{\ddagger}_{\text{Me}} < \Delta G^{\ddagger}_{\text{OMe}}$, which is in agreement with the electronic effect observed experimentally. The computed ρ parameter (5.7) is larger than the experimental value of 4.08. The hydride transfer to **9y** has to overcome a transition state $4.3 \text{ kcal}\cdot\text{mol}^{-1}$ higher in energy than the same for **9a**, which is also in agreement with the experimentally observed reactivity patterns for these substrates (Figure IX. 21).

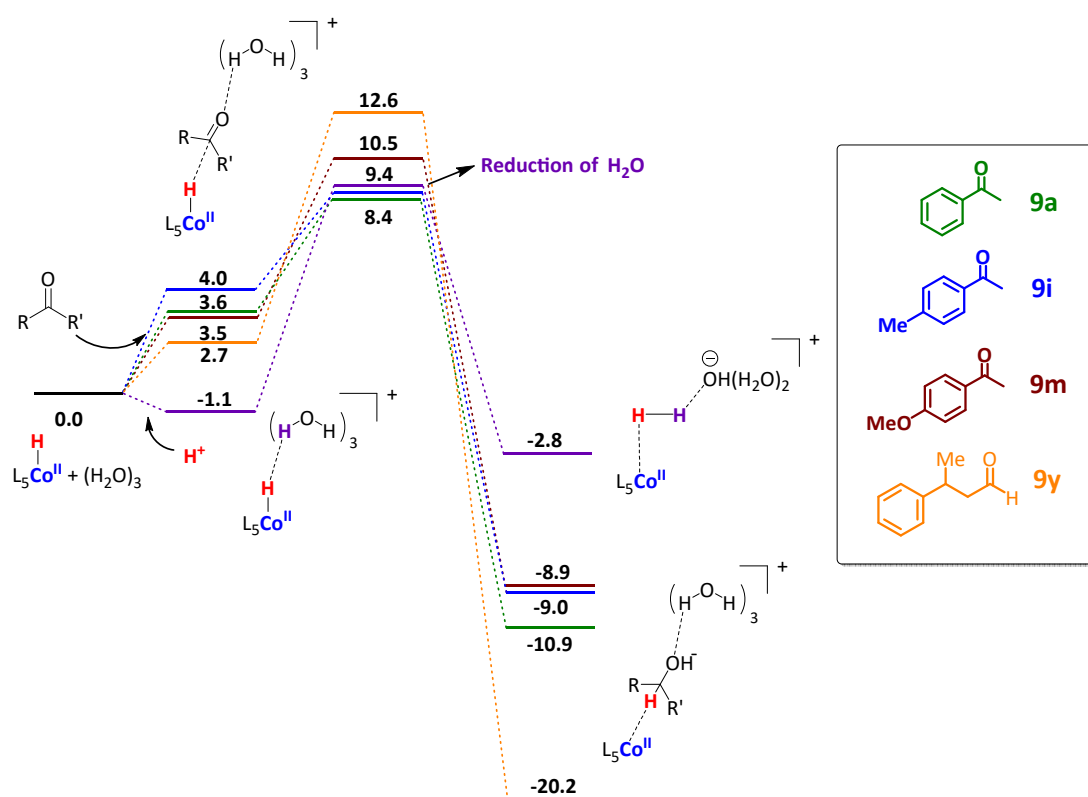


Figure IX. 21. Heterolytic reduction performed by $\text{L}_5\text{Co}^{\text{II}}\text{-H}$. Comparison between the free energy profiles for the reduction reaction of different organic substrates and water. The L_5 label refers to the pentadentate $\text{Py}_2^{\text{Ts}}\text{tacn}$ ligand. Gibbs energies are in $\text{kcal}\cdot\text{mol}^{-1}$.

Finally, we also evaluated the heterolytic mechanism involving the $\text{Co}^{\text{III}}\text{-H}$ species, and we found that this reaction pathway has an inaccessible energy barrier under catalytic conditions ($\Delta G^\ddagger > 30.0 \text{ kcal}\cdot\text{mol}^{-1}$) due to the poor hydride character of the $\text{Co}^{\text{II}}\text{-H}$ intermediate. Therefore, we believe that if $\text{Co}^{\text{III}}\text{-H}$ is directly involved in the formation of alcohols it may operate through a HAT mechanism instead of a hydride mechanism. The free energy profiles for the $\text{Co}^{\text{II}}\text{-H}$ heterolytic and $\text{Co}^{\text{III}}\text{-H}$ homolytic **9a** reduction reactions are presented in Figure IX. 20. DFT calculations indicate that the $\text{Co}^{\text{II}}\text{-H}$ heterolytic mechanism is kinetically preferred by $19.5 \text{ kcal}\cdot\text{mol}^{-1}$, which is in agreement with the experimental data. However, the contribution of a HAT mechanism cannot be discarded, and it can be relevant in electron poor substrates such as aldehydes or ketones with electron withdrawing groups, as suggested by the SDKIE experiments.

In summary, experimental and theoretical data suggest that the heterolytic pathway can be operative in the reduction of organic compounds, however, we can not discard the contribution of the homolytic pathway. The heterolytic mechanism would explain the electronic effects on the metal described in Chapter VIII.

IX.4. EXPERIMENTAL SECTION

IX.4.1. Material and Reagents

Reagents and solvents were purchased from commercial sources as used as received unless otherwise stated. Anhydrous acetonitrile was purchased from Scharlab. Water (18.2 M Ω ·cm) was purified with a Milli-Q Millipore Gradient AIS system. All solvents were strictly degassed and stored under anaerobic conditions.

IX.4.2. Instrumentation

Nuclear magnetic resonance (NMR) spectra were recorded on Bruker Fourier300, AV400, AV500 and AVIII500 spectrometers using standard conditions (300 K). All ^1H chemical shifts are reported in ppm and have been internally calibrated to the residual protons of the deuterated solvent. The ^{13}C chemical shifts have been internally calibrated to the carbon atoms of the deuterated solvent. The coupling constants were measured in Hz.

UV/Vis spectra were recorded on an Agilent 8453 diode array spectrophotometer (190–1100 nm range) in 1 cm quartz cells. A cryostat from Unisoku Scientific Instruments was used for the temperature control.

Mass Spectrometry. Electrospray ionization mass spectrometry (ESI-MS) experiments were performed on a Bruker Daltonics Esquire 3000 Spectrometer using a 1 mM solution of the analyzed compound, by introducing the sample directly into the ESI-source using a syringe. High resolution mass spectra (HRMS) were recorded on a Bruker MicroTOF-Q IITM instrument with an ESI source at Serveis Tècnics of the University of Girona. Samples were introduced into the mass spectrometer ion source by direct infusion through a syringe pump and were externally calibrated using sodium formate.

Electrochemistry. A standard three-electrode configuration was employed in conjunction with CHI Instruments potentiostat interfaced to a computer with CHI Instruments 600D software. Using one-compartment cell, all voltammetric scans were recorded using glassy carbon working electrode which was treated between experiments by means of a sequence of polishing with MicroPolish Powder (0.05 micron) before washing and sonification. Saturated calomel electrode (SCE) and Pt wire were used as reference and counter electrodes respectively.

Gas chromatography analysis. The analysis and quantification of the starting materials and products were carried out on an Agilent 7820A gas chromatograph (HP5 column, 30m or Cyclosil-B column, 30m) and a flame ionization detector. The enantioselectivity was determined by comparison with the pure samples synthesized by the reported procedures.⁴⁸⁴

GC-MS spectral analyses were performed on an Agilent 7890A gas chromatograph interfaced with an Agilent 5975c MS mass spectrometer.

Photochemical analysis. Fluorescence measurements were carried out on a Fluorolog Horiba Jobin Yvon spectrofluorimeter equipped with photomultiplier detector, double monochromator and Xenon light source. All **PS_{ir}** solutions were excited at 450 nm and the emission intensity was collected from 520 to 800 nm. In a typical experiment, to a 10 μ M solution of **PS_{ir}** in MeCN:H₂O (0.6:1.4) was added the appropriate amount of quencher in a screw-top quartz cuvette. All of the quencher stock solutions were prepared under strict anaerobic conditions. After degassing the sample with a stream of argon for 10 minutes, the emission of the sample was collected.

Online MS measurements have been performed using Omnistar GSD 301 C (Pfeiffer) quadrupole mass spectrometer apparatus.

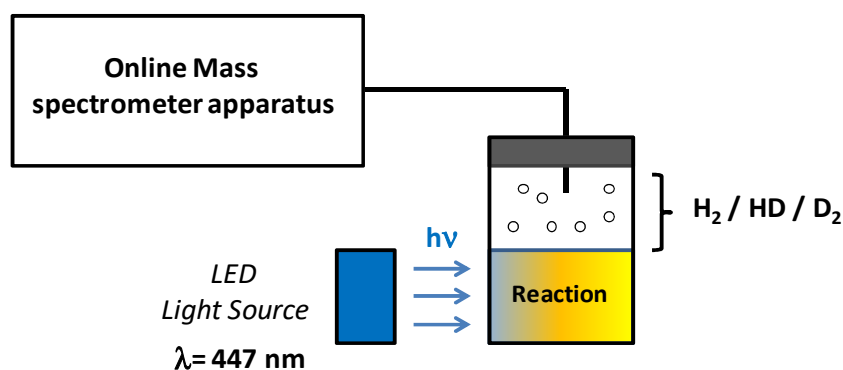


Figure IX. 22. Setup for the online measurement of the H₂, HD and D₂ ratios formed under light-driven conditions.

Parallel Pressure Transducer Hardware. The parallel pressure transducer that we used for these studies is the same that previously was developed and described for water oxidation studies.³⁰⁴ This is composed by 8 differential pressure transducers (Honeywell-ASCX15DN, ± 15 psi) connected to a hardware data-acquisition system (base on Atmega microcontroller) controlled by a home-developed software program. The differential pressure transducer Honeywell-ASCX15DN is a 100 microseconds response, signal-conditioned (high level span, 4.5 V) output, calibrated and temperature compensated (0 $^{\circ}$ C to 70 $^{\circ}$ C) sensor. The differential sensor has two sensing ports that can be used for differential pressure measurements. The pressure calibrated devices to within ± 0.5 matm was offset and span calibrated *via* software with a high precision pressure transducer (PX409-030GUSB, 0.08% Accuracy). Each of the 8 differential pressure transducers (Honeywell-ASCX15DN, ± 15 psi) produce a voltage outputs that can directly transformed to a pressure difference between the two measuring ports. The voltage outputs were digitalized with a resolution of 0.25 matm from 0 to 175 matm and 1 matm from 176 to 1000 matm using an Atmega microcontroller with an independent voltage auto-calibration. Firmware Atmega microcontroller and control software were home-

developed. The sensitivity of H₂ analytics allows quantifying the gas formed when low H₂ volumes are generated. Therefore, it could not be discarded that small amounts of H₂ were produced by inactive complexes.

Gas chromatography identification and quantification of gases. Gases at the headspace were analyzed with an Agilent 7820A GC System equipped with columns Washed Molecular Sieve 5A, 2m x 1/8" OD, Mesh 60/80 SS and Porapak Q, 4m x 1/8" OD, SS, Mesh: 80/100 SS and a Thermal Conductivity Detector. The quantification of the H₂ obtained was measured through the interpolation of a previous calibration using different H₂/N₂ mixtures.

Light source. The reactions were performed using Royal-Blue ($\lambda = 447 \pm 20$ nm) LUXEON Rebel ES LED, Mounted on a 10mm Square Saber - 1030 mW @ 700mA (Datasheet: <https://www.luxeonstar.com/assets/downloads/ds68.pdf>) as a light source.

IX.4.3. General procedure for KIE determination using H₂O and D₂O

KIE determined by NMR. By direct irradiation for 2.5, 7.5 13 and 18 min and subsequent analysis of reactions carried out in an NMR tube at $\lambda = 447$ nm and 30 °C, under N₂. Conditions: **1c_o** (0.189 μ mol, 3 mol%), **PS_{Ir}** (0.076 μ mol, 1.2 mol%) and **9a** (6.30 μ mol, 12.6 mM) irradiated in CH₃CN:H₂O(or D₂O):Et₃N (0.15:0.35:0.01 mL) as indicated. Only 1.2 mol% of **PS_{Ir}** was employed to guarantee the solubility of all components in D₂O (See section A.6.1.1 for detailed information).

KIE determined by GC analysis. The study was carried out under N₂ using CH₃CN:H₂O:Et₃N or CH₃CN:D₂O:Et₃N (3:7:0.2 mL) as a solvent mixture. Conditions: **1c_o** (3.8 μ mol, 3 mol%), (**PS_{Ir}** (2.5 μ mol, 2 mol%), substrate (0.126 mmol, 12.4 mM) under irradiation ($\lambda = 447$ nm) at 30 °C. The amount of **10a** in each reaction time was determined through quenching the reaction carried out under the same catalytic conditions at different reaction times. The **10a** formed was determined by GC analysis after the reaction workup and relative to a calibrated internal standard (See section A.6.1.2 for detailed information).

IX.4.4. General Procedure of NMR Measurements for ^{13}C KIE Determination

^{13}C measurements were carried out by 27 catalytic reactions under the same catalytic conditions. All employed acetophenone was used from the same commercial lot. After the irradiation time, the crude mixtures of all of the 27 reactions were combined and purified and the final isolated product was subjected to ^{13}C -NMR analysis. The ^{13}C values are the average from 6 ^{13}C -NMR measurements of the same sample. The ^{13}C -NMR samples of starting and recovered material were prepared identically, using 100 mg of acetophenone in 5 mm NMR tubes in CDCl_3 with a constant height of 5.0 cm.

To avoid integration problems by possible paramagnetic impurities, a T_1 determination by the inversion-recovery method was carried out for each NMR sample. T_1 values were examined to exclude artefacts. The ^{13}C spectra were recorded at 125.94 MHz, on a Bruker 500 MHz spectrometer, using inverse gated decoupling, 100 s delays between calibrated $\pi/2$ pulses, and a 5.999 s acquisition time to collect 191360 points. Integrations were determined numerically using a constant integration region for each peak. Six spectra were obtained for each sample of recovered acetophenone along with corresponding samples of acetophenone that were not subjected to the reaction conditions. From the ^{13}C integrations the ^{13}C KIEs and uncertainties were calculated as previously described.⁵⁴⁰

NMR Results. The integration average for the 27 samples are shown in Table IX. 4. The carbon (C_F) was used as reference and was set up at 1000.

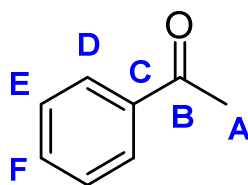


Table IX. 4 Average ^{13}C integration values for acetophenone

Conversion (%)	C_A	C_B	C_C	C_D	C_E	C_F	n
Standard ^[a]	944.36	1001.55	1013.03	997.65	997.65	1000	6
89.5 ± 1 % ^[b]	948.72	1057.92	1018.84	1001.17	1001.17	1000	6

[a] ^{13}C integrations of the commercial acetophenone not subjected to the reaction. [b] ^{13}C integrations of the recovered acetophenone from the reaction at 89.5% of conversion.

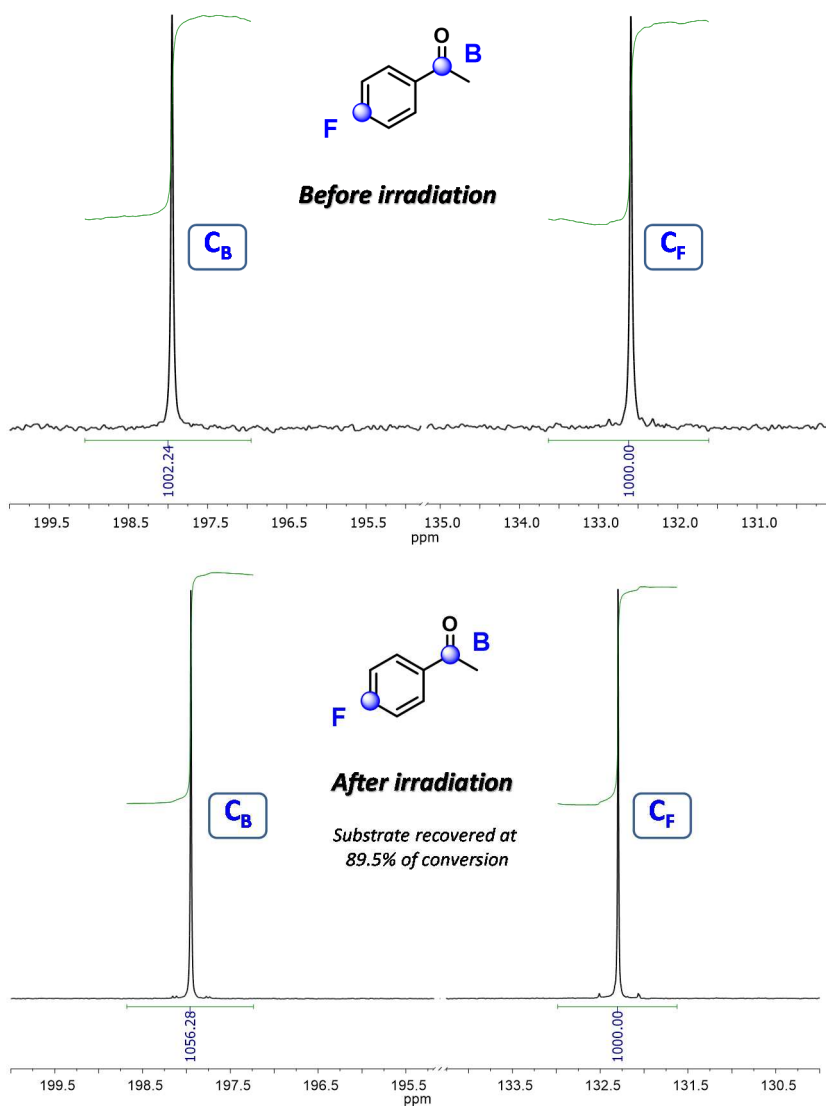


Figure IX. 23. ^{13}C enrichment after the reaction. Integration values of the C_B carbon compared to the para carbon set at 1000 before (Top) and after the recovery of the acetophenone at 89.5% of conversion (Bottom).

As described by *Singleton et al.*,⁵⁴⁰ Equation 1 holds the relation between the proportion of a minor isotopic component in the recovered material compared to the original material (R/R_0), with the conversion of the reactants (F) and KIE (Relative rate for major/minor isotopic components). As shown in Eq. IX. 2, R/R_0 values are magnified at higher conversions ($F \rightarrow 1$) (Figure IX. 24, left), and thus it can improve the precision of KIE determinations (Figure IX. 24, right).

$$\frac{R}{R_0} = (1 - F)^{(1/\text{KIE})-1} \quad (\text{Eq. IX. 2})$$

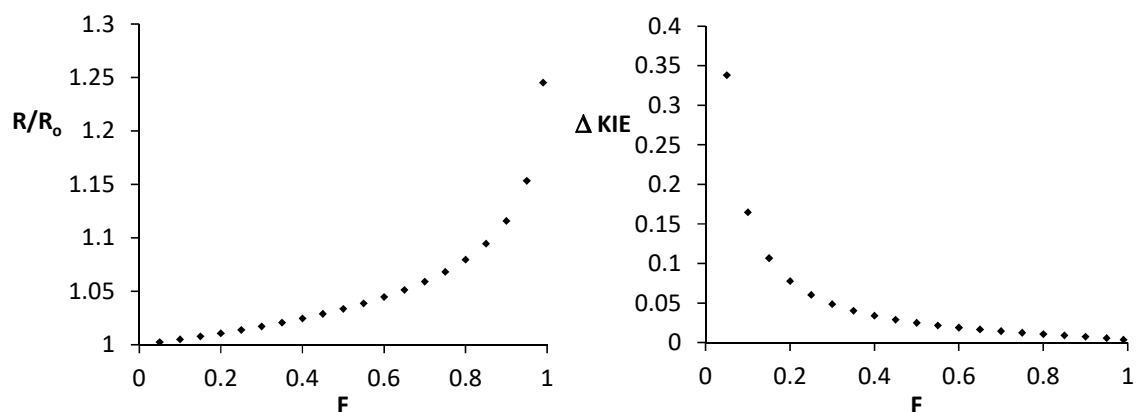


Figure IX. 24. *Left:* Simulated R/R_0 values versus the conversion for a KIE value of 1.05. *Right:* Simulated KIE uncertainties versus the conversion. Uncertainties calculated with the Equation 6.

The R/R_0 values can be determined using the integrations values ratios of the carbons. The values for R/R_0 , calculated as the ratio of average integrations in Table IX. 4 relative to the standard, are shown in Table IX. 5. Standard deviations were determined with Eq. IX. 3.

$$\Delta R/R_0 = R/R_0 \times \left(\left(\frac{\Delta \text{IntSample}}{\text{IntSample}} \right)^2 + \left(\frac{\Delta \text{IntStandard}}{\text{IntStandard}} \right)^2 \right)^{1/2} \quad (\text{Eq. IX. 3})$$

Table IX. 5. R/R_0 calculated values for acetophenone.

R/R_0 and Stand. Dev.	C_A	C_B	C_C	C_D	C_E	C_F
R/R_0	1.004	1.056	1.005	1.003	1.003	1.000
Stand. Dev.	0.011	0.013	0.009	0.011	0.011	0.000

R/R_0 values calculated from the integrations obtained at 89.5% of conversion. R : ^{13}C integrations of the commercial acetophenone not subjected to the reaction. R_0 : ^{13}C integrations of the recovered acetophenone from the reaction at 89.5% of conversion.

^{13}C KIEs for acetophenone were then calculated from Eq. IX. 4, with the standard deviations calculated according to Eq. IX. 5, IX. 6 and IX. 7. All formulas were taken from: Singleton, D. A.; Thomas, A. A. *J. Am. Chem. Soc.* **1995**, *117*, 9357.

$$\text{KIE}_{\text{calcd}} = \frac{\ln(1-F)}{\ln(1-F)R/R_0} \quad (\text{Eq. IX. 4})$$

$$\Delta \text{KIE}_F = \frac{\partial \text{KIE}}{\partial F} \Delta F = \frac{-\ln(R/R_0)}{(1-F)\ln^2 [(1-F)R/R_0]} \Delta F \quad (\text{Eq. IX. 5})$$

$$\Delta \text{KIE}_R = \frac{\partial \text{KIE}}{\partial (R/R_0)} \Delta (R/R_0) = \frac{-\ln(1-F)}{(R/R_0)\ln^2 [(1-F)R/R_0]} \Delta R/R_0 \quad (\text{Eq. IX. 6})$$

$$\Delta \text{KIE} = \text{KIE} \times \left(\left(\frac{\Delta \text{KIE}_R}{\text{KIE}} \right)^2 + \left(\frac{\Delta \text{KIE}_F}{\text{KIE}} \right)^2 \right)^{1/2} \quad (\text{Eq. IX. 7})$$

Table IX. 6. ^{13}C KIEs values calculated from Table IX. 5 and Eq. IX. 4.

KIE and Stand. Dev.	C_A	C_B	C_C	C_D	C_E	C_F
^{13}C KIE	1.002	1.025	1.002	1.001	1.001	1.000
Δ KIE	0.005	0.006	0.004	0.005	0.005	0.000

IX.4.5. SDKIE Determination

IX.4.5.1. General procedure

The determination of the SDKIE for the series of the benzaldehydes-H/D were conducted in a 15 mL capped vials with a septum under nitrogen atmosphere at room temperature. A typical experiment was conducted using a solution of MeCN:H₂O:Et₃N (2:8:0.2 mL), **1c_o** (5 μmol , 3 mol%), **PS_{Ir}** (2.5 μmol , 1.5 mol%) containing benzaldehyde-*H* (0.084 mmol, 8.2 mM) and the same amount of the corresponding deuterated benzaldehyde-*D* (0.084 mmol, 8.2 mM), and it was irradiated for 15 min at $\lambda = 447$ nm under N₂. After the irradiation, the mixture was extracted using CH₂Cl₂ (3 x 2 mL) and the combined organic layers were dried over MgSO₄ and evaporated under the reduced pressure. The resulting crude oil was dissolved with CH₂Cl₂ (1 mL) and it was passed through a silica plug, which was eluded with Hexane:AcOEt (8:2).

IX.4.5.2. Synthetic procedures

Synthesis of labelled benzaldehydes. Commercially available R-substituted benzoic acids were converted to the corresponding benzyl-deuterated benzaldehydes following the synthetic procedures described below. Ethyl 4-methylbenzoate and ethyl 4-methoxybenzoate were prepared following the procedure reported in the literature.⁵⁶⁰

IX.4.5.2.1. Synthesis of 4-methyl-1-d₁-benzaldehyde (**[D]-9w**)

***p*-tolylmethan-*d*₂-ol:** LiAlD₄ (86 mg, 1.85 mmol, 0.54 eq.) was suspended in Et₂O (6 mL) at 0°C, under an argon atmosphere. Ethyl 4-methylbenzoate (507 mg, 3.37 mmol, 1 eq) was added dropwise and the reaction was allowed to come to room temperature and stirred for 3 hours. The reaction was quenched by the addition of 4 M NaOH aq and extraction with ethyl acetate three times furnished an organic layer, which was dried and concentrated under reduced pressure to give the desired *p*-tolylmethan-*d*₂-ol as a white solid in a quantitative yield. ¹H-NMR (CDCl₃, 400 MHz, 300 K) δ , ppm: 7.27 (d, 2H), 7.20 (d, 2H), 2.39 (s, 3H, CH₃), 2.03 (br, 1H, OH) ¹³C{¹H}-NMR (CDCl₃, 101 MHz, 300 K) δ , ppm: 137.8, 137.4, 129.2, 127.2, 64.5 (quint, $J = 21.8$ Hz), 21.2. GC-MS (m/z) = 124.1

4-methyl-1-*d*₁-benzaldehyde. Pyridinium chlorochromate (PCC) (2.15 g, 10 mmol) was added to a solution of *p*-tolylmethan-*d*₂-ol (6.66 mmol) in anhydrous dichloromethane, under argon atmosphere. The resulting solution was left stirred overnight at room temperature. After that, Celite was added to the brown crude mixture and filtered,

washing with CH_2Cl_2 . Column chromatography on silica gel using Hexane:AcOEt (9:1) yielded the deuterated benzaldehyde as a colorless oil (0.800 g, 6.60 mmol, 99 % yield). $^1\text{H-NMR}$ (CDCl_3 , 500 MHz, 300 K) δ , ppm: 7.8 (d, $J = 8.3$ Hz, 2H), 7.35 (d, $J = 8.3$ Hz, 2H), 2.46 (s, 3H). $^{13}\text{C-NMR}$ (CDCl_3 , 126 MHz, 300 K) δ , ppm: 191.7 (t, $J = 26.43$ Hz), 145.6, 134.1 (t, $J = 3.8$ Hz), 129.7, 21.9. GC-MS (m/z) = 121.1

IX.4.5.2.2. Synthesis of 4-methoxy-1- d_1 -benzaldehyde ([D]-9v)

(4-methoxyphenyl)methan- d_2 -ol: LiAlD_4 (283 mg, 6.06 mmol, 0.54 eq.) was suspended in Et_2O (10 mL) at 0°C , under an argon atmosphere. Ethyl 4-methoxybenzoate (2 g, 11.1 mmol, 1 eq) was added dropwise and the reaction was allowed to come to room temperature and stirred for 3 hours. The reaction was quenched by the addition of 4 M NaOH aq and extraction with ethyl acetate three times furnished an organic layer, which was dried and concentrated under reduced pressure to give the desired (4-methoxyphenyl)methan- d_2 -ol as a colourless oil in a quantitative yield. $^1\text{H-NMR}$ (CDCl_3 , 400 MHz, 300 K) δ , ppm: 7.30 (dt, $J = 8.8$ Hz, $J' = 2.9$ Hz, 2H), 6.90 (dt, $J = 8.8$ Hz, $J' = 2.9$ Hz, 2H), 3.83 (s, 3H, OCH_3), 1.85 (s, 1H, OH). $^{13}\text{C}\{^1\text{H}\}$ -NMR (CDCl_3 , 101 MHz, 300 K) δ , ppm: 159.2, 133.0, 128.8, 113.9, 64.3 (quint, $J = 21.7$ Hz), 55.3. GC-MS (m/z) = 140.0

4-methoxy-1- d_1 -benzaldehyde. Pyridinium chlorochromate (PCC) (2.31 g, 10.7 mmol) was added to a solution of (4-methoxyphenyl)methan- d_2 -ol (7.13 mmol) in anhydrous dichloromethane, under argon atmosphere. The resulting solution was left stirred overnight at room temperature. After that, Celite was added to the brown crude mixture and filtered, washing with CH_2Cl_2 . Column chromatography on silica gel using Hexane:AcOEt (9:1) yielded the deuterated benzaldehyde as a colourless oil (0.577 g, 4.08 mmol, 58 % yield). $^1\text{H-NMR}$ (CDCl_3 , 500 MHz, 300 K) δ , ppm: 7.86 (d, $J = 8.9$ Hz, 1H), 7.02 (d, $J = 8.8$ Hz, 1H), 3.90 (s, 3H). $^{13}\text{C}\{^1\text{H}\}$ -NMR (CDCl_3 , 126 MHz, 300 K) δ , ppm: 190.7 (t, $J = 26.4$ Hz), 164.6, 131.9, 129.9 (t, $J = 3.78$ Hz), 114.3, 55.6. GC-MS (m/z) = 137.1

IX.4.5.2.3. Synthesis of 3,5-di-*tert*-butyl-1- d_1 -benzaldehyde ([D]-9x).

Ethyl 3,5-di-*tert*-butylbenzoate. A solution of 3,5-di-*tert*-butylbenzoic acid (0.8 g, 3.4 mmol) and H_2SO_4 (2.6 mL, 49.11 mmol) in EtOH was refluxed for 24 hours. After removing the EtOH, CH_2Cl_2 followed by saturated aqueous Na_2CO_3 (60 mL) were added and the mixture was extracted with CH_2Cl_2 (3 x 50 mL) and then dried over MgSO_4 . By removing CH_2Cl_2 , 0.81 g (91% yield) of ethyl 3,5-di-*tert*-butylbenzoate were obtained. $^1\text{H-NMR}$ (CDCl_3 , 400 MHz, 300 K) δ , ppm: 7.78 (s, 2H), 7.68 (s, 1H), 4.30 (q, 2H), 1.35 (s, 18H), 1.30 (t, 3H).

(3,5-di-*tert*-butylphenyl)methan- d_2 -ol: LiAlD_4 (67 mg, 1.43 mmol, 0.54 eq.) was suspended in Et_2O (10 mL) at 0°C , under an argon atmosphere. Ethyl 3,5-di-*tert*-butylbenzoate (0.7 g, 2.66 mmol, 1 eq) was added dropwise and the reaction was allowed to come to room temperature and stirred for 3 hours. The reaction was

quenched by the addition of 4 M NaOH aq and extraction with ethyl acetate three times furnished an organic layer, which was dried and concentrated under reduced pressure to give the desired (3,5-di-*tert*-butylphenyl)methan-*d*₂-ol as a white solid in a quantitative yield. ¹H-NMR (CDCl₃, 400 MHz, 300 K) δ, ppm: 7.41 (s, 1H), 7.17 (s, 2H), 1.78 (s, OH), 1.38 (s, 18H). ¹³C{¹H}-NMR (CDCl₃, 101 MHz, 300 K) δ, ppm: 151.1, 139.9, 121.8, 121.4, 65.9, 65.4 (quint, *J* = 21.7 Hz), 34.9, 31.5. GC-MS (*m/z*) = 221.1.

3,5-di-*tert*-butyl-1-*d*₁-benzaldehyde. Pyridinium chlorochromate (PCC) (860 mg 4 mmol) was added to a solution of (4-methoxyphenyl)methan-*d*₂-ol (2.66 mmol) in anhydrous dichloromethane, under argon atmosphere. The resulting solution was left stirred overnight at room temperature. After that, Celite was added to the brown crude mixture and filtered, washing with CH₂Cl₂. Column chromatography on silica gel using Hexane:AcOEt (9:1) yielded the deuterated benzaldehyde as a white solid (430 mg, 1.96 mmol, 75 % yield). ¹H-NMR (CDCl₃, 500 MHz, 300 K) δ, ppm: 7.75 (m, 3H), 1.39 (s, 18H). ¹³C-NMR (CDCl₃, 126 MHz, 300 K) δ, ppm: 192.8 (m), 151.8, 136.1, 128.9, 124.1, 34.9, 31.3. GC-MS (*m/z*) = 219.1.

IX.4.6. Theoretical Studies

IX.4.6.1. Computational details

The DFT quantum mechanical exploration of the ketone reduction mechanism was carried out using the Gaussian09 program.³⁰¹ Geometry optimizations were performed in the unrestricted spin formalism, with the B3LYP hybrid exchange-correlation functional³⁰⁵⁻³⁰⁷ and the standard 6-31G* basis set for all atoms. The solvation effect of water was introduced in geometry optimizations and energy through the SMD polarizable continuum model.³⁰⁸ Dispersion effects were also included using the Grimme D₂ correction.³⁰⁹ The located stationary points were characterized by analytical frequency calculations at the same level of theory than geometry optimizations. Gibbs energy values (G) were obtained by including thermal, solvation and Grimme corrections to the potential energy computed with the 6-311+G** basis set on equilibrium geometries:

$$G = E_{6-311+G^{**}} + G_{\text{corr.}} + G_{\text{solv.}} + E_{\text{disp.}} \quad (\text{Eq. IX. 8})$$

where the thermal correction ($G_{\text{corr.}}$) was obtained from gas phase analytical Hessians calculations at 298.15 K, the solvation energy ($G_{\text{solv.}}$) was calculated as the difference of the total free energy in gas phase and in water at the same level of theory and geometry and $E_{\text{disp.}}$ is the dispersion correction.

Hirshfeld's charges and Mayer bond order indexes^{561,562} were computed to rationalize the reactivity trends of Co-H species.

Labels **I**, **TS** and **II** were used as short nomenclature of reactant complexes, transition states and products involved in the C-H bond formation event. The **homo** and **heter** notations are related to the homolytic or heterolytic nature of the C-H bond formation. Labels **d**, **q**, **s**, **t** are used to specify the doublet, quartet, singlet and triplet spin states of the cobalt complexes, respectively.

IX.4.6.2. Redox potentials, pK_a values and hydricities

The pK_a can be quantified by:

$$pK_a = \frac{\Delta G^\circ}{RT \ln(10)} \quad (\text{Eq. IX. 9})$$

where R is the universal gas constant and T is the temperature.³¹¹ The ΔG° (standard dissociation free energy change between an acid (AH) and its conjugate base (A⁻) in aqueous phase) may be expressed using the following equations:

$$\Delta G^\circ = G(A_{\text{aq}}^-) + G(H_{\text{aq}}^+) - G(AH_{\text{aq}}) + \Delta G^* \quad (\text{Eq. IX. 10})$$

$$G(H_{\text{aq}}^+) = G(H_{\text{gas}}^+) + \Delta G_{\text{solv}}^{H^+} \quad (\text{Eq. IX. 11})$$

where $G(AH_{\text{aq}})$ and $G(A_{\text{aq}}^-)$ are standard free energies of the acid and its conjugate base, respectively. The $G(H_{\text{aq}}^+)$ is the free energy of the proton in water, obtained from the experimental solvation free energy of a proton ($\Delta G_{\text{solv}}^{H^+} = -265.9 \text{ kcal} \cdot \text{mol}^{-1}$) and its gas-phase free energy ($G(H_{\text{gas}}^+) = -6.3 \text{ kcal} \cdot \text{mol}^{-1}$).³¹² ΔG^* is the free energy change associated with the conversion from a standard-state of 1 M in the aqueous phase and 1 atm in gas phase, to 1 M in both phases. Its value is $1.89 \text{ kcal} \cdot \text{mol}^{-1}$ at 298 K.

In the free energy balances, the following concentrations were used to adjust the final free energies: 16.8 mM for acetophenone and cyclohexanone, 40 M for water and 5.7 M for acetonitrile (the concentrations of water and acetonitrile were derived from the 7:3 H₂O/CH₃CN solvent mixture used in catalysis). The previous concentrations translate into $\Delta G^{o/*}$ values (at 298.15 K) of $-0.53 \text{ kcal} \cdot \text{mol}^{-1}$ for ketone substrates, $4.1 \text{ kcal} \cdot \text{mol}^{-1}$ for water and $2.9 \text{ kcal} \cdot \text{mol}^{-1}$ for acetonitrile.

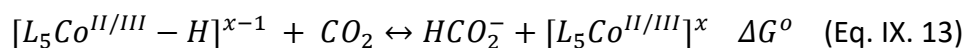
The standard one electron redox potentials relative to the SHE electrode were calculated by:

$$E^\circ = -\frac{\Delta G^* - \Delta G_{\text{SHE}}}{F} \quad (\text{Eq. IX. 12})$$

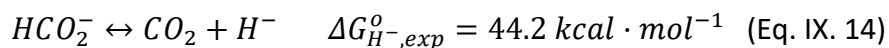
where ΔG^* is the standard free energy change associated with the reduction reaction, F is the Faraday constant and ΔG_{SHE} is the free energy change associated with the proton reduction to H₂ (-4.24 eV). The ΔG_{SHE} value was derived using the Fermi-Dirac statistics for the treatment of electron thermodynamics.⁵⁶³

Energetics for the reduction steps were calculated relative to the redox potential of the iridium photosensitizer ($E^{\circ}(\text{Ir}^{\text{II}}/\text{Ir}^{\text{III}}) = -1.38 \text{ V vs. SHE}$). The reduction of an acetophenone molecule to the corresponding protonated ketyl radical supposes an energetic cost of $3.2 \text{ kcal}\cdot\text{mol}^{-1}$ respect to the $\text{Ir}^{\text{III}}/\text{Ir}^{\text{II}}$ redox couple. Taking into account the previous value, the relationship $\Delta G^{\circ} = -RT\ln(K)$ and a 16.8 mM for acetophenone, we derived a protonated ketyl radical concentration of $75.8 \text{ }\mu\text{M}$, with a $\Delta G^{0/*}$ value of $-3.7 \text{ kcal}\cdot\text{mol}^{-1}$. The generation of a diradical adduct from the protonated ketyl radical is an endergonic process with a free energy of $13.5 \text{ kcal}\cdot\text{mol}^{-1}$. From this data, we calculate a diradical adduct concentration of $7.55\cdot 10^{-14} \text{ }\mu\text{M}$ and $\Delta G^{0/*} = -22.8 \text{ kcal}\cdot\text{mol}^{-1}$.

The hydricities of Co-H species in acetonitrile were evaluated employing the isodesmic scheme:⁵⁶⁴



where,



CHAPTER X

General Conclusions

X. GENERAL CONCLUSIONS

In **Chapter III** three complexes based on Fe (**1_{Fe}**), Co (**1_{Co}**) and Ni (**1_{Ni}**) sharing the same aminopyridine ligand Py₂^Tstacn were tested in electro and photocatalytic H₂ production. While all three complexes were found active under electrocatalytic conditions, only the cobalt-based complex was able to efficiently catalyze the reduction of water when paired with **PS_{Ir}** as photoredox catalyst. By DLS, NTA and poisoning experiments we confirmed the formation of inactive nanoparticles during the irradiation time, suggesting that the real catalyst is molecular in nature. The sum of our mechanistic observations together with DFT calculations allowed us to elucidate the factors that controlled the activity among the three complexes. Under photocatalytic conditions, **1_{Ni}** and **1_{Co}** can achieve the M^I oxidation state with the aim of the photoredox system, which is not the case of **1_{Fe}**. However, the Co^I specie was found to be the only one capable to generate a stable Co^{III}-H species in the basic solution, leading to the generation of H₂.
“Understanding the role of the metal center on water reduction catalysis may allow the design of new active systems.”

In **Chapter IV** the systematic tuning of the electronic properties on **1^H** ([Co(OTf)₂(Py^{Me}tacn)]) have been found to impact directly on water reduction activity, strongly supporting that the catalytic activity is originated from the molecular system. The photocatalytic activity dependence was clearly illustrated in the excellent linear correlations observed in the Hammett analysis of the relative reaction rates (log(rate **1^R**/rate **1^H**) versus Hammett values of substituents (σ), showing two different regimens of activity. Towards a better mechanistic understanding, kinetic experiments and DFT calculations suggested that the electronic nature of the ligand controlled the formation of Co^I and Co^{III}-H species. Presumably, the appropriate combination of the Co^{II/I} redox couple and pK_a (Co^{III}-H) value is sustained by the catalyst **1^{CO₂Et}**, which is the most active from the series (up to 8500 TON). In contrast, the electrocatalytic activity of these complexes obeys an opposite trend, being enhanced with more donating ligands. We proposed that a decoordination of the pyridine through a PCET step is involved.

“The water reduction activity can be modulated through the electronic modification of the ligand.”

In **Chapter V** we demonstrated that the modular nature of tacn ligands let to modulate the activity through the modification of the second-sphere of the catalyst. It was achieved by the introduction of the biotinylated cobalt catalysts **1^{Biotin}** and **1^{Spacer-Biotin}** into streptavidin. The resulting cobalt metalloenzymes provides a decrease in the water reduction overpotential and enhance the photocatalytic activity of the molecular cobalt complex.

“The introduction of Co aminopyridine cobalt complexes into proteins lead to an activity enhancement”.

In **Chapter VI** we have synthesized and characterized the $\text{Py}_2^{\text{T5tacn}}$ cobalt complex in oxidation state (I) by NMR, XAS and SQUID magnetometry. Presumably Co^{I} species possesses an extra electron respect to Co^{II} and could be interpreted as $\text{Co}^{\text{II}} \text{S} = 3/2$. However, in contrast to Co^{II} species, Co^{I} efficiently reacts with protons, and O_2 to give rise Co^{III} species. With the aim the give some light into this intriguing discrepancy between XAS, SQUID and observed reactivity, DFT modelled structures suggested that Co^{I} species has an important spin density located over one of the pyridines of $\text{Py}_2^{\text{T5tacn}}$ ligand leading to a formal Co^{II} metal center.

“The metal center of the Co^{I} species is electronically similar to the Co^{II} species but has a reactivity against protons, water and O_2 as expected for a Co^{I} most probably due to the unusual non-innocent character of the pyridine”.

In **Chapter VII**, cobalt aminopyridine complexes were found active for the photocatalytic reduction of ketones and aldehydes using H_2O as source of hydrogen and visible-light as driving force to regenerate to Co-based active species. Ligand availability, modularity and versatility of this type of coordination complexes open up to systematically study a family of cobalt structures. This allowed us to pinpointing preferred ligand structures to sustain efficient ketone reduction. Kinetic studies performed with catalyst **1_{Co}** showed that water reduction to H_2 and ketone reduction to alcohols are competing reactions, strongly supporting that both share a common well-defined intermediate. The catalytic system provides remarkable selectivities towards the reduction of aromatic ketones. Remarkably, up to 37 % ee using the chiral cobalt complex $[\text{Co}(\text{OTf})_2((S,S)\text{-PDP})]$ could be obtained. The use of **PS_{Cu}** as photoredox catalyst

led to an improvement of the catalytic activity together with decreased catalyst loadings.

“Aminopyridine cobalt complexes for H₂ evolution can also photocatalytically reduce ketones”.

In **Chapter VIII**, the electronic tuning of the tetra- and penta-dentate aminopyridine cobalt complexes allows an easy modulation of the photocatalytic activity in ketone reduction. The use of donating ligands affords more selectivity towards the reduction of ketones, whereas electron withdrawing ligands favors the selectivity towards H₂ production.

“The photocatalytic ketone reduction activity can be modulated and improved by the electronic modification of the ligand”.

In **Chapter IX**, towards the understanding of the operative mechanism of light-driven ketone reduction, fluorescence quenching, UV/Vis, electrochemical, kinetic and isotope labelling experiments were performed. Under photochemical conditions the starting Co^{II} species can be reduced to Co^I with the aid of the photoredox catalyst **PS_{Ir}^{II}** generating the formal Co^I species, which then evolves to Co-H species. We concluded that these species preferred react with the substrate through a heterolytic pathway involving Co^{II}-H species. However, the contribution of a homolytic pathway in some substrates involving a HAT mechanism with ketyl radical species cannot be discarded since ketyl radical species can be formed in solution.

“The photocatalytic reduction of ketones can occur through a heterolytic mechanism”.

References

REFERENCES

- (1) Lewis, N. S.; Nocera, D. G. *Proc. Natl. Acad. Sci. U. S. A.* **2006**, *103*, 15729.
- (2) Barber, J. *Chem. Soc. Rev.* **2009**, *38*, 185.
- (3) Ronge, J.; Bosserez, T.; Martel, D.; Nervi, C.; Boarino, L.; Taulelle, F.; Decher, G.; Bordiga, S.; Martens, J. A. *Chem. Soc. Rev.* **2014**, *43*, 7963.
- (4) Lewis, N. S.; Nocera, D. G. *Proc. Natl. Acad. Sci.* **2006**, *103*, 15729.
- (5) Barber, J. *Int. J. Photoenergy* **2004**, *6*, 43.
- (6) Ferreira, K. N.; Iverson, T. M.; Maghlaoui, K.; Barber, J.; Iwata, S. *Science* **2004**, *303*, 1831.
- (7) Nocera, D. G. *Acc. Chem. Res.* **2012**, *45*, 767.
- (8) Blankenship, R. E.; Tiede, D. M.; Barber, J.; Brudvig, G. W.; Fleming, G.; Ghirardi, M.; Gunner, M. R.; Junge, W.; Kramer, D. M.; Melis, A.; Moore, T. A.; Moser, C. C.; Nocera, D. G.; Nozik, A. J.; Ort, D. R.; Parson, W. W.; Prince, R. C.; Sayre, R. T. *Science* **2011**, *332*, 805.
- (9) Berardi, S.; Drouet, S.; Francas, L.; Gimbert-Surinach, C.; Guttentag, M.; Richmond, C.; Stoll, T.; Llobet, A. *Chem. Soc. Rev.* **2014**, *43*, 7501.
- (10) Fontecilla-Camps, J. C.; Volbeda, A.; Cavazza, C.; Nicolet, Y. *Chem. Rev.* **2007**, *107*, 4273.
- (11) Fontecilla-Camps, J. C.; Amara, P.; Cavazza, C.; Nicolet, Y.; Volbeda, A. *Nature* **2009**, *460*, 814.
- (12) Peters, J. W.; Lanzilotta, W. N.; Lemon, B. L.; Seefeldt, L. C. *Science* **1998**, *282*, 1853.
- (13) Volbeda, A.; Charon, M.-H.; Piras, C.; Hatchikian, E. C.; Frey, M.; Fontecilla-Camps, J. C. *Nature* **1995**, *373*, 580
- (14) Nicolet, Y.; Piras, C.; Legrand, P.; Hatchikian, C. E.; Fontecilla-Camps, J. C. *Structure* **1999**, *7*, 13.
- (15) Montet, Y.; Amara, P.; Volbeda, A.; Venede, X.; Hatchikian, E. C.; Field, M. J.; Frey, M.; Fontecilla-Camps, J. C. *Nat. Struct. Biol.* **1997**, *4*, 523.
- (16) Volbeda, A.; Garcin, E.; Piras, C.; Lacey, A. L. d.; Fernandez, V. M.; Hatchikian, E. C.; Frey, M.; Fontecilla-Camps, J. C. *J. Am. Chem. Soc.* **1996**, *118*, 12989.
- (17) Appel, A. M.; Bercaw, J. E.; Bocarsly, A. B.; Dobbek, H.; DuBois, D. L.; Dupuis, M.; Ferry, J. G.; Fujita, E.; Hille, R.; Kenis, P. J.; Kerfeld, C. A.; Morris, R. H.; Peden, C. H.; Portis, A. R.; Ragsdale, S. W.; Rauchfuss, T. B.; Reek, J. N.; Seefeldt, L. C.; Thauer, R. K.; Waldrop, G. L. *Chem. Rev.* **2013**, *113*, 6621.
- (18) Wang, Y.; Wang, M.; Sun, L.; Ahlquist, M. S. *Chem. Commun.* **2012**, *48*, 4450.
- (19) Sit, P. H.; Car, R.; Cohen, M. H.; Selloni, A. *Proc. Natl. Acad. Sci. U. S. A.* **2013**, *110*, 2017.
- (20) Lunsford, A. M.; Blank, J. H.; Moncho, S.; Haas, S. C.; Muhammad, S.; Brothers, E. N.; Darensbourg, M. Y.; Bengali, A. A. *Inorg. Chem.* **2016**, *55*, 964.
- (21) Streich, D.; Astuti, Y.; Orlandi, M.; Schwartz, L.; Lomoth, R.; Hammarstrom, L.; Ott, S. *Chem. Eur. J.* **2010**, *16*, 60.
- (22) Wang, H. Y.; Wang, W. G.; Si, G.; Wang, F.; Tung, C. H.; Wu, L. Z. *Langmuir* **2010**, *26*, 9766.
- (23) Cao, W. N.; Wang, F.; Wang, H. Y.; Chen, B.; Feng, K.; Tung, C. H.; Wu, L. Z. *Chem. Commun.* **2012**, *48*, 8081.
- (24) Frederix, P. W.; Kania, R.; Wright, J. A.; Lamprou, D. A.; Ulijn, R. V.; Pickett, C. J.; Hunt, N. T. *Dalton Trans.* **2012**, *41*, 13112.
- (25) Wang, F.; Wang, W.-G.; Wang, H.-Y.; Si, G.; Tung, C.-H.; Wu, L.-Z. *ACS Catal.* **2012**, *2*, 407.
- (26) Ghosh, S.; Hogarth, G.; Hollingsworth, N.; Holt, K. B.; Richards, I.; Richmond, M. G.; Sanchez, B. E.; Unwin, D. *Dalton Trans.* **2013**, *42*, 6775.

REFERENCES

- (27) Tard, C.; Pickett, C. J. *Chem. Rev.* **2009**, *109*, 2245.
- (28) Barton, B. E.; Rauchfuss, T. B. *Inorg. Chem.* **2008**, *47*, 2261.
- (29) Song, L.-C.; Yang, Z.-Y.; Hua, Y.-J.; Wang, H.-T.; Liu, Y.; Hu, Q.-M. *Organometallics* **2007**, *26*, 2106.
- (30) Chiang, M. H.; Liu, Y. C.; Yang, S. T.; Lee, G. H. *Inorg. Chem.* **2009**, *48*, 7604.
- (31) Hartley, C. L.; DiRisio, R. J.; Chang, T. Y.; Zhang, W.; McNamara, W. R. *Polyhedron* **2016**, *114*, 133.
- (32) Cavell, A. C.; Hartley, C. L.; Liu, D.; Tribble, C. S.; McNamara, W. R. *Inorg. Chem.* **2015**, *54*, 3325.
- (33) Connor, G. P.; Mayer, K. J.; Tribble, C. S.; McNamara, W. R. *Inorg. Chem.* **2014**, *53*, 5408.
- (34) Tang, L.-Z.; Lin, C.-N.; Zhan, S.-Z. *Polyhedron* **2016**, *110*, 247.
- (35) Zhou, L.-L.; Tang, L.-Z.; Zhang, Y.-X.; Zhan, S.-Z. *Polyhedron* **2015**, *92*, 124.
- (36) Zhang, Y.-X.; Fu, L.-Z.; Zhou, L.-L.; Tang, L.-Z.; Zhan, S.-Z. *J. Coord. Chem.* **2015**, *68*, 2286.
- (37) Fu, L.-Z.; Zhou, L.-L.; Tang, L.-Z.; Zhang, Y.-X.; Zhan, S.-Z. *Int. J. Hydrogen Energy* **2015**, *40*, 8688.
- (38) Canaguier, S.; Artero, V.; Fontecave, M. *Dalton Trans.* **2008**, 315.
- (39) Barton, B. E.; Whaley, C. M.; Rauchfuss, T. B.; Gray, D. L. *J. Am. Chem. Soc.* **2009**, *131*, 6942.
- (40) Ogo, S.; Ichikawa, K.; Kishima, T.; Matsumoto, T.; Nakai, H.; Kusaka, K.; Ohhara, T. *Science* **2013**, *339*, 682.
- (41) Rakowski DuBois, M.; DuBois, D. L. *Chem. Soc. Rev.* **2009**, *38*, 62.
- (42) Wiedner, E. S.; Yang, J. Y.; Dougherty, W. G.; Kassel, W. S.; Bullock, R. M.; DuBois, M. R.; DuBois, D. L. *Organometallics* **2010**, *29*, 5390.
- (43) Appel, A. M.; Pool, D. H.; O'Hagan, M.; Shaw, W. J.; Yang, J. Y.; Rakowski DuBois, M.; DuBois, D. L.; Bullock, R. M. *ACS Catalysis* **2011**, *1*, 777.
- (44) Kilgore, U. J.; Stewart, M. P.; Helm, M. L.; Dougherty, W. G.; Kassel, W. S.; DuBois, M. R.; DuBois, D. L.; Bullock, R. M. *Inorg. Chem.* **2011**, *50*, 10908.
- (45) Fernandez, L. E.; Horvath, S.; Hammes-Schiffer, S. *J. Phys. Chem.* **2012**, *116*, 3171.
- (46) Wiese, S.; Kilgore, U. J.; DuBois, D. L.; Bullock, R. M. *ACS Catal.* **2012**, *2*, 720.
- (47) Dutta, A.; Lense, S.; Hou, J.; Engelhard, M. H.; Roberts, J. A.; Shaw, W. J. *J. Am. Chem. Soc.* **2013**, *135*, 18490.
- (48) Hoffert, W. A.; Roberts, J. A.; Morris Bullock, R.; Helm, M. L. *Chem. Commun.* **2013**, *49*, 7767.
- (49) Horvath, S.; Fernandez, L. E.; Appel, A. M.; Hammes-Schiffer, S. *Inorg. Chem.* **2013**, *52*, 3643.
- (50) Wiese, S.; Kilgore, U. J.; Ho, M.-H.; Raugei, S.; DuBois, D. L.; Bullock, R. M.; Helm, M. L. *ACS Catal.* **2013**, *3*, 2527.
- (51) DuBois, D. L. *Inorg. Chem.* **2014**, *53*, 3935.
- (52) Song, L.-C.; Tan, H.; Luo, F.-X.; Wang, Y.-X.; Ma, Z.; Niu, Z. *Organometallics* **2014**, *33*, 5246.
- (53) Brown, H. J. S.; Wiese, S.; Roberts, J. A. S.; Bullock, R. M.; Helm, M. L. *ACS Catal.* **2015**, *5*, 2116.
- (54) Curtis, C. J.; Miedaner, A.; Ciancanelli, R.; Ellis, W. W.; Noll, B. C.; DuBois, M. R.; DuBois, D. L. *Inorg. Chem.* **2003**, *42*, 216.
- (55) Yang, J. Y.; Smith, S. E.; Liu, T.; Dougherty, W. G.; Hoffert, W. A.; Kassel, W. S.; Rakowski DuBois, M.; DuBois, D. L.; Bullock, R. M. *J. Am. Chem. Soc.* **2013**, *135*, 9700.
- (56) Wilson, A. D.; Newell, R. H.; McNevin, M. J.; Muckerman, J. T.; M., R. D.; DuBois, D. L. *J. Am. Chem. Soc.* **2006**, *128*, 358–366.

REFERENCES

- (57) Kilgore, U. J.; Roberts, J. A.; Pool, D. H.; Appel, A. M.; Stewart, M. P.; DuBois, M. R.; Dougherty, W. G.; Kassel, W. S.; Bullock, R. M.; DuBois, D. L. *J. Am. Chem. Soc.* **2011**, *133*, 5861.
- (58) Smith, S. E.; Yang, J. Y.; DuBois, D. L.; Bullock, R. M. *Angew. Chem. Int. Ed. Engl.* **2012**, *51*, 3152.
- (59) Helm, M. L.; Stewart, M. P.; Bullock, R. M.; DuBois, M. R.; DuBois, D. L. *Science* **2011**, *333*, 863.
- (60) Le Goff, A.; Artero, V.; Jusselme, B.; Tran, P. D.; Guillet, N.; Metaye, R.; Fihri, A.; Palacin, S.; Fontecave, M. *Science* **2009**, *326*, 1384.
- (61) McLaughlin, M. P.; McCormick, T. M.; Eisenberg, R.; Holland, P. L. *Chem. Commun.* **2011**, *47*, 7989.
- (62) Han, Z.; Eisenberg, R. *Acc. Chem. Res.* **2014**, *47*, 2537.
- (63) Han, Z.; McNamara, W. R.; Eum, M. S.; Holland, P. L.; Eisenberg, R. *Angew. Chem. Int. Ed.* **2012**, *51*, 1667.
- (64) Han, Z.; Shen, L.; Brennessel, W. W.; Holland, P. L.; Eisenberg, R. *J. Am. Chem. Soc.* **2013**, *135*, 14659.
- (65) Rao, H.; Yu, W.-Q.; Zheng, H.-Q.; Bonin, J.; Fan, Y.-T.; Hou, H.-W. *J. Power Sources* **2016**, *324*, 253.
- (66) Ezzaher, S.; Capon, J.-F.; Gloaguen, F.; Pétillon, F. Y.; Schollhammer, P.; Talarmin, J. *Inorg. Chem.* **2009**, *48*, 2.
- (67) Helm, M. L.; Stewart, M. P.; Bullock, R. M.; DuBois, M. R.; DuBois, D. L. *Science* **2011**, *333*, 863.
- (68) Das, A.; Han, Z.; Brennessel, W. W.; Holland, P. L.; Eisenberg, R. *ACS Catal.* **2015**, *5*, 1397.
- (69) Zhang, W.; Hong, J.; Zheng, J.; Huang, Z.; Zhou, J. S.; Xu, R. *J. Am. Chem. Soc.* **2011**, *133*, 20680.
- (70) Han, J.; Zhang, W.; Zhou, T.; Wang, X.; Xu, R. *RSC Adv.* **2012**, *2*, 8293.
- (71) Gan, L.; Groy, T. L.; Tarakeshwar, P.; Mazinani, S. K. S.; Shearer, J.; Mujica, V.; Jones, A. K. *J. Am. Chem. Soc.* **2015**, *137*, 1109.
- (72) Fisher, B. J.; Eisenberg, R. *J. Am. Chem. Soc.* **1980**, *102*, 7361.
- (73) Collin, J.-P.; Jouaiti, A.; Sauvage, J.-P. *Inorg. Chem.* **1988**, *27*, 1986.
- (74) Yuan, Y. J.; Lu, H. W.; Tu, J. R.; Fang, Y.; Yu, Z. T.; Fan, X. X.; Zou, Z. G. *ChemPhysChem.* **2015**, *16*, 2925.
- (75) Yang, Y.; Wang, M.; Xue, L.; Zhang, F.; Chen, L.; Ahlquist, M. S.; Sun, L. *ChemSusChem* **2014**, *7*, 2889.
- (76) Yuan, Y.-J.; Tu, J.-R.; Lu, H.-W.; Yu, Z.-T.; Fan, X.-X.; Zou, Z.-G. *Dalton Trans.* **2016**, *45*, 1359.
- (77) Chen, L.; Chen, G.; Leung, C.-F.; Yiu, S.-M.; Ko, C.-C.; Anxolabéhère-Mallart, E.; Robert, M.; Lau, T.-C. *ACS Catal.* **2015**, *5*, 356.
- (78) Luca, O. R.; Konezny, S. J.; Blakemore, J. D.; Colosi, D. M.; Saha, S.; Brudvig, G. W.; Batista, V. S.; Crabtree, R. H. *New J. Chem.* **2012**, *36*, 1149.
- (79) Luca, O. R.; Blakemore, J. D.; Konezny, S. J.; Praetorius, J. M.; Schmeier, T. J.; Hunsinger, G. B.; Batista, V. S.; Brudvig, G. W.; Hazari, N.; Crabtree, R. H. *Inorg. Chem.* **2012**, *51*, 8704.
- (80) Jacques, P. A.; Artero, V.; Pecaut, J.; Fontecave, M. *Proc. Natl. Acad. Sci. U. S. A.* **2009**, *106*, 20627.
- (81) Pantani, O.; Anxolabéhère-Mallart, E.; Aukauloo, A.; Millet, P. *Electrochem. Commun.* **2007**, *9*, 54.
- (82) Cherdo, S.; Ghachtouli, S. E.; Sircoglou, M.; Brisset, F.; Orio, M.; Aukauloo, A. *Chem. Commun.* **2014**, *50*, 13514.
- (83) Artero, V.; Chavarot-Kerlidou, M.; Fontecave, M. *Angew. Chem. Int. Ed.* **2011**, *50*, 7238.

REFERENCES

- (84) Losse, S.; Vos, J. G.; Rau, S. *Coord. Chem. Rev.* **2010**, *254*, 2492.
- (85) Beyene, B. B.; Mane, S. B.; Hung, C.-H. *Chem. Commun.* **2015**, *51*, 15067.
- (86) McCrory, C. C.; Uyeda, C.; Peters, J. C. *J. Am. Chem. Soc.* **2012**, *134*, 3164.
- (87) Kaeffer, N.; Chavarot-Kerlidou, M.; Artero, V. *Acc. Chem. Res.* **2015**, *48*, 1286.
- (88) Dempsey, J. L.; Brunschwig, B. S.; Winkler, J. R.; Gray, H. B. *Acc. Chem. Res.* **2009**, *42*, 1995.
- (89) Baffert, C.; Artero, V.; Fontecave, M. *Inorg. Chem.* **2007**, *46*, 1817.
- (90) Anxolabehere-Mallart, E.; Costentin, C.; Fournier, M.; Nowak, S.; Robert, M.; Saveant, J. M. *J. Am. Chem. Soc.* **2012**, *134*, 6104.
- (91) Krawicz, A.; Yang, J.; Anzenberg, E.; Yano, J.; Sharp, I. D.; Moore, G. F. *J. Am. Chem. Soc.* **2013**, *135*, 11861.
- (92) Reuillard, B.; Warnan, J.; Leung, J. J.; Wakerley, D. W.; Reisner, E. *Angew. Chem. Int. Ed. Engl.* **2016**.
- (93) Andreiadis, E. S.; Jacques, P.-A.; D., T. P.; Leyris, A.; Chavarot-Kerlidou, M.; Jusselme, B.; Matheron, M.; Pécaut, J.; Palacin, S.; Fontecave, M.; Artero, V. *Nat Chem.* **2013**, *5*, 48.
- (94) Krishnan, C. V.; Sutin, N. *J. Am. Chem. Soc.* **1981**, 2141.
- (95) Creutz, C.; Sutin, N. *Coord. Chem. Rev.* **1985**, 321.
- (96) Bigi, J. P.; Hanna, T. E.; Harman, W. H.; Chang, A.; Chang, C. J. *Chem. Commun.* **2010**, *46*, 958.
- (97) Khnayzer, R. S.; Thoi, V. S.; Nippe, M.; King, A. E.; Jurss, J. W.; El Roz, K. A.; Long, J. R.; Chang, C. J.; Castellano, F. N. *Energy Environ. Sci.* **2014**, *7*, 1477.
- (98) Sun, Y.; Sun, J.; Long, J. R.; Yang, P.; Chang, C. J. *Chem. Sci.* **2013**, *4*, 118.
- (99) Sun, Y.; Bigi, J. P.; Piro, N. A.; Tang, M. L.; Long, J. R.; Chang, C. J. *J. Am. Chem. Soc.* **2011**, *133*, 9212.
- (100) Nippe, M.; Khnayzer, R. S.; Panetier, J. A.; Zee, D. Z.; Olaiya, B. S.; Head-Gordon, M.; Chang, C. J.; Castellano, F. N.; Long, J. R. *Chem. Sci.* **2013**, *4*, 3934.
- (101) King, A. E.; Surendranath, Y.; Piro, N. A.; Bigi, J. P.; Long, J. R.; Chang, C. J. *Chem. Sci.* **2013**, *4*, 1578.
- (102) Guttentag, M.; Rodenberg, A.; Bachmann, C.; Senn, A.; Hamm, P.; Alberto, R. *Dalton Trans.* **2013**, *42*, 334.
- (103) Bachmann, C.; Guttentag, M.; Spingler, B.; Alberto, R. *Inorg. Chem.* **2013**, *52*, 6055.
- (104) Xie, J.; Zhou, Q.; Li, C.; Wang, W.; Hou, Y.; Zhang, B.; Wang, X. *Chem. Commun.* **2014**, *50*, 6520.
- (105) Lewandowska-Andralojc, A.; Baine, T.; Zhao, X.; Muckerman, J. T.; Fujita, E.; Polyansky, D. E. *Inorg. Chem.* **2015**, *54*, 4310.
- (106) Tong, L.; Zong, R.; Thummel, R. P. *J. Am. Chem. Soc.* **2014**, *136*, 4881.
- (107) Leung, C.-F.; Ng, S.-M.; Ko, C.-C.; Man, W.-L.; Wu, J.; Chen, L.; Lau, T.-C. *Energy Environ. Sci.* **2012**, *5*, 7903.
- (108) Singh, W. M.; Baine, T.; Kudo, S.; Tian, S.; Ma, X. A.; Zhou, H.; DeYonker, N. J.; Pham, T. C.; Bollinger, J. C.; Baker, D. L.; Yan, B.; Webster, C. E.; Zhao, X. *Angew. Chem. Int. Ed.* **2012**, *51*, 5941.
- (109) Vennampalli, M.; Liang, G.; Katta, L.; Webster, C. E.; Zhao, X. *Inorg. Chem.* **2014**, *53*, 10094.
- (110) Song, X.; Wen, H.; Ma, C.; Chen, H.; Chen, C. *New J. Chem.* **2015**, *39*, 1734–1741.
- (111) Zhang, P.; Wang, M.; Gloaguen, F.; Chen, L.; Quentel, F.; Sun, L. *Chem. Commun.* **2013**, *49*, 9455.
- (112) Lo, W. K.; Castillo, C. E.; Gueret, R.; Fortage, J.; Rebarz, M.; Sliwa, M.; Thomas, F.; McAdam, C. J.; Jameson, G. B.; McMorran, D. A.; Crowley, J. D.; Collomb, M. N.; Blackman, A. G. *Inorg. Chem.* **2016**, *55*, 4564.

- (113) Mandal, S.; Shikano, S.; Yamada, Y.; Lee, Y. M.; Nam, W.; Llobet, A.; Fukuzumi, S. *J. Am. Chem. Soc.* **2013**, *135*, 15294.
- (114) Di Giovanni, C.; Gimbert-Surinach, C.; Nippe, M.; Benet-Buchholz, J.; Long, J. R.; Sala, X.; Llobet, A. *Chem. Eur J.* **2016**, *22*, 361.
- (115) McNamara, W. R.; Han, Z.; Yin, C.-J. M.; Brennessel, W. W.; Holland, P. L.; Eisenberg, R. *Proc. Natl. Acad. Sci. U. S. A.* **2012**, *109*, 15594.
- (116) Zhang, P.; Wang, M.; Yang, Y.; Yao, T.; Sun, L. *Angew. Chem. Int. Ed.* **2014**, *53*, 1.
- (117) Thompson, E. J.; Berben, L. A. *Angew. Chem.* **2015**, *127*, 11808.
- (118) Karunadasa, H. I.; Chang, C. J.; Long, J. R. *Nature* **2010**, *464*, 1329.
- (119) Karunadasa, H. I.; Montalvo, E.; Sun, Y.; Majda, M.; Long, J. R.; Chang, C. J. *Science* **2012**, *335*, 698.
- (120) Elvington, M.; Brown, J.; Arachchige, S. M.; Brewer, K. J. *J. Am. Chem. Soc.* **2007**, *129*, 10644.
- (121) Rangan, K.; Arachchige, S. M.; Brown, J. R.; Brewer, K. J. *Energy Environ. Sci.* **2009**, *2*, 410.
- (122) Mori, K.; Ogawa, S.; Martis, M.; Yamashita, H. *J. Phys. Chem.* **2012**, *116*, 18873.
- (123) Ozawa, H.; Haga, M.-a.; Sakai, K. *J. Am. Chem. Soc.* **2006**, *128*, 4926.
- (124) Yamauchi, K.; Masaoka, S.; Sakai, K. *Dalton Trans.* **2011**, *40*, 12447.
- (125) Ozawa, H.; Sakai, K. *Chem. Commun.* **2011**, *47*, 2227.
- (126) Muckerman, J. T.; Fujita, E. *Chem. Commun.* **2011**, *47*, 12456.
- (127) Solis, B. H.; Hammes-Schiffer, S. *Inorg. Chem.* **2011**, *50*, 11252.
- (128) Solis, B. H.; Yu, Y.; Hammes-Schiffer, S. *Inorg. Chem.* **2013**, *52*, 6994.
- (129) Razavet, M.; Artero, V.; Fontecave, M. *Inorg. Chem.* **2005**, *44*, 4786.
- (130) Dempsey, J. L.; Winkler, J. R.; Gray, H. B. *J. Am. Chem. Soc.* **2010**, *132*, 1060.
- (131) Bhattacharjee, A.; Chavarot-Kerlidou, M.; Andreiadis, E. S.; Fontecave, M.; Field, M. J.; Artero, V. *Inorg. Chem.* **2012**, *51*, 7087.
- (132) Lacy, D. C.; Roberts, G. M.; Peters, J. C. *J. Am. Chem. Soc.* **2015**, *137*, 4860.
- (133) Singh, W. M.; Mirmohades, M.; Jane, R. T.; White, T. A.; Hammarstrom, L.; Thapper, A.; Lomoth, R.; Ott, S. *Chem. Commun.* **2013**, *49*, 8638.
- (134) Estes, D. P.; Grills, D. C.; Norton, J. R. *J. Am. Chem. Soc.* **2014**, *136*, 17362.
- (135) Dempsey, J. L.; Winkler, J. R.; Gray, H. B. *J. Am. Chem. Soc.* **2010**, *132*, 16774.
- (136) Marinescu, S. C.; Winkler, J. R.; Gray, H. B. *Proc. Natl. Acad. Sci. U. S. A.* **2012**, *109*, 15127–15131.
- (137) Costentin, C.; Dridi, H.; Saveant, J. M. *J. Am. Chem. Soc.* **2014**, *136*, 13727.
- (138) Kahnt, A.; Peuntinger, K.; Dammann, C.; Drewello, T.; Hermann, R.; Naumov, S.; Abel, B.; Guldi, D. M. *J. Phys. Chem. A* **2014**, *118*, 4382.
- (139) Smolentsev, G.; Ceconi, B.; Guda, A.; Chavarot-Kerlidou, M.; van Bokhoven, J. A.; Nachttegaal, M.; Artero, V. *Chem. Eur. J.* **2015**, *21*, 15158.
- (140) Shan, B.; Baine, T.; Ma, X. A.; Zhao, X.; Schmehl, R. H. *Inorg. Chem.* **2013**, *52*, 4853.
- (141) Rodenberg, A.; Oraziotti, M.; Probst, B.; Bachmann, C.; Alberto, R.; Baldrige, K. K.; Hamm, P. *Inorg. Chem.* **2015**, *54*, 646.
- (142) Varma, S.; Castillo, C. E.; Stoll, T.; Fortage, J.; Blackman, A. G.; Molton, F.; Deronzier, A.; Collomb, M. N. *Phys. Chem. Chem. Phys.* **2013**, *15*, 17544.
- (143) Sakai, T.; Mersch, D.; Reisner, E. *Angew. Chem. Int. Ed.* **2013**, *52*, 12313.
- (144) Eckenhoff, W. T.; Eisenberg, R. *Dalton Trans.* **2012**, *41*, 13004.
- (145) Queyriaux, N.; Jane, R. T.; Massin, J.; Artero, V.; Chavarot-Kerlidou, M. *Coord. Chem. Rev.* **2015**, *304-305*, 3.
- (146) Du, P.; Eisenberg, R. *Energy Environ. Sci.* **2012**, *5*, 6012.

REFERENCES

- (147) McKone, J. R.; Marinescu, S. C.; Brunschwig, B. S.; Winkler, J. R.; Gray, H. B. *Chem. Sci.* **2014**, *5*, 865.
- (148) Thoi, V. S.; Sun, Y.; Long, J. R.; Chang, C. J. *Chem. Soc. Rev.* **2013**, *42*, 2388.
- (149) Graham, D. J.; Nocera, D. G. *Organometallics* **2014**, *33*, 4994.
- (150) Lee, C. H.; Dogutan, D. K.; Nocera, D. G. *J. Am. Chem. Soc.* **2011**, *133*, 8775.
- (151) Ginovska-Pangovska, B.; Dutta, A.; Reback, M. L.; Linehan, J. C.; Shaw, W. J. *Acc. Chem. Res.* **2014**, *47*, 2621.
- (152) Wiedner, E. S.; Roberts, J. A.; Dougherty, W. G.; Kassel, W. S.; DuBois, D. L.; Bullock, R. M. *Inorg. Chem.* **2013**, *52*, 9975.
- (153) Jian, J. X.; Liu, Q.; Li, Z. J.; Wang, F.; Li, X. B.; Li, C. B.; Liu, B.; Meng, Q. Y.; Chen, B.; Feng, K.; Tung, C. H.; Wu, L. Z. *Nat. Commun.* **2013**, *4*, 2695.
- (154) Singleton, M. L.; Reibenspies, J. H.; Darensbourg, M. Y. *J. Am. Chem. Soc.* **2010**, *132*, 8870.
- (155) Orain, C.; Quentel, F.; Gloaguen, F. *ChemSusChem* **2014**, *7*, 638.
- (156) Pullen, S.; Fei, H.; Orthaber, A.; Cohen, S. M.; Ott, S. *J. Am. Chem. Soc.* **2013**, *135*, 16997.
- (157) Yu, T.; Zeng, Y.; Chen, J.; Li, Y. Y.; Yang, G.; Li, Y. *Angew. Chem. Int. Ed.* **2013**, *52*, 5631.
- (158) Okura, I.; Kim-Thuan, N. *J. Chem. Soc. Faraday Trans.1* **1980**, *76*, 2209.
- (159) Okura, I.; Takeuchi, M.; Kusunoki, S.; Aono, S. *Inorg. Chim. Acta* **1982**, *63*, 157.
- (160) Ihara, M.; Nishihara, H.; Yoon, K. S.; Lenz, O.; Friedrich, B.; Nakamoto, H.; Kojima, K.; Honma, D.; Kamachi, T.; Okura, I. *Photochem. Photobiol.* **2006**, *82*, 676.
- (161) Reisner, E.; Fontecilla-Camps, J. C.; Armstrong, F. A. *Chem. Commun.* **2009**, 550.
- (162) Reisner, E.; Powell, D. J.; Cavazza, C.; Fontecilla-Camps, J. C.; Armstrong, F. A. *J. Am. Chem. Soc.* **2009**, *131*, 18457.
- (163) Lubner, C. E.; Knorz, P.; Silva, P. J.; Vincent, K. A.; Happe, T.; Bryant, D. A.; Golbeck, J. H. *Biochemistry-Us* **2010**, *49*, 10264.
- (164) Brown, K. A.; Wilker, M. B.; Boehm, M.; Dukovic, G.; King, P. W. *J. Am. Chem. Soc.* **2012**, *134*, 5627.
- (165) Zadvornyy, O. A.; Lucon, J. E.; Gerlach, R.; Zorin, N. A.; Douglas, T.; Elgren, T. E.; Peters, J. W. *J. Inorg. Biochem.* **2012**, *106*, 151.
- (166) Roy, A.; Sarrou, I.; Vaughn, M. D.; Astashkin, A. V.; Ghirlanda, G. *Biochemistry-Us* **2013**, *52*, 7586.
- (167) Sommer, D. J.; Roy, A.; Astashkin, A.; Ghirlanda, G. *Biopolymers* **2015**, *104*, 412.
- (168) Jones, A. K.; Lichtenstein, B. R.; Dutta, A.; Gordon, G.; Dutton, P. L. *J. Am. Chem. Soc.* **2007**, *129*, 14844.
- (169) Roy, A.; Madden, C.; Ghirlanda, G. *Chem. Commun.* **2012**, *48*, 9816.
- (170) Sano, Y.; Onoda, A.; Hayashi, T. *Chem. Commun.* **2011**, *47*, 8229.
- (171) Sano, Y.; Onoda, A.; Hayashi, T. *J. Inorg. Biochem.* **2012**, *108*, 159.
- (172) Onoda, A.; Kihara, Y.; Fukumoto, K.; Sano, Y.; Hayashi, T. *ACS Catal.* **2014**, *4*, 2645.
- (173) Utschig, L. M.; Silver, S. C.; Mulfort, K. L.; Tiede, D. M. *J. Am. Chem. Soc.* **2011**, *133*, 16334.
- (174) McCormick, T. M.; Calitree, B. D.; Orchard, A.; Kraut, N. D.; Bright, F. V.; Detty, M. R.; Eisenberg, R. *J. Am. Chem. Soc.* **2010**, *132*, 15480.
- (175) Bullock, R. M.; Helm, M. L. *Acc. Chem. Res.* **2015**, *48*, 2017.
- (176) Silver, S. C.; Niklas, J.; Du, P.; Poluektov, O. G.; Tiede, D. M.; Utschig, L. M. *J. Am. Chem. Soc.* **2013**, *135*, 13246.
- (177) Bacchi, M.; Berggren, G.; Niklas, J.; Veinberg, E.; Mara, M. W.; Shelby, M. L.; Poluektov, O. G.; Chen, L. X.; Tiede, D. M.; Cavazza, C.; Field, M. J.; Fontecave, M.; Artero, V. *Inorg. Chem.* **2014**, *53*, 8071.
- (178) Gray, H. B.; Winkler, J. R. *Q. Rev. Biophys.* **2003**, *36*, 341.

REFERENCES

- (179) Soltau, S. R.; Niklas, J.; Dahlberg, P. D.; Poluektov, O. G.; Tiede, D. M.; Mulforta, K. L.; Utschig, L. M. *Chem. Commun.* **2015**, 51, 10628.
- (180) Marcus, R. A.; Sutin, N. *Biochim. Biophys. Acta, Rev. Bioenerg.* **1985**, 811, 265.
- (181) Saint-Martin, P.; Lespinat, P. A.; Fauque, G.; Berlier, Y.; Legall, J.; Moura, I.; Teixeira, M.; Xavier, A. V.; Moura, J. J. G. *Proc. Natl. Acad. Sci. U. S. A.* **1988**, 85, 9378.
- (182) Lubitz, W.; Ogata, H.; Rudiger, O.; Reijerse, E. *Chem. Rev.* **2014**, 114, 4081.
- (183) Slater, J. W.; Shafaat, H. S. *J. Phys. Chem. Lett.* **2015**, 6, 3731.
- (184) Sommer, D. J.; Vaughn, M. D.; Ghirlanda, G. *Chem. Commun.* **2014**, 50, 15852.
- (185) Sommer, D. J.; Vaughn, M. D.; Clark, B. C.; Tomlin, J.; Roy, A.; Ghirlanda, G. *Biochim. Biophys. Acta, Bioenerg.* **2015**, 1857, 598.
- (186) Kleingardner, J. G.; Kandemir, B.; Bren, K. L. *J. Am. Chem. Soc.* **2014**, 136, 4.
- (187) Kleingardner, J. G.; Bren, K. L. *Acc. Chem. Res.* **2015**, 48, 1845.
- (188) Beyene, B. B.; Mane, S. B.; Hung, C.-H. *Chem. Commun.* **2015**, 51.
- (189) Kellett, R. M.; Spiro, T. G. *Inorg. Chem.* **1985**, 24, 2373.
- (190) Kellett, R. M.; Spiro, T. G. *Inorg. Chem.* **1985**, 24.
- (191) Kandemir, B.; Chakraborty, S.; Guo, Y.; Bren, K. L. *Inorg. Chem.* **2016**, 55, 467.
- (192) Wen, X.; Bren, K. L. *Biochemistry-Us* **2005**, 44, 5225.
- (193) Wen, X.; Patel, K. M.; Russell, B. S.; Bren, K. L. *Biochemistry-Us* **2007**, 46, 2537.
- (194) Massari, A. M.; McClain, B. L.; Finkelstein, I. J.; Lee, A. P.; Reynolds, H. L.; Bren, K. L.; Fayer, M. D. *J. Phys. Chem. B* **2006**, 110, 18803.
- (195) Yoon, T. P.; Ischay, M. A.; J.N. *Nat. Chem.* **2010**, 2, 527.
- (196) Zeitler, K. *Angew. Chem. Int. Ed. Engl.* **2009**, 48, 9785.
- (197) Prier, C. K.; Rankic, D. A.; MacMillan, D. W. *Chem. Rev.* **2013**, 113, 5322.
- (198) Rueping, M.; Vila, C.; Bootwicha, T. *ACS Catal.* **2013**, 3, 1676.
- (199) Narayanam, J. M.; Stephenson, C. R. *Chem. Soc. Rev.* **2011**, 40, 102.
- (200) Narayanam, J. M. R.; Tucker, J. W.; Stephenson, C. R. *J. Am. Chem. Soc.* **2009**, 131, 8756.
- (201) Pitre, S. P.; McTiernan, C. D.; Scaiano, J. C. *Acc. Chem. Res.* **2016**, 49, 1320.
- (202) Maji, T.; Karmakar, A.; Reiser, O. *J. Org. Chem.* **2011**, 76, 736.
- (203) Ghosh, I.; Ghosh, T.; Bardagi, J. I.; König, B. *Science* **2014**, 346, 725.
- (204) Ryu, D.; Primer, D. N.; Tellis, J. C.; Molander, G. A. *Chem. Eur. J.* **2016**, 22, 120.
- (205) Rono, L. J.; Yayla, H. G.; Wang, D. Y.; Armstrong, M. F.; Knowles, R. R. *J. Am. Chem. Soc.* **2013**, 135, 17735.
- (206) Chen, Y.; Feng, G. *Org. Biomol. Chem.* **2015**, 13, 4260.
- (207) Jin, J.; MacMillan, D. W. *Nature* **2015**, 525, 87.
- (208) Nguyen, T. M.; Nicewicz, D. A. *J. Am. Chem. Soc.* **2013**, 135, 9588.
- (209) Lu, Z.; Shen, M.; Yoon, T. P. *J. Am. Chem. Soc.* **2011**, 133, 1162.
- (210) Hari, D. P.; König, B. *Chem. Commun.* **2011**, 13, 3852.
- (211) Beatty, J. W.; Stephenson, C. R. *Acc. Chem. Res.* **2015**, 48, 1474.
- (212) Imamura, K.; Iwasaki, S.; Maeda, T.; Hashimoto, K.; Ohtani, B.; Kominami, H. *Phys. Chem. Chem. Phys.* **2011**, 13, 5114.
- (213) Imamura, K.; Hashimoto, K.; Kominami, H. *Chem. Commun.* **2012**, 48, 4356.
- (214) Kamegawa, T.; Seto, H.; Matsuura, S.; Yamashita, H. *ACS Appl. Mater. Interfaces* **2012**, 4, 6635.
- (215) Shiraishi, Y.; Togawa, Y.; Tsukamoto, D.; Tanaka, S.; Hirai, T. *ACS Catal.* **2012**, 2, 2475.
- (216) Imamura, K.; Yoshikawa, T.; Hashimoto, K.; Kominami, H. *Appl. Catal., B* **2013**, 134-135, 193.
- (217) Shiraishi, Y.; Hirakawa, H.; Togawa, Y.; Sugano, Y.; Ichikawa, S.; Hirai, T. *ACS Catal.* **2013**, 3, 2318.
- (218) Tanaka, A.; Nishino, Y.; Sakaguchi, S.; Yoshikawa, T.; Imamura, K.; Hashimoto, K.; Kominami, H. *Chem. Commun.* **2013**, 49, 2551.

REFERENCES

- (219) Xu, C.; Yuan, Y.; Yuan, R.; Fu, X. *RSC Adv.* **2013**, *3*, 18002.
- (220) Wu, W.; Liu, G.; Xie, Q.; Liang, S.; Zheng, H.; Yuan, R.; Su, W.; Wu, L. *Green Chem.* **2012**, *14*, 1705.
- (221) Eskandari, P.; Kazemi, F.; Zand, Z. *J. Photochem. Photobiol., A* **2014**, *274*, 7.
- (222) Wu, W.; Wen, L.; Shen, L.; Liang, R.; Yuan, R.; Wu, L. *Appl. Catal., B* **2013**, *130-131*, 163.
- (223) Ke, X.; Sarina, S.; Zhao, J.; Zhang, X.; Chang, J.; Zhu, H. *Chem. Commun.* **2012**, *48*, 3509.
- (224) Ke, X.; Zhang, X.; Zhao, J.; Sarina, S.; Barry, J.; Zhu, H. *Green Chem.* **2013**, *15*, 236.
- (225) Sarina, S.; Waclawik, E. R.; Zhu, H. *Green Chem.* **2013**, *15*, 1814.
- (226) Wang, C.; Astruc, D. *Chem. Soc. Rev.* **2014**, *43*, 7188.
- (227) Guo, X.; Hao, C.; Jin, G.; Zhu, H. Y.; Guo, X. Y. *Angew. Chem. Int. Ed. Engl.* **2014**, *53*, 1973.
- (228) Wu, W.; Liang, S.; Chen, Y.; Shen, L.; Zheng, H.; Wu, L. *Catal. Commun.* **2012**, *17*, 39.
- (229) Wu, W.; Liu, G.; Liang, S.; Chen, Y.; Shen, L.; Zheng, H.; Yuan, R.; Hou, Y.; Wu, L. *J. Catal.* **2012**, *290*, 13.
- (230) Wu, W.; Lin, R.; Shen, L.; Liang, R.; Yuan, R.; Wu, L. *Catal. Commun.* **2013**, *40*, 1.
- (231) Fu, L.; Cai, W.; Wang, A.; Zheng, Y. *Mater. Lett.* **2015**, *142*, 201.
- (232) Ghosh, S.; Khamarui, S.; Saha, M.; De, S. K. *RSC Adv.* **2015**, *5*, 38971.
- (233) Yang, X.-J.; Chen, B.; Zheng, L.-Q.; Wu, L.-Z.; Tung, C.-H. *Green Chem.* **2014**, *16*, 1082.
- (234) Gazi, S.; Ananthakrishnan, R. *Appl. Catal., B* **2011**, *105*, 317.
- (235) Toyao, T.; Saito, M.; Horiuchi, Y.; Mochizuki, K.; Iwata, M.; Higashimura, H.; Matsuoka, M. *Catal. Sci. Technol.* **2013**, *3*, 2092.
- (236) Lin, C. W.; Hong, B. C.; Chang, W. C.; Lee, G. H. *Org. Lett.* **2015**, *17*, 2314.
- (237) Cai, S.; Zhang, S.; Zhao, Y.; Wang, D. Z. *Org. Lett.* **2013**, *15*, 2660.
- (238) Molinari, R.; Lavorato, C.; Argurio, P. *Chem. Eng. J.* **2015**, *274*, 307.
- (239) Kohtani, S.; Kamoi, Y.; Yoshioka, E.; Miyabe, H. *Catal. Sci. Technol.* **2014**, *4*, 1084.
- (240) Kohtani, S.; Yoshioka, E.; Saito, K.; Kudo, A.; Miyabe, H. *J. Phys. Chem. C* **2012**, *116*, 17705.
- (241) Kohtani, S.; Yoshioka, E.; Saito, K.; Kudo, A.; Miyabe, H. *Catal. Commun.* **2010**, *11*, 1049.
- (242) Kohtani, S.; Nishioka, S.; Yoshioka, E.; Miyabe, H. *Catal. Commun.* **2014**, *43*, 61.
- (243) Kohtani, S.; Mori, M.; Yoshioka, E.; Miyabe, H. *Catalysts* **2015**, *5*, 1417.
- (244) Shiragami, T.; Pac, C.; Yanagida, S. *J. Chem. Soc., Chem. Commun.* **1989**, 831.
- (245) Shiragami, T.; Pac, C.; Yanagida, S. *J. Phys. Chem.* **1990**, *94*, 504.
- (246) Matsuoka, S.; Kohzuki, T.; Kuwana, Y.; Nakamura, A.; Yanagida, S. *J. Chem. Soc. Perkin Trans. 2* **1992**, 679.
- (247) Matsuoka, S.; Kohzuki, T.; Nakamura, A.; Pac, C.; Yanagida, S. *J. Chem. Soc., Chem. Commun.* **1991**, 580.
- (248) Pac, C.; Ihama, M.; Yasuda, M.; Miyauchi, Y.; Sakurai, H. *J. Am. Chem. Soc.* **1981**, *103*, 6495.
- (249) Nakajima, M.; Fava, E.; Loescher, S.; Jiang, Z.; Rueping, M. *Angew. Chem. Int. Ed. Engl.* **2015**, *54*, 8828.
- (250) Lang, X.; Zhao, J.; Chen, X. *Chem. Soc. Rev.* **2016**, *45*, 3026.
- (251) Lee, S. H.; Kim, J. H.; Park, C. B. *Chem. Eur. J.* **2013**, *19*, 4392
- (252) Jaegfeldt, H. J. *Electroanal. Chem.* **1981**, *128*, 355.
- (253) Hollmann, F.; Arends, I. W. C. E.; Buehler, K. *Chemcatchem* **2010**, *2*, 762.
- (254) Goren, Z.; Lapidot, N.; Willner, I. *J. Mol. Catal.* **1988**, *47*, 21.
- (255) Mandler, D.; Willner, I. *J. Chem. Soc. Chem. Commun.* **1986**, 851.
- (256) Wienkamp, R.; Steckhan, E. *Angew. Chem. Int. Ed. Engl.* **1983**, *22*, 497

REFERENCES

- (257) Steckhan, E.; Herrmann, S.; Ruppert, R.; Dietz, E.; Frede, M.; Spika, E. *Organometallics* **1991**, *10*, 1568.
- (258) Hollmann, F.; Witholt, B.; Schmid, A. *J. Mol. Catal. B* **2002**, *19-20*, 167.
- (259) Lo, H. C.; Buriez, O.; Kerr, J. B.; Fish, R. H. *Angew. Chem. Int. Ed.* **1999**, *38*, 1429.
- (260) Lo, H. C.; Leiva, C.; Buriez, O.; Kerr, J. B.; Olmstead, M. M.; Richard, H. *Inorg. Chem.* **2001**, *40*, 6705.
- (261) Choudhury, S.; Baeg, J. O.; Park, N. J.; Yadav, R. K. *Angew. Chem. Int. Ed.* **2012**, *51*, 11624.
- (262) Choudhury, S.; Baeg, J.-O.; Park, N.-J.; Yadav, R. K. *Green Chem.* **2014**, *16*, 4389.
- (263) Kudo, A.; Miseki, Y. *Chem. Soc. Rev.* **2009**, *38*, 253.
- (264) Jiang, Z.; Lü, C.; Wu, H. *Ind. Eng. Chem. Res.* **2005**, *44*, 4165
- (265) Chen, D.; Yang, D.; Wang, Q.; Jiang, Z. *Ind. Eng. Chem. Res.* **2006**, *45*, 4110
- (266) Shi, Q.; Yang, D.; Jiang, Z.; Li, J. *J. Mol. Catal. B* **2006**, *43*, 44.
- (267) Dijken, A. V.; Makkinje, J.; Meijerink, A. *J. Lumin.* **2001**, *92*, 323
- (268) Nam, D. H.; Lee, S. H.; Park, C. B. *Small* **2010**, *6*, 922.
- (269) Lee, S. H.; Ryu, J.; Nam, D. H.; Park, C. B. *Chem. Commun.* **2011**, *47*, 4643.
- (270) Ryu, J.; Lee, S. H.; Nam, D. H.; Park, C. B. *Adv. Mater.* **2011**, *23*, 1883.
- (271) Bhoware, S. S.; Kim, K. Y.; Kim, J. A.; Wu, Q.; Kim, J. *J. Phys. Chem. C* **2011**, *115*, 2553.
- (272) Zhang, H.; Chen, G.; Bahnemann, D. W. *J. Mater. Chem.* **2009**, *19*, 5089.
- (273) Park, C. B.; Lee, S. H.; Subramanian, E.; Kale, B. B.; Lee, S. M.; Baeg, J. O. *Chem. Commun.* **2008**, 5423.
- (274) Garnett, E.; Yang, P. *Nano Lett.* **2010**, *10*, 1082.
- (275) Oh, I.; Kye, J.; Hwang, S. *Nano Lett.* **2012**, *12*, 298.
- (276) Lee, H. Y.; Ryu, J.; Kim, J. H.; Lee, S. H.; Park, C. B. *ChemSusChem* **2012**, *5*, 2129
- (277) Nolan, M.; O'Callaghan, S.; Fagas, G.; Greer, J. C. *Nano Lett.* **2007**, *7*, 34.
- (278) Mifsud, M.; Gargiulo, S.; Iborra, S.; Arends, I. W.; Hollmann, F.; Corma, A. *Nature Commun.* **2014**, *5*, 3145.
- (279) Ryu, J.; Nam, D. H.; Lee, S. H.; Park, C. B. *Chem. Eur. J.* **2014**, *20*, 12020.
- (280) Yadav, R. K.; Baeg, J. O.; Oh, G. H.; Park, N. J.; Kong, K. J.; Kim, J.; Hwang, D. W.; Biswas, S. K. *J. Am. Chem. Soc.* **2012**, *134*, 11455.
- (281) Woolerton, T. W.; Sheard, S.; Pierce, E.; Ragsdale, S. W.; Armstrong, F. A. *Energy Environ. Sci.* **2011**, *4*, 2393.
- (282) Hentall, P. L.; Flowers, N.; Bugg, T. D. H. *Chem. Commun.* **2001**, 2098
- (283) Lee, H. J.; Lee, S. H.; Park, C. B.; Won, K. *Chem. Commun.* **2011**, *47*, 12538.
- (284) Li, J.; Yang, J.; Wen, F.; Li, C. *Chem. Commun.* **2011**, *47*, 7080.
- (285) Liu, X.; Sun, D.; Yuan, R.; Fu, X.; Li, Z. *J. Catal.* **2013**, *304*, 1.
- (286) Ghosh, T.; Slanina, T.; König, B. *Chem. Sci.* **2015**, *6*, 2027.
- (287) Imamura, K.; Okubo, Y.; Ito, T.; Tanaka, A.; Hashimoto, K.; Kominami, H. *RSC Adv.* **2014**, *4*, 19883.
- (288) Zhao, X.; Long, R.; Liu, D.; Luo, B.; Xiong, Y. *J. Mater. Chem. A* **2015**, *3*, 9390.
- (289) Shimakoshi, H.; Hisaeda, Y. *ChemPlusChem* **2014**, *79*, 1250.
- (290) Zhong, J.-J.; Liu, Q.; Wu, C.-J.; Meng, Q.-Y.; Gao, X.-W.; Li, Z.-J.; Chen, B.; Tung, C.-H.; Wu, L.-Z. *Chem. Commun.* **2016**, *52*, 1800.
- (291) Solis, B. H.; Hammes-Schiffer, S. *J. Am. Chem. Soc.* **2011**, *133*, 19036.
- (292) Newkome, G. R.; Gupta, V. K.; Fronczek, F. R.; Pappalardo, S. *Inorg. Chem.* **1984**, *23*, 2400.
- (293) Kochem, A.; Thomas, F.; Jarjayes, O.; Gellon, G.; Philouze, C.; Weyhermüller, T.; Neese, F.; van Gastel, M. *Inorg. Chem.* **2013**, *52*, 14428.
- (294) Enachescu, C.; Krivokapic, I.; Zerara, M.; Real, J. A.; Amstutz, N.; Hauser, A. *Inorg. Chim. Acta* **2007**, *360*, 3945.

REFERENCES

- (295) Goldsmith, J. I.; Hudson, W. R.; Lowry, M. S.; Anderson, T. H.; Bernhard, S. *J. Am. Chem. Soc.* **2005**, *127*, 7502.
- (296) Bock, C. R.; Connor, J. A.; Gutierrez, A. R.; Meyer, T. J.; Whitten, D. G.; Sullivan, B. P.; Nagle, J. K. *J. Am. Chem. Soc.* **1979**, *101*, 4815.
- (297) DeRosa, M. C.; Crutchley, R. J. *Coord. Chem. Rev.* **2002**, *233-234*, 351.
- (298) Lakadamyali, F.; Kato, M.; Muresan, N. M.; Reisner, E. *Angew. Chem. Int. Ed.* **2012**, *51*, 9381.
- (299) Artero, V.; Fontecave, M. *Chem. Soc. Rev.* **2013**, *42*, 2338.
- (300) A. J. Bard, L. R. Faulkner, *Electrochemical Methods: Fundamentals and Applications*, 2 ed., Wiley, New York, 2001.
- (301) Scuseria, G. E. R., M. A.; Cheeseman, J. R.; Scalmani, G.; Barone, V.; Mennucci, B. P., G. A.; Nakatsuji, H.; Caricato, M.; Li, X.; Hratchian, H. P.; Izmaylov, A. F. B., J.; Zheng, G.; Sonnenberg, J. L.; Hada, M.; Ehara, M. T., K.; Fukuda, R.; Hasegawa, J.; Ishida, M.; Nakajima, T.; Honda, Y. K., O.; Nakai, H.; Vreven, T.; Montgomery, Jr., J. A.; Peralta, J. E.; Ogliaro, F. B., M.; Heyd, J. J.; Brothers, E.; Kudin, K. N.; Staroverov, V. N. K., R.; Normand, J.; Raghavachari, K.; Rendell, A.; Burant, J. C. I., S. S.; Tomasi, J.; Cossi, M.; Rega, N.; Millam, J. M.; Klene, M. K., J. E.; Cross, J. B.; Bakken, V.; Adamo, C.; Jaramillo, J.; Gomperts, R. S., R. E.; Yazyev, O.; Austin, A. J.; Cammi, R.; Pomelli, C. O., J. W.; Martin, R. L.; Morokuma, K.; Zakrzewski, V. G.; Voth, G. A. S., P.; Dannenberg, J. J.; Dapprich, S.; Daniels, A. D.; Farkas, F., J. B.; Ortiz, J. V.; Cioslowski, J.; Fox, D. J.; Gaussian, I., Wallingford CT, 2009.
- (302) Flassbeck, C.; Wieghardt, K. *Z. Anorg. Allg. Chem.* **1992**, *608*, 60.
- (303) Cline, E. D.; Adamson, S. E.; Bernhard, S. *Inorg. Chem.* **2008**, *47*, 10378.
- (304) Lloret-Fillol, J.; Codolà, Z.; Garcia-Bosch, I.; Gómez, L.; Pla, J. J.; Costas, M. *Nat. Chem.* **2011**, *3*, 807
- (305) Becke, A. D. *J. Chem. Phys.* **1993**, *98*, 1372.
- (306) Becke, A. D. *J. Chem. Phys.* **1993**, *98*, 5648.
- (307) Lee, C. T.; Yang, W. T.; Parr, R. G. *Phys. Rev. B* **1988**, *37*, 785.
- (308) Marenich, A. V.; Cramer, C. J.; Truhlar, D. G. *J. Phys. Chem. B* **2009**, *113*, 6378.
- (309) Schwabe, T.; Grimme, S. *Phys. Chem. Chem. Phys.* **2007**, *9*, 3397.
- (310) Swart, M.; Güell, M.; Luis, J. M.; Solà, M. *J. Phys. Chem. A* **2010**, *114*, 7191.
- (311) Kelly, C. P.; Cramer, C. J.; Truhlar, D. G. *J. Phys. Chem. B* **2006**, *110*, 2493.
- (312) Winget, P.; Cramer, C. J.; Truhlar, D. G. *Theor. Chem. Acc.* **2004**, *112*, 217.
- (313) Mahammed, A.; Mondal, B.; Rana, A.; Dey, A.; Gross, Z. *Chem. Commun.* **2014**, *50*, 2725.
- (314) Call, A.; Codolà, Z.; Acuña-Parés, F.; Lloret-Fillol, J. *Chem. Eur. J.* **2014**, *20*, 6171.
- (315) Prat, I.; Company, A.; Corona, T.; Parella, T.; Ribas, X.; Costas, M. *Inorg. Chem.* **2013**, *52*, 9229.
- (316) Garcia-Bosch, I.; Codola, Z.; Prat, I.; Ribas, X.; Lloret-Fillol, J.; Costas, M. *Chem. Eur. J.* **2012**, *18*, 13269.
- (317) Company, A.; Gomez, L.; Fontrodona, X.; Ribas, X.; Costas, M. *Chem. Eur. J.* **2008**, *14*, 5727.
- (318) Company, A.; Gómez, L.; Güell, M.; Ribas, X.; Luis, J. M.; Lawrence Que, J.; Costas, M. *J. Am. Chem. Soc.* **2007**, *129*, 15766.
- (319) Prat, I.; Font, D.; Company, A.; Junge, K.; Ribas, X.; Beller, M.; Costas, M. *Adv. Synth. Catal.* **2013**, *355*, 947.
- (320) Prat, I.; Gomez, L.; Canta, M.; Ribas, X.; Costas, M. *Chem. Eur. J.* **2013**, *19*, 1908.
- (321) Garcia-Bosch, I.; Company, A.; Fontrodona, X.; Ribas, X.; Costas, M. *Org. Lett.* **2008**, *10*, 2095.
- (322) Garcia-Bosch, I.; Ribas, X.; Costas, M. *Adv Synth Catal* **2009**, *351*, 348.
- (323) Hammett, L. P. *J. Am. Chem. Soc.* **1937**, *59*, 96.

REFERENCES

- (324) Hansch, C.; Leo, A.; Taft, R. W. *Chem. Rev.* **1991**, *91*, 165.
- (325) Prat, I.; Font, D.; Company, A.; Junge, K.; Ribas, X.; Beller, M.; Costas, M. *Adv. Synth. Catal.* **2013**, *355*, 947.
- (326) Zhang, C. X.; Kaderli, S.; Costas, M.; Kim, E.-i.; Neuhold, Y.-M.; Karlin, K. D.; Zuberbühler, A. D. *Inorg. Chem.* **2003**, *42*, 1807.
- (327) Lever, A. B. P. *Coord. Chem. Rev.* **1996**, *150*, 77.
- (328) Ward, A. L.; Elbaz, L.; Kerr, J. B.; Arnold, J. *Inorg. Chem.* **2012**, *51*, 4694–4706.
- (329) Zang, Y.; Kim, J.; Dong, Y.; Wilkinson, E. C.; Appelman, E. H.; Lawrence Que, J. J. *Am. Chem. Soc.* **1997**, *119*, 4197.
- (330) Fryzuk, M. D.; Leznoff, D. B.; Thompson, R. C.; Rettig, S. J. *J. Am. Chem. Soc.* **1998**, *120*, 10126.
- (331) Evans, D. F. *J. Chem. Soc.* **1959**, 2003.
- (332) Pigué, C. *J. Chem. Educ.* **1997**, *74*, 815.
- (333) Naklicki, M. L.; White, C. A.; Plante, L. L.; Evans, C. E. B.; Crutchley, R. J. *Inorg. Chem.* **1998**, *37*, 1880.
- (334) Das, U. K.; Bobak, J.; Fowler, C.; Hann, S. E.; Petten, C. F.; Dawe, L. N.; Decken, A.; Kerton, F. M.; Kozak, C. M. *Dalton Trans.* **2010**, *39*, 5462.
- (335) Matsumoto, J.; Suzuki, T.; Kajita, Y.; Masuda, H. *Dalton Trans.* **2012**, *41*, 4107.
- (336) England, J.; Gondhia, R.; Bigorra-Lopez, L.; Petersen, A. R.; White, A. J.; Britovsek, G. J. *Dalton Trans.* **2009**, 5319.
- (337) Benhamou, L.; Thibon, A.; Brelot, L.; Lachkar, M.; Mandon, D. *Dalton Trans.* **2012**, *41*, 14369.
- (338) Artero, V.; Chavarot-Kerlidou, M.; Fontecave, M. *Angew. Chem. Int. Ed.* **2011**, *50*, 7238.
- (339) Solis, B. H.; Hammes-Schiffer, S. *J. Am. Chem. Soc.* **2011**, *133*, 19036.
- (340) Artero, V.; Fontecave, M. *Chem. Soc. Rev.* **2013**, *42*, 2338.
- (341) Bachmann, C.; Probst, B.; Guttentag, M.; Alberto, R. *Chem. Commun.* **2014**, *50*, 6737.
- (342) Joliat, E.; Schnidrig, S.; Probst, B.; Bachmann, C.; Spingler, B.; Baldrige, K. K.; von Rohr, F.; Schilling, A.; Alberto, R. *Dalton Trans.* **2015**.
- (343) Bachmann, C.; Guttentag, M.; Spingler, B.; Alberto, R. *Inorg. Chem.* **2013**, *52*, 6055.
- (344) Hollmann, D.; Gartner, F.; Ludwig, R.; Barsch, E.; Junge, H.; Blug, M.; Hoch, S.; Beller, M.; Bruckner, A. *Angew. Chem. Int. Ed.* **2011**, *50*, 10246.
- (345) Aoi, S.; Mase, K.; Ohkubo, K.; Fukuzumi, S. *Chem. Commun.* **2015**, *51*, 15145.
- (346) Hollmann, D.; Gärtner, F.; Ludwig, R.; Barsch, E.; Junge, H.; Blug, M.; Hoch, S.; Beller, M.; Bückner, A.; Ed., A. C. I. *Angew. Chem. Int. Ed.* **2011**, *50*, 10246
- (347) Lakadamyali, F.; Kato, M.; Muresan, N. M.; Reisner, E. *Angew. Chem. Int. Ed.* **2012**, *51*, 9381.
- (348) Wakerley, D. W.; Gross, M. A.; Reisner, E. *Chem. Commun.* **2014**, *50*, 15995.
- (349) Mondal, B.; Sengupta, K.; Rana, A.; Mahammed, A.; Botoshansky, M.; Dey, S. G.; Gross, Z.; Dey, A. *Inorg. Chem.* **2013**, *52*, 3381.
- (350) Kaeffer, N.; Morozan, A.; Artero, V. *J. Phys. Chem.* **2015**, *119*, 13707.
- (351) Losse, S.; Vos, J. G.; Rau, S. *Coord. Chem. Rev.* **2010**, *254*, 2492.
- (352) Fukuzumi, S.; Mandal, S.; Mase, K.; Ohkubo, K.; Park, H.; Benet-Buchholz, J.; Nam, W.; Llobet, A. *J. Am. Chem. Soc.* **2012**, *134*, 9906.
- (353) Palmisano, G.; Augugliaro, V.; Pagliaro, M.; Palmisano, L. *Chem. Commun.* **2007**, 3425.
- (354) Mohamed, M. M.; Al-Sharif, M. S. *Appl. Catal., B* **2013**, *142-143*, 432.
- (355) Bhattacharjee, A.; Andreiadis, E. S.; Chavarot-Kerlidou, M.; Fontecave, M.; Field, M. J.; Artero, V. *Chem. Eur. J.* **2013**, *19*, 15166.

REFERENCES

- (356) Roy, L. E.; Jakubikova, E.; Guthrie, M. G.; Batista, E. R. *J. Phys. Chem. A* **2009**, *113*, 6745.
- (357) Niu, S.; Hall, M. B. *Inorg. Chem.* **2001**, *40*, 6201.
- (358) Simmons, T. R.; Berggren, G.; Bacchi, M.; Fontecave, M.; Artero, V. *Coord. Chem. Rev.* **2014**, *270-271*, 127.
- (359) Kaljurand, I.; Kütt, A.; Sooväli, L.; Rodima, T.; Mäemets, V.; Leito, I.; Koppel, I. A. *J. Org. Chem.* **2005**, *70*, 1019.
- (360) McCarthy, B. D.; Martin, D. J.; Rountree, E. S.; Ullman, A. C.; Dempsey, J. L. *Inorg. Chem.* **2014**, *53*, 8350.
- (361) Flassbeck, C.; Wieghardt, K. *Z. Anorg. Allg. Chem.* **1992**, *608*, 60.
- (362) Ashimori, A.; Ono, T.; Uchida, T.; Ohtaki, Y.; Fukaya, C.; Watanabe, M.; Yokoyama, K. *Chem. Pharm. Bull.* **1990**, *38*, 2446.
- (363) Kojima, T.; Hayashi, K.; Iizuka, S. Y.; Tani, F.; Naruta, Y.; Kawano, M.; Ohashi, Y.; Hirai, Y.; Ohkubo, K.; Matsuda, Y.; Fukuzumi, S. *Chem. Eur. J.* **2007**, *13*, 8212.
- (364) Weber, P. C.; Ohlendorf, D. H.; Wendoloski, J. J.; Salemme, F. R. *Science* **1989**, *243*, 85.
- (365) Wilson, M. E.; Whitesides, G. M. *J. Am. Chem. Soc.* **1978**, *100*, 306.
- (366) Ward, T. R. *Acc. Chem. Res.* **2011**, *444*, 47.
- (367) Letondor, C.; Ward, T. R. *ChemBioChem.* **2006**, *7*, 1845.
- (368) Collot, J.; Gradinaru, J.; Humbert, N.; Skande, M.; Zocchi, A.; Ward, T. R. *J. Am. Chem. Soc.* **2003**, *125*, 9030.
- (369) Skander, M.; Humbert, N.; Collot, J.; Gradinaru, J.; Klein, G.; Loosli, A.; Sauser, J.; Zocchi, A.; Gilardoni, F.; Ward, T. R. *J. Am. Chem. Soc.* **2004**, *126*, 14411.
- (370) Letondor, C.; Pordea, A.; Humbert, N.; Ivanova, A.; Mazurek, S.; Novic, M.; Ward, T. R. *J. Am. Chem. Soc.* **2006**, *128*, 8320.
- (371) Zimbron, J. M.; Heinisch, T.; Schmid, M.; Hamels, D.; Nogueira, E. S.; Schirmer, T.; Ward, T. R. *J. Am. Chem. Soc.* **2013**, *135*, 5384.
- (372) Pierron, J.; Malan, C.; Creus, M.; Gradinaru, J.; Hafner, I.; Ivanova, A.; Sardo, A.; Ward, T. R. *Angewandte Chemie* **2008**, *120*, 713.
- (373) Pordea, A.; Creus, M.; Panek, J.; Duboc, C.; Mathis, D.; Novic, M.; Ward, T. R. *J. Am. Chem. Soc.* **2008**, *130*.
- (374) Lo, C.; Ringenberg, M. R.; Gnanndt, D.; Wilson, Y.; Ward, T. R. *Chem. Commun.* **2011**, *47*, 12065.
- (375) Chatterjee, A.; Mallin, H.; Klehr, J.; Vallapurackal, J.; Finke, A. D.; Vera, L.; Marsh, M.; Ward, T. R. *Chem. Sci.* **2016**, *7*, 673.
- (376) Wilson, M. E.; Nuzzo, R. G.; Whitesides, G. M. *J. Am. Chem. Soc.* **1978**, *100*, 2269.
- (377) Hofmann, K.; Titus, G.; Montibeller, J. A.; Finn, F. M. *Biochemistry-U.S.* **1982**, *21*, 978.
- (378) Freitag, S.; Trong, I. L.; Klumb, L.; Stayton, P. S.; Stenkamp, R. E. *Protein Sci* **1997**, *6*, 1157.
- (379) Jones, M. L.; Kurzban, G. P. *Biochemistry-U.S.* **1995**, *34*, 11750.
- (380) Green, N. M. *Methods Enzymol.* **1970**, *18*, 418.
- (381) Gill, S. C.; Hippel, P. H. v. *Anal. Biochem.* **1989**, *182*, 319.
- (382) Masarik, M.; Kizek, R.; Kramer, K. J.; Billova, S.; Brazdova, M.; Vacek, J.; Bailey, M.; Jelen, F.; Howard, J. A. *Anal. Chem.* **2003**, *75*, 2663.
- (383) Loosli, A.; Rusbandi, U. E.; Gradinaru, J.; Bernauer, K.; Schlaepfer, C. W.; Meyer, M.; Mazurek, S.; Novic, M.; Ward, T. R. *Inorg. Chem.* **2006**, *45*, 660.
- (384) Livnah, O.; Bayer, E. A.; Wilchek, M.; Sussman, J. L. *Proc. Natl. Acad. Sci. U.S.A.* **1993**, *90*, 5076.
- (385) Girault, S.; Chassaing, G.; Blais, J. C.; Brunot, A.; Bolbach, G. *Anal. Chem.* **1996**, *68*, 2122.

REFERENCES

- (386) The overpotential is defined as the difference between the applied potential and the standard potential in the reduction of protons at a given conditions.
- (387) The termodinamic potential vs. SCE at a given pH under 1 atm H₂ for the electrocatalytic H₂ evolution from water is given by $E(\text{pH}) = -0.241\text{V} - 0.059\text{V} \times \text{pH}$.
- (388) Abe, T.; Kaneko, M. *J. Mol. Catal. A: Chem.* **2001**, *169*, 177.
- (389) Slattery, S. J.; K., B. J.; J., L.; A., G. K. *Coord. Chem. Rev.* **1998**, *174*, 391–416.
- (390) Savéant, J.-M. *Elements of Molecular and Biomolecular Electrochemistry: An Electrochemical Approach to Electron Transfer Chemistry*; Wiley-Interscience: Hoboken, NJ, 2006.
- (391) Curtin, P. N.; Tinker, L. L.; Burgess, C. M.; Cline, E. D.; Bernhard, S. *Inorg. Chem.* **2009**, *48*, 10498.
- (392) Hanss, D.; Freys, J. C.; Bernardinelli, G. r.; Wenger, O. S. *Eur. J. Inorg. Chem.* **2009**, *2009*, 4850.
- (393) Ladouceur, S.; Fortin, D.; Zysman-Colman, E. *Inorg. Chem.* **2010**, *49*, 5625.
- (394) Luo, S. P.; Mejia, E.; Friedrich, A.; Pazidis, A.; Junge, H.; Surkus, A. E.; Jackstell, R.; Denurra, S.; Gladiali, S.; Lochbrunner, S.; Beller, M. *Angew. Chem. Int. Ed.* **2013**, *52*, 419.
- (395) Luo, S.-P.; Mejía, E.; Friedrich, A.; Pazidis, A.; Junge, H.; Surkus, A.-E.; Jackstell, R.; Denurra, S.; Gladiali, S.; Lochbrunner, S.; Beller, M. *Angew. Chem. Int. Ed.* **2013**, *52*, 419.
- (396) Zee, D. Z.; Chantarojsiri, T.; Long, J. R.; Chang, C. J. *Acc. Chem. Res.* **2015**, *48*, 2027.
- (397) Wender, P. A.; Quiroz, R. V.; Stevens, M. C. *Acc. Chem. Res.* **2015**, *48*, 752.
- (398) Deponti, E.; Luisa, A.; Natali, M.; Iengo, E.; Scandola, F. *Dalton Trans.* **2014**, *43*, 16345.
- (399) Lazarides, T.; McCormick, T.; Du, P.; Luo, G.; Lindley, B.; Eisenberg, R. *J. Am. Chem. Soc.* **2009**, *131*, 9192.
- (400) Basu, D.; Mazumder, S.; Niklas, J.; Baydoun, H.; Wanniarachchi, D.; Shi, X.; Staples, R. J.; Poluektov, O.; Schlegel, H. B.; Verani, C. N. *Chem. Sci.* **2016**.
- (401) Probst, B.; Guttentag, M.; Rodenberg, A.; Hamm, P.; Alberto, R. *Inorg. Chem.* **2011**, *50*, 3404.
- (402) Probst, B.; Kolano, C.; Hamm, P.; Alberto, R. *Inorg. Chem.* **2009**, *48*, 1836.
- (403) Smolentsev, G.; Guda, A.; Zhang, X.; Haldrup, K.; Andreiadis, E.; Chavarot-Kerlidou, M.; Canton, S. E.; Nachtegaal, M.; Artero, V.; Sundstrom, V. *J. Phys. Chem C* **2013**, *117*, 17367.
- (404) Chirik, P. J.; Wieghardt, K. *Science* **2010**, *327*, 794.
- (405) Luca, O. R.; Crabtree, R. H. *Chem. Soc. Rev.* **2013**, *42*, 1440.
- (406) Blanchard, S.; Derat, E.; Desage-El Murr, M.; Fensterbank, L.; Malacria, M.; Mouriès-Mansuy, V. *Eur. J. Inorg. Chem.* **2012**, *2012*, 376.
- (407) Lyaskovskyy, V.; de Bruin, B. *ACS Catal.* **2012**, *2*, 270.
- (408) Dugan, T. R.; Bill, E.; MacLeod, K. C.; Christian, G. J.; Cowley, R. E.; Brennessel, W. W.; Ye, S.; Neese, F.; Holland, P. L. *J. Am. Chem. Soc.* **2012**, *134*, 20352.
- (409) Lewis, R. A.; MacLeod, K. C.; Mercado, B. Q.; Holland, P. L. *Chem. Commun.* **2014**, *50*, 11114.
- (410) Broere, D. L. J.; Plessius, R.; Vlugt, J. I. v. d. *Chem. Soc. Rev.* **2015**, *44*, 6886.
- (411) Chirik, P. J. *Acc. Chem. Res.* **2015**, *48*, 1687.
- (412) Stubbert, B. D.; Peters, J. C.; Gray, H. B. *J. Am. Chem. Soc.* **2011**, *133*, 18070.
- (413) Jurss, J. W.; Khnayzer, R. S.; Panetier, J. A.; Roz, K. A. E.; Nichols, E. M.; Head-Gordon, M.; Long, J. R.; Castellano, F. N.; Chang, C. J. *Chem. Sci.* **2015**, *6*, 4954.
- (414) Shearer, J.; Kung, I. Y.; Lovell, S.; Kaminsky, W.; Kovacs, J. A. *J. Am. Chem. Soc.* **2001**, *123*, 463.
- (415) Kau, L. S.; Spira-Solomon, D. J.; Penner-Hahn, J. E.; Hodgson, K. O.; Solomon, E. I. *J. Am. Chem. Soc.* **1987**, *109*, 6433.

REFERENCES

- (416) Roemelt, M.; Beckwith, M. A.; Duboc, C.; Collomb, M. N.; Neese, F.; DeBeer, S. *Inorg. Chem.* **2012**, *51*, 680.
- (417) Nemec, I.; Marx, R.; Herchel, R.; Neugebauer, P.; van Slageren, J.; Travnicek, Z. *Dalton Trans.* **2015**, *44*, 15014.
- (418) Colpas, G. J.; Maroney, M. J.; Bagyinka, C.; Kumar, M.; Willis, W. S.; Suib, S. L.; Baidya, N.; Mascharak, P. K. *Inorg. Chem.* **1991**, *30*, 920.
- (419) Ravel, B.; Newville, M. J. *Synchrotron Radiat.* **2005**, *12*, 537.
- (420) Newville, M. J. *Synchrotron Radiat.* **2001**, *8*, 96.
- (421) Rehr, J. J.; Albers, R. C. *Rev. Mod. Phys.* **2000**, *72*, 621.
- (422) Martin-Diaconescu, V.; Bellucci, M.; Musiani, F.; Ciurli, S.; Maroney, M. J. *J. Biol. Inorg. Chem.* **2012**, *17*, 353.
- (423) Zambelli, B.; Berardi, A.; Martin-Diaconescu, V.; Mazzei, L.; Musiani, F.; Maroney, M. J.; Ciurli, S. *J. Biol. Inorg. Chem.* **2014**, *19*, 319.
- (424) Yano, J.; Yachandra, V. K. *Photosynth. Res.* **2009**, *102*, 241.
- (425) Yang, Q.; Cui, P.; Ye, Q.; Chen, S.; Wu, Z. *J. Mol. Struct.* **2015**, *1098*, 306.
- (426) Bordage, A.; Trannoy, V.; Proux, O.; Vitoux, H.; Moulin, R.; Bleuzen, A. *Phys. Chem. Chem. Phys.* **2015**, *17*, 17260.
- (427) Goswami, M.; Lyaskovskyy, V.; Domingos, S. R.; Buma, W. J.; Woutersen, S.; Troeppner, O.; Ivanovic-Burmazovic, I.; Lu, H.; Cui, X.; Zhang, X. P.; Reijerse, E. J.; DeBeer, S.; van Schooneveld, M. M.; Pfaff, F. F.; Ray, K.; de Bruin, B. *J. Am. Chem. Soc.* **2015**, *137*, 5468.
- (428) Bonnitcha, P. D.; Hall, M. D.; Underwood, C. K.; Foran, G. J.; Zhang, M.; Beale, P. J.; Hambley, T. W. *J. Inorg. Biochem.* **2006**, *100*, 963.
- (429) Krogman, J. P.; Gallagher, J. R.; Zhang, G.; Hock, A. S.; Miller, J. T.; Thomas, C. M. *Dalton Trans.* **2014**, *43*, 13852.
- (430) Liebeskind, L. S.; Baysdon, S. L.; South, M. S.; Iyer, S.; Leeds, J. P. *Tetrahedron* **1985**, *41*, 5839.
- (431) Barber, J.; Tran, P. D. *J. R. Soc. Interface* **2013**, *10*, 20120984.
- (432) Macia-Agullo, J. A.; Corma, A.; Garcia, H. *Chem. Eur. J.* **2015**, *21*, 10940.
- (433) Finholt, A. E.; Bond, A. C.; Schlesinger, H. I. *J. Am. Chem. Soc.* **1947**, *69*, 1199.
- (434) Cook, P. L. *J. Org. Chem.* **1962**, *27*, 3873.
- (435) Figadère, B.; Chaboche, C.; Franck, X.; Peyrat, J.-F.; Cavé, A. *J. Org. Chem.* **1994**, *59*, 7138.
- (436) Babler, J. H.; Sarussi, S. J. *J. Org. Chem.* **1981**, *46*, 3369.
- (437) Zhang, W.; Shi, M. *Chem. Commun.* **2006**, 1218.
- (438) Wang, Z.; Wroblewski, A. E.; Verkade, J. G. *J. Org. Chem.* **1999**, *64*, 8021.
- (439) Sarkar, D. C.; Das, A. R.; Ranu, B. C. *J. Org. Chem.* **1990**, *55*, 5801.
- (440) Kim, J.; De Castro, K. A.; Lim, M.; Rhee, H. *Tetrahedron* **2010**, *66*, 3995.
- (441) Borch, R. F.; Bernstein, M. D.; Durst, H. D. *J. Am. Chem. Soc.* **1971**, *93*, 2897.
- (442) Cha, J. S.; Moon, S. J.; Park, J. H. *J. Org. Chem.* **2001**, *66*, 7514.
- (443) Burkhardt, E. R.; Matos, K. *Chem. Rev.* **2006**, *106*, 2617.
- (444) Shi, L.; Liu, Y.; Liu, Q.; Wei, B.; Zhang, G. *Green Chem.* **2012**, *14*, 1372.
- (445) Bullock, R. M. *Science* **2013**, *342*, 1054.
- (446) Mikhailine, A.; Lough, A. J.; Morris, R. H. *J. Am. Chem. Soc.* **2009**, *131*, 1394.
- (447) Sui-Seng, C.; Freutel, F.; Lough, A. J.; Morris, R. H. *Angew. Chem. Int. Ed.* **2008**, *47*, 940.
- (448) Friedfeld, M. R.; Shevlin, M.; Hoyt, J. M.; Krska, S. W.; Tudge, M. T.; Chirik, P. J. *Science* **2013**, *342*, 1076.
- (449) Zuo, W.; Lough, A. J.; Li, Y. F.; Morris, R. H. *Science* **2013**, *342*, 1080.
- (450) Zhang, G.; Scott, B. L.; Hanson, S. K. *Angew. Chem. Int. Ed.* **2012**, *51*, 1.
- (451) Du, P.; Knowles, K.; Eisenberg, R. *J. Am. Chem. Soc.* **2008**, *130*, 12576.
- (452) Du, P.; Schneider, J.; Luo, G.; Brennessel, W. W.; Eisenberg, R. *Inorg. Chem.* **2009**, *48*, 4952.

REFERENCES

- (453) McMillin, D. R.; Kirchoff, J. R.; Goodwin, K. V. *Coord. Chem. Rev.* **1985**, *64*, 83
- (454) Riesgo, E. C.; Hu, Y.-Z.; Bouvier, F.; Thummel, R. P.; Scaltrito, D. V.; Meyer, G. J. *Inorg. Chem.* **2001**, *40*, 3413
- (455) Jahng, Y.; Hazelrigg, J.; Kimball, D.; Riesgo, E.; Wu, F.; Thummel, R. P. *Inorg. Chem.* **1997**, *36*, 5390.
- (456) Cuttell, D. G.; Kuang, S.-M.; Fanwick, P. E.; McMillin, D. R.; Walton, R. A. *J. Am. Chem. Soc.* **2002**, *124*, 6.
- (457) Wang, Z. Y.; Rao, H.; Deng, M. F.; Fan, Y. T.; Hou, H. W. *Phys Chem Chem Phys* **2013**, *15*, 16665.
- (458) Free ligand from PSCu.
- (459) We previously determined by Dynamic light scattering (DLS) and Nanoparticle Tracking Analysis (NTA) the formation of nanoparticles in low concentration (1:108).
- (460) Atzrodt, J.; Derdau, V.; Fey, T.; Zimmermann, J. *Angew. Chem. Int. Ed.* **2007**, *46*, 7744.
- (461) Cambeiro, F.; Lopez, S.; Varela, J. A.; Saa, C. *Angew. Chem. Int. Ed.* **2014**, *53*, 5959.
- (462) He, Z.; Qi, X.; Li, S.; Zhao, Y.; Gao, G.; Lan, Y.; Wu, Y.; Lan, J.; You, J. *Angew. Chem. Int. Ed.* **2015**, *53*, 1.
- (463) Lin, T. P.; Peters, J. C. *J. Am. Chem. Soc.* **2013**, *135*, 15310.
- (464) Zhang, G.; Vasudevan, K. V.; Scott, B. L.; Hanson, S. K. *J. Am. Chem. Soc.* **2013**, *135*, 8668.
- (465) Li, Y.; Hou, C.; Jiang, J.; Zhang, Z.; Zhao, C.; Page, A. J.; Ke, Z. *ACS Catal.* **2016**, *6*, 1655.
- (466) Jing, Y.; Chen, X.; Yang, X. *Organometallics* **2015**, *34*, 5716.
- (467) Atzrodt, J.; Derdau, V.; Fey, T.; Zimmermann, J. *Angew. Chem. Int. Ed.* **2007**, *46*, 7744
- (468) Wang, Q.; Sheng, X.; Horner, J. H.; Newcomb, M. J. *J. Am. Chem. Soc.* **2009**, *131*, 10629–10636.
- (469) Yung, C. M.; Skaddan, M. B.; Bergman, R. G. *J. Am. Chem. Soc.* **2004**, *126*, 13033–13043.
- (470) Khaskin, E.; Milstein, D. *ACS Catal.* **2013**, *3*, 448–452.
- (471) Artero, V.; Fontecave, M. *Coord. Chem. Rev.* **2005**, *249*, 1518.
- (472) Yamada, T.; Nagata, T.; Sugi, K. D.; Yorozu, K.; Ikeno, T.; Ohtsuka, Y.; Miyazaki, D.; Mukaiyama, T. *Chem. Eur. J.* **2003**, *9*, 4485.
- (473) Sigman, M. S.; Miller, J. J. *J. Org. Chem.* **2009**, *74*, 7633.
- (474) Mantilli, L.; Gerard, D.; Torche, S.; Besnard, C.; Mazet, C. *Chem. Eur. J.* **2010**, *16*, 12736.
- (475) Giri, S.; Wang, D. Z.; Chattaraj, P. K. *Tetrahedron* **2010**, *66*, 4560.
- (476) Minakata, S.; Ando, T.; Nishimura, M.; Ryu, I.; Komatsu, M. *Angew. Chem. Int. Ed.* **1998**, *37*, 3392.
- (477) Wu, X.; Li, X.; Hems, W.; King, F.; Xiao, J. *Org. Biomol. Chem.* **2004**, *2*, 1818.
- (478) Mao, J.; Wan, B.; Wu, F.; Lu, S. *Tetrahedron Lett.* **2005**, *46*, 7341.
- (479) Wu, X.; Li, X.; Zanotti-Gerosa, A.; Pettman, A.; Liu, J.; Mills, A. J.; Xiao, J. *Chem. Eur. J.* **2008**, *14*, 2209.
- (480) Wu, X.; Wang, C.; Xiao, J. *Platinum Metals Rev.* **2010**, *54*, 3.
- (481) Sinou, D. *Adv. Synth. Catal.* **2002**, *344*, 221.
- (482) Dwars, T.; Oehme, G. *Adv. Synth. Catal.* **2002**, *344*, 239.
- (483) Yoshimura, M.; Tanaka, S.; Kitamura, M. *Tetrahedron Lett.* **2014**, *55*, 3635.
- (484) Wu, X.; Li, X.; Hems, W.; King, F.; Xiao, J. *Org. Biomol. Chem.* **2004**, *2*, 1818.
- (485) Ramírez-Monroy, A.; Swager, T. M. *Organometallics* **2011**, *30*, 2464.
- (486) Uenishi, J. i.; Tanaka, T.; Nishiwaki, K.; Wakabayashi, S.; Oae, S.; Tsukubet, H. *J. Org. Chem.* **1993**, *58*, 4382.

REFERENCES

- (487) Radaram, B.; Ivie, J. A.; Singh, W. M.; Grudzien, R. M.; Reibenspies, J. H.; Webster, C. E.; Zhao, X. *Inorg. Chem.* **2011**, *50*, 10564.
- (488) Comba, P.; Rudolf, H.; HubertWadepohl *Dalton Trans.* **2015**, *44*, 2724.
- (489) Roefles, G.; Lubben, M.; Hage, R.; Jr., L. Q.; Feringa, B. L. *Chem. Eur. J.* **2000**, *6*, 2152.
- (490) Chen, M. S.; White, M. C. *Science* **2007**, *318*, 783.
- (491) Maity, N. C.; Kumar Bera, P.; Ghosh, D.; Abdi, S. H. R.; Kureshy, R. I.; Khan, N.-u. H.; Bajaj, H. C.; Suresh, E. *Catal. Sci. Technol.* **2014**, *4*, 208.
- (492) Kooistra, T. M.; Hekking, K. F. W.; Knijnenburg, Q.; Bruin, B. d.; Budzelaar, P. H. M.; Gelder, R. d.; Smits, J. M. M.; Gal, A. *Eur. J. Inorg. Chem.* **2003**, 648.
- (493) Hammoud, M. M.; McKamie, J. J.; Heeg, M. J.; Kodanko, J. J. *Dalton Trans.* **2008**, 4843.
- (494) Abouelatta, A. I.; Sonk, J. A.; Hammoud, M. M.; Zurcher, D. M.; McKamie, J. J.; Schlegel, H. B.; Kodanko, J. J. *Inorg. Chem.* **2010**, *49*, 5202.
- (495) Hu, X.; Brunschwig, B. S.; Peters, J. C. *J. Am. Chem. Soc.* **2007**, *129*, 8988.
- (496) Jeletic, M. S.; Helm, M. L.; Hulley, E. B.; Mock, M. T.; Appel, A. M.; Linehan, J. C. *ACS Catal.* **2014**, *4*, 3755.
- (497) Eisenberg, D. C.; Norton, J. R. *Isr. J. Chem.* **1991**, *31*, 55.
- (498) Tang, L.; Papish, E. T.; Abramo, G. P.; Norton, J. R.; Baik, M.-H.; Friesner, R. A.; Rappe, A. *J. Am. Chem. Soc.* **2003**, *125*, 10093.
- (499) Bullock, R. M.; Samsel, E. G. *J. Am. Chem. Soc.* **1990**, *112*, 6886.
- (500) Choi, J.; Pulling, M. E.; Smith, D. M.; Norton, J. R. *J. Am. Chem. Soc.* **2008**, *130*, 4250.
- (501) Sweany, R. L.; Halpern, J. *J. Am. Chem. Soc.* **1977**, *99*, 8335.
- (502) Feder, H. M.; Halpern, J. *J. Am. Chem. Soc.* **1975**, *97*, 7186.
- (503) Weil, T. A.; Friedman, S.; Wender, I. *J. Org. Chem.* **1974**, *39*, 48.
- (504) Burczyk, A. F.; O'Driscoll, K. F.; Rempel, G. L. *Polym. Chem.* **1984**, *22*, 3255.
- (505) King, S. M.; Ma, X.; Herzon, S. B. *J. Am. Chem. Soc.* **2014**, *136*, 6884.
- (506) Obradors, C.; Martinez, R. M.; Shenvi, R. A. *J. Am. Chem. Soc.* **2016**, *138*, 4962.
- (507) Li, G.; Han, A.; Pulling, M. E.; Estes, D. P.; Norton, J. R. *J. Am. Chem. Soc.* **2012**, *134*, 14662.
- (508) Crossley, S. W.; Barabe, F.; Shenvi, R. A. *J. Am. Chem. Soc.* **2014**, *136*, 16788.
- (509) Hayon, E.; Ibata, T.; Lichtin, N. N.; Simic, M. *J. Phys. Chem.* **1972**, *76*, 2072.
- (510) Weiss, M. E.; Kreis, L. M.; Lauber, A.; Carreira, E. M. *Angew. Chem. Int. Ed. Engl.* **2011**, *50*, 11125.
- (511) Reckenthäler, M.; Griesbeck, A. G. *Adv. Synth. Catal.* **2013**, *355*, 2727.
- (512) Tinker, L. L.; McDaniel, N. D.; Curtin, P. N.; Smith, C. K.; Ireland, M. J.; Bernhard, S. *Chem. Eur. J.* **2007**, *13*, 8726.
- (513) Zhang, P.; Wang, M.; Na, Y.; Li, X.; Jiang, Y.; Sun, L. *Dalton Trans* **2010**, *39*, 1204.
- (514) Luo, S. P.; Mejia, E.; Friedrich, A.; Pazidis, A.; Junge, H.; Surkus, A. E.; Jackstell, R.; Denurra, S.; Gladiali, S.; Lochbrunner, S.; Beller, M. *Angew Chem Int Ed Engl* **2013**, *52*, 419.
- (515) Tinker, L. L.; Bernhard, S. *Inorg.Chem.* **2009**, *48*, 10507.
- (516) Tinker, L. L.; McDaniel, N. D.; Curtin, P. N.; Smith, C. K.; Ireland, M. J.; Bernhard, S.; J., C. E. *Chem. Eur. J.* **2007**, *13*, 8726.
- (517) Goldsmith, J. I.; Hudson, W. R.; Lowry, M. S.; Anderson, T. H.; Bernhard, S. *J. Am. Chem. Soc.* **2005**, *127*, 7502.
- (518) Tarantino, K. T.; Liu, P.; Knowles, R. R. *J. Am. Chem. Soc.* **2013**, *135*, 10022.
- (519) Kodama, Y.; Imoto, M.; Ohta, N.; Kitani, A.; Ito, S. *J. Electroanal. Chem.* **2001**, *507*, 103.
- (520) Noel, M.; Rajini, I.; Srinivasan, R. K. *B. Electrochem.* **1988**.
- (521) Wawzonek, S.; Gundersen, A. *J. Electrochem. Soc.* **1960**, *107*, 537.
- (522) Nicewicz, D.; Roth, H.; Romero, N. *Synlett* **2015**, *27*, 714.

REFERENCES

- (523) Tanko, J. M.; Drumright, R. E. *J. Am. Chem. Soc.* **1992**, *114*, 1844.
- (524) Yang, D.; Tanner, D. D. *J. Org. Chem.* **1986**, *51*, 2267.
- (525) Tanko, J. M.; Drumright, R. E. *J. Am. Chem. Soc.* **1990**, *112*, 5362.
- (526) Griller, D.; Ingold, K. U. *Acc. Chem. Res.* **1980**, *13*, 317.
- (527) Stevenson, J. P.; Jackson, W. F.; Tanko, J. M. *J. Am. Chem. Soc.* **2002**, *124*, 4271.
- (528) Murphy, W. S.; Wattanasin, S. *J. Chem. Soc. Perkin. Trans.* **1986**, 1445.
- (529) Nakahara, K.; Iwasa, S.; Iriyama, J.; Morioka, Y.; Suguro, M.; Satoh, M.; Cairns, E. *J. Electrochim Acta* **2006**, *52*, 921.
- (530) Swain, C. G.; Elmer C. Lupton, J. *J. Am. Chem. Soc.* **1968**, *90*, 4328.
- (531) Bowden, K.; Hardy, M. *Tetrahedron* **1966**, *22*, 1169.
- (532) Wieggers, K. E.; Smith, S. G. *J. Am. Chem. Soc.* **1977**, *99*, 1480.
- (533) Noyori, R.; Ohkuma, T. *Angew. Chem. Int. Ed.* **2001**, *40*, 40.
- (534) Jacobs, J. W.; McFarland, J. T.; Wainer, I.; Jeanmaier, D.; Ham, C.; Hamm, K.; Wnuk, M.; Lam, M. *Biochemistry-Us* **1974**, *13*, 60.
- (535) Nowlan, D. T.; Gregg, T. M.; Davies, H. M. L.; Singleton, D. A. *J. Am. Chem. Soc.* **2003**, *125*, 15902.
- (536) Yamataka, H.; Sasaki, D.; Kuwatani, Y.; Mishima, M.; Tsuno, Y. *J. Am. Chem. Soc.* **1997**, *119*, 9975.
- (537) Yamataka, H.; Fujimura, N.; Kawafuji, Y.; Hanafusa, T. *J. Am. Chem. Soc.* **1987**, *109*, 4305.
- (538) Yamataka, H.; Ando, T. *J. Phys. Chem.* **1981**, *85*, 2281.
- (539) Yamataka, H.; Tamura, S.; Hanafusa, T.; Ando, T. *J. Am. Chem. Soc.* **1985**, *107*, 5429.
- (540) Singleton, D. A.; Thomas, A. A. *J. Am. Chem. Soc.* **1995**, *117*, 9357.
- (541) Yamataka, H.; Hanafusa, T. *J. Org. Chem.* **1988**, *53*, 772.
- (542) Yamataka, H.; Hanafusa, T. *J. Am. Chem. Soc.* **1986**, *108*, 6643.
- (543) Yamataka, H.; Kawafuji, Y.; Katsushi Nagareda; Miyano, N.; Hanafusa, T. *J. Org. Chem.* **1989**, *54*, 4706.
- (544) Amaral, L. D.; Bull, H. G.; Cordes, E. H. *J. Am. Chem. Soc.* **1972**, *94*, 7579.
- (545) Simmons, E. M.; Hartwig, J. F. *Angew. Chem. Int. Ed. Engl.* **2012**, *51*, 3066.
- (546) Plata, R. E.; Singleton, D. A. *J. Am. Chem. Soc.* **2015**, *137*, 3811.
- (547) Gajewski, J. J.; Bocian, W.; Brichford, N. L.; Henderson, J. L. *J. Org. Chem.* **2002**, *67*, 4236.
- (548) Gajewski, J. J.; Bocian, W.; Harris, N. J.; Olson, L. P.; Gajewski, J. P. *J. Am. Chem. Soc.* **1999**, *121*, 326.
- (549) Shapley, P. A.; Zhang, N.; Allen, J. L.; Pool, D. H.; Liang, H.-C. *J. Am. Chem. Soc.* **2000**, *122*, 1079.
- (550) Amorati, R.; Lynett, P. T.; Valgimigli, L.; Pratt, D. A. *Chem. Eur. J.* **2012**, *18*, 6370.
- (551) Pozzi, M. H.; Gawandi, V.; Fitzpatrick, P. F. *Biochemistry-Us* **2009**, *48*, 12305.
- (552) Heiden, Z. M.; Lathem, A. P. *Organometallics* **2015**, *34*, 1818.
- (553) Li, X.; Li, L.; Tang, Y.; Zhong, L.; Cun, L.; Zhu, J.; Liao, J.; Deng, J. *J. Org. Chem.* **2010**, *75*, 2981.
- (554) Nordin, M.; Liao, R.-Z.; Ahlford, K.; Adolfsson, H.; Himo, F. *Chemcatchem* **2012**, *4*, 1095.
- (555) Abdur-Rashid, K.; Clapham, S. E.; Hadzovic, A.; Harvey, J. N.; Lough, A. J.; Morris, R. H. *J. Am. Chem. Soc.* **2002**, *124*, 15104.
- (556) Hedberg, C.; Källström, K.; Arvidsson, P. I.; Brandt, P.; Andersson, P. G. *J. Am. Chem. Soc.* **2005**, *127*, 15083.
- (557) Sui-Seng, C.; Haque, F. N.; Hadzovic, A.; Pütz, A.-M.; Reuss, V.; Meyer, N.; Lough, A. J.; Iuliis, M. Z.-D.; Morris, R. H. *Inorg. Chem.* **2009**, *48*, 735.
- (558) Langer, R.; Iron, M. A.; Konstantinovski, L.; Diskin-Posner, Y.; Leitun, G.; Ben-David, Y.; Milstein, D. *Chem. Eur. J.* **2012**, *18*, 7196.

REFERENCES

- (559) Suzuki, Y.; Kaneno, D.; Tomoda, S. *J. Phys. Chem. A* **2009**, *113*, 2578.
- (560) Aziz ur, R.; Gul, S.; Abbasi, M. A.; Nafeesa, K.; Akhtar, M. N.; Ahmad, I.; Afzal, S. *Phosphorus Sulfur Silicon Relat Elem* **2014**, *190*, 1045.
- (561) Mayer, I. *Int. J. Quantum Chem.* **1984**, *26*, 151.
- (562) Mayer, I. *Chem. Phys. Lett.* **1983**, *97*, 270.
- (563) Kelly, C. P.; Cramer, C. J.; Truhlar, D. G. *J. Phys. Chem. B* **2007**, *111*, 408.
- (564) Xue, L.; Ahlquist, M. S. *Inorg. Chem.* **2014**, *53*, 3281.

Annex

A.1. ANNEX CHAPTER III

A.1.1. Characterization of $\text{Py}_2^{\text{Tstacn}}$ by NMR

The signals in ^1H and ^{13}C NMR have been fully assigned by using ^1H - ^1H COSY, ^1H - ^{13}C HSQC and ^1H - ^{13}C HMBC techniques. The assignment is depicted as follows:

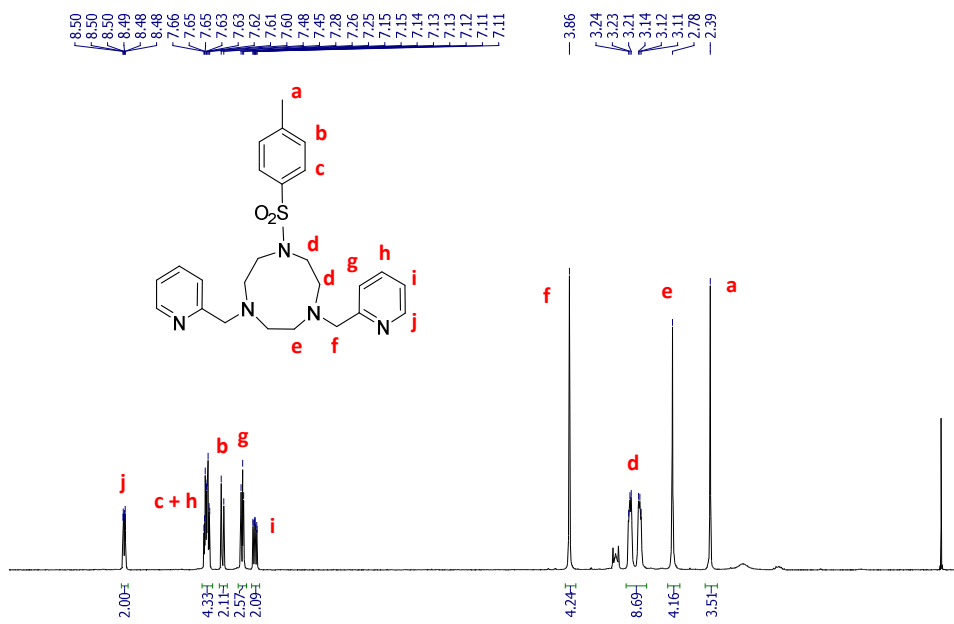


Figure A. 1. 1. ^1H NMR (CDCl_3 , 400 MHz, 300 K) spectrum of $\text{Py}_2^{\text{Tstacn}}$.

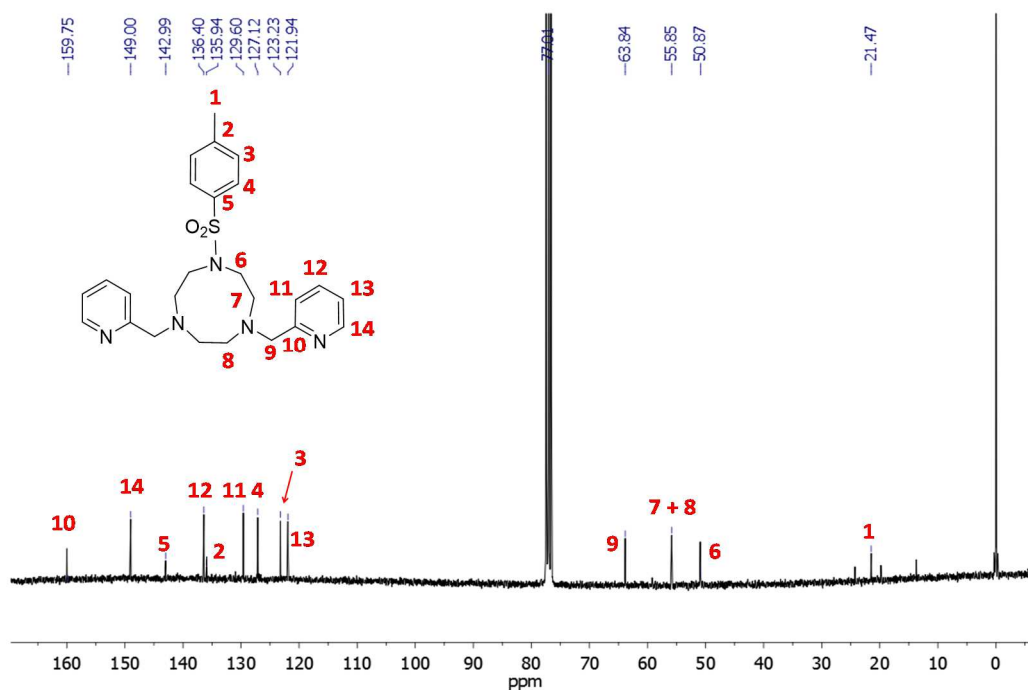


Figure A. 1. 2. $^{13}\text{C}\{^1\text{H}\}$ NMR (CDCl_3 , 101 MHz, 300 K) spectrum of $\text{Py}_2^{\text{Tstacn}}$.

A.1.2. Solid State Characterization $\text{Py}_2^{\text{Tstacn}}$, $\mathbf{1}_{\text{Co}}$ and $\mathbf{1}_{\text{Ni}}$ Table A. 1. 1. Crystal data and refinement details for $\text{Py}_2^{\text{Tstacn}}$, $\mathbf{1}_{\text{Co}}$ and $\mathbf{1}_{\text{Ni}}$.

Compound	$\text{Py}_2^{\text{Tstacn}}$	$\mathbf{1}_{\text{Co}}$	$\mathbf{1}_{\text{Ni}}$
Empirical formula	$\text{C}_{25}\text{H}_{31}\text{N}_5\text{O}_2\text{S}$	$\text{C}_{27}\text{H}_{31}\text{F}_6\text{N}_5\text{CoO}_8\text{S}_3$	$\text{C}_{27}\text{H}_{31}\text{F}_6\text{N}_5\text{NiO}_8\text{S}_3$
Formula weight	465.61	822.68	822.44
Temperature	100(2) K	149.95(10) K	100(2) K
Wavelength	0.71073 Å	0.71073 Å	0.71073 Å
Crystal system	Monoclinic	Triclinic	Triclinic
Space group	P2(1)	P-1	P-1
Unit cell dimensions	a = 5.5750(2) Å $\alpha = 90^\circ$ b = 11.8796(5) Å $\beta = 92.3874(12)^\circ$ c = 17.9224(7) Å $\gamma = 90^\circ$	a = 8.7900(2) Å $\alpha = 82.753(3)^\circ$ b = 12.7933(6) Å $\beta = 81.162(3)^\circ$ c = 17.2259(6) Å $\gamma = 75.372(3)^\circ$	a = 8.753(3) Å $\alpha = 83.287(6)^\circ$ b = 12.741(4) Å $\beta = 81.785(6)^\circ$ c = 17.037(6) Å $\gamma = 74.860(6)^\circ$
Volume	1185.95(8) Å ³	1844.32(12) Å ³	1808.7(11) Å ³
Z	2	2	2
Density (calculated)	1.304 Mg/m ³	1.634 g·cm ⁻³	1.666 g·cm ⁻³
Adsorption coefficient	0.169 mm ⁻¹	0.864 mm ⁻¹	0.943 mm ⁻¹
F(000)	496	926	928
Crystal size	0.30 x 0.25 x 0.15 mm ³	0.38 x 0.066 x 0.056 mm ³	0.8 x 0.2 x 0.08 mm ³
Reflections collected	20516	41023	27736
Independent reflections	5894	9300	8644
Final R indices	[R(int) = 0.0420]	[R(int) = 0.0476]	[R(int) = 0.0497]
R indices (all data)	R1 = 0.0297 wR2 = 0.0795	R1 = 0.0396 wR2 = 0.0979	R1 = 0.0419 wR2 = 0.0933

$$R1 = R = \frac{\sum ||F_o| - |F_c||}{\sum F_o} \quad wR2 = \left[\frac{\sum w (F_o^2 - F_c^2)^2}{\sum w (F_o^2)^2} \right]^{1/2}$$

A.1.3. Photochemical Hydrogen Generation Studies

Table A. 1. 2. Screening catalytic conditions of photochemical water reduction of **1_{Co}**.

[1_{Co}] (μM)	[PS_{ir}] (μM)	MeCN:H ₂ O:Et ₃ N	TON _{Cat} ^[a]	TON _{PS} ^[b]	TOF _{Cat} ^[c]
50	250	2:8:2	5	1	-
50	250	2:8:1.5	23	5	48
50	250	2:8:1	45	9	63
50	250	2:8:0.6	89	18	70
50	250	2:8:0.4	123	25	70
50	250	2:8:0.3	137	27	105
50	250	2:8:0.2	178	36	106
50	250	2:8:0.1	162	32	104
50	250	0:10:0.2	4	1	-
50	250	1:9:0.2	26	5	12
50	250	2:8:0.2	178	36	75
50	250	2.5:7.5:0.2	226	45	84
50	250	3:7:0.2	259	52	139
50	250	3.5:6.5:0.2	222	44	127
50	250	5:5:0.2	96	19	118
50	50	3:7:0.2	68	68	92
50	100	3:7:0.2	135	68	96
50	200	3:7:0.2	241	60	122
50	300	3:7:0.2	327	55	137
50	400	3:7:0.2	236	30	87
5	100	2:8:0.2	685	34	702
12.5	100	2:8:0.2	360	45	319
25	100	2:8:0.2	226	57	184
50	100	2:8:0.2	133	67	119
75	100	2:8:0.2	106	80	99
100	100	2:8:0.2	93	93	76
50	25	2:8:0.2	35	7	70
50	50	2:8:0.2	89	18	89
50	75	2:8:0.2	121	24	81
50	100	2:8:0.2	133	27	66
50	125	2:8:0.2	165	33	66

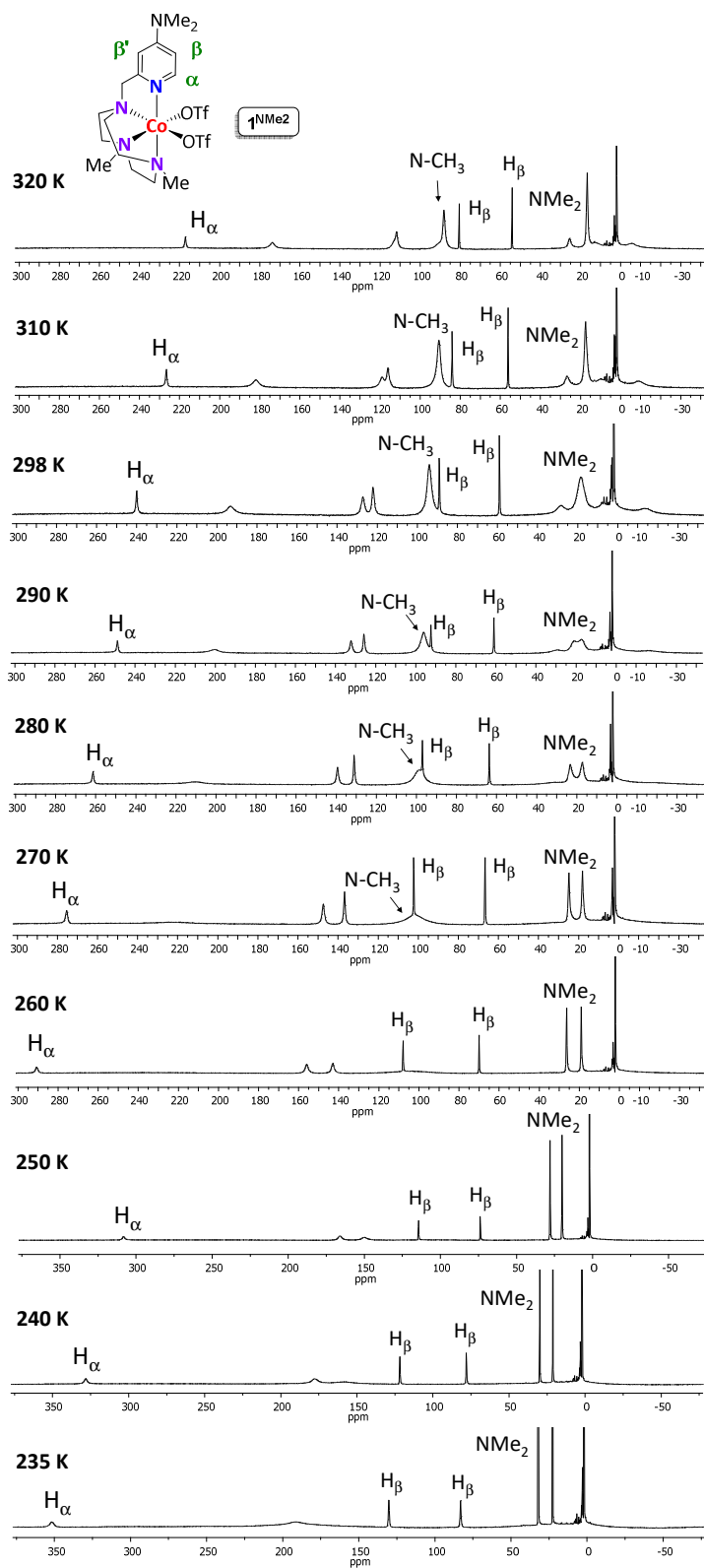
All reactions were performed at RT, irradiating at $\lambda = 447$ nm under strict anaerobic conditions.

[a] Turnover number respect to the catalyst, $\text{TON}_{\text{Cat}} = (\text{mol H}_2 / \text{mol } \mathbf{1}_{\text{Co}})$. [b] Turnover number respect to the PS, $\text{TON}_{\text{PS}} = (\text{mol H}_2 / \text{mol } \mathbf{PS}_{\text{ir}})$. [c] Initial turnover frequency calculated at 10 % of conversion, $\text{TOF}_{\text{Cat}} = \text{TON}_{\text{Cat}} \cdot \text{h}^{-1}$.

A.2. ANNEX CHAPTER IV

A.2.1. Characterization of Complexes

A.2.1.1. Paramagnetic NMR spectra

Figure A. 2. 1. ^1H -NMR spectra (500 MHz) of $^1\text{NMe}_2$ in CD_3CN at different temperatures.

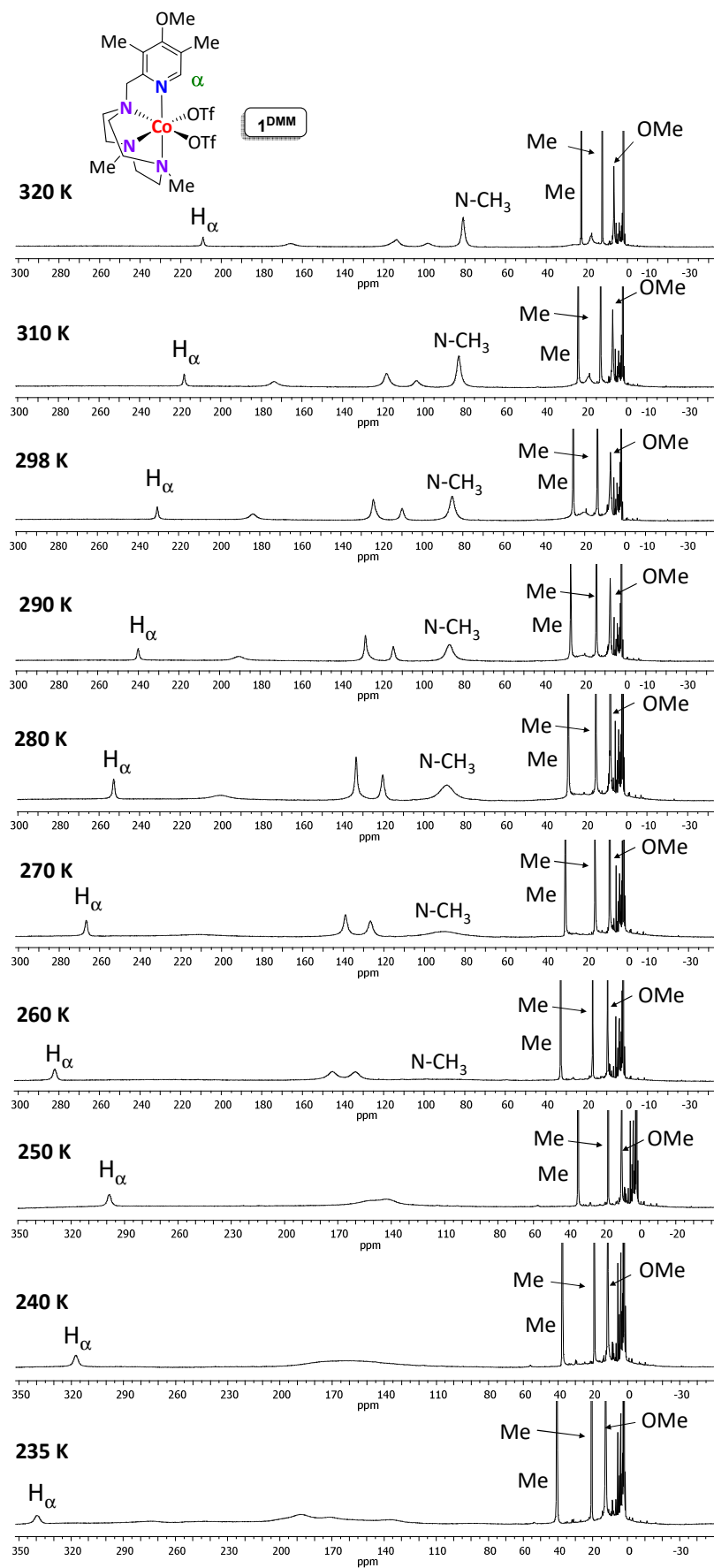


Figure A. 2. 2. ^1H -NMR spectra (500 MHz) of 1^{DMM} in CD_3CN at different temperatures.

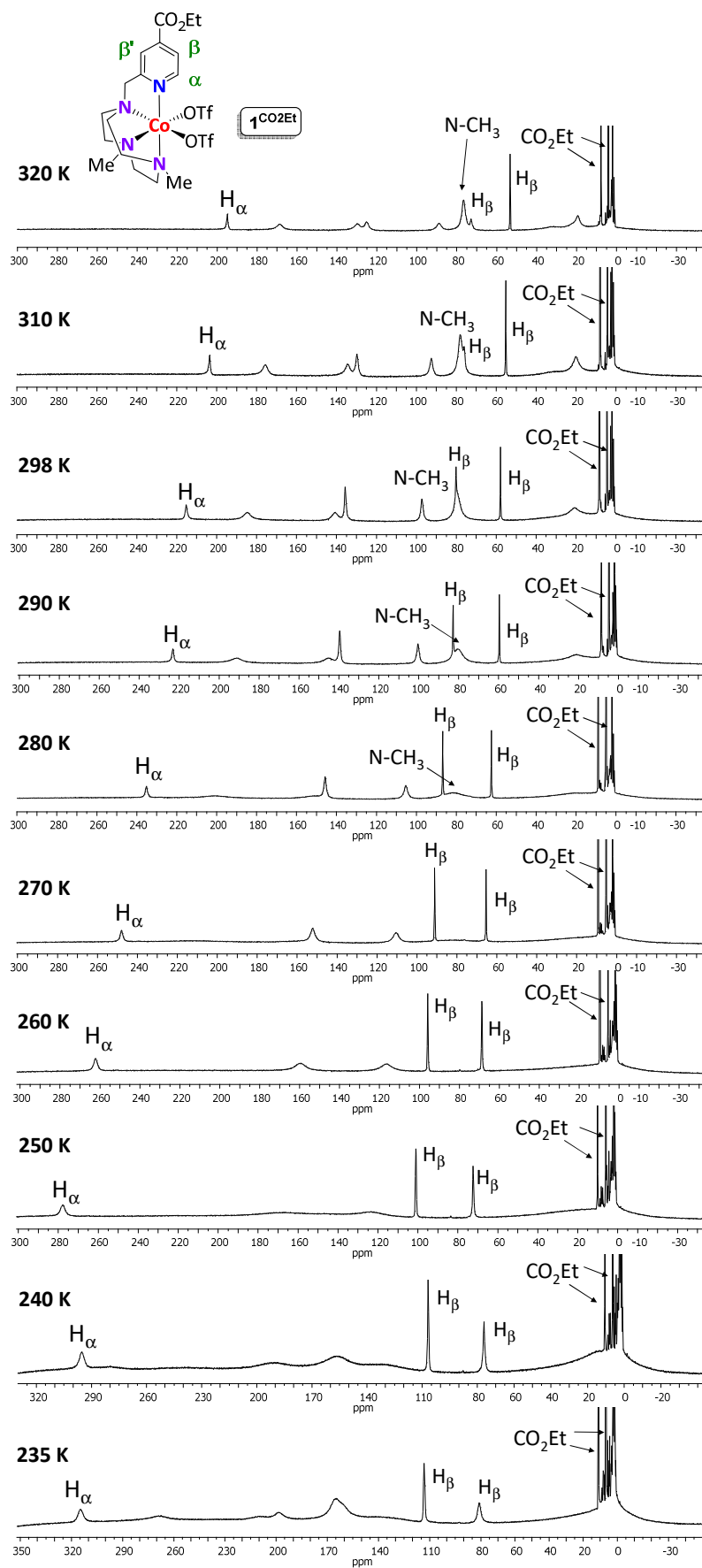


Figure A. 2. 3. $^1\text{H-NMR}$ spectra (500 MHz) of $1^{\text{CO}_2\text{Et}}$ in CD_3CN at different temperatures.

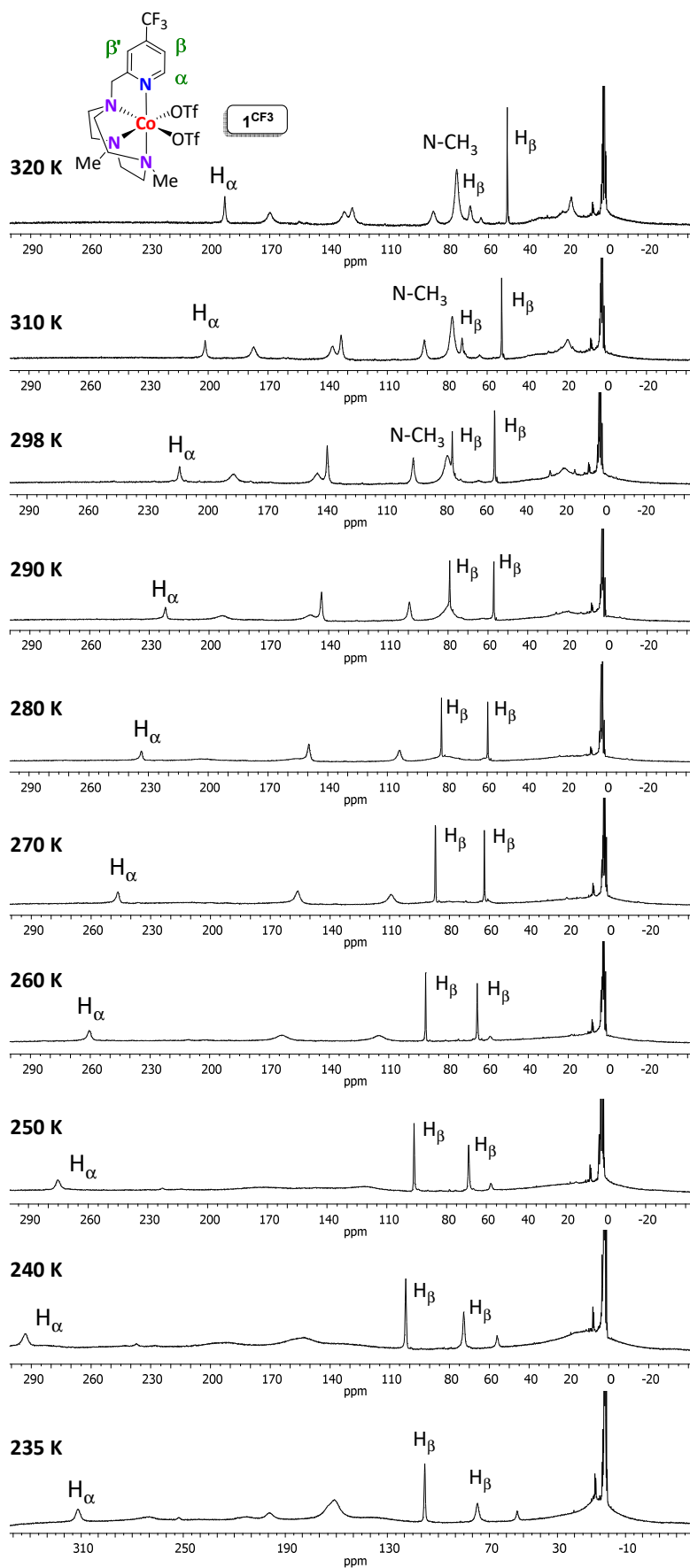


Figure A. 2. 4. ^1H -NMR spectra (500 MHz) of 1^{CF_3} in CD_3CN at different temperatures.

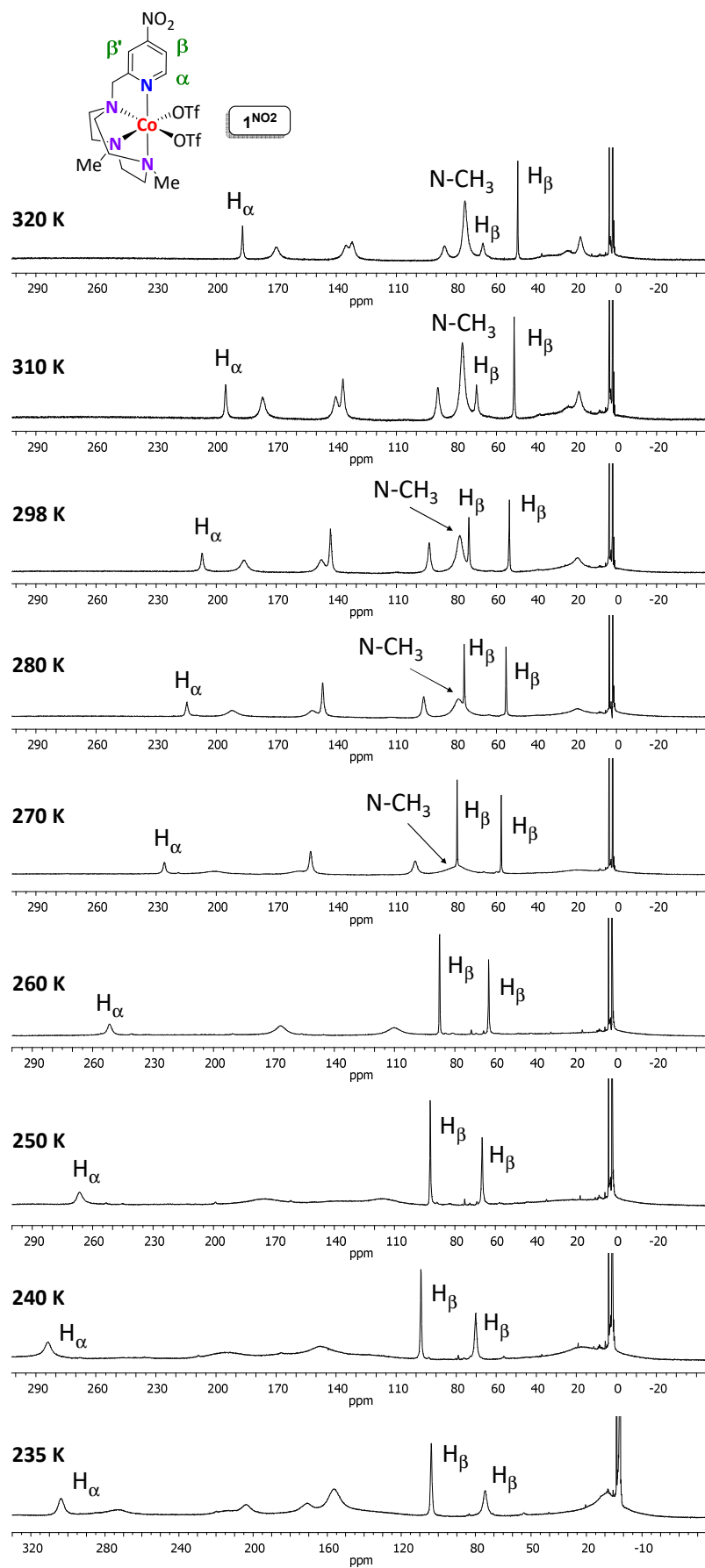


Figure A. 2. 5. $^1\text{H-NMR}$ spectra (500 MHz) of $\mathbf{1}^{\text{NO}_2}$ in CD_3CN at different temperatures.

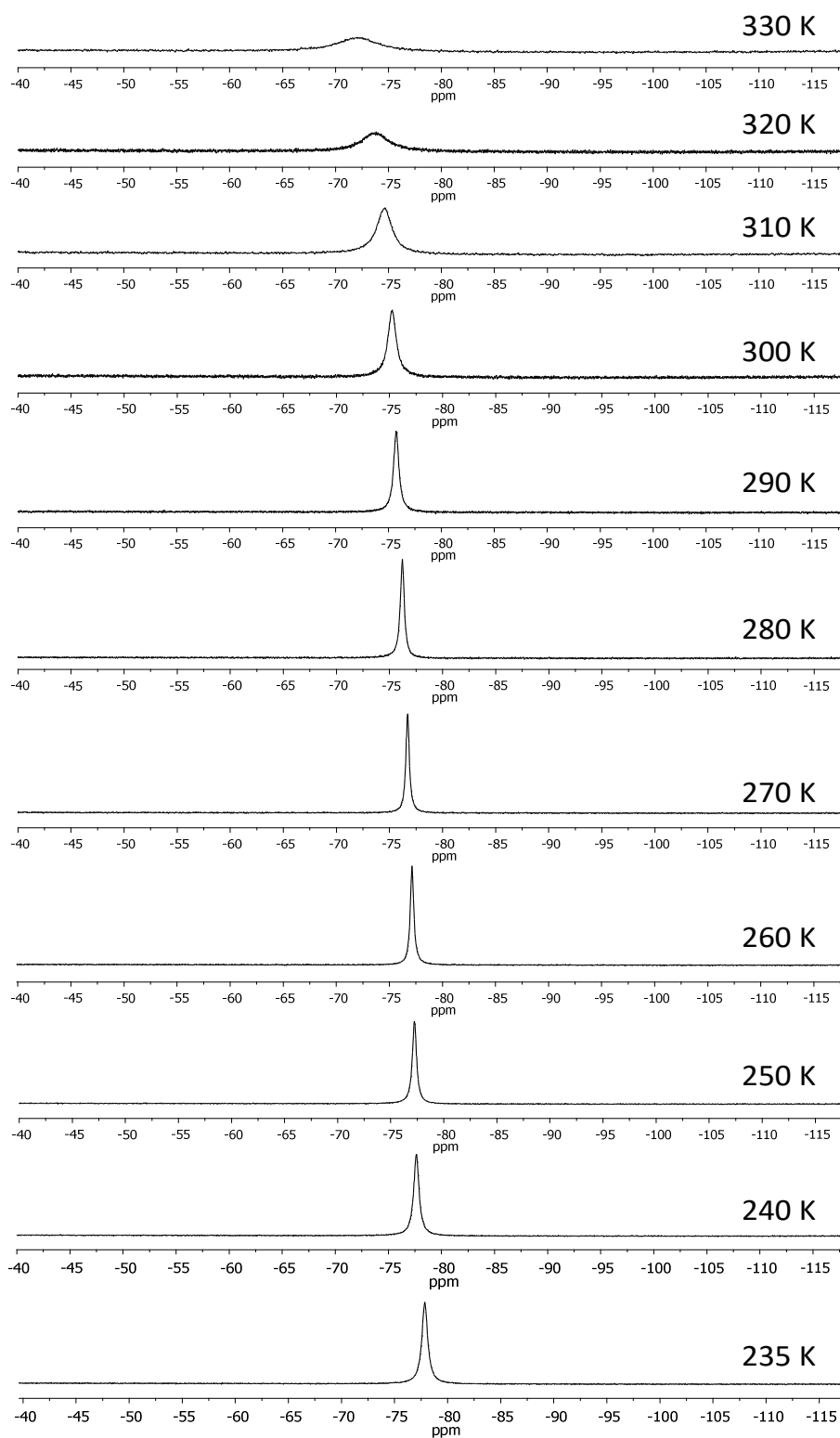


Figure A. 2. 6. ^{19}F -NMR spectra (500 MHz) of 1^{H} in CD_3CN at different temperatures.

A.2.1.2. FT-IR characterization of the 1^R complexes

Although in FT-IR 1^R complexes exhibit similar pattern, compounds 1^{NO_2} and 1^{CO_2Et} show characteristic bands at 1541 and 1731 cm^{-1} attributed to the NO_2 and $C=O$ stretching frequencies.

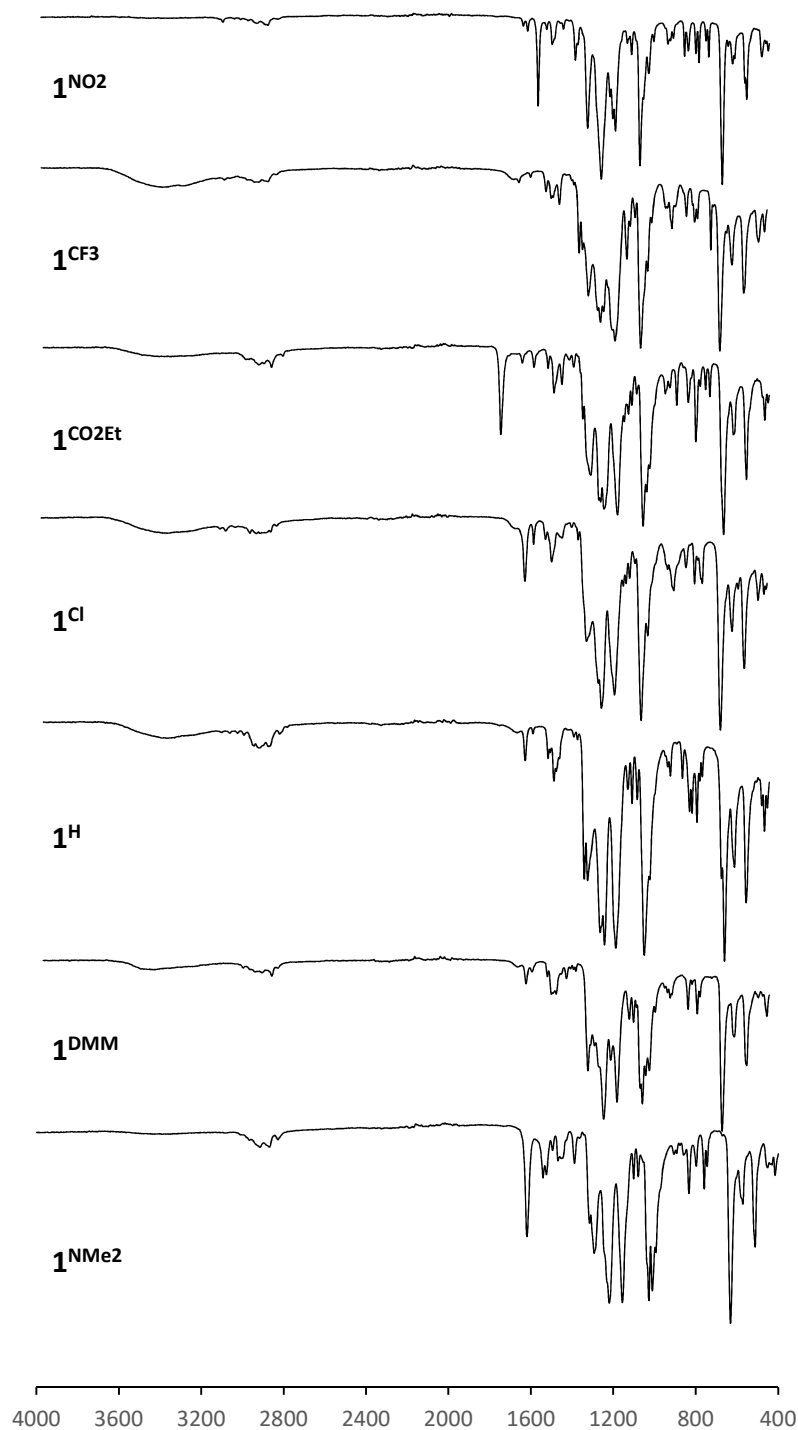


Figure A. 2. 7. FT-IR spectra of 1^R complexes.

A.2.1.3. Solid state characterization of complexes**Table A. 2. 1.** Selected Bond Lengths (Å) and Angles (°) for **1^{NO2}**, **1^{CO2Et}** and **1^{Cl}**.

	1^{NO2}	1^{CO2Et}	1^{Cl}		
Co-N1	2.1325(13)	Co-N1	2.1175(17)	Co-N1	2.116(2)
Co-N2	2.1262(13)	Co-N2	2.1451(17)	Co-N2	2.154(2)
Co-N3	2.1548(14)	Co-N3	2.157(2)	Co-N3	2.155(2)
Co-N4	2.1473(13)	Co-N4	2.1436(18)	Co-N4	2.145(2)
Co-O1	2.0497(12)	Co-O1	2.0450(15)	Co-O1	2.0861(19)
Co-O2	2.1432(13)	Co-O2	2.2089(17)	Co-O2	2.175(2)
N1-Co-N2	79.42(5)	N1-Co-N2	78.00(7)	N1-Co-N2	79.92(9)
N1-Co-N3	83.55(5)	N1-Co-N3	110.39(7)	N1-Co-N3	101.19(8)
N1-Co-N4	162.50(5)	N1-Co-N4	155.68(7)	N1-Co-N4	161.69(9)
N1-Co-O1	104.62(5)	N1-Co-O1	99.25(7)	N1-Co-O1	104.77(8)
N1-Co-O2	83.70(5)	N1-Co-O2	82.81(6)	N1-Co-O2	85.26(8)
N2-Co-N3	83.52(5)	N2-Co-N3	81.59(7)	N2-Co-N3	82.01(8)
N2-Co-N4	83.16(5)	N2-Co-N4	84.06(7)	N2-Co-N4	83.30(9)
N2-Co-O1	175.94(5)	N2-Co-O1	169.72(7)	N2-Co-O1	170.61(8)
N2-Co-O2	93.10(5)	N2-Co-O2	100.94(7)	N2-Co-O2	100.02(9)
N3-Co-N4	96.14(5)	N3-Co-N4	82.69(7)	N3-Co-N4	83.57(8)
N3-Co-O1	96.30(5)	N3-Co-O1	90.23(7)	N3-Co-O1	89.04(8)
N3-Co-O2	176.58(5)	N3-Co-O2	166.77(7)	N3-Co-O2	173.52(8)
N4-Co-O1	92.78(5)	N4-Co-O1	101.15(7)	N4-Co-O1	92.90(8)
N4-Co-O2	95.58(5)	N4-Co-O2	84.65(7)	N4-Co-O2	90.53(8)
O1-Co-O2	87.04(5)	O1-Co-O2	88.44(6)	O1-Co-O2	88.57(8)

Table A. 2. 2. Selected Bond Lengths (Å) and Angles (°) for **1^H**, **1^{DMM}** and **1^{NMe2}**.

	1^H		1^{DMM}		1^{NMe2}
Co-N1	2.0969(12)	Co-N1	2.0883(13)	Co-N1	2.088(4)
Co-N2	2.1309(12)	Co-N2	2.1263(13)	Co-N2	2.160(4)
Co-N3	2.1667(12)	Co-N3	2.1628(14)	Co-N3	2.172(5)
Co-N4	2.1458(12)	Co-N4	2.1427(13)	Co-N4	2.150(4)
Co-O1	2.1684(10)	Co-O1	2.0596(13)	Co-O1	2.083(4)
Co-O2	2.0689(10)	Co-O2	2.2230(12)	Co-O2	2.225(4)
N1-Co-N2	80.26(5)	N1-Co-N2	78.21(5)	N1-Co-N2	79.03(15)
N1-Co-N3	95.45(5)	N1-Co-N3	108.01(5)	N1-Co-N3	106.7(2)
N1-Co-N4	163.27(5)	N1-Co-N4	157.25(5)	N1-Co-N4	158.05(18)
N1-Co-O1	87.37(4)	N1-Co-O1	100.22(6)	N1-Co-O1	101.75(15)
N1-Co-O2	103.44(5)	N1-Co-O2	84.44(5)	N1-Co-O2	86.73(15)
N2-Co-N3	82.84(5)	N2-Co-N3	82.26(5)	N2-Co-N3	81.31(19)
N2-Co-N4	83.02(5)	N2-Co-N4	83.64(5)	N2-Co-N4	82.75(17)
N2-Co-O1	96.60(4)	N2-Co-O1	175.82(6)	N2-Co-O1	171.35(17)
N2-Co-O2	174.14(4)	N2-Co-O2	97.98(5)	N2-Co-O2	101.10(17)
N3-Co-N4	82.95(5)	N3-Co-N4	82.71(5)	N3-Co-N4	82.4(2)
N3-Co-O1	176.98(4)	N3-Co-O1	94.62(6)	N3-Co-O1	90.26(19)
N3-Co-O2	92.24(4)	N3-Co-O2	167.23(5)	N3-Co-O2	166.6(2)
N4-Co-O1	94.03(4)	N4-Co-O1	98.77(6)	N4-Co-O1	98.12(18)
N4-Co-O2	93.27(4)	N4-Co-O2	84.62(5)	N4-Co-O2	84.86(18)
O1-Co-O2	88.16(4)	O1-Co-O2	85.68(6)	O1-Co-O2	87.55(17)

Table A. 2. 3. Crystal Data for **1^{NO2}**, **1^{CO2Et}** and **1^{Cl}**.

Compound	1^{NO2}	1^{CO2Et}	1^{Cl}
Empirical formula	C ₁₆ H ₂₃ CoF ₆ N ₅ O ₈ S	C ₁₉ H ₂₈ CoF ₆ N ₄ O ₈ S ₂	C ₁₆ H ₂₃ ClCoF ₆ N ₄ O ₆ S ₂
Formula weight	650.44	677.50	639.88
Temperature	100(2) K	100(2) K	100(2) K
Wavelength	0.71073 Å	null Å	0.71073 Å
Crystal system	Monoclinic	Monoclinic	Monoclinic
Space group	P2(1)/c	Cc	P 21/n
Unit cell dimensions	a = 9.5156(16) Å α = 90° b = 14.818(2) Å β = 95.229(5)° c = 17.273(3) Å γ = 90°	a = 12.8115(16) Å α = 90° b = 24.0973(19) Å β = 96.927(5)° c = 8.7902(10) Å γ = 90°	a = 8.8511(7) Å α = 90° b = 24.5258(19) Å β = 97.0660(10)° c = 11.1501(9) Å γ = 90°
Volume	2425.3(7) Å ³	2693.9(5) Å ³	2402.1(3) Å ³
Z	4	4	4
Density (calculated)	1.781 Mg/m ³	1.670 Mg/m ³	1.769 Mg/m ³
Adsorption coefficient	0.980 mm ⁻¹	0.885 mm ⁻¹	1.088 mm ⁻¹
F(000)	1324	1388	1300
Crystal size	0.51 x 0.30 x 0.15 mm ³	0.30 x 0.30 x 0.15 mm ³	0.25 x 0.15 x 0.08 mm ³
Θ range for data collection	1.814 to 32.332°	1.811 to 32.527°	1.661 to 28.302°
Index ranges	-13 ≤ h ≤ 13 -22 ≤ k ≤ 14 -25 ≤ l ≤ 20	-19 ≤ h ≤ 19 -25 ≤ k ≤ 36 -12 ≤ l ≤ 6	-8 ≤ h ≤ 11 -32 ≤ k ≤ 31 -13 ≤ l ≤ 14
Reflections collected	31525	16431	14849
Independent reflections	8149	6178	5575
Completeness to Θ	[R(int) = 0.0542] 94.0% (Θ = 32.332°)	[R(int) = 0.0251] 92.0% (Θ = 32.527°)	[R(int) = 0.0250] 99.9% (Θ = 25.242°)
Absorption correction	Empirical	Multi-scan	Empirical
Max. and min. transmission	0.867 and 0.605	0.879 and 0.777	1 and 0.783
Refinement method	Full-matrix least-squares on F ²	Full-matrix least-squares on F ²	Full-matrix least-squares on F ²
Data / restraints / parameters	8149/0/345	6178/2/364	5575/0/327
Goodness-of-fit on F ²	1.030	1.034	1.031
Final R indices [I > 2σ(I)]	R1 = 0.0365	R1 = 0.0259	R1 = 0.0426
R indices (all data)	wR2 = 0.0844 R1 = 0.0528 wR2 = 0.0926	wR2 = 0.0595 R1 = 0.0280 wR2 = 0.0605	wR2 = 0.1065 R1 = 0.0538 wR2 = 0.1133
Largest diff. peak and hole	0.673 and -0.802 e ⁻ Å ⁻³	0.377 and -0.373 e ⁻ Å ⁻³	0.941 and -0.635 e ⁻ Å ⁻³

Table A. 2. 4. Crystal Data for **1^H**, **1^{DMM}** and **1^{NMe2}**.

Compound	1^H	1^{DMM}	1^{NMe2}
Empirical formula	C ₁₆ H ₂₄ CoF ₆ N ₄ O ₆ S ₂	C ₁₉ H ₃₀ CoF ₆ N ₄ O ₇ S ₂	C ₁₈ H ₂₉ CoF ₆ N ₅ O ₆ S ₂
Formula weight	605.44	663.52	648.51
Temperature	100(2) K	100(2) K	298(2) K
Wavelength	0.71073 Å	0.71073 Å	0.71073 Å
Crystal system	Orthorhombic	Monoclinic	Monoclinic
Space group	Pbca	P2(1)/c	P 21/n
Unit cell dimensions	a = 9.312(2) Å α = 90 b = 16.956(4) Å β = 90° c = 29.498(7) Å γ = 90°	a = 11.9921(9) Å α = 90° b = 15.4423(14) Å β = 108.403(2)° c = 15.8756(13) Å γ = 90°	a = 8.802(2) Å α = 90° b = 24.936(6) Å β = 94.038(5)° c = 12.694(3) Å γ = 90°
Volume	4657.5(19) Å ³	2789.6(4) Å ³	2779.3(12) Å ³
Z	8	4	4
Density (calculated)	1.727 Mg/m ³	1.580 Mg/m ³	1.550 Mg/m ³
Adsorption coefficient	1.006 mm ⁻¹	0.850 mm ⁻¹	0.849 mm ⁻¹
F(000)	2472	1364	1332
Crystal size	0.20 x 0.20 x 0.05 mm ³	0.40 x 0.35 x 0.10 mm ³	0.35 x 0.20 x 0.12 mm ³
Θ range for data collection	2.402 to 27.573°	1.790 to 30.537°	2.292 to 27.498°
Index ranges	-11 ≤ h ≤ 12 -22 ≤ k ≤ 20 -38 ≤ l ≤ 38	-15 ≤ h ≤ 17 -21 ≤ k ≤ 22 -16 ≤ l ≤ 22	-11 ≤ h ≤ 11 -32 ≤ k ≤ 32 -16 ≤ l ≤ 16
Reflections collected	20276	29373	41842
Independent reflections	5153	8352	6388
Completeness to Θ	[R(int) = 0.0216] 95.6% (Θ = 27.573°)	[R(int) = 0.0381] 97.89% (Θ = 30.537°)	[R(int) = 0.0479] 95.6% (Θ = 25.242°)
Absorption correction	Empirical	Multi-scan	Empirical
Max. and min. transmission	0.951 and 0.732	0.920 and 0.733	1.0 and 0.843
Refinement method	Full-matrix least-squares on F ²	Full-matrix least-squares on F ²	Full-matrix least-squares on F ²
Data / restraints / parameters	5153/6/318	8352/0/357	6388/6/330
Goodness-of-fit on F ²	1.091	1.035	1.036
Final R indices [I > 2σ(I)]	R1 = 0.0227	R1 = 0.0353	R1 = 0.0767
R indices (all data)	wR2 = 0.0556 R1 = 0.0251 wR2 = 0.0568	wR2 = 0.0873 R1 = 0.0458 wR2 = 0.0933	wR2 = 0.2182 R1 = 0.1031 wR2 = 0.2483
Largest diff. peak and hole	0.397 and -0.369 e·Å ⁻³	1.509 and -0.603 e·Å ⁻³	1.005 and -0.656 e·Å ⁻³

Table A. 2. 5. Crystal Data for $\text{Co}(\text{H,NO}_2\text{Py}^{\text{Me}}\text{tacn})(\text{MeCN})_2(\text{OTf})_2$.

Compound	1^H
Empirical formula	$\text{C}_{20}\text{H}_{29}\text{CoF}_6\text{N}_7\text{O}_8\text{S}_2$
Formula weight	732.55
Temperature	298(2) K
Wavelength	Monoclinic
Crystal system	P2(1)/c
Space group	P2(1)/c
Unit cell dimensions	a = 14.625 (4) Å α = 90 b = 13.233 (3) Å β = 130.498(12)° c = 20.411(4) Å γ = 90°
Volume	3003.8(12) Å ³
Z	4
Density (calculated)	1.620 Mg/m ³
Adsorption coefficient	0.803 mm ⁻¹
F(000)	1500
Crystal size	0.40 x 0.20 x 0.10 mm ³
Θ range for data collection	2.00 to 28.43°
Index ranges	-19 ≤ h ≤ 19 -17 ≤ k ≤ 17 -27 ≤ l ≤ 26
Reflections collected	46939
Independent reflections	7490 [R(int) = 0.0216]
Completeness to Θ	99.0 % (Θ = 28.43°)
Absorption correction	Empirical
Max. and min. transmission	1.0 and 0.825975
Refinement method	Full-matrix least-squares on F ²
Data / restraints / parameters	7490/0/399
Goodness-of-fit on F ²	1.016
Final R indices [I > 2σ(I)]	R1 = 0.0639 wR2 = 0.1446
R indices (all data)	R1 = 0.1637 wR2 = 0.1853
Largest diff. peak and hole	0.645 and -0.377 e·Å ⁻³

A.2.2. Electrochemical Studies

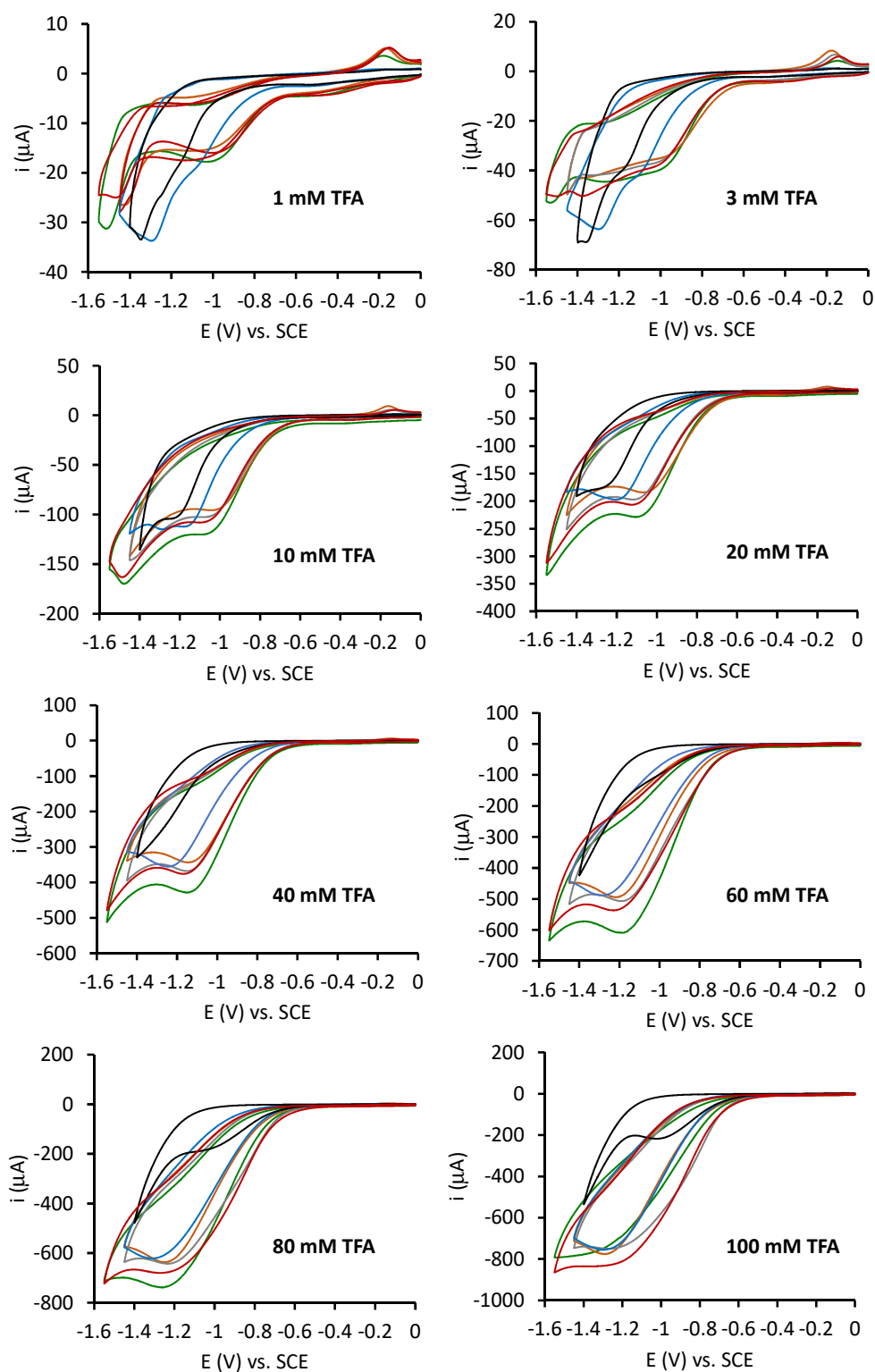


Figure A. 2. 8. Successive cyclic voltammograms obtained at different concentrations of TFA with different 1^R complexes (1^{NMe_2} (green), 1^{DMM} (red), 1^H (grey), 1^{Cl} (orange), 1^{CO_2Et} (blue) and 1^{CF_3} (black)). Conditions: 1^R (1 mM) in acetonitrile containing Bu_4NPF_6 (0.1 M) in the presence of TFA (1 – 100 mM, as indicated in each case). Scan rate of $100 \text{ mV}\cdot\text{s}^{-1}$.

A.3. ANNEX CHAPTER VI

A.3.1. Characterization of Complexes

A.3.1.1. Paramagnetic NMR spectra

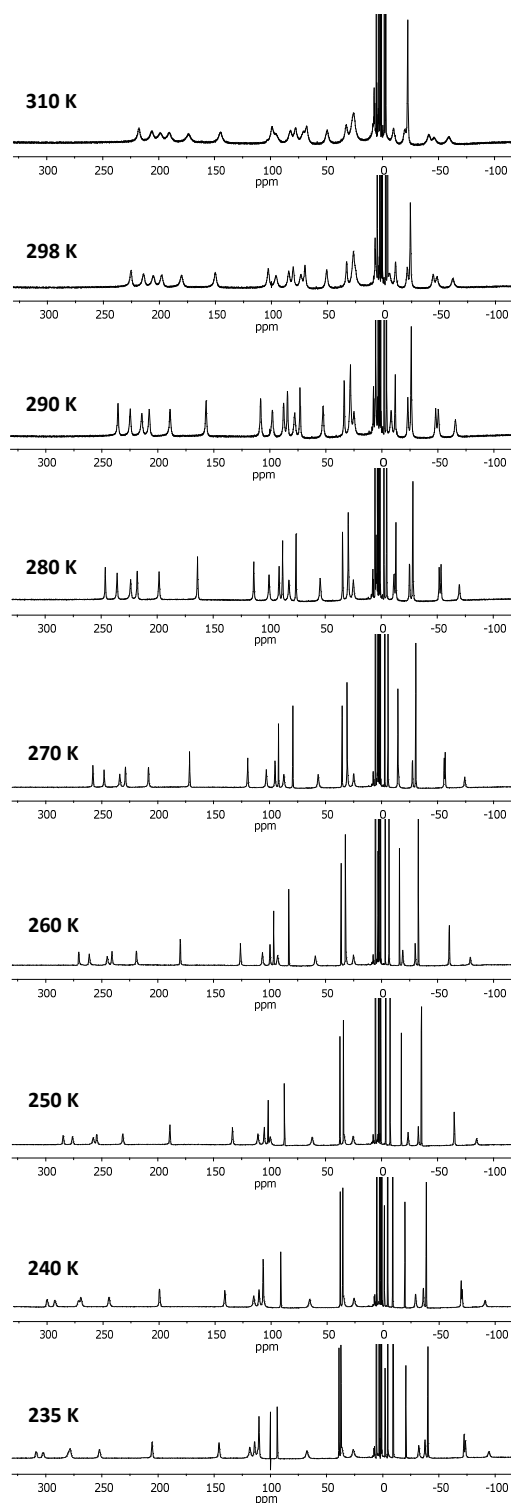


Figure A. 3. 1. $^1\text{H-NMR}$ spectra (500 MHz) of $1_{\text{Co}}^{\text{II}} \text{Cl}$ in CD_3CN at different temperatures.

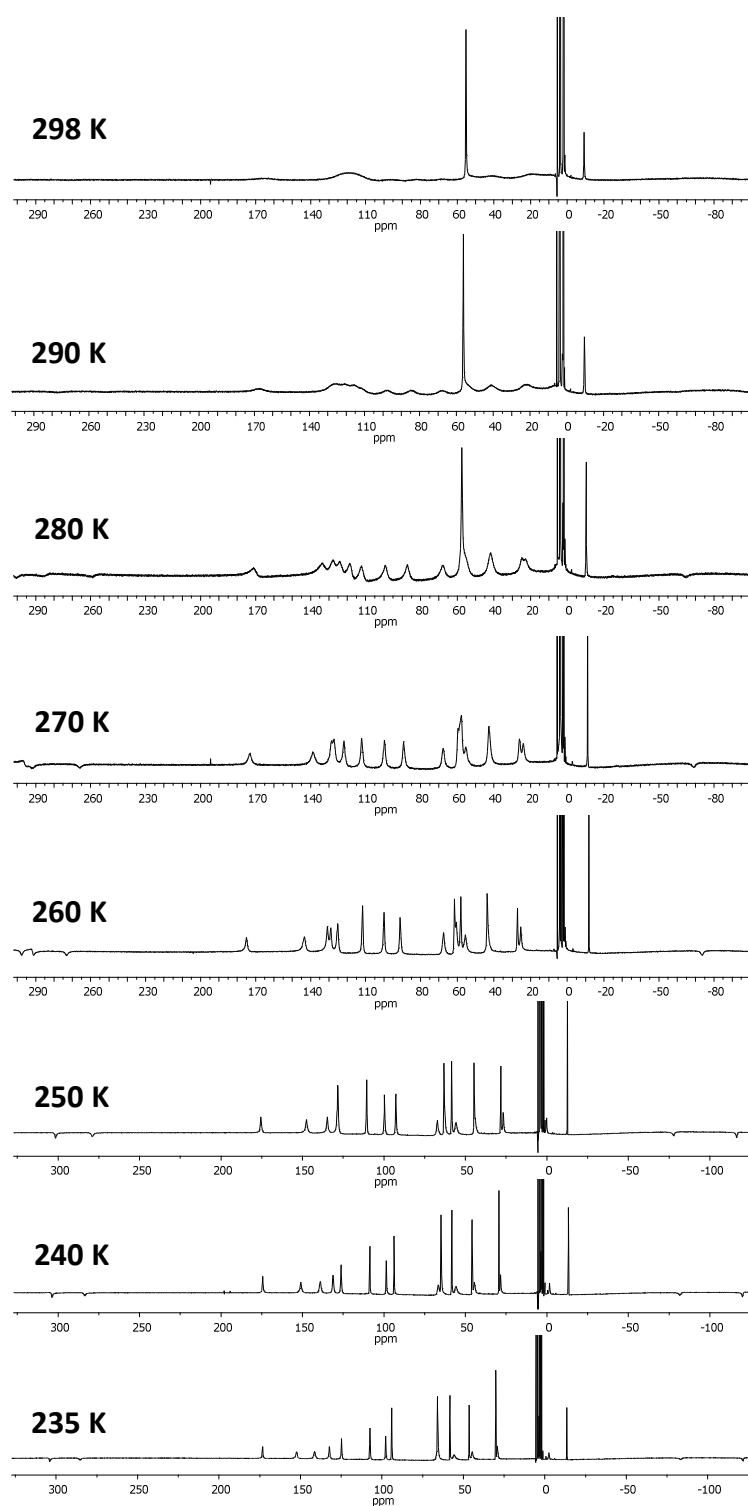


Figure A. 3. 2. $^1\text{H-NMR}$ spectra (500 MHz) of $1_{\text{Co}^{\text{II}}}\text{CH}_3\text{CN}$ in CD_3CN at different temperatures.

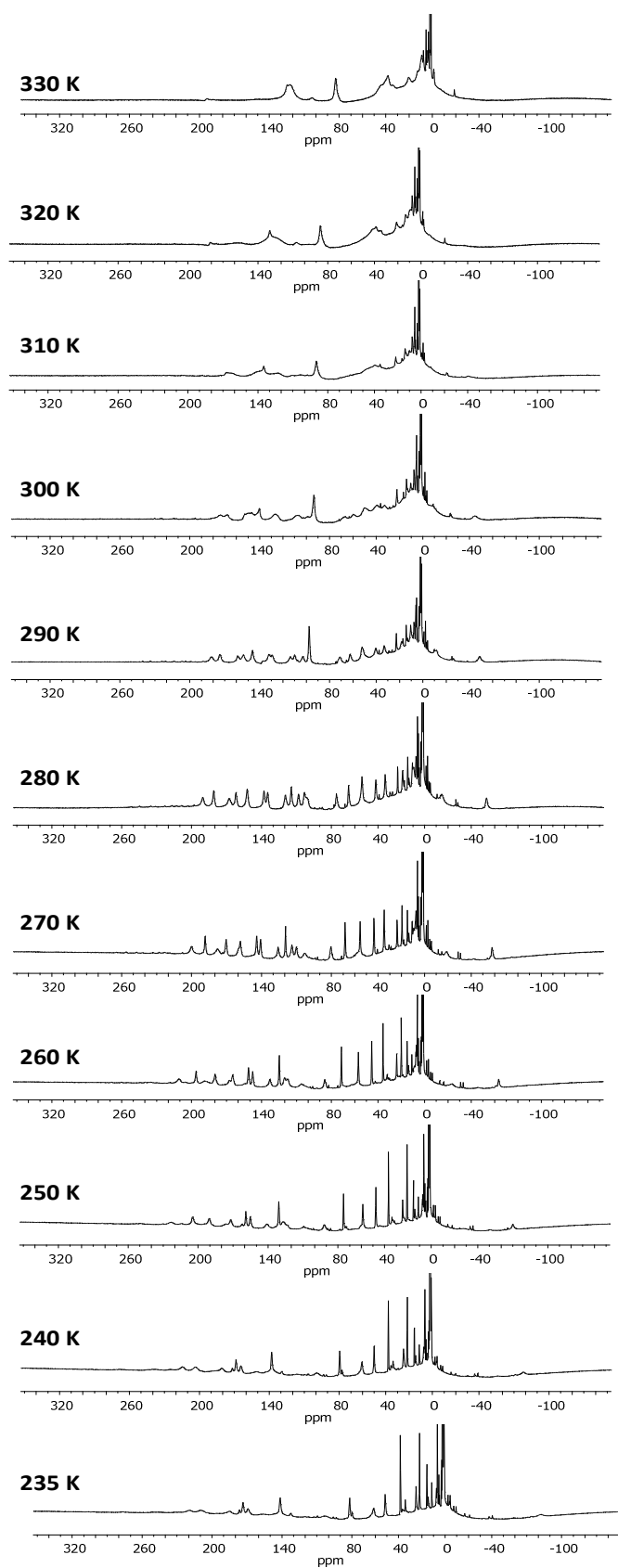


Figure A. 3. 3. $^1\text{H-NMR}$ spectra (500 MHz) of $1_{\text{Co}}^{\text{Cl}}$ in CD_3CN at different temperatures.

A.3.1.2. Solid state characterization of the complexes**Table A. 3.** 1. Crystal Data for $1_{\text{Co}}^{\text{II}}_{\text{CH}_3\text{CN}}$, $1_{\text{Co}}^{\text{II}}_{\text{Cl}}$ and $1_{\text{Co}}^{\text{III}}_{\text{CH}_3\text{CN}}$.

Compound	$1_{\text{Co}}^{\text{II}}_{\text{CH}_3\text{CN}}$	$1_{\text{Co}}^{\text{II}}_{\text{Cl}}$	$1_{\text{Co}}^{\text{III}}_{\text{CH}_3\text{CN}}$
Empirical formula	$\text{C}_{29}\text{H}_{34}\text{CoF}_6\text{N}_6\text{O}_8\text{S}_3$	$\text{C}_{28}\text{H}_{37}\text{Cl}_8\text{CoN}_5\text{O}_2\text{S}$	$\text{C}_{31}\text{H}_{37}\text{BCoF}_{10}\text{N}_7\text{O}_8\text{S}_3$
Formula weight	863.73	850.21	991.59
Temperature	100(2) K	100(2) K	100(2) K
Wavelength	0.71073 Å	0.71073 Å	0.71073 Å
Crystal system	Monoclinic	Triclinic	Triclinic
Space group	P2(1)/n	P-1	P-1
Unit cell dimensions	a = 20.705(3) Å $\alpha = 90^\circ$ b = 9.1952(12) Å $\beta = 118.582(4)^\circ$ c = 20.933(3) Å $\gamma = 90^\circ$	a = 10.4564(14) Å $\alpha = 62.094(4)^\circ$ b = 19.696(3) Å $\beta = 89.700^\circ$ c = 19.910(3) Å $\gamma = 88.428(4)^\circ$	a = 11.2011(8) Å $\alpha = 67.278(2)^\circ$ b = 12.9653(9) Å $\beta = 83.647(2)^\circ$ c = 14.8648(11) Å $\gamma = 86.401(2)^\circ$
Volume	3499.7(9) Å ³	3622.1(9) Å ³	1978.5(2) Å ³
Z	4	4	2
Density (calculated)	1.639 Mg/m ³	1.559 Mg/m ³	1.664 Mg/m ³
Adsorption coefficient	0.760 mm ⁻¹	1.157 mm ⁻¹	0.698 mm ⁻¹
F(000)	1772	1740	1012
Crystal size	0.40 x 0.12 x 0.08 mm ³	0.355 x 0.30 x 0.10 mm ³	0.20 x 0.03 x 0.02 mm ³
Θ range for data collection	2.216 to 30.168°	1.157 to 26.546°	1.784 to 27.273°
Index ranges	-29 ≤ h ≤ 23 -12 ≤ k ≤ 10 -29 ≤ l ≤ 28	-13 ≤ h ≤ 13 -21 ≤ k ≤ 24 0 ≤ l ≤ 24	-14 ≤ h ≤ 9 -16 ≤ k ≤ 16 -19 ≤ l ≤ 18
Reflections collected	37031	14800	26306
Independent reflections	10235 [R(int) = 0.0577]	14800 [R(int) = ?]	8784 [R(int) = 0.0737]
Completeness to Θ	98.9 % ($\Theta = 30.168^\circ$)	98.2 % ($\Theta = 26.546^\circ$)	98.8 % ($\Theta = 27.273^\circ$)
Absorption correction	Empirical	Empirical	Multi-scan
Max. and min. transmission	0.942 and 0.823	0.893 and 0.687	0.986 and 0.596
Refinement method	Full-matrix least-squares on F ²	Full-matrix least-squares on F ²	Full-matrix least-squares on F ²
Data / restraints / parameters	10235/0/480	14800/99/894	8784/69/581
Goodness-of-fit on F ²	1.035	1.035	1.025
Final R indices [$I > 2\sigma(I)$]	R1 = 0.0405 wR2 = 0.0945	R1 = 0.0755 wR2 = 0.1923	R1 = 0.0639 wR2 = 0.1570
R indices (all data)	R1 = 0.0581 wR2 = 0.1041	R1 = 0.1162 wR2 = 0.2260	R1 = 0.1147 wR2 = 0.1831
Largest diff. peak and hole	0.829 and -0.552 e·Å ⁻³	1.502 and -1.024 e·Å ⁻³	0.986 and -0.817e·Å ⁻³ 3

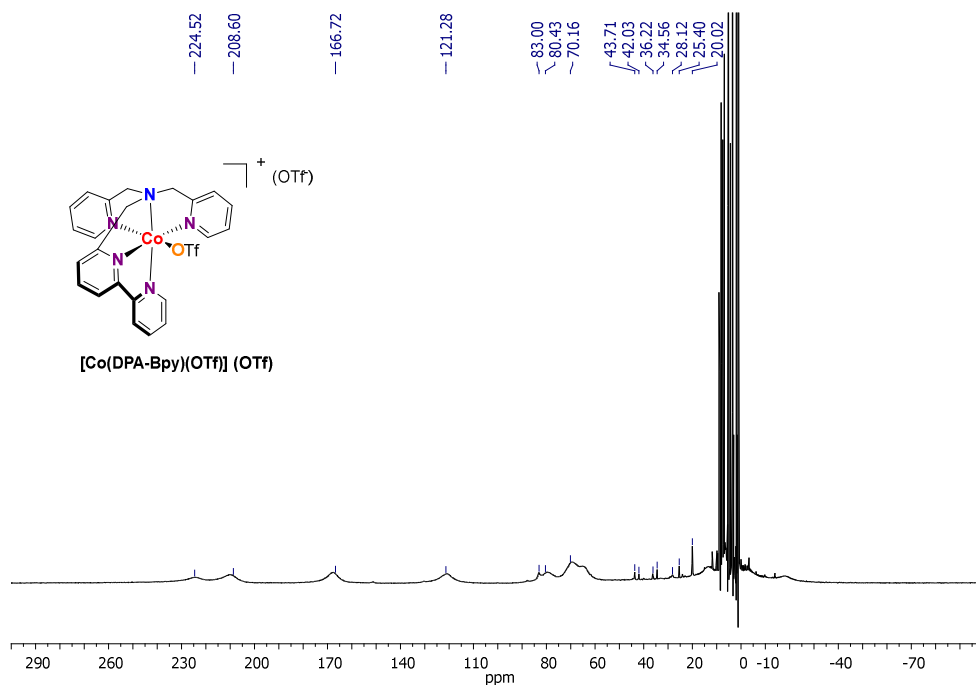
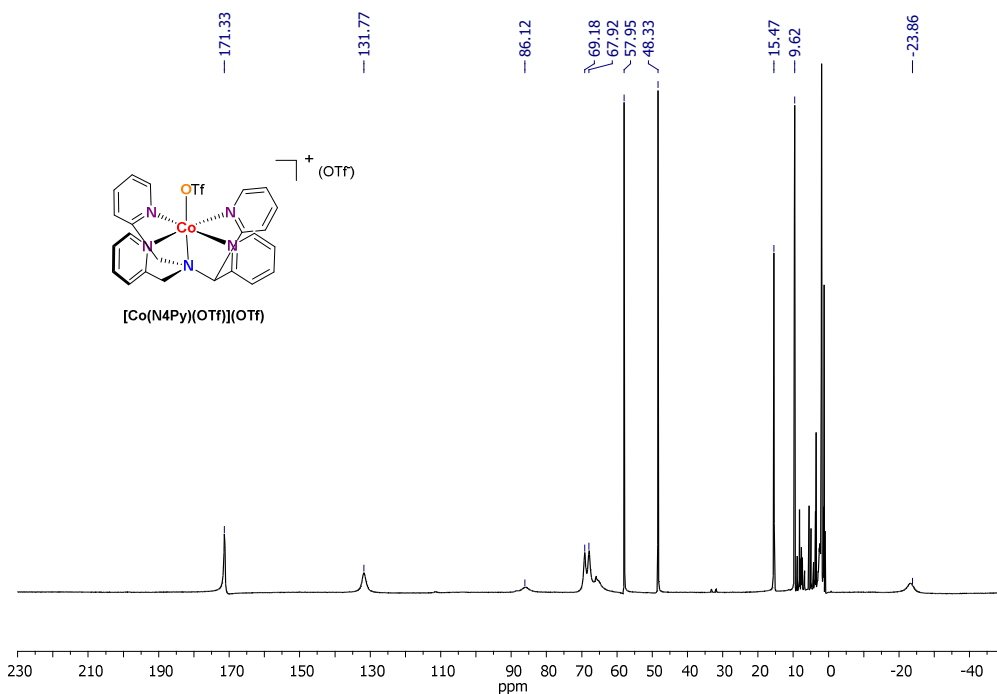
Table A. 3. 2. Selected Bond Lengths (Å) and Angles (°) for $1_{\text{Co}^{\text{II}}\text{CH}_3\text{CN}}$, $1_{\text{Co}^{\text{II}}\text{Cl}}$ and $1_{\text{Co}^{\text{III}}\text{CH}_3\text{CN}}$.

$1_{\text{Co}^{\text{II}}\text{CH}_3\text{CN}}$		$1_{\text{Co}^{\text{II}}\text{Cl}}$		$1_{\text{Co}^{\text{III}}\text{CH}_3\text{CN}}$	
Co-N1	1.9885(16)	Co-N1	2.135(5)	Co-N1	1.937(4)
Co-N2	1.9745(16)	Co-N2	2.110(5)	Co-N2	1.952(3)
Co-N3	2.3856(17)	Co-N3	2.433(5)	Co-N3	2.073(4)
Co-N4	2.0224(16)	Co-N4	2.190(5)	Co-N4	1.953(3)
Co-N5	2.1496(17)	Co-N5	2.086(5)	Co-N5	1.956(4)
Co-N6	1.9466(17)	Co-Cl	2.3007(15)	Co-N6	1.905(4)
N1-Co-N2	83.41(6)	N1-Co-N2	79.5(2)	N1-Co-N2	84.55(14)
N1-Co-N3	83.85(6)	N1-Co-N3	78.18(18)	N1-Co-N3	86.78(14)
N1-Co-N4	85.28(6)	N1-Co-N4	79.55(19)	N1-Co-N4	87.00(14)
N1-Co-N5	96.57(6)	N1-Co-N5	157.29(19)	N1-Co-N5	94.04(15)
N1-Co-N6	174.67(7)	N1-Co-Cl	101.38(14)	N1-Co-N6	178.88(14)
N2-Co-N3	97.83(6)	N2-Co-N3	157.27(18)	N2-Co-N3	97.72(13)
N2-Co-N4	168.68(6)	N2-Co-N4	92.08(18)	N2-Co-N4	170.71(15)
N2-Co-N5	100.22(7)	N2-Co-N5	100.4(2)	N2-Co-N5	92.56(14)
N2-Co-N6	96.20(7)	N2-Co-Cl	91.57(14)	N2-Co-N6	94.66(14)
N3-Co-N4	81.30(6)	N3-Co-N4	79.87(18)	N3-Co-N4	85.63(13)
N3-Co-N5	161.88(6)	N3-Co-N5	98.59(18)	N3-Co-N5	169.72(13)
N3-Co-N6	90.95(6)	N3-Co-Cl	96.82(12)	N3-Co-N6	92.55(14)
N4-Co-N5	80.69(6)	N4-Co-N5	77.76(19)	N4-Co-N5	84.18(14)
N4-Co-N6	95.10(6)	N4-Co-Cl	176.34(14)	N4-Co-N6	93.84(14)
N5-Co-N6	88.74(7)	N5-Co-Cl	101.33(14)	N5-Co-N6	86.78(15)

A.4. ANNEX CHAPTER VII

A.4.1. Characterization of Complexes

A.4.1.1. Paramagnetic NMR spectra

Figure A. 4. 1. $^1\text{H-NMR}$ (CD_3CN , 400 MHz, 260 K) spectrum of $[\text{Co}(\text{OTf})(\text{DPA-Bpy})](\text{OTf})$.Figure A. 4. 2. $^1\text{H-NMR}$ (CD_3CN , 400 MHz, 260 K) spectrum of $[\text{Co}(\text{N4Py})(\text{OTf})](\text{OTf})$.

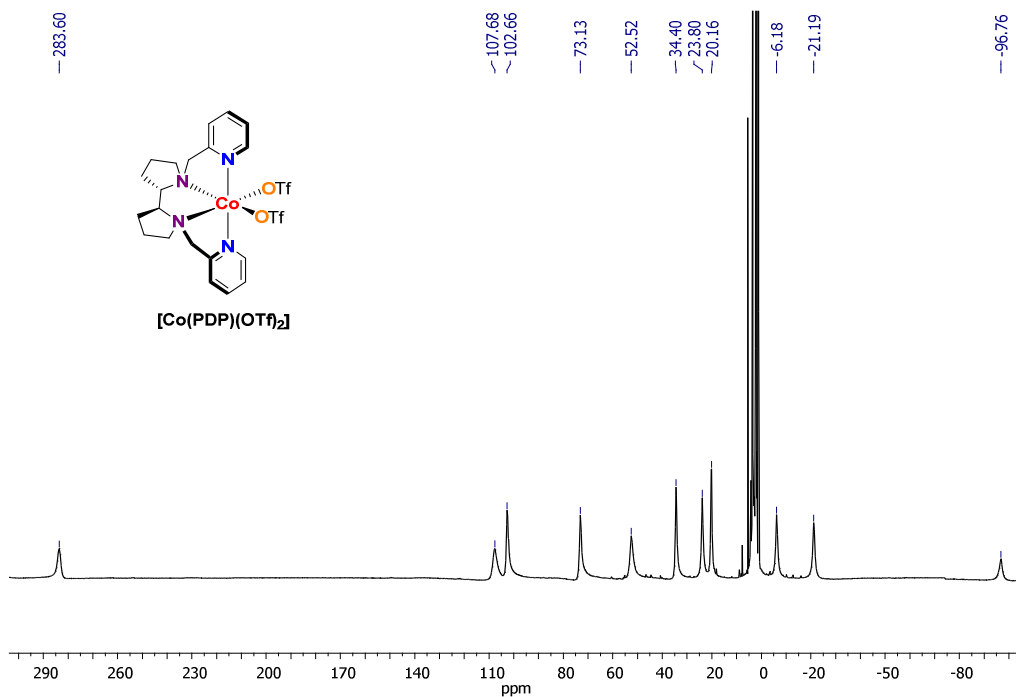


Figure A. 4. 3. $^1\text{H-NMR}$ (CD_3CN , 400 MHz, 260 K) spectrum of $[\text{Co}(\text{OTf})_2((S,S)\text{-PDP})]$.

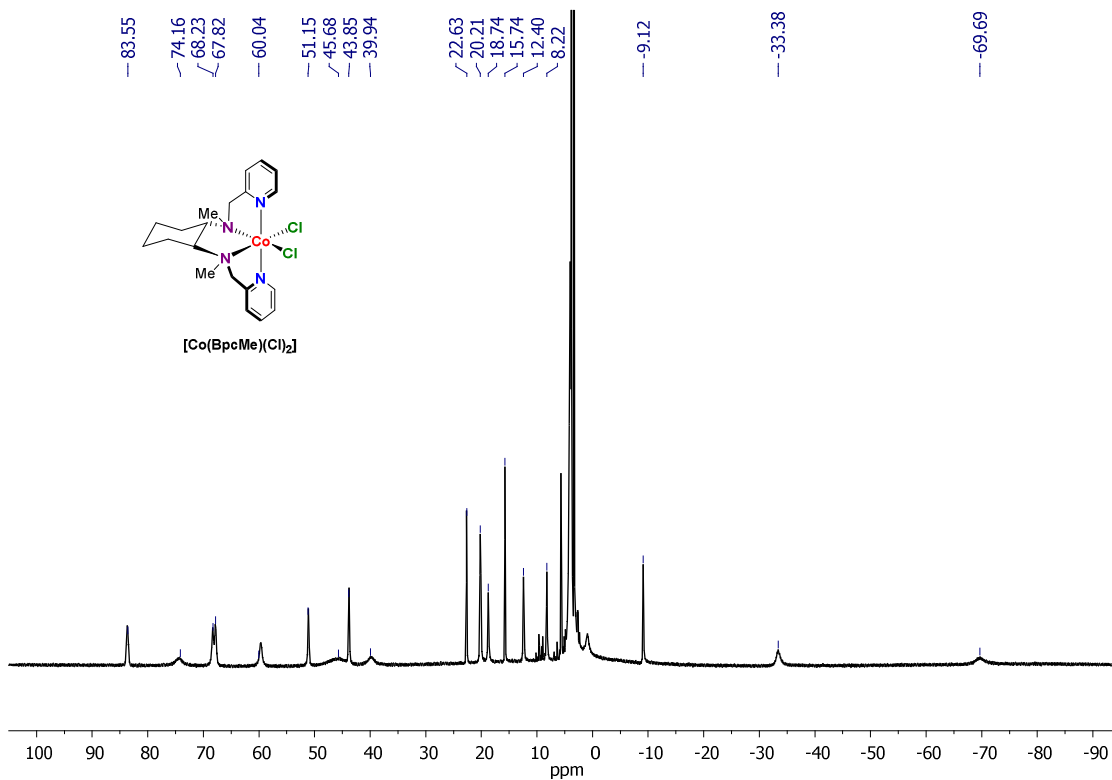


Figure A. 4. 4. $^1\text{H-NMR}$ (CD_3CN , 500 MHz, 260 K) spectrum of $[\text{Co}(\text{Cl})_2(\text{BpcMe})]$.

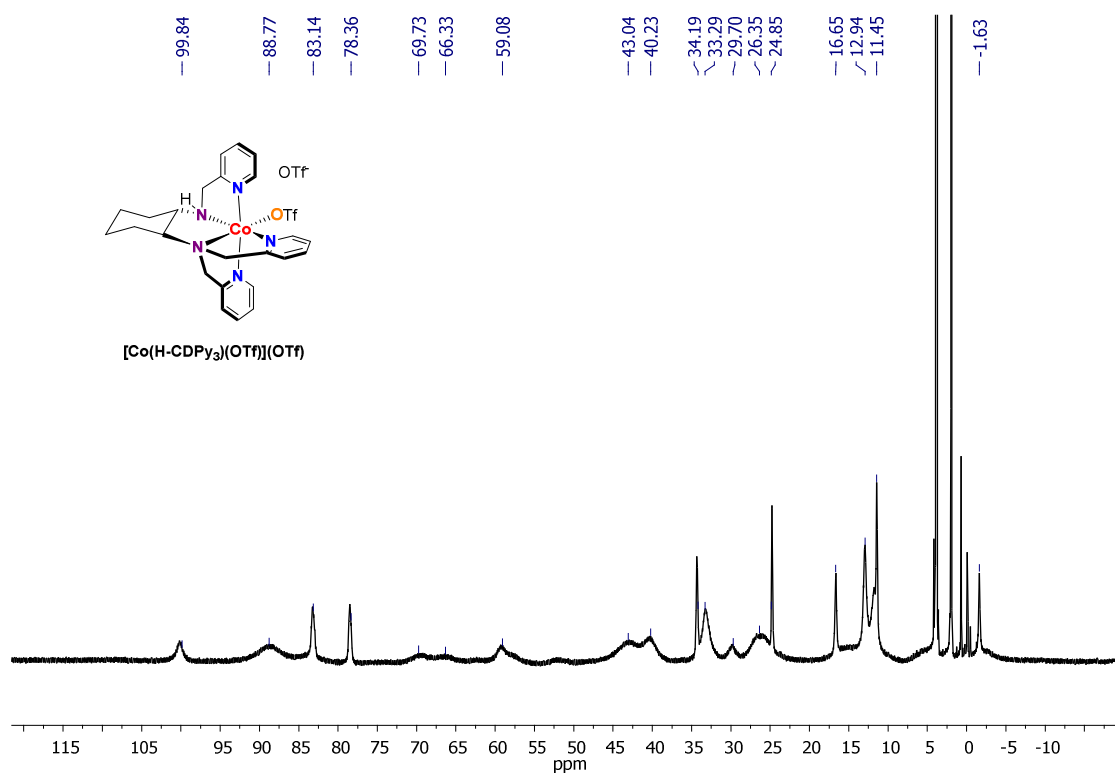


Figure A. 4. 5. $^1\text{H-NMR}$ (CD_3CN , 500 MHz, 260 K) spectrum of $[\text{Co}(\text{OTf})(\text{H-CDPy}_3)](\text{OTf})$.

A.4.2. Catalytic Studies Using PS_{Cu} as Photoredox Catalyst

A.4.2.1. Optimization of the solvent mixture

Acetophenone (**9a**) was used as a model substrate for the optimization of the catalytic conditions when using PS_{Cu} as chromophore.

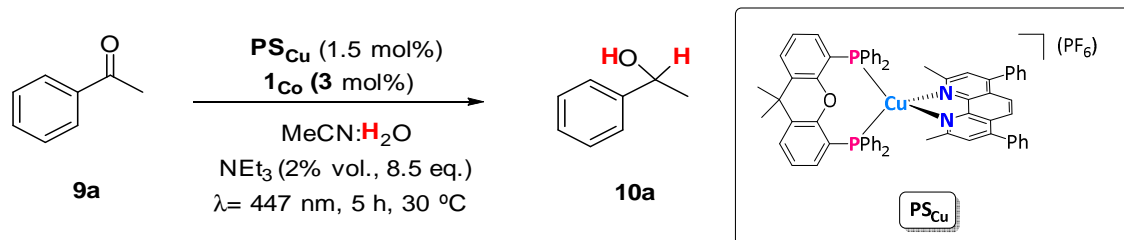


Table A. 4. 1. Photocatalytic reduction of **9a** with PS_{Cu} at different ratios of MeCN:H₂O.

Entry	Solvent mixture (MeCN:H ₂ O)	Subs (%)	Yield 10a (%)
1	2:8	93	<1
2	3:7	5	93
3	3.5:6.5	0	90
4	4:6	0	92
5	4.5:5.5	0	92
6	5:5	5	92
7	6:4	28	63
8	7:3	52	38

Optimization of the solvent mixture. Reaction conditions: [**9a**] (0.168 mmol, 16.5 mM), $\mathbf{1}_{\text{Co}}$ (5 μmol , 3 mol%), PS_{Cu} (2.5 μmol , 1.5 mol%), 0.2 mL Et₃N (8.5 eq.) irradiating at $\lambda = 447 \text{ nm}$ for 5 h at 30 °C under N₂. Total volume mixture: 10 mL. The amount of the starting material **9a** and the yields of **10a** were determined by GC after the reaction workup relative to the calibrated internal standard. Sub = substrate unreacted. $\text{PS}_{\text{Cu}} = [\text{Cu}(\text{bathocuproine})(\text{Xantphos})]\text{PF}_6$.

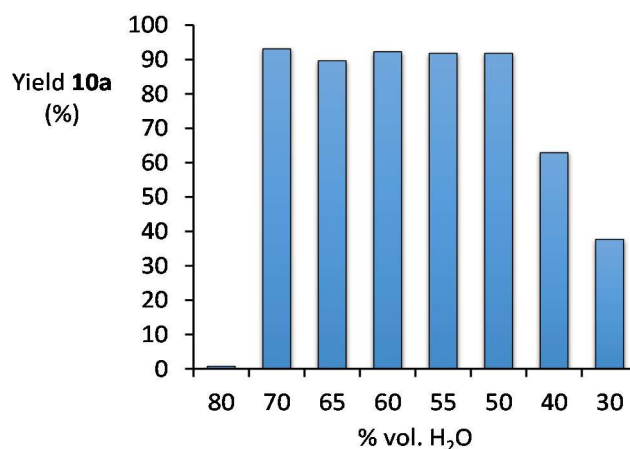


Figure A. 4. 6. Photocatalytic reduction of **9a** into **10a** with PS_{Cu} at different ratios of MeCN:H₂O.

A.4.2.2. Optimization of the PS_{Cu} loading

Acetophenone (**9a**) was used as a model substrate for the optimization of the catalytic conditions when using PS_{Cu} as chromophore.

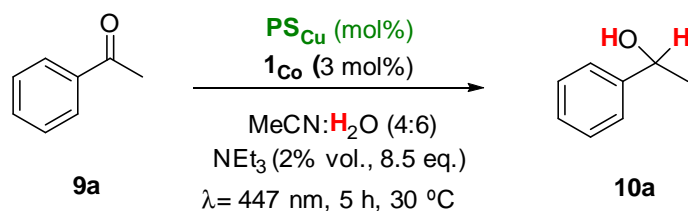


Table A. 4. 2. Photocatalytic reduction of **9a** using different PS_{Cu} loadings.

Entry	PS _{Cu} (%mol)	Subs (%)	Yield 10a (%)
1	0	90	0
2	0.3	70	20
3	0.6	53	36
4	0.9	28	62
5	1.2	0	92
6	1.5	0	92
7	1.8	0	93
8	2.1	0	92
9	2.4	0	91

Optimization of the PS_{Cu} loading. Reaction conditions: [**9a**] (0.168 mmol, 16.5 mM), **1_{Co}** (5 μmol, 3 mol%), PS_{Cu} (0-2.4 mol%), 0.2 mL Et₃N (8.5 eq.) irradiating at λ = 447 nm for 5 h at 30 °C under N₂. Total volume mixture: 10 mL. The amount of the starting material **9a** and the yields of **10a** were determined by GC after the reaction workup relative to the calibrated internal standard. Sub = substrate unreacted.

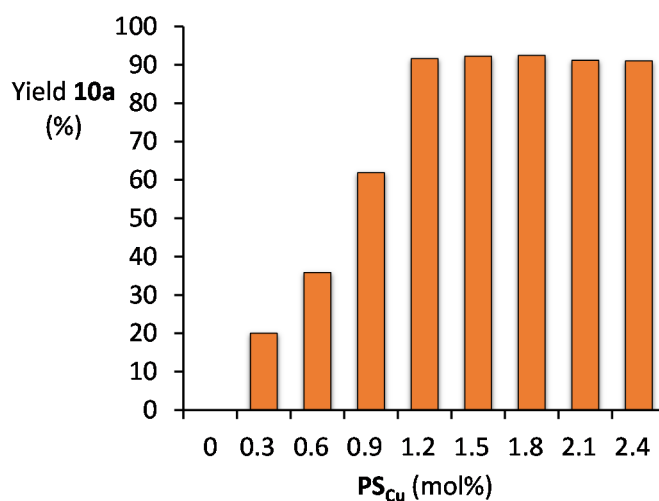


Figure A. 4. 7. Photocatalytic reduction of **9a** into **10a** with PS_{Cu} at different ratios of MeCN:H₂O.

A.4.2.3. Optimization of the cobalt catalyst 1_{Co} loading.

Acetophenone (**9a**) was used as a model substrate for the optimization of the catalytic conditions when using PS_{Cu} as chromophore.

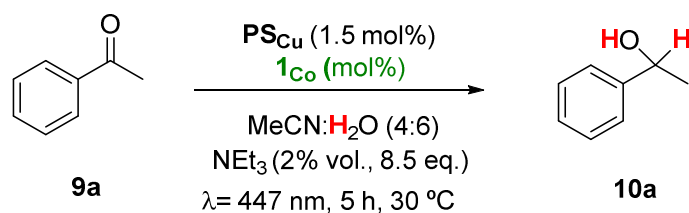


Table A. 4. 3. Photocatalytic reduction of **9a** using different 1_{Co} loadings.

Entry	1_{Co} (mol%)	Sub (%)	Yield 10a (%)	TON _{cat}
1	5	0	93	18
2	4	0	92	22
3	3.5	0	92	27
4	3	0	91	31
5	2.5	0	92	36
6	2	0	93	44
7	1	0	92	88
8	0.5	0	91	173
9	0.25	0	90	353
10	0.1	44	45	449
11	0.05	54	35	700
12	0.03	67	23	900
13	0.01	80	11	1100
14	0.005	85	7	1400
15	0	92	n.d.	-

Optimization of the 1_{Co} loading. Reaction conditions: [**9a**] (0.168 mmol, 16.5 mM), PS_{Cu} (2.5 μ mol, 1.5 mol%), 1_{Co} (0.005-5 mol%), 0.2 mL Et₃N (8.5 eq.) irradiating at $\lambda = 447 \text{ nm}$ for 5 h at 30 $^\circ\text{C}$ under N₂. Total volume mixture: 10 mL. The amount of the starting material **9a** and the yields of **10a** were determined by GC after the reaction workup relative to the calibrated internal standard. Sub = substrate unreacted. TON_{cat} = mol **10a** / mol 1_{Co} .

A.4.3. NMR Spectra of the deuterated alcohols

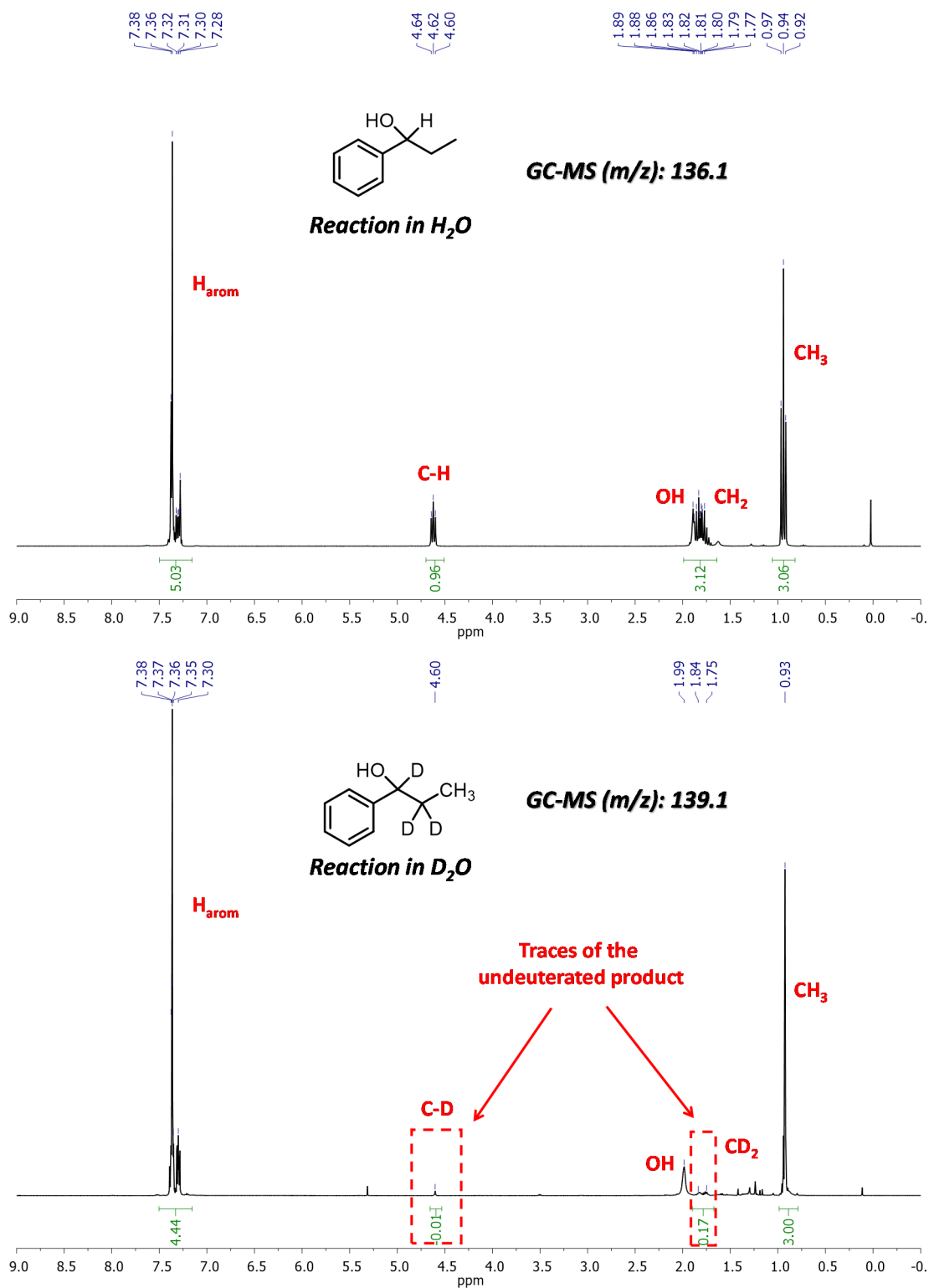


Figure A. 4. 8. ¹H-NMR spectrum (CDCl₃, 400 MHz, 300 K) of the isolated product **10b** using H₂O (Top) or D₂O (99.9 % in deuterium) (Bottom) in the solvent mixture. Conditions: **1c_o** (3.8 μmol, 3 mol%), **PS_{ir}** (2.5 μmol, 2 mol%), substrate (0.126 mmol, 12.4 mM) in MeCN:H₂O(or D₂O):Et₃N (3:7:0.2 mL) irradiated at λ= 447 nm and 30 °C, under N₂.

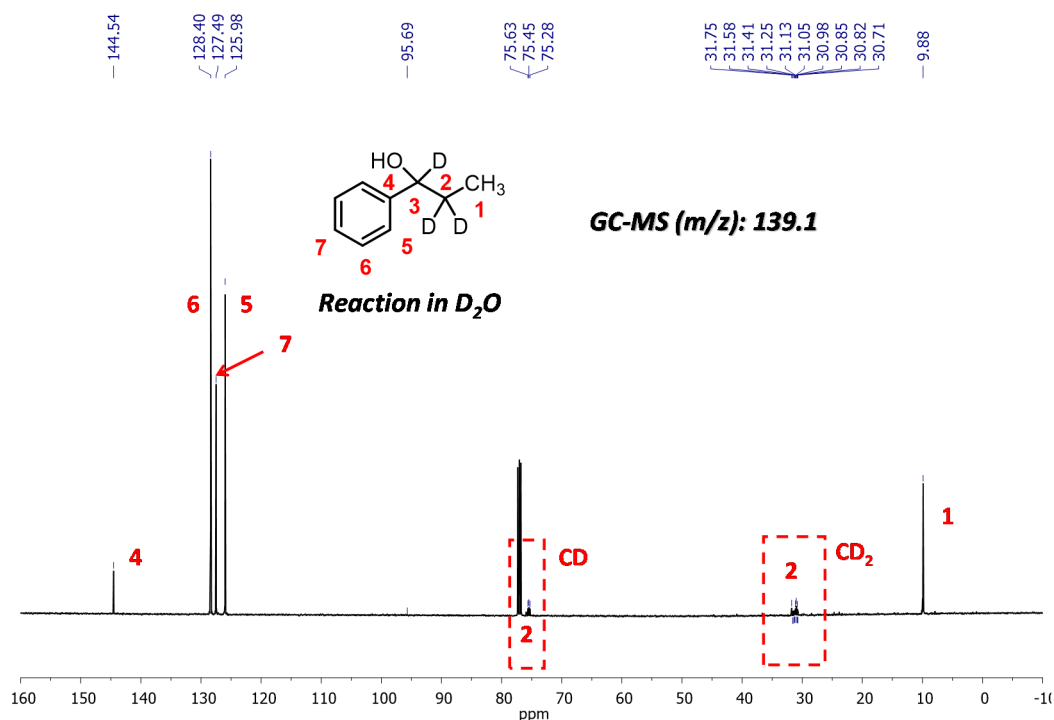
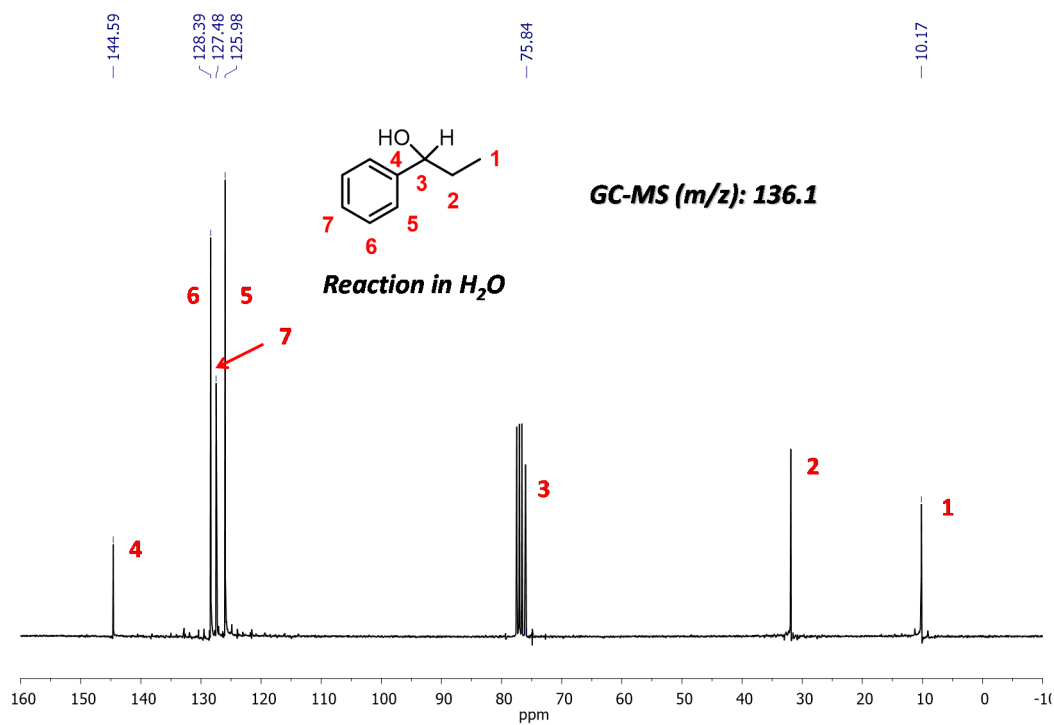


Figure A. 4. 9. ¹³C-NMR spectrum (CDCl₃, 101 MHz, 300 K) of the isolated product **10b** using H₂O (Top) or D₂O (99.9 % in deuterium) (Bottom) in the solvent mixture. Conditions: **1c_o** (3.8 μmol, 3 mol%), **PS_r** (2.5 μmol, 2 mol%), substrate (0.126 mmol, 12.4 mM) in MeCN:H₂O(or D₂O):Et₃N (3:7:0.2 mL) irradiated at λ= 447 nm and 30 °C, under N₂.

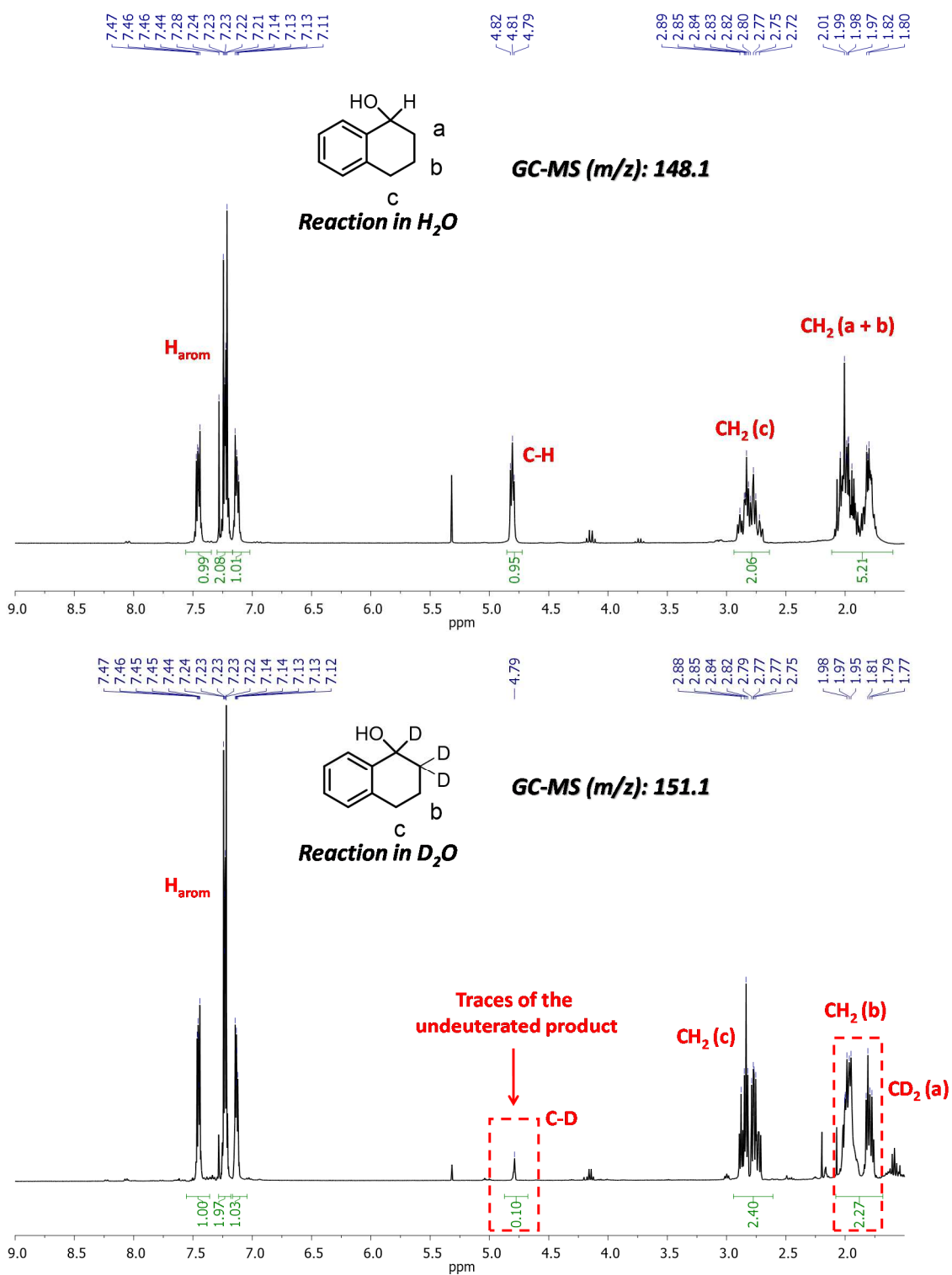


Figure A. 4. 10. ¹H-NMR spectrum (CDCl₃, 400 MHz, 300 K) of the isolated product **10g** using H₂O (Top) or D₂O (99.9 % in deuterium) (Bottom) in the solvent mixture. Conditions: **1c_o** (3.8 μmol, 3 mol%), **PS_{Ir}** (2.5 μmol, 2 mol%), substrate (0.126 mmol, 12.4 mM) in MeCN:H₂O(or D₂O):Et₃N (3:7:0.2 mL) irradiated at λ= 447 nm and 30 °C, under N₂.

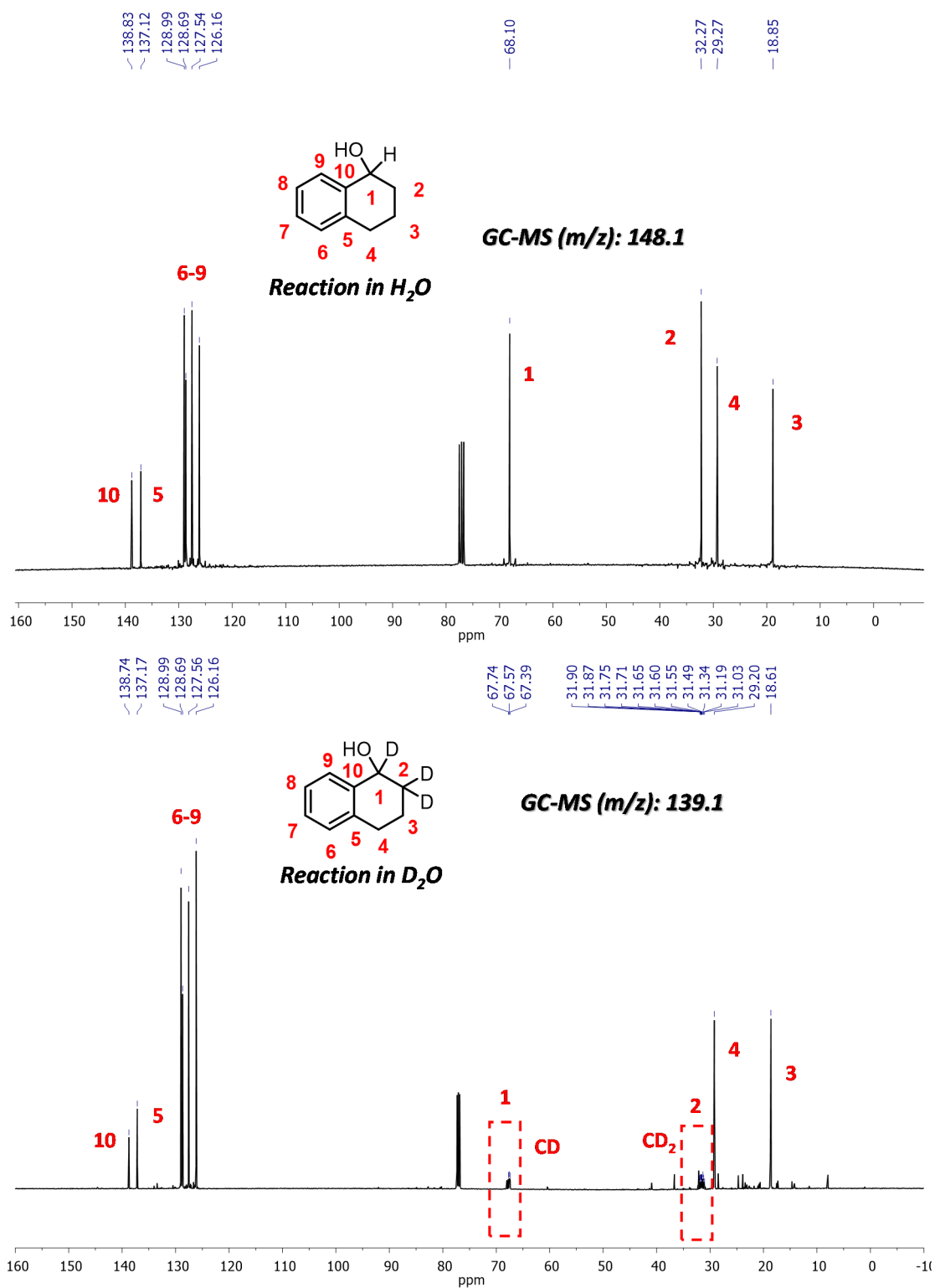


Figure A. 4. 11. ¹H-NMR spectrum (CDCl₃, 400 MHz, 300 K) of the isolated product **10g** using H₂O (Top) or D₂O (99.9 % in deuterium) (Bottom) in the solvent mixture. Conditions: **1c_o** (3.8 μmol, 3 mol%), **PS_{ir}** (2.5 μmol, 2 mol%), substrate (0.126 mmol, 12.4 mM) in MeCN:H₂O(or D₂O):Et₃N (3:7:0.2 mL) irradiated at λ= 447 nm and 30 °C, under N₂.

A.4.4. NMR Spectra of the isolated alcohols 10ah, 10ai and 10aj.

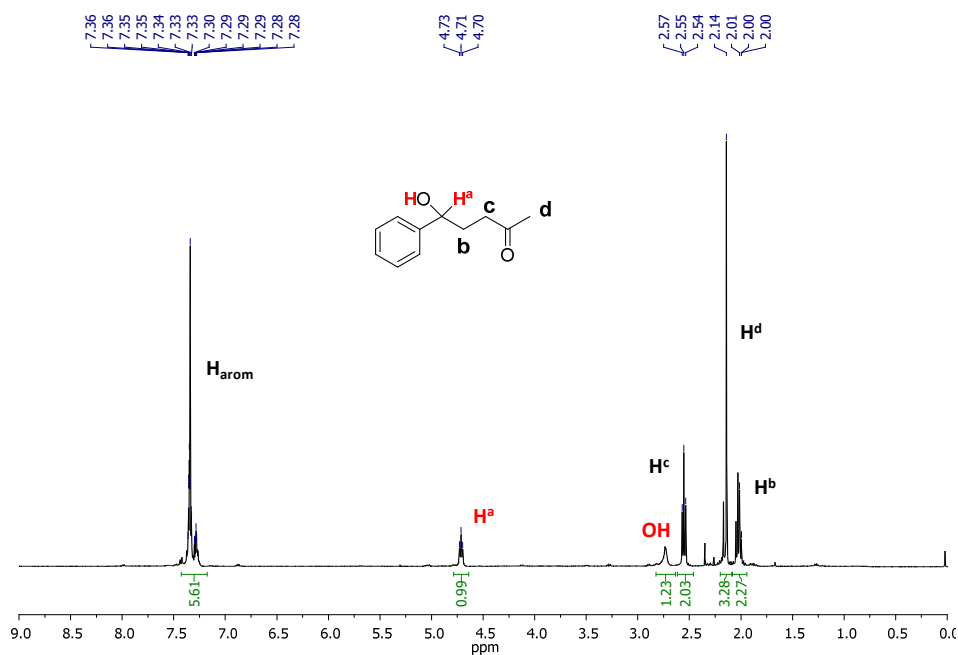


Figure A. 4. 12. $^1\text{H-NMR}$ (CDCl_3 , 400 MHz, 300 K) spectrum of the isolated product **5-Hydroxy-5-phenylpentan-2-one**.

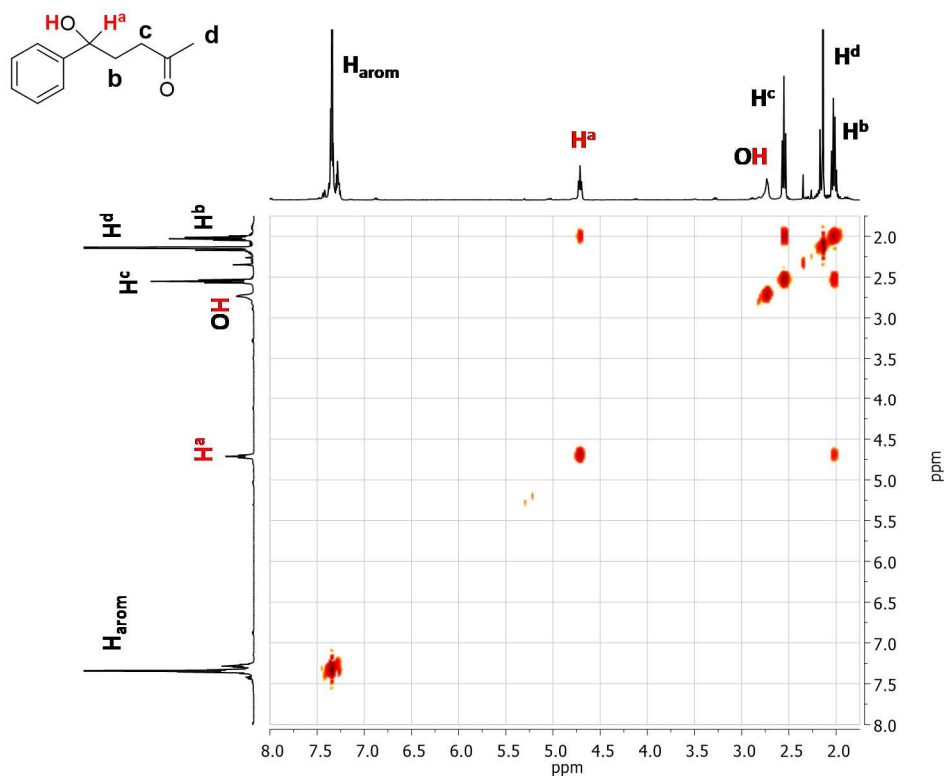


Figure A. 4. 13. $^1\text{H-}^1\text{H COSY}$ (CDCl_3 , 400 MHz, 300 K) spectrum of the isolated product **5-Hydroxy-5-phenylpentan-2-one**.

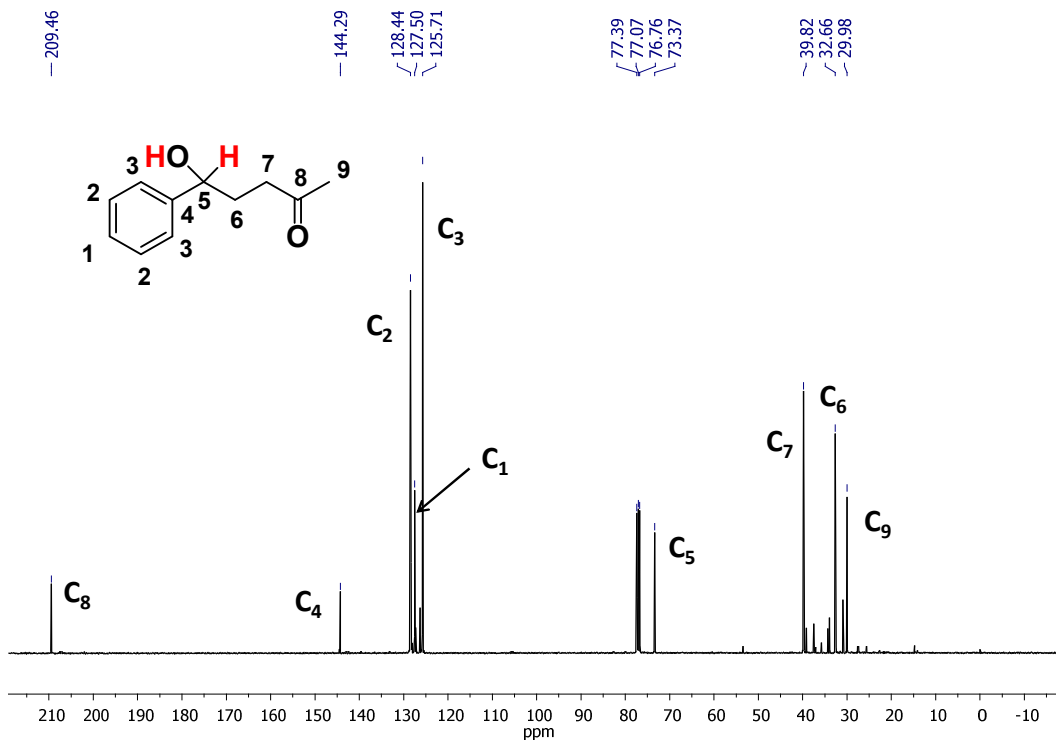


Figure A. 4. 14. $^{13}\text{C}\{^1\text{H}\}$ -NMR (CDCl_3 , 101 MHz, 300 K) spectrum of the isolated product 5-Hydroxy-5-phenylpentan-2-one.

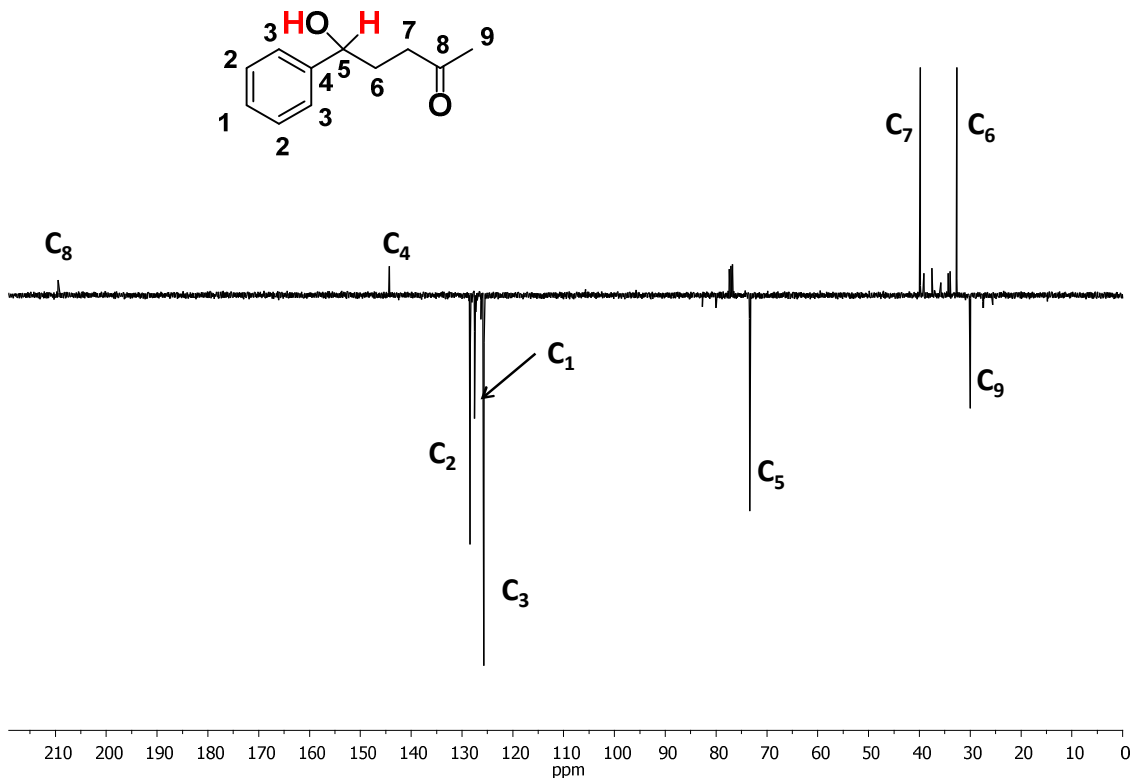


Figure A. 4. 15. DEPTQ135 (CDCl_3 , 400 MHz, 300 K) spectrum of the isolated product 5-Hydroxy-5-phenylpentan-2-one.

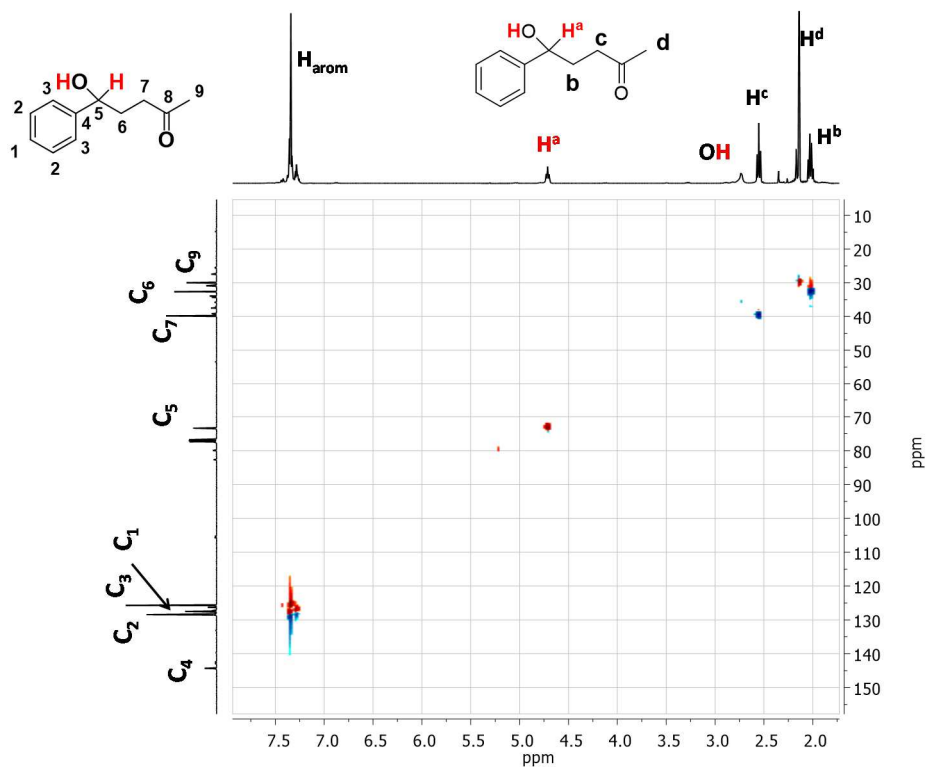


Figure A. 4. 16. ^1H - ^{13}C HSQC (CDCl_3 , 400 MHz, 300 K) phase sensitive spectrum of the isolated product **5-Hydroxy-5-phenylpentan-2-one**.

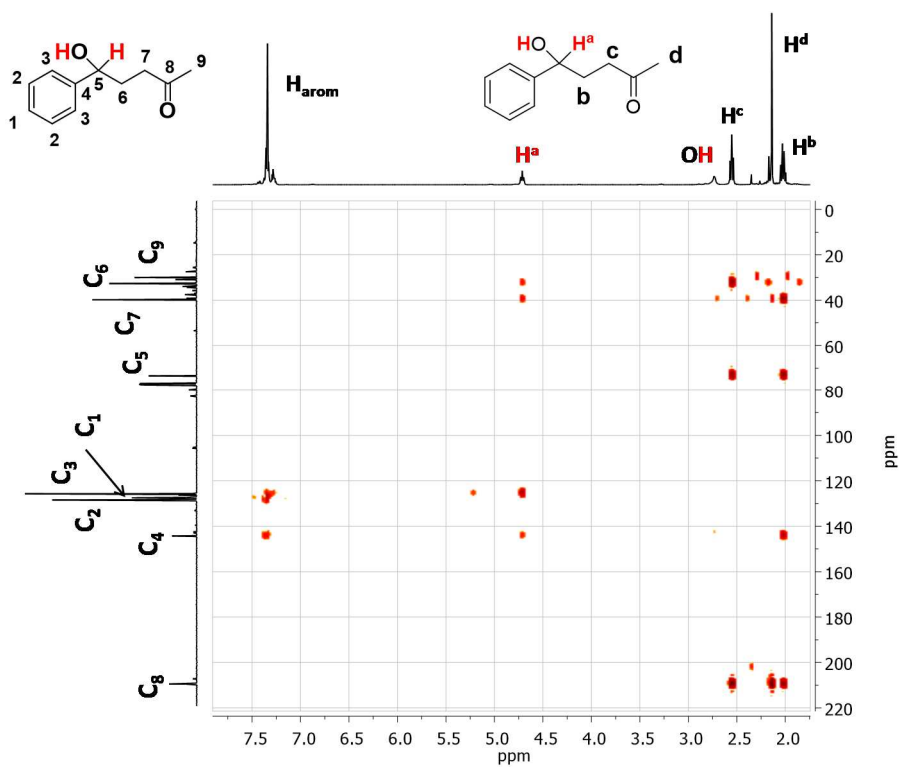


Figure A. 4. 17. ^1H - ^{13}C HMBC (CDCl_3 , 400 MHz, 300 K) phase sensitive spectrum of the isolated product **5-Hydroxy-5-phenylpentan-2-one**.

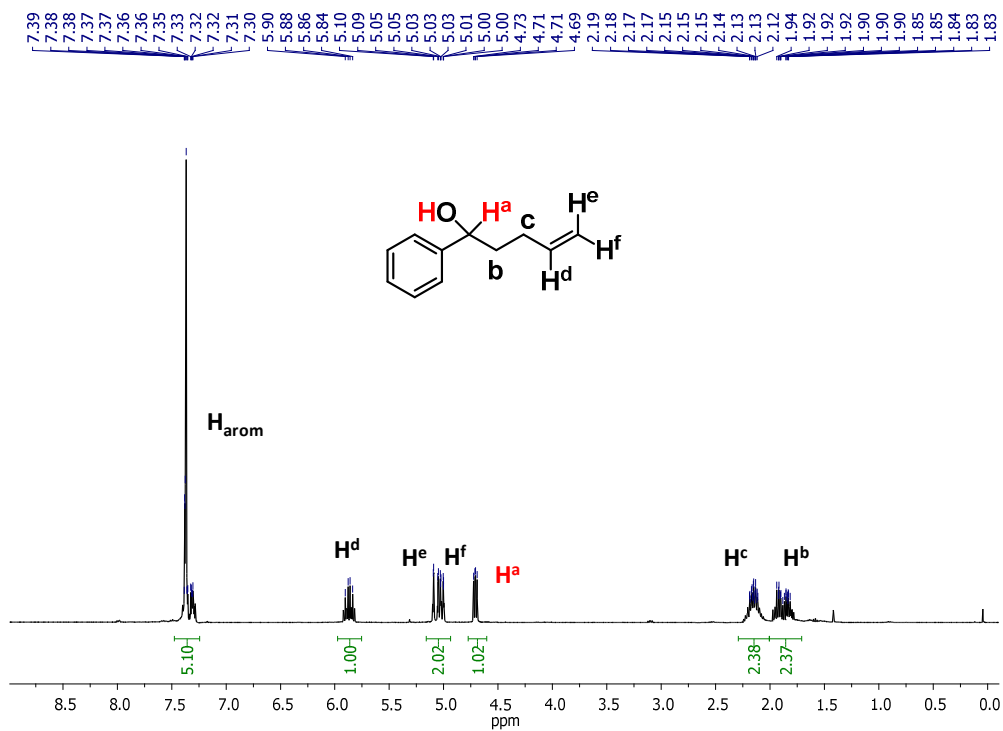


Figure A. 4. 18. $^1\text{H-NMR}$ (CDCl_3 , 400 MHz, 300 K) spectrum of the isolated product **1-Phenyl-4-penten-1-ol**.

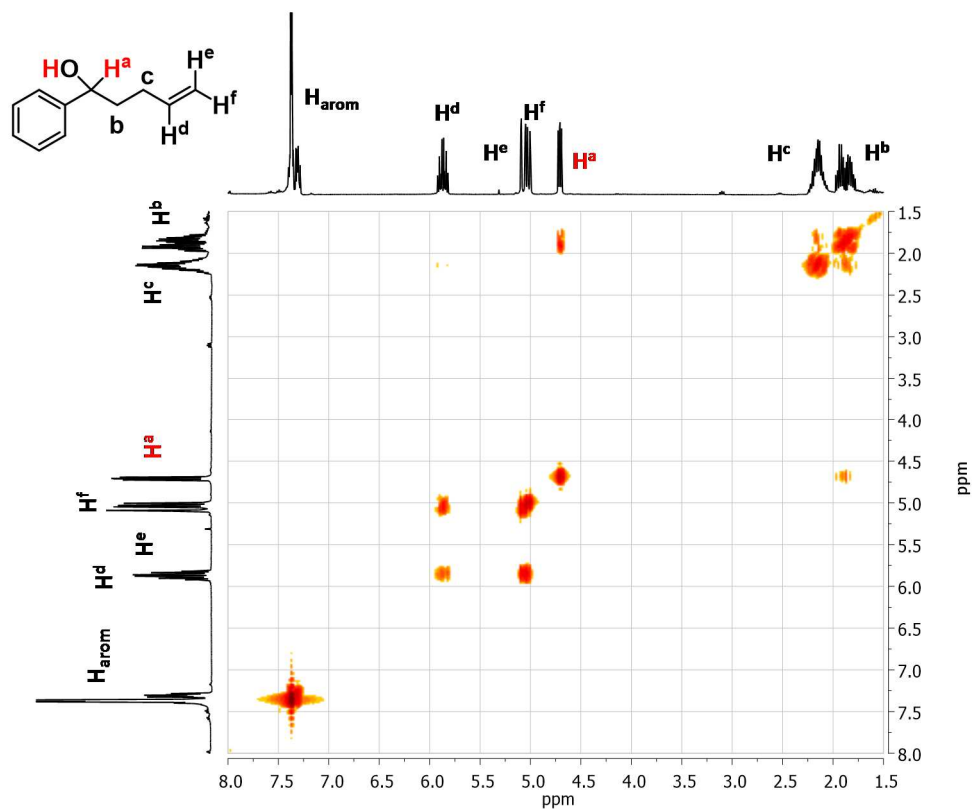


Figure A. 4. 19. $^1\text{H-}^1\text{H}$ COSY (CDCl_3 , 400 MHz, 300 K) spectrum of the isolated product **1-Phenyl-4-penten-1-ol**.

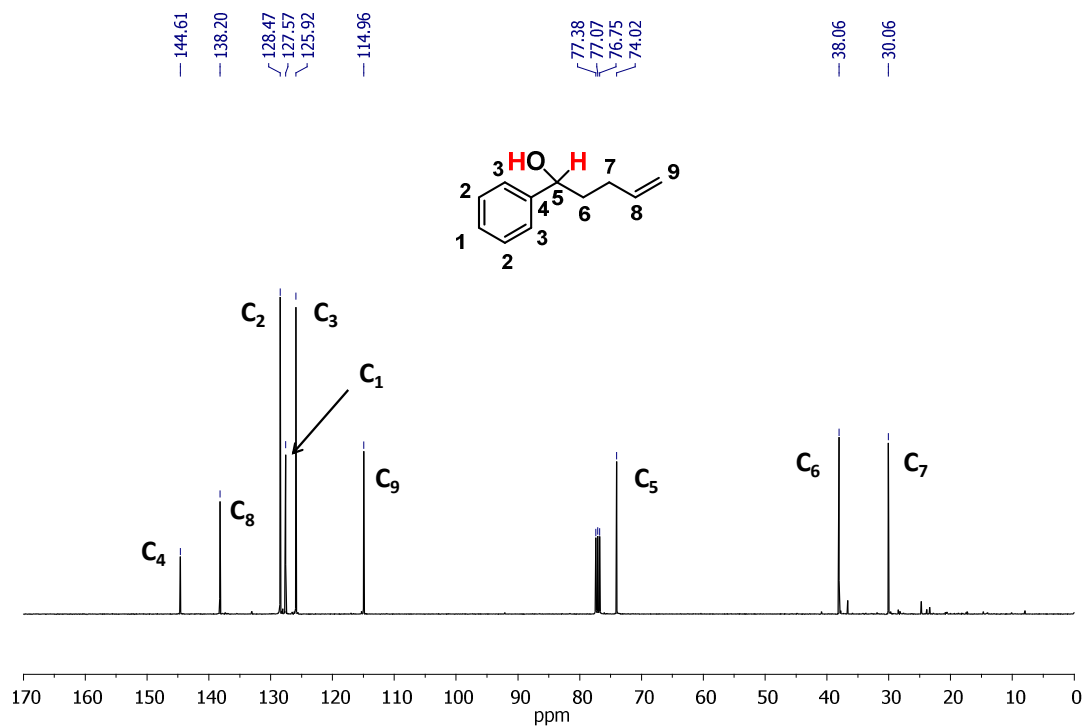


Figure A. 4. 20. $^{13}\text{C}\{^1\text{H}\}$ -NMR (CDCl_3 , 101 MHz, 300 K) spectrum of the isolated product **1-Phenyl-4-penten-1-ol**.

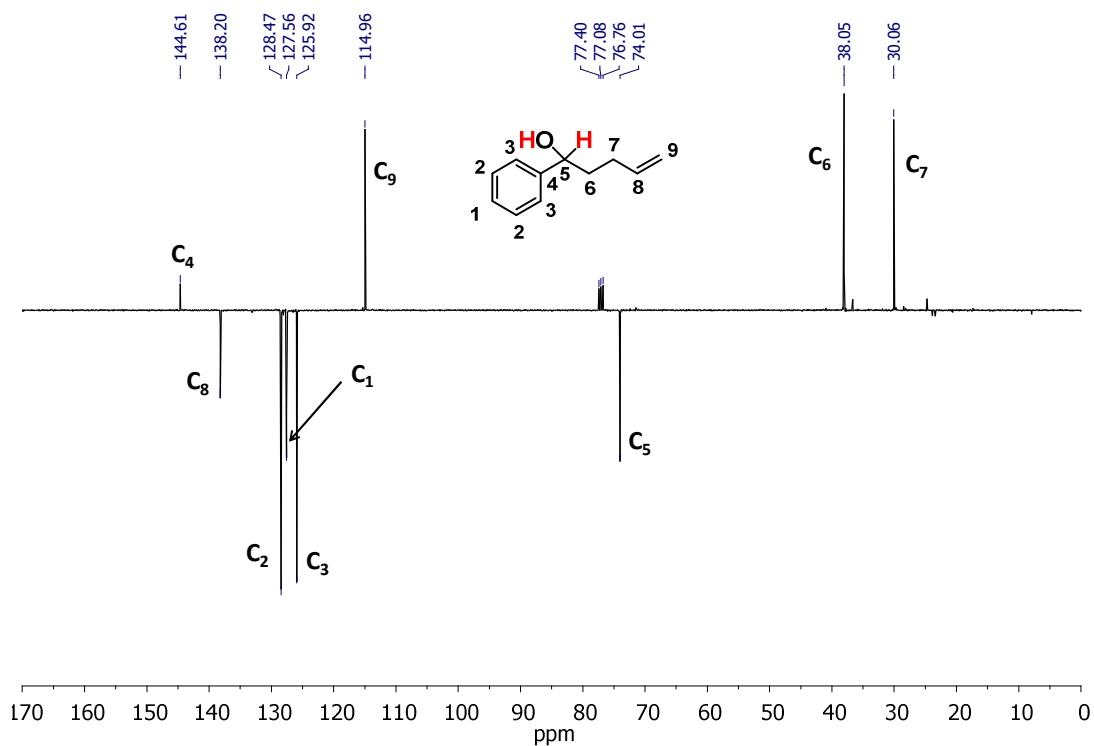


Figure A. 4. 21. DEPTQ135 (CDCl_3 , 400 MHz, 300 K) spectrum of the isolated product **1-Phenyl-4-penten-1-ol**.

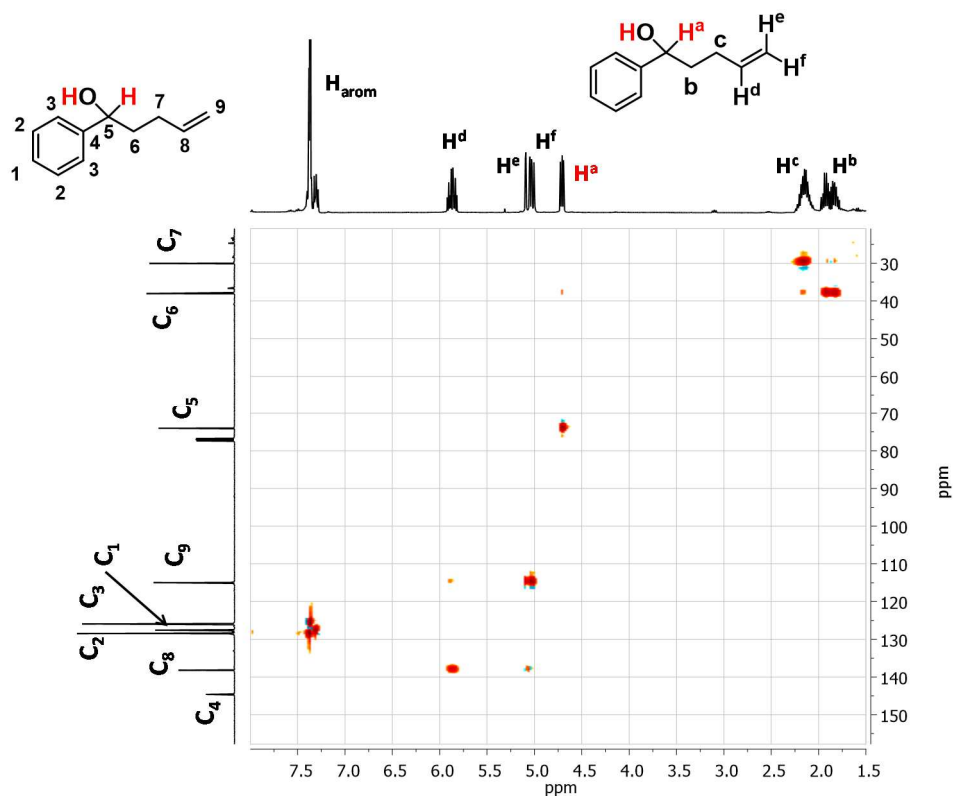


Figure A. 4. 22. ^1H - ^{13}C HSQC (CDCl_3 , 400 MHz, 300 K) phase sensitive spectrum of the isolated product **1-Phenyl-4-penten-1-ol**.

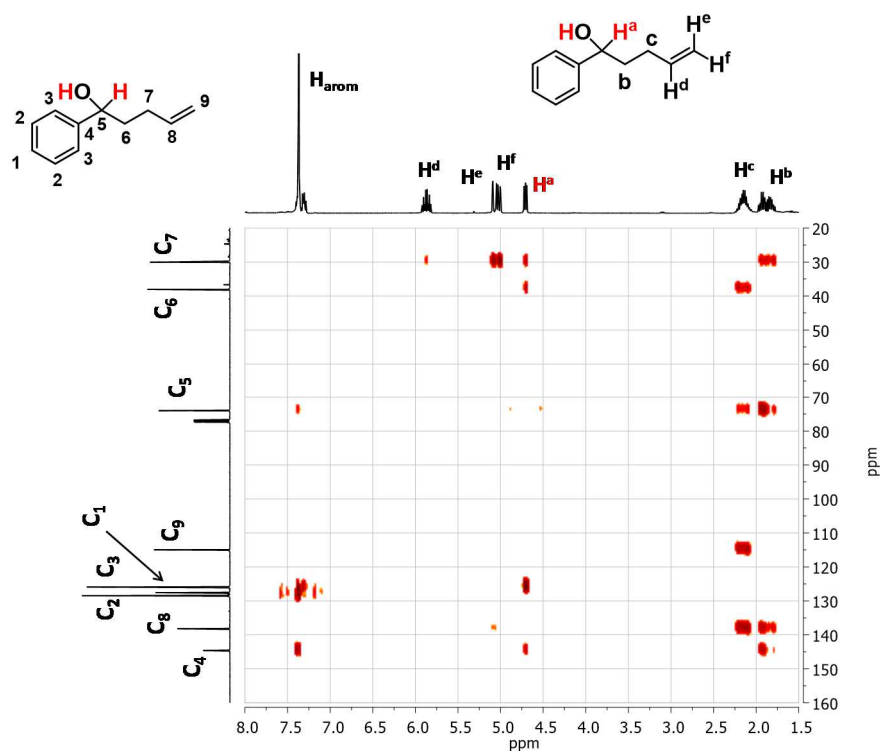


Figure A. 4. 23. ^1H - ^{13}C HMBC (CDCl_3 , 400 MHz, 300 K) phase sensitive spectrum of the isolated product **1-Phenyl-4-penten-1-ol**.

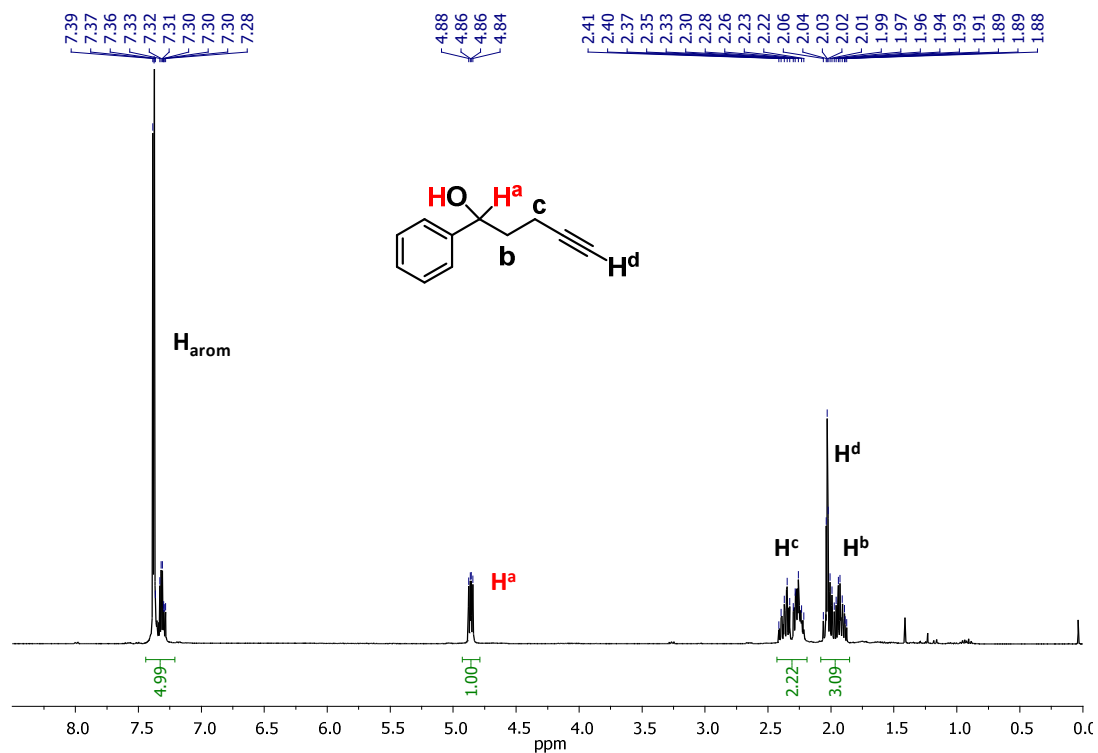


Figure A. 4. 24. $^1\text{H-NMR}$ (CDCl_3 , 400 MHz, 300 K) spectrum of the isolated product **1-Phenyl-4-pentyn-1-ol**.

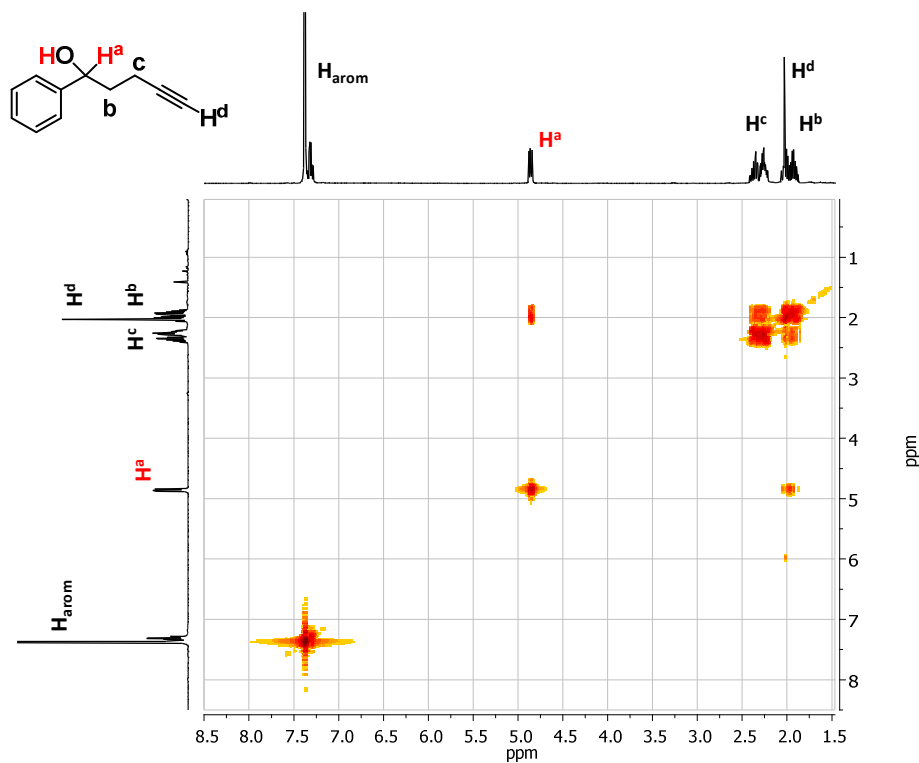


Figure A. 4. 25. $^1\text{H-}^1\text{H COSY}$ (CDCl_3 , 400 MHz, 300 K) spectrum of the isolated product **1-Phenyl-4-pentyn-1-ol**.

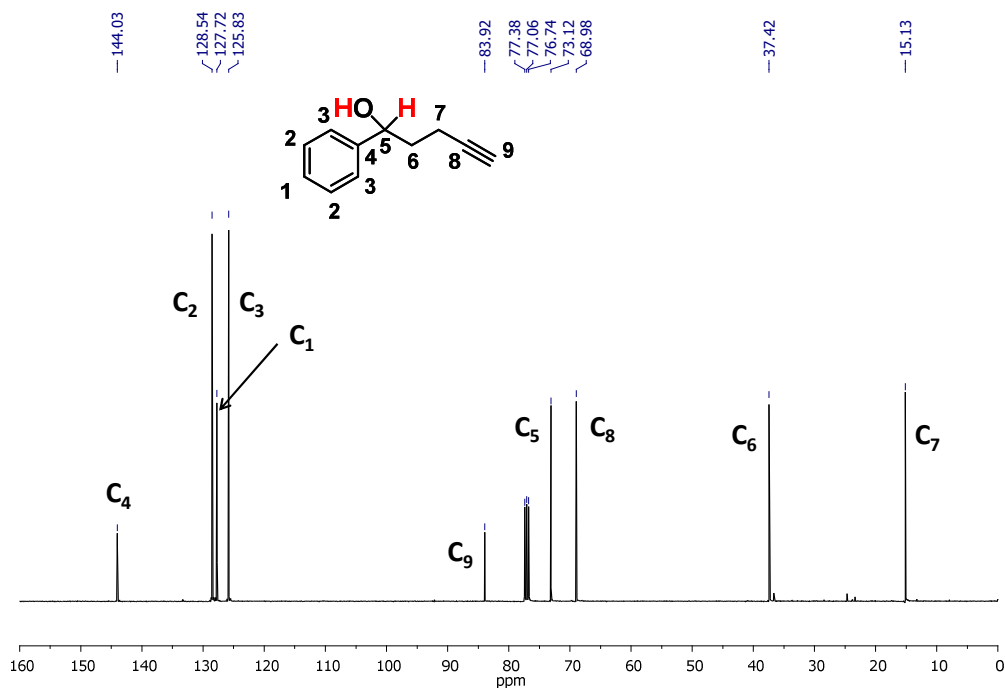


Figure A. 4. 26. $^{13}\text{C}\{^1\text{H}\}$ -NMR (CDCl_3 , 101 MHz, 300 K) spectrum of the isolated product **1-Phenyl-4-pentyn-1-ol**.

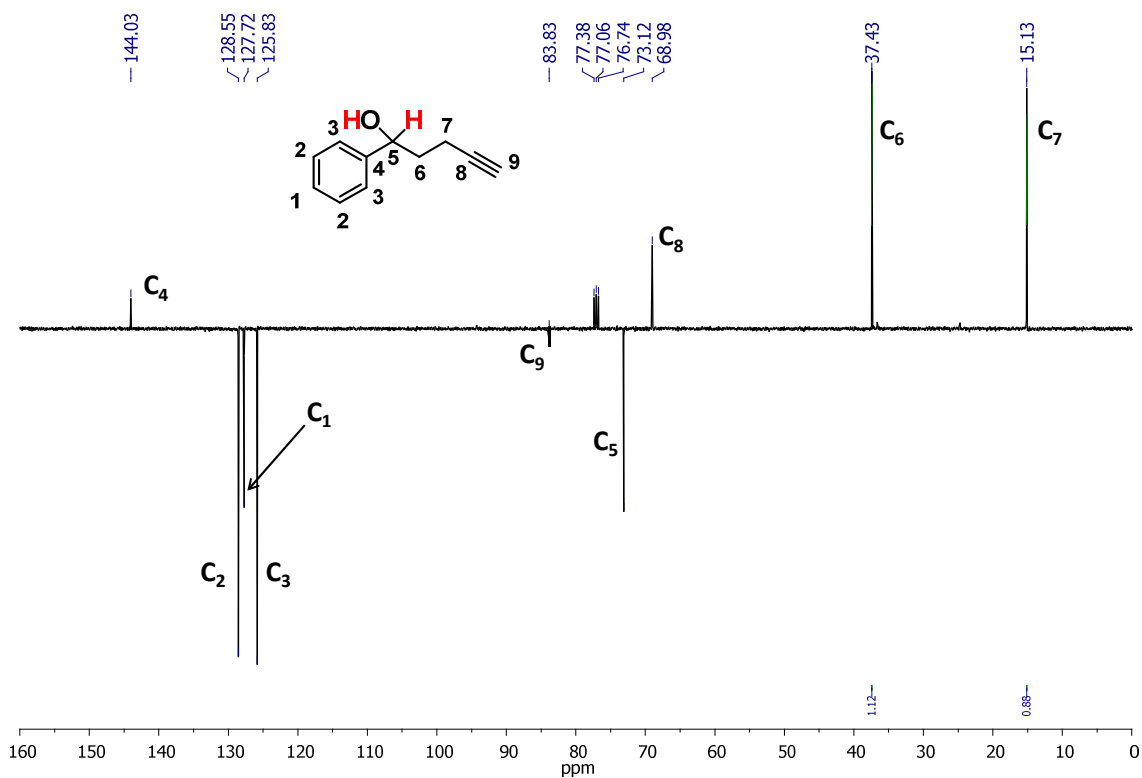


Figure A. 4. 27. DEPTQ135 (CDCl_3 , 400 MHz, 300 K) spectrum of the isolated product **1-Phenyl-4-pentyn-1-ol**.

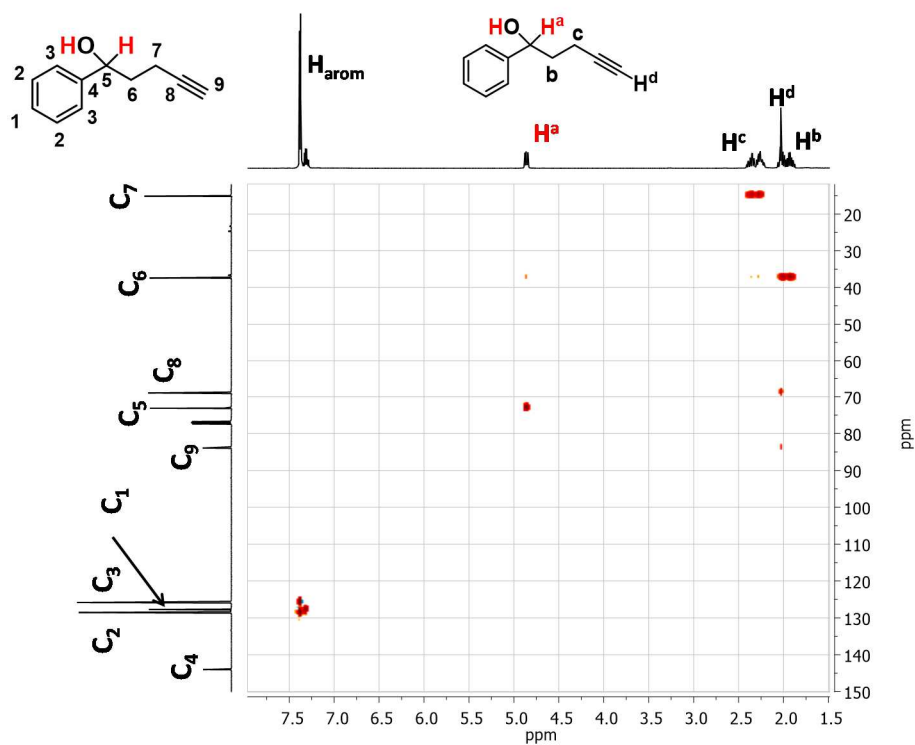


Figure A. 4. 28. ^1H - ^{13}C HSQC (CDCl_3 , 400 MHz, 300 K) phase sensitive spectrum of the isolated product 1-Phenyl-4-pentyn-1-ol.

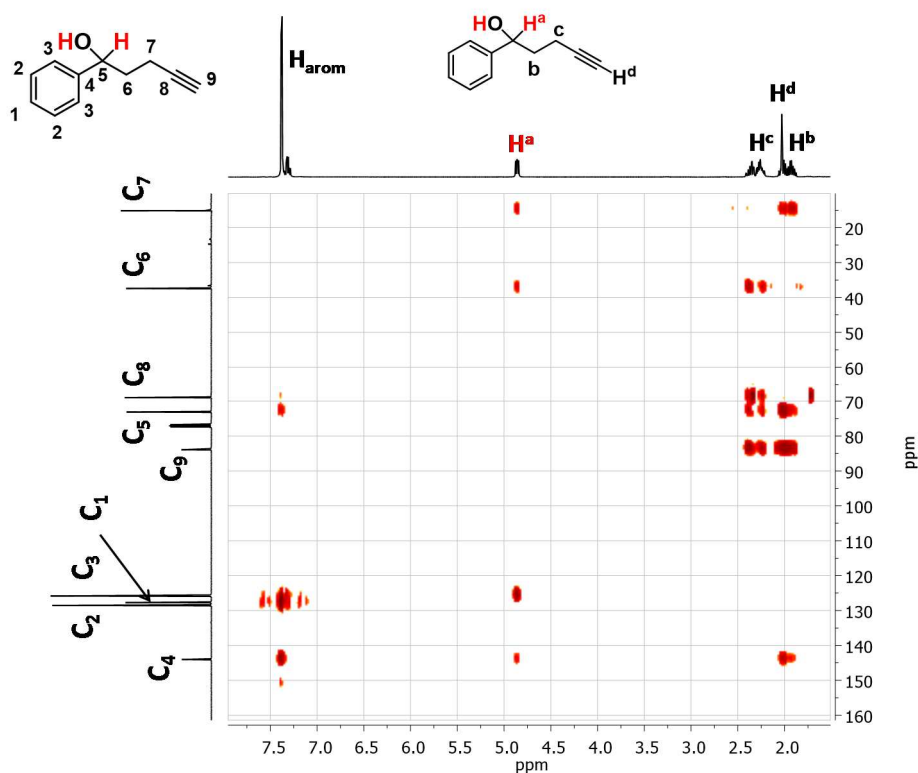
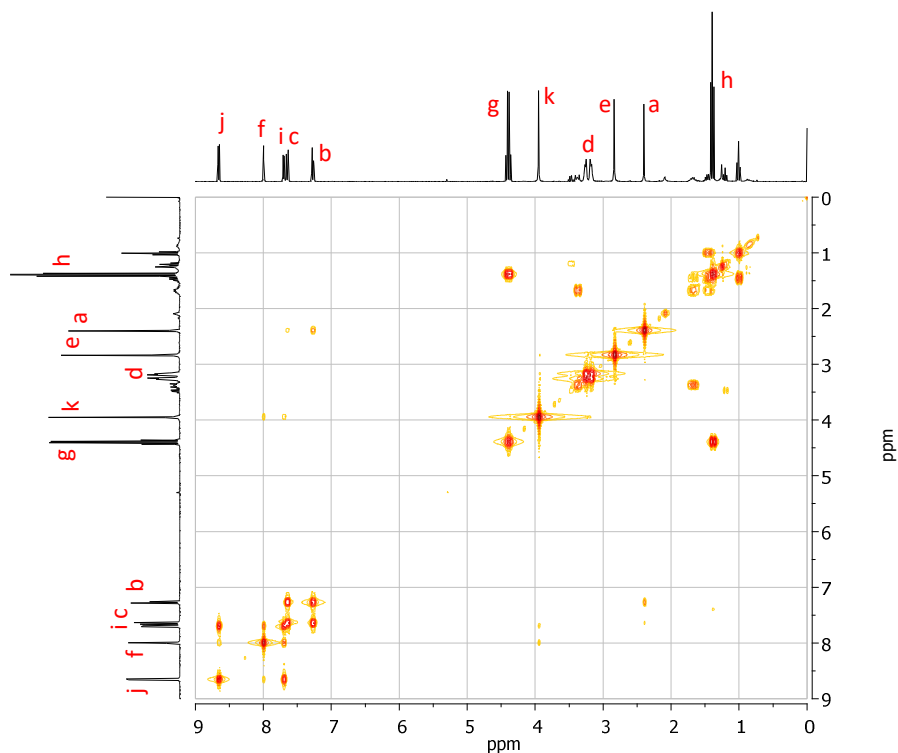
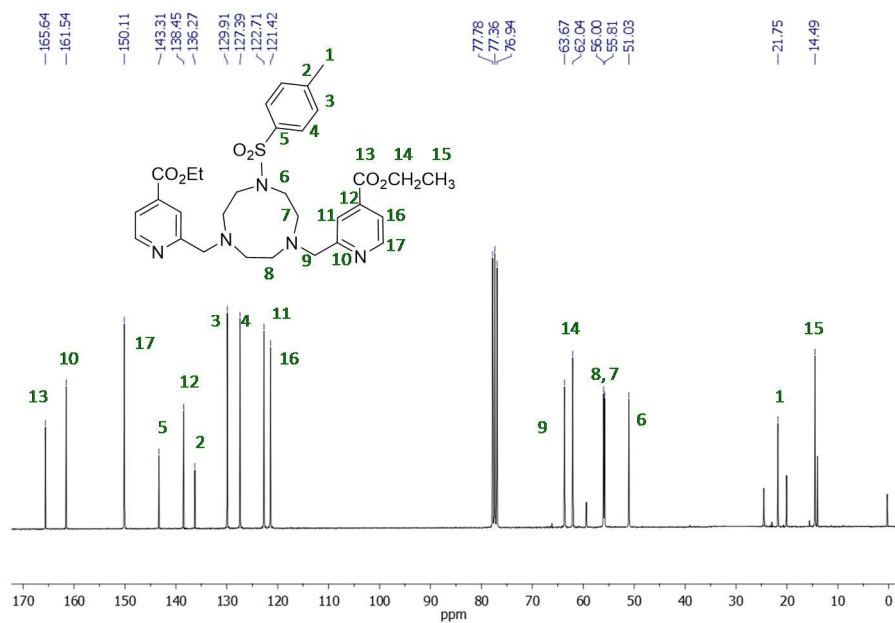


Figure A. 4. 29. ^1H - ^{13}C HMBC (CDCl_3 , 400 MHz, 300 K) phase sensitive spectrum of the isolated product 1-Phenyl-4-pentyn-1-ol.

A.5. ANNEX CHAPTER VIII

A.5.1. NMR spectra

A.5.1.1. NMR spectra of the ligands $^{H,CO_2Et}Py_2^{Ts}taccn$ and $^{Me,OMe}Py_2^{Ts}taccn$ Figure A. 5. 1. 1H - 1H COSY ($CDCl_3$, 400 MHz, 300 K) spectrum of $^{H,CO_2Et}Py_2^{Ts}taccn$.Figure A. 5. 2. $^{13}C\{^1H\}$ -NMR ($CDCl_3$, 101 MHz, 300 K) spectrum of $^{Me,OMe}Py_2^{Ts}taccn$.

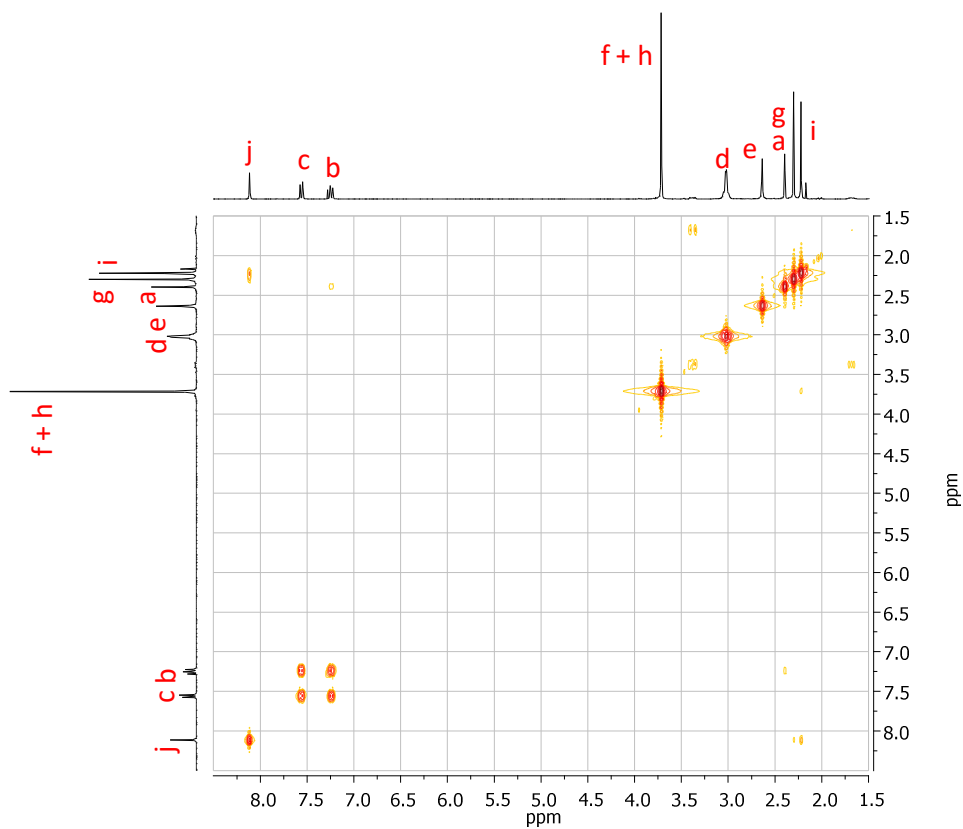


Figure A. 5. 3. ^1H - ^1H COSY (CDCl_3 , 400 MHz, 300 K) spectrum of $\text{Me,OMe-Py}_2\text{-Ts-tacn}$.

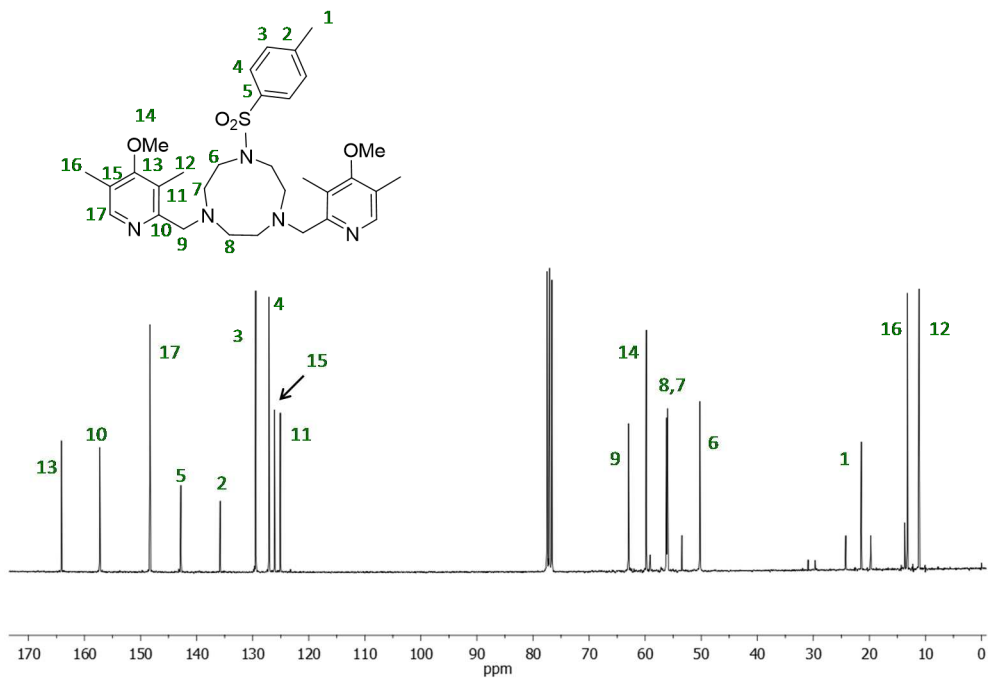


Figure A. 5. 4. $^{13}\text{C}\{^1\text{H}\}$ NMR (CDCl_3 , 101 MHz, 300 K) spectrum of $\text{Me,OMe-Py}_2\text{-Ts-tacn}$.

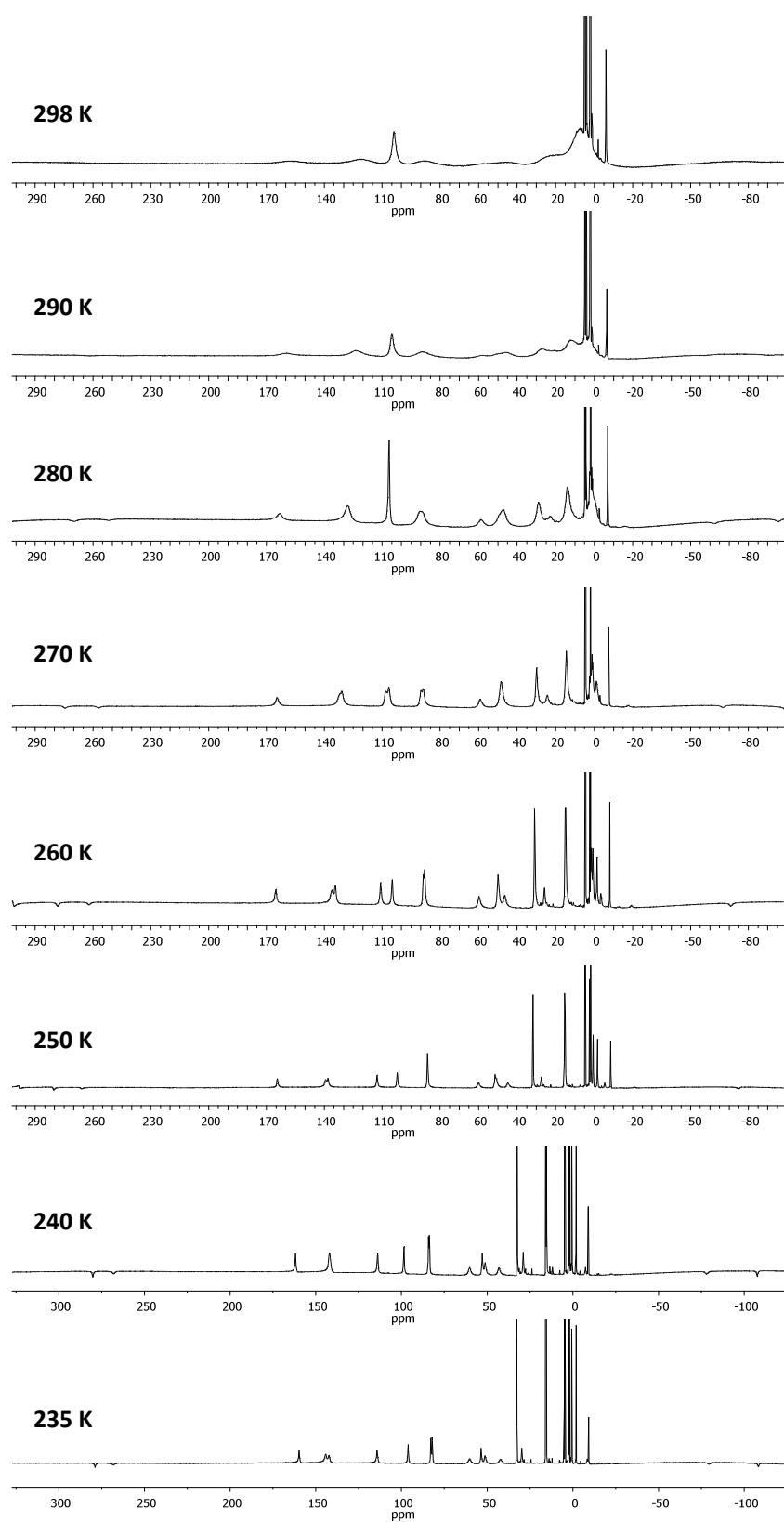
A.5.1.2. Paramagnetic NMR spectra

Figure A. 5. 5. $^1\text{H-NMR}$ spectra (500 MHz) of $1_{\text{Co}}^{\text{DMM}}$ in CD_3CN at different temperatures.

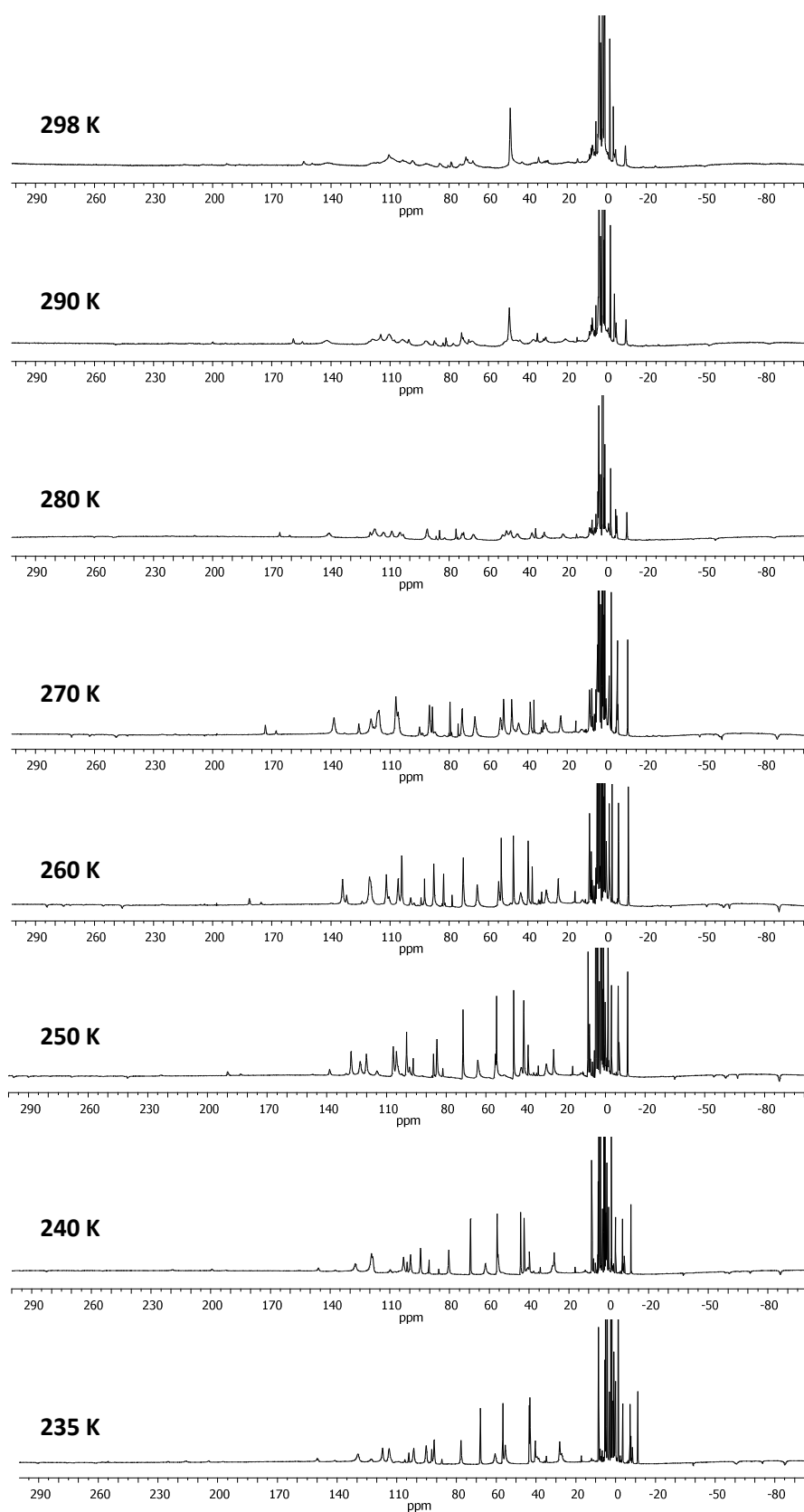


Figure A. 5. 6. ¹H-NMR spectra (500 MHz) of **1c^O^{CO₂Et}** in CD₃CN at different temperatures.

A.5.1.2. Solid state characterization**Table A. 5. 1.** Crystal Data for $1_{\text{Co}}^{\text{II}}_{\text{MeCN}}$, $1_{\text{Co}}^{\text{II}}_{\text{Cl}}$ and $1_{\text{Co}}^{\text{III}}_{\text{MeCN}}$.

Compound	$1_{\text{Co}}^{\text{DMM}}$	$\text{Me}1_{\text{Co}}^{\text{DMM}}$
Empirical formula	$\text{C}_{38.25}\text{H}_{47.50}\text{CoF}_{7.50}\text{N}_5\text{O}_{10}\text{S}_3$	$\text{C}_{27}\text{H}_{39}\text{CoF}_6\text{N}_5\text{O}_8\text{S}_2$
Formula weight	1088.09	798.68
Temperature	100(2) K	298(2) K
Wavelength	0.71073 Å	0.71073 Å
Crystal system	Monoclinic	Triclinic
Space group	Cs/c	P-1
Unit cell dimensions	$a = 42.0464(14)$ Å $\alpha = 90^\circ$ $b = 9.0171(3)$ Å $\beta = 124.4553(11)^\circ$ $c = 29.4652(11)$ Å $\gamma = 90^\circ$	$a = 9.1795(14)$ Å $\alpha = 89.698(3)^\circ$ $b = 11.9258(19)$ Å $\beta = 86.165(3)^\circ$ $c = 15.999(3)$ Å $\gamma = 81.913(3)^\circ$
Volume	$9211.5(6)$ Å ³	$1730.1(5)$ Å ³
Z	8	2
Density (calculated)	1.569 Mg/m ³	1.533 Mg/m ³
Absorption coefficient	0.686 mm ⁻¹	0.702 mm ⁻¹
F(000)	4480	826
Crystal size	0.20 x 0.04 x 0.02 mm ³	0.30 x 0.20 x 0.10 mm ³
Θ range for data collection	1.175 to 25.076°	2.14 to 28.37°
Index ranges	$-43 \leq h \leq 50$ $-10 \leq k \leq 10$ $-35 \leq l \leq 27$	$-12 \leq h \leq 12$ $-15 \leq k \leq 15$ $-21 \leq l \leq 21$
Reflections collected	49533	25478
Independent reflections	8166	8395
	[R(int) = 0.0592]	[R(int) = 0.0569]
Completeness to Θ	99.9 % ($\Theta = 25.076^\circ$)	96.80 % ($\Theta = 28.37^\circ$)
Absorption correction	Multi-scan	Empirical
Max. and min. transmission	0.986 and 0.891	1.0 and 0.860795
Refinement method	Full-matrix least-squares on F ²	Full-matrix least-squares on F ²
Data / restraints / parameters	8166/348/755	8395/11/494
Goodness-of-fit on F ²	1.069	1.035
Final R indices [$I > 2\sigma(I)$]	R1 = 0.0602 wR2 = 0.1497	R1 = 0.0669 wR2 = 0.1767
R indices (all data)	R1 = 0.0892 wR2 = 0.1669	R1 = 0.1022 wR2 = 0.2052
Largest diff. peak and hole	0.949 and -1.042 e·Å ⁻³	0.625 and -0.483 e·Å ⁻³

Table A. 5. 2. Selected Bond Lengths (Å) and Angles (°) for $1_{\text{Co}}^{\text{II}}_{\text{MeCN}}$, $1_{\text{Co}}^{\text{II}}_{\text{Cl}}$ and $1_{\text{Co}}^{\text{III}}_{\text{MeCN}}$.

$1_{\text{Co}}^{\text{DMM}}$		Me $1_{\text{Co}}^{\text{DMM}}$	
Co-N1	2.142(4)	Co-N1	2.133(3)
Co-N2	2.071(4)	Co-N2	2.092(3)
Co-N3	2.326(4)	Co-N3	2.174(3)
Co-N4	2.113(4)	Co-N4	2.125(3)
Co-N5	2.123(4)	Co-N5	2.135(3)
Co-O1	2.058(3)	Co-O1	2.117(3)
N1-Co-N2	79.69(14)	N1-Co-N2	79.48(11)
N1-Co-N3	81.85(13)	N1-Co-N3	82.79(14)
N1-Co-N4	82.96(14)	N1-Co-N4	83.32(11)
N1-Co-N5	96.46(14)	N1-Co-N5	97.66(13)
N1-Co-O1	173.16(13)	N1-Co-O1	172.68(12)
N2-Co-N3	99.57(13)	N2-Co-N3	98.99(12)
N2-Co-N4	162.40(14)	N2-Co-N4	162.30(12)
N2-Co-N5	99.50(15)	N2-Co-N5	99.25(12)
N2-Co-O1	99.70(13)	N2-Co-O1	97.61(12)
N3-Co-N4	80.78(13)	N3-Co-N4	82.87(12)
N3-Co-N5	160.21(14)	N3-Co-N5	161.52(11)
N3-Co-O1	91.57(12)	N3-Co-O1	91.09(13)
N4-Co-N5	79.45(14)	N4-Co-N5	78.85(11)
N4-Co-O1	97.88(14)	N4-Co-O1	99.95(12)
N5-Co-O1	90.36(14)	N5-Co-O1	89.41(12)

A.6. ANNEX CHAPTER IX

A.6.1. KIE determination

A.6.1.1. KIE determined by NMR

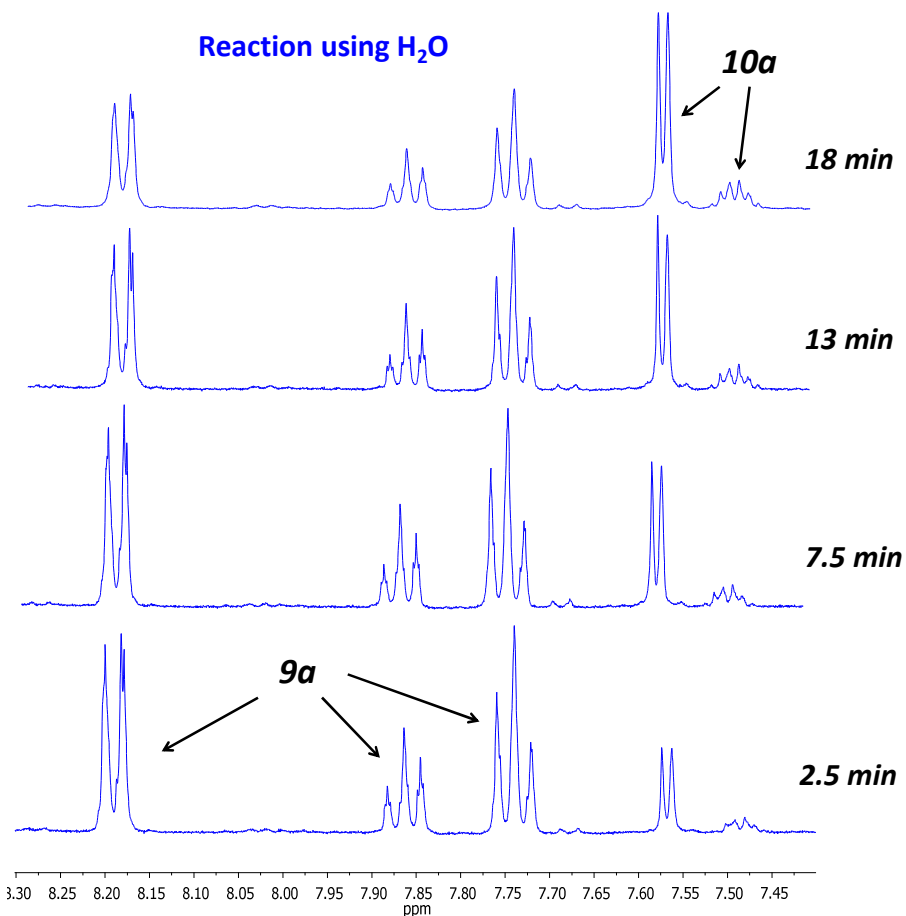


Figure A. 6. 1. ¹H-NMR (400 MHz, 300 K) recorded at variable irradiation times (2.5-18 min) using CH₃CN:H₂O:Et₃N (0.15:0.35:0.01 mL) as solvent mixture. Conditions: **1**_{Co} (0.189 μmol, 3 mol%), **PS**_{Ir} (0.076 μmol, 1.2 mol%) and **9a** (6.30 μmol, 12.6 mM) irradiated at λ = 447 nm in a NMR tube.

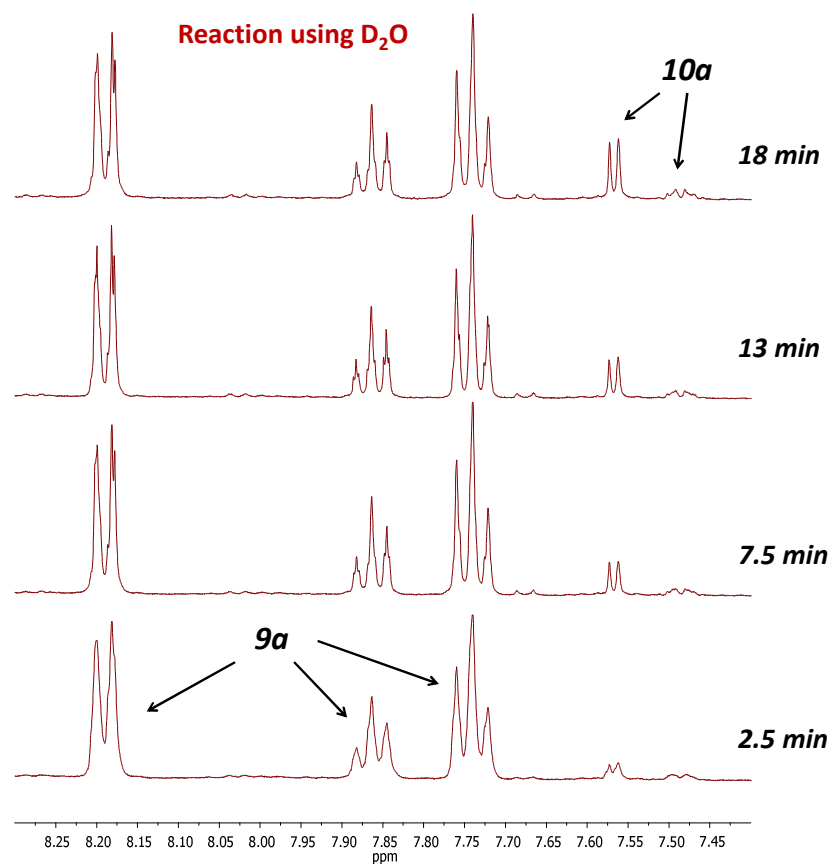


Figure A. 6. 2. ¹H-NMR (400 MHz, 300 K) recorded at variable irradiation times (2.5-18 min) using CH₃CN:D₂O:Et₃N (0.15:0.35:0.01 mL) as solvent mixture. Conditions: **1**_{c_o} (0.189 μmol, 3 mol%), **PS**_{ir} (0.076 μmol, 1.2 mol%) and **9a** (6.30 μmol, 12.6 mM) irradiated at λ = 447 nm in a NMR tube.

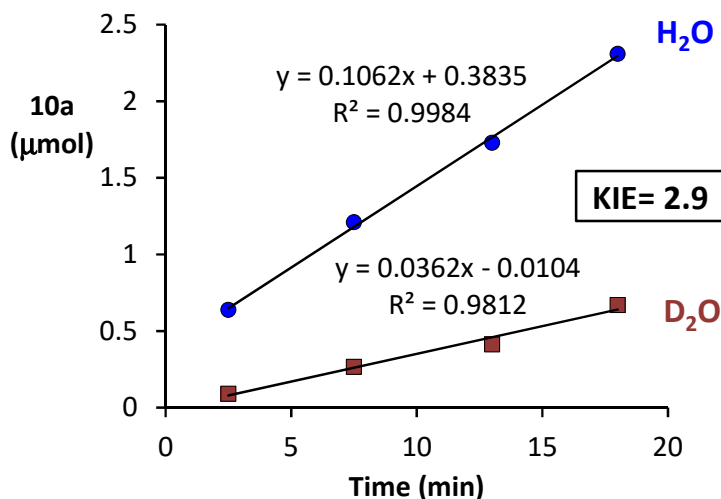


Figure A. 6. 3. Determination of KIE by NMR. Formation of **10a** (μmol) versus time (min) in $\text{CH}_3\text{CN}:\text{H}_2\text{O}:\text{Et}_3\text{N}$ (3:7:0.2 mL) (blue dots, derived from **Figure A. 6. 1**) and $\text{CH}_3\text{CN}:\text{D}_2\text{O}:\text{Et}_3\text{N}$ (3:7:0.2 mL) (red squares, derived from **Figure A. 6. 2**), **1_{co}** (0.189 μmol , 3 mol%), **PS_{ir}** (0.076 μmol , 1.2 mol%) and **9a** (6.30 μmol , 12.6 mM) irradiated at $\lambda = 447$ nm in a NMR tube. The amount of **10a** was determined by $^1\text{H-NMR}$ (400 MHz, 300 K) using 4-nitroacetophenone as internal standard. $\text{KIE} = \text{rate in H}_2\text{O} / \text{rate in D}_2\text{O}$.

A.6.1.2. KIE determined by GC

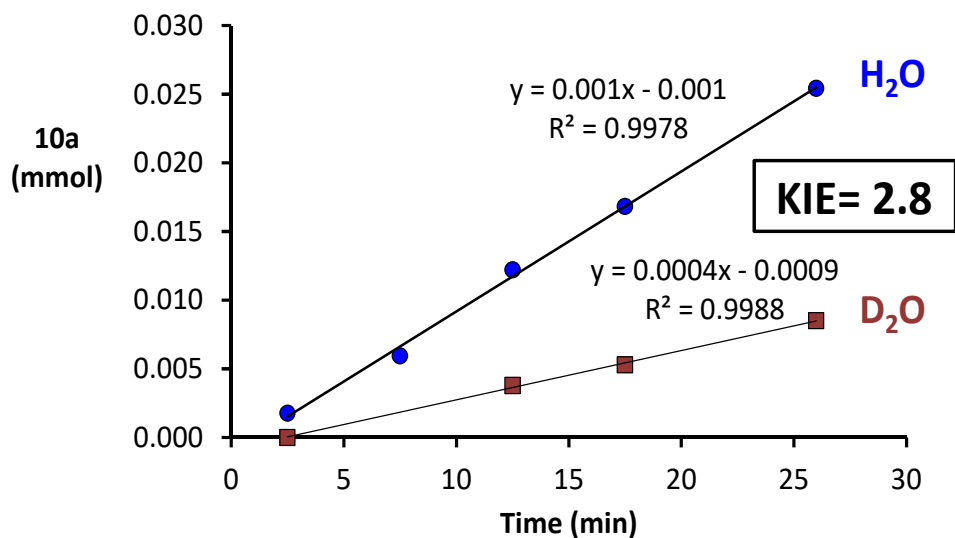


Figure A. 6. 4. Plot **10a** (mmol) produced versus time (min) in $\text{CH}_3\text{CN}:\text{H}_2\text{O}:\text{Et}_3\text{N}$ (3:7:0.2 mL) (blue dots) and $\text{CH}_3\text{CN}:\text{D}_2\text{O}:\text{Et}_3\text{N}$ (3:7:0.2 mL) (red squares). Conditions: **1_{co}** (3.8 μmol , 3 mol%), (**PS_{ir}** (2.5 μmol , 2 mol%), substrate (0.126 mmol, 12.4 mM) under irradiation ($\lambda = 447$ nm). The amount of **10a** was determined by GC using 1,3,5-trimethoxybenzene as an internal standard. $\text{KIE} = \text{rate in H}_2\text{O} / \text{rate in D}_2\text{O}$.

A.6.2. Oxidation of the In-situ Photogenerated $\text{PS}_{\text{Ir}}^{\text{II}}$ Species with Different Amounts of $\mathbf{1}_{\text{Co}}$.

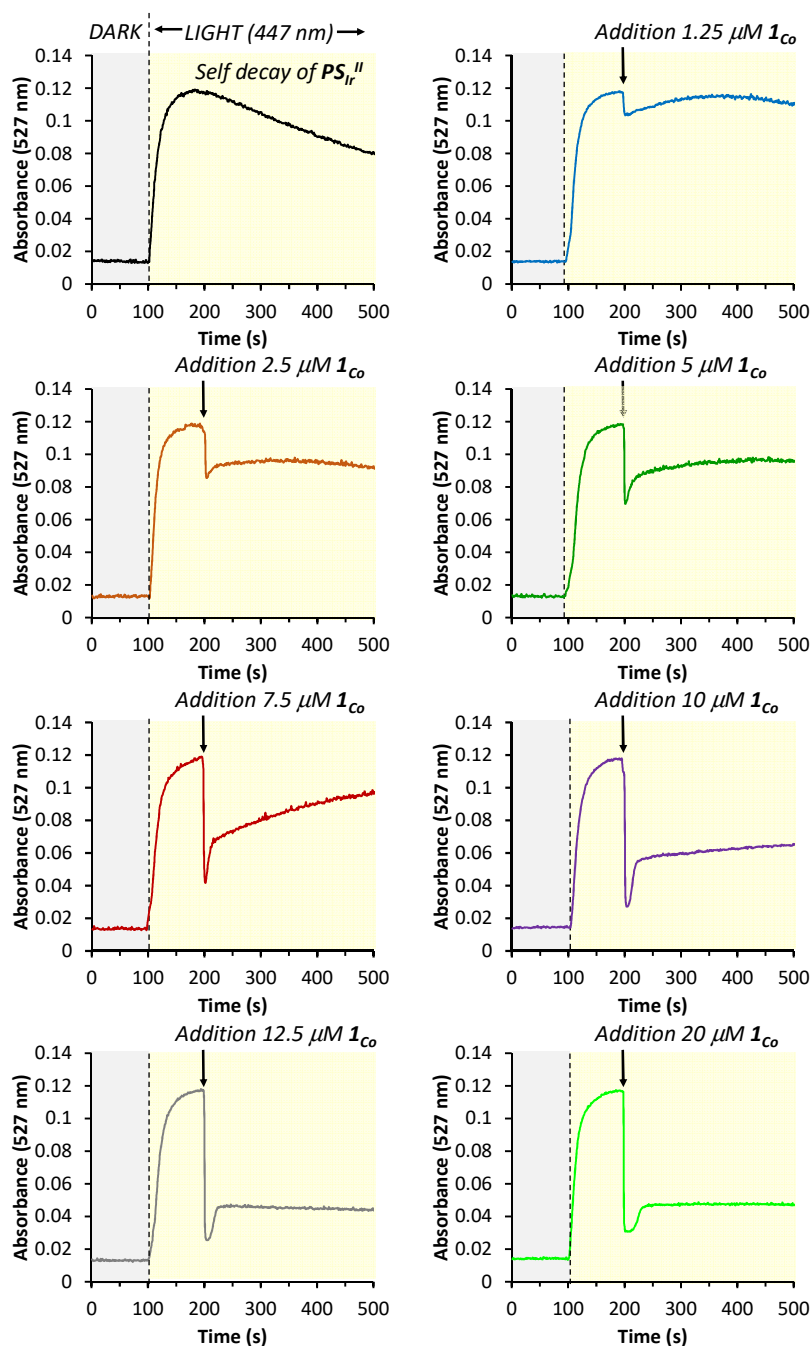


Figure A. 6. 5. UV/Vis monitoring ($\lambda = 527 \text{ nm}$) of $\text{PS}_{\text{Ir}}^{\text{III}}$ photoreduction with Et_3N to form $\text{PS}_{\text{Ir}}^{\text{II}}$ at $\lambda = 447 \text{ nm}$ and subsequent addition of different amounts of $\mathbf{1}_{\text{Co}}^{\text{II}}$ catalyst (0, 1.25, 2.5, 5, 7.5, 10, 12.5 and 20 μM). Conditions: $[\text{PS}_{\text{Ir}}^{\text{III}}] = 50 \mu\text{M}$, $\text{Et}_3\text{N} = 2000 \text{ eq.}$, reaction volume = 2 mL, $\text{CH}_3\text{CN}:\text{H}_2\text{O}$ (0.6 : 1.4) at 5°C , under N_2 . Dark trace corresponds to the self-decay of the photogenerated $\text{PS}_{\text{Ir}}^{\text{II}}$ in the absence of $\mathbf{1}_{\text{Co}}^{\text{II}}$.

A.6.3. Cyclic Voltammograms of the Substrates Under Reaction Solvent Mixture

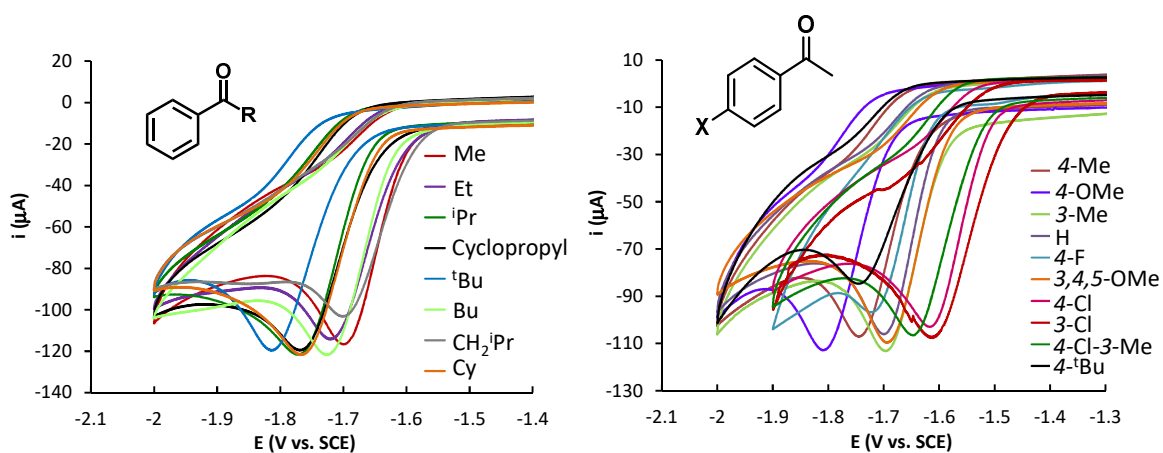


Figure A. 6. 6. Cyclic voltammograms obtained with different substituted acetophenones (5 mM) in the solvent mixture MeCN:H₂O:Et₃N (4:6:0.2 mL) using KNO₃ (0.1 M) as a supporting electrolyte. Scan rate= 100 mV/s, glassy carbon working electrode. Potentials are referenced versus SCE.

A.6.4. NMR data of 1,4-diphenylbutan-1-one (10ap)

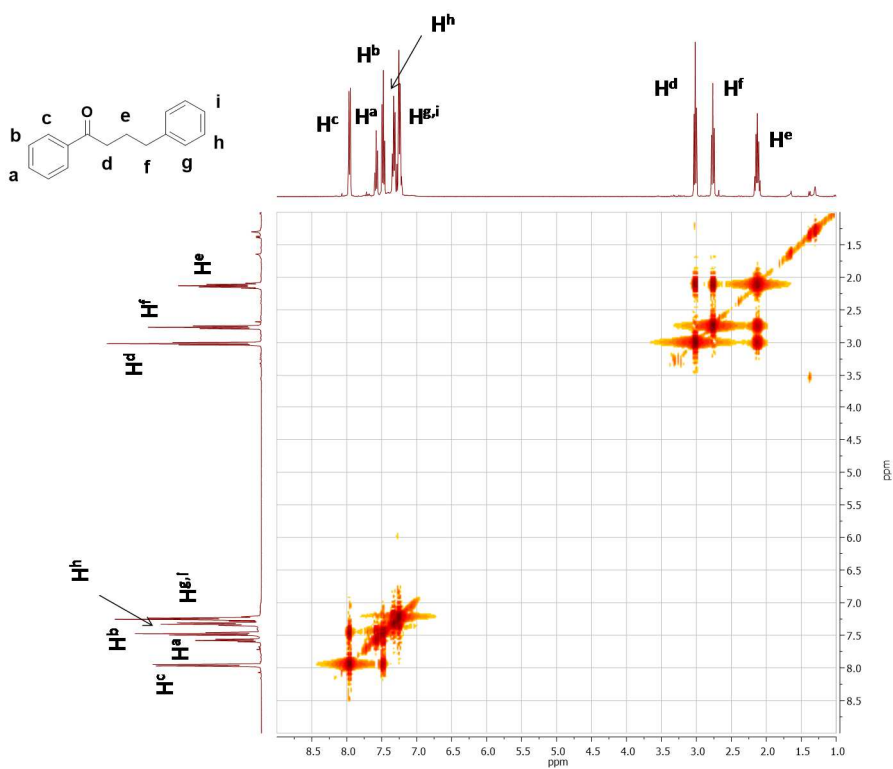


Figure A. 6. 7. ^1H - ^1H COSY (CDCl_3 , 400 MHz, 300 K) spectrum of the isolated product **1,4-diphenylbutan-1-one (10ap)**.

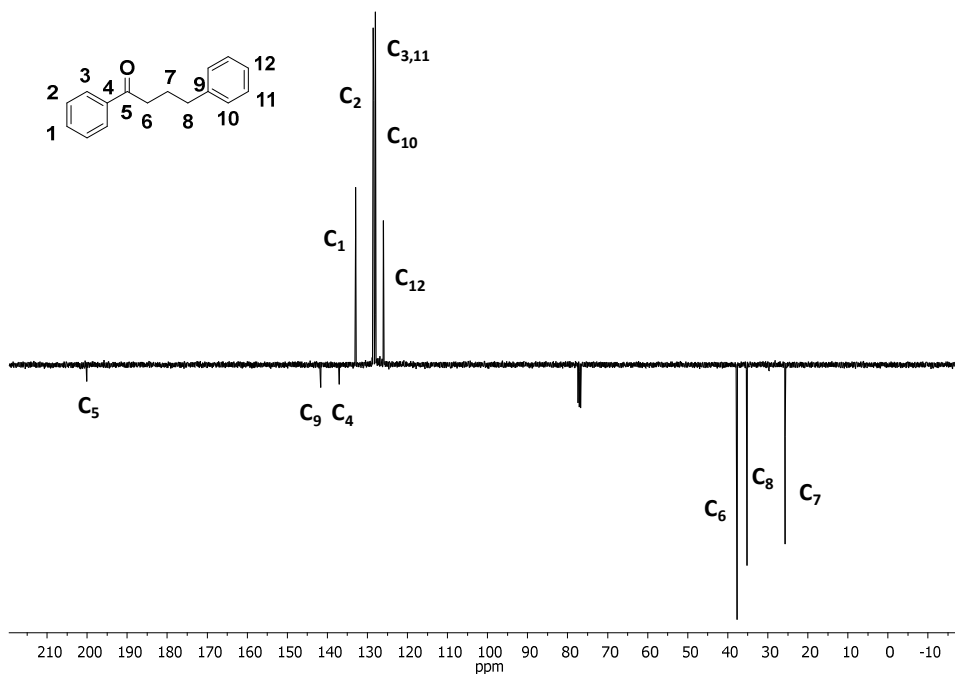


Figure A. 6. 8. ^{13}C DEPT135 (CDCl_3 , 101 MHz, 300 K) spectrum of **1,4-diphenylbutan-1-one (10ap)**.

A.6.5. NMR spectra of the labelled products p-tolymethan-d₂-ol and 4-methyl-1-d₁-benzaldehyde

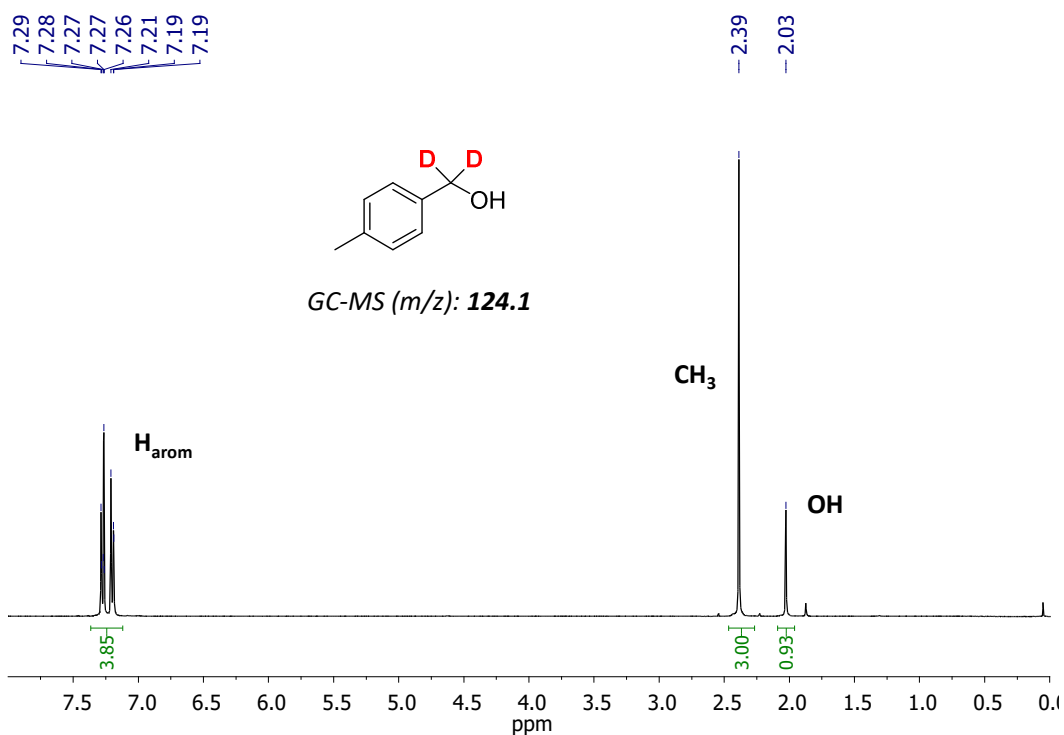


Figure A. 6. 9. ¹H-NMR (CDCl₃, 400 MHz, 300 K) spectrum of p-tolymethan-d₂-ol ([D]-10v).

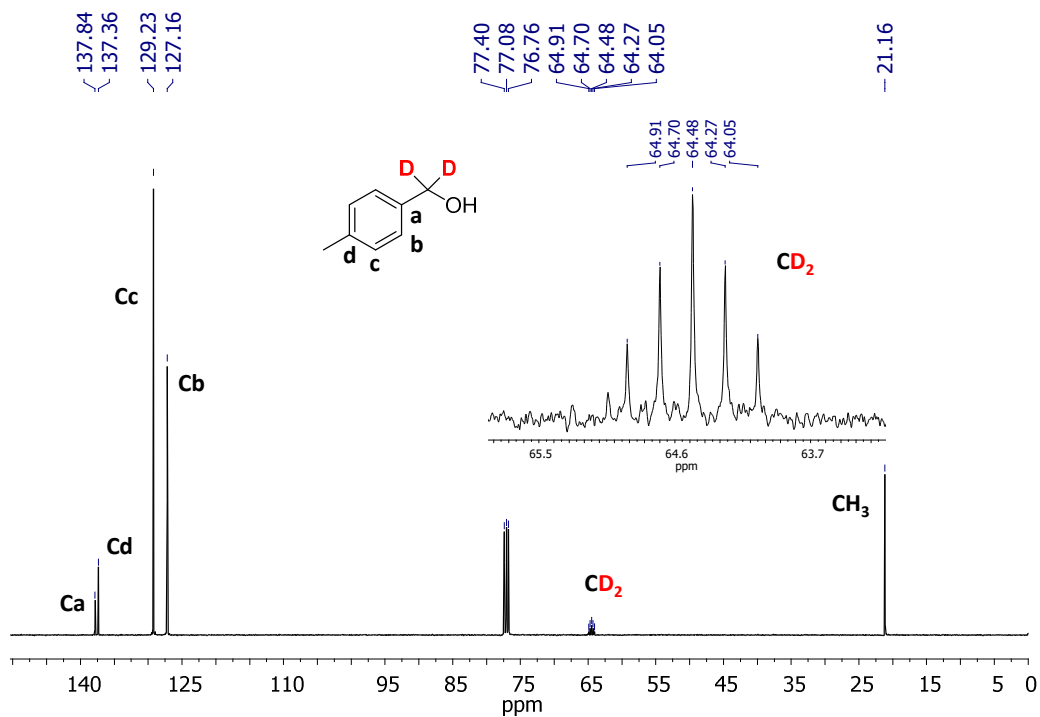


Figure A. 6. 10. ¹³C{¹H}-NMR (CDCl₃, 101 MHz, 300 K) spectrum of p-tolymethan-d₂-ol ([D]-10v).

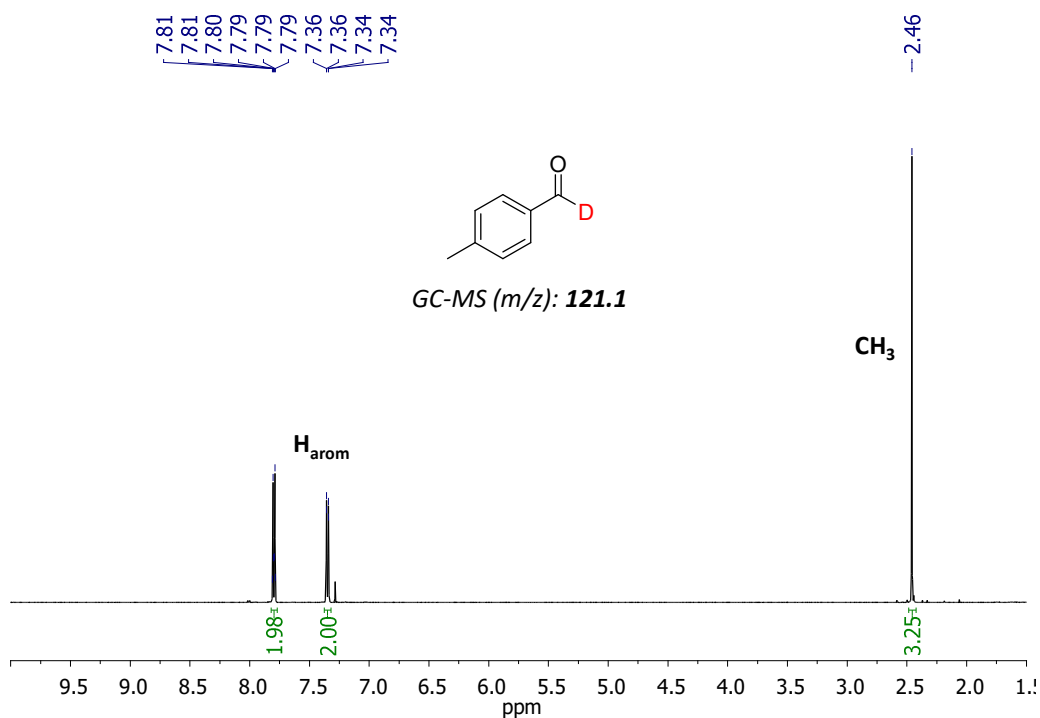


Figure A. 6. 11. 1H -NMR ($CDCl_3$, 400 MHz, 300 K) spectrum of 4-methyl-1- d_1 -benzaldehyde ([D]-9v).

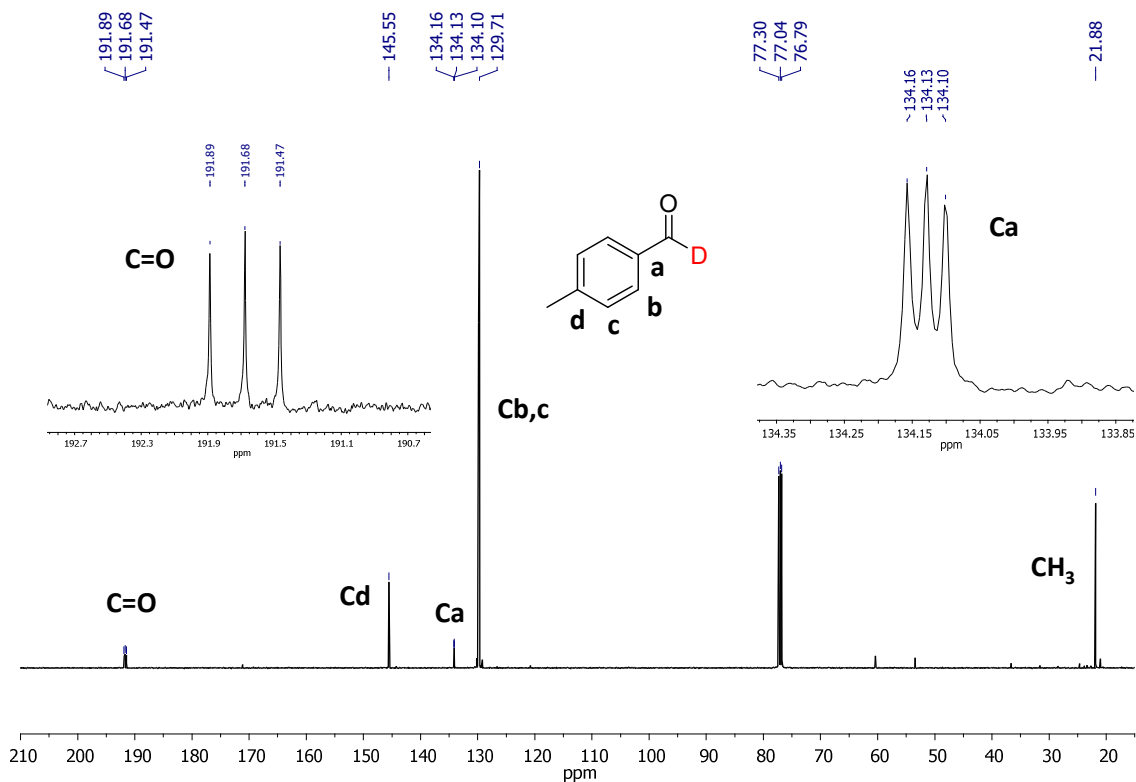


Figure A. 6. 12. $^{13}C\{^1H\}$ -NMR ($CDCl_3$, 400 MHz, 300 K) spectrum of 4-methyl-1- d_1 -benzaldehyde ([D]-9v).

A.6.6. Determination of the SDKIE in the substrates [D]-9v and [D]-9x

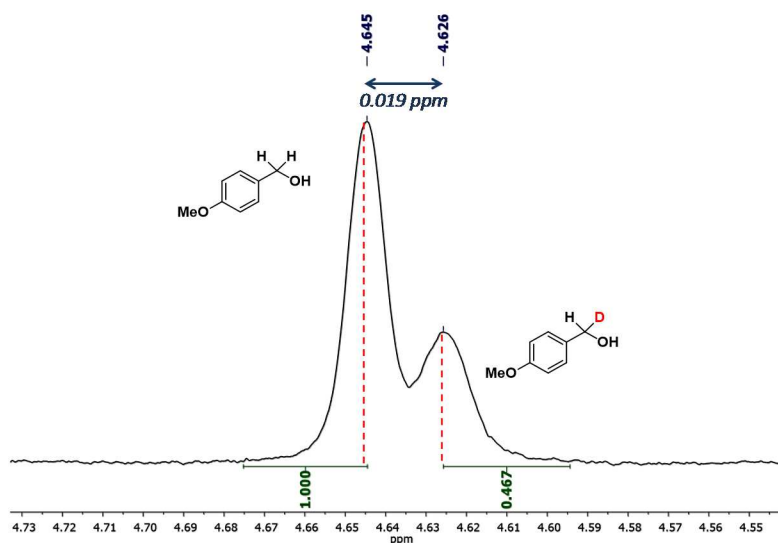


Figure A. 6. 13. ¹H-NMR spectrum (CDCl₃, 500 MHz) of the benzylic CH₂:CHD signals. The ratio of the labelled:unlabelled products for the 4-OMe-PhCHO:4-OMe-PhCDO (1:1) reduction products was found to be 1.07. $\text{SDKIE} = \frac{{}^{\text{OMe}}k_{\text{H}}}{{}^{\text{OMe}}k_{\text{D}}} = 1.07$.

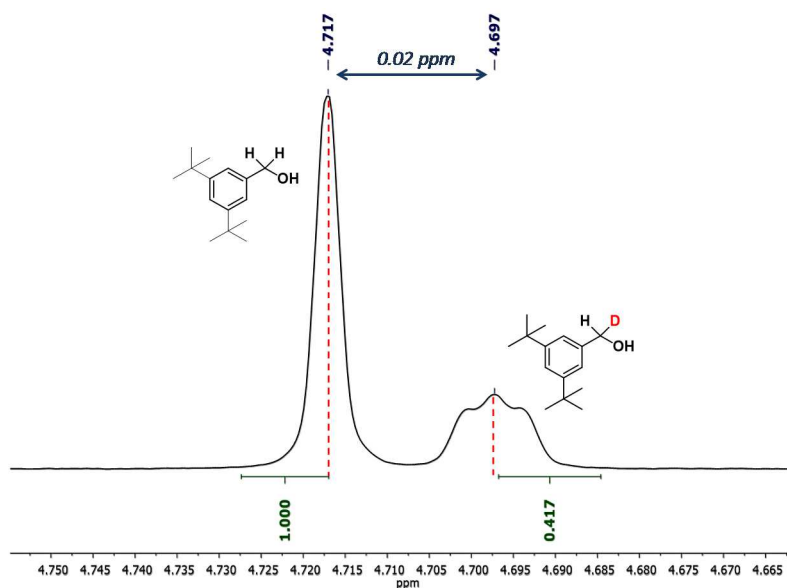


Figure A. 6. 14. ¹H-NMR spectrum (CDCl₃, 500 MHz) of the benzylic CH₂:CHD signals. The ratio of the labelled:unlabelled products for the 3,5-Di-^tBu-PhCHO: 3,5-Di-^tBu-PhCDO (1:1) reduction products was found to be 1.19. $\text{SDKIE} = \frac{{}^{\text{tBu}}k_{\text{H}}}{{}^{\text{tBu}}k_{\text{D}}} = 1.19$.